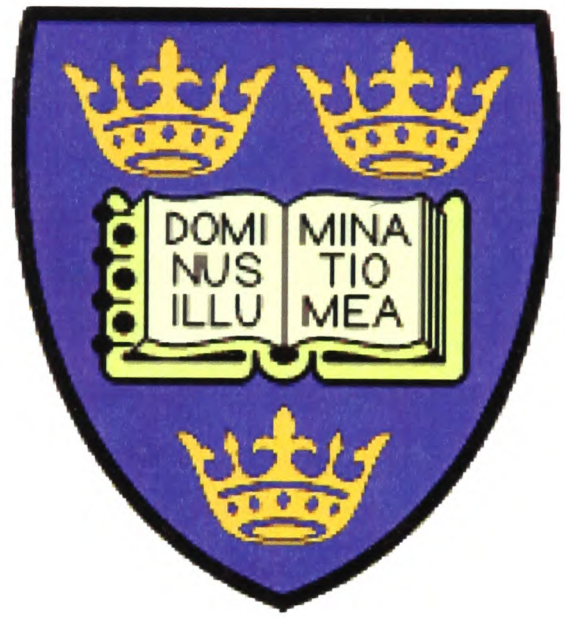
Marine Geophysical Studies of the Southern Margins of the Iberian Peninsula

by

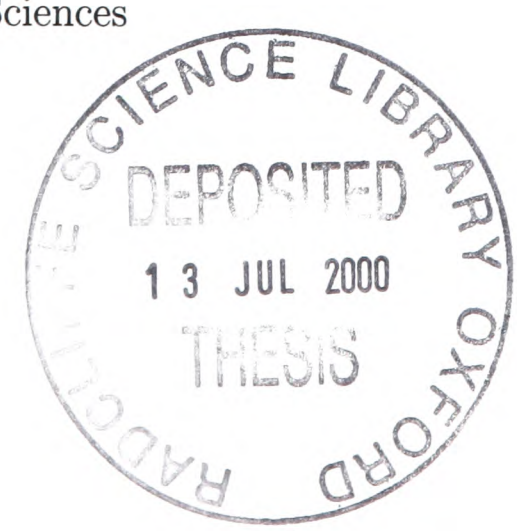
Suman Chowdhury



Thesis submitted for the Degree of Doctor of Philosophy, University of Oxford

University College &
Department of Earth Sciences

Michaelmas Term 1999



Marine Geophysical Studies of the Southern Margins of the Iberian Peninsula

Suman Chowdhury

University College and Department of Earth Sciences, University of Oxford

Michaelmas Term 1999

A wide variety of tectonic settings are juxtaposed at the southern margins of the Iberian Peninsula. The regional geology comprises an Atlantic passive margin in western Iberia, the convergent eastern part of the Azores-Gibraltar plate boundary zone between Africa and Eurasia, and an orogenic arc (the Betic-Rif mountains) surrounding an extensional basin (the Alboran Sea). The complex tectonic history of the southern Iberian margins is recorded in its sediments and structure, and these were investigated in this study using multichannel seismic reflection techniques in conjunction with other marine geophysical data.

Multichannel seismic reflection and well data from the Gulf of Cadiz have shown that the earliest sediments are Triassic evaporites, followed by Jurassic carbonates, which form rotated fault blocks in the Gulf of Cadiz. Backstripping and thermal modelling has indicated that a rifting event took place in the Late Jurassic, which stretched the crust by ~20–50%. Gravity modelling, and mapping of stretching factors, has suggested that two zones of thinning underlie the Gulf of Cadiz, which are related to the original rifting event. Backstripped subsidence curves indicate passive margin thermal subsidence until the Miocene, when westward-directed thrusting and loading from the Betic–Rif mountain belt is reflected in a typical foreland basin tectonic subsidence signature of accelerated subsidence with time.

A giant, chaotic body of allochthonous sediment was emplaced into the central Gulf of Cadiz as westward migration of the Gibraltar Arc led to oversteepening of the margin west of the Gibraltar Straits, while the Alboran Sea was simultaneously undergoing active extension. These allochthonous deposits are composed mainly of Triassic evaporites and Palaeogene shales. In the Gulf of Cadiz and Seine Abyssal Plains this body has the appearance of an accretionary wedge, but a 300 km long northern lobe of the body extends into the Horseshoe Abyssal Plain. This lobe is interpreted as being a cumulative mass wasting feature, formed by the gravity-driven downslope transport of large allochthonous masses as debris flows and slides and slumps, encouraged by a regional gradient and a pre-existing trough in the Horseshoe Abyssal Plain. The total volume of sediments involved was of the order of 72 000 km^3, and the time of emplacement has been estimated as being Tortonian on the basis of seismic correlation with core data at DSDP site 135. This chaotic unit has formed a series of longitudinal diapiric ridges in the northern Gulf of Cadiz, which have been interpreted to act as a transport system for gas generated in the lower slope area to migrate to the upper slope where gas-related features are seen. Gas hydrates are present beneath the lower continental slope, as inferred from a bottom–simulating reflection on seismic reflection profiles.

Extended Abstract

The goal of this research was to use marine geophysical techniques, with particular emphasis on the multichannel seismic reflection method, to understand a tectonically complex area at the convergent eastern segment of the Azores–Gibraltar plate boundary zone between Africa and Eurasia, offshore southern Iberia. The complexity of the southern Iberian margins is a result of a series of major tectonic processes, with the region being shaped since the Mesozoic by the opening of the central eastern Atlantic Ocean and lateral plate motions between Africa and Iberia, followed by plate convergence, culminating with the formation of the Alpine Betic-Rif orogenic belt of Spain and north Africa. In this study, new multichannel seismic reflection images have been produced and interpreted in conjunction with marine geophysical and geological data, to study structure, sedimentary fill, and evolution of the Gulf of Cadiz (GOC) continental margin, the Gorringe Bank Region (GBR) and the Alboran Sea (ABS) in the western Mediterranean.

Multichannel seismic profiles from the GOC region were interpreted on the basis of five major seismic stratigraphic units (units CI to CV). The sediments are of Triassic to Recent in age, and rest on a Hercynian basement which is an extension of the Iberian Massif. A complex tectonic history is indicated by the presence of extensional, compressional and diapiric structures, and the widespread occurrence of allochthonous sediments. The seismic data was tied to well data, which was also used to determine the subsidence and uplift history of the basin through backstripping studies. The resulting tectonic subsidence curves displayed a period of rapid subsidence in the Late Jurassic (154.1 Ma) which correlated with the M25 (157 Ma) spreading anomaly in the NE Atlantic - the oldest magnetic spreading anomaly west of the Gulf of Cadiz. This rifting phase was followed by a long period of gentle tectonic subsidence, reflecting post-rift cooling when the region as a whole was a passive margin. The tectonic subsidence curves revealed an accelerating subsidence in the Miocene as a foreland basin developed ahead of the advancing Betic–Rif thrust wedge.

Prominent SE–dipping reflections in the western GOC are interpreted to be due to a reflective lower crust 3 s thick, typical of Hercynian crust in SW Europe [e.g., Watts *et al.*, 1990]. These reflections stop below a zone of tilted basement/Mesozoic fault blocks and an overlying graben structure, which may indicate these originated with rifting with an asymmetric simple shear component. Alternatively, strike slip motion may have juxtaposed two different crusts.

β values averaging 1.2–1.5 were obtained from wells in the northeast GOC, using a finite duration rifting model, with an Upper Jurassic time of rifting and a rift duration of ~10 Ma. Assuming an unstretched crustal thickness of 35 km, these results produced backstrip Moho estimates that were in agreement with seismic refraction/wide-angle reflection data of González *et al.* [1998]. This suggests that the thinned crust observed in the NE GOC at the present day is a relict of the original rifting event. Mapping and contouring of stretching factors from well and gravity modelling reveals lateral zones of thinning in the GOC, which trend away from the margin, and which are associated with gravity anomaly highs. These are thought to be a result of Mesozoic rifting, subsequent lateral movements and the structure of the Betic–Rif belt. A possible continent–ocean boundary zone runs approximately at the base of the continental slope, on the basis $\beta > 4$ produces oceanic crust.

The first reported gas hydrate occurrence from the eastern margin of the central Atlantic, has been inferred from the presence of a bottom-simulating reflection and acoustic blanking on two MCS profiles from the Gulf of Cadiz. The BSR is observed in slope sediments at water depths of 1275–1575 m (1.7–2.1 s TWTT) and from 0.4–0.5 s TWTT beneath the seabed. Velocities implied hydrate concentrations were low above the BSR, and that gas volumes below the BSR may be <1% of pore volume. A positive reflection beneath the BSR may mark a base of the gas layer, which may be up to 36 m thick. BSR reflection coefficients varied from -0.02 to -0.07, which were comparable to values observed from a BSR off the Cascadia Margin [Fink & Spence, 1999]. The BSR may cover 3500 km^2, but this may be an underestimate if hydrate exists at depths below 1575 m. The extent of the BSR implies that hydrates are limited to a local concentration in the Gulf of Cadiz. Possible migration pathways between the BSR region, a system of longitudinal diapiric ridges and valleys (and associated faults), and gas–affected sediments in the upper slope and shelf area have been mapped. Mass wasting associated with free gas has been noted in certain areas of the Gulf of Cadiz. Large mass wasting events appear to have been recorded in the Pliocene to Recent sediments of intraslope basins downslope of the Gibraltar Straits. It has been shown that bottom waters were

up to 5°C colder before the onset of the Mediterranean outflow, and so hydrates would have been stable at much shallower depths. Dissociation of these hydrates caused by the warm Mediterranean Outflow Water at the early Pliocene highstand may have been responsible for the observed mass wasting in Pliocene sediments.

Multichannel seismic reflection data were used to study a giant, acoustically chaotic body which underlies the Iberian continental slope from the Gulf of Cadiz to the Horseshoe and Seine Abyssal Plains west of Gibraltar. The data, acquired with a powerful 116 litre airgun array and a 192-channel 5 km long streamer, have been used to constrain the age, thickness and origin of the chaotic body. Nearshore drilling in the Gulf of Cadiz suggests that the body is made up of allochthonous Triassic evaporites and Palaeogene marls. A seismic profile correlated with core data from DSDP Site 135, suggests a mid-late Miocene age for the chaotic body. An isopach of the chaotic body was produced by the depth conversion of a time thickness map compiled from interpretation of available seismic reflection data. The depth converted data indicates that the chaotic units form a lobate body beneath the Horseshoe Abyssal Plain, of a maximum thickness of 5 km beneath the base of the continental rise and thinning westwards over some 250 km. Calculations of thickness and area allow a volume estimate of some 72,000 km^3 to be made for the northern lobe of the chaotic body, which extends west of 8W into the Horseshoe Abyssal Plain. The lobe has several features that suggest an origin through cumulative gravity-driven mass flow processes, as evidenced by the imaging of three individual flows on Profiles 4E and GB1. Based on its large volume, seismic fabric and the regional physiographic and tectonic settings, the Horseshoe lobe is interpreted to be a giant cumulative mass wasting deposit from several pulses of slope failure caused by seismicity or tectonic oversteepening upslope near the Gulf of Cadiz "hinge" of the Gibraltar Arc (Betic and Rif orogens), associated with its westward movement and rapid uplift. The geometries observed on seismic profiles indicate that the chaotic units have an eastern origin, rather than being sourced from bathymetric highs flanking the Horseshoe Abyssal Plain. The pre-existing trough between Gorringe Bank and Coral Patch seamounts provided the accomodation space, and possibly the constraint which allowed long runouts, for the GCB.

Regional 2D seismic profiles of the *Conrad* RC2911 cruise from the Alboran Sea Basin have been migrated and interpreted. A variety of structural features observed on these profiles provide evidence for the extensional nature of the Alboran Sea, and a transpressive regime after the Messinian. Normal faulting has been observed affecting Miocene sediments in the West Alboran Basin, indicating an extension in the Miocene. Reverse

faults are seen bounding the Alboran Ridge and Xauen Bank basement highs, indicating a compressive regime after the Miocene. Strike-slip systems also affect the present day ABS, and have produced a pull–apart basin south of the Yusuf fault. South-dipping intracrustal reflections and layered lower crust have been imaged on Lines 824 and 827. These may be associated with the early Miocene rifting of the Alboran Sea, although the lower crustal layering may have been a feature of the crust prior to stretching. The thickest sediments were observed in the West Alboran Basin where thick Miocene successions were up to 5 s TWTT thick, indicating a thickness of several kms. A large volume of volcanic material is also present in this basin, both overlying basement, and as ridges and seamounts. This is related to thinning and heating of the crust during Miocene rifting [e.g., Watts *et al.*, 1993; Willet, 1996].

Acknowledgements

I thank my supervisor, Tony Watts, for his sage counsel, and Jenny Collier whose help with seismic processing and interpretion extending to organising a term at the Bullard Laboratories, Cambridge, where I learnt much at BIRPS. I must also thank the Marine Lab team at Oxford (Neil Mitchell , Rupert Dalwood, Nathan Hayward, Audrey Willet, Jonathan Stewart, David Haddad, Martin Gee, Emily Black, Gareth Armstrong, Paul Wyer and Mohammed Ali) and Cambridge (Simon Dean in particular) for stimulating discussions and day-to-day help. Liz Ross, Emily Black, David Haddad, Paul Wyer, Fiona Grant, Jenefer Brett, Margaret Moore and Darren Randall kindly proof–read chapters. Karine David helped with French papers; John Platt and Menchu Comas for discussions on the geology of the Alboran Sea; Steve Usher solved many computing problems. Thanks are also due to those many people who made a difference but who I have been unable to thank individually.

Mr Hayler, my humourous school geology teacher, was responsible for my early interest in geology, which was nurtured under the watchful eye of my early mentor at Univ, David Bell. I have also enjoyed the great friendship of the Jolly Boys (senior member K.G. Cox, sadly no longer with us), the Budly Brothers (Arun, Roshan, Ankush, Sumit and Surajit), the 1994–95 committees of the Oxford Asia Society, and the 1995–96 Univ rugby 1st XV. I also thank Mrinalini, Rita, and Darakhshan. A big thank you to Karine for all her help and patience. Greatest thanks of all to my loving and patient parents, Dulal and Shefali, my sister Subhra, and brothers Subhashis and Sujan, the Wrestlemaniac and teenage geology enthusiast.

IAM data acquisition and commercial processing were funded by EEC project JOU-CT92-0177 and carried out by GECO-PRAKLA. I acknowledge NERC funds for PhD studentship GT4/94/224/G and offshore safety training at Warsash Maritime Institute in Southampton. I also thank NERC for funding participation in the 1996 BIRPS Chicxulub Crater marine seismic survey off Mexico on the *R/V Geco-Sigma.* Bursaries were kindly provided by Shell International Petroleum Company and University College, Oxford.

Glossary of Terms and Abbreviations

The following abbreviations and acronyms are used throughout this thesis:

ABS	Alboran Sea
AGC	Automatic Gain Control
AGFZ	Azores–Gibraltar Fracture Zone
BA	Bouguer gravity anomaly
BROB	Betic-Rif orogenic belt
BSR	Bottom Simulating Reflection
CDP	Common depth point
CMQZ	Cretaceous Magnetic Quiet Zone
COE	Cross-over error
DOBS	Digital ocean bottom seismometer
DSDP	Deep Sea Drilling Project
EHAP	Eastern Horseshoe Abyssal Plain
FAA	Free-air gravity anomaly
FD	Finite Difference
FZ	Fracture Zone
GAR	Gibraltar Arc Region
GQB	Guadalquivir Basin
GBR	Gorringe Bank Region
GCB	Giant Chaotic Body
GCTZ	Gulf of Cadiz Thinned Zone
GHSZ	Gas Hydrate Stability Zone
GOC	Gulf of Cadiz
GPS	Global Positioning System
IAM	Iberian Atlantic Margins
IB	Iberian plate
IGME	Instituto Geologico y Minero de Espana

IGRF	International Geomagnetic Reference Field
JMQZ	Jurassic Magnetic Quiet Zone
LDGO	Lamont-Doherty Geological Observatory
Ma	Million years ago
MOW	Mediterrean
NA	North American plate
NERC	Natural Environment Research Council
OCT	Ocean Continent Transition
ODP	Ocean Drilling Program
PBZ	Plate Boundary Zone
SAP	Seine Abyssal Plain
SEG-Y	Trace sequential seismic recording standard [Barry *et al.*, 1975]
SCBA	Sediment corrected Bouguer gravity anomaly
TAP	Tagus Abyssal Plain
T_e	The effective elastic thickness of the lithosphere
TTS	Total Tectonic Subsidence
TWTT	Two-Way Travel Time
V_p	P-wave velocity
WAM	Wrap Around Multiple

Contents

Short Abstract i

Extended Abstract ii

Acknowledgements vi

Glossary of Terms and Abbreviations vii

Contents ix

List of Figures xiv

List of Tables xviii

1 Introduction 1

1.1 Aims of the Study 1

1.2 Data 3

1.3 Thesis Outline 4

2 Tectonic Setting 5

2.1 The Study Region in the Context of the African–Eurasian Plate Boundary 5

2.1.1 Physiography 5

2.1.2 Seismicity 9

2.1.3 Kinematics 12

2.1.4 The Ocean-Continent Transition 13

2.2 The Gibraltar Arc and Betic-Rif Orogenic Belt 18

2.2.1 Introduction 18

2.2.2 Geological Units 19

2.2.3 Key observations 20

2.2.4 Models of Formation 21

2.3 Geological Development of the Study Region 24

3 Multichannel Seismic Data Acquisition and Processing 31

3.1 Introduction to The Iberian Atlantic Margins (IAM) Dataset 31

3.2 Acquisition of IAM Data 33
3.2.1 Navigation 33
3.2.2 Acquisition of Seismic Reflection Data 34
3.3 Processing to Stack of IAM MCS Data 36
3.4 Post–stack Processing and Migration of IAM MCS Data 42
3.4.1 Post-Stack Data Enhancement 42
3.4.2 Migration 45
3.5 Reprocessing of R/V Conrad Cruise RC2911 MCS Data 53
3.6 Seismic Processing Synopsis 55

4 Crustal Structure, Subsidence History and Gravity Anomalies of the Gulf of Cadiz 56

4.1 Introduction 56
4.2 Geological and Geophysical Setting 59
4.2.1 Gulf of Cadiz 59
4.2.2 Guadalquivir Basin and the Betic Cordillera 60
4.3 Data 64
4.3.1 Well data 64
4.3.2 Seismic reflection data 64
4.4 Observations from Well Data 66
4.5 Seismic Stratigraphy and Well Ties 68
4.5.1 Seismic Facies 68
4.5.2 Sonic Data, Synthetic Velocity Profiles and Well Ties 71
4.6 Interpretation of Seismic Reflection Profiles 77
4.6.1 Deep Reflectivity 86
4.6.2 Upper Crustal Structure 90
4.7 Subsidence and Uplift History 92
4.7.1 Methodology 92
4.7.2 Results 93
4.8 Crustal Structure 107
4.8.1 Introduction 107
4.8.2 Comparison of seismic and backstrip Moho 109
4.8.3 Gravity modelling 111
4.8.4 Mapping of stretching factors 118
4.9 Conclusions 120

5 A Seismic Study of Hydrates and Mass Wasting in the Gulf of Cadiz 122

5.1 Introduction 122

5.2 Background to gas hydrates 123

5.2.1 Occurrence 123

5.2.2 Bottom Simulating Reflectors 124

5.2.3 Hydrates and Slope Stability 126

5.3 Tectonic and geological setting 127

5.4 Multichannel Seismic Reflection Data 129

5.4.1 Seismic Profiles 129

5.4.2 Observations of Anomalous Reflectivity 130

5.4.3 Analysis of the interpreted BSR 134

5.4.4 Intraslope Basins and Observations of Mass Wasting Upslope of the Observed BSR 140

5.5 Discussion 145

5.6 Conclusions 156

6 A Seismic Study of The Giant Chaotic Body Beneath the Horseshoe Abyssal Plain 158

6.1 Introduction 158

6.2 Previous Work 160

6.3 Mass Flow Processes in the Deep Sea 162

6.4 Data Acquisition and Processing 164

6.5 Observations 166

6.5.1 Seismic Character and Correlation 166

6.5.2 Observations from Seismic Profiles 170

6.5.3 Age of Emplacement of the Chaotic Body 171

6.5.4 Dimensions 175

6.6 Discussion 177

6.7 Conclusions 181

7 A Seismic Study of the Alboran Sea Basin in the Western Mediterranean 182

7.1 Introduction 182

7.2 Methodology 184

7.3 Observations from Seismic Profiles 186

7.4 Conclusions 191

8 Conclusions **192**

8.1 Gulf of Cadiz . . . 192

8.2 Gorringe Bank and Horseshoe Abyssal Plain . . . 194

8.3 The Alboran Sea . . . 195

8.4 Further Work . . . 195

Appendices **197**

A Regional datasets **198**

A.1 Topography/Bathymetry . . . 198

A.2 Gravity . . . 198

A.2.1 Global Geopotential Model OSU91a . . . 200

A.3 Well Data . . . 202

A.4 Earthquake Relocation and Focal Mechanisms . . . 203

A.4.1 Methodology . . . 203

A.4.2 Relocation Results . . . 204

A.5 Heat Flow Data . . . 206

A.6 Summary . . . 209

B Well Data **210**

B.1 Description of wells . . . 212

B.1.1 Wells with available logs . . . 212

B.1.2 Well Correlation Profile A-A' . . . 216

B.2 Backstripping Input and Output Tabulated For Selected Wells . . . 219

B.3 Backstripping Results For All Available Gulf of Cadiz Wells . . . 225

C Basin Analysis Methods **228**

C.1 Introduction . . . 228

C.2 Backstripping Methodology . . . 228

C.2.1 Sediment Compaction and Decompaction . . . 229

C.2.2 Absolute Ages, Palaeobathymetry and Sea Level . . . 236

C.2.3 Airy (1D) Backstripping . . . 237

C.2.4 Flexural Backstripping . . . 239

C.3 Calculation of Stretching Factor, β . . . 244

C.3.1 Thermo-Mechanical Models of Extensional Basins . . . 244

C.3.2 Pure Shear Model of Lithospheric Extension [McKenzie, 1978] . . . 245

C.4 Gravity Modelling . . . 248

C.4.1 Two-Dimensional Gravity modelling - forward method . . . 249

Bibliography **251**

List of Figures

1.1 Location of the study region 1
1.2 Bathymetric features of the NE Atlantic. 2
1.3 Map of study region showing location of MCS profiles. 3

2.1 3D Relief of the central North Atlantic and western Mediterranean 6
2.2 3D illuminated relief of the study region. 8
2.3 Seismicity (M_b >4) of the African-Eurasian plate boundary. 11
2.4 Regional tectonic map of the Azores-Gibraltar plate boundary 14
2.5 Location of the ocean-continent transition zone 16
2.6 Tectonic map of the Mediterranean showing the arcuate belts of the Alpine mountain chain and Neogene basins. 18
2.7 Simplified geological map of the Gibraltar Arc 19
2.8 Models for the formation of the Gibraltar Arc 22
2.9 Plate reconstructions for the Northeast Atlantic from chron M25 to chron 6. 25
2.10 Correlation chart showing general direction of the motion of Africa with respect to Europe, after Dewey *et al.* [1989]. 27

3.1 IAM Survey Locations 32
3.2 IAM seismic acqusition geometries 34
3.3 Spectral characteristics of airgun source array 35
3.4 Generalized IAM processing scheme 36
3.5 Amplitude spectrum of raw IAM shot data 38
3.6 IAM-4 shotgather 39
3.7 Amplitude spectrum of a stacked portion of data from IAM-4 41
3.8 Location of T3 and IAM-4 Panels 43
3.9 T3 Post-Stack Enhancement Panels 44
3.10 IAM-T3 Migration Panels 48
3.11 IAM-4 Migration Panels 50
3.12 Location of Line 823 Panel 54
3.13 A segment of RC2911 Line 823 showing post-migration improvement . . . 54

4.1 Regional relief and tectonic map 57
4.2 Sections across the GOC and Guadalquivir Basin 61
4.3 Strike section of the Gudalquivir Basin 62
4.4 Well data and seismic ties over relief map of SW Iberia and the northern GOC. 65
4.5 Stratigraphic well correlation profile A-A' 67
4.6 Well ties to seismic profile IAM GC3 70
4.7 Example of sonic data from a Gulf of Cadiz well. 72
4.8 Compilation of sonic velocity data in the GOC 73
4.9 Histogram of sonic velocities in the GOC 75
4.10 Comparison of sonic versus interval velocities for IAM-GC3 76
4.11 Migrated Profile GC3 and interpretation. 79
4.12 Interpreted Migrated Profile GC2. 80
4.13 Interpreted salt structures at north end of Profile GC2 81
4.14 Detail of Facies CIII from Profile T3 83
4.15 Interpreted Migrated Profile GC1 85
4.16 Interpreted Migrated Profile T3 87
4.17 Interpreted Stack 829 in the central GOC. 89
4.18 1D backstripping methodology flowchart 94
4.19 Sonic to porosity conversion of GOC well data 95
4.20 Sonic to porosity conversion of GQB well data 96
4.21 Plot of compressibility parameters for studied wells 98
4.22 1-D backstripping results for selected wells of the GOC and GQB 100
4.23 Tectonic subsidence curves for all Gulf of Cadiz wells with available data . 102
4.24 Airy backstripping results for wells 241, 296 and 314 in the northern GOC. See text for full explanation. 105
4.25 Free-air gravity anomaly map of the Gorringe Bank–Gulf of Cadiz region. 108
4.26 Comparison of Airy backstrip Moho against refraction Moho 110
4.27 Gulf of Cadiz profiles and gravity anomaly I. 112
4.28 Wide-angle profile R2 - velocity and density. 113
4.29 Free-air anomaly gravity model **A–A'** (South Portugal to Morocco profile) 114
4.30 Estimate of depths to discrete density boundaries using the power spectrum of the free-air gravity anomaly over profile GC1 116
4.31 Map of contoured stretching factors (β) superimposed on a gravity anomaly map of the Gulf of Cadiz region. 118

5.1 Global gas hydrate occurence 124

5.2 Gas hydrate stability field 125
5.3 Mass flow processes operating on the continental slope 126
5.4 ERMapper-processed perspective image of the bathymetry of the central North Atlantic viewed from the south-west. 128
5.5 Location of seismic profiles studied. 129
5.6 Interpreted Migrated Profile IAM–T3 131
5.7 Interpreted Migrated Profile GC1 132
5.8 Detail of BSR on Profiles IAM-T3 and IAM-GC1 133
5.9 BSR Polarity on IAM-T3 135
5.10 Relation of observed seismic velocity inversions to free gas concentration. 136
5.11 Derivation of BSR reflection coefficients from analysis of seafloor and BSR amplitudes. 139
5.12 Mid- to upper slope features of the central GOC as seen on migrated Profile IAM-T3: 0–3 s TWTT. 141
5.13 Upper slope features of the central GOC illustrated with migrated MCS profile Conrad 829. 143
5.14 Example of a BSR from the Outer Blake Ridge. 145
5.15 BSR burial TWTT versus water depth for worldwide BSRs observed on seismic reflection profiles. 146
5.16 Summary map of gas–related observations in the Gulf of Cadiz. 149
5.17 The current system of the Gibraltar Straits and Gulf of Cadiz and eustatic sealevel change. 153
5.18 Salinity and temperature of water bodies either side of the Gibraltar Straits. 155

6.1 Map of the Gibraltar Arc-eastern Atlantic region. 159
6.2 Seafloor processes 163
6.3 Comparison of acquisition parameters for IAM and AR92 profiles 165
6.4 DSDP site 135 correlation with seismic data. 167
6.5 Interpreted seismic profile IAM-4. 169
6.6 Interpreted depth-converted seismic profile GC2. 172
6.7 Interpreted seismic profile GB1. 173
6.8 Interpreted seismic profile GB2. 174
6.9 Depth-converted thickness of unit C-III/HAP-II. 176
6.10 Model for the formation of the giant chaotic body in the Gulf of Cadiz and Horseshoe Abyssal Plain. 179

7.1 Location of the Alboran Sea Basin in relation to elements of the Betic–Rif orogenic belt, superimposed on relief. 183
7.2 Major bathymetric features of the Alboran Sea Basin. 184
7.3 Seismic profile and well locations in the Alboran Sea Basin. 185
7.4 Correlation of ODP and commercial wells in the Alboran Sea Basin, after Comas *et al.* [1999]. 186
7.5 RC2911 Profiles 823 and 824. See text for explanation 187
7.6 RC2911 Profiles 825 and 827. See text for explanation 190

A.1 Relief and well data in the study area 199
A.2 Gravity anomaly map of study area 201
A.3 Degree 16 gravity field determined from geopotential model OSU91a . . . 202
A.4 Flow chart of earthquake hypocentre relocation method 204
A.5 Results of JHD hypocentre relocation 205
A.6 Heat flow density map of study region 207

B.1 Petrophysical data from the GOC 214
B.2 Petrophysical data from the western GQB 215
B.3 1-D backstripping results for GOC wells penetrating only Miocene to Recent sediment 225
B.4 1-D backstripping results for GOC wells penetrating only the Tertiary. . . 226
B.5 1-D backstripping results for GOC wells penetrating the Mesozoic. 227

C.1 The backstripping method 229
C.2 Calibration procedure for porosity–sonic transit time equations 232
C.3 Published porosity-depth relationships 234
C.4 Sea level curves used for backstripping corrections 237
C.5 1D backstripping methodology flowchart 238
C.6 Illustration of variation of response function Φ with wavenumber 240
C.7 Parameters involved in flexural backstripping 241
C.8 Representative present-day $T_e$values from oceanic to continental lithosphere243
C.9 $T_e$against age for the oceanic lithosphere (Watts, 1994) 244
C.10 Uniform stretching model of McKenzie [1978] 246
C.11 The use of local (Pratt) isostasy in the uniform stretching model 247
C.12 Parameters used in calculating the gravity field caused by a semi-infinite slab with a sloping edge 249

List of Tables

2.1 Euler poles for the African plate 13
2.2 Criteria for distinguishing oceanic from continental crust. 15
2.3 Criteria used to locate the Ocean-Continent Transition 16

3.1 Final IAM commercial processing sequence 37
3.2 Time migration algorithms 47

4.1 Seismic facies classification in the Gulf of Cadiz 69
4.2 Theoretical compaction curve properties of analysed wells 97
4.3 Stretching factors for northeastern GOC wells 241, 296 and 314. 109

6.1 Volumes of rock involved in mass wasting. 178

A.1 Average heat flow values from two global studies 206

B.1 Well data from the Gulf of Cadiz, Campo de Gibraltar and Alboran Sea, as outlined in IGME[1987]. 210
B.2 Wells from the western Betic Cordillera and Guadalquivir Basin, as outlined in IGME[1987]. 211
B.3 IGME 296 (Cadiz B1) stratigraphy. 219
B.4 IGME 296 (Cadiz B1) backstripping results. Thickness and subsidence values in kilometres. 219
B.5 IGME 241 (Cadiz D1) stratigraphy. 220
B.6 IGME 241 (Cadiz D1) backstripping results. Thickness & subsidence in kilometres. 220
B.7 IGME 314 (Cadiz D2) stratigraphy. 221
B.8 IGME 314 (Cadiz D2) backstripping results. Thickness & subsidence in kilometres. 221
B.9 IGME 288 (Cadiz C1) stratigraphy. 222
B.10 IGME 288 (Cadiz C1) backstripping results. Thickness & subsidence in kilometres. Sealevel corrections not applied as negligible in Neogene and Quaternary. 222

B.11 IGME 245 (Cadiz G1) stratigraphy. 222
B.12 IGME 245 (Cadiz G1) backstripping results. Thickness & subsidence in kilometres. Sealevel corrections not applied as negligible in Neogene and Quaternary. 222
B.13 IGME 533 stratigraphy. Sealevel corrections prior to the mid-Jurassic are extrapolated constants from the oldest mid-Jurassic sealevel curve values. Palaeobathymetry not available. 223
B.14 IGME 533 backstripping results. Thickness & subsidence in kilometres. . 223
B.15 IGME 223 stratigraphy and backstripping results. Sealevel corrections not applied as negligible in Neogene and Quaternary. Palaeobathymetry not available. 223
B.16 IGME 225 stratigraphy and backstripping results. Sealevel corrections not applied as negligible in Neogene and Quaternary. Palaeobathymetry not available. 224

C.1 Sonic velocities and interval transit times for various rock types. ϕ=0 in all cases. (After Schlumberger Well Interpretation Charts, 1972 and 1991). 231
C.2 List of assumed palaeodepth ranges for given environments of deposition, for use in backstripping corrections. 237
C.3 List of physical parameters used in backstripping and gravity modelling analysis. 248

Chapter 1

Introduction

1.1 Aims of the Study

The goal of this research was to understand a tectonically complex area at the convergent eastern segment of the Azores–Gibraltar plate boundary zone (PBZ) between Africa and Eurasia (Figure 1.1). This thesis reports investigations in this area based primarily on marine geological and geophysical data on the southern margins of the Iberian Peninsula.



Figure 1.1: Location of the study region between the African and Eurasian plates.

The complexity of the southern Iberian margins is a result of a series of major tectonic processes, with the region being shaped since the Mesozoic by the opening of the central eastern Atlantic Ocean and lateral plate motions between Africa and Iberia, followed by plate convergence, culminating with the formation of the Alpine Betic-Rif orogenic belt of Spain and north Africa. The present day regional geology can be summarised as an Atlantic passive margin in western Iberia, the eastern part of the Azores-Gibraltar plate boundary zone between Africa and Eurasia, and an orogenic arc (the Betic-Rif mountains) surrounding the Alboran Sea basin, which is an extensional basin within a region of overall convergence. The sediments and structures of the southern Iberian margins provide a record of the complex tectonic history, which can be unravelled through their

analysis. In this study, new multichannel seismic reflection images have been produced and interpreted in conjunction with previous geophysical and geological data, in order to understand better the structure, sedimentary fill, and evolution of the Gulf of Cadiz (GOC) continental margin, the Gorringe Bank Region (GBR) and the Alboran Sea (ABS) in the western Mediterranean (Figure 1.2, Figure 1.3).

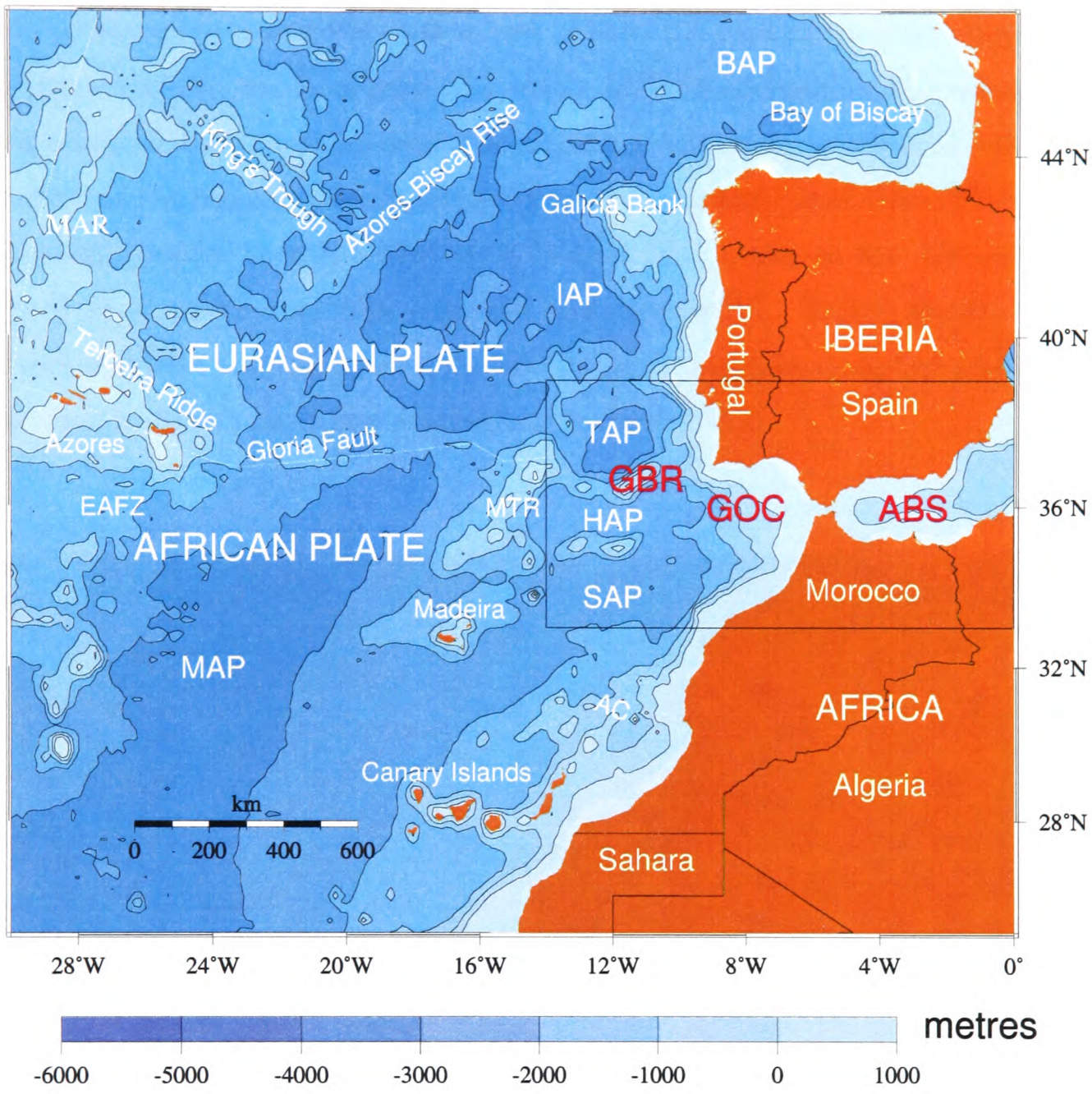


Figure 1.2: Bathymetric features of the plate boundary zone between African and Eurasian plates in the NE Atlantic and western Mediterranean (nomenclature follows that in *General Bathymetric Chart of the Oceans, GEBCO, 1984*). MAR=Mid Atlantic Ridge, EAFZ=East Azores Fracture Zone, AC=Agadir Canyon, MAP=Madeira Abyssal Plain, SAP=Seine Abyssal Plain, HAP=Horseshoe Abyssal Plain, TAP=Tagus Abyssal Plain, IAP=Iberian Abyssal Plain, BAP=Biscay Abyssal Plain. The study regions dealt with in this thesis are shown within a black box and labelled in red: GBR=Gorringe Bank Region, GOC=Gulf of Cadiz, ABS=Alboran Sea.

1.2 Data

This thesis is mainly concerned with the processing and interpretation of multichannel seismic reflection data in the regions offshore southern Iberia, from Gorringe Bank to the Alboran Sea in the western Mediterranean. The primary dataset for this study comprises 3800 km of near-vertical multichannel seismic reflection data (Figure 1.3) which were collected offshore Spain and Portugal in late 1993 by the Iberian Atlantic Margins (IAM) group [Banda *et al.*, 1995], aboard the vessel *M/V* Geco-Sigma. The seismic survey utilized a large 116 litre volume airgun array, and a 5 km long streamer of 192 channels, which allowed the imaging of reflectivity up to 14 s two-way travel time (TWTT). Deep multichannel profiles from the 1988 *R/V* Conrad 2911 cruise in the Alboran Sea and eastern Gulf of Cadiz were also migrated and interpreted. Relief, gravity, borehole, seismicity, and heat flow data across the study region have been compiled and processed, as described in Appendix A and summarised in Section A.6.



Figure 1.3: A relief map of the study region, with major onshore and offshore features marked. Locations of multichannel seismic profiles of Iberian Atlantic Margins Project (in red) and Lamont Doherty Geological Observatory cruise RC2911 (in black). GBR=Gorringe Bank Region, GOC=Gulf of Cadiz, ABS=Alboran Sea. The possible position of the African–Eurasian plate boundary in this region is shown as a dashed black line (taken from Hayward *et al.* [1999]).

1.3 Thesis Outline

- **Chapter 1** is an introduction to the aims of this study and the data used.
- **Chapter 2** is a description of the tectonic setting of the study regions in terms of their location at the intersection between the African–Eurasian plate boundary and the Betic–Rif orogenic belt. The known geological development of the region is summarised.
- **Chapter 3** is concerned with the acquisition and processing of the IAM multichannel seismic reflection profiles, and the reprocessing of MCS profiles from the Conrad 2911 cruise.
- **Chapter 4** reports an integrated study of the Gulf of Cadiz margin involving a seismic stratigraphic analysis of multichannel seismic data, and the modelling of gravity anomalies and well data in order to elucidate the deep structure of the Gulf of Cadiz.
- **Chapter 5** presents a seismic study of a bottom-simulating reflection observed on IAM MCS profiles from the continental slope of the Gulf of Cadiz margin, indicating the presence of hydrates and free gas. A possible link between this gas and upslope mass wasting is explored.
- **Chapter 6** analyses the sedimentary fill and structure of the Gorringe Bank Region using well-seismic ties and seismic stratigraphic techniques. The study is focussed on a seismically chaotic body underlying much of the continental slope west of Gibraltar, and in particular the lobe which extends beneath the Eastern Horseshoe Abyssal Plain.
- **Chapter 7** is a basinwide seismic study of the Alboran Sea, involving the interpretion of structure and sedimentary fill from new multichannel seismic reflection images.
- **Chapter 8** summarises the main findings of this work.

Chapter 2

Tectonic Setting

2.1 The Study Region in the Context of the African–Eurasian Plate Boundary

The position of the present-day African-Eurasian plate boundary zone is thought to extend from the Azores triple junction to the region of Gibraltar (Azores-Gibraltar Fracture Zone, AGFZ), and into the North Africa–Alboran Sea region [Arana & Vegas, 1974], as illustrated in Figure 2.1. The Azores-Gibraltar-Mediterranean-Alpine region marks a broad lithospheric transition zone between African and Eurasian plates. A higher spreading rate in the South Atlantic relative to the North Atlantic led to a gradual anticlockwise rotation of the African plate, and thus the zone of Eurasian/African plate contact is largely under compression [e.g., Collette & Roest, 1992]. West of Gibraltar, an eastward transition occurs from convergence of ocean-ocean lithosphere to continental-continental lithosphere near the southern Iberian margins. This provides the framework for mountain building processes accompanied by active rifting in preconditioned zones of lithospheric weakness [Kahle & Mueller, 1998], as is seen around the Alpine arcs of the western Mediterranean. In the Atlantic, the plate boundary is marked by the AGFZ, which since the early Oligocene (36 Ma, Chron 13) has exhibited extension near the Azores triple junction, dextral strike-slip along the Gloria fault and compression across the Gibraltar Arc [e.g., Roest & Srivastava, 1991]. To the east of the Azores-Gibraltar lineament, Arana & Vegas [1974] place the boundary behind the calc-alkaline volcanism of northern Africa.

2.1.1 Physiography

Buforn *et al.* [1988] divide this Azores-Mediterranean zone into three sections according to bathymetry, seismicity and tectonics. The **Azores** section, from 35° to 24° W on Figure 1.2, includes the Azores triple junction, where the North American, Eurasian, and African plates meet at a point [Searle, 1980]. Triple junctions are most commonly a "T" or a "Y" shape. The Azores triple junction is a ridge-ridge-ridge T-shaped triple junction; the Mid-Atlantic Ridge (MAR) forms two arms of the "T", and the third

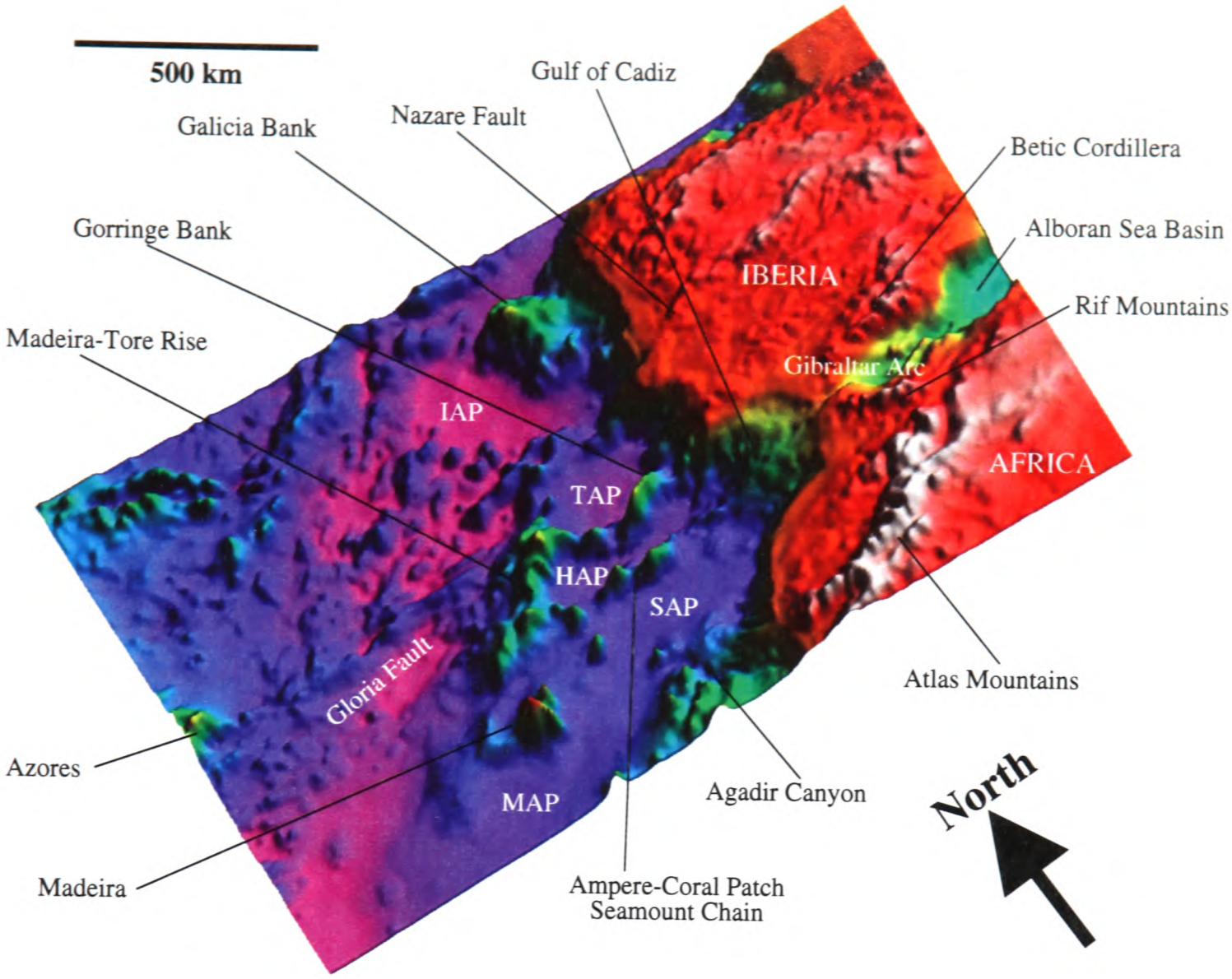


Figure 2.1: 3D Relief of the central North Atlantic and western Mediterranean: the Africa-Eurasia plate boundary zone. Image processing of relief data within the ERMapper GIS package, illumination from the SE. MAP=Madeira Abyssal Plain, SAP=Seine Abyssal Plain, HAP=Horseshoe Abyssal Plain, TAP=Tagus Abyssal Plain, IAP=Iberian Abyssal Plain.

the third is formed by the Azores spreading centre, otherwise known as the Terceira Ridge (see Figure 1.2). This actively volcanic spreading centre rises above sealevel at the Azores, and was thought to be a hotspot feature [e.g., Flower *et al.*, 1976]. However, this has been disputed [e.g., Moore, 1990; Simkin & Siebert, 1994] since the volcanoes of the Azores lack the linear age progression seen in volcanic island chains associated with hot spots such as the Hawaiian and Canary islands [Simkin & Siebert, 1994]. The eastern part of the Terceira Ridge terminates at about 24° W against the East Azores Fracture Zone (EAFZ) which strikes E-W to the MAR (Figure 1.2).

Further east, the **Central** section (24°-13° W, Figure 1.2) is formed by an approximately rectilinear fracture zone. In the west the plate boundary is clearly defined along the Gloria Fault, a well-mapped [e.g., Laughton *et al.*, 1972; Laughton & Whitmarsh, 1974] 400km long, linear bathymetric feature. It is considered to be an extension of the

EAFZ, and is illustrated in Figure 2.1. Geological Long Range Inclined Asdic (GLORIA) data [Searle, 1979] show the Gloria Fault as a series of parallel to near parallel echos, possibly cut by weak WNW-NW normal faults near to 21° W. At its eastern end, the Gloria Fault is less well defined and may pass into the most northerly seamount of the Madeira-Tore Rise (Figure 2.1).

The **East** section (13° -0° W, Figure 1.2) lies to the east of the Madeira-Tore Rise. It is a region of complex bathymetry, dominated by large seamounts and deep abyssal plains. The principal features from north to south are the Galicia Bank, Tagus abyssal plain, Gorringe Bank, Horseshoe abyssal plain, Ampere-Coral Patch seamount chain and the Seine abyssal plain. Onshore, topographic features such as the Atlas Mountains, the Betic and Rif arms of the Gibraltar Arc, and the trace of the Nazaré Fault are clearly illustrated on a relief image (Figure 2.1). Prolongation onto the ocean floor of land structures, such as the Guadalquivir Basin and Nazaré Fault, have been recognized for some time [e.g., Roberts, 1970; Buforn *et al.*, 1988]. There is no obvious feature delimiting the contact between African and Eurasian plates in this region, and the complex relief is described in detail in the next section.

Physiography of the Study Region

The study region lies east of the Madeira-Tore Rise (Figure 2.2), where in the Gorringe Bank Region the bathymetry is complex (Figure 2.1). A series of small, deep abyssal plains (Tagus, Horseshoe and Seine abyssal plains) are separated by the Gorringe Bank and Ampere-Coral Patch Ridge, which form two eastward stretching arms extending from the NNE-SSW trending Madeira Tore Rise.

The Gorringe Bank lies on the northerm arm and is 180 km long, and 80 km wide at the base, trending approximately NE-SW, and rising from abyssal depths to within 25 m of sealevel (Figure 2.2). It was formed by overthrusting of the African plate upon the Eurasian plate in the Middle Miocene at $\sim$ 10 Ma [e.g., LePichon *et al.*, 1970; Hayward *et al.*, 1999]. The southern seamount arm comprises the less well-studied Ampere and Coral Patch seamounts (Figure 2.2). These form a pair of overlapping ridges with a trend of approximately N65° E, in contrast to Gorringe Bank which trends N50° E. The Ampere seamount in the west has a width of approximately 80 km and length 120 km with a main peak and a few smaller lateral peaks [Litvin *et al.*, 1982]. It is of Pliocene to Miocene age [Matveyenkov *et al.*, 1994] with a volcanic origin and partial subaerial formation [Litvin *et al.*, 1982; Marova & Yevsyukov, 1988]. the Coral Patch seamount lies to the east of the Ampere seamount with a width of approximately 80 km, a length

of 150 km and a depth of within 1200 m of sea level. This seamount also extends to the east to form the more minor bathymetric feature of the Coral Patch Ridge.

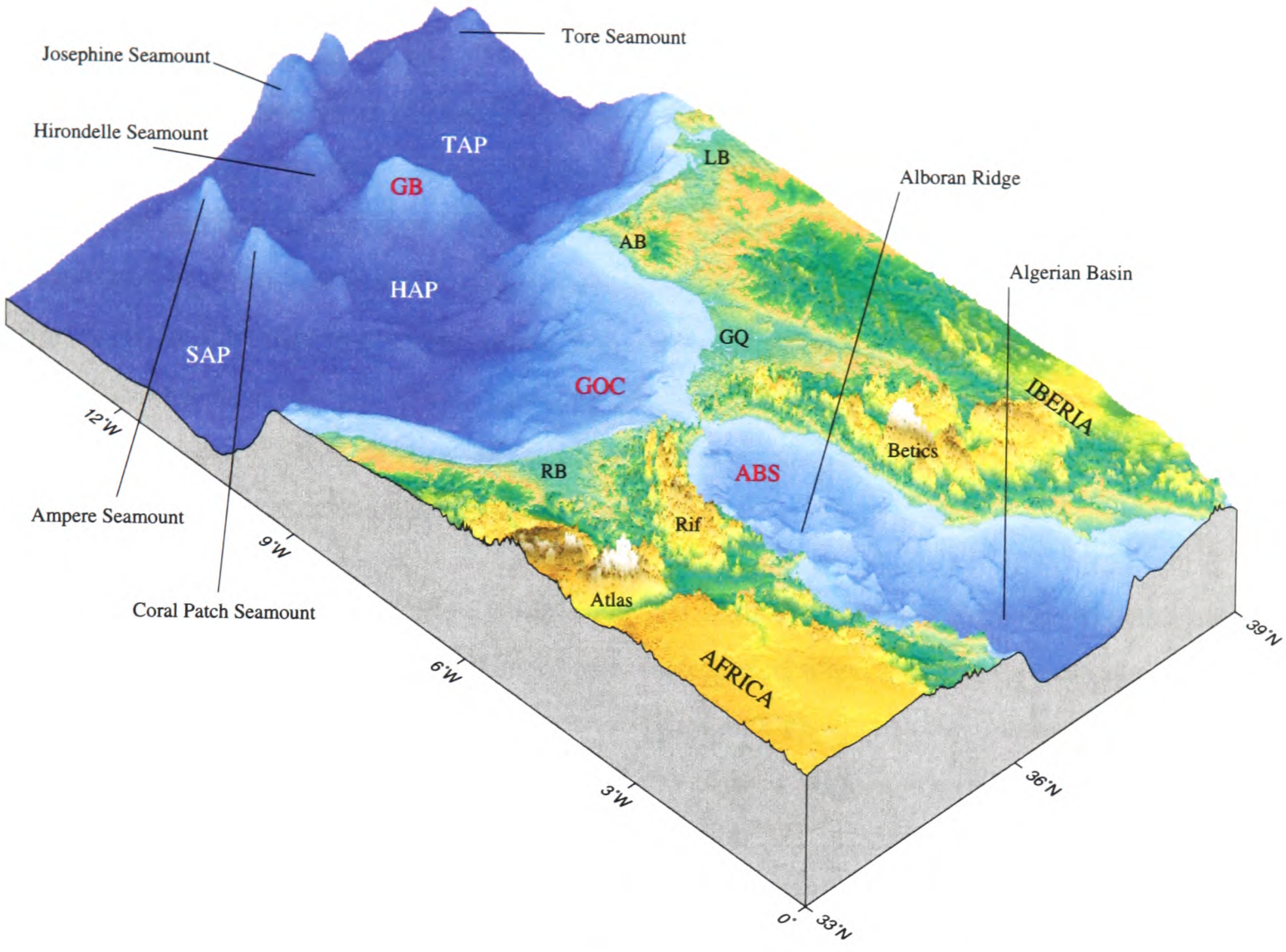


Figure 2.2: 3D relief of the study region illuminated from the SE. GB=Gorringe Bank, GOC=Gulf of Cadiz, ABS=Alboran Sea, TAP=Tagus Abyssal Plain, HAP=Horseshoe Abyssal Plain, SAP=Seine Abyssal Plain, GQ=Guadalquivir Basin, RB=Rharb Basin, AB=Algarve Basin, LB=Lusitanian Basin.

The Iberian and north African passive continental margins form the eastern boundary of the seamount arms and the small abyssal plains east of the Madeira-Tore Rise, and both continental slopes rise relatively rapidly from abyssal depths, but in the central sector of the Gulf of Cadiz to the Straits of Gibraltar slopes are lower (Figure 2.1). The Iberian shelf is incised by many submarine canyons, which are associated with fault zones; from north to south: the Nazaré, Tejo-Sado, and São Vicente canyons, supply terrigenous sediment from Iberia to the Iberian, Tagus, and Horseshoe abyssal plains respectively. The African shelf is incised by the continuation of the South Atlas Fault, the Agadir Canyon (Figure 2.1).

The Tagus, Horseshoe and Seine abyssal plains (TAP, HAP and SAP on Figure 2.1 and Figure 2.2) resemble the major abyssal plains of the Atlantic Ocean, such as the Madeira Abyssal Plain (Figure 1.2), in being very flat with undisturbed sediments, yet they are of a far smaller scale. The HAP is a narrow, elongate dumbell-shaped basin which is divided into East (EHAP) and West sub-basins by a narrow strait 11km wide at its centre [e.g., Hayward *et al.*, 1999]. The average water depth in both Tagus and Horseshoe abyssal plains is $\sim$ 5000m [Lebreiro, 1995] and both are ringed by shallower seamounts at their distal ends. This makes them effective stores for sediment derived from terrigenous sources upslope, or shallow-water material from surrounding carbonate-capped seamounts. To the south, the Seine abyssal plain is the shallowest abyssal plain in the region at $\sim$ 4500 metres, with low gradient slopes onto the base of Coral Patch and Ampere seamounts at the northern boundary.

Figure 2.2 shows the re-entrant position of the Gulf of Cadiz between the Iberian and African margins. It consists of two elements: a steep and narrow upper slope and a broad convex-up terrace dipping gently to the west (Figure 2.2). In the NE of the GOC (8° W and 36.5° N) the terrace is cut by a series of curvilinear valleys which channel sediment into the Horseshoe abyssal plain [Roberts, 1970].

The Alboran Sea is a semi–enclosed basin at the westernmost end of the Mediterranean, flanked by the Betic–Rif orogenic belt and opening out to the east into the Algerian Basin, which is known to be floored by oceanic crust [Mauffret *et al.*, 1992]. The Alboran Sea has a number of bathymetric features, the largest of which is the volcanic Alboran Ridge (Figure 2.2), which rises to the surface at Alboran Island, and divides the Alboran Sea into sub-basins [e.g., Willet, 1996].

2.1.2 Seismicity

Seismicity is an important tool in tectonic studies: epicentre distributions help establish plate boundaries, and focal mechanisms give insight into the dynamics of plate motions and strain release. The study of earthquake data from the Azores-Gibraltar region is important because of its large magnitude seismicity, which apart from yielding geological information also has significant environmental implications through its effects on human population centres. For example, since 1931, three events of M_b >8 and six events of M_b >7 have been recorded [e.g., Fukao, 1973; Udias *et al.*, 1976]. The giant 1755 Lisbon earthquake (possibly the world's largest magnitude recorded event) had an epicentre seaward of Lisbon, and produced the only known Atlantic earthquake tsunami [Muzcua *et al.*, 1991].

The main trend of seismicity from the Azores triple junction to the Alboran Sea is illustrated on Figure 2.3. Early workers [e.g., Rothé, 1954; Gutenberg & Richter, 1954] observed that there existed a belt of seismic activity extending from the Azores on the Mid-Atlantic Ridge to the Straits of Gibraltar and then again across North Africa to Sicily, marking the main interplate boundary between African and Eurasian plates. Subsequently, several regional seismotectonic studies of this region have been undertaken [e.g., McKenzie, 1972; Grimison & Chen, 1986; Buforn *et al.*, 1988; Udias & Buforn, 1991; Muzcua *et al.*, 1991; Vegas, 1991; Galindo-Zaldívar *et al.*, 1993; Kiratzi & Papazachos, 1995]. The studies, which examined earthquake focal mechanisms, arrived at similar conclusions concerning plate motions: the Africa-Eurasian PBZ consists of a western section with strike-slip motion with an extensional component (Azores); a central dextral strike-slip section (Gloria Fault) and an eastern compressional region with strike-slip components (Gorringe Bank - Mediterranean region) (Figure 2.3).

In the **Azores** section, W of 24° W, seismicity is generally of moderate magnitude, shallow depth, and concentrated on the MAR and Terceira Ridge. At the Terceira Ridge, earthquake derived slip vectors [Udias & Buforn, 1991] indicate NE-SW extension. Activity on the East Azores Fracture Zone is of low frequency and magnitude [Buforn *et al.*, 1988].

In the **Central** section, epicentres follow a linear trend along the Gloria Fault, and focal mechanisms are clearly strike-slip, with only dextral motion compatible with the E-W strike of the Gloria Fault. The cluster of earthquakes seen to the south of this trend, centred at about -18° W and 36° N, may be related to a NW-SE trend of earthquakes ending in the Agadir Canyon. Some workers interpret this as one edge of a triangular subplate bounded to the north by the E-W trend of seismicity and the NE-SW seismic trend associated with the Atlas Mountains of N. Africa [e.g., Buforn *et al.*, 1988; Westaway, 1990]. A clear seismic gap exists between 20° -24° W, but the eastern part of this region has given rise to two events of M_b >8 since 1912.

In the **East** section landward of the Madeira–Tore Rise, seismicity is more diffuse; focal mechanisms near the Gorringe Bank indicate predominantly reverse faulting with a strike slip component (Figure 2.3). However, a trend in the data can be made out, changing from an E-W to NW-SE direction at the Gulf of Cadiz and continuing across N. Africa. P axes (principal axes of stress) have a mean trend of N30° W [Buforn *et al.*, 1988] and slip vectors, calculated from focal mechanisms, have a trend of about N35° W [Udias & Buforn, 1991]. To the north of the trend, earthquakes have been associated with

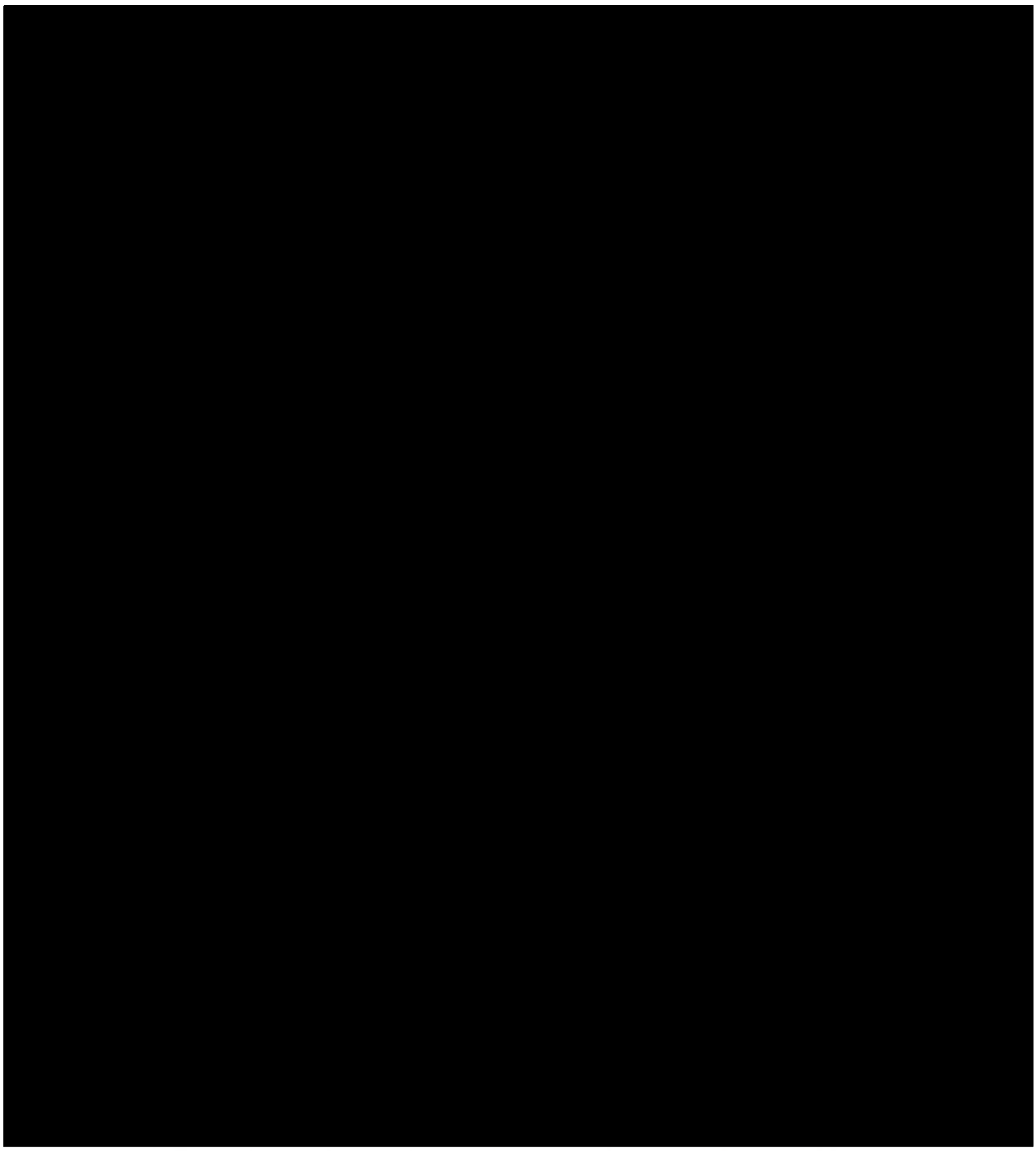


Figure 2.3: a) Seismicity (M_b >4) of the African-Eurasian plate boundary. Data are from the catalogue of the International Seismological Centre (ISC). Focal mechanisms are compiled from the ISC and published data, ISC depths are given in km and compressional quadrants are shown shaded. (Modified from Hayward [1996]). b) Regional pattern of seismic stresses and tectonic features from the Azores Triple Junction to Mediterranean (Med.) regions, from Udias [1985].

land fractures and their oceanic extensions, such as the Nazaré Fault on Figure 2.1 [e.g., Buforn *et al.*, 1988]. Kiratzi & Papazachos [1995] examined crustal deformation using moment tensor summation of post-1964 events of M_s >=5. They concluded that from the Azores to Italy, the mean direction of compression was N40° W at a rate of between 1.1-2.8mm/yr, and that at the Gloria Fault, dextral strike-slip occured at 11mm/yr. Shallow and intermediate depth seismicity occurs throughout this eastern region, with oblique convergence between African and Eurasian plates being indicated by the largest earthquakes (Figure 2.3). In the Alboran Sea region, seismic gaps have been observed between 60-100 km depth and 150-600 km [Seber *et al.*, 1996]. Deep seismic activity associated with the Gibraltar Arc is revealed mainly by the 1954 earthquake of M_b =7.1 at a depth of ~630 km, and two smaller events also recorded at this depth [Grimison & Chen, 1986; Udias & Buforn, 1991]. All three events have P-axes which steeply dip east, and these events have been cited as evidence for a detached N-S striking subducted slab beneath southern Spain [e.g., Lonergan & White, 1997]. This is also supported by seismic tomography which shows an anomalously fast and cold region in the upper mantle below southern Spain [Blanco & Spakman, 1993].

Early plate models [e.g., McKenzie, 1972], postulated the existence of an E-W trending active margin through the Straits of Gibraltar, which would be obliquely convergent in nature. It would be expected that the slip on this plate boundary would result in a concentrated band of seismicity, but this is not supported by seismological evidence [e.g., Purdy, 1975; Grimison & Chen, 1986; Argus *et al.*, 1989]. A geodetic determination of crustal deformation across the Straits indicates instead that E-W compression and N-S extension are taking place [Reilly *et al.*, 1992]; however, their study samples only a minor portion of a region ~200km wide of diffuse deformation over which interplate motion is being accommodated. Figure 2.3b summarises the tectonic divisions and the seismic stresses (indicated by arrows), and is a synthesis of many results [Udias, 1985].

2.1.3 Kinematics

Analysis of North Atlantic magnetic lineations allows the history of Africa-Eurasia kinematics to be derived independently from plate movement reconstruction of these plates with respect to North America [e.g., Dewey *et al.*, 1973, 1989; Laughton & Whitmarsh, 1974; Olivet *et al.*, 1984; Srivastava *et al.*, 1990; Roest & Srivastava, 1991]. Such studies have suggested that convergence along a NW-SE or N-S trend has occurred over the past 10 Ma in the Mediterranean area, which is consistent with results from most present-day plate motion reconstructions [e.g., Chase, 1978; Minster & Jordan, 1978; Argus *et al.*, 1989; DeMets *et al.*, 1990; Westaway, 1990; DeMets *et al.*, 1994]. These workers

have tried to constrain the relative velocity of Africa and Eurasia, which can be described in terms of rotation of rigid blocks about an Euler pole. Current African-Eurasian plate interactions can be described through the anticlockwise rotation of Africa with respect to a stable Europe. Most kinematic studies have located the Euler pole for the rotation of Africa in the eastern Atlantic near the Canaries. Table 2.1 summarises Euler poles for the African plate with respect to the Eurasian plate that have been calculated by various authors. The locations of these Euler poles are shown on the regional tectonic map in Figure 2.4, on which the main magnetic anomalies observed about the AGFZ have also been plotted.

LATITUDE	**LONGITUDE**	**REFERENCE**
22.7° N	-28.2°	McKenzie [1972]
29.2° N ± 500 km	-23.5° ± 200 km	Chase [1978]
25.2° N ± 500 km	-21.2° ± 100 km	RM2 [Minster & Jordan, 1978]
21.3° N ± 70 km	-21.0° ± 60 km	Searle [1980]
21.0° N ± 700 km	-20.6° ± 70 km	NUVEL 1A [DeMets *et al.*, 1990, 1994]
21.0° N ± 100 km	-21.0° ± 100 km	Westaway [1990]

Table 2.1: Euler poles for the rotation of the African plate with respect to a stable Eurasia. Uncertainty in kilometres.

NUVEL 1A [DeMets *et al.*, 1994] is the most comprehensive model, being the modified version of NUVEL 1 [DeMets *et al.*, 1990], which utilised fault azimuths, focal mechanisms and slip vectors. Model NUVEL 1A was used to calculate the relative motion of Africa with respect to a fixed Europe at specified locations along the plate boundary zone; these are shown as red arrows with the rate of motion in mmyr^{-1} in Figure 2.4. It is clear that the relative motion vector of Africa changes from NW at a rate of 4-5 mmyr^{-1} in the GOC-ABS region, to being westward-directed at $\sim$3.6 mmyr^{-1} at the Gloria Fault, to WSW at $\sim$4.2 mmyr^{-1} at the Terceira Ridge/Azores. Thus, the plate boundary is extensional at the Azores, transform at the Gloria Fault and convergent in the study area east of the Madeira–Tore Rise at 4-5 mmyr^{-1}.

2.1.4 The Ocean-Continent Transition

The boundary between oceanic and continental crust is not a well determined feature, but is often modelled as being relatively abrupt, and commonly placed beneath the continental shelf or slope [Rosendahl *et al.*, 1992]. However, at rifted margins, the change from extended continental crust to oceanic crust is more likely to occur over a finite region

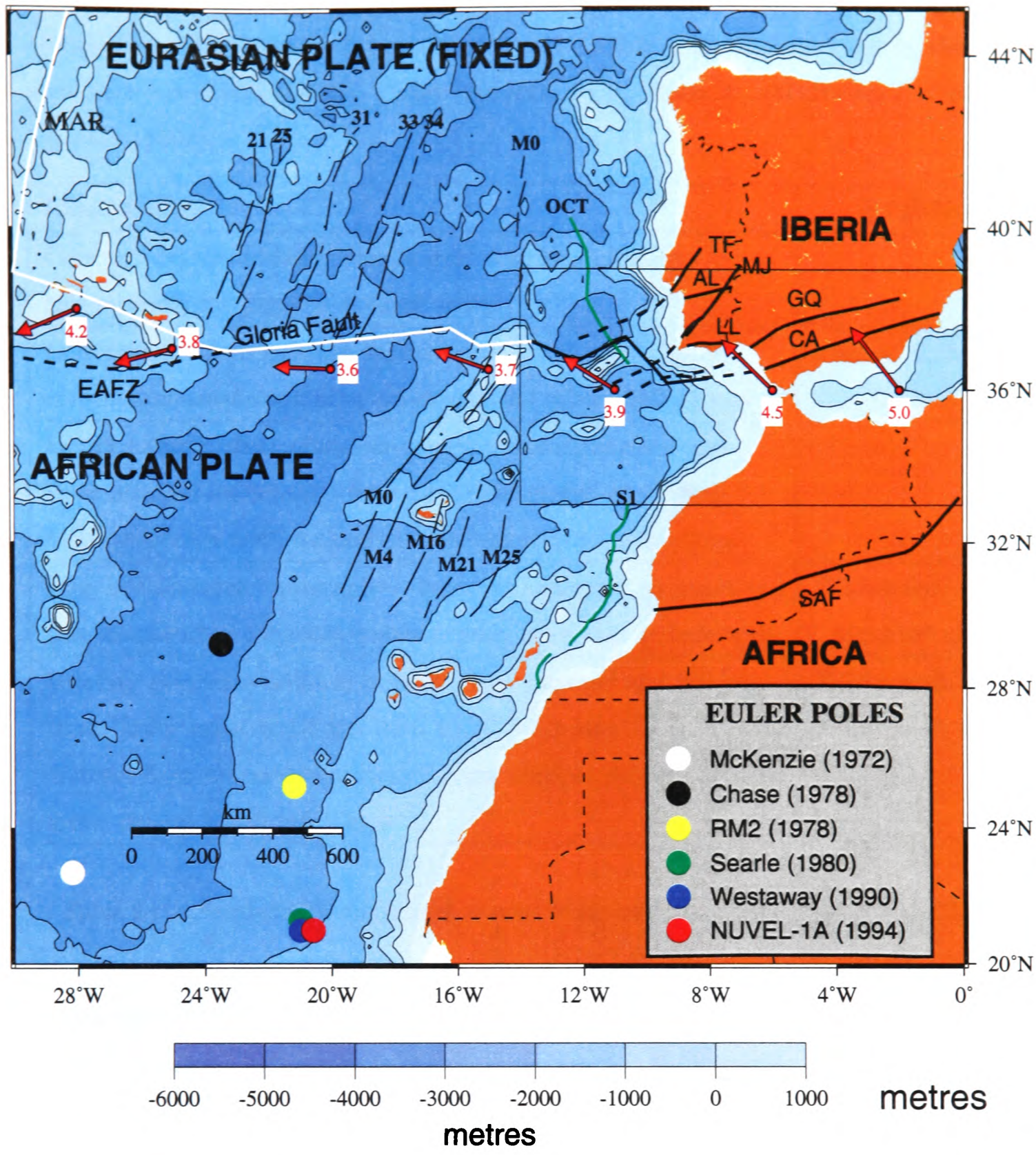


Figure 2.4: Regional tectonic map of the Azores-Gibraltar plate boundary between Eurasian and African plates in the NE Atlantic. White lines mark the current plate boundaries: MAR=Mid-Atlantic Ridge. Black lines mark major fault zones and lineations: EAFZ=East Azores Fault Zone, TF=Lower Valley of the Tagus, AL=Alandroal, MJ=Messejana, LL=Loule, GQ=Gaudalquivir lineament, CA=Crevillente (Cadiz-Alicante) fault zone, SAF=Southern Atlas Fault zone. Euler poles fromWestaway [1990]; magnetic anomalies from Srivastava *et al.* [1990]; Verhoef *et al.* [1991]; OCT=ocean-continent transition - from Mauffret *et al.* [1989]; S1 anomaly from Verhoef *et al.* [1991]. Red arrows indicate the motion of the African plate relative to a stable Eurasia, with the length of arrow and associated value by it indicating the velocity in mm/yr with respect to the NUVEL-1A pole of rotation (calculated from the model of DeMets *et al.* [1990, 1994]).

of transition, tens of kms wide. Different geophysical criteria are used for distinguishing thinned continental crust from oceanic crust (Table 2.2), and to identify the ocean–continent transition (OCT). These are outlined in Table 2.3 [Whitmarsh *et al.*, 1993; Pinheiro, 1994].



Table 2.2: Criteria for distinguishing oceanic from continental crust, from Pinheiro [1994].

The OCT is yet to be conclusively identified in the Gorringe Bank/Horseshoe abyssal plain area, where differences in the crustal structure from west to east in the Horseshoe abyssal plain have been indicated from early refraction models [e.g., Purdy, 1975]. These differences were assumed to be due to tectonic alteration of crustal structure in the EHAP (associated with its shallow seismicity). Geophysical study of the regions north and south of the EHAP, utilising criteria given in Table 2.2 and Table 2.3, gives some constraint to the OCT location in the Horseshoe abyssal plain. Magnetic lineations are shown on Figure 2.4, illustrating the difference north and south of the African-Eurasian PBZ. The oldest identified seafloor spreading anomaly west of Iberia is the 118 Ma **M0** anomaly (formerly known as the J-anomaly). This anomaly transgresses the Madeira–Tore Rise, which is believed to have a hotspot origin [e.g., Peirce & Barton, 1991], indicating that the Rise formed at the same time as the surrounding ocean floor. The OCT indicated on Figure 2.4, from Mauffret *et al.* [1989], is landward of the **M0** anomaly and is in approximate agreement (at this regional scale) with subsequent estimates of the OCT location by Whitmarsh *et al.* [1990, 1993]; Pinheiro *et al.* [1992]; Pinheiro [1994] (Figure 2.5).

Table 2.3: Criteria used to locate the Ocean-Continent Transition (at non-volcanic rifted margins such as W. Iberia). Taken from Whitmarsh *et al.* [1993].

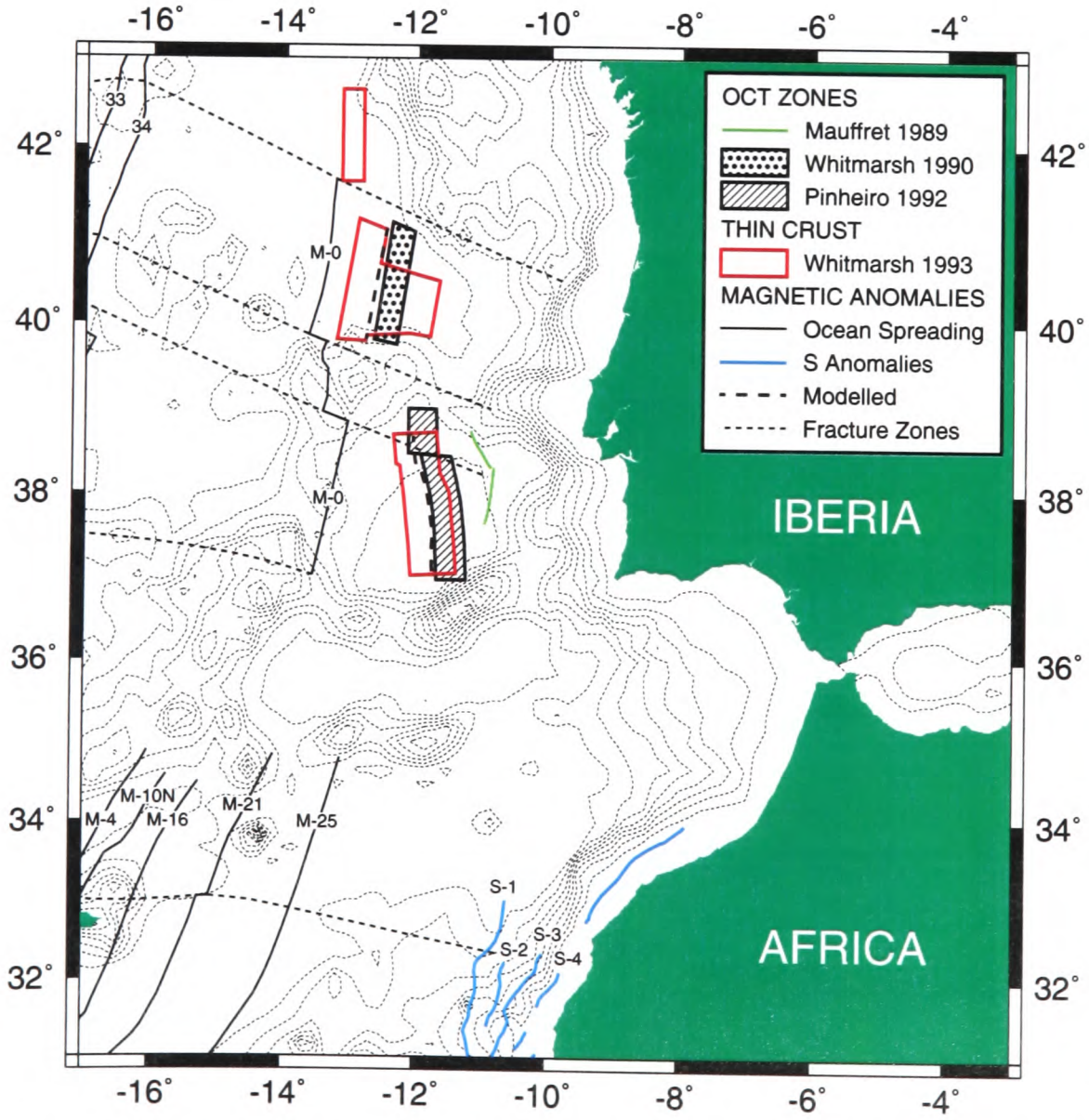


Figure 2.5: Location of the Ocean-Continent Transition zone (OCT) seaward of Iberian and North African margins. Red boxes show the possible extent of thin crust underlain by serpentinised peridotite [Whitmarsh *et al.*, 1993]. Figure after Hayward [1996].

To the south of the Horseshoe abyssal plain, off the west coast of North Africa, the oldest magnetic spreading anomaly is the **M-25** anomaly (~156 Ma). However, the eastern boundary of oceanic crust is believed to be marked by the **S1** anomaly. This also corresponds to the eastward extent of a series of salt diapirs [Roeser, 1982; Hinz *et al.*, 1982]. The salt diapirism is related to the presence of evaporites laid down during early rifting and subsidence, and is found around the North Atlantic margins [Pautot *et al.*, 1970]. Between the **S1** and **M-25** anomalies is an area of uniform magnetisation called the Jurassic Magnetic Quiet Zone (JMQZ). The OCT off Africa is marked as the **S1** anomaly on Figure 2.4, which is only one of a group of anomalies on the African margin (Figure 2.5). However, seismic experiments showed that anomalies S2 to S4 east of S1 lie on continental lithosphere [Roeser, 1982], whereas the S1 anomaly is oblique to the African margin and thought to be related to the initial rifting of Africa and North America [Roeser, 1982; Roest *et al.*, 1992].

On the basis of magnetic anomalies, and the criteria given in this section, the crust underlying the Gorringe Bank Region is likely to be oceanic and that under the Gulf of Cadiz is likely to be continental (Figure 2.5). The Alboran Sea is known to be underlain by thin continental crust[Comas *et al.*, 1992; Watts *et al.*, 1993].

2.2 The Gibraltar Arc and Betic-Rif Orogenic Belt

2.2.1 Introduction

The Betic Cordillera of southern Spain and the Rif Mountains of Morocco join across the Straits of Gibraltar to form an arcuate mountain belt (the Gibraltar Arc) surrounding the Alboran Sea at the western end of the Mediterranean. Similar geometries are found in several cases where arcuate mountain belts surround Neogene sedimentary basins in the Mediterranean (Figure 2.6). These basins formed in a convergent setting between African and Eurasian plates in late Oligocene–Miocene times, on the sites of Late Cretaceous to Tertiary Alpine mountain belts. Characteristically, the basins are floored by stretched continental crust but oceanic crust is present beneath parts of the Ligurian and Tyrrhenian basins (Figure 2.6).

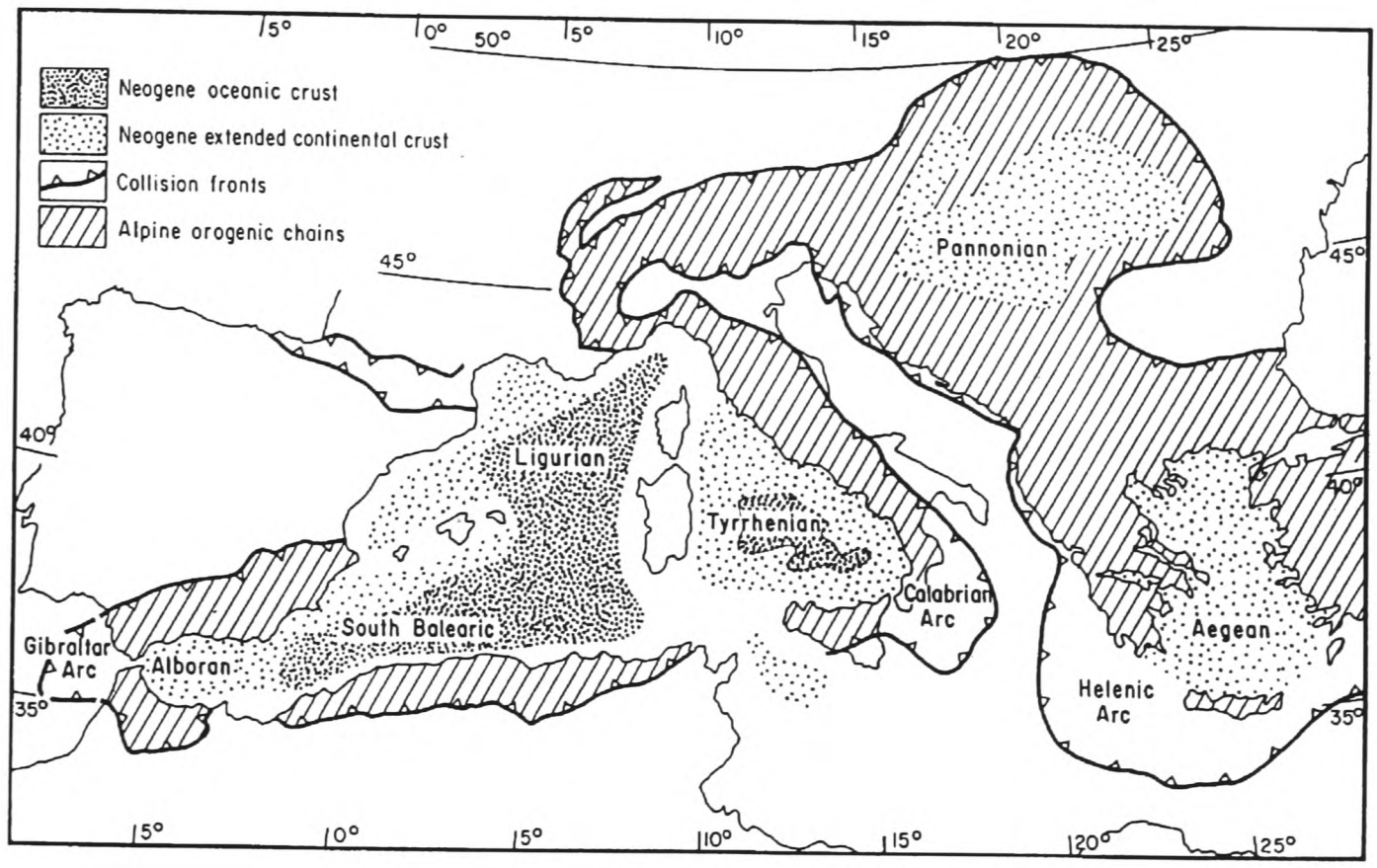


Figure 2.6: Tectonic map of the Mediterranean showing the arcuate belts of the Alpine mountain chain and Neogene basins.

Extensional basins associated with convergent plate boundaries are found in the western Pacific and in the Mediterranean [Lonergan & White, 1997]. However, whereas the Pacific basins are often clear cut cases of back-arc extension through subduction rollback, this is not the case for the Alboran Sea basin, where geophysical evidence has led to the proposal of several formative mechanisms, which are still under debate.

2.2.2 Geological Units



Figure 2.7: Simplified geological map of the Gibraltar Arc, Betic-Rif orogenic belt and Alboran Sea. From Stromberg & Bluck [1998], modified after Platt & Vissers [1989].

The Betic and Rif Cordilleras have commonly been divided into Internal Zones, External Zones and Flysch nappes, as shown on Figure 2.7. The **External Zone** of the **Betics** is made up of non-metamorphic Mesozoic–Tertiary sediments deposited in basinal (Subbetic) and shelf (Prebetic) environments on the former Southern Iberian Margin of the Tethyan Ocean [Vissers *et al.*, 1995; Vera *et al.*, 1997]. Northwest-directed, thin-skinned thrusting and deformation through the Miocene strongly shortened these rocks [e.g., Garcia-Hernandez *et al.*, 1989; Banks & Warburton, 1991; Allerton *et al.*, 1993]. Thrusting and shortening led to flexural loading of Iberian lithosphere and the development of the Guadalquivir foreland basin ahead of the thrust front. The **Internal Zone** to the south is made up of Palaeozoic and Mesozoic rocks, penetratively deformed to various metamorphic grades. These rocks are now exposed in elongate ridges 15-30km wide, parallel to the general trend of the belt, and separated by intramontane basins containing Neogene-Recent sediments.

In the **Rif**, the **Internal Zone** contains metamorphosed rocks similar to those in the corresponding part of the Betics, and the **External Zone** is made up of Mesozoic–

Tertiary sediments deposited on the North African margin. The Gibraltar Arc Flysch Zone (Figure 2.7) is made up of allochthonous thrust sheets (nappes), containing mostly Early Cretaceous–Early Miocene deep marine clastics, found between the Internal and External Zones at either side of the Gibraltar Straits. In the early Miocene, the Rifian External Zone was thrust onto the Flysch, and, with continued convergence through the Miocene, the External Zone deformed as a thin-skinned fold-and-thrust belt [e.g., Andrieux *et al.*, 1971; Morley, 1993] like its Betic counterpart.

The Internal Betic-Rif Zones are considered part of the Alboran Domain, most of which underlies the Alboran Sea, which is known to be underlain by thin continental crust of a suite of metamorphic rocks similar to those found in the Internal Zones onshore [Comas *et al.*, 1992; Platt *et al.*, 1996]. The current Alboran Sea area was a Mesozoic marine basin that closed progressively in the Tertiary such that in the Oligocene an emergent collisional orogen stood in its place [Platt & Vissers, 1989]. Early to mid-Miocene extension and subsidence created the present-day Alboran Sea Basin, and smaller onshore basins [Watts *et al.*, 1993], accompanied by volcanism [Hernandez *et al.*, 1987]. At the end of the Tortonian, the whole region was composed of elongate mountainous islands surrounded by marine basins; from the Messinian a regional transpressional regime prevailed [Watts *et al.*, 1993], and the Betic-Rif was uplifted while the Alboran Sea subsided [Vissers *et al.*, 1995].

2.2.3 Key observations

A brief summary of the major geological and geophysical observations that a model for the formation of the Gibraltar Arc should satisfy is given below.

- Extension of the Alboran Domain and Internal Zones, coeval with radial outward thrusting around the Betic-Rif arc, within an overall environment of plate convergence.

- Westward displacement of the Internal zones by 100-200 km in the early to middle Miocene, and their rapid exhumation during the same period [e.g., Lonergan & Mange-Rajetsky, 1994; Zeck, 1997].

- Presence of graphite-pseudomorphed diamonds in peridotite bodies, which represent tectonic allochthonous slices of mantle rocks within the Internal Zones of the Gibraltar Arc, indicating a mantle origin at 150-200 km [Davies *et al.*, 1993; Zeck, 1997].

- Thinning of previously thickened continental crust to form a deep sedimentary basin underlain by thinned continental crust. Modelling of wide-angle data indicates that crustal thickness decreases from 40km at the Betic Internal-External boundary to ~15km in the central Alboran Sea [e.g., Torne & Banda, 1992].

- From palaeomagnetic studies, post-Oligocene block rotations of 130° clockwise [e.g., Platzman, 1992; Allerton *et al.*, 1993; Platt *et al.*, 1995] of thrust sheets in the Betic External Zone, and of ~100° anticlockwise [Platzman *et al.*, 1993] in the Rif.

- Regional metamorphism that locally reached very high temperatures

- Basaltic dike swarms in the central and western Betics, dated at ~22 Ma (K/Ar), representing the earliest igneous activity [Torresroldan *et al.*, 1986].

- Substantial Serravallian to Pliocene calc-alkaline volcanism in SE Spain, eastern Morocco and east of 3° W in the Alboran Sea Basin [Hernandez *et al.*, 1987].

- Three deep (600km plus) earthquakes beneath SE Spain, with steeply east–dipping P-axes [Buforn *et al.*, 1991], possibly indicating a cold, detached slab of subducted lithosphere [e.g., Lonergan & White, 1997].

2.2.4 Models of Formation

The seeming geological paradox of simultaneous extension and shortening observed in the Gibraltar Arc has led to the proposal of many geodynamic models for its evolution. Figure 2.8 presents all the main models to date in cartoon form. Theories include **curved indenter** models (Figure 2.8B) involving westward motion of an Alboran microplate [Andrieux *et al.*, 1971; Kampschuur & Rondeel, 1975; Leblanc & Olivier, 1984; Bouillin *et al.*, 1987; Leblanc, 1990; Degaldeano, 1990]; **oroclinal bending** models, where an originally linear mountain chain is tectonically curved [Carey, 1958; Tubia & Cuevas, 1987]; and **mantle diapirism and gravitational nappe shedding**, (Figure 2.8A.b) where a rising mantle diapir would cause doming of the lithosphere and nappe shedding, followed by thermal contraction and subsidence in the Alboran region [Didon, 1977; Dubourdieu, 1964; Weijermars, 1985a,b]. However, these models, as well as those involving traditional subduction, have largely been discounted because they fail to account for some or most of the observations listed in the previous section. The remaining contenders may be divided into two camps: those models involving **convective removal or delamination** (Figure 2.8A.d and A.f), and those invoking **subduction roll-back** (Figure 2.8A.c and Figure 2.8C). These models attempt to explain observations from seismicity studies, where Grimison & Chen [1986] had inferred a fragment of detached lithosphere from their

teleseismic earthquake study, and a clear NE-SW positive velocity anomaly 200-600km below the Alboran Sea had been observed from seismic tomographic studies [Blanco & Spakman, 1993].



Figure 2.8: Cartoons illustrating various mechanisms proposed for the formation of the Gibraltar Arc Betic-Rif-Alboran system. **A** is an illustration in cross-section of processes that have been invoked for the formation of the Gibraltar Arc (after Calvert, pers. comm.); **B** illustrates the indenter model from Andrieux *et al.* [1971]; and **C** illustrates the subduction rollback model, where a) is before rollback, b) after rollback and c) plan view showing coeval thrusting and extension plus block rotations (from Lonergan & White [1997])

Several workers [e.g., Dewey, 1988; Platt & Vissers, 1989; Doblas & Oyarzun, 1989] have proposed that the Betic-Rif-Alboran system formed through gravitational extensional

collapse driven by rapid convective removal of part of, or delamination of the whole of, previously thickened lithospheric mantle [Houseman *et al.*, 1981; England & Houseman, 1986], in a manner similar to that thought to be responsible for the Tibetan Plateau. This **extensional collapse** model has subsequently been further developed [e.g., Platzman, 1992; Mandeville, 1993; Vissers *et al.*, 1995; Mezcua & Rueda, 1997]. The main problems with these models are that shortening occurs on only three sides of the Gibraltar Arc, but the free eastern side of the Alboran Sea is not accounted for [Lonergan & White, 1997], nor are the large block rotations in the Betic and Rif inferred from palaeomagnetic studies. Willet [1996], observing that the Alboran Basin has a complex structure and a diachronous extensional history, proposed a hybrid model with an initial deblobbing, followed by delamination of lithosphere peeling away to the SW.

Subduction zone roll-back occurs where old oceanic crust is being subducted into warmer, less dense mantle. The subducting slab then retreats from the subduction zone as its front edge is pulled downwards into the mantle, thus generating and maintaining back-arc extension (Figure 2.8A.c and Figure 2.8C). Many workers have invoked this mechanism together with delamination of the lithosphere [e.g., Frizon De Lamotte *et al.*, 1991; Garciaduenas *et al.*, 1992; Royden, 1993b,a; Morley, 1993], or with slab breakoff and detachment [e.g., Zeck, 1996, 1997; Lonergan & White, 1997; Carminati *et al.*, 1998a,b]. Delamination or slab sinking allows upwelling of hot asthenospheric mantle, which causes initial uplift and erosion followed by cooling and subsidence to produce a large sag basin, such as the Western Alboran Basin [Morley, 1992, 1993]. Some authors [e.g., Royden, 1993b,a; Morley, 1993; Lonergan & White, 1997] suggest that extensional collapse alone cannot generate sufficient thermal decay to generate such a thick sag basin. Lonergan & White [1997] suggest that, as shortening and extension had ceased in Betic External zones and Alboran Sea respectively by the end of the Tortonian, west-ward rollback occured in the Alboran Sea between 23 – 10 Ma, and the slab was stopped by continental crust at the Straits of Gibraltar.

2.3 Geological Development of the Study Region

The evolution of the study region is largely coupled to the complex spreading history of the North Atlantic Ocean, and the interaction between the North American (NA), Eurasian (EU) and African (AF) plates. The magnetic anomaly record of the North Atlantic has allowed plate reconstructions to be made, giving an insight into the relative motion of these plates through time [e.g., Klitgord & Schouten, 1986; Dewey *et al.*, 1989; Ziegler, 1989; Srivastava *et al.*, 1990; Roest & Srivastava, 1991; Olivet, 1996]. The plate reconstructions give insight into the regional development through time, as described below. Figure 2.9 shows plate reconstructions for the North Atlantic [Srivastava *et al.*, 1990] from the Late Jurassic to the Miocene (chron M-25 to chron 6), and Figure 2.10 correlates chrons, ages and relative motions of Africa with respect to Eurasia from the Triassic onward [Dewey *et al.*, 1989].

Breakup of Pangea and the Mesozoic Margins

Plate reconstructions, such as that of Ziegler [1989], indicate that in the Triassic, the study region was part of the Tethys-related rift systems. Pangea breakup led to Late Triassic rifting and associated basic volcanism, and the subsequent formation of the margins of southern Iberia and north Africa [Heymann, 1989]. The rifting between the North American and African plates (opening of the Central Atlantic) began at about 175 Ma [Klitgord & Schouten, 1986], with the Central Atlantic Ridge ending at the Gloria Transform Fault, a major tectonic boundary in the early Mesozoic that was probably connected with the deep oceanic basins of the Tethys to the east. Extension between Iberia (IB) and the Grand Banks of North America commenced in the Late Jurassic at anomaly **M-25** (156 Ma) (Figure 2.9a).

The former Mesozoic Southern Iberian passive margin has largely been incorporated into the present-day External Zones of the Betics, but is still preserved beneath the eastern Gulf of Cadiz and in the Algarve Basin of southern Portugal. Workers studying the External Betics in SE Spain [e.g., Garcia-Hernandez *et al.*, 1980; Rey, 1998] have found evidence for a Jurassic rifting event from Pleinsbachian (190 Ma) to late Callovian (157 Ma). Rey [1998] has suggested that periods of increased subsidence in the early-mid Jurassic were related to opening of the southern North Atlantic, and Peper & Cloetingh [1992] also considered that phases of rapid subsidence co-incided with Atlantic transtensional tectonics.

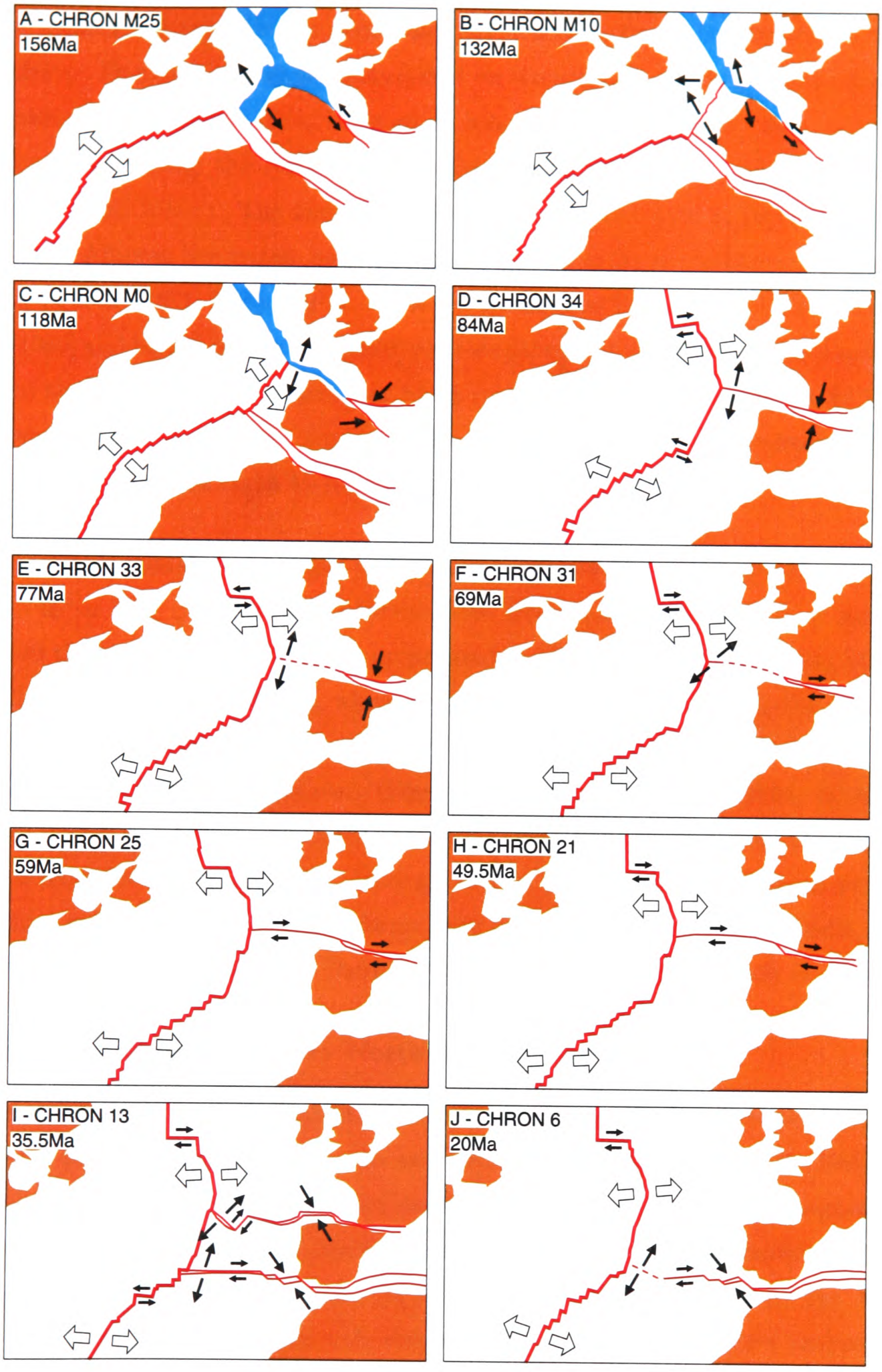


Figure 2.9: Plate reconstructions of North American and Iberian plate motions relative to a fixed Eurasian plate from chron M25 to chron 6. Motions along boundaries from previous times are shown as small arrows, while relative motion is indicated by large arrows. Blue shaded areas are plate overlaps implying later extension in those regions. [After Srivastava *et al.*, 1990]

During the Late Jurassic to Early Cretaceous, anomaly M-25 to M-0 (156-118Ma), central Atlantic spreading led to major sinistral strike-slip translation between Laurasia and Africa. This motion was accommodated on wrench-induced deep crustal fractures [Laughton & Whitmarsh, 1974; Klitgord & Schouten, 1986; Ziegler, 1989], with plate boundaries separating the North African and Iberian margins as well as Iberia from Eurasia (Figure 2.9a-c). The major transcurrent fault zone south of Iberia ran though the present Alboran Sea region, and may have extended as far as the Gorringe Bank area [Andrieux *et al.*, 1971; Feraud *et al.*, 1986]. In the eastern Tagus abyssal plain, Mauffret *et al.* [1989] and Malod & Mauffret [1990] propose the presence of an abandoned spreading ridge at the ocean continent transition, which corresponds to an age of chron M-21 (150 Ma), and which subsequently jumped to the west in the earliest Cretaceous, between chron 16 (142 Ma) and chron M-10 (130 Ma).

The western continental margin of Iberia is a non-volcanic rifted margin extending from N43° to N37°, formed when Iberia rifted from North America. It is generally accepted that sea-floor spreading has propagated northwards along this margin based on modelling of magnetic anomalies, which decrease in age northwards from 137 Ma in the Tagus abyssal plain [e.g., Pinheiro, 1994; Whitmarsh & Miles, 1995] to 130 Ma (M10 anomaly) in the Iberian abyssal plain (Figure 2.9b) [Whitmarsh *et al.*, 1993; Whitmarsh & Miles, 1995]. In addition, drilling of the Galicia Bank yields a 114 Ma age for a breakup unconformity [Boillot *et al.*, 1987]. During this late Jurassic-early Cretaceous period, a spreading axis and associated transforms were present near the Gulf of Cadiz, and a triple junction near the Gorringe Bank region (Figure 2.9b-c) [Maldonado *et al.*, 1999].

Cretaceous and early Tertiary North Atlantic spreading

The opening of the North Atlantic through the Cretaceous and Tertiary led to the rotational divergence of North America away from Eurasia [Srivastava *et al.*, 1990]. The Iberian plate remained independent for most of the mid-Cretaceous: paleomagnetic evidence indicates that Iberia had rotated some 30° anti-clockwise with respect to Eurasia between chron M-10 and chron M-0 [Galdeano *et al.*, 1989], dragged by the African plate during its eastward motion with respect to Europe. Sometime after anomaly MO (118Ma), the relative plate motion of Africa with respect to Eurasia became NE-oriented convergence instead of E–W oriented strike-slip (Figure 2.10). Sometime before chron 34 (84 Ma) the plate boundary between Iberia and Africa jumped northwards to the Bay of Biscay (Figure 2.9d), which experienced extensional tectonics due to the continuing rotation of Iberia. The exact timing of these events is difficult to discern because of the absence of magnetic anomalies between chrons M0 and 34 (Cretaceous Magnetic Quiet

Zone). Multichannel seismic data in the EHAP indicate Jurassic sediments below a major reflection that represents a pre-Aptian angular unconformity [Mauffret *et al.*, 1989; Sartori *et al.*, 1994; Hayward *et al.*, 1999].

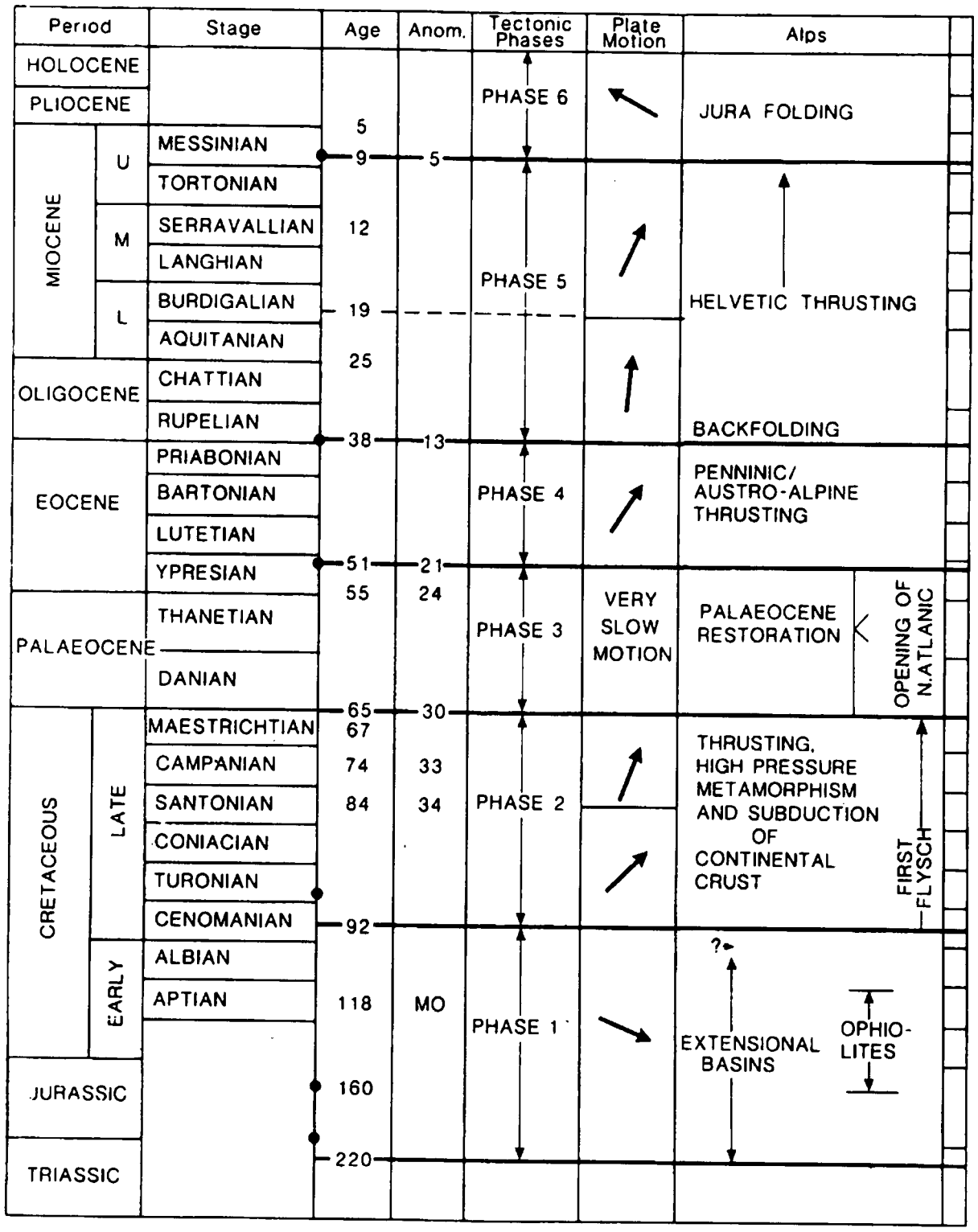


Figure 2.10: Correlation chart showing general direction of the motion of Africa with respect to Europe, after Dewey *et al.* [1989].

The Bay of Biscay plate boundary was the main Africa-Eurasia plate boundary from chron 34 (84 Ma) to chron 17 (40 Ma) [Roest & Srivastava, 1991]. Chron 34 (84 Ma) to chron 31 (69 Ma) (Figure 2.9f) saw extensional motion on this boundary, followed by extension with an increasing strike slip component until chron 25 (59 Ma) when motion became largely strike slip (see small arrows around triple junction on Figure 2.9d-g).

Iberia became independent once more in the mid-Eocene at chron 18 (42 Ma), with the formation of two new plate boundaries (Figure 2.9i), and remained independent until chron 6c (20Ma) [Roest & Srivastava, 1991]. The northern boundary extended from the King's Trough (Figure 1.2) to the Pyrenees, and to the south the transforms along the Gloria Fault zone passed through the convergent GBR in an arrangement similar to the present-day Azores-Gibraltar fracture zone (AGFZ). Compression in the Pyrenees region led to the Pyrenean orogeny between 30-35 Ma [Roest & Srivastava, 1991]. Throughout the mid-Eocene to late Oligocene, motion of Africa with respect to Eurasia proceeded in a N-NE direction (Figure 2.10), which meant that by the end of the Oligocene the oceanic crust of the Neo–Tethys in the western Mediterranean had been completely subducted and replaced by an emergent collisional belt as part of the Alpine orogenic process [Dewey *et al.*, 1989; Platt & Vissers, 1989]. Between chrons 18-13 (42-35 Ma), the compressional regime east of Gorringe Bank resulted in significant shortening in the GOC [Maldonado *et al.*, 1999], with regional uplift reflected in the major Early Eocene–Late Oligocene unconformity seen at DSDP Site 135 [Hayes *et al.*, 1972] and in the Ampere-Coral Patch area [e.g., Hayward, 1996].

Late Cenozoic evolution

The African–Eurasian plate boundary jumped to its present position along the AGFZ when Iberia became part of the Eurasian plate at chron 6 (20 Ma) (Figure 2.9j). Plate motions along the AGFZ have since been extensional near the Azores, right lateral slip along the Gloria Fault and compressional in the Gorringe Bank – Alboran Sea region, causing crustal shortening. According to Dewey *et al.* [1989], the GOC-ABS area experienced some 200km of N-S shortening between mid-Oligocene to late Miocene times, and 50 km of NW-directed oblique convergence since the late Miocene (Figure 2.10). In the GBR, a shortening rate of $\sim$11 mmyr^{-1} over the past 10 Ma was estimated by Purdy [1974, 1975], giving some 110 km of shortening since the Tortonian. The present day shortening rates are 4-5 mmyr^{-1} across the study area (Figure 2.4).

Apart from causing the progressive closure of the Neo–Tethyan basins, the northward drift and anticlockwise rotation of Africa with respect to Eurasia caused the rapid westward propagation of the Gibraltar Arc (GA) [Balanya & Garciaduenas, 1987]. The Gibraltar Arc is a major tectonic feature in the study region, with the Betic-Rif fold-and-thrust belts comprising the two arms of this highly arcuate, Alpine orogenic belt. The Betic-Rif chains and the Alboran Domain they enclose represent the fragments of an interplate collisional belt formed through the compressional regime prevalent across the study region from the late Cretaceous to late Miocene [e.g., Dewey *et al.*, 1989;

Platt & Vissers, 1989; DeJong, 1990; Garciaduenas *et al.*, 1992]. In the Lower Miocene (Aquitanian-Burdigalian), rifting and creation of new oceanic crust gave rise to the Western Mediterranean Sea. The Alboran Sea developed as a type of Mediterranean back-arc basin [e.g., Comas *et al.*, 1992; Morley, 1993; Lonergan & White, 1997]. The Alboran Domain and adjacent Internal Zones are known to have undergone significant crustal thinning [Platt & Vissers, 1989; Watts *et al.*, 1993; Docherty & Banda, 1995; Seber *et al.*, 1996] coeval with radial thrusting in the External Zones of the Betic and Rif Cordilleras. Radiometric dating and stratigraphic provenance studies demonstrate that metamorphic rocks in the Betic Zone have been rapidly exhumed and cooled in the period from 23-15 Ma (earliest-mid Miocene), coeval with extension [e.g., Zeck *et al.*, 1992; Lonergan & Mange-Rajetsky, 1994]. The possible mechanisms for generating late orogenic extension within the Gibraltar Arc have been a topic of much discussion in recent years [e.g., Lonergan & White, 1997]. The Guadalquivir and Rharb Basins (Figure 1.3) are the Neogene foreland basins to the Betic and Rif orogens respectively, and have formed in response to loading by the advancing fold-and-thrust belts of the Arc.

West of Iberia, Gorringe Bank and Ampere-Coral Patch seamounts formed in response to the Neogene convergence across the GBR (Figure 1.3). Recent broken plate flexure gravity modelling over the Gorringe Bank [Hayward, 1996; Hayward *et al.*, 1999] suggest that the Gorringe Bank is the result of the overthrusting of a portion of the African plate onto the Eurasian plate, which has then partially supported the African plate through lithospheric flexure below the Tagus Abyssal Plain. The timing of overthrusting was mid-Miocene (approximately 10 Ma), identified from correlation of the unconformity between pre- and post-loading sediments in the Tagus Abyssal Plain [Mauffret *et al.*, 1989].

Quaternary to Recent Tectonics

Present-day kinematics along the AGFZ plate boundary region are complex (Figure 2.4) and from W to E can be summarised as a) transtensional in the **Azores** section ; b) dextral strike-slip along the Gloria Transform Fault of the **Central** section (24–18° W; c) distributed/diffusely compressional at the GBR, and transpressional in the GOC and Gibraltar Arc region [e.g., Westaway, 1990; Sartori *et al.*, 1994; Meghraoui *et al.*, 1996].

Diffuse seismicity, with no Benioff plane, and enormous gravity anomalies over the Gorringe Bank and Ampere-Coral Patch Seamounts characterise the study region which lies east of the Madeira-Tore Rise (MTR in Figure 1.2), whereas to the west, seismicity is very localized (Figure 2.3), suggesting a definite change in tectonic style. The increasingly complex patterns of seismicity and distributed deformation observed in the study region

relate to the change in nature of colliding lithosphere, from ocean-ocean near Gorringe Bank to continent-continent further east, with the superimposed radial deformation due to tectonic transport around the Gibraltar Arc. A zone of deformation 50-100km wide, from Gorringe Bank across the southern Alboran Sea Basin and Tell Atlas mountains, is thought to form the PBZ (equivalent to the GALTEL zone of Meghraoui *et al.* [1996]).

In summary, active but slow interplate convergence has taken place across the study region since the Oligocene, with the entire region currently in an approximately NW-SE orientated compressive regime. The Alpine Betic-Rif-Gibraltar Arc is incorporated into a broad region of compression, but encloses the extensional Alboran Sea Basin. The present-day convergence rate of Africa with respect to Eurasia at the study region is calculated to be 4 $mmyr^{-1}$ to the NW at the GBR and 5 $mmyr^{-1}$ at the ABS, in the most comprehensive NUVEL-1A kinematic model [DeMets *et al.*, 1990, 1994].

Chapter 3

Multichannel Seismic Data Acquisition and Processing

3.1 Introduction to The Iberian Atlantic Margins (IAM) Dataset

During the latter part of 1993, 3800 km of near-vertical seismic 2D reflection data were collected offshore Spain and Portugal by the Iberian Atlantic Margins (IAM) group, aboard the vessel M/V Geco-Sigma [Banda *et al.*, 1995]. The profiles of the IAM Project are shown in Figure 3.1, although IAM-12 was collected during a previous survey. The seismic survey utilised a very large, 116 litre volume airgun array, and a 5 km long streamer of 192 channels, resulting in high quality images. The acquisition of the marine geophysical data is described in Section 3.2. Land recording was carried out for some profiles, excluding IAM-4, GB1, GB2, GB3. Ocean bottom seismometers (OBS) were deployed for profiles 5, 6 and 2W. In this study, seismic profiles from the Gulf of Cadiz to the Eastern Horseshoe Abyssal Plain were used, namely those lines between 35–37°N and 347–354° in longitude (Figure 3.1).

Onboard processing tests were carried out during acquisition for quality control purposes. Noise problems, such as low frequency swell-generated noise due to rough weather, or the contamination of near traces by coherent water column noise (probably due to internal reflections from temperature/salinity stratification), were identified at this stage, and solutions recommended for further processing [Torne *et al.*, 1993].

The IAM seismic data acquired was commercially processed by GECO-PRAKLA Ltd after the cruise, using standard processing techniques [Yilmaz, 1987]. Filtered stacks of the IAM profiles were released by GECO-PRAKLA Ltd in late 1995. The final commercial processing scheme to stack adopted was: reformat to SEGY, bandpass filter, resample to 8 ms, trace edit, trace equalisation, sum adjacent traces, CDP gather with 25m bin and 32 fold, spherical divergence correction, deconvolution, fk demultiple, nor-

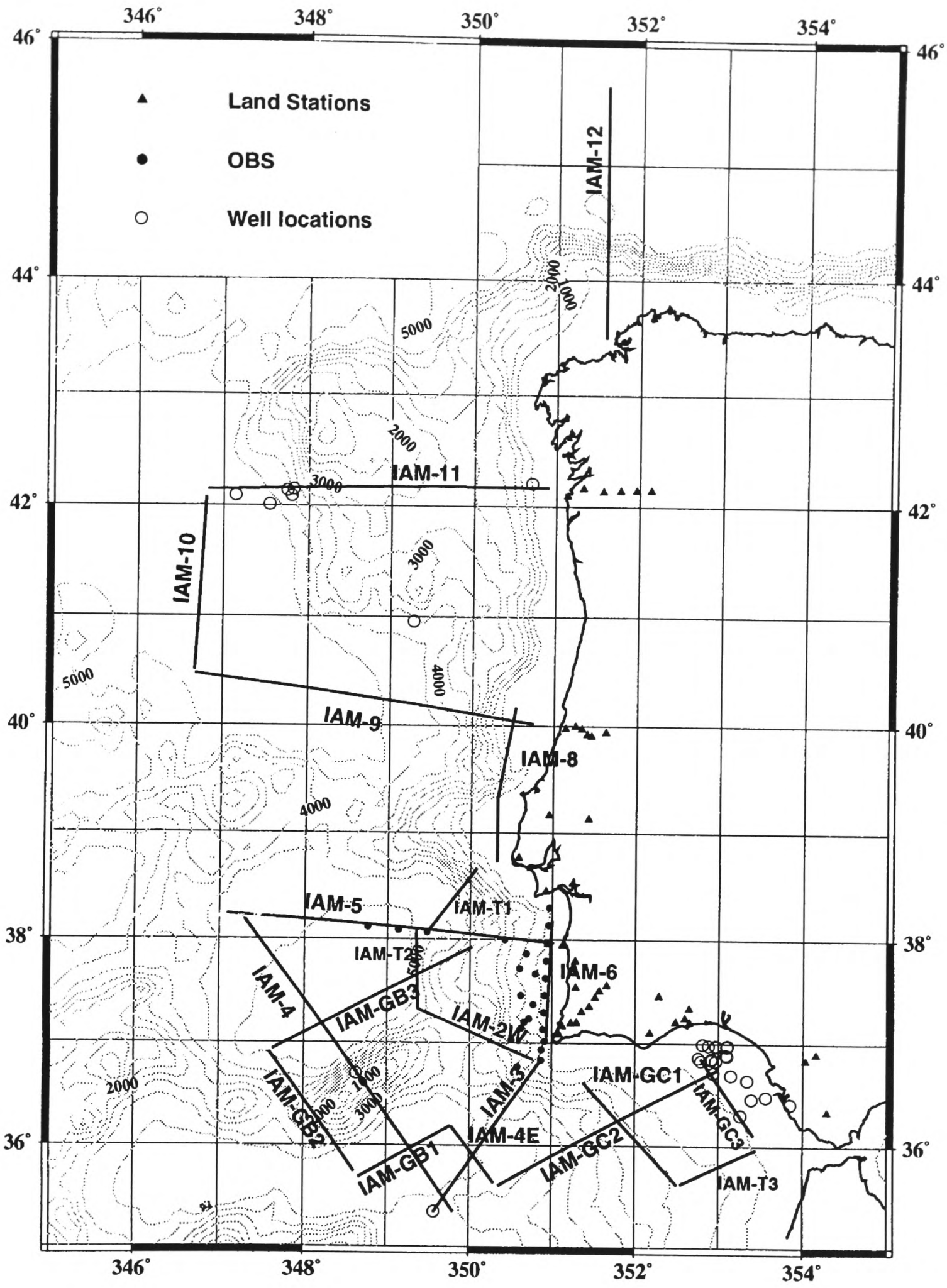


Figure 3.1: Location of all IAM Project track lines and recording land stations and OBS.

mal move-out correction, front end and inner trace mute, spherical divergence correction using stacking velocity field to replace initial correction, CDP stack, noise attenuation,

time and space variant bandpass filter. Constant–velocity migrated stacks of the IAM profiles were released in 1996.

Prior to the release of commercially processed stacks, some processing of IAM shot data had been carried out on IAM data in academic institutions. For example, in a seismic study of sediments of the Tagus abyssal plain at Imperial College, London, Chowdhury [1994] produced a filtered and stacked profile from shotgathers from the northernmost 30 km segment of profile IAM-4 (Figure 3.1). The major findings of this study were that seismic stacking velocities were reasonably invariant along a sequence of abyssal plain sediments, and that the IAM profile was successful in imaging a diffractive basement, and an intra–basement dipping reflection down to 11 s TWTT. Some processing of shotgathers was also carried out at Oxford University, from upper continental slope profile GC3 and deep–water profile IAM-4, to look at problems of noise, multiples and velocity analysis. The steps in commercial processing to stack, and additional work done at Oxford, are summarised in Section 3.3.

The commercially processed GECO filtered and migrated stacks were not successful at imaging deep reflectivity because of the prevalence of noise on the profiles, and poor lateral coherency of reflections at depth. The top of basement was difficult to pick, particularly in the more shallow–water profiles in the Gulf of Cadiz and interpretation was restricted to the upper 4 s TWTT, as seen in the GECO profiles published in Tortella *et al.* [1997] (GC1-GC3). Because of the large volume of IAM data, it was not practicable to reprocess the entire dataset. Thus, after the release of commercial stacks, further work was concentrated on post–stack processing to produce the best possible images for interpretation, concentrating on noise reduction and the enhancing of deeper events, including the Moho. Post-stack work was carried out at Oxford University using the Advance geophysical processing package Promax Version 6.0 on a Sun Sparcstation 20 platform, as well as at Cambridge University, under the auspices of BIRPS, where Promax Version 5.1 was available on a Sparcstation 2. Different post-stack filtering and migration algorithms were tested in order to improve the profiles, and these are described in Section 3.4.

3.2 Acquisition of IAM Data

3.2.1 Navigation

The onboard NORSTAR integrated navigation system on the *R/V* Geco Sigma utilised the Skyfix Differential GPS system with a Trimble 4000DL receiver as its primary navigation tool, with secondary backup from Transit satellites and a Magnavox receiver. The

Global Positioning System (GPS) network utilised 24 satellites, with a coverage of at least four satellites guaranteed. The reference station for corrections was Cadiz, with the secondary system using corrections from Aberdeen or Rome. The two GPS receivers on board were interfaced such that the primary system would output data when differential signals came in, whereas if this were not the case the secondary system would output raw GPS.

3.2.2 Acquisition of Seismic Reflection Data

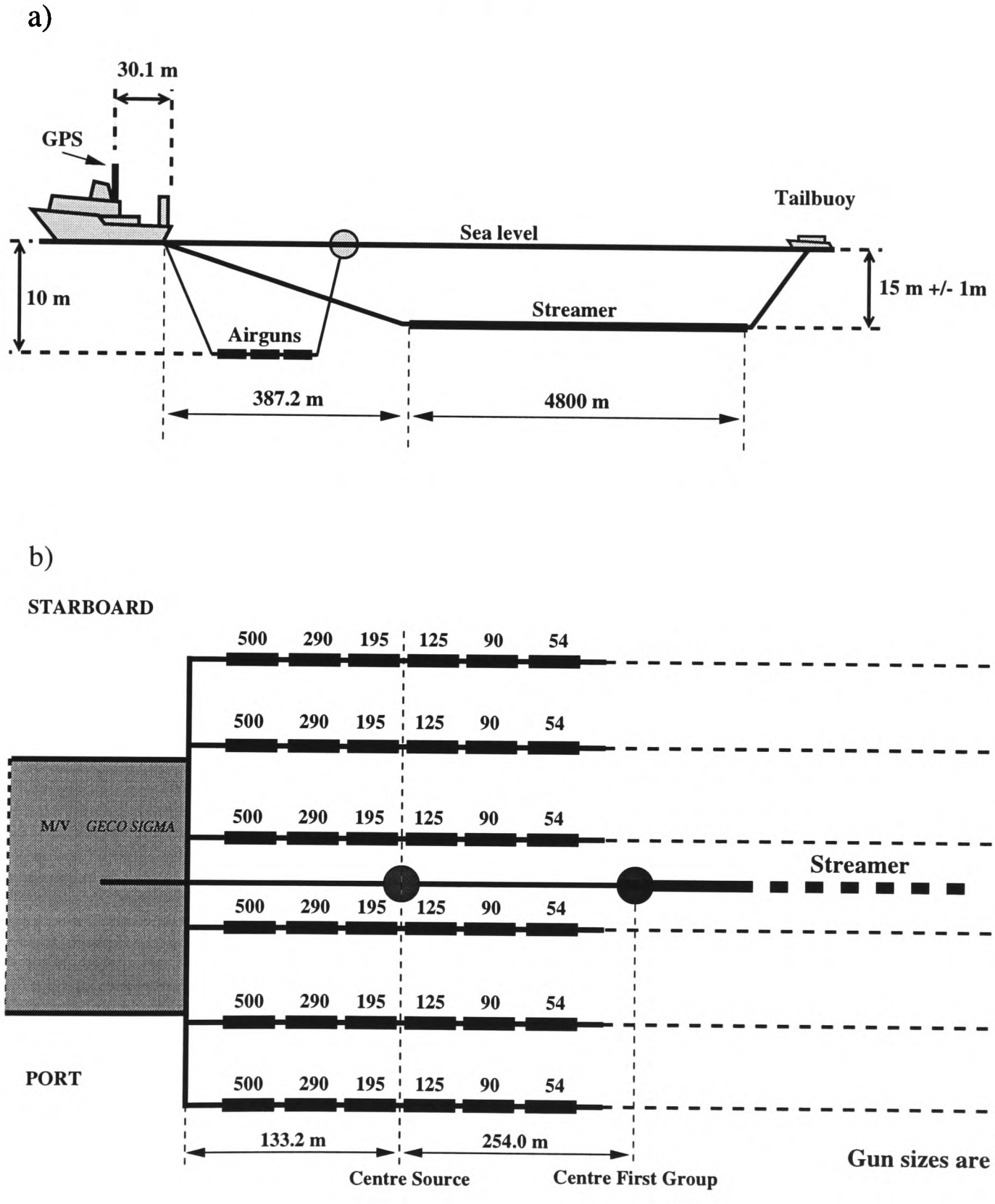


Figure 3.2: a) A schematic diagram of the seismic acquisition geometry used in the IAM cruise. b) Airgun array configuration.

The streamer geometry used in IAM data acquisition is shown in Figure 3.2a: an active 4.8km section of 192 channels organised in 25m groups. It was towed deep at $\sim$ 15m depth, to reduce surface noise and noise from turbulence from the preceding gun array. As attenuation results in little energy being returned from the lower crust at frequencies greater than 35 Hz [Scheirer & Hobbs, 1990], a 4ms sampling interval was acceptable [Hobbs & Snyder, 1992]. Incoming data was recorded at 4ms sample rate by a DFSV recording instrument and written directly to demultiplexed SEGD format on 360 Mbyte seismic data cartridges. Data was recorded to 25s, with a high-cut of 90Hz and no low-cut filters in order not to lose very deep, low frequency data.

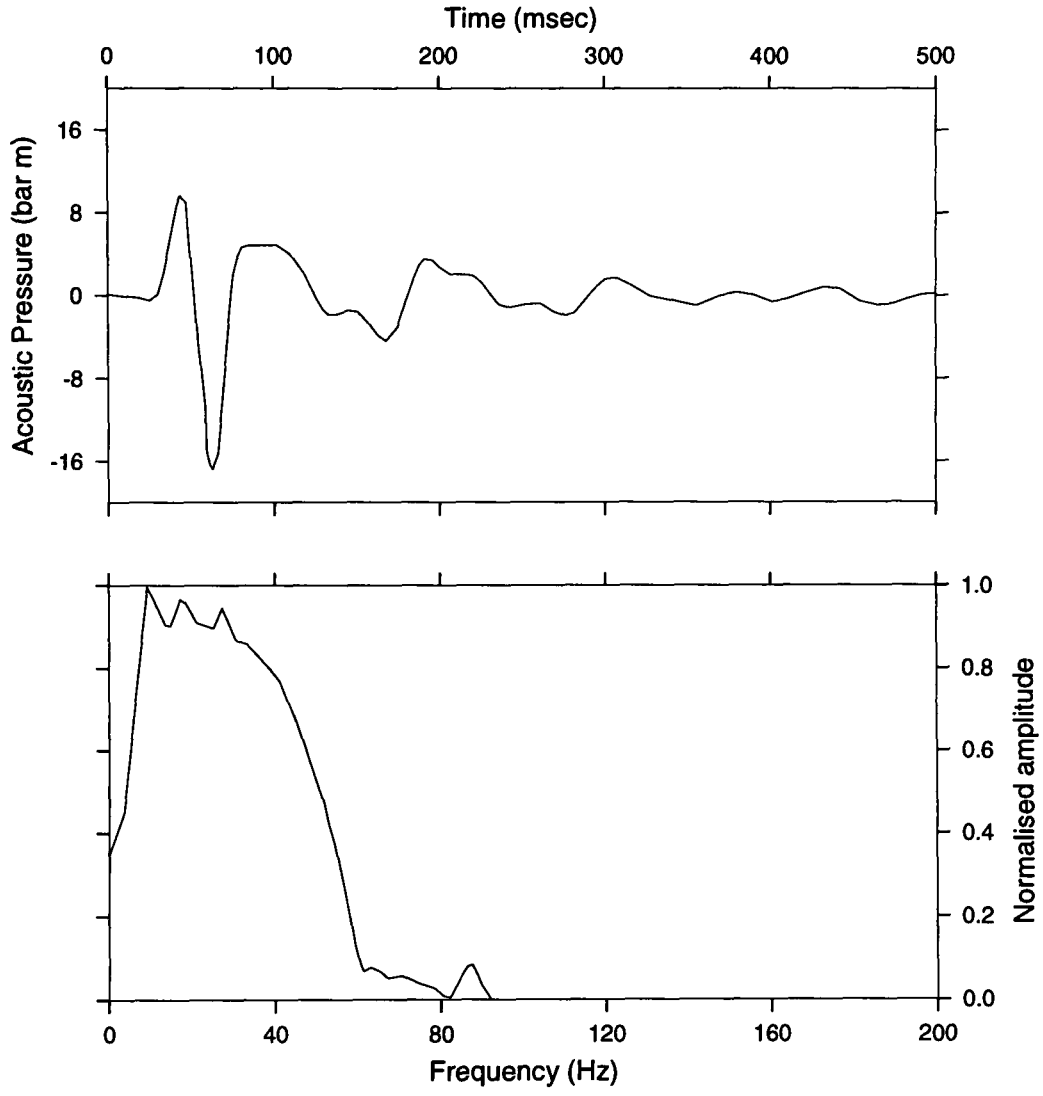


Figure 3.3: Spectral characteristics of airgun source array recorded by DFSV recording instrument: predicted wavelet (top) and amplitude spectra (bottom), 0-90 Hz filter.

The GECO Super Wide Air Gun (SWAG) array was made up of 36 guns in 6 identical strings (Figure 3.2b), with a total volume of 7524 in^3, equivalent to 116 litres, towed at 10m depth. The SWAG array is efficient in focussing and directing the source energy downwards in-line with the shooting profile [Hobbs & Snyder, 1992] and is the established optimum deep seismic source geometry. Guns were synchronised, with tests indicating that redundancy up to 20% would not significantly affect the amplitude content of the desired frequency range. The predicted wavelet and amplitude spectra of the source

recorded by the DFSV instrument are shown in Figure 3.3.

A shot-point interval of 75m was used, in order to ensure sufficient spacing for land recording and also to try to avoid deep-water multiples interfering with the primary arrivals of the next shot.

3.3 Processing to Stack of IAM MCS Data

With some field tapes becoming available in 1994–95, it was possible to do some QC pre–stack processing at Oxford, to look at problems of noise, multiples and velocity analysis. The major pre-stack processing effort was undertaken by GECO-PRAKLA under contract from the IAM Consortium, with feedback from academic parties at various stages. Figure 3.4 illustrates the major process steps used on data pre-stack and post-stack.

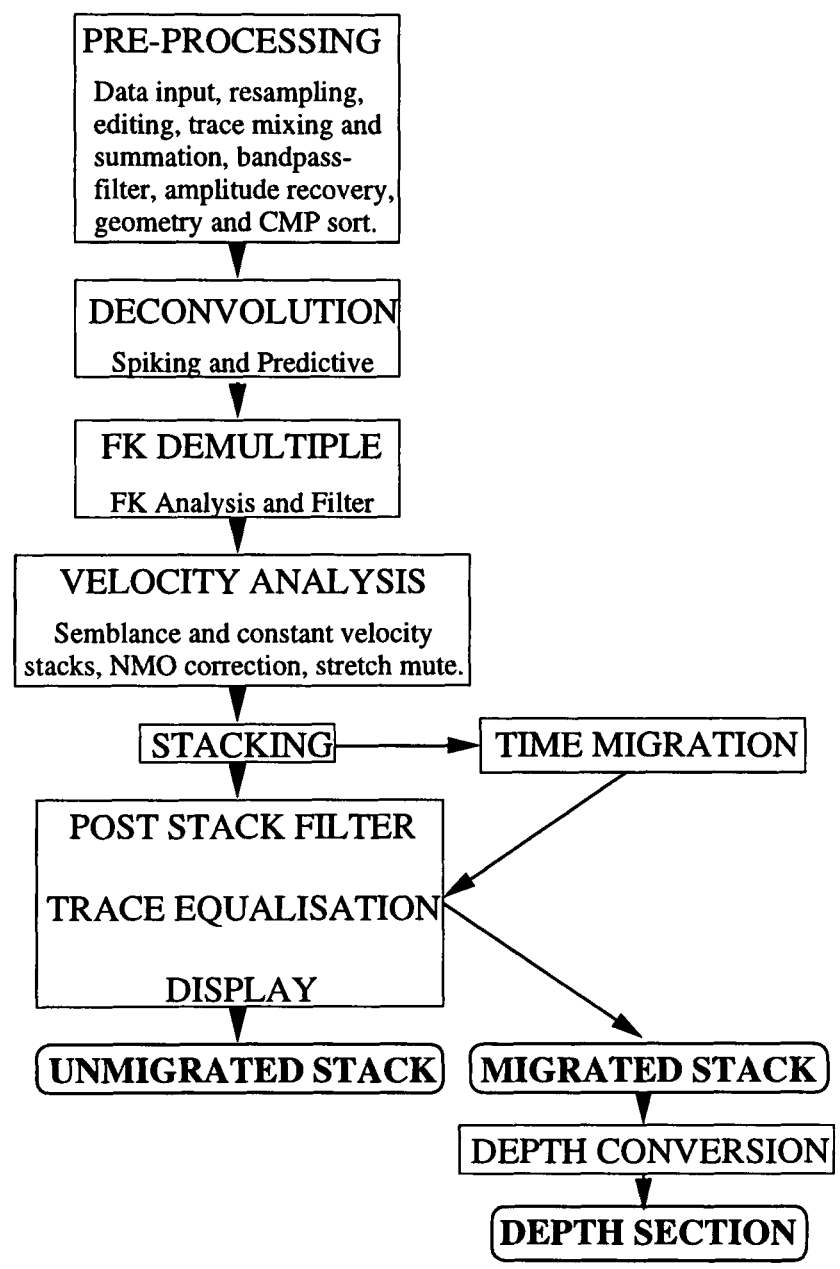


Figure 3.4: Generalized IAM processing scheme showing the major processing steps taken from field tape to final migrated and unmigrated stacks and depth sections.

Table 3.1 summarizes the processing parameters used in the final commercial processing to stack, for the entire survey. These are described in more detail in the following section, along with description of other steps tested at Oxford University.

PROCESSING SEQUENCE	14s record
1. Reformat	SEGD to SEGY
2. Bandpass filter	6 Hz (36 db/Oct) – 55 Hz (130 db/Oct)
3. Temporal Resample	4ms to 8ms and anti-alias filter
4. Trace Edit	
5. Trace Equalization	8-12 s window
6. Adjacent Trace Summation	
7. Common Mid-Point Gather	25 m bin, 32 fold
8. Spherical Divergence Correction	Initial velocity function
9. Predictive Deconvolution	300 ms operator , 32 ms gap
10. FK Demultiple	
11. Velocity Analysis	6 km interval
12. Normal Moveout Correction	
13. Space Variant Front End Mute	
14. Space Variant Inner Trace Mute	From above first seabed multiple
15. Spherical Divergence Correction	Replace initial with stacking velocity
16. CDP Stack	
17. Static Correction	Source and streamer static of +16.9 ms
18. Noise Attenuation F-K Filter	
19. Kichoff Diffraction Migration (optional)	Max dip 60° , $1700ms^{-1}$ constant velocity
20. Bandpass Filter	Time and space variant
21. AGC Scaling	1000 ms window

Table 3.1: Final IAM commercial processing sequence parameters to stack and migrated stack

Pre-processing

The "pre-processing" stage of data processing can be considered as the data preparation stage, the purpose of which is to prepare field data for input into the mathematical algorithms used in data enhancement, and also to reduce dataset size to enable efficient and speedy computation.

Data Input Field tapes were in demultiplexed SEGD (directly readable by Promax 6.0) accompanied by Observer's Logs, which gave details of each shot, including noisy

channels. Observations from onboard and early commercial post-cruise processing had revealed that little useful data were present below 14s TWTT. Figure 3.5 illustrates the varying amplitudes over the 0–60Hz bandwidth for typical shotgathers taken from Profile IAM-4.

Resampling The sample rate was changed from 4ms to 8ms, to compress the dataset without compromising temporal resolution. The new Nyquist frequency was therefore 62.5 Hz. Onboard gun tests had shown that the energy of the gun signal was almost entirely contained in the 0–60Hz frequency band so the new Nyquist limit was quite acceptable.

Trace editing Quality Control plots such as single trace monitor, shotgather plots and brutestacks using generalized velocity functions were used to aid in detection of noisy traces, which needed to be partly muted or killed. Reversed traces were manually reversed. Noise bursts and reversals can be due to faults in a hydrophone array or in the recording system, rather than the reflected wavefield.

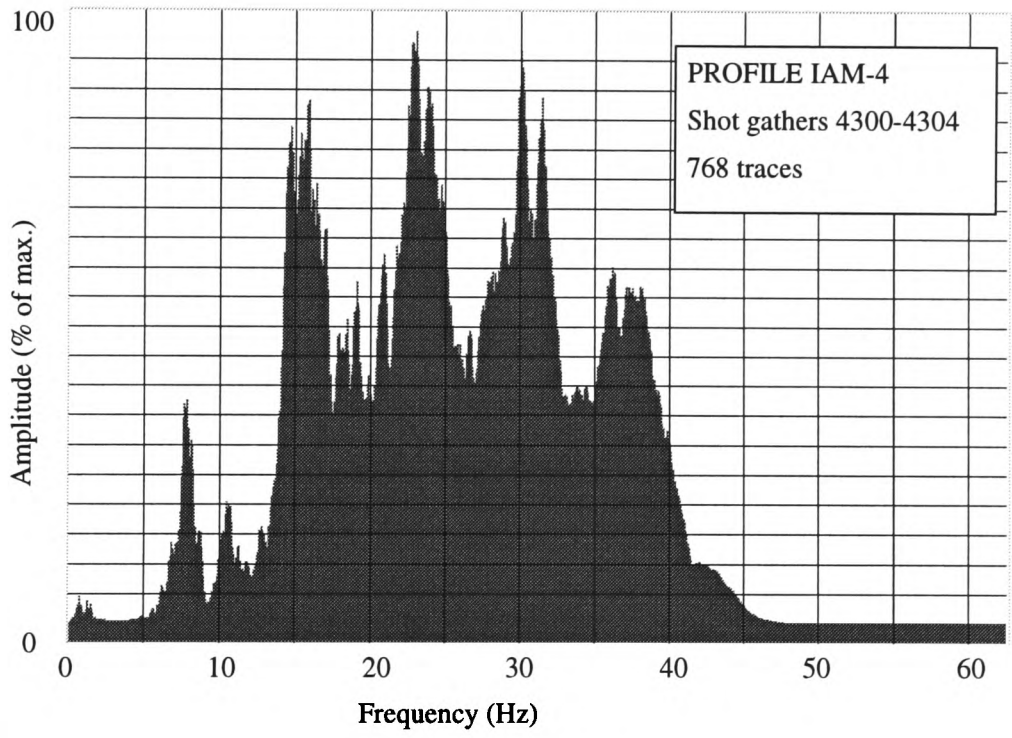


Figure 3.5: Amplitude spectra of raw IAM shot data, 0–14s TWTT.

Trace Mixing and Summation A weighted trace mix applied to the data enhances laterally coherent events, and subsequent trace summation halved the data volume while enhancing signal coherency, although at the expense of lateral resolution.

Bandpass filter A Butterworth frequency domain filter was applied to the data: a low-cut at 6 Hz to eliminate low frequency noise (e.g., swell-generated noise), and an

anti-alias high-cut at 55Hz (well below the Nyquist frequency, and above peak source frequencies).

Amplitude Recovery A spherical divergence correction was applied using the generalized RMS velocities picked for the brutestack, using the True Amplitude Recovery tool in Promax. This correction was removed directly before stack and a spherical divergence correction using the velocity function picked from the detailed velocity analysis was applied. Figure 3.6 below illustrates a typical shot-gather from Profile IAM-4 after application of this correction.

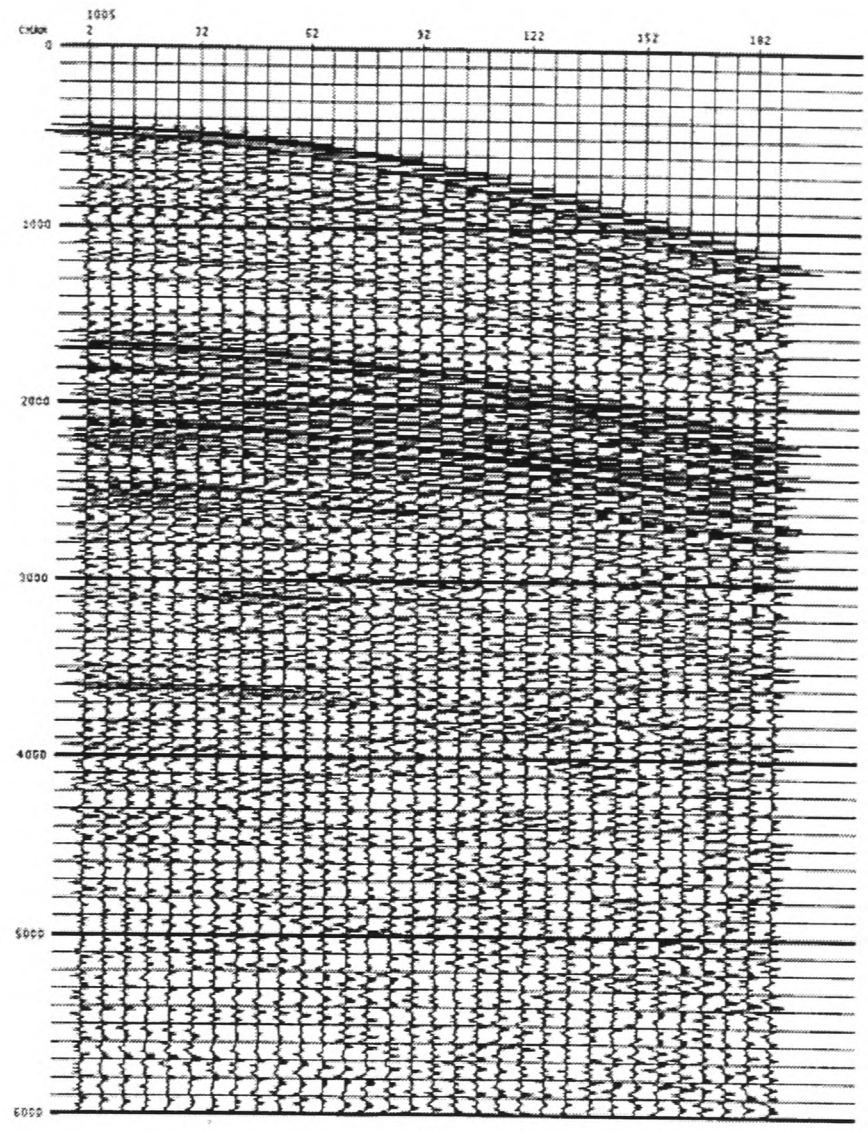


Figure 3.6: Top 6s of an IAM-4 shotgather, with every 5th trace of 192 traces shown. A spherical divergence correction has been applied, bringing up the strength of reflections lower down.

Geometry and CDP sorting Geometry was assigned to each line using PROMAX. A database of the position of each channel (trace) and shot position relative to the beginning of the line was created. CDP binning was performed using this database and the trace headers were then updated to include CDP-gather number and position. A CDP bin of 25m was used to avoid FK aliasing, and maintain a 32-fold coverage, despite earlier trace summation.

Deconvolution

Source signature deconvolution was not attempted, as onboard processing had shown that the IAM airgun array successfully produced an impulsive source with only a short bubble pulse component. *Predictive deconvolution* was applied before stack to suppress short-period multiples, of concern in shallow-water areas. After commercial testing a predictive least-square deconvolution filter with the following parameters was chosen: operator length 300 ms, gap 32 ms and white noise of 0.1% added before deconvolution.

FK multiple attenuation

To achieve multiple attenuation in deeper water, the moveout filtering method is often used [Ryu, 1982; Hardy & Hobbs, 1991]. A NMO correction which undercorrects the multiple and overcorrects the primaries is applied. The data are transformed into the frequency-wavenumber (F-K) domain [March & Bailey, 1983] where the positive quadrant, which contains the multiple, is removed. This method is more effective on far traces where NMO moveout between traces is greatest. A post-NMO inner trace mute, starting above the first multiples and extending until the end of the trace, attenuates multiples at near offsets. As the success of this procedure is dependent on the trace to trace moveout at far offsets, and thus streamer length, the 5 km streamer was useful in enabling removal of far-offset multiples. In very deep water, the first seabed multiples arrived at traveltimes where no real events were evident, and so multiple suppression was less important.

Wave Equation Multiple Removal (WEMR)

Seabed multiples are prominent in the shallow-water areas of the Gulf of Cadiz. The water-bottom reflection had to be picked on shot records and input to the WEMR program in Promax 6.0, which performed an FK extrapolation of shot records to estimate water-bottom related multiples and subtract them from the records. A portion of the profile IAM-GC3 was tested, as it was the shallowest profile in the survey, with water depths between 300-400m. The first seabed multiple clearly passed through sedimentary reflections on stack, and post-WEMR results illustrated that the first multiple was reasonably well attenuated, but the prominent peg-leg multiples were not. This method was recommended for use on near flat water-bottoms. However, IAM-GC2 and IAM-T3 are sloping, and IAM-GC1 has rough seabed topography. As the simple water-bottom multiples did not generally obscure reflections of interest on IAM profiles this step was not applied in general.

Dip Move-out (DMO)

The aim of seismic processing is to produce an accurate zero-offset section, assuming a layered earth. Dipping events do not stack properly, and if dips conflict one event will not stack at all. The aim of *dip move-out* [Deregowski, 1986] is to equalize stacking velocities at the point of dip crossover, so such conflicting-dip events are not lost. Testing of a common-offset DMO algorithm on a segment of IAM-4 revealed little change in subsequently picked velocities and resultant stack, and so was not implemented further [Chowdhury, 1994].

Velocity Analysis

Semblance velocity analysis was performed interactively using the Interactive Velocity Analysis tool in PROMAX, which allows editing of the velocity function while simultaneously viewing real-time moveout of the analysis CDP gather and the effect on the stack. Velocity anaysis was carried out every 6 km for the survey, but 3 km on test profiles. Constant velocity stacks were used for checking small variations in stacking velocities.

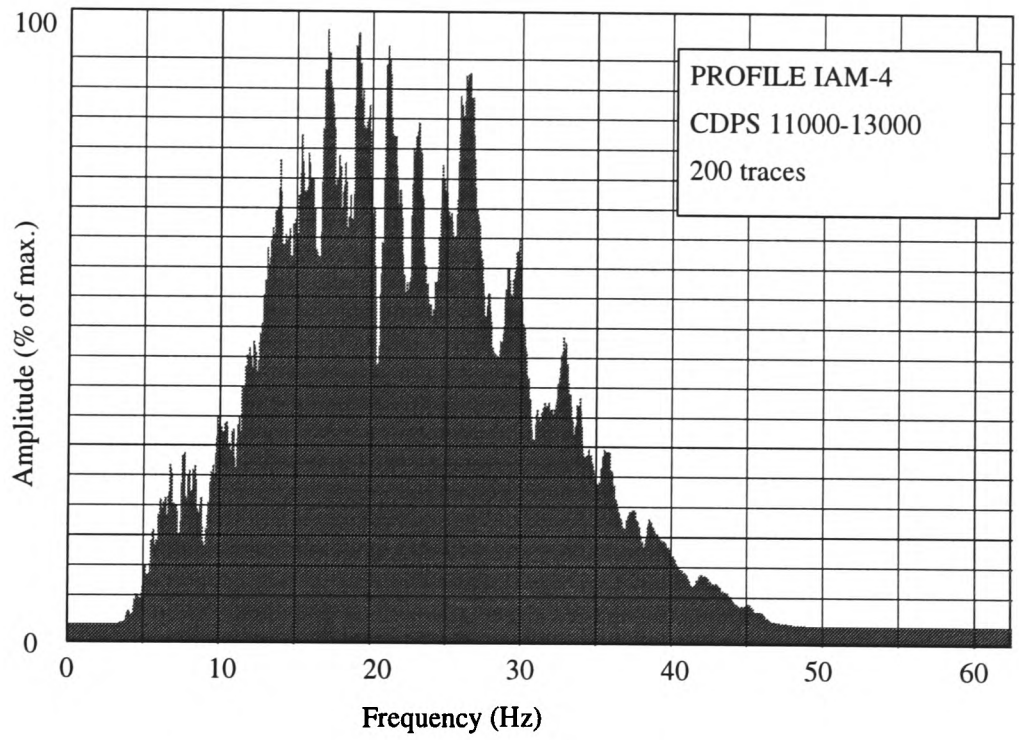


Figure 3.7: Amplitude spectra of a stacked portion of data from IAM-4

Stacking

The most important step in S/N improvement, is the adding together of traces which have reflections beneath a common depth-point (CDP). In this case the S/N improvement is by a ratio of $1/\sqrt{n}$, where n is the number of traces stacked, which is 32 in the case where a 25 m bin is used for trace-summed shot gathers. The effect of processing to stack can be seen in Figure 3.7 which illustrates the amplitude spectrum of a stacked portion

of IAM-4 in the Horseshoe Abyssal Plain, and the improvement in terms of a more even frequency distribution peaking at 20 Hz can be seen by comparison with the spectrum for raw shot data (Figure 3.5).

Summary

Table 3.1 summarized the processing parameters used in the final commercial processing to stack, for the entire survey. QC processing had shown that steps such as DMO and WEMR did not make a sufficient enough improvement to be applied to the entire survey pre-stack. The IAM-4 seismic data used in the spectral analysis of Figure 3.7 is shown on Figure 3.11A below. Many diffractions can be seen on this stacked data, particularly between 7–9 s TWTT where stratigraphic discontinuities within the chaotic unit and structural discontinuities from the fault zone (arrow) source the diffraction hyperbolae. Steeply, dipping diffraction tails can also be seen throughout the section. The acoustic basement is not well-imaged. The next steps involved post-stack filtering to enhance the S/N ratio of the data, and migration to collapse diffractions and provide a more structurally accurate image. Two panels, a deep-water IAM-4 panel and a Cadiz margin T-3 panel, are used to illustrate these steps, as shown on Figure 3.8.

3.4 Post–stack Processing and Migration of IAM MCS Data

3.4.1 Post-Stack Data Enhancement

The purpose of these processes is largely to improve the stacked image for further processing and interpretation. Noise suppression and coherency filtering were used to produce clean stack sections with enhanced deep reflectivity for input to the migration process. Data volume reduction was also required to speed up migration run times which can be very computer intensive. The basic steps are illustrated for a panel of IAM-T3 on Figure 3.9, from the Cadiz continental margin (Figure 3.8).

Dip-Filtering Figure 3.9A is the result of commercial processing by GECO of a segment of IAM-T3 from the Gulf of Cadiz (Figure 3.8). Steeply dipping coherent noise can be seen on this data, dipping both left and right, and affecting the entire section. Some dipping noise trains are due to the tails of diffraction hyperbolae, while others are typically due to side-reflections through the water or shallow sediment layers [Klemperer, 1987]. This problem affects all the stacks produced by commercial processing. A weak *Frequency-Wavenumber (FK) Filter* was applied in commercial processing to deal with this problem (Table 3.1,Banda *et al.* [1995]) but was overcautious and therefore not effective.

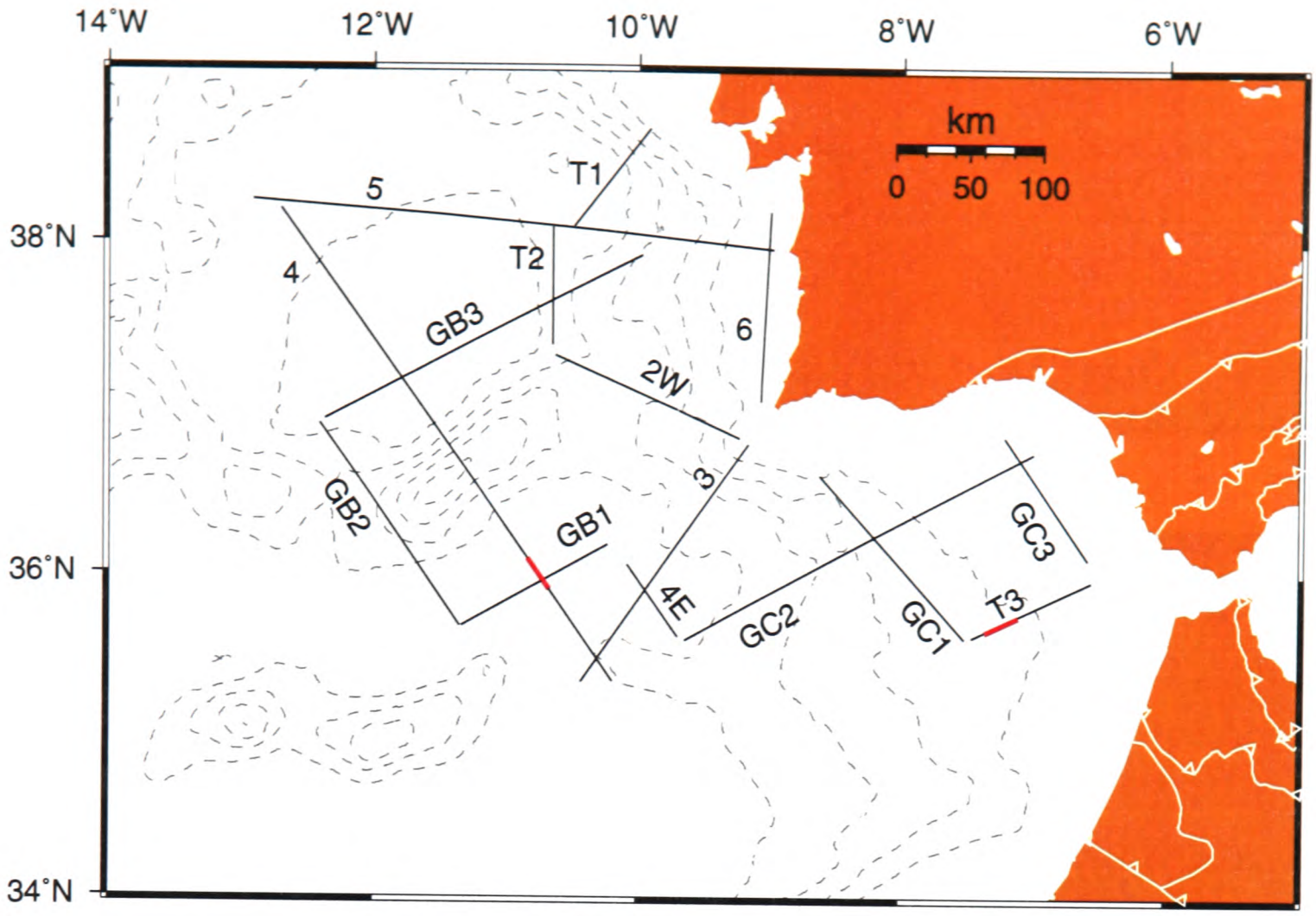


Figure 3.8: Location of IAM-T3 Panel (CDP 500-1500) and IAM-4 Panel (CDP 11500-12500), over bathymetry contoured at 1000m intervals, for illustration of post-stack processing and migration in Figure 3.9, Figure 3.10 and Figure 3.11.

The **Dip Scan Stack** algorithm in Promax was used to eliminate steep-dipping events that were obviously spurious. Tests were carried out for different dips, and suitable maximum and minimum dip ranges were chosen so that no real events were removed. The Dip Scan Stack algorithm performs a limited aperture Tau–P transform of the input x–t traces to a selected range of dip traces, each of which is weighted by the semblance along that dip, and inverse Tau–P transformed back. Coherent events are enhanced, dips to be excluded can be chosen, and unlike FK-filtering, the process is insensitive to aliasing, and was effective in excluding steep dip noise. This is illustrated in Figure 3.9B, where a filter excluding dips outside the range ±10ms/tr yielded the best result. The diffractions between 2–5s TWTT are attenuated, but the greatest improvement is in the deeper section, particularly between 8–13 s TWTT where a series of brighter reflections now stand out from the background noise.

Trace mixing This is a standard coherency enhancement tool, but entails some degree of lateral smearing, as does FK filtering for example. This arises through inclusion of portion of neighbouring traces in the filtered trace. A short mix (3-5 traces) median

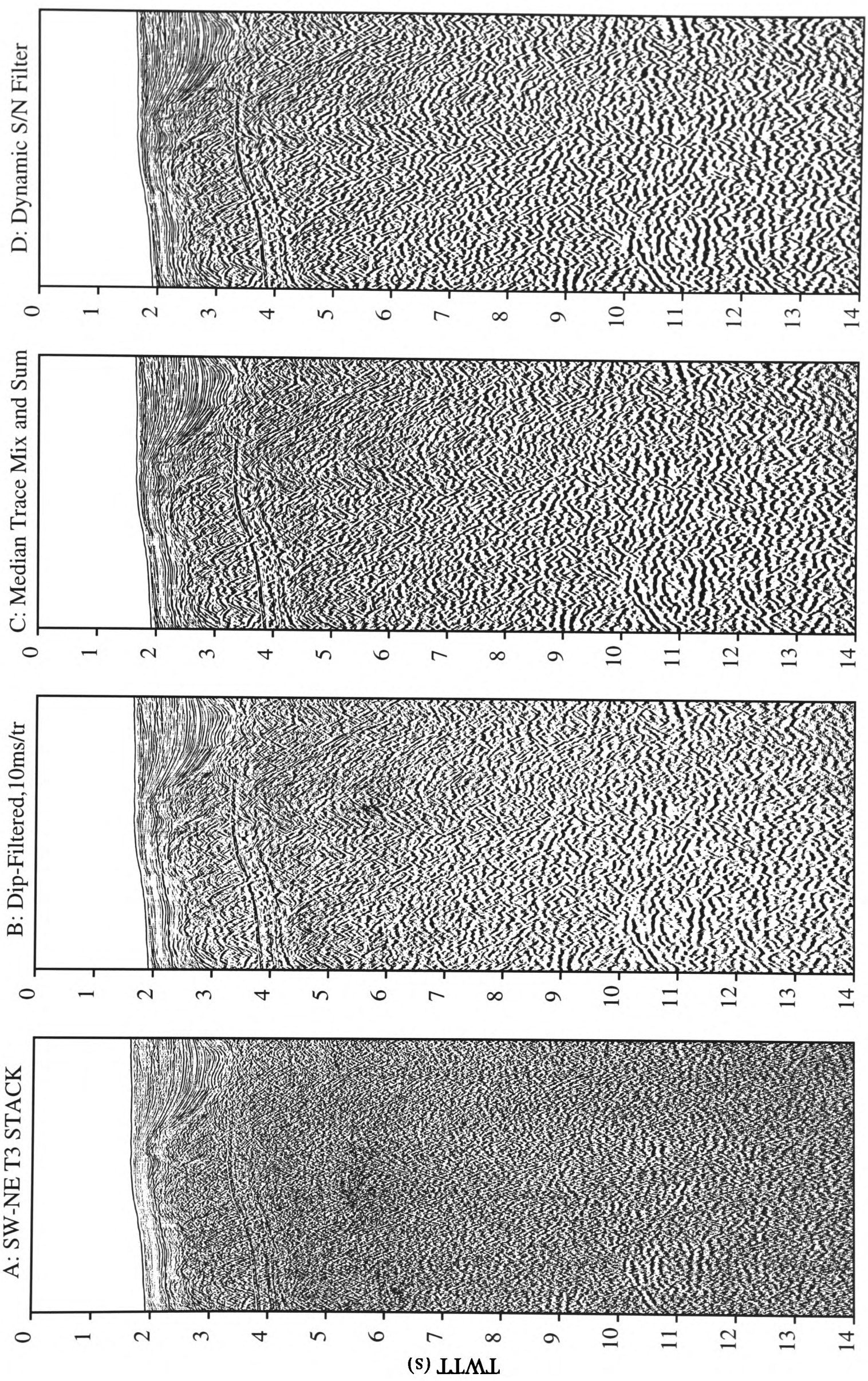


Figure 3.9: IAM-T3 Panel (CDPs 500-1500) in the Gulf of Cadiz, illustrating the effects of post-stack data enhancement steps. A) raw stack after commercial processing; B) Stack in A) after dip-filtering; C) median trace mix and summation; D) dynamic signal/noise filtering. See text for further explanation.

filter was applied, which excluded extreme points, whereas a weighted mean mix would have included some portion of these. Longer mixes of 9 and 11 traces produced coherent events from random noise, and so were discarded. This process was applied to improve reflection continuity before summation.

Adjacent Trace Summation This step has the double advantage of reducing data volume by a half, as well as increasing the signal/random noise ratio by a factor of 1.4 ($\sqrt{2}$). The trace mixing in the previous step helped to overcome the inevitable loss of spatial resolution. The trace separation was now 50m, and this was the limit for this data because further summations would lead to spatial aliassing on migration [p.320 Yilmaz, 1987]. The effects of median mixing and summation on the T3 panel are shown on Figure 3.9C. Coherent reflections have been brought up in strength throughout the section, but especially so for the low frequency sub-horizontal events seen within 8–14s TWTT.

Dynamic S/N Filtering This algorithm enhances lateral coherency – especially important with weak deep reflections – by weighting each frequency by a function derived from the local S/N ratio, where the weighting function approaches 1.0 for high S/N, and 0 for low S/N. Thus, although the filter is derived from nearby traces it does not include any portion of them, applied as it is as a simple, convolutional filter. This process is best used as a final post-stack filter, eliminating the need for a **time and space variant bandpass filter** (see Table 3.1 Step 19). The effects are most dramatic in noisy data, but produce some noise reduction and improvement in reflection coherency even on relatively clean data, as shown on Figure 3.9D.

3.4.2 Migration

Migration is a seismic inversion operation which "involves repositioning of data elements to make their locations appropriate to the locations of the associated reflectors and diffracting points." [Sheriff & Geldart, 1983]. In other words, migration collapses or focuses the recorded wave-field to its correct subsurface position. Several categories of migration techniques exist, based on algorithm implementation. An algorithm using RMS velocities analytically, which does not account for ray bending at interfaces, is called a time migration. One which uses interval velocities and accounts for ray bending at interfaces, is characterized as a depth migration. Mathematically, ray bending is accounted for by the "thin-lens term" which appears in certain solutions of the scalar wave equation. This leads to an alternative definition of depth migration as "a migration method that includes the effects of the thin lens term"[Yilmaz, 1987]. The migration

method assumes that diffractions come from point sources and so a correct model of the velocity structure will result in a transform which collapses the diffractions.

Migration is necessary to obtain a structural picture. The production of depth sections, either by depth-conversion of a time-migrated stack or depth migration, helps further in structural interpretation by approximating a true geological section through the earth. The accuracy of the depth section is completely dependent on the accuracy of the velocity field used in processing, the limitations of which must be understood so that the depth section is not taken as a true geological section, but as our best approximation through geophysical remote-sensing. For example, small errors in measuring NMO lead to larger errors in stacking velocities (particularly for deep reflections) which can cause large errors in subsequent calculation of interval velocities [Sheriff & Geldart, 1983]. As a good knowledge of the velocity field is fundamental to the success of the migration operator, some attention has to be paid to this aspect. Where there are bright reflection horizons, such as sedimentary layering, these can be easily identified on stacking velocity semblance plots and a reliable velocity derived. However, this is difficult within the chaotic zone seen between 2.5–4s TWTT on Figure 3.10A, and between between 7–8s on Figure 3.11A. Similarly, at the basement interface, out-of-plane effects come into play and scattered energy from nearby diffractions confuses the semblance procedure. In these cases, such as below the basement, refraction velocities become important, but these are sparse in the study region. Stolt migrated time sections [Stolt, 1978] can also provide velocity information but preliminary tests indicated that the deeper data had noise problems and did not migrate well at high velocities. These limitations in velocity models, and problems inherently associated with migration of deep events [Warner, 1987] meant that the migration scheme for the data would not be over-ambitious, but concentrate on collapsing diffractions in order to image diffractive basement and faults, while not interfering too much with the deeper section. Thus, only time migrations were used, as a direct comparison could be made between stack and migrated stack.

In this section, the effects of different post-stack time migration algorithms on IAM data are discussed, using panels from IAM-4 and T3 for illustration (Figure 3.8). Processing was carried out on a Sun Sparcstation20, running Promax 2D Version 6 software. Table 3.2 lists the time migrations attempted on IAM data, along with their key characteristics with respect to handling of lateral velocity variation, V(x), vertical velocity variation in time, V(t) and steep dips. The relative run times are not controlled benchmarks but results from Landmark Corporation tests on these Promax algorithms, which nevertheless give an idea of run times when one considers that a phase-shift migration

for 4,000 traces will take $\sim$ 1 hour. It can also be seen from the table that different types of velocity are required: rms stacking velocities and interval velocities, which are related by the Dix equation [Dix, 1955]. Velocity conversions were carried out within Promax using the Velocity Manipulation tool.

Migration name	Velocity	V(x)	V(t)	Steep Dip	Rel Run Time
Memory Stolt F-K	V_{RMS}(x,t)	Poor	Poor	Fair	0.2
Phase-shift	V_{INT}(t)	None	Good	Good	1.0
Fast explicit FD	V_{INT}(x,t)	Fair	Good	Fair	9.6
Kirchoff	V_{RMS}(x,t)	Fair	Good	Good	14.6

Table 3.2: Time migration algorithms

Kirchoff Time Migration The commercial processing by GECO produced migrated stacks of IAM data using a Kirchoff diffraction stack using a constant velocity function of 1700 ms^{-1}. This collapsed some, but not all diffractions, and obviously did not reposition elements as accurately as a migration incorporating some velocity variation would.

Stolt F-K Time Migration Stolt F-K Migration [Stolt, 1978] is the fastest algorithm. It involves a Fourier transform from the T-X (time-space) domain to the F-K (frequency-wavenumber) domain where a mapping operation using a single velocity is carried out. A subsequent inverse Fourier transform from the F-K to T-X Domain generates the migrated image. This method works best for a single velocity, but with the Promax algorithm used, lateral and vertical velocity variations can be accommodated using a stretch function to the T-X data pre-, and an inverse stretch post-migration. However, tests showed a poor response to velocity variations (see also Table 3.2). This method was used with constant velocities, mainly for migration velocity test panels, which were necessary as the best velocity function for migration is not always the same as the best stacking field, especially deeper in the section where overmigration is a common problem [Klemperer, 1987].

Phase-Shift Time Migration This migration algorithm is based on the downward continuation of Gazdag [1978] which is equivalent to phase-shifts in the F-K domain. It accurately repositions events of up to 90 °dip assuming that there is no lateral change in velocity. This method is relatively quick, with run-times of 30–90minutes for an entire profile. It was found to be particularly satisfactory in the abyssal plain sediments where there was no large lateral change of velocity. In these cases an average velocity function

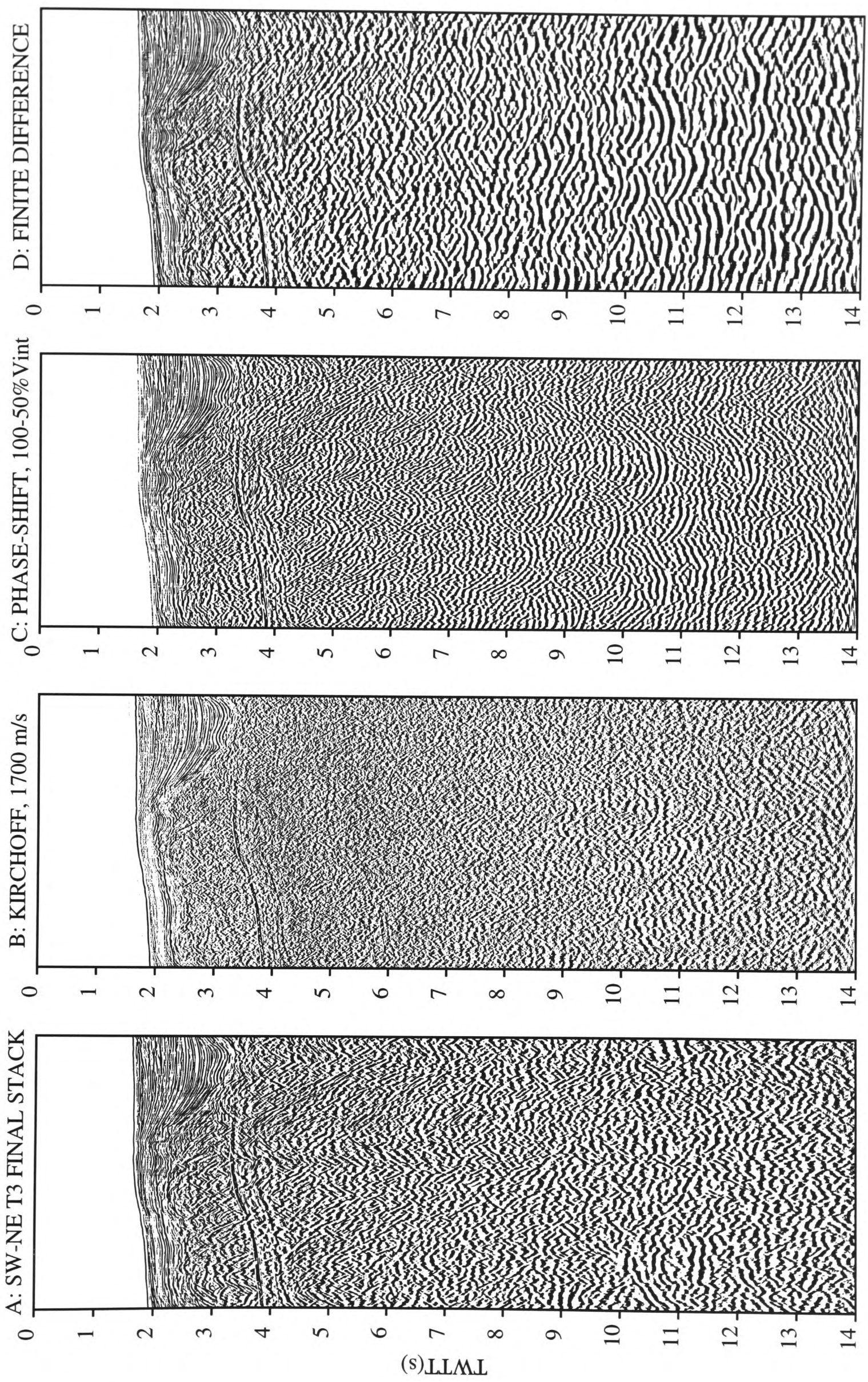


Figure 3.10: SW–NE IAM-T3 panel (CDPs 500-1500), illustrating the effects of A) no migration; B) Kirchoff migration at $1700ms^{-1}$ (commercial processing); C) phase-shift migration with vertically varying velocity field: D) fast explicit finite-difference migration with vertically and laterally variant velocity field

was computed and applied to the whole line. Migrated images were generally well-imaged right down to basement.

Finite–Difference Time Migration This method use finite-difference methods to solve the appropriate wave equation, and uses time and spatially variant RMS velocity fields [Claerbout, 1985]. Various assumptions can be made to simplify the scalar wave equation, so FD implementations can be accurate to different levels of dip; tests on PROMAX used the 65°dip option on structurally complex sections. These methods are much slower than phase-shift migration (Table 3.2). Care had to be taken with velocities because of the presence of a diffractive chaotic layer, and out of plane effects, which were blown up if migration velocity was even a little too high. Because of these limitations this method was used on limited portions of the data.

Migration Panels Time migrations of a continental slope panel from Profile T3, and an abyssal plain panel from Profile IAM-4, are presented in Figure 3.10 and Figure 3.11.

Continental Margin Panel T3 panel Figure 3.10A represents the final stack after post-stack data enhancement discussed earlier in the chapter (Figure 3.9). On the commercially-processed Figure 3.10B the base of the layered sediments, between 2–3s TWTT, still have a diffractive appearance, and the deep reflections (9–14s) look hardly migrated at all.The overgentle dip-filtering has left the section obscured by steep-dipping noise, especially between 4–8s TWTT. Phase-shift migration using an averaged function from nearby velocity analyses, scaled down to 50% velocities at 14s TWTT, produced Figure 3.10C. The base of layered sediment is much better imaged than in Figure 3.10B. Coherent events can be seen throughout the section below, and are visible because of their higher amplitude and lower frequency relative to the background noise. The events between 9–14s TWTT are much clearer and easier to pick. The explicit finite-difference method used to produce panel Figure 3.10D, required an interval velocity field, which was produced from the stacking velocity field, adjusted by percentages, and smoothed. The deep section contains noise which was prone to produce "smiles" and so the maximum migration velocity was pegged at 3500 ms^{-1}. This produced the best image of the layered sediment-chaotic unit interface, but although deeper reflections are still visible in the deep section, the migration has produced some smearing of noise with signal, but events can still be picked.

Abyssal Plain Panel Figure Figure 3.11 illustrates a segment of profile IAM-4 over the Horseshoe Abyssal Plain (Figure 3.8. The chaotic unit beneath the upper layered

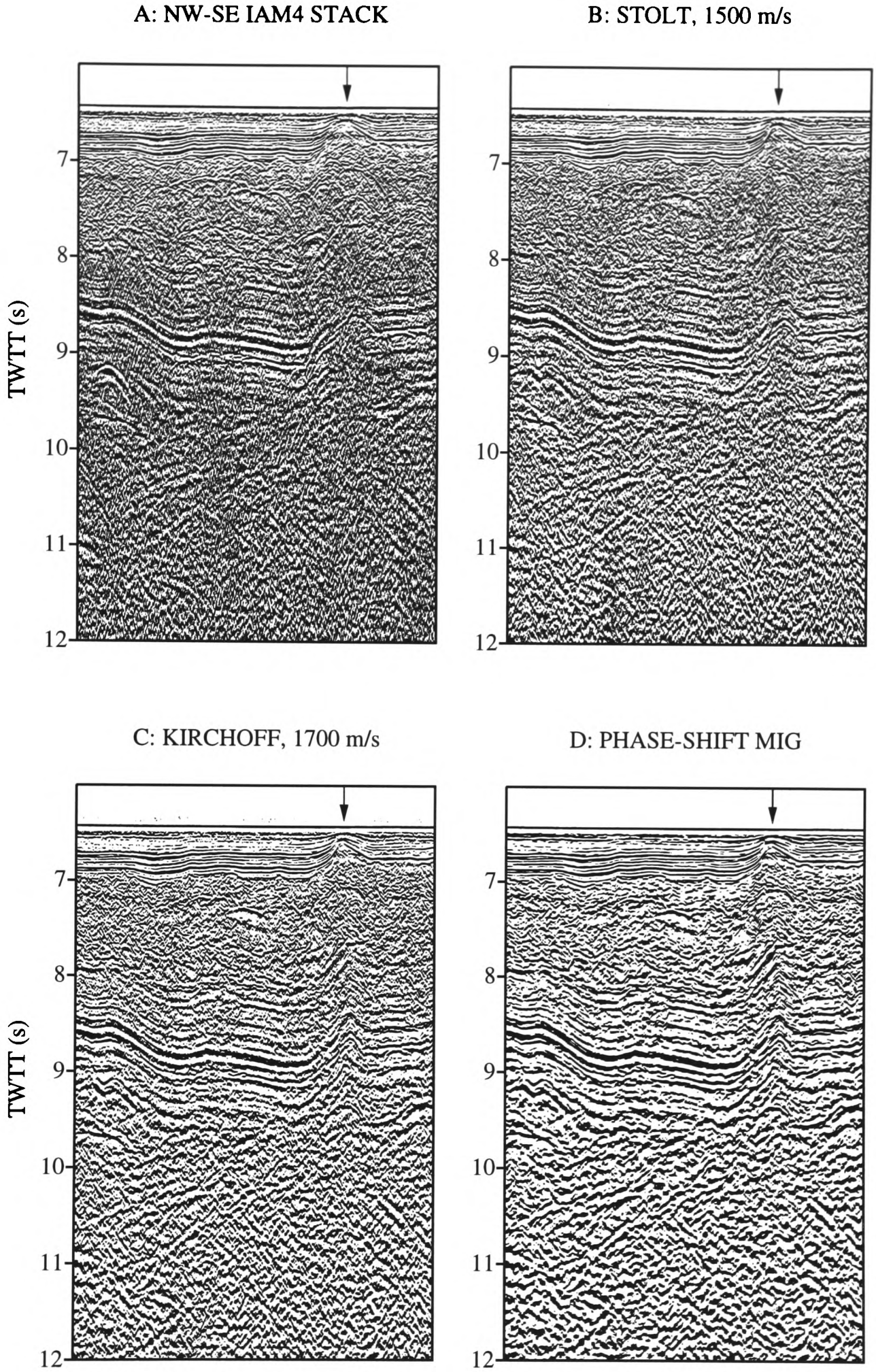


Figure 3.11: NW–SE IAM-4 panel (CDPs 11500-12500) in the Horseshoe Abyssal Plain, illustrating the effects of A) no migration; B) migration at water velocity; C) migration at $1700 ms^{-1}$ (commercial processing); D) phase-shift migrated stack with vertically varying velocity field.

sediments on Figure 3.10 is also seen the raw stack of Figure 3.11A, as a very diffractive layer with small scale seismic fabric, between 7–8s TWTT. However, layered reflections are visible below the chaotic unit, and the basement lies between 9–10s TWTT, although it is obscured by noise on the stack. The arrow points to a feature where the layered sediments above 7s are thinned, and which produces diffraction hyperbolae down to 9s. A simple, cosmetic Stolt migration at water velocity (1500 ms^{-1}) was applied in Figure 3.11B. This was sufficient to collapse many of the diffraction hyperbolae in the chaotic unit, which also led to a lower section with far less contamination from steep noise. Some diffractions are still seen below the arrow, associated with what now appears to be a fault zone. Subcrustal reflections at 10.5–11s are clearer. The commercial processing, with a single velocity of 1700 ms^{-1}, is shown on Figure 3.11C. The higher velocity is much more appropriate than water velocity for collapsing diffractions, with few diffractions left in the chaotic unit between 7–8s TWTT. The basement surface is becoming clearer, with sub-basement events between 11-12 s beginning to emerge from the noise. The best panel is produced by phase-shift migration, where the base of the chaotic unit, top of basement, and intra-chaotic unit and intra-basement events are much more clearly imaged than in the other panels. The fault zone beneath the arrow is well defined through the sediment column by the position of the sedimentary layers offset by it, which can clearly be seen to be downthrown to the left.

Depth conversion

Depth conversion was carried out by mapping reflections from the x-t to x-z domain using an interval velocity field derived from 100% stacking velocities. The stacking velocity field was checked and any other velocity information (from wells, refraction, wide-angle surveys) was used to check, and correct, the derived interval velocity field at this stage. This was done for all cases where the geometry of a particular structure was useful for interpretation.

Display

Initial sections and interpretation displays were plotted on a Versatec 24" plotter using rasterized CGM output from Promax. Final profiles were generally displayed with a 500 ms AGC scalar, using Seismic Unix [Cohen & Stockwell, 1996] and GMT [Wessel & Smith, 1991] software packages.

Processing to reveal the Moho reflection

Previous deep seismic experiments in the North Atlantic have, in a few cases, imaged the Moho as a strong, sometimes banded, reflection event occurring at approximately 2.0 s TWTT below the top of the oceanic basement [e.g., NAT Study Group, 1985; Banda *et al.*, 1992; Sartori *et al.*, 1994; Collier *et al.*, 1998]. Moho reflections can sometimes be observed as a high amplitude event on initial stacks, but this was not the case with any of the IAM profiles. Post-stack processing of good data is normally applied to enhance the reflection rather than to reveal it. In this study, band-pass filters and trace mixing up to 21 traces were employed to enhance any candidate reflections for a Moho, particularly to enhance low frequencies (< 25 Hz) and weakly coherent events at depth. On the IAM data no strong reflections that might mark the Moho were seen on the unmigrated stacks, although several intracrustal reflections were noted. At the continental slope, on IAM-GC1 and T-3 a series of high-amplitude reflections were seen at 8-12 s TWTT, possibly representing layered lower crust. One reason for lack of a clear Moho on IAM lines over TAP and HAP regions may be the presence of a gradational Moho, with no large impedance contrasts to act as a strong reflector. In the region of the central North Atlantic studied here, the lack of a Moho reflection may be related to crust formation under slow spreading conditions. If a Moho event is weak compared to other non-coherent events at similar arrival times, attempts to increase the amplitude and coherency of this event (trace mixing, filtering to remove dipping energy, band-pass filters) will also increase the amplitude of the non-coherent events so the Moho will not be easily identified.

3.5 Reprocessing of R/V Conrad Cruise RC2911 MCS Data

Acquisition Multichannel seismic data of cruise RC2911 were acquired in the western Mediterranean in 1989 by the Lamont–Doherty Geophysical Observatory (LDGO) vessel *R/V Robert D. Conrad.* The survey used a tuned 10-element BOLT airgun array (5346 cubic inch total vol); a DIGICON 2.4 km streamer with 48 channels with a 50m hydrophone group spacing; 50m shot spacing (23s shot interval at a survey speed of 4.2 knots) ; 20s recording window with a 4 ms sample interval.

Original Processing Scheme Standard processing steps were applied to the multichannel seismic data at the LDGO, with 25m CDP binning giving 24-fold stacks. Velocity analysis determined semblance velocities for sedimentary reflections at 1.25 km intervals (50 CDP) along each seismic line [Watts *et al.*, 1993], but acoustic basement velocities used in stacking were taken from previous published refraction experiments. Normal moveout corrections, variable range mute, velocity filtering (multiple removal) were also applied.

Further Processing The following post-stack processing sequence was carried out during this study: trace summation, resampling from 4 ms to 8 ms, phase-shift migration using an average function derived from stacking velocities, Tau-P dip filter, dynamic S/N coherency filtering, automatic gain control, display. The panel shown below in Figure 3.13, is from the eastern Alboran Sea (Figure 3.12), and illustrates the dramatic improvement in the data produced by migration, for example. Figure 3.13a is a portion of the original stack after processing by LDGO. The basement is obscured by diffractions , and there are strong water-bottom and peg-leg multiples (marked M on the figure). On the same panel after migration, in Figure 3.13b, the top of the acoustic basement is imaged as most of the diffractions have collapse. Discrete sedimentary bodies can be seen, as can the base of the mini-basin in the centre of the profile (CDP 600, 3–5 s TWTT). Diffraction "smiles" dominate below about 5s TWTT, and result from migration of the multiples, which have lower velocities than expected for real events at that depth, and so appear overmigrated.

Of the profiles, only 827 had been previously migrated (at LDGO) but this data was not available for this study. Migrated stacks of profiles 823–829 of the RC2911 survey were produced, and with careful post–stack filtering, greatly improved images were obtained. The new migrated profiles were interpreted as part of this study: the regional profiles 823, 824, 825, 827 have since been published as a foldout in Comas *et al.* [1999].

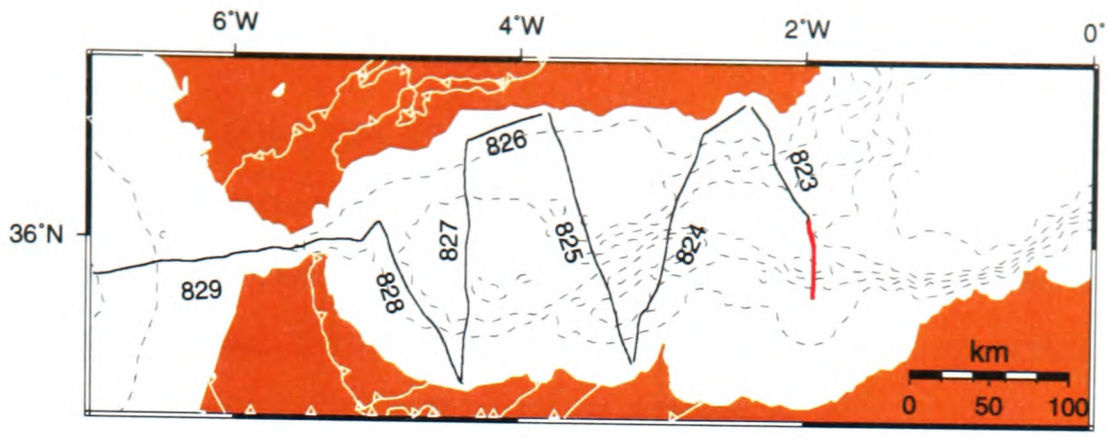


Figure 3.12: Location of Line 823 Panel shown in Figure 3.13, over bathymetry contoured at 500m intervals.

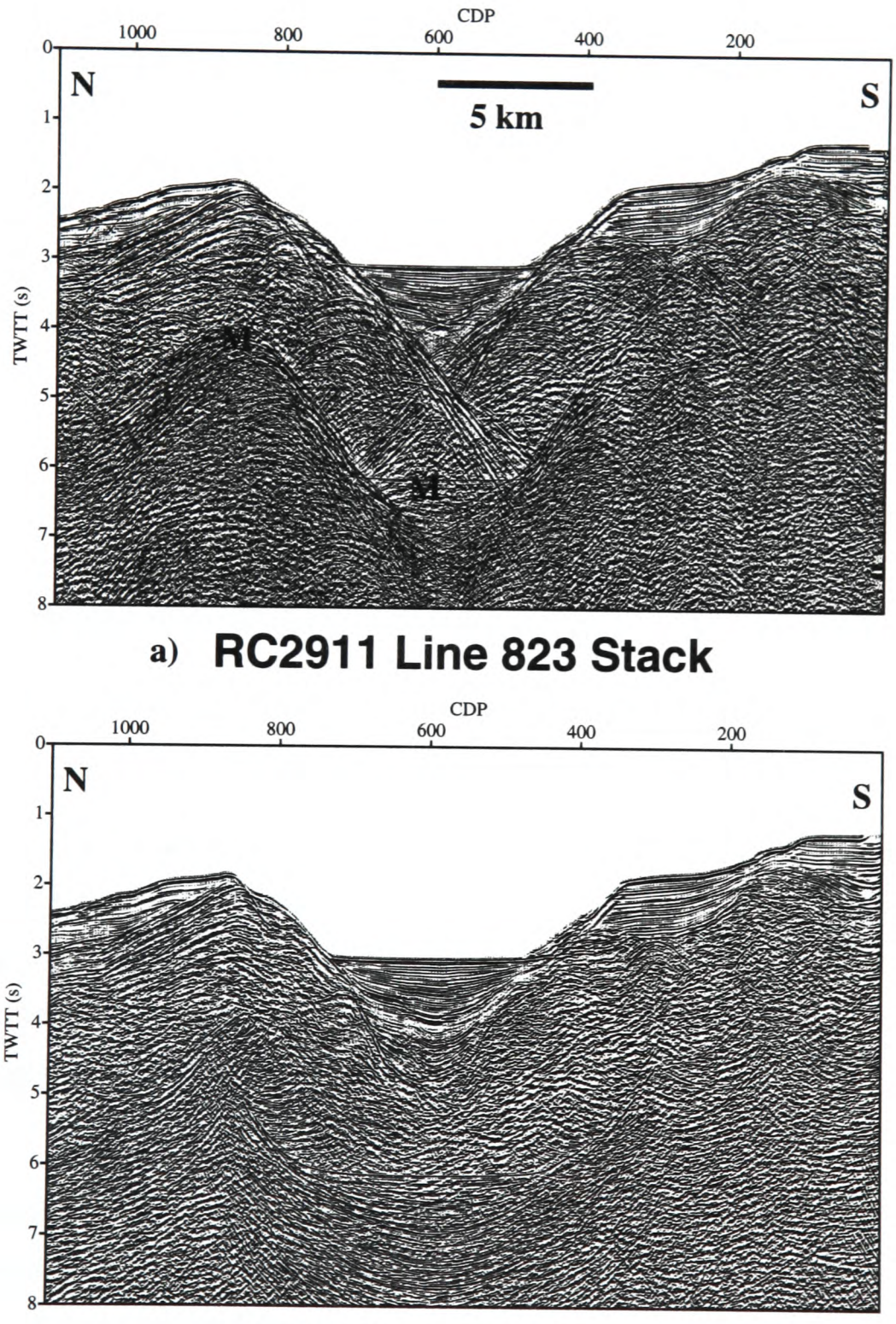


Figure 3.13: A segment of RC2911 Line 823 showing post-migration improvement. A phase-shift migration algorithm was used, and a 500ms AGC applied before display.

3.6 Seismic Processing Synopsis

- In terms of acquisition, the GECO-PRAKLA SWAG airgun array used for the IAM survey, was successful in producing a sharp, impulsive source signal rich in low frequencies. The well-tuned source was able to provide returns from deep in the crust, and through thick sections of the regional chaotic unit which had proved to be seismically impenetrable to previous surveys.

- Commercial processing of the data was carried out by GECO–PRAKLA. Commercial filtered stacks became available in late 1995 and single–velocity migrated stacks in 1996. In-house QC processing of pre-stack data was carried out at Oxford University in order to validate processing steps taken, and to test different schemes. The final commercial data did not image deep reflectivity nor basement well, and so post–stack processing steps were carried out in order to reduce noise and enhance coherent reflectivity at depth.

- Post-stack processing, carried out at Cambridge and Oxford Universities, led to image improvements to the commercial stacks through post-stack filtering and migration. Depth sections were produced for structural analysis e.g.,GC3.

- Careful dip-filtering was necessary to remove the steep-dipping noise present on IAM profiles, and this was achieved using a limited-aperture Tau-P transform and inverse transform excluding selected dips.

- Coherency filtering was applied to the profiles to enhance deep reflectivity in particular.

- Migration was found to be necessary to eliminate the large number of diffractions from the regional chaotic unit and numerous structural discontinuities. Migrations incorporating velocity variation produced significantly better results than single-velocity migrations, especially of structure and at the basement interface. Phase-shift migration proved to be a successful, and relatively economic, migration to use.

- Post-migration cosmetic steps include gentle trace mixing to remove migration-introduced noise, and other filters were applied as necessary. The final migrated stack could then be used for depth conversion.

Chapter 4

Crustal Structure, Subsidence History and Gravity Anomalies of the Gulf of Cadiz

4.1 Introduction

The Gulf of Cadiz (GOC) lies in the eastern Atlantic between southern Iberia and north Africa. The regional relief is shown in Figure 4.1 with major tectonic and physiographic features labelled, and with the location of well and seismic data available for this study. In particular, the tectonic elements of the arcuate Betic-Rif orogen are shown, which have been explained in detail in Section 2.2. The GOC is underlain by continental crust, although the position of the ocean-continent transition (OCT) west of the GOC is under debate [e.g., Pinheiro *et al.*, 1992]; the green lines on Figure 4.1 illustrate the position of the OCT from Mauffret *et al.* [1989] in the Tagus Abyssal Plain (based on seismic data and a magnetic ridge), and from Verhoef *et al.* [1991] in the Seine Abyssal Plain (the S1 magnetic anomaly). Between Seine and Tagus Abyssal Plains the OCT may run approximately along the base of the continental slope, although this is a matter of speculation in the absence of any clear indicators such as a magnetic anomaly (as discussed in Whitmarsh *et al.* [1993]).

Since the Mesozoic, the evolution of the GOC has involved several phases of extension, compression and strike-slip motions with large lateral displacements [e.g., Dewey *et al.*, 1989]. Following the inception of the Southern Iberian Margin in the late Triassic through the breakup of the Pangaean landmass, the GOC region has been shaped by the tectonic interplay of Atlantic opening, Africa-Eurasian collision and Tertiary Alpine deformation leading to formation of the Betic-Rifian orogenic arc. A GOC-Guadalquivir basin formed at the end of the Early Miocene Alpine compression [Riaza & Martinez del Olmo, 1996].

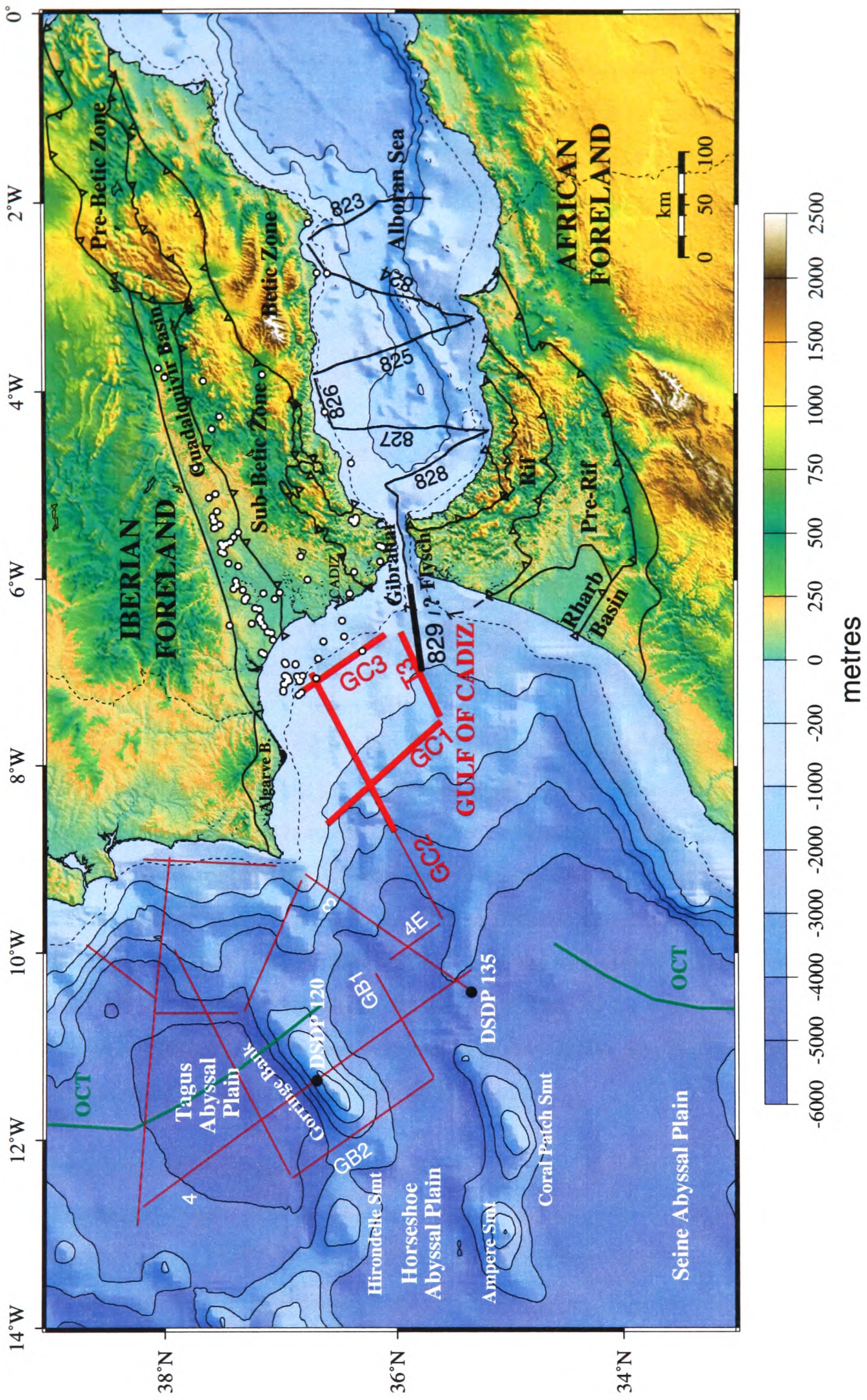


Figure 4.1: Regional relief map, including tectonic domains of the Betic-Rif orogenic arc. DSDP wells 120 and 135 are labelled; other well data from IGME [1987] shown as white circles. Heavy lines indicate MCS profiles used in this chapter. Green lines offshore indicate the probable position of the ocean-continent transition (OCT), as reported by Mauffret *et al.* [1989]; Verhoef *et al.* [1991].

A number of previous geophysical studies have been reported [e.g., Malod & Mougenot, 1979; Delaplanche *et al.*, 1982; Flinch *et al.*, 1996; Maldonado *et al.*, 1999] but these surveys were carried out within 50 km of the Spanish coast and therefore do not provide a regional coverage of the GOC. The Iberian Atlantic margins survey provides a regional deep seismic survey all the way up the Cadiz continental margin. Tortella *et al.* [1997] published initial interpretations of the commercial stacks of some lines used in this study, but did not interpret below 4s TWTT. Further post-stack processing, enabling better and deeper interpretation, was applied to the profiles utilised in this study, which include previously unpublished IAM and RC2911 cruise data from the GOC.

In order to address the limitations of previous studies with regards to their lack of a regional treatment of the GOC, an integrated study was carried out involving the processing and interpretation of multichannel seismic (MCS) data, and the modelling of gravity anomalies and well data in order to elucidate the deep structure of the GOC. The case study of the GOC region presented here provides tectonic insights into the evolution of continental margins in complex plate boundary settings.

Quantitative analysis of petrophysical data enabled physical properties of sediments to be derived, and backstripping [e.g., Steckler & Watts, 1978] was carried out to obtain burial histories. Porosity-depth relationships for backstripping were calculated using the soil mechanics–based method of Audet [1995] rather than the traditional empirical exponential curve-fitting of Athy [1930], in order to prevent the underestimation of shallow porosity [e.g., Baldwin & Butler, 1985], and hence the calculated magnitude of tectonic subsidence, and subsequent stretching factors modelled to fit the tectonic subsidence. Analysis of well data allowed a comparative study between the Neogene Guadalquivir foreland basin and the adjacent, offshore GOC.

Seismic data was tied to well lithological data, allowing five seismic stratigraphic units to be distinguished, comprising sediments ranging from Triassic to Recent in age. Interval velocities derived from NMO correction and stacking of reflection data, were compared to available downhole sonic log velocities, and physical properties for each unit were derived from the velocity data. Physical parameters thus derived, depth-converted seismic reflection interpretations, and published refraction data, were used as constraints in forward gravity modelling in order to predict crustal thickness changes on a regional scale across the western GOC. Stretching factor calculations over the GOC allowed the estimation of the ocean-continent transition west of the Gibraltar Straits.

4.2 Geological and Geophysical Setting

The Gulf of Cadiz is located at the intersection of the Atlantic passive margin of western Iberia, the eastern part of the Azores-Gibraltar boundary between African and Eurasian plates, and the Gibraltar Arc - an arcuate Alpine orogenic belt comprising the Betic-Rif mountains surrounding the Alboran Sea basin. The Iberian Peninsula is mainly comprised of Hercynian rocks of the Iberian Massif, to the south of which lies a Neogene orogenic belt (the Betic Cordillera). The studied area lies in the SW corner (Figure 4.1), where the Iberian Massif meets the western end of the Betic orogen, across the Guadalquivir Basin (GQB). The deposits of the GQB have long been known to extend out into the GOC [e.g., Roberts, 1970], and the western GQB and northeast GOC can be considered as a single basin for much of the Tertiary [e.g., Riaza & Martinez del Olmo, 1996].

The tectonic elements of the Betic orogen have been described in Section 2.2, and consist of the following: the Internal Zones of the Gibraltar Arc and Alboran Sea continental crust to the east; the Gibraltar Flysch units of the Campo de Gibraltar complex either side of the Gibraltar Strait (Figure 2.7, Figure 4.1), composed of Cretaceous–Lower Eocene flysch of Ultra-Betic origin; the Subbetics; and the Neogene Guadalquivir foreland basin [e.g., Platt & Vissers, 1989; Stromberg & Bluck, 1998]. This geometry is mirrored to the south by the Rif orogen, its External Zones, and the Rharb foreland basin. The present-day position of these units results from the Late Cretaceous to present convergence of Africa and Eurasia, which has led to westward displacement of the Alboran and Flysch Trough basin units, which were eventually overthrust onto both the African and Iberian Mesozoic margins, forming the Gibraltar Arc. The External Zones of the Betic-Rif (Subbetics and Pre-Rif) are the deformed Mesozoic margins, whereas the Algarve Basin represents the undeformed equivalent of the Subbetic Mesozoic margin of the Iberian massif. The main phase of compression was during the mid- to late Miocene (Late Langhian to Serravalian), with slower compression continuing until the present [Dewey *et al.*, 1989]. The Guadalquivir and Rharb Neogene basins are generally considered the foreland basins formed by flexural loading ahead of the outwardly-thrusting Betic-Rif fold-and-thrust belts [e.g., Platt & Vissers, 1989; Pratsch, 1996].

4.2.1 Gulf of Cadiz

Well and seismic data shows that the basement underlying the GOC comprises of elements of Palaeozoic rocks of the Iberian Massif, deformed rocks of the Betic-Rif orogen, and Neogene foreland basin infill [e.g., Drake *et al.*, 1959; Malod & Mougenot, 1979;

IGME, 1987]. Drake *et al.* [1959] tied early seismic data with boreholes to establish that Palaeozoic (Hercynian) basement overlain by a series of Mesozoic sediments extended offshore as the bottom structure of the northern GOC, as confirmed by subsequent offshore wells [IGME, 1987]. Fault-bounded blocks of flysch and Subbetic units have been interpreted to crop out in the SE Iberian shelf near Gibraltar [Maldonado *et al.*, 1999]. Roberts [1970] speculated on the extension of Betic-Rif structures into the Gulf of Cadiz on the basis of free-air gravity anomalies, and correctly correlated a zone of slope-parallel diapiric ridges and valleys observed in the central Cadiz continental slope (Figure 4.4) with the extension of a widespread allochthonous unit drilled in the GQB (the "olistostrome" of Perconig [1962]), where the ridges are currently thought to be due to shale mobility and halokinetic response of the allochthonous unit to the compressional stress regime [Baraza *et al.*, 1999]. Later papers used single-channel seismic reflection profiles which penetrated to 1s TWTT [e.g., Watkins & Hoppe, 1979; Hinz *et al.*, 1982; Veeken & Schwander, 1988]. The tectonics, stratigraphy and development of the GOC margin have been the subject of several other studies [e.g., Lajat *et al.*, 1975; Malod & Mougenot, 1979; Maldonado *et al.*, 1989]. The 1992 cruise of the *RV Explora* collected multichannel seismic data over the lower continental slope in the westernmost GOC, and in the Horseshoe Abyssal Plain [Sartori *et al.*, 1994; Torelli *et al.*, 1997].

The GOC margin has been the locus of much oil and gas exploration [e.g., Melendez-Hevia & Alvarez de Buergo, 1996], as a result of which borehole and seismic data have been available [Delaplanche *et al.*, 1982; Flinch *et al.*, 1996; Maldonado *et al.*, 1999]. Figure 4.2 presents interpreted cross-sections based on seismic and well data. Figure 4.2A [Flinch, 1993] is perpendicular to, and Figure 4.2B [Maldonado *et al.*, 1999] is parallel to, the Spanish coast in the NE GOC. Rifted Mesozoic sediments of the Tethyan margin form tilted fault blocks on a detachment surface of mobile Triassic evaporites on Figure 4.2A. A diapir of salt and anhydrite has been drilled at well C1 (IGME well number 288, Table B.1 and Figure B.1). Figure 4.2B is an interpretative summary section along the Spanish margin of the Gulf where the basal layers were not imaged but are inferred from several seismic sections [Maldonado *et al.*, 1999]. In the NW of this profile, extensional fault blocks of basement and Mesozoic sediment are recorded, whereas to the SE a buried accretionary wedge (consisting of thrust slices of "olistostrome" material and possible Flysch units) is observed, all below thick Neogene sediments (Figure 4.2B).

4.2.2 Guadalquivir Basin and the Betic Cordillera

The structure and stratigraphy of the western Betic Cordillera, from the Flysch units in the South, to the Iberian Massif in the North, is important due to its influence on

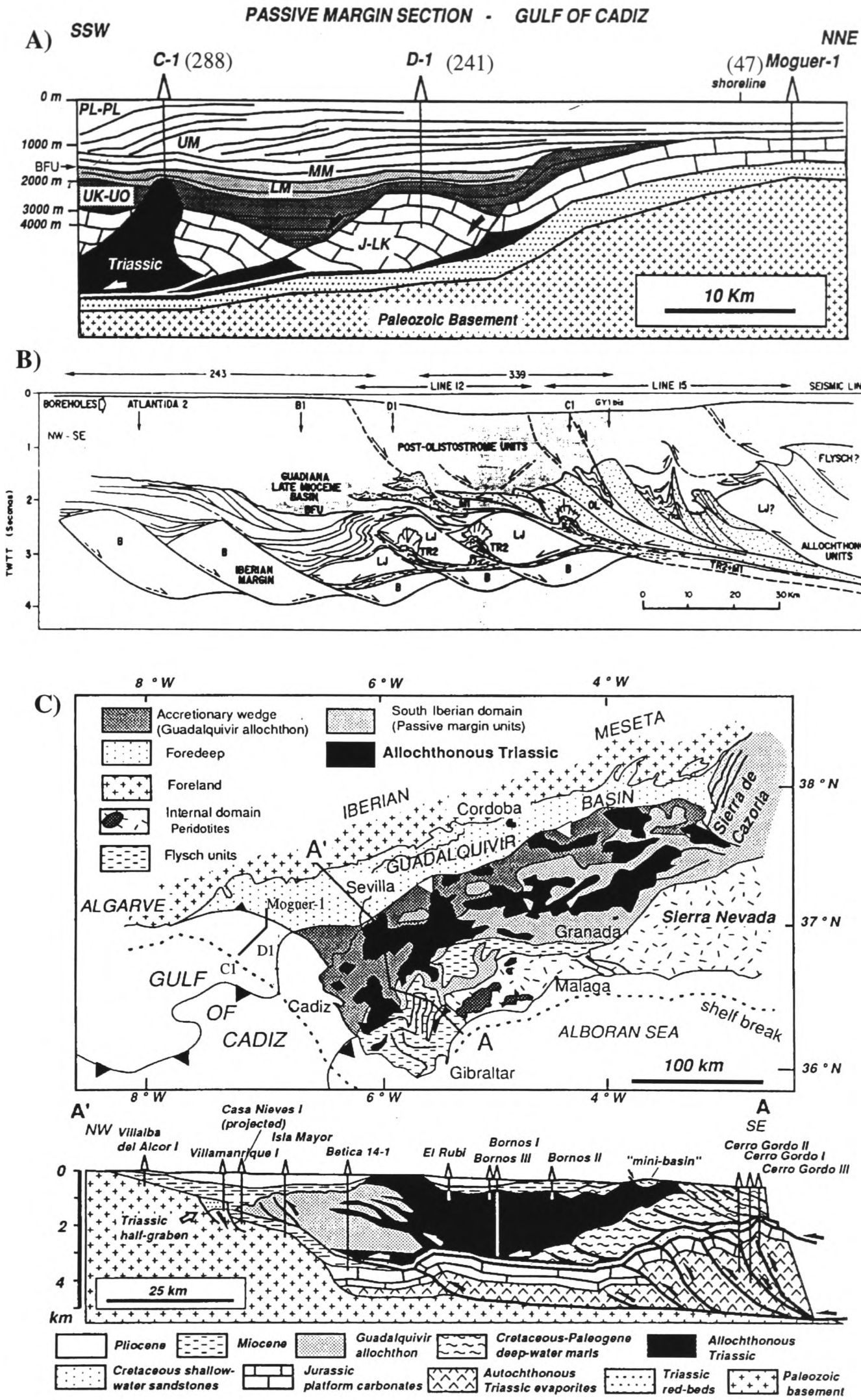


Figure 4.2: Sections across the GOC and Guadalquivir Basin: A) Well-constrained geological cross-section from Flinch [1993] in the northern GOC (IGME87 well numbers in brackets, location shown in C); B) A schematic cross-section through the NE GOC (after Maldonado *et al.* [1999]); C) Map of the western Betic Cordillera and cross section based on well and surface data from Flinch *et al.* [1996].

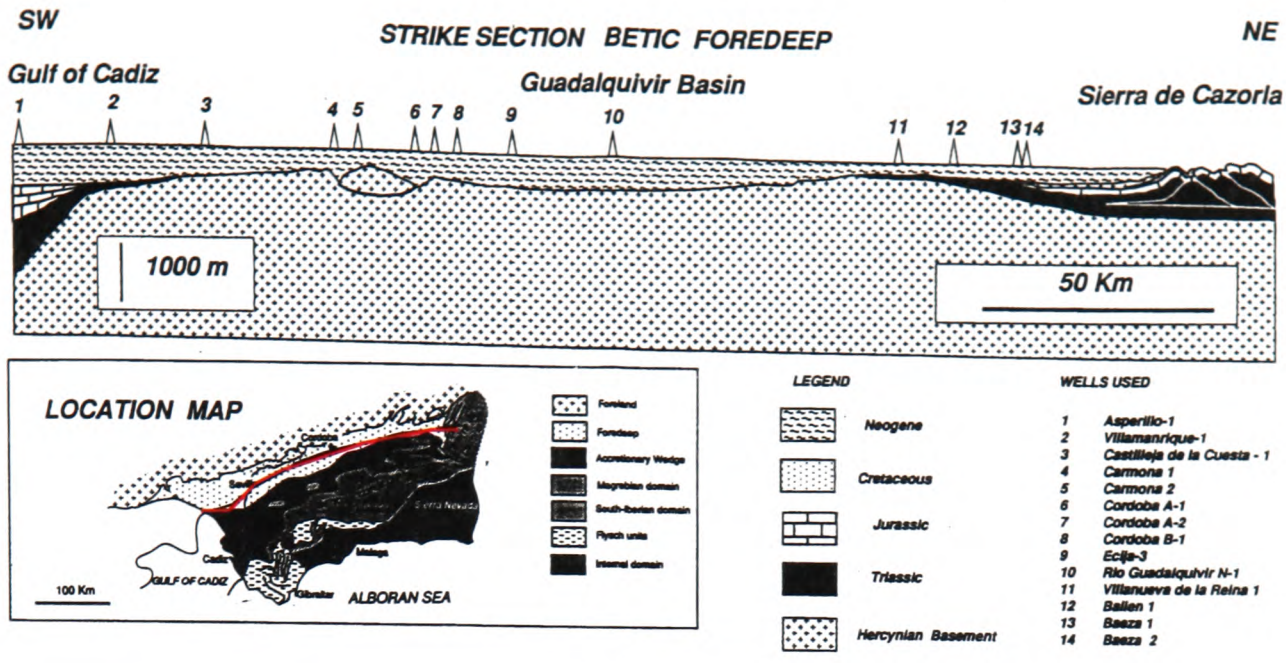


Figure 4.3: A strike section along the entire length of the Gudalquivir Basin, illustrating the distribution of Mesozoic sediments within the basin (After Flinch [1993]).

the stratigraphy in the adjacent GOC. A brief review of the geology of the GQB is now presented [Roberts, 1970; Flinch *et al.*, 1996; Riaza & Martinez del Olmo, 1996].

In the western Betic Cordillera, the high ridges of the Betics and Sub-Betics are separated from the high plateau of the Iberian Massif by the wide River *Guadalquivir* ("Great River" in Arabic) valley. A sharp contact between basinal sediments of the Guadalquivir Valley and rocks of the Iberian Massif runs straight for 400 km, obliquely cutting the NW-SE fabric of the Hercynian Massif rocks [Ager, 1980]. This "Guadalquivir Lineament" was originally thought to be a classic example of a normal fault [e.g., Rey, 1954], but after seismic reflection surveys and deep wells showed that the Palaeozic "basement" dipped gently southwards beneath the basin [Perconig, 1962] its true nature as a flexural forebulge was recognised. The GQB is thus the flexural foreland basin [e.g., Fernandez *et al.*, 1998a] formed ahead of the central and western parts of the Betic thrust front in southern Spain as a consequence of the Miocene-Recent Alpine Betic orogenic loading of the Hercynian basement of the Iberian massif (Figure 4.1), as the Alboran Sea underwent extension, resulting in the contemporaneous radial outward thrusting of the Betic-Rif Arc [Watts *et al.*, 1993].

Figure 4.2C illustrates the geological structure of the western Betic Cordillera. The thrusted Mesozoic and Palaeogene units of the Flysch and Subbetics lie to the south, while undeformed Neogene sediments of the GQB are shown to the North. In between,

infilling much of the onshore Subbetics and lying beneath the southern half of the GQB, is a body of allochthonous sediments, which has been subdivided by Flinch *et al.* [1996] into allochthonous Triassic at the back, and the Guadalquivir allochthon under the clastic foredeep sediments.

The sedimentary fill of the GQB is Neogene in age and comprises mainly marine marls with sandy intercalations, above a "basal calcarenite" unconformably overlying a pre-Miocene basement [Riaza & Martinez del Olmo, 1996; Fernandez *et al.*, 1998a]. Deposition in the Miocene took place in the North-Betic Strait which linked the Atlantic and Mediterranean until ongoing convergence closed the seaway in the Late Miocene [Riaza & Martinez del Olmo, 1996].

The Palaeozoic basement beneath the transgressive Neogene fill of the GQB has been found to consist mainly of metasediments, with some granites and gneisses (e.g., IGME [1987], wells 71, 75, 82, 87). Marine Jurassic and Triassic facies form the pre-Miocene basement at either extermity of the GQB, indicating that the Mesozoic shoreline reached inland as far as the drilled extent of Mesozoic marine sediments (Figure 4.3, Figure 4.4), as also found in the Algarve Basin (Figure 4.1). Seismic data from the western GQB [Fernandez *et al.*, 1998a] have revealed faulted Palaeozoic to Mesozoic units (Profile I, Figure 4.4), overlain by onlapping Neogene sediments, with late Messinian to Plio-Quaternary sediments prograding westwards in a trough-parallel direction (Profile II, Figure 4.4). On the basis of proprietary commercial seismic data from the GQB, Fernandez *et al.* [1998a] relate observed NE-SW-trending pre-Miocene "basement" faults, downthrown both to the north and the south, to crustal arching in response to Betic orogenic loading in Mid-Miocene times.

Boreholes along the southern band of the GQB penetrate large thicknesses of a chaotic allochthonous unit (the Guadalquivir allochthon of Figure 4.2C), consisting largely of chaotic Triassic facies containing clasts of younger rocks, which is known to fill over half the basin [Perconig, 1962]. This allochthon is exposed at the surface in the south but pinches out towards the north as a wedge buried within Miocene sediments (Figure 4.2C). The position of this buried front in the GQB is marked on Figure 4.4. The Betica-14 well (IGME87 604) penetrated 2 km of the allochthon, and sampled undercompacted shales, clays and Triassic evaporite layers up to 160 m thick. Most authors from Perconig [1962] onwards have interpreted this unit to be the result of a large-scale gravitational collapse of sediments from the External Zones of the Betic Cordillera into a pre-Guadalquivir foredeep. Other explanations include northward tectonic displacement of passive margin

salt deposits followed by deformation from below by Subbetic and Prebetic thrust sheets [Flinch *et al.*, 1996](see Figure 4.2C), and lateral diapiric movement of Triassic evaporites under loading by the Betic thrust belt [Berastegui *et al.*, 1998; Fernandez *et al.*, 1998a].

In summary, previous regional interpretations surmised that a clastic infill was sourced from a northern passive margin (Iberian foreland) and a gravitational infill from an active southern margin (External Zones of the Betics). However, the extent of gravitational filling of the southern part of the basin [e.g., Perconig, 1962] has not been universally accepted, and other credible mechanisms for allochthon emplacement have been proposed [e.g., Flinch *et al.*, 1996; Berastegui *et al.*, 1998].

4.3 Data

4.3.1 Well data

Well data for this study included public-domain and proprietary commercial borehole logs, plus lithologic and stratigraphic information reported in IGME [1987]. These data were used in lithological and subsidence analysis, as well as for ties to seismic data. The Spanish governmental compilation, IGME [1987], provided limited well data at locations shown on Figure 4.1. Due to the search for hydrocarbons, the bulk of boreholes have been drilled in the western GQB and NE GOC (Figure 4.1). The Neogene basin comprising the northern GOC and the GQB has yielded several discoveries of dry, biogenic gas, sourced from the Miocene shales of the basin [Melendez-Hevia & Alvarez de Buergo, 1996].

Figure 4.4 shows well locations in the GOC/western GQB study region, with their IGME [1987] catalogue numbers, which are used throughout this chapter. A full IGME [1987] listing of wells in southern Iberia is given in Appendix B, Table B.1 and Table B.2, with name, location, elevation, depth, and oldest formation drilled given for each well. Commercial data were provided by Shell International Oil Company for 5 wells in the GOC (Figure B.1) , while Chevron (COPI) provided a suite of well data for 3 wells in the westernmost GQB (Figure B.2A). Sonic logs for wells 223, 225 and 604 in the GQB were digitised from Fernandez *et al.* [1998a] (Figure B.2B). The locations of these commercial wells are shown in red on Figure 4.4, and the data is described in detail in Section B.1.1.

4.3.2 Seismic reflection data

The seismic profiles shown in bold red on Figure 4.1 are lines GC1, GC2, GC3 and T3 of the IAM project [Banda *et al.*, 1995]. Stacks of profiles GC3, GC2 and GC1 have previously been published by Tortella *et al.* [1997], but the prevalence of deeper noise

Figure 4.4: Well data and seismic ties superimposed on a relief map of SW Iberia and the northern GOC. GB = Guadalquivir Basin; AB = Algarve Basin. The term "Ultra-Betics" is synonymous with the "Campo de Gibraltar Flysch Complex" [Ager, 1980]. Well data numbered according to order in IGME [1987]; wells with gas shows are infilled, wells with available geophysical downhole data shown in red. Seismic profiles in red: GC2, GC3 offshore; locations of I and II onshore [Fernandez *et al.*, 1998a](discussed in text). Continental slope ridges (purple lines) and valleys (purple dots) shown in the SW corner [Roberts, 1970; Nelson *et al.*, 1993]. Profile A-A' is the location of a well correlation section based on data from IGME [1987]. The extent of marine Mesozoic pre-Miocene "basement" beneath the Guadalquivir Neogene infill is shown as a thick black line. North of this line, Miocene sediments rest above Palaeozoic rocks of the Hercynian foreland of the Iberian Massif. The extent of a buried wedge of allochthonous sediments within the GQB is shown as a red line with ticks.

restricted their interpretations to the top 4s TWTT, and generally did not allow identification of basement and intra-basement reflectivity over the GOC. This study uses profiles to which several additional post-stack data processing steps have been carried out, followed by migration (see Section ??). The resulting profiles display less noise and clearer reflections than the stacks in Tortella *et al.* [1997], and are more spatially ac-

accurate due to better migration. Deep reflections have been enhanced through improved noise suppression and coherency filtering, and allow image resolution below the top of the chaotic unit. As a result of the improved interpretability of the IAM profiles, interpretations have been possible as deep as 14s TWTT. Migration redistributes the energy of the reflected wavefield, thus unmigrated data is often better for displaying the presence and form of weak amplitude deep crustal structures, as individual unmigrated reflections tend to be stronger and display greater lateral continuity [e.g., Drummond *et al.*, 1998]. The profiles used here were migrated with low velocities at depth in order to avoid pitfalls associated with migrating deep continental data [Warner, 1987], such as weakening of reflections and unjustifiably large migrations of deep events. In addition to the improved IAM profiles, a noisy initial stack of unpublished Lamont Doherty MCS profile 829 from the Gibraltar Straits (Figure 4.1) was reprocessed, and a new interpretation presented.

4.4 Observations from Well Data

Well profile A-A' (Figure 4.5), was constructed using available well information along a NW-SE transect (Figure 4.4) from the northeastern GOC shelf to the Ultra-Betics (Campo de Gibraltar Flysch Complex). Well logs were available for wells 245, 288, 296 (Figure B.1). Correlations between wells have been made for four surfaces on Figure 4.5 (and Figure B.1): seabed, base Pliocene (black), base Miocene (green), and base Tertiary (purple). The lithologies are classified into the main categories of shale, sandstone, limestone, dolomite, marl, evaporite and the more genetic "allochthonous unit".

Palaeozoic basement has been penetrated only in well 533 (Figure 4.6), and the Mesozoic mainly in the northern GOC (Figure 4.5, Figure 4.4). Triassic rocks comprise clastic redbeds (well 296) and evaporites (well 288; well 363, Figure 4.6). Drilled Jurassic rocks (e.g., wells 241, 296, 314; well 533, Figure 4.6) are carbonate-dominated, with dolomite and limestone interbedded with thinner layers of marls and shales. The Jurassic is up to 2000 m thick (well 533, Figure 4.6). The Cretaceous sequence is more shale-dominated (e.g., wells 296 and 241, Figure B.1; well 526, Figure 4.6), with carbonate and sandstone intervals (e.g., well 427, Figure 4.5; well 241, Figure B.1).

The Mesozoic-Cenozoic transition in the northern GOC is marked by a stratigraphic break (Figure 4.5). Above this correlated base Tertiary unconformity are Palaeogene rocks varying from Palaeocene to Oligocene in age, with sands, shales, limstones and dolomites all represented. The Palaeogene displays considerable thickness variations, with a thick (up to 1200 m) sequence of carbonate shelf limestones in the northern GOC

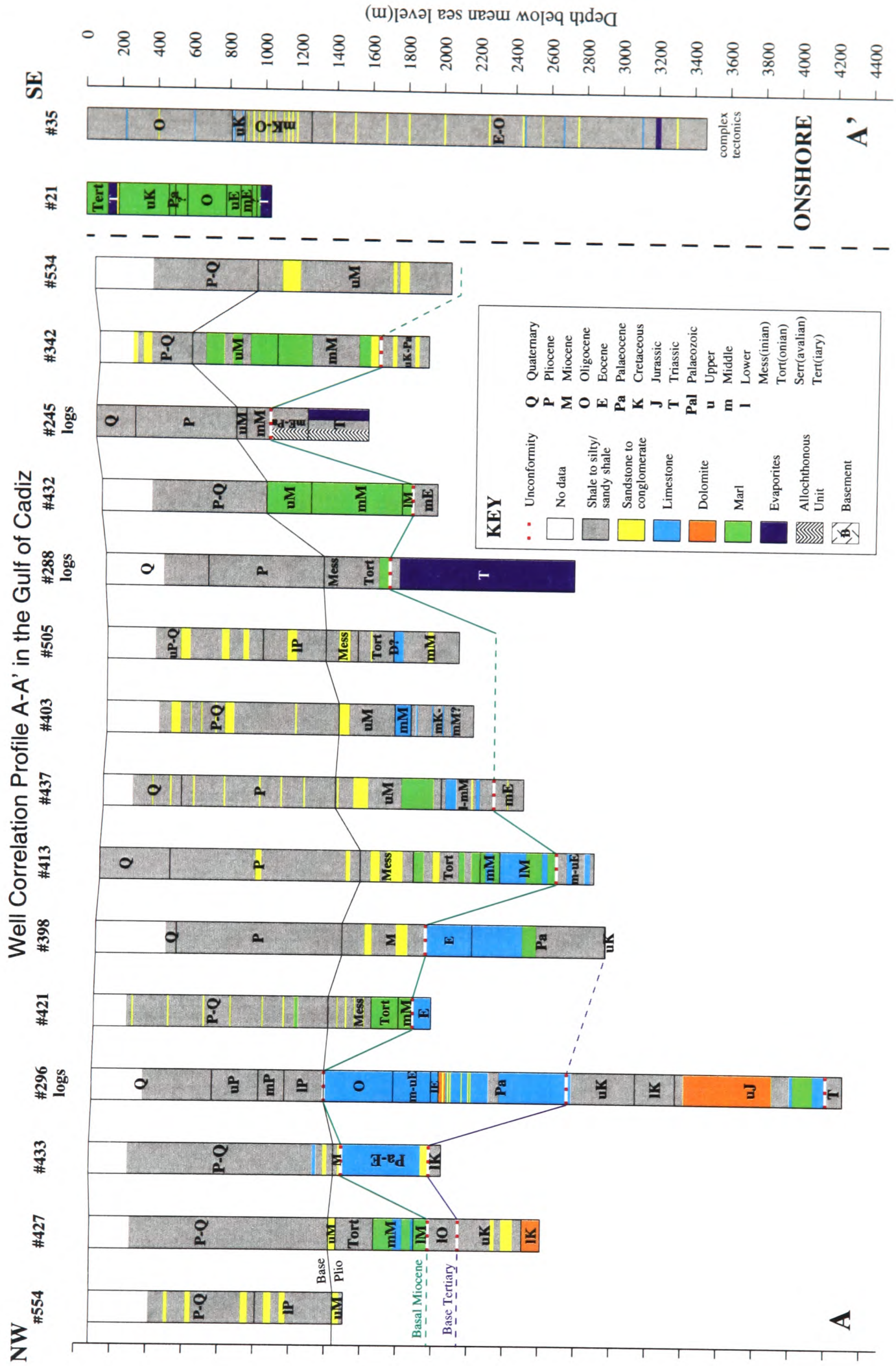


Figure 4.5: Stratigraphic well correlation profile **A-A'** (Figure 4.4), from the northern GOC to the Ultra-Betics (Campo de Gibraltar Flysch complex). Horizontal well separation is not to scale; depths are in metres below mean sealevel. Borehole data was available for Wells 245, 288 and 296, as indicated; sonic velocities for these are shown on Figure B.1.

(e.g., wells 296, 398, 421, and 433), whereas the interval is absent above the saline diapir of well 288 on Figure 4.5. An erosional unconformity due to an Oligocene–lower Miocene stratigraphic break (basal Miocene surface, Figure 4.5) separates Neogene sediments of Lower or Mid–Miocene age above from the Palaeogene sediments below.

The Neogene comprises Miocene and Pliocene–Quaternary intervals, with the transitional base-Pliocene surface correlated on Figure 4.5. The Miocene is variable in lithology and thickness, with a maximum thicknesses up to ~1200 m in local depocentres (wells 413 and 534, Figure 4.5; well 241, Figure B.1), to minimal thicknesses over autochthonous and allochthonous evaporites and clays (wells 288 and 245, Figure 4.5, respectively) and Palaeogene carbonate buildups (wells 433 to 398). Allochthonous sediments drilled below the Mid–Miocene of well 245 consist of upper redeposited Palaeogene deep-water sediments, while the lower part is a chaotic mixture of mainly Triassic clay with some evaporites, thought to be supratidal flat deposits redeposited in a deepwater environment. Drilled Plio-Quaternary sediments in the GOC consist largely of calcareous muds, shales and some sandy intercalations, which are up to ~1500 m thick in the northern GOC, thinning towards the SE towards the Gibraltar Straits (Figure 4.5).

Onshore, thrusting is indicated by stratigraphic repetition seen in wells 21 and 35 at the southern end of Figure 4.5, which are attributable to Sub-Betic and Ultra-Betic deformation respectively (Figure 4.4). Onshore data from the GQB (Figure B.2) indicate a Neogene infill, and a pre-Miocene basement of Palaeozoic metamorphic rocks or Mesozoic sediments (Figure 4.3). As in the GOC, the Neogene foreland sediments of the GQB are mainly shales with some sand and carbonate interlayers. The southern GQB is also known to be filled with intra-Miocene allochthonous deposits (Figure 4.4, Figure B.2B) [e.g., Perconig, 1962; Flinch *et al.*, 1996; Berastegui *et al.*, 1998].

4.5 Seismic Stratigraphy and Well Ties

4.5.1 Seismic Facies

To characterise the sedimentary fill of the GOC a seismic stratigraphic scheme for the Gulf of Cadiz has been developed, on the basis of seismic character and reflector terminations [e.g., Mitchum *et al.*, 1977]. It was necessary that each seismic facies could be distinguished regionally, with prominent boundary reflections which correlated with expected changes in acoustic impedance based on well–derived information on stratigraphic breaks, lithology and sonic velocity. Five major seismic stratigraphic units (units CI to CV) were identified, picked on the basis of seismic character, and well calibration. These,

and their typical pattern of reflectivity, are shown in Table 4.1, together with descriptions of each facies and correlated ages.

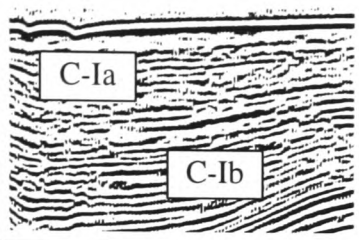
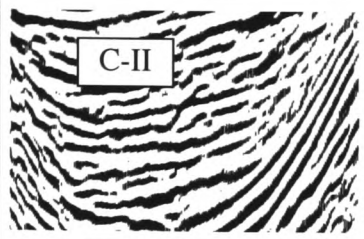
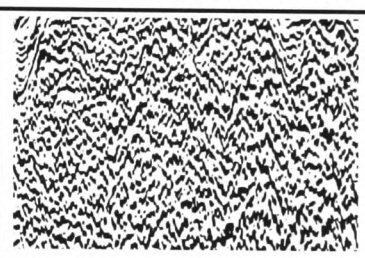
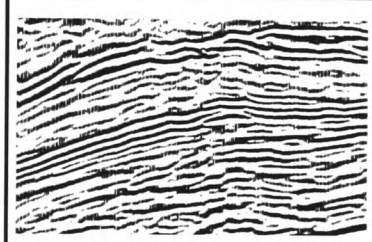
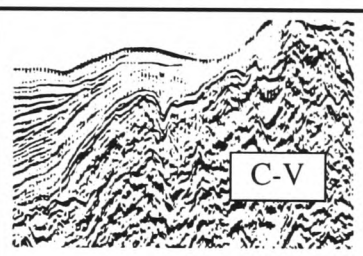
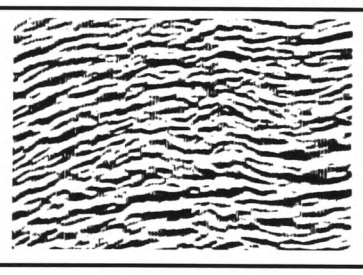
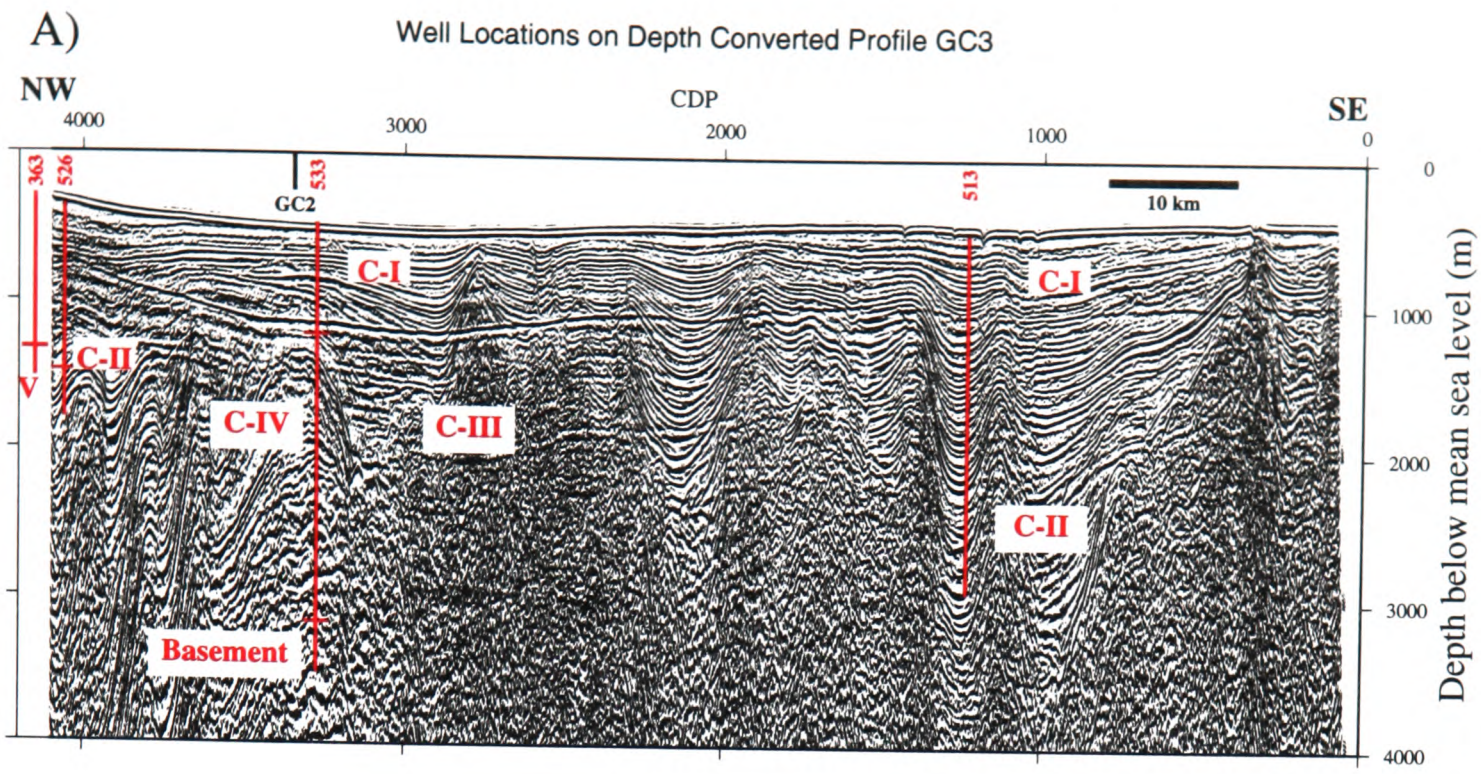
SEISMIC UNITS	SEISMIC FACIES	DESCRIPTION OF FACIES	AGE
C-I		Medium-low amplitude, continuous to semi-continuous. C-Ia generally parallel, onlapping, separated from generally divergent subunit C-Ib by an erosional unconformity. Internal discon-formities. Variable thickness. Basal unconformity.	Pliocene-Quaternary
C-II		Variable seismic fabric and thickness. Generally continuous to semi-continuous, sub-parallel to divergent. Basal unconformity marked by a high amplitude reflection.	Miocene
C-III		Small-scale chaotic seismic fabric , associated with diffraction hyperbolae and steep dipping noise. Internal structure of semi-continuous reflections and internal angular unconformities. Generally lenticular or wedge-like form. Allochthonous.	intra-Miocene
C-IV		High amplitude upper surface marking an angular unconformity. Variable internal character, with generally high amplitude , parallel-subparallel reflections with some low amplitude intervals. Faulted and folded, sometimes seen as tilted blocks.	Oligocene-Jurassic
C-V		Low frequency, mid-high amplitude, noncoherent reflectivity. Upper surface generally deformed and marked by a high amplitude, irregular reflection. Displays variable form: lenses, pillows, diapirs.	Triassic
BASEMENT		Top basement marked by a high amplitude reflect-ion where not obscured by noise. High amplitude layering seen in top 1s TWTT, otherwise noise dominates. Upper layer correlates with drilled metasediments and volcanics of Hercynian age.	Palaeozoic

Table 4.1: Seismic facies classification in stratigraphic context, youngest at the top. Each box is 10 km wide and 1 s TWTT deep, except that for C-II which is 10 km by 0.6 s TWTT.

Figure 4.6 illustrates the four wells (IGME [1987] numbers 363, 526, 533 and 513) that are within 2 km of IAM profile GC3 (Figure 4.4). Figure 4.6A shows the position and penetration of these wells superimposed on depth-converted seismic profile GC3 and Figure 4.6B illustrates the lithological and stratigraphic data available from IGME [1987]. The seismic facies divisions on Figure 4.6 illustrate the seismic–well correlation. Well 533



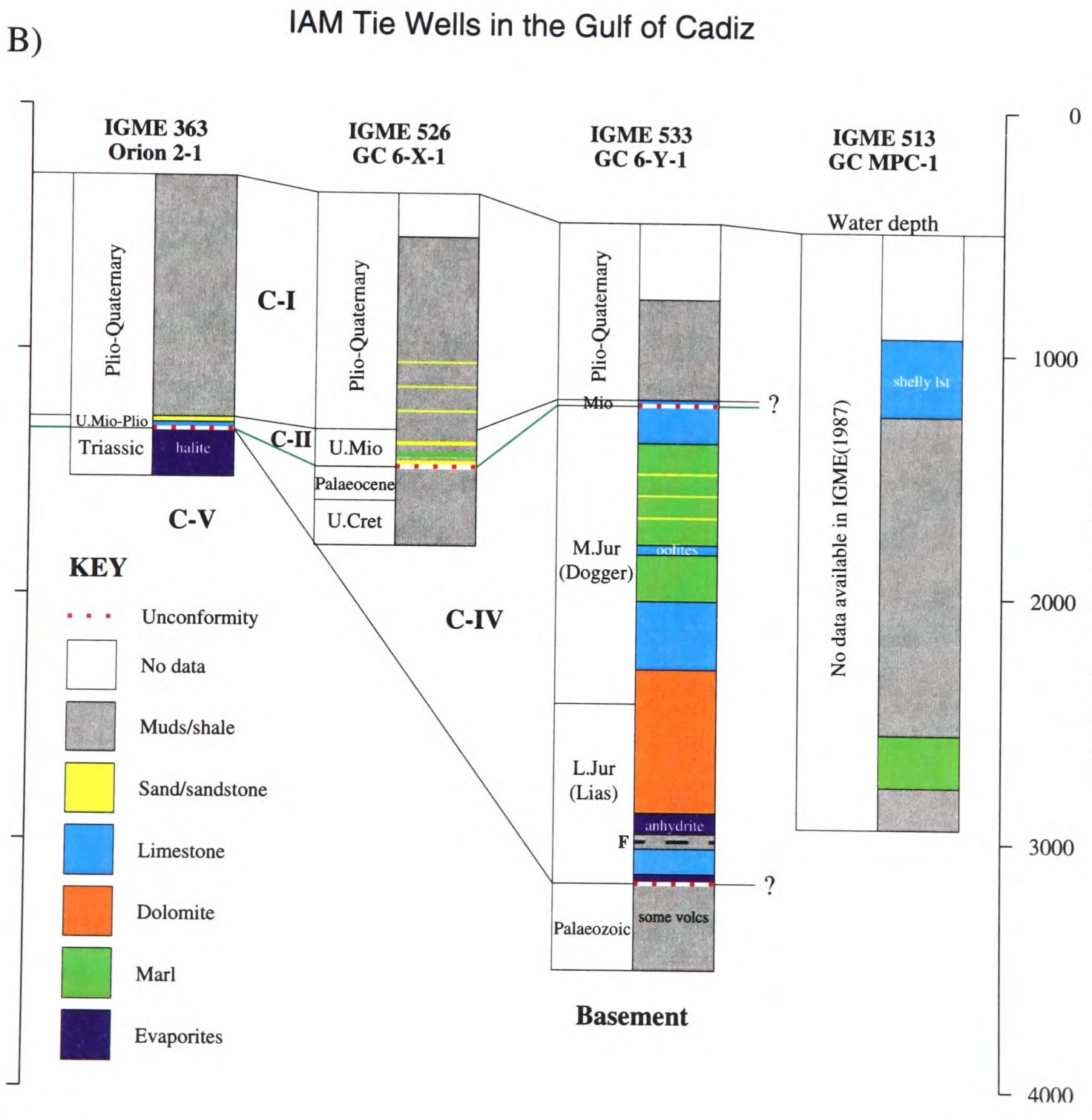


Figure 4.6: Well lithostratigraphy and ties with depth converted profile GC3: A) Well locations and penetration projected onto Profile GC3 depth converted with stacking velocities; B) Lithostratigraphy of wells close to profile GC3. Sonic data was not available for these wells.

was also correlated with Profile GC2 (Figure 4.4).

Previous seismic stratigraphic schemes for the GOC have been produced by Tortella *et al.* [1997] and Maldonado *et al.* [1999], and for the GQB by Riaza & Martinez del Olmo [1996]; Berastegui *et al.* [1998]. The GQB schemes span only the mid-Miocene (Langhian)–Recent infill of the basin and were largely based on detailed geophysical log correlations, making them unsuitable for regional extrapolation to the Gulf. The scheme used in this study has a more detailed Miocene–Recent classification than that of Tortella *et al.* [1997], and is also integrated with recent studies [e.g., Berastegui *et al.*, 1998; Maldonado *et al.*, 1999] and a larger number of wells, giving the scheme outlined here greater validity. The detailed scheme of Maldonado *et al.* [1999] was not used here as the identification of seismic units was dependent on dense borehole and seismic coverage, which in the GOC was only available along the marginal shelf of SW Spain, east of IAM Profile GC3 (Figure 4.4). This scheme was not viable for the regional IAM profiles as there was insufficient well control away from the northeast GOC shelf, so the relatively simple scheme outlined here was used.

4.5.2 Sonic Data, Synthetic Velocity Profiles and Well Ties

The correlation of stratigraphic data in wells to seismic data (as shown in Figure 4.6) depends on the velocity profile used to convert the seismic profile to depth, as well as matching unconformities and lithological boundaries to the correct reflections. The velocity profile used in depth conversion can be validated by comparing it to sonic velocity in the wells. As pointed out previously, sonic data were not available for the four wells drilled within 2 km of either IAM Profiles GC2 or GC3 (Figure 4.4). However, by examining sonic velocity data from all the other available wells in the GOC and western GQB, with respect to principal lithologies and stratigraphic units, it is possible to construct pseudo–synthetic sonic velocity profiles for the tie wells of Figure 4.6B. These profiles were then compared to seismic velocity profiles taken from the nearest analysis points on the seismic data.

Sonic logs show the variation in sonic slowness measured downhole by logging tools, and by taking the inverse of sonic slowness, the sonic velocity of drilled formations is obtained. An example of a sonic log for one of the wells is shown in Figure 4.7. Densities in the figure have been derived from sonic velocities using the empirical relationship of Gardner *et al.* [1974] (Equation (B.1)). The product of velocity and density of the layers above and below a discontinuity define their respective acoustic impedances. If the contrast in acoustic impedance is large and widespread it will produce a prominent

seismic reflection. Thus, large changes in sonic velocity (and hence, the derived density) can be taken as a proxy for a large impedance contrast.

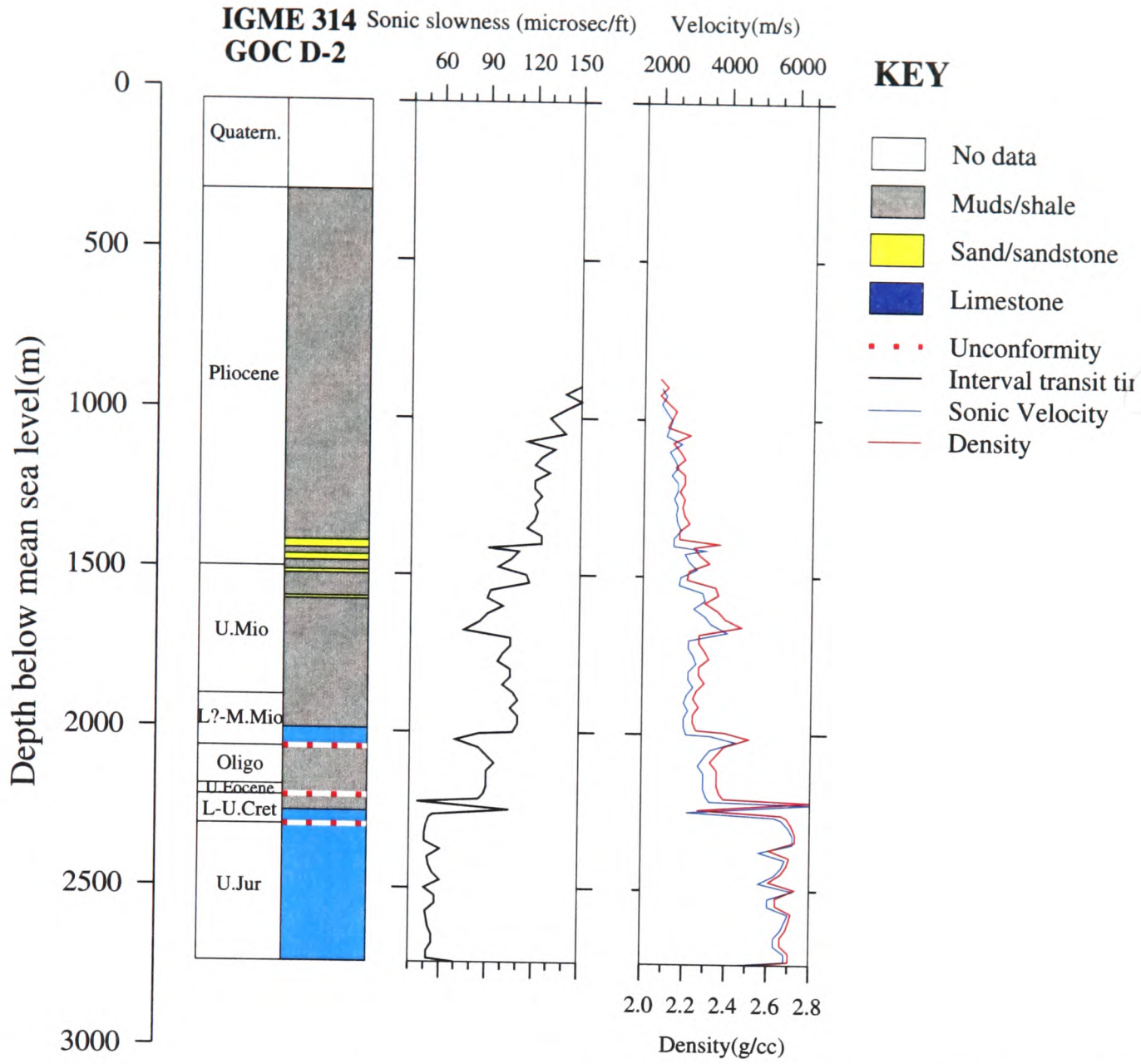


Figure 4.7: An example of sonic data from a Gulf of Cadiz well, IGME [1987] 314 (D–2).

Figure 4.8 is a compilation of all the available sonic velocity data from the northeast GOC and western GQB (which can be considered parts of the same depositional basin), plotted with respect to depth and seismic unit (common rock ranges have been included for reference). Data from the GQB was available for Miocene to Recent sediments and so was assigned a seismic unit on age, as per the GOC scheme of Table 4.1.

Velocities generally increase with depth on Figure 4.8, as expected in normal compacting sequences. However, large differences occur between the separate units. Units C-I and C-II are composed of clastic sediments (Figure B.1) and display velocity values which follow an approximately linear trend, with a best-fit line (velocity(m/s)=0.8*Depth(m) + 1600) as shown on Figure 4.8; synthetic velocity values for C-I and C-II of the tie wells of Figure 4.6 were calculated on this basis. Values from unit C-III also display a roughly

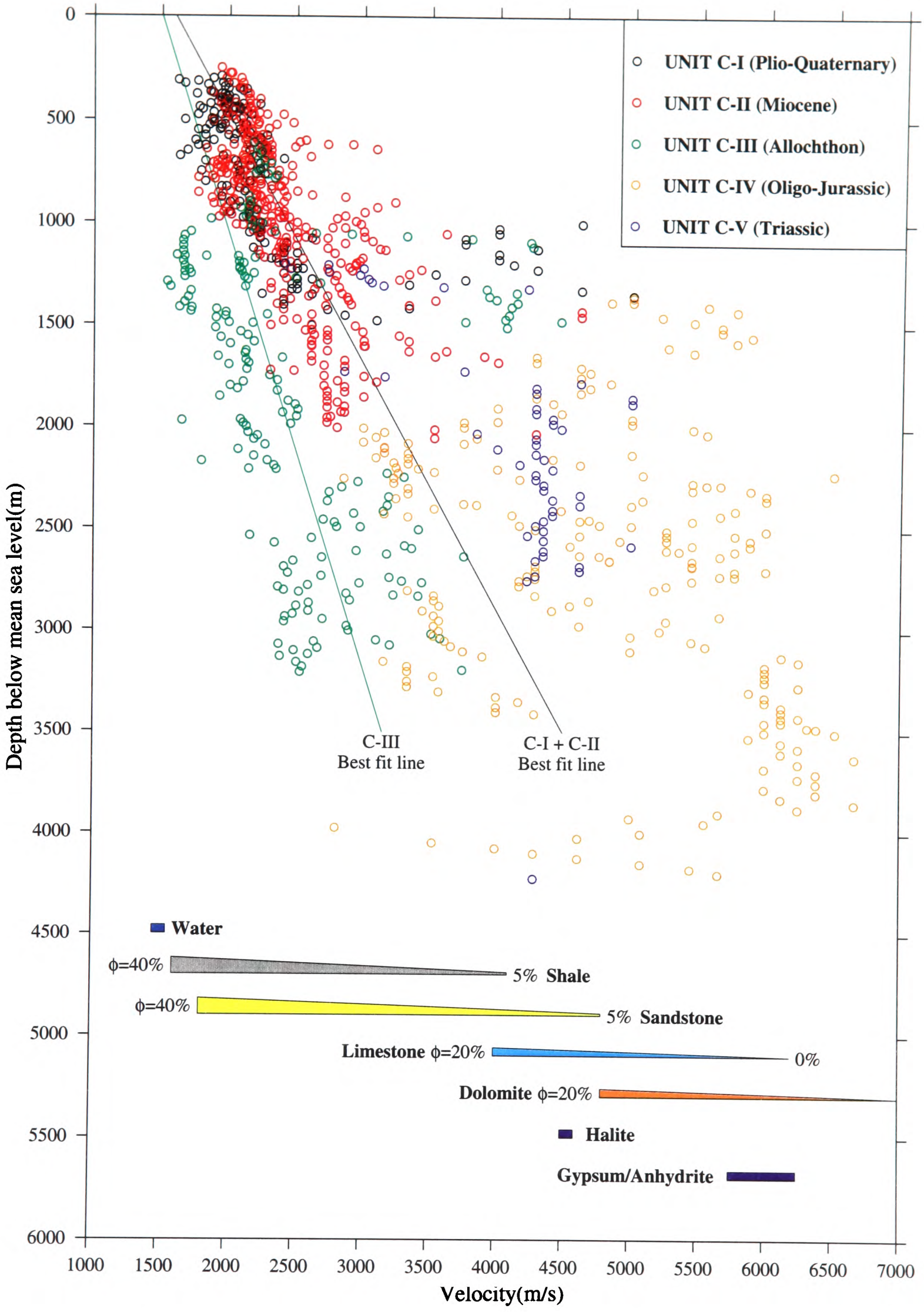


Figure 4.8: Compilation of sonic velocity data obtained from available sonic logs (see Appendix C) from the Gulf of Cadiz (IGME [1987] 241, 245, 288, 296, 314; Figure B.1) and the western Guadalquivir Basin (wells 223, 225, 482, 483, 581, 604; Figure B.2), colour coded by seismic unit.

linear trend (best-fit line shown on Figure 4.8), with anomalously high values away from this C-III trend due to the presence of high velocity salt layers (Figure B.2). The C-III trend is similar in gradient to that of C-I+C-II, but with lower values for a given depth, although all these units are largely shales and muds (Figure B.1, Figure B.2). The most plausible explanation for this observation is that compaction has been retarded by overpressuring in C-III, which may be caused by pore water being trapped in sediments by shale and evaporitic layers during rapid deposition of the allochthon. The presence of overpressures within the allochthonous unit has recently been speculated upon by Somoza *et al.* [1999]. Unit C-IV values range from 3000–6500 ms^{-1}, corresponding with limestone/dolomite to shale velocities. Unit C-V values tend to fall around halite values, as expected given that the bulk of these values are from a saline diapir (well 288, Figure B.1).

The sonic velocity data were also analysed to gauge representative values and the spread of data for each unit, as shown in Figure 4.9 where normalized histograms for each unit are shown, as well as for shale-dominated Units I, II, and III combined. All the distributions are unimodal, except for Unit C-IV, which is related to the variety of lithology in CIV. The mean values calculated for sonic velocity and derived density were representative of each unit.

The analysis of well log-derived sonic velocities was used to construct synthetic sonic velocity profiles for the tie–wells of Figure 4.6 by assigning representative velocities to each well interval on the basis of bulk lithology and burial depth (Figure 4.8). The resulting synthetic sonic velocity profiles were compared to interval velocities derived from the seismic data at the nearest velocity analysis locations of profile GC3, as shown in Figure 4.10. Seismic interval velocities were derived from RMS stacking velocities by means of the Dix equation which relates them [Dix, 1955]. Errors in seismic velocities are $\sim$10% [e.g., Sheriff & Geldart, 1983; Yilmaz, 1987], whereas the sonic velocity values are based on representative values for lithology and depth from Figure 4.8 and Figure 4.9, and hence are subject to greater errors, with standard deviation $\sigma \approx$20–25% from the histograms of Figure 4.9.

Synthetic sonic velocity profiles for Wells 513 and 526 (Figure 4.10) display the best agreement between seismic and sonic velocity profiles. In wells 363 and 533 the sonic-based velocities agree with the seismic interval velocities in the sections shallower than about 1200 m, but at deeper levels the sonic velocities assigned to the synthetic profile is significantly larger than seismic interval velocities. The intervals where the sonic velocity

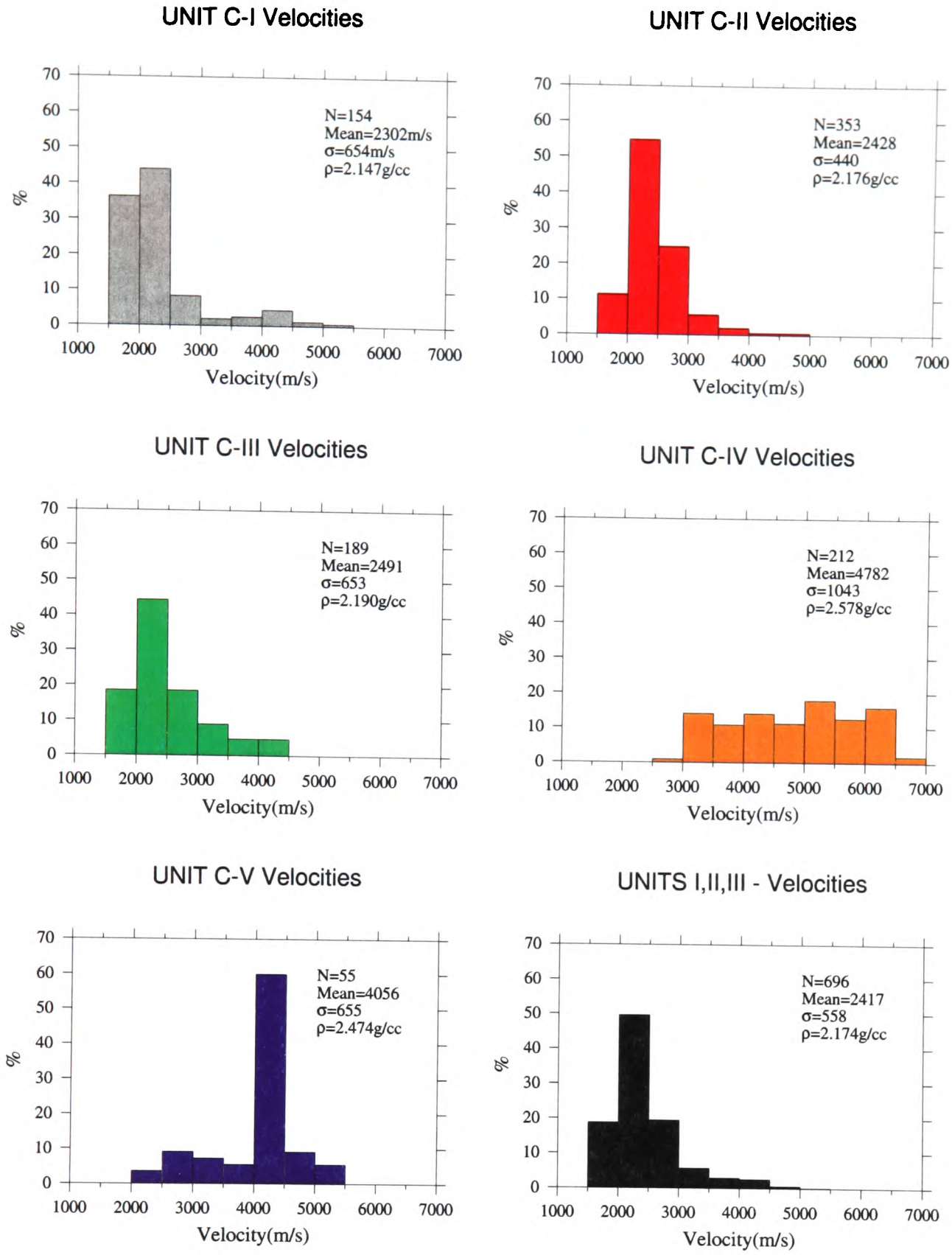


Figure 4.9: Histogram of sonic velocities in the GOC; statistics by unit.

profile exceeds the seismic values coincide with carbonate or halite intervals (Figure 4.6, Figure 4.10). The difference is not significant for the halite in well 363 but is large for the carbonate intervals in well 533.

Sonic measurements maybe biased towards higher values for theoretical reasons according to Sheriff & Geldart [1983]. The sonic log measures vertical seismic velocities, at kilohertz frequencies, of the fastest path within a small sample of rock near the borehole, which is unlikely to be representative of the formation bulk sonic velocity. Velocity anal-

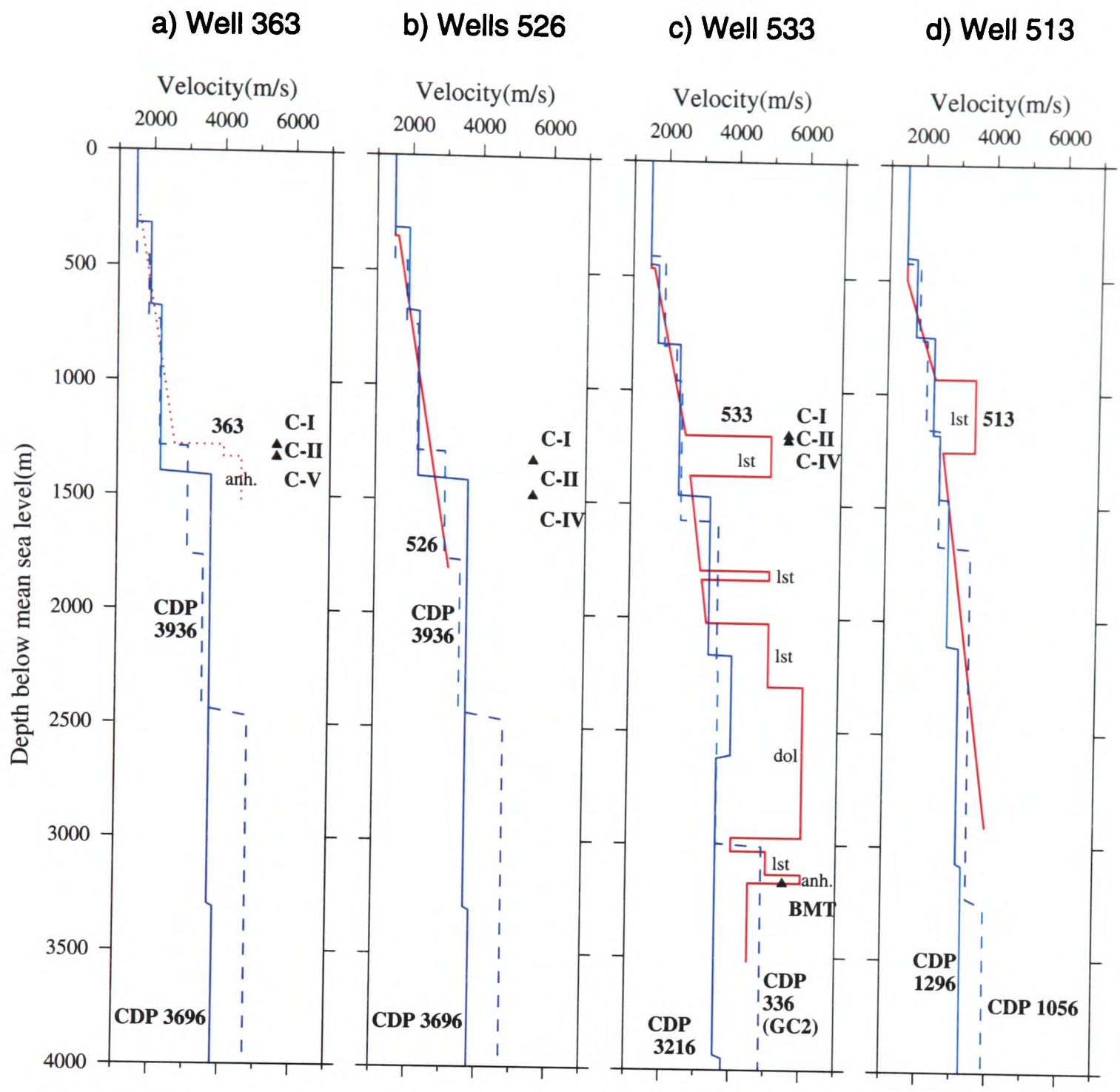


Figure 4.10: Comparison of sonic velocities assigned to Profile GC3 Tie wells on the basis of the log data in nearby wells (red), and interval velocities derived from seismic stacking velocities (blue) using the Dix equation [Yilmaz, 1987]. CDP locations refer to IAM profile GC3 unless otherwise stated. Boundaries between seismic units shown as filled triangles. Limestone (lst), dolomite (dol), and anhydrite (anh.) horizons are labelled.

ysis of seismic data through normal moveout corrections of CDP gathers from the seismic datasets measures a quantity closer to the horizontal bulk velocity of a material as seismic reflection techniques sample a much larger quantity of rock, at normal seismic frequencies of a few tens of Hz. For example, each source-reflector-receiver path involves a cylinder of rock around the path and a Fresnel zone diameter of typically 200-400m on the reflector itself, depending on the velocity of the medium [Sheriff & Geldart, 1983]. Hence, interval velocity computations from the seismic RMS stacking velocities represent the bulk horizontal velocity at seismic frequencies for the sampled interval within a disc-shaped

segment of the subsurface. Some rocks, such as stratified shales, show marked anisotropy with faster bedding-parallel velocities, which is why a distinction between horizontal and vertical bulk velocity has been made in this discussion. The source frequency range also contributes to the bias towards higher velocities of sonic measurement due to dispersive effects on its higher frequencies. With regard to Figure 4.10, the higher synthetic sonic values for limestone and dolomite are based on localised sonic measurements, whereas the seismic velocity is likely to be more realistic as it samples a much larger volume and so would incorporate such effects as mud interlayers, large scale fracturing and vuggy porosity, which all serve to reduce velocities through carbonate rocks.

In conclusion, the synthetic sonic velocity profiles and seismic velocities were in general agreement, although carbonates displayed higher sonic velocities for specific reasons, as given above. The seismic velocities were taken to be realistic bulk values, and therefore depth conversion with these values could be taken to produce a realistic depth profile (e.g., Figure 4.6A). The accuracy of the well-ties to seismic data was also aided by the correlation of lithologic and synthetic velocity changes from the tie wells in Figure 4.6B to seismic events on Figure 4.6A, although these were not always reflected in the seismic interval velocity functions, as the boundaries between seismic units C-I, C-II and C-IV/CV were relatively small (wells 363, 526 and 533, Figure 4.10). The collection of both check shot well data and sonic logs is industry standard in most modern wells, and if these become available for the tie wells in Figure 4.6, very accurate ties between well and seismic data will become possible through the use of check-shot calibrated synthetic seismograms.

4.6 Interpretation of Seismic Reflection Profiles

Basement

On the seismic reflection data, identifying basement definitively is difficult, due to the presence of salt diapirism, thick overlying chaotic sediments and widespread faulting. On Figure 4.11, it was possible to correlate the drilled top basement with a high amplitude reflection, which could be traced reasonably near well 533, but which became more uncertain away from the well. Below about 6s on Profile GC3, little signal reflectivity was visible amidst strong noise. This is due to attenuation of signal within the chaotic unit C-III to the southeast, and structure-related noise beneath the folded and overthrust C-IV layers seen NW of well 533 between 2-4 s. The basement of the GOC has only been drilled by well 533 (Figure 4.11), where it consists of Palaeozoic rocks (metasediments, coals and volcanics) similar to the Hercynian basement of the Iberian

Massif. Recent refraction data indicates a similar velocity basement underlies most of the GOC [González *et al.*, 1996, 1998], and is interpreted to be the offshore extension of the Hercynian basement beneath the GQB.

The basement at well 533 correlates with a high amplitude reflection on Figure 4.12 which can be traced to south away from the well. Between CDPs 2000-4000 there is a basement high (Figure 4.12). High amplitude layering is visible within 1s TWTT of the picked top basement on both GC2 and GC3. This is interpreted to be due to depositional layering leading to impedance contrasts in the Palaeozoic metasediments and volcanics that make up the basement. In the central and eastern GOC, where thick chaotic sequences occur, the top basement is obscured, but a high amplitude reflection with some layering below, which is inferred to be basement, can be picked (e.g., Figure 4.16).

Facies C-V

The oldest facies that has been identified above basement has very low amplitude, and incoherent reflectivity, and is best observed in the northern GOC (e.g., Figure 4.12). It correlates with autochthonous Triassic rocks of a lower unit of siliciclastic type (continental red beds with volcanics in well 296) and a upper unit of evaporites and red clays (wells 288 and 363 in the northeast GOC). The top is usually a strong reflection (indicating a high impedance contrast) with a hummocky appearance, inferred to be due to salt movement. The base is generally less clear and is identified as acoustic basement. Internal reflectivity ranges from being reflection–free to low frequency and chaotic (see Figure 4.12 and Figure 4.15).

The disturbed sediments observed between CDPs 0–500 and 1–3 s TWTT on Figure 4.12 are interpreted to be due to the mobility of this unit. This segment of seismic data is displayed in greater detail as Figure 4.13, with opposite polarity to Figure 4.12, with red being equivalent to negative (white) and blue equivalent to positive (black) on Figure 4.12. The presence of thick salt layers close to this northernmost end of Profile GC2 has been established by drilling of Triassic evaporitic formations in two nearby wells, 363 and 288 (Figure 4.4). Well 288 is nearest, and penetrates over a thousand metres of mostly halite (Figure B.1), whereas well 363 penetrated 150 m of halite before drilling was stopped. On the basis of its seismic character and the drilled salt nearby, the unit with a distinctive lenticular shape with a ragged extremity seen in the shallowest 1 s of Figure 4.13 is interpreted to be due to salt movements, with the apparent interfingering with the C-I layers thought to be caused by salt intruding into less competent horizons. The sediment beneath the domal structure between CDPs 200–300 of Figure 4.13 is frac-

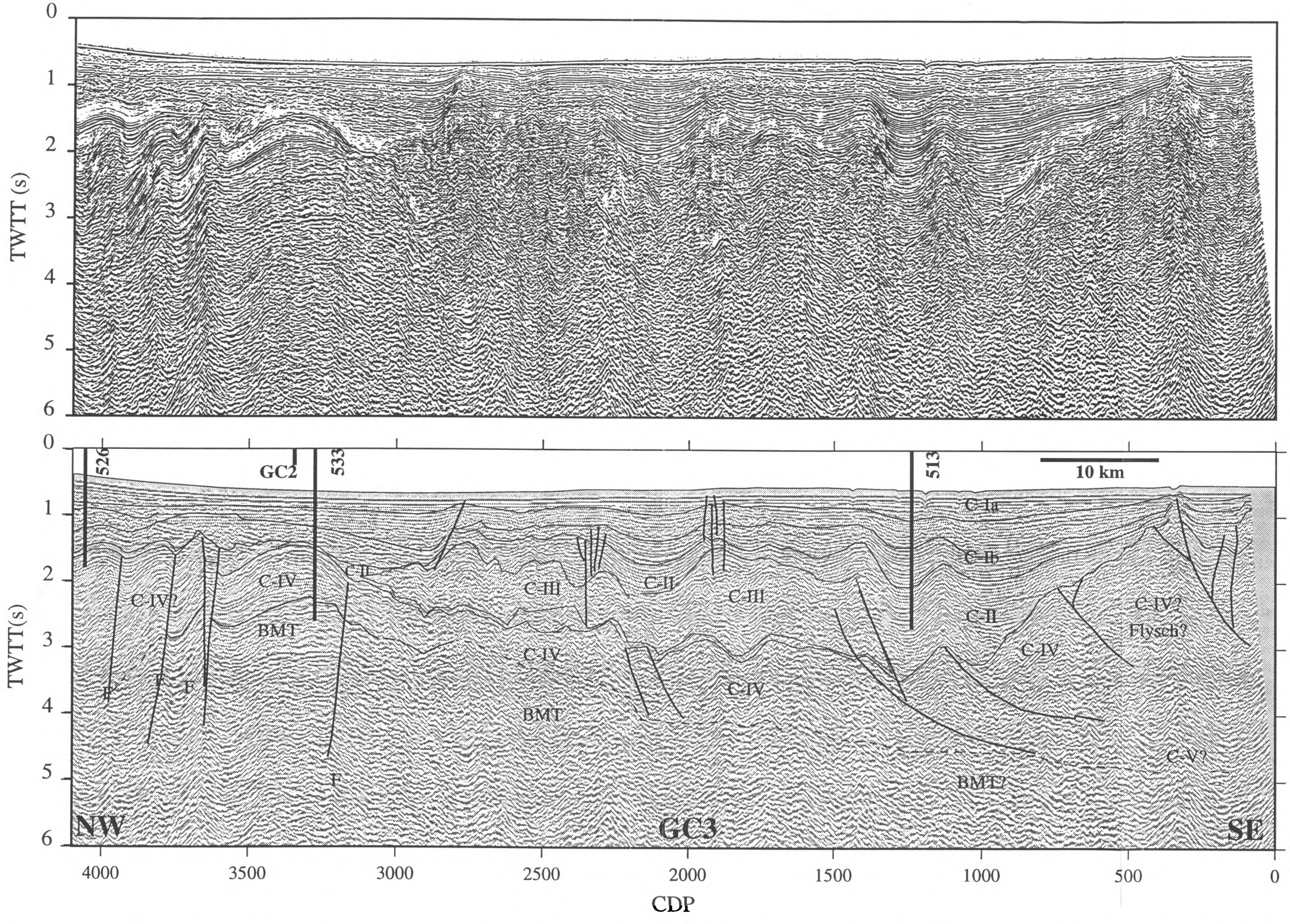


Figure 4.11: Migrated Profile GC3 and interpretation. Wells numbered as per IGME [1987]. No vertical exaggeration at V_p=6 kms^{-1}.

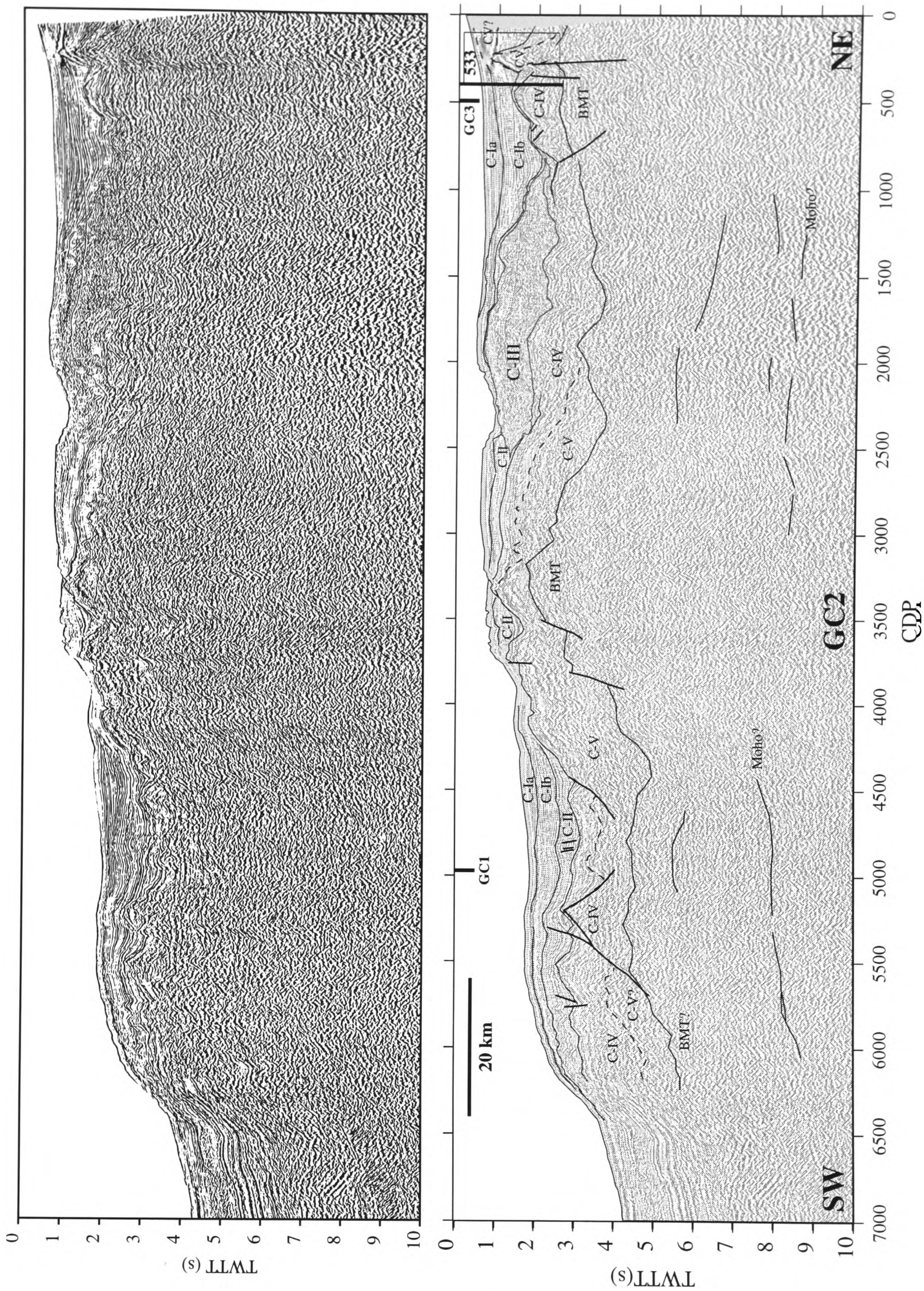


Figure 4.12: Interpreted Migrated Profile GC2. Little reflectivity beneath ~8 s TWTT. HAP=Horseshoe Abyssal Plain. Profile GC3 crosses GC2 at CDP 500. Box in the NE shows location of Figure 4.13. No vertical exaggeration at V_p=6 kms^{-1}.

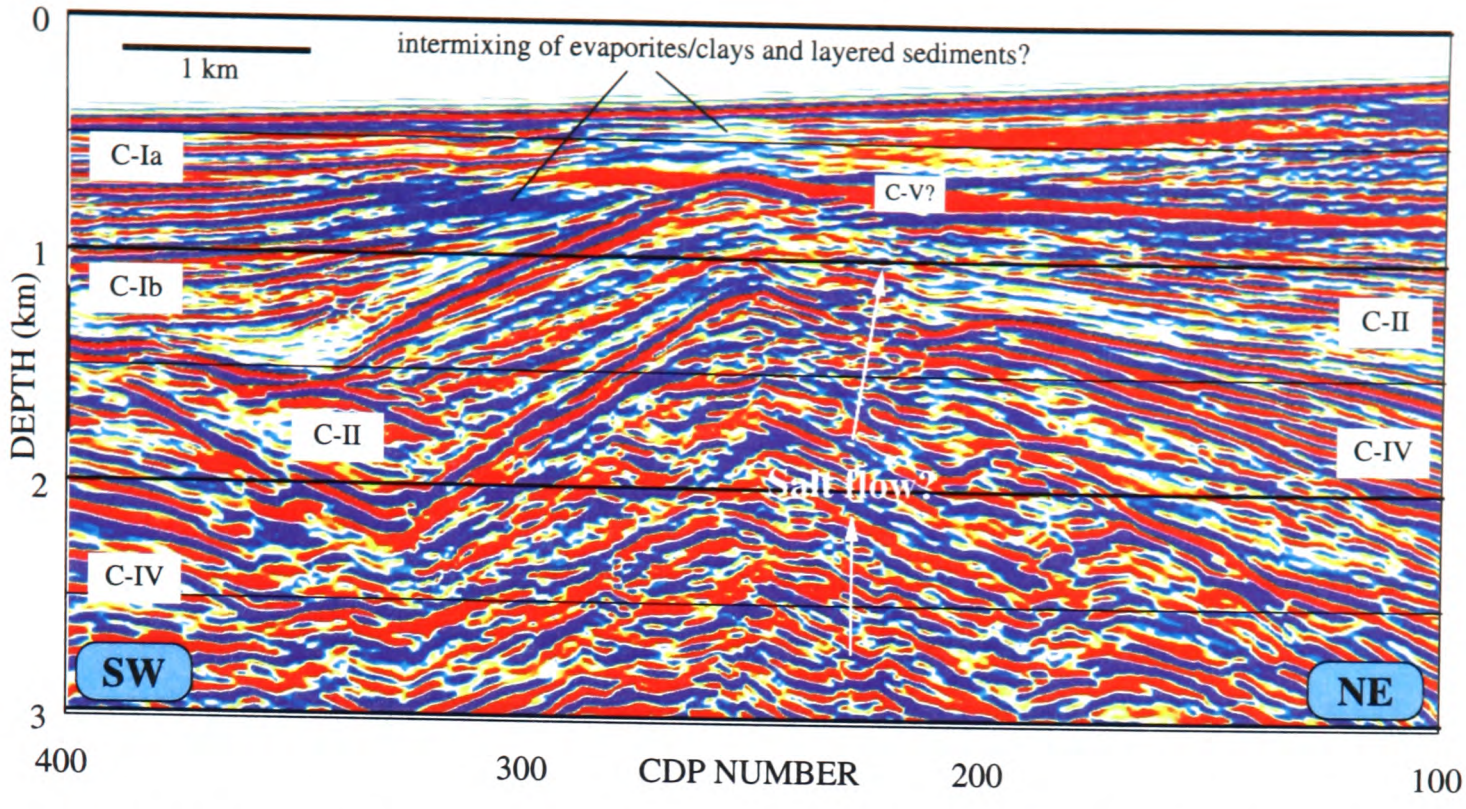


Figure 4.13: Interpreted salt structures at north end of Profile GC2. Location shown by small box at NE end of Figure 4.12.

tured through compression, and perhaps these have allowed upward salt movement which has fed the shallower salt bodies.

Elsewhere, C-V occurs at depth, so the shallow location interpreted on GC2 is unusual. A diapir of this unit is interpreted to cross–cut unit C-IV on Figure 4.15 between CDPs 2600–2800, 3–4s TWTT. The presence of a weak detachment layer of Triassic evaporites has previously been inferred below rotated fault blocks (e.g., Figure 4.11) in the northern GOC [e.g., Flinch, 1993; Maldonado *et al.*, 1999], although any such layer is not directly observed on the seismic data.

Facies C-IV

This facies is variable in character, ranging from parallel layering to non coherent reflections. It is best expressed in the northern GOC where it can be traced away from boreholes (Figure 4.11 and Figure 4.12) and appears with a low frequency sub-parallel reflection appearance. It is affected by thrusts near the northeast shelf (NW end of Figure 4.11 and NE end of Figure 4.12). Towards the southern and western Gulf it is seen as tilted, fault-bounded blocks (SE end of Figure 4.11 and CDPs 5000–6000 of Figure 4.12). The upper boundary is a high amplitude reflection in the northern GOC, which corresponds to an unconformity bounding mid-Miocene deposits from the Palaeogene carbonate platform below (Figure 4.5). Towards the central GOC this boundary dips below thick chaotic deposits of Facies C-III, and becomes obscured. As a result, away

from the Spanish shelf, its presence is largely inferred, as its seismic character makes it difficult to identify without some borehole control. Published seismic data have shown that there exists a lower Jurassic limestone section of massive, reflection free character, occurring to the northeast of IAM-GC3 as rotated fault blocks [Maldonado *et al.*, 1999]. The unit as a whole is composed of Palaeogene-Jurassic limestones and dolomites of the Mesozoic Tethyan carbonate platform, with Cretaceous clays and marls (e.g., wells 526, 533).

In the central-east sector of the GOC, towards the Gibraltar Straits, fault bounded blocks below Neogene sediments have been interpreted, which form part of the thrust units at the back of allochthonous CIII facies (Figure 4.11, Figure 4.16, Figure 4.17). The main faults verge downslope and away from the Gibraltar Straits area, and are interpreted to be due to radial Subbetic and Gibraltar Arc related structures. The internal structure of these blocks is of lower frequency layering than unit C-III. These are interpreted as Palaeogene flysch units of the Campo de Gibraltar Complex, as have been recorded in wells 21 and 35 of Figure 4.5. These inferred flysch deposits are considered as part of unit C-IV and are largely made up of redeposited marls and shales of Eocene–Oligocene age.

Facies C-III

This seismic facies has a distinctive small scale chaotic reflection fabric, and is observed on all the profiles in the GOC. On unmigrated sections it is characterised by many diffraction hyperbolae and steeply dipping noise, whereas after migration and post-stack filtering internal structure can be observed. It generally has the form of an accretionary wedge, thinning to the north and pinching out within sediments of facies C-II (Figure 4.11, Figure 4.15). On Profile GC2 (Figure 4.12), a northern lobe of the unit can be seen in cross-section (CDPS 500–2500), within CII strata, and above which is an eroded channel of the "ridge-and-valley" type of Roberts [1970]. The main body of this facies has a lensate or lenticular shape (e.g., Figure 4.15). The upper boundary is generally uneven, with folds and faults affecting overlying rocks. Some of this deformation appears due to mobility of sediments within this body, e.g., Profile GC3 (Figure 4.11) CDP 2750 and 1.5s TWTT, which may be due to mobility of overpressured shales [Maldonado *et al.*, 1989]. The lower boundary is a high amplitude reflection, visible near the pinchout of the wedge, but obscured beneath the thicker chaotic sediments in the central GOC basin.

On Profiles GC1 (Figure 4.15) and T3 (Figure 4.16), the water-bottom multiple has been suppressed where there are laterally continuous reflections but is prominent in the

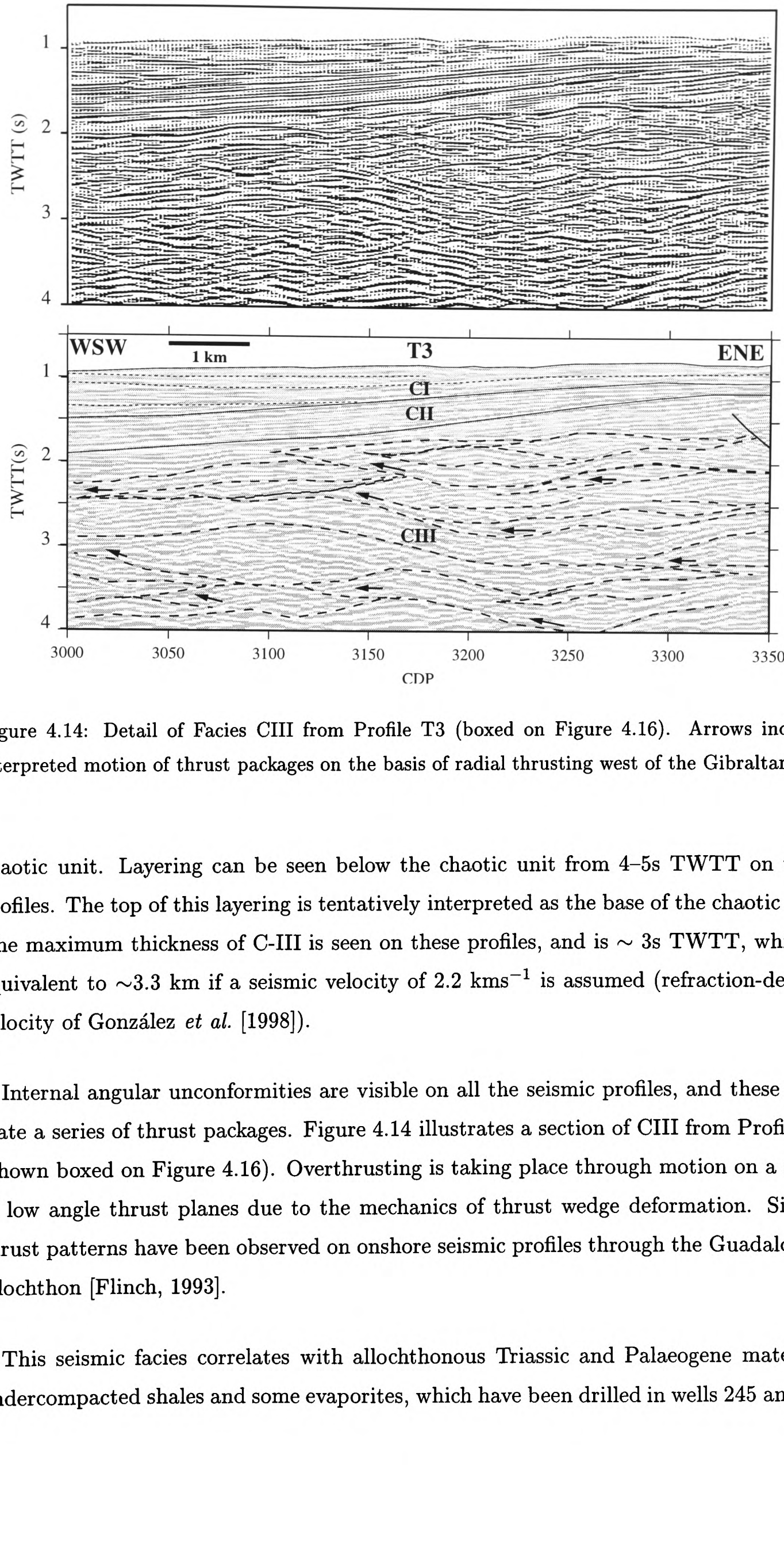


Figure 4.14: Detail of Facies CIII from Profile T3 (boxed on Figure 4.16). Arrows indicate interpreted motion of thrust packages on the basis of radial thrusting west of the Gibraltar Arc.

chaotic unit. Layering can be seen below the chaotic unit from 4–5s TWTT on these profiles. The top of this layering is tentatively interpreted as the base of the chaotic unit. The maximum thickness of C-III is seen on these profiles, and is $\sim$ 3s TWTT, which is equivalent to $\sim$3.3 km if a seismic velocity of 2.2 kms^{-1} is assumed (refraction-derived velocity of González *et al.* [1998]).

Internal angular unconformities are visible on all the seismic profiles, and these illustrate a series of thrust packages. Figure 4.14 illustrates a section of CIII from Profile T3 (shown boxed on Figure 4.16). Overthrusting is taking place through motion on a series of low angle thrust planes due to the mechanics of thrust wedge deformation. Similar thrust patterns have been observed on onshore seismic profiles through the Guadalquivir allochthon [Flinch, 1993].

This seismic facies correlates with allochthonous Triassic and Palaeogene materials, undercompacted shales and some evaporites, which have been drilled in wells 245 and 495

offshore, and a 2500 m section of which has been drilled onshore in well 604 (Figure B.2). The front of the C-III wedge pinchout in the GOC is a direct continuation of the buried wedge front of the Guadalquivir allochthon onshore (Figure 4.4). Wells and the seismic data indicate that this intra-Miocene allochthonous, chaotic unit had an approximately mid-Miocene time of emplacement.

A prominent reflection runs $\sim$ 0.5s TWTT below the seabed of the central GOC slope on Figure 4.16 (CDPs 1-1500, 2-2.5s TWTT) and Figure 4.15 (CDPs 4500-6000, 2-3s TWTT), and crosses reflections of both units C-III and C-II. This bottom simulating reflection (BSR) is interpreted to be diagenetic in origin and is an indicator of the presence of gas hydrates. The BSR feature is reported in more detail in Chapter 5.

Facies C-II

Seismic facies C-II has a variable seismic fabric, but with generally continuous to semi-continuous and sub-parallel internal reflection character. Facies C-III wedges out within this unit, as described above. The base of the unit is a high amplitude reflection representing a prominent unconformity between underlying Palaeogene rocks of Facies C-IV and overlying Neogene rocks. The rocks of this facies correlate with lower to late Miocene shales, sands and limestones (e.g., Figure 4.5). The upper surface is also a prominent reflection due to a widespread disconformity (e.g., Figure 4.11), with local angular unconformities (e.g., the western end of Profile 829 on Figure 4.17), between C-II and the strata of facies C-I above it.

The unit is variable in thickness and character. Above the deformed Jurassic–Palaeogene of Figure 4.11, CDPs 3000-4000, C-II is also involved in folding and thrusting, and is truncated at the top by an unconformity marking the end of the thrust activity of the C-III allochthonous wedge to the SE. C-II sediment infills depressions of the underlying units, and drapes facies C-III. Its thickness is greatest when underlying faults and folding have created depressions into which greater thicknesses of C-II have been deposited. Much of this deformation appears to be syn-depositional, leading to divergent fill patterns in reflectivity e.g., the Miocene sub-basin on Figure 4.11 between CDPs 500–1500, which is up to 1.5s TWTT deep. Large thicknesses of C-II are also present in the NE GOC, where up to 1200 m of Miocene sediment has been drilled in well 413 (Figure 4.5, Figure 4.4), for example.

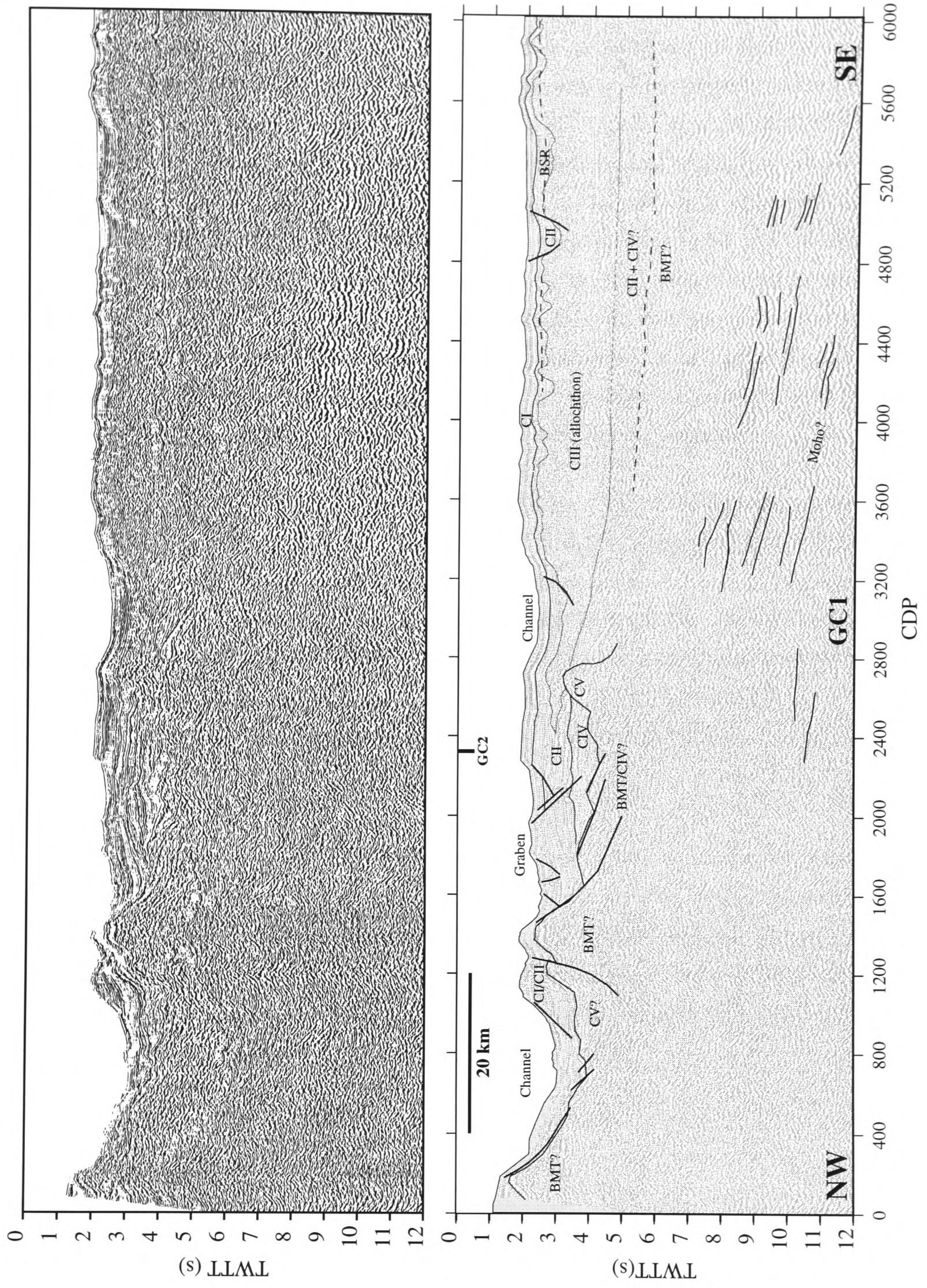


Figure 4.15: Interpreted Migrated Profile GC1. Labelled seismic units as defined in the text. BSR=Bottom Simulating Reflector. Vertical exaggeration 0.7 at V_p=6 kms^{-1}.

Facies C-I

The base of this unit is characterised by a basin-wide unconformity of Messinian to early Pliocene age. The Pliocene sediments of C-I are generally disconformable with the underlying Miocene, but angular erosional relationships are seen, for example, on Profiles GC3 and GC2 around well 533. Facies C-I has variable thickness and continuous to semi-continuous layering which varies from parallel to divergent. Internal disconformities can be seen, controlled by evolution of structures in lower units. This facies can be sub-divided into two units: an upper unit C-Ia with generally parallel, onlapping reflections, separated by an erosional unconformity from the generally more divergent reflections of lower unit C-Ib below. This unit correlates with Plio-Quaternary clastics (e.g., Figure 4.6, Figure 4.11), predominantly muds, with turbidites. C-Ia correlates to upper-Pliocene to Quaternary sediments, while C-Ib correlates to mid-lower Pliocene sediments.

C-Ia is up to 0.5s TWTT thick on profile GC2 (Figure 4.12). C-Ib displays greater variations in thickness, reaching a thickness of 1s TWTT in the depocentre around CDP 3000 on GC3 (Figure 4.11). Another possible deep depocentre is in a graben structure on Profile 829 near the Gibraltar Straits (CDPs 4500–5500 Figure 4.17). The alternating reflection-free (massive), chaotic and layered sequence suggest periods of large-scale mass flow into this depocentre, while the parallel configuration suggests deposition post-dating the main deformational episodes affecting the Strait through the Miocene.

4.6.1 Deep Reflectivity

On the seismic profiles shown on Figure 4.11 to Figure 4.17, a number of planar reflectors are imaged below 6s TWTT on profiles GC2, GC1 and T3. Deeper sections of GC3 and 829 are noisy and little signal reflection could be picked out from the ambient noise. On profiles GC1, GC2 and T3 laterally coherent events with greater amplitude and lateral coherency than the surrounding section are identified, and shown on the profile interpretation.

Profile GC1 (Figure 4.15) offers the best evidence for lower crustal reflectivity. A series of strong amplitude SE-dipping reflections are clearly visible in the SE half of the profile, with horizontal reflection segments up to ~15 km long. These are interpreted to be reflective lower crust, with the deepest segments tentatively interpreted as a Moho dipping SE. This zone of reflectivity is ~3 s TWTT in thickness, which is equivalent to 10.5 km if a typical velocity of 7 kms^{-1} is assumed for this layer [Watts *et al.*, 1990]. These deep reflections may be linked to the faults bounding half grabens of basement, or

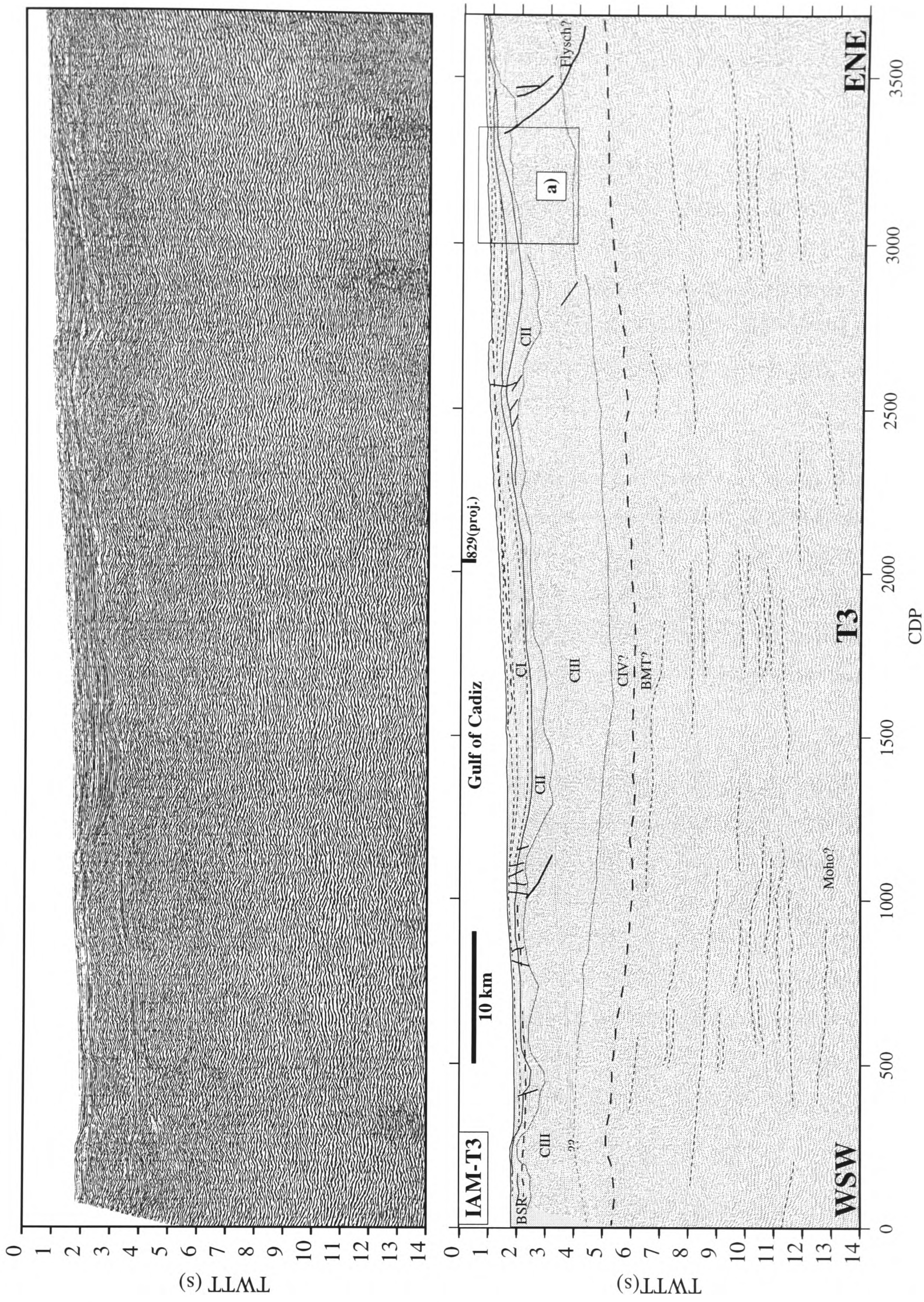


Figure 4.16: Interpretion of migrated profile T3. Labelled seismic units as defined in the text. Box a) shows location of the enlargement shown in Figure 4.14. Vertical exaggeration ~0.4 at V_p=6 kms^{-1}.

possibly C-IV, seen between 3–5 s TWTT, CDPs 1200–2400 on Figure 4.15. Curiously, this high amplitude reflectivity is not seen in the noisy section below 6 s at the NW end of GC1.

Profile T3 (Figure 4.16) images downslope through the central GOC, revealing strong reflections in the section below 6s TWTT. Those between 6–8s are interpreted to be upper crustal reflections, whereas the more laterally continuous reflections around 8s are tentatively interpreted as the top of a reflective lower crust. The deep reflections on Figure 4.16 appear to dip towards the centre of the profile, which could indicate crustal warping. On profile GC2 (Figure 4.12) the sub-basement is generally unreflective but some brighter reflections are apparent between 6–9s TWTT.

Deep seismic reflection profiles have revealed strongly reflective lower continental crust in many regions, including the Valencia Trough off SE Spain [e.g., Watts *et al.*, 1990], and have imaged reflections deep into the mantle lithosphere [e.g., Lie *et al.*, 1990]. Possible origins for these reflections that have been proposed include shear zones, mafic igneous rocks and fluids [e.g., Wever & Meissner, 1987]. Each of these mechanisms juxtapose rocks with different densities and P-wave velocities, thus giving rise to a strong impedance contrast which leads to a strong reflection from the interface.

The GOC is known to be underlain by Hercynian rocks of the Iberian foreland [González *et al.*, 1998]. Reflection profiling of Hercynian crust has also revealed strongly reflective lower crust beneath the Pyrenees and the Ebro basin [ESCI data, e.g., Gallart *et al.*, 1994] and the Ardennes Massif, with typical thicknesses in TWTT of 2–4 s [Watts *et al.*, 1990], which is in agreement with the thickness of 3 s TWTT of the layering observed on Figure 4.15. In some cases, reflectivity can be attributed to shear zones because it can be correlated directly with surface structures, as for example in the North Sea where a number of reflections in the lower crust and upper mantle dip away from the Central Graben, where the crust is about 5 km thinner than the surrounding area [Abramovitz *et al.*, 1997].

The SE–dipping reflections beneath the southern 100 km of profile GC1 (Figure 4.15) indicate that the Moho is shallowing, and therefore crustal thickness is decreasing, to the NW. The SE–dipping half-graben–bounding extensional faults seen on GC1 (3–5 s TWTT, CDPs 1200–2400, Figure 4.15) indicate early extension, and these faults are likely to be syn-rift structures. However, it cannot be ruled out that the reflective lower crustal layer developed in the Hercynian crust before rifting. However, the SE–dipping

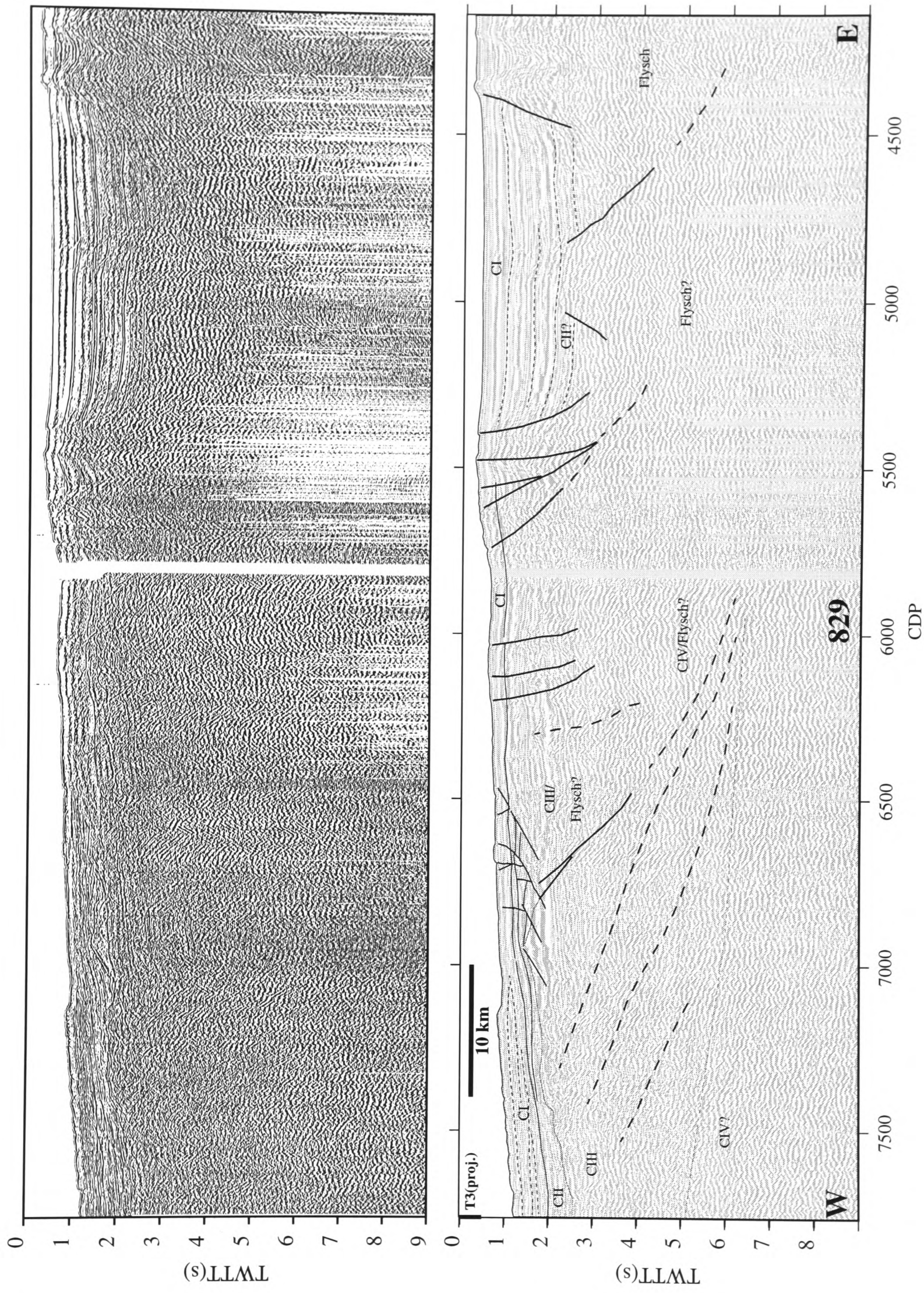


Figure 4.17: Interpreted Stack 829 in the central GOC. Vertical exaggeration 0.5 at V_p=6 kms^{-1}.

deep reflections may extend up to join the extensional faults around CDP 2000–2400 on GC1, perhaps suggesting a common origin, in a rifting event in the early Mesozoic perhaps, in which case the deep reflections would be magmatic or ductile features. The common orientation of the reflective crust and basement faulting indicates an asymmetry in extension, which suggests a degree of simple–shear during rifting [Wernicke, 1985]. The abrupt end of the deeper reflections around CDP 2400 on GC1 (Figure 4.15) may not be due just to seismic noise, but may be real. One very tentative explanation for this is that the crust from CDP 0–2000, on GC1, may have been offset from that of CDP 2000–6000, by strike-slip displacement.

4.6.2 Upper Crustal Structure

The upper crustal structure of the GOC reflects its complex geological history and evolution. Structures observed in the sedimentary layers have been active at different times and indicate the varying stress regimes that the region has undergone. Compressional fold and thrust structures are observed, as well as extensional normal faulting, and widespread diapirism. The region is known to have undergone transpression [Dewey *et al.*, 1989] so some strike-slip component to fault motions is expected, but cannot be resolved from a 2-D seismic profile.

The oldest structures identified in the profiles of this seismic study are the lower crustal layering best seen in Profile GC1 (Figure 4.15). These may be Palaeozoic if they were developed in Hercynian crust prior to any stretching. If the lower crustal reflectivity is due to an extensional event, such as Tethyan rifting in the Triassic–Jurassic, then they may be coeval with the half-grabens also seen on Profile GC1. Other structures seen in the Gulf of Cadiz profiles are much younger than early Mesozoic in age.

Thrust faults, and their associated folds, affect basement and sediments up to CII (Miocene) in age (Figure 4.11). These largely Miocene structures are buried beneath younger sediments of Facies C-I, which are also affected by deformation in underlying sediments. Some of the larger faults may be reactivated, such as the steeply dipping thrusts in the northeast GOC (Figure 4.11, Figure 4.12). Compression is also responsible for the presence of allochthonous units of chaotic reflection character. These appear to be of tectonic origin, with the form and internal character of an accretionary wedge, rather than a purely chaotic internal character attributable to an entirely olistostromic depositional mechanism, as has been postulated by many previous authors, [e.g., Lajat *et al.*, 1975; Maldonado *et al.*, 1999]. The intra-Miocene CIII is an accretionary wedge with internal low angle thrusting (Figure 4.14). At the rear of this wedge, thrust units

comprise blocks of Subbetic and Flysch material of Mesozoic and Palaeogene age, seen in the seismic data in the proximity of the Straits of Gibraltar (Figure 4.11, Figure 4.16, Figure 4.17). Thrust splays reaching the surface are seen here (Figure 4.17, CDP 5500), which are reminiscent of flower structures.

Extensional structures are observed in the northwest GOC, where normal faults bound graben structures of profile GC1 (Figure 4.15) and are exposed at the surface. Towards the base of the continental slope on Profile GC2 (Figure 4.12) normal faults are observed affecting sub–Pliocene units seaward of the interpreted basement high. Elsewhere, extensional structures are associated with movements in the roof of the allochthonous units (e.g., a graben on GC1, Figure 4.15, CDP 5000, 3 s TWTT; rotational normal faults antithetic to W-verging thrusts on 829, Figure 4.15, CDPs 6500-7000). A sub-basin with a flat, horizontal, low amplitude parallel fill is observed on Profile 829 near the Gibraltar Straits (CDPs 4500–5500 Figure 4.17), and is interpreted to be a fault-bounded graben-type structure. The mechanism for formation of the original accommodation space is not resolved from the seismic data, but may have occurred in the last major deformational phase affecting the Strait through the Miocene, as the parallel infill configuration suggests aggradational deposition post-dating this deformational episode.

Post-depositional flow structures of evaporites and clays are dominant in the study region, and these features have complicated the assessment of compressional and extensional structures. In the northern GOC, structures involving flow of Triassic evaporites of seismic facies C-V, are observed (Figure 4.15, Figure 4.12). Diapirs of C-V are seen on GC1 (Figure 4.15, CDP 2800) and GC2 (Figure 4.12, CDP 250). The GC2 diapir appears to be feeding a salt pillow within Facies C-I (Plio-Quaternary) sediments, which is probably part of the same Triassic halite body drilled by well 363 just off the north end of Profile GC3 (Figure 4.6). Elsewhere on GC2, unit C-V has a pillow-like form, with an irregular top surface implying sediment flow. Diapiric activity through salt flow of the autochthonous Triassic of the northern GOC has been active since Mesozoic times.

Diapirism also affects Facies C-III. On GC3 (Figure 4.11) a diapir penetrates overlying Plio-Quaternary C-I strata at CDP 2750 and 1.5s TWTT. Fluid escape from C-III also causes characteristic faulting in the overlying sediments, as seen at CDP 2400 and at CDP 2000. All these structures occur above local C-III highs caused by thrusting and folding of C-III, and accentuated by diapirism, above which the draping sediments of C-II and C-I units thin. Similar is the diapir visible at the west end of profile T3 (Figure 4.16, CDP 200). The corrugated upper surface of C-III sediments on GC1 (Figure 4.15) is also

due to a combination of folding and diapirism.

The formation and structural trends of many of the compressional and diapiric features seen in the Gulf of Cadiz are a response to the oblique NW–SE directed regional compressive regime between Iberia and Africa over the last 10 Ma or so [DeMets *et al.*, 1990; Westaway, 1990; DeMets *et al.*, 1994]. The $\sim$ 5 km wavelength folds and subsequent diapirism of Facies C-III observed on Figure 4.11 find surface expression in a series of NE-SW oriented ridges and valleys in the central slope region (Figure 4.4). The ridges correlate with C-III highs, whereas the slope valleys have been accentuated by pathway incision by downslope currents (e.g., Figure 4.12, CDPs 2000–2500; Figure 4.15, CDPs 2400–3600). The linear diapiric ridges were originally attributed to Triassic evaporites [Roberts, 1970; Lajat *et al.*, 1975], but shallow cores taken from a ridge axis have yielded blue marls of Miocene age [Maldonado *et al.*, 1989; Nelson *et al.*, 1993]. Well logs through C-III indicate that sonic velocities are lower than would be expected for normally compacted sediments at similar depths (Figure 4.8), which, together with the cores, indicates that diapirism within C-III is mainly due to undercompacted clays and muds, with the diapirism being triggered by regional compression and subsequent folding.

4.7 Subsidence and Uplift History

Backstripping is a technique that is designed to correct the basement depth for the effects of sediment loading and compaction, in order to estimate the tectonic subsidence component of basin subsidence [e.g., Watts & Ryan, 1976]. This allows a better understanding of the evolution of the crust in terms of the timing of tectonic events and the driving mechanisms such as crustal thinning or thrust loading [e.g., Watts & Ryan, 1976]. Where sedimentary history is known only at a point, such as a well, Airy (1-D) backstripping is used [Watts & Ryan, 1976; Steckler & Watts, 1978; Watts, 1988]. The 1-D backstripping equation (Equation (C.9)) is based on simple balancing of columns of unit cross-sectional area (columns b) and c) of Figure C.1), assuming Airy isostatic compensation. In the case of extension, this 1-D technique allows the estimation of crustal thinning, and discrimination between instantaneous and finite duration rifting models, by comparison of the backstripped tectonic subsidence curve and theoretical curves.

4.7.1 Methodology

The backstripping technique was applied to wells from the GOC and the adjacent Guadalquivir foreland basin of Spain, following the procedure outlined below. Sonic logs obtained from the Shell International and Chevron (COPI) oil companies (Figure 4.4)

were converted to porosity points, to which compaction curves based on soil mechanics theory and observations [Audet, 1995, 1996] were fitted, using a least squares method. Published well data [IGME, 1987] was also backstripped (see Figure 4.4, Table B.1, Table B.2).

The major steps in the analysis are as follows:

1. Conversion of sonic log data from sonic slowness to porosity using the combined empirical relationships of Raymer *et al.* [1980]; Issler [1992].

2. Derivation of best–fit porosity–depth relationships using the method of Audet [1995], based on theoretical soil compaction curves rather than the empirical exponential curve fitting of Athy [1930]. The Audet [1995] method has the added advantage of yielding data on the physical properties of the sediments under study.

3. Compilation of stratigraphic, palaeodepth and palaeo-sealevel data, used in conjunction with porosity–depth functions to backstrip the well data.

4. Comparison of observed tectonic subsidence with theoretical subsidence curves for different models based on thermal contraction.

The data sources and required inputs for the analysis of well data are summarised in the flowchart in Figure 4.18. The individual steps, the theory behind them, and specific information pertaining to the studied dataset, are laid out in Section C.2 of Appendix C.

4.7.2 Results

Porosity-Depth Relationships

Rock volumes change with time and depth due to factors such as dewatering and diagenesis. Before the final backstripping stage it is necessary to correct for these changes so true thicknesses at the time of deposition can be estimated for the backstripping process. In this study, only porosity loss through mechanical compaction is compensated for, through decompaction along soil mechanics–based theoretical porosity–depth curves fitted to the observed sonic–derived porosity, using a least squares method (Section C.2.1). Figure 4.19 and Figure 4.20 illustrate logged sonic interval transit times (sonic slowness) against depth, and the derived sonic porosity against depth, for five wells from the GOC and six wells from Guadalquivir Basin. The best-fit theoretical compaction curve [Audet, 1995, 1996] for each well is also shown. An observation can be made on Figure 4.19 that intervals of lower porosity than would be expected by simple mechanical compaction (i.e.,

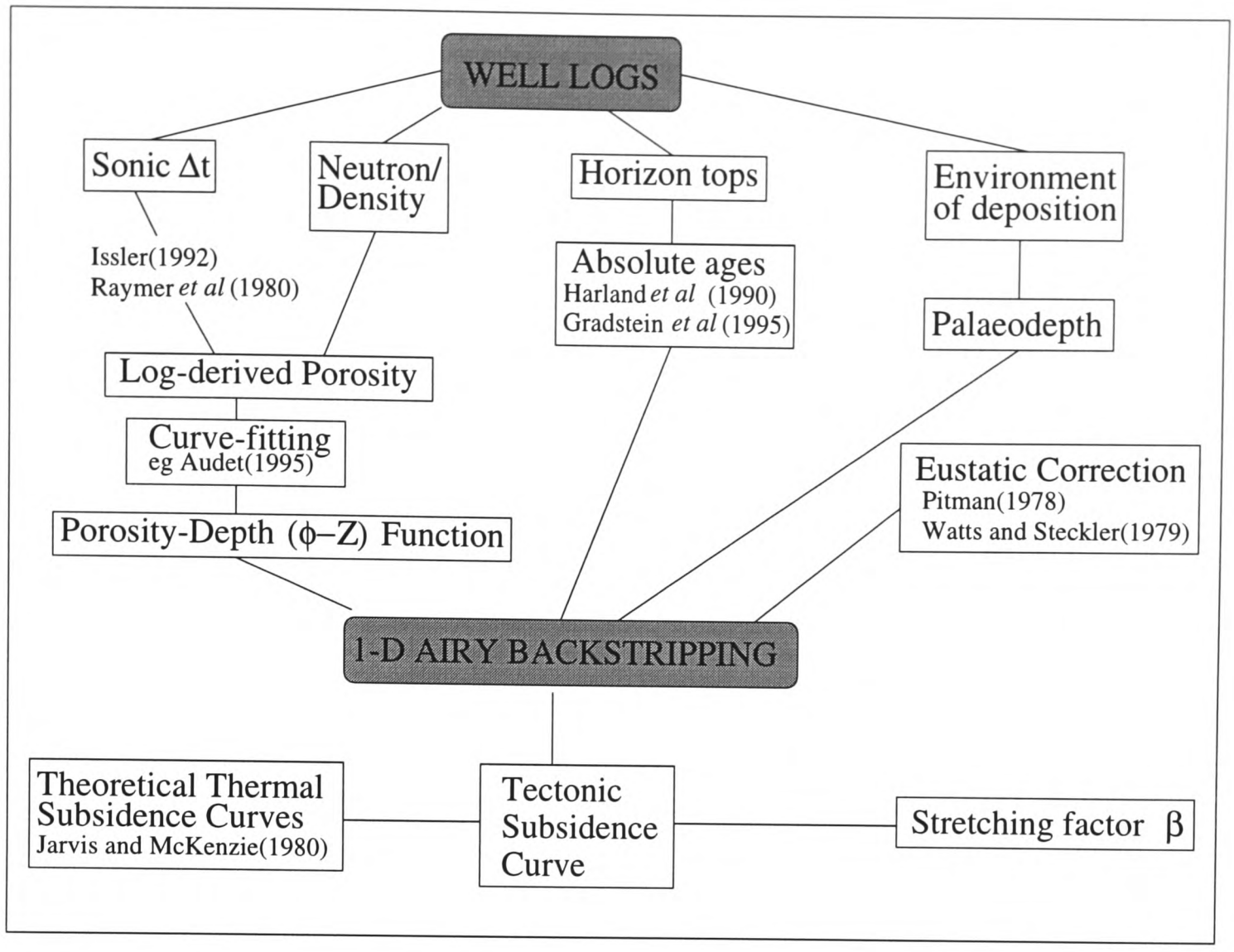


Figure 4.18: Flowchart illustrating the methodology of 1D Airy backstripping as carried out with well data in this study.

with ϕ less than predicted by the theoretical curves shown) are present in the midsection of wells 296 and 288, and at the bottom of wells 241 and 314. These formations of lower-than-expected porosity are all either limestone, dolomite or very calcareous, and thus subject to porosity loss through non-mechanical mechanisms such as chemical solution and precipitation. Well 245 samples a chaotic unit comprising allochthonous evaporites and Triassic sediments. These allochthonous sediments have anomalously low sonic velocities, which yield porosity values which deviate from the normal compaction trend in the well. This is highlighted in Figure 4.19f, which shows that the compaction curves for the three deep wells (241, 296 and 314) have similar compaction trends whereas the curve fit to the autochonous sediments of well 245 show a relatively lower loss of porosity with depth. The allochthonous sediments of well 245 contain salt and clay layers, found in a chaotic mixture at the base of the well, which may have acted as barriers, preventing fluid migration and dewatering. These sediments may have been redeposited quickly, forming fluid-bearing compartments with salt and clay seals, which would become overpressured and thus undercompacted with increasing depth of burial.

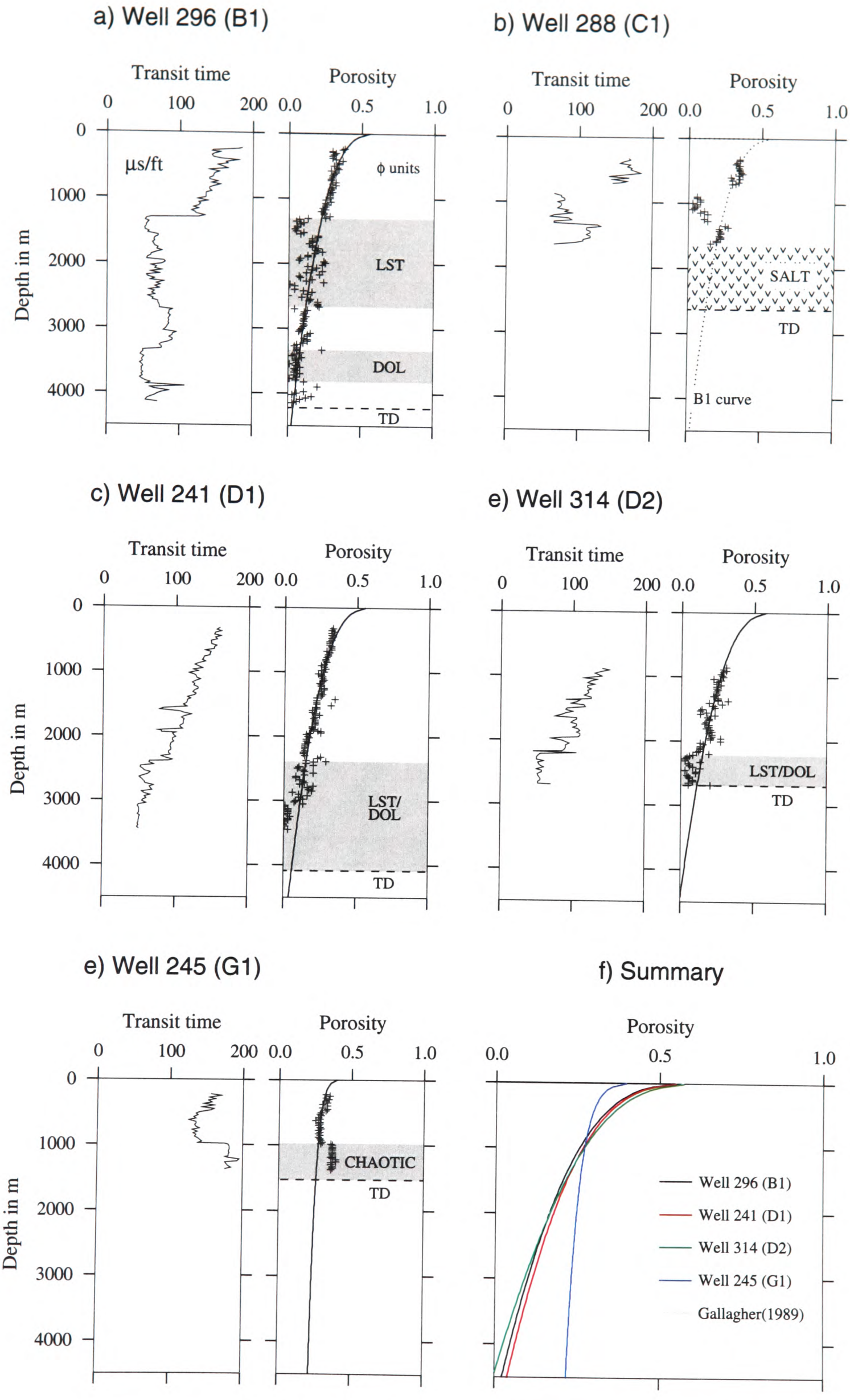


Figure 4.19: Wireline sonic interval transit time and porosity conversion of GOC wells.

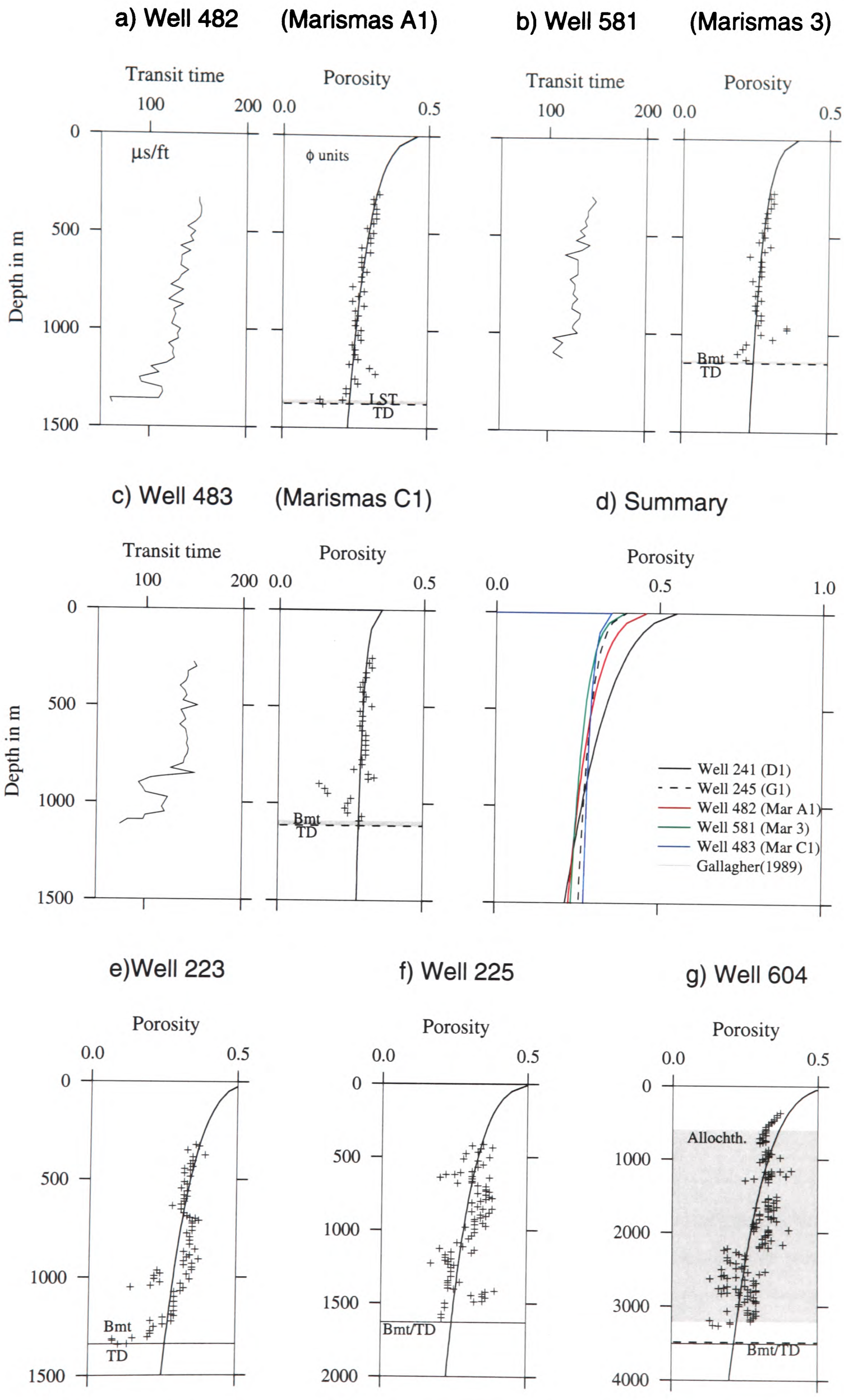


Figure 4.20: Wireline sonic interval transit time and porosity-depth relationships of onshore wells from the western GQB.

The GQB wells of Figure 4.20 penetrate Miocene–Recent sediments which are mostly clays with coarser components. Theoretical compaction curves provide a good fit to the porosity data of the wells, with the greatest scatter being exhibited by the two wells which penetrate the Guadalquivir allochonous unit (wells 225, 604).

Mechanical parameters

The strength of sediments (i.e., their ability to support mechanical loading) is related to the effective stress, which depends in turn on the porosity. It can be shown that two mechanical parameters are sufficient to describe a realistic porosity-depth function [Audet, 1995]: the compression index C_c and the void ratio e_{100} which is the ratio of pores to matrix (Equation (C.8)). The strength is characterised by a constant, C_c, called the compression index, which indicates the compressibility of a sediment. For example, values of typically 0.1–0.3 for silts are measured, and 0.7 or higher for much more compressible organic-rich clays. The reference void ratio, e_{100}, is at a reference effective stress, which in this study is 100 kPa, as recommended in Audet [1995]. Both parameters can also be determined in the laboratory using uniaxial compression methods, and many such values for both clays and coarser clastics are found in the geotechnical literature [e.g., Burland, 1990]. Thus, log-derived values can be experimentally checked with this method.

Well Name	296 B1	241 D1	314 D2	245 G1	482 MA1	581 M3	483 MC1
C_c	0.42797	0.43071	0.48710	0.13959	0.24823	0.14986	0.07552
e_{100}	1.21761	1.23878	1.35565	0.66078	0.85123	0.64507	0.54547

Well Name	223 VM-1	225 CN-1	604 Bet 14-1
C_c	0.36359	0.31077	0.36865
e_{100}	1.13963	1.02788	1.23197

Table 4.2: Theoretical compaction curve properties (compression indicies, C_c, and void ratios, e_{100}) at 100 kPa for wells used to derive porosity–depth relationships for backstripping.

Table 4.2 summarises the mechanical parameters describing the theoretical compaction curves that best fit the log–derived porosities for each of the wells for which logs were available. These points are plotted on Figure 4.21. Trends of experimentally tested sediments [Parasnis, 1986] and remoulded clays [Burland, 1990] are shown, and it can be seen that the sediments in the well logs lie within the narrow band defined by these

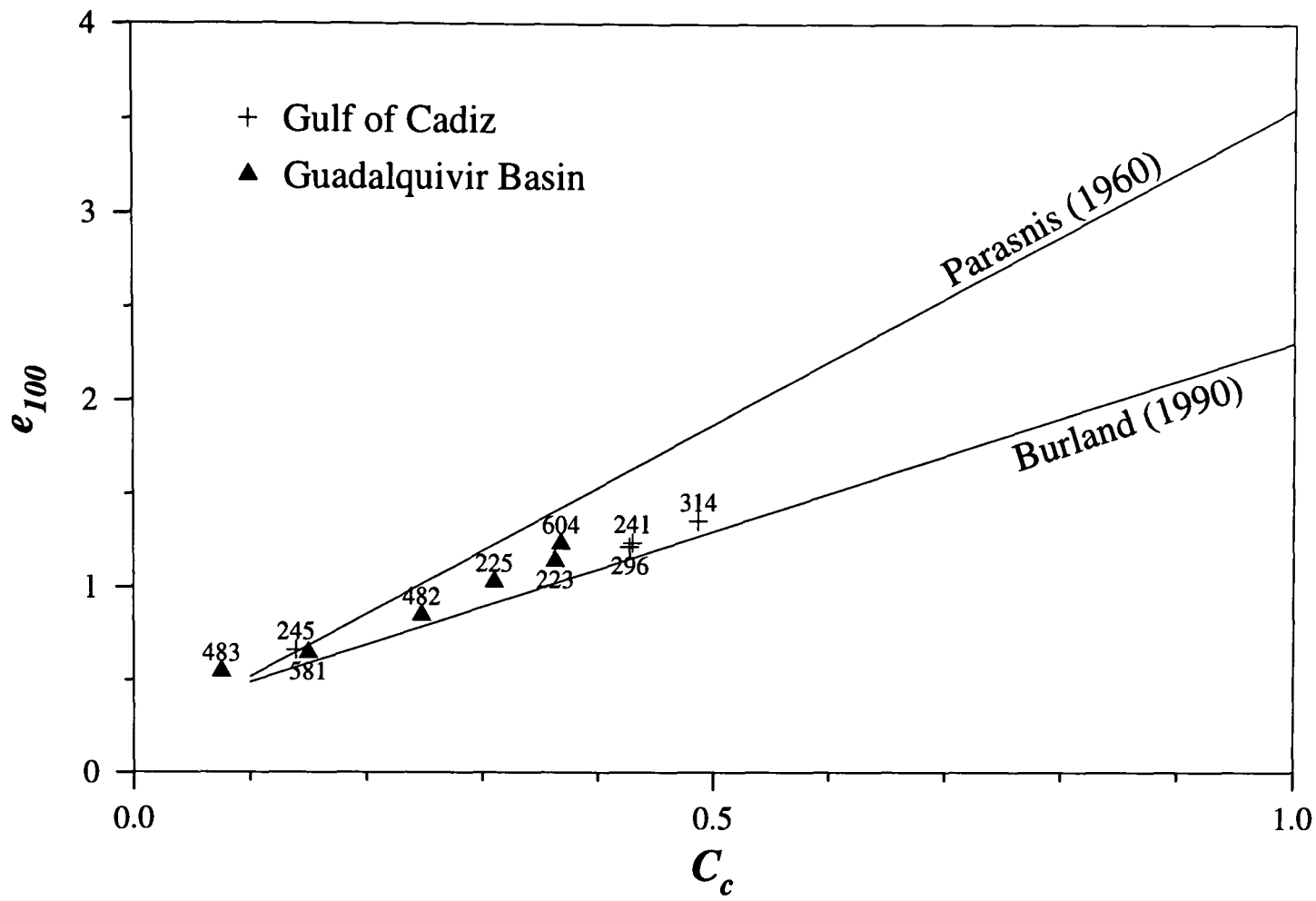


Figure 4.21: Plot of compressibility parameters (C_c and e_{100}) for wells used in the one-dimensional backstripping analysis. Both GOC and Guadalquivir basin wells plot on a linear trend close to experimental measurements from triaxial tests on clays [Burland, 1990], and below the experimental values for naturally-deposited sediments of Parasnis [1986].

two experimental trends. Wells from the Guadalquivir basin generally lie in the less compressible region of the plot, with the exception of well **245** from the GOC. The overall trend of increasing compressiblity from the most inland well (483) to the GOC is interpreted to reflect a decreasing trend in grain size, probably from muds with sands and silts at the more inland wells to a predominance of mud offshore, which reflects the greater transporting power of stronger currents in the fluvial GQB.

Results of 1D (Airy) Backstripping

The data points on a subsidence curve originate from the stratigraphic boundaries, of presumed known absolute age, defining stratigraphic units of known present-day thickness. The stratigraphic periods for horizons given in IGME [1987] and commercial well data were converted to absolute ages using the following standard time scales: Harland *et al.* [1990] for the Cenozoic and Gradstein *et al.* [1995] for Mesozoic. Thus, each horizon top had a given age. Unconformities were given age brackets i.e., two ages, to represent the period of non-deposition or erosion. The unconformities were shown simply as periods of non-deposition as estimates of erosion were beyond this study, though they are

possible [e.g., Issler, 1992].

The subsidence curves shown in Figure 4.22 a,b,c,g,h represent the midpoints of the error ranges of tectonic subsidence due to uncertainties in the palaeobathymetry, as shown in Figure 4.22 g and h. The palaeobathymetric ranges are based on palaeoenvironment interpretations given in well logs, using the scheme outlined in Table C.2, Appendix C. Wells 241, 296, 314, and 533 (Figure 4.22a–d) have penetrated the oldest sediments in the GOC. Well 533 (Figure 4.22d) records subsidence and deposition (of largely shallow water carbonates) from late Triassic to late Jurassic, with an apparent step in subsidence in the early Jurassic. This initial subsidence is followed by a period of non-deposition or erosion covering ~140 Ma until the Miocene, when subsidence recommenced. Well 296 (Figure 4.22b) samples a Triassic–Jurassic unconformity above which are Upper Jurassic rocks, of carbonate platform facies (Figure B.1), whereas wells 241 and 314 (Figure 4.22a and c) penetrate into the Upper Jurassic. The subsidence histories of the latter (palaeobathymetry corrected) three wells display an initial period of accelerated subsidence followed by a gentle decrease interpreted as being due to thermal subsidence, which is modified by end Cretaceous and Miocene tectonism. Where palaebathymetric corrections are not applied the resulting tectonic subsidence curves display an initial subsidence followed by little subsidence until the Miocene when an abrupt increase is observed (curves shown dashed in Figure 4.23). For all these wells, the effect of using the Pitman [1978] sealevel correction is that the tectonic subsidence is reduced relative to that obtained by applying the lower magnitude sealevel corrections of Watts & Steckler [1979].

Wells 342 and 398 (Figure 4.22e and f) are examples of wells that span the Cenozoic, showing subsidence rates decreasing across the Palaeocene, and increasing in the Miocene. Figure 4.22g and h show wells 245 and 288 from the GOC which overlie allochthonous sediments and a Triassic saltdome respectively. Well 245 indicates uplift in the Tortonian, followed by subsidence in the Pliocene onwards, whereas the subsidence history of 288 is linked to salt movement, showing a sharp decrease in subsidence in the Quaternary.

Wells 223 and 225 (Figure 4.22i and j) only record tectonic subsidence and sediment accumulation from Langhian to recent times, as the GQB foreland basin is only of Neogene age. Wells 482 (Marismas A-1), 483 (Marismas C-1), 581 (Marismas 3) of Figure B.2a have not been backstripped due to too few data points, with large age uncertainties and no palaeobathymetric control on the logs. Wells 223 and 225 (Figure B.2b) have more temporal control points and were therefore analysed, with the backstrip method using

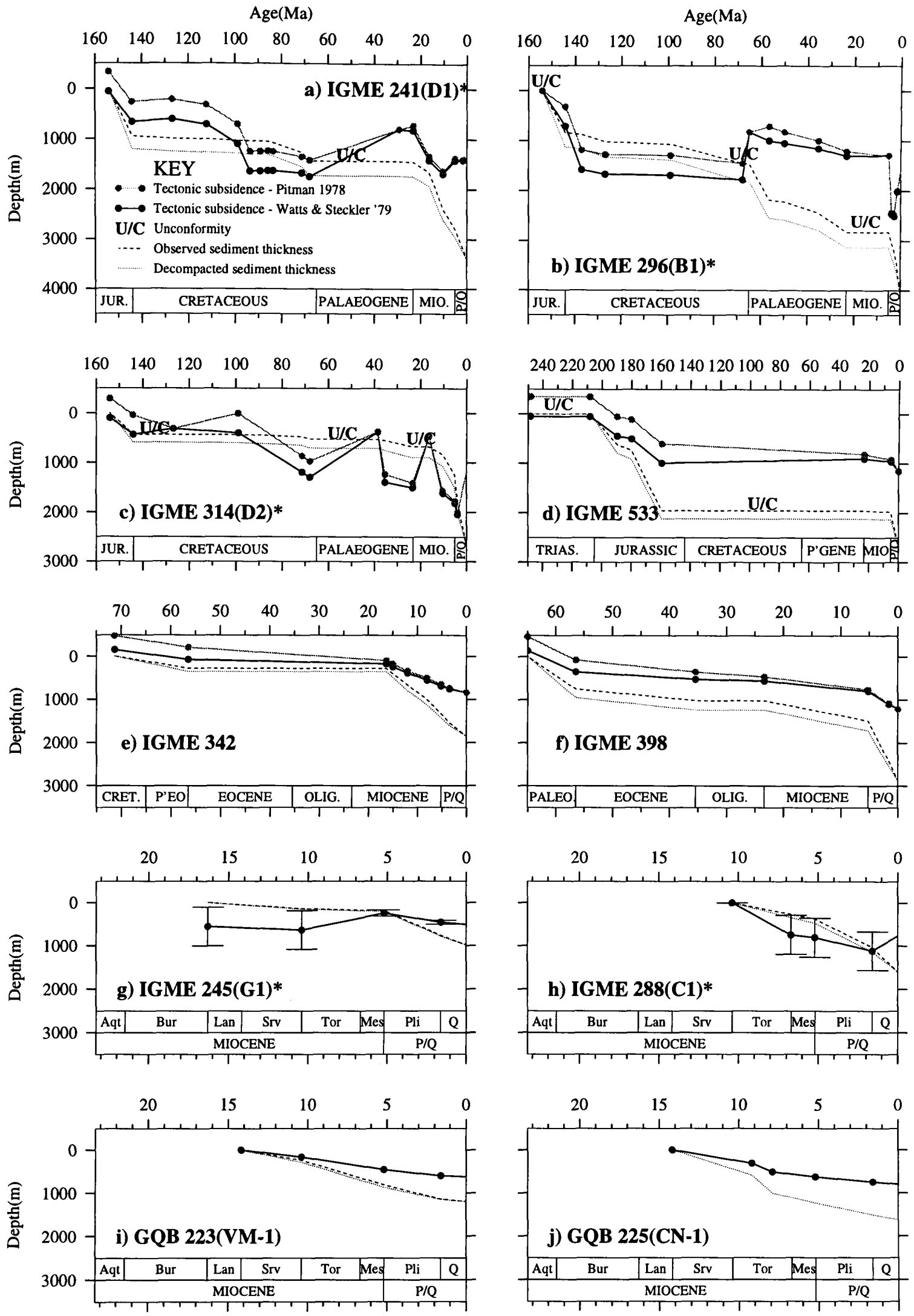


Figure 4.22: 1-D backstripping results for selected wells of the GOC and GQB . Backstrips for starred wells have incorporated palaeobathymetric data.

the porosity curves fitted to the well sonic data in Figure 4.20. Well 604 has also not been backstripped due to the difficulties of assigning dates to the allochthonous sediments which make up the bulk of the sampled sediments.

Figure 4.23 summarises the tectonic subsidence and uplift curves for all the analysed wells from the GOC. In each case, sealevel corrections based on the Watts & Steckler [1979] curve were applied. Wells for which log data and palaeobathymetry data were available are shown in red; the other wells were backstripped using an average porosity–depth relationship. The wells are ordered NW–SE, perpendicular to the structural grain of the adjacent Betic Cordillera. The main feature of Figure 4.23 is that subsidence has been generally slow prior to the Miocene, when a phase of rapid subsidence begins which continues to the present day.

Major events that have affected the development of the study area and northeast Atlantic Ocean have been outlined in Section 2.3. The slow subsidence can be attributed to developments after the breakup of Pangea led to late Triassic rifting and associated basic volcanism, and the subsequent formation of the margins of southern Iberia and north Africa [Heymann, 1989]. Extensional tectonics commenced at 220 Ma in the Late Triassic (Figure 2.10, Dewey *et al.* [1989]), shown as event A on Figure 4.23. This extensional event is reflected in the subsidence recorded at well 363 within red beds and evaporites. Well 533 is the sole well that penetrates the Palaeozic offshore and while subsidence and deposition in the Early-Mid Jurassic is recorded, the Triassic is marked by an unconformity. For both these wells on Figure 4.23, early subsidence associated with Pangean extension is succeeded by non-deposition or erosion until Neogene times.

One feature of the generally slow GOC subsidence (Figure 4.23) is a period of rapid subsidence in the Late Jurassic (wells 296, 241 and 314 of Figure 4.23). Each subsidence history starts with a period of accelerated subsidence interpreted as rifting, followed by a gentle decrease, interpreted as being due to thermal subsidence. The well logs date the oldest Jurassic as Kimmeridgian, and therefore the date of rifting is taken to be at the Kimmeridgian-Oxfordian boundary at 154.1 Ma [Gradstein *et al.*, 1995]. This correlates closely with the M25 (157 Ma) spreading anomaly in the NE Atlantic, which is the oldest magnetic spreading anomaly west of the Gulf of Cadiz (Figure 2.4). A breakup anomaly is not readily identifiable on the seismic reflection data because of poor imaging at depth and the presence of mobile Triassic evaporites. Interestingly, the curves for wells 241 and 314 display a slight uplift after the initial subsidence, then gentle subsidence, imparting a concave down pattern to the curves until the end of the Creataceous. This

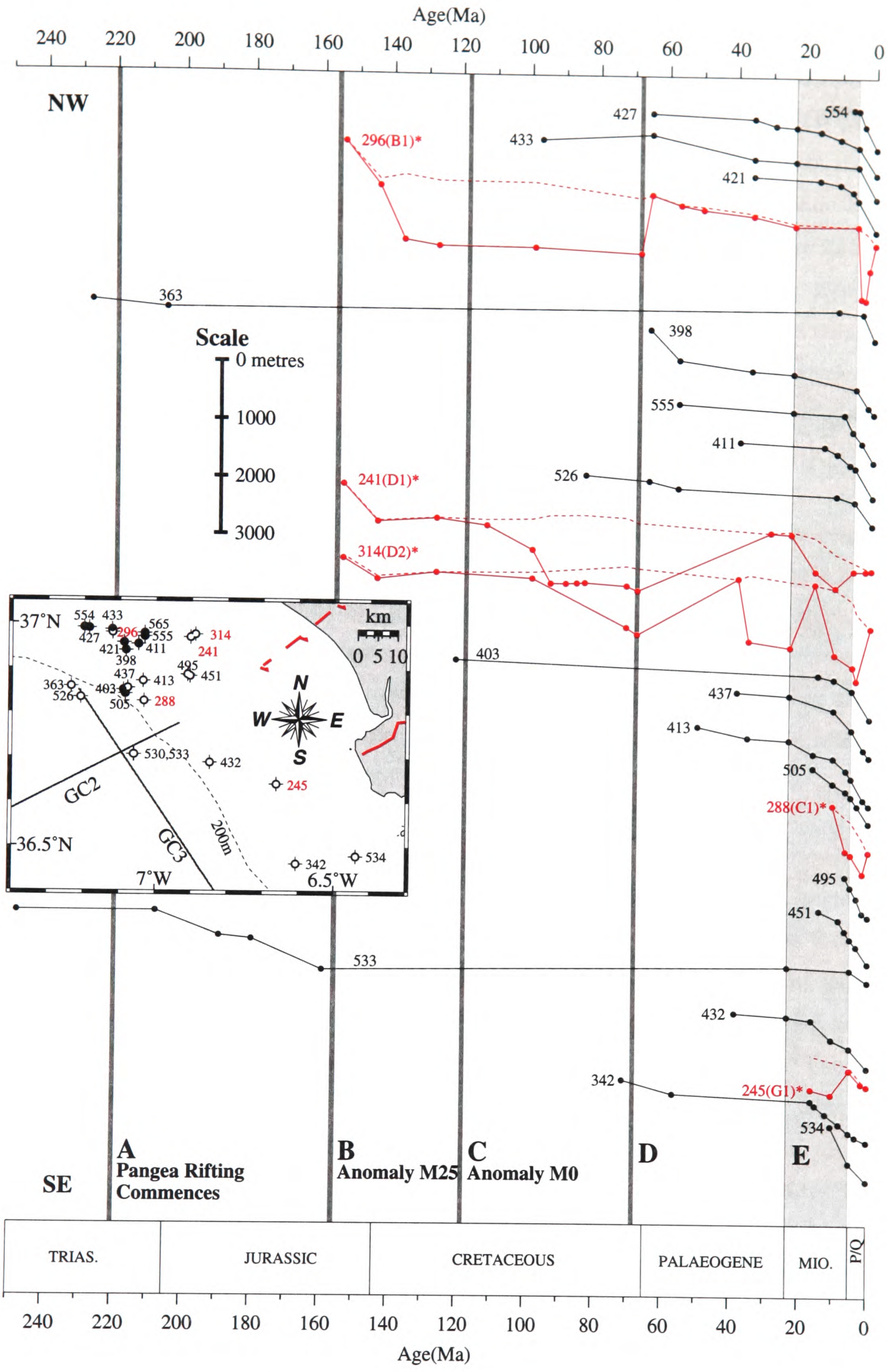


Figure 4.23: Tectonic subsidence curves for all Gulf of Cadiz wells with available data, ordered from northwest to southeast (locations on inset map). Sealevel corrections have been applied using the curve of Watts & Steckler [1979]. Starred wells shown in red display tectonic subsidence curves which incorporate palaeobathymetric data; subsidence curves without palaebathymetry are shown dashed for these wells. Events A–E are discussed in the text.

modification of the basic concave-up pattern which is typical of rift-type basins (due to thermal subsidence after rifting) is speculated to be caused by transpression affecting the Azores–Gibraltar Fracture Zone in the Gulf of Cadiz region due to sinistral wrench faulting and the rotation of Iberia, which palaeomagnetic evidence indicates rotated by 30°between anomaly M-10 (130 Ma) and anomaly MO (118Ma) [Galdeano *et al.*, 1989]. It must be borne in mind, however, that the "uplift" seen in wells 241 and 314 may be an artifact of palaeobathymetric corrections applied, although these are relatively small until the Late Cretaceous for these wells (Figure 4.24). Authors who have examined subsidence histories in the Subbetics generally agree that periods of accelerated subsidence coincided with Atlantic transtensional tectonics [e.g., Garcia-Hernandez *et al.*, 1980; Peper & Cloetingh, 1992; Rey, 1998].

Most wells penetrating the Cretaceous and Palaeogene periods have little subsidence or sedimentation, with one possible uplift event marked as Event D on Figure 4.23. In many GOC wells much of this period is marked by an unconformity (e.g., Figure 4.5), which through plate kinematic reconstructions has been shown to be one of continental convergence between Africa and Eurasia, with some 200km of N–S shortening taking place across the GOC and Alboran Sea regions in the mid-Oligocene to Late Miocene [e.g., Dewey *et al.*, 1989].

A major feature of the tectonic subsidence and uplift curves is the concave–down pattern that begins in the Miocene (Event E on Figure 4.23). This concave-down pattern is associated with foreland-type basins ahead of thrust loads: as the load thrusts forward, the rate of tectonic subsidence increases [e.g., Watts, 1992]. In this case the loading is due to the outwardly thrusting Alpine Betic-Rif orogenic belt, which has led to the superposition of a foreland basin signal above that of the older passive margin. The time of onset of this thrusting, as recorded in accelerated subsidence rates, varies from well to well, but in general goes from early to late Miocene as one goes from SE to NW, which is in agreement with the radial thrust directions of the External Zones of the Betic Cordillera, which are west to northwest in the GOC [e.g., Platt & Vissers, 1989; Maldonado *et al.*, 1989]. In wells uncorrected for palaeobathymetry, the subsidence continues to the present, and these can be compared with the continuous subsidence and sediment accumulation recorded in wells 223 and 225 from the western Guadalaquivir foreland basin (Figure 4.22i and j). However, when wells with palaebathymetric corrections are examined, an early Pliocene uplift event is observed on wells 296, 241, and 314: this may imply an increase in the convergence rate between Africa and Eurasia, which competes with the effect of flexural loading by thrust-and-fold loads in the Betics. Well 288 records

a late Pliocene/early Pleistocene uplift, whereas well 245 records a late Miocene uplift then Pliocene to Recent subsidence.

Both wells 288 and 245 penetrate sediments which are associated with mobile sediment (autochthonous Triassic evaporites and allochthonous Triassic/Palaeogene clays and evaporites respectively). In these wells, sedimentological factors may have affected the tectonic signal, as vertical movements cannot be attributed simply to compaction and subsidence (tectonic or thermal), but may be due to salt or shale movements, which are unquantifiable in this study.

Stretching Factor

The early subsidence seen on Figure 4.24 for backstripped wells 296, 241, and 314 from the NE of the GOC (see inset map, Figure 4.23) is intrepeted to be due to a rifting event. The observation of tilted fault blocks of Mesozoic sediments and basement beneath the GOC e.g., Flinch [1993]; Maldonado *et al.* [1999] indicate that the GOC is underlain by a rifted margin. (Figure 4.2). Tilted fault blocks of basement and/or unit C-IV are also seen on GC1, Figure 4.15. The initiaton of the subsidence in wells 296, 241, and 314 appears to coincide with the onset of Late Jurassic seafloor spreading in the central Atlantic marked by anomaly M25 (157 Ma), shown as event B on Figure 4.23. The early subsidence is rapid early on then slows, which is a pattern expected in models of theoretical rifting [e.g., McKenzie, 1978] and is similar to modern margins such as the Atlantic margin of North America [e.g., Steckler & Watts, 1978; Royden & Keen, 1980].

This rifting event was modelled to obtain stretching factors (β) using the finite duration rifting model of Jarvis & McKenzie [1980], which includes the consideration of lateral heat flow (Section C.3). The theoretical subsidence curves shown on Figure 4.24 were produced from the rifting model using a rift time at 154.1 Ma and a short duration of 10 Ma (the event duration in wells 241 and 314). Well 296 (Figure 4.24a), however, is the most reliable as it penetrates the Upper Jurassic/Triassic unconformity, whereas the other two wells have in all probability not penetrated the full thickness of Jurassic sediments, and so any derived β will be an underestimate. The initial subsidence event in well 296 is 17 Ma in duration, and this produces a better fit for the tectonic subsidence in this well as illustrated for the Watts & Steckler [1979] case in Figure 4.24a where the theoretical curve for β of 1.5 and 17 Ma rift duration (heavy dashed) fits the initial tectonic subsidence with mean palaebathymetry corrections (heavy line with filled circles) better than the theoretical curve for β of 1.5 and 10 Ma rift duration (light dashed). The main period of thermal subsidence in well 296 appears to be from ~140–70 Ma, but the

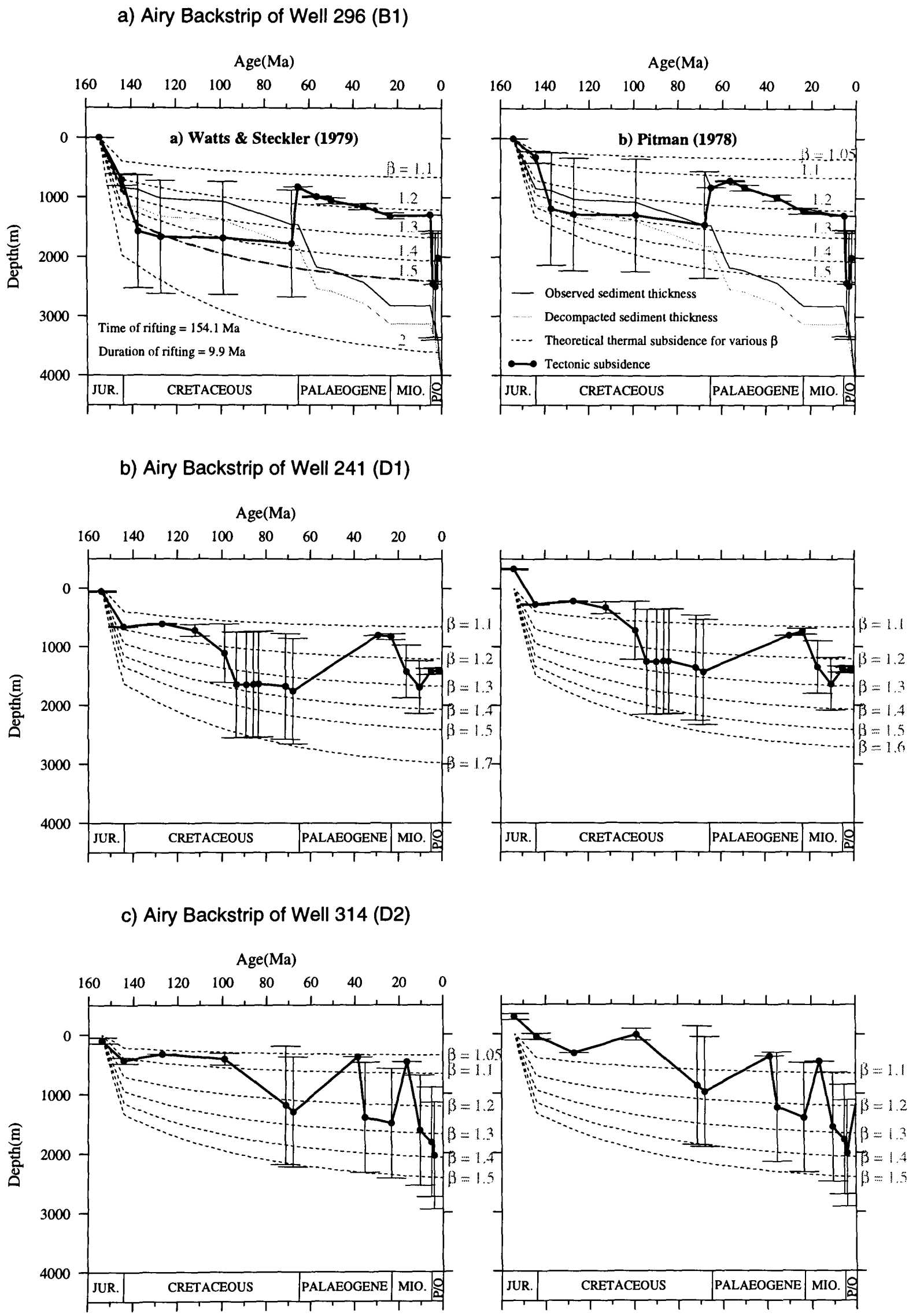


Figure 4.24: Airy backstripping results for wells 241, 296 and 314 in the northern GOC. See text for full explanation.

palaeobathymetric errors are large so the tectonic subsidence is not well constrained, unlike the well-defined Tertiary values. For the case where Watts & Steckler [1979] sealevel corrections have been applied, minimum palaeobathymetry corrections yield a simple thermal subsidence to the Pliocene fitted to a curve of $\beta \sim 1.2$: in the maximum water depth case a β of 2 would fit the early subsidence better. For the Pitman [1978] sealevel case, maximum, minimum and mean subsidence values fit to curves of β about 0.1 less than in the equivalent Watts & Steckler [1979] case.

The tectonic subsidence curves for wells 241 and 314 (Figure 4.24b and c) display a rapid initial subsidence, followed by a well-defined concave down curve characteristic of compression [Watts, 1992], then poorly-defined values in the late Mesozoic. The Tertiary in both cases is marked by uplift. If it is assumed that the concave-up part of the curve is due to some element of compression overprinting the passive margin thermal subsidence, the β values that fit the Mesozoic subsidence of these two wells range from a minimum of 1.05–1.1 (5%to 10% stretching) to a maximum of 1.7, for the Watts & Steckler [1979] case. These are lower than for well 296, but may merely be a reflection of an incomplete penetration of Upper Jurassic sediment in these wells. For example, if the undifferentiated Jurassic drilled in the base of well 241 was dated Upper Jurassic the initial subsidence, and hence β, would have been greater. The limited Triassic subsidence recorded at well 533 (Figure 4.23) was not modelled as the post–rift thermal subsidence and possibly some of the syn-rift subsidence has been obscured by an unconformity.

In summary, the tectonic subsidence displayed in the wells analysed here resembles that of modern passive margins in the sense of a rapid initial subsidence followed by slow (thermal) subsidence. However, there is a considerable scatter in the values compared to the predictions of rifting models. Part of this variation is due to the large uncertainties in palaeobathymetry estimates. Part, however, is also due to the effect of episodes of compressional deformation caused by regional convergence of African and Eurasian plates, from Late Cretaceous to Palaeogene times [e.g., Dewey *et al.*, 1989], after which the loading effect of the Betic fold-and-thrust belt becomes the dominant mechanism driving subsidence and uplift.

4.8 Crustal Structure

4.8.1 Introduction

Previous seismic refraction surveys have constrained the structure of the two main crustal domains of southern Iberia that border the GOC: the South Portugese Zone of the Iberian Massif, and the western end of the Betic Cordillera. The earliest information came from earthquake travel-time inversion [Payo, 1972], followed by seismic refraction profiling [Mueller *et al.*, 1973; Banda & Garin, 1975]. In 1974 and 1975 a number of profiles were shot in the Betic Cordilleras and Alboran Sea [Working Group for Deep Seismic Sounding in Spain 1974-1975, 1977] and for Deep Seismic Sounding in the Alboran Sea 1974 [1978]. Several subsequent refraction surveys were carried out in the southern Iberian region [Grupo de Trabajo de perfiles sísmicos profundos, 1983; Emery & Uchupi, 1984; Medialdea *et al.*, 1986; Banda, 1988; Mueller & Kahle, 1993; ILIHA DSS Group, 1993; González, 1996; González *et al.*, 1998]. Fernandez *et al.* [1998a] compiled this data to generate a Moho depth map of southern Iberia, which revealed typical values of 32–34 km thick crust for the Iberian Massif, and a decrease of crustal thickness from 30+ km beneath the Betics to 15 km in the central Alboran Sea. González *et al.* [1998] reinterpreted older refraction and wide-angle data using constraints from IGME [1987] well data and commercial seismic reflection and borehole data from Repsol. Their study indicated that crustal thickness varies from 29 km at the Guadalquivir Basin (GQB)–Iberian Massif contact to a maximum of 35 km in the South Portugese Zone.

There is relatively little refraction and wide-angle reflection data offshore GOC. González *et al.* [1998] published a 1981 vintage marine seismic refraction/wide-angle reflection profile across the SW Spanish shelf (Profile R1, Figure 4.25) which indicated a previously thinned crust which maintained a thickness of 30 km due to a thick sediment cover (Figure 4.26a and c). Recent wide-angle and refraction data were collected as part of the IAM project (see Section 3.1), involving landstation and OBS recording of the marine shots. One recent model along the profile IAM-3 (Profile R3 Figure 4.25) revealed crustal thinning from 30 km at the South Portugese Zone to 15 km only 120 km to the SW, in the vicinity of Coral Patch Ridge [González *et al.*, 1996]. A land-recorded velocity–depth section along the northern part of IAM-GC1 was recently published in Dañobeitia *et al.* [1999] (Profile R2 Figure 4.25), which indicates crustal thinning from 30 km to the north of the profile to $\sim$ 20 km beneath a large positive free-air gravity anomaly (Anomaly I in Figure 4.25).

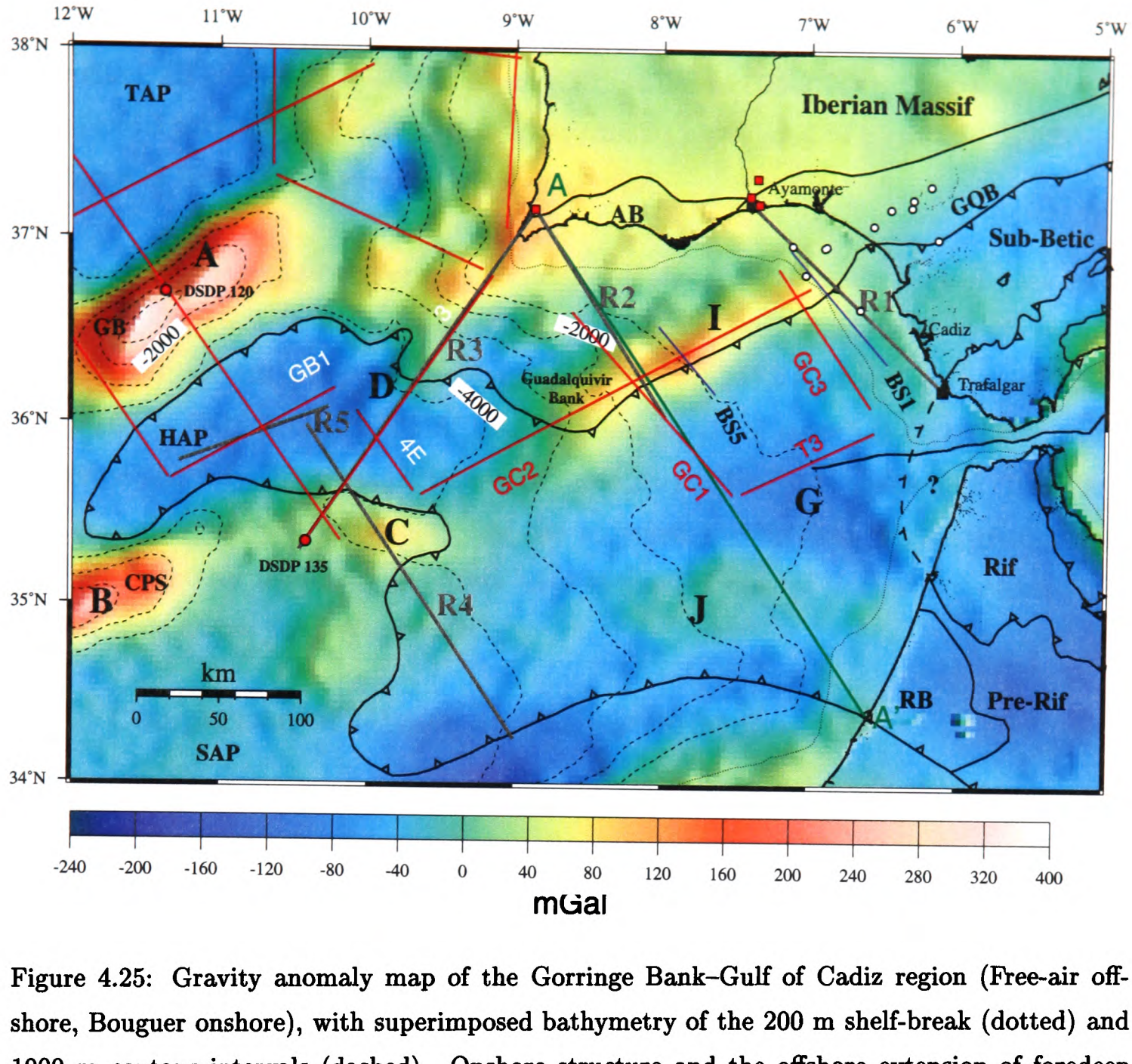


Figure 4.25: Gravity anomaly map of the Gorringe Bank–Gulf of Cadiz region (Free-air offshore, Bouguer onshore), with superimposed bathymetry of the 200 m shelf-break (dotted) and 1000 m contour intervals (dashed). Onshore structure and the offshore extension of foredeep allochthonous units west of the Betic-Rif Arc are shown. Prominent anomalies labelled A, B, C, D, I, G, J. Abbreviations: HAP=Horseshoe Abyssal Plain; TAP=Tagus Abyssal Plain; SAP=Seine Abyssal Plain; GB=Gorringe Bank; CPS=Coral Patch Seamounts; AB=Algarve Basin; RB=Rharb Basin; GQB=Guadalquivir Basin. Seismic refraction/wide-angle lines shown in grey: R1 from González *et al.* [1998]; R2 from González [1996]; Dañobeitia *et al.* [1999]; R3 from González *et al.* [1996]; R4 is taken from the crustal model of Hayward *et al.* [1999]; R5 is profile B-BR' in Purdy [1974]. The location of MCS profiles of IAM, Conrad RC2911, and the recent BIGSETS 98 cruise [BS1 and BS5, Bartolomé *et al.*, 1999] are shown. IAM Project land recording stations are shown as red squares, boreholes are shown as white circles. Forward gravity model A–A' shown in green (Figure 4.29).

The GOC margin displays an atypical pattern of free-air gravity anomalies (Figure 4.25), which trend orthoganal to it, rather than the typical FAA "edge-effect" of a rifted margin [Roberts, 1970; Watts & Marr, 1995], which is a large positive gravity anomaly caused by mantle shallowing seawards of the margin. Anomaly I (Figure 4.25) is a prominent linear anomaly trending away from the margin, which appears to be as-

sociated with the Guadalquivir Bank, a bathymetric high above shallow basement seen on Profile GC2 (CDPs 2500–4000, Figure 4.12; ~8°W and 36.2°N on Figure 4.25). The highs I and J and gravity low G have been previously postulated to be related to offshore extensions of Betic-Rifian structure [Roberts, 1970].

In order to investigate the crustal structure of the GOC several types of data have been used, as shown on Figure 4.25: offshore seismic refraction and wide-angle profiles (R1–R3, R5); seismic reflection profiles of IAM and BIGSETS [Bartolomé *et al.*, 1999] cruises (GC1, GC2, GC3, BS1, BS5); a published profile of modelled crustal structure, R4, across anomaly C for comparison with those perpendicular to anomaly I. These are used in conjunction with well data and the observed gravity field to constrain crustal structure. Gravity modelling has been used to predict crustal thickness changes on a regional scale across the western GOC.

4.8.2 Comparison of seismic and backstrip Moho

Estimates of β from Airy backstripping results of wells 241, 296 and 314 (Figure 4.24, Section 4.7.2) are tabulated in Table 4.3. Predicted crustal thicknesses were calculated from these β values, assuming a 35 km thick unstretched continental crust, based on data from the Iberian Peninsula [e.g., Medialdea *et al.*, 1986; González *et al.*, 1998] and shown on Figure 4.26a. The positions of the backstrip Moho values calculated from the backstrip estimates of thinning are plotted on Figure 4.26a and b, against the observed seismic refraction/wide-angle reflection Moho of González *et al.* [1998] (Profile R1, Figure 4.25).

	Y at Well 296 (B1)			Y at Well 241 (D1)			Y at Well 314 (D2)		
	Min	Max	Mean	Min	Max	Mean	Min	Max	Mean
β	1.2	2.0	1.5	1.15	1.7	1.3	1.05	1.5	1.2
35km/β	29.17	17.50	23.33	30.43	20.59	26.92	33.33	23.33	29.17

Table 4.3: Stretching factors for northeastern GOC wells 241, 296 and 314 shown in Figure 4.24. Best-fit β for minimum, maximum and mean tectonic subsidence values with Watts & Steckler [1979] sealevel corrections. Y is tectonic subsidence (see Section C.2).

The results on Figure 4.26 show that one well matches the refraction Moho (241), one is above (296) and one is below (314), although the refraction Moho depth falls within the error bars of all three wells. The rifting and loading history from well data therefore agrees with the seismic refraction data, within errors. The significance of this result is that it is likely that the present-day thickness of the crust beneath the eastern GOC can

be explained by the original thinning event modelled in the well data i.e., rifting coeval with the seafloor spreading that produced the M25 (157 Ma) magnetic anomaly of the NE Atlantic, which is the oldest spreading anomaly west of the GOC (Figure 2.4).

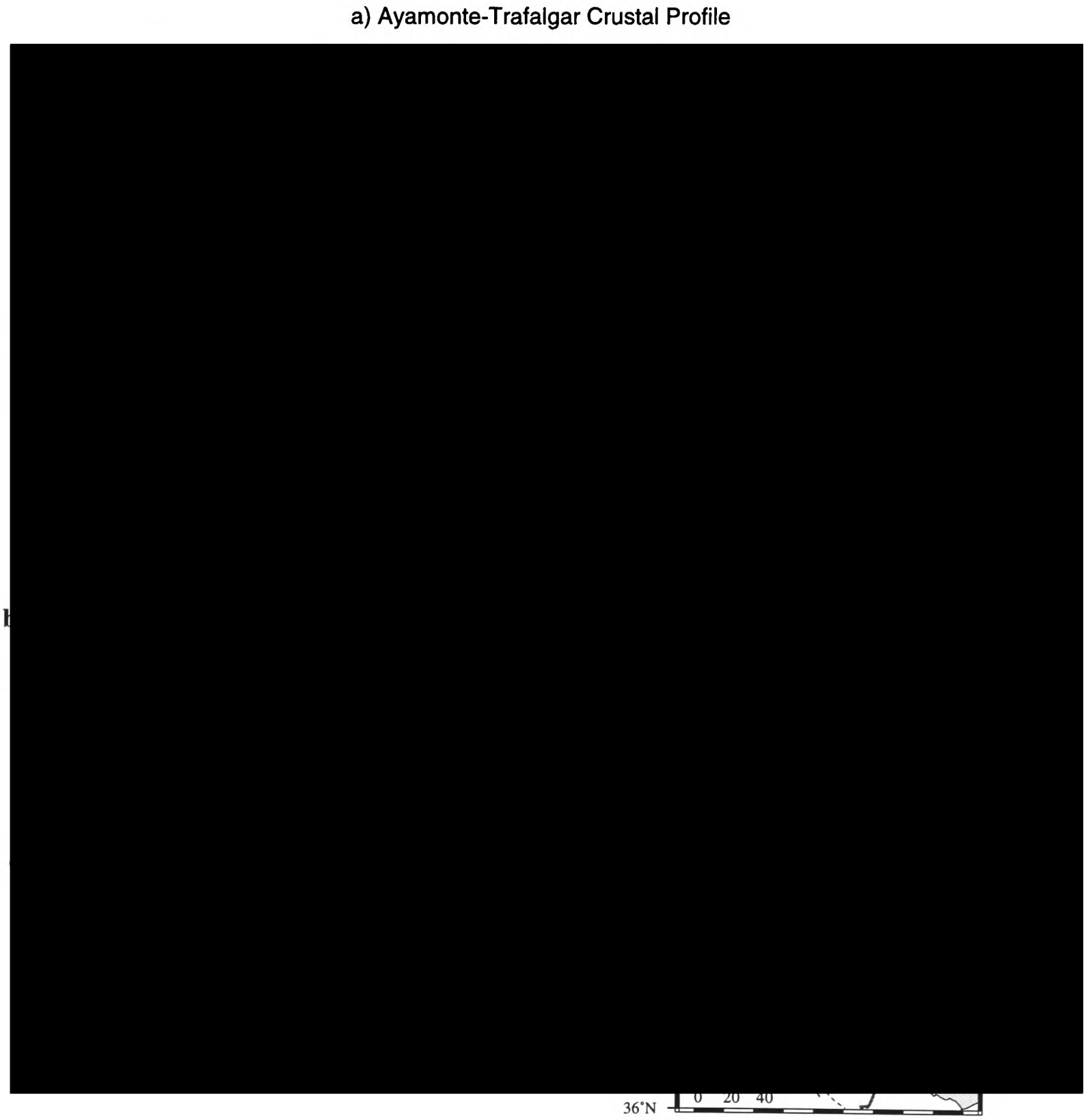


Figure 4.26: a) Crustal stucture in the eastern Gulf of Cadiz (based on refraction/wide-angle profile R1), with estimates of Moho depths obtained from the Airy backstripping of wells 241, 296 and 314 superimposed; b) values for the stretching factor obtained from the crustal model shown in c); c) original refraction/wide-angle profile from González *et al.* [1998]; d) location map for the Ayamonte–Trafalgar profile and the positions of wells with available log data.

4.8.3 Gravity modelling

Three free-air gravity anomalies, trending away from the reentrant Atlantic margin between SW Spain and NW Morocco, are marked G, I, and J on Figure 4.25. Seismic profiles GC3 and BS5 (Figure 4.27b and c) cross anomaly I, and suggest an intimate link between the anomaly and a basement high. However, this is not necessarily the case, as seismic profile BS1 (Figure 4.27a) apparently has no basement high beneath the axis of anomaly I, and the interpreted basement ridge on profile GC1 (Figure 4.27d) is offset from the anomaly axis by 20 km. Hence, profiles BS1 and GC1 suggest a source for anomaly I which is deeper than the basement–sediment interface.

Data which constrain the crustal structure in the region of anomalies G, I, and J on Figure 4.25 include wide-angle data (profile R2), seismic reflection data (e.g., IAM-GC1) and published gravimetric and seismic data from the Morocco margin [Tadili *et al.*, 1986; Favre, 1995; Pratsch, 1996]. In order to provide further constraints on regional crustal structure across the western GOC and Moroccan margin, a gravity model was carried out of a 400 km long NW–SE profile from the SW tip of Iberia to the Rharb Basin of Morocco (A–A', Figure 4.25), using prior data to constrain the initial model.

Wide-angle seismic reflection profile R2 [González, 1996; Dañobeitia *et al.*, 1999] constrains the northerly 150 km of profile A-A'(Figure 4.25). Figure 4.28 shows the original velocity–depth section, and the equivalent density model. The large anomaly to the NW has been shown to be associated with a wedge of dense lower crust (Profile R3, Figure 4.25, González *et al.* [1996]), whereas profile R2 indicates that the large positive gravity anomaly to the SE (Anomaly I, Figure 4.25) is associated with a NW–SE decrease in Moho depth from 30 km to 21 km. The positions of the intracrustal divisions were stated to be the least reliable layers in the model [González *et al.*, 1998].

Seismic reflectivity patterns can be used to constrain gravity models [e.g., Setto & Meissner, 1987], and the main boundaries for the model obtained from a depth-conversion of profile GC1 were a) the base of sedimentary layers, and b) the base of reflective lower crust, which is a common feature of European Hercynian crust and is considered as the Moho boundary based on reflection-refraction profile comparisons [e.g., Wever & Meissner, 1987; Meissner *et al.*, 1986; Watts *et al.*, 1990]. The top of the layered crust from seismic profile GC1 is interpreted to indicate the intra-crustal Conrad discontinuity [Setto & Meissner, 1987] and thus represents a velocity and density contrast which is equivalent to the top of the lower crust, which beneath gravity anomaly I lies at ~15 km according to profile R2 Figure 4.28b. However, the depth-conversion of profile GC1 indicates a

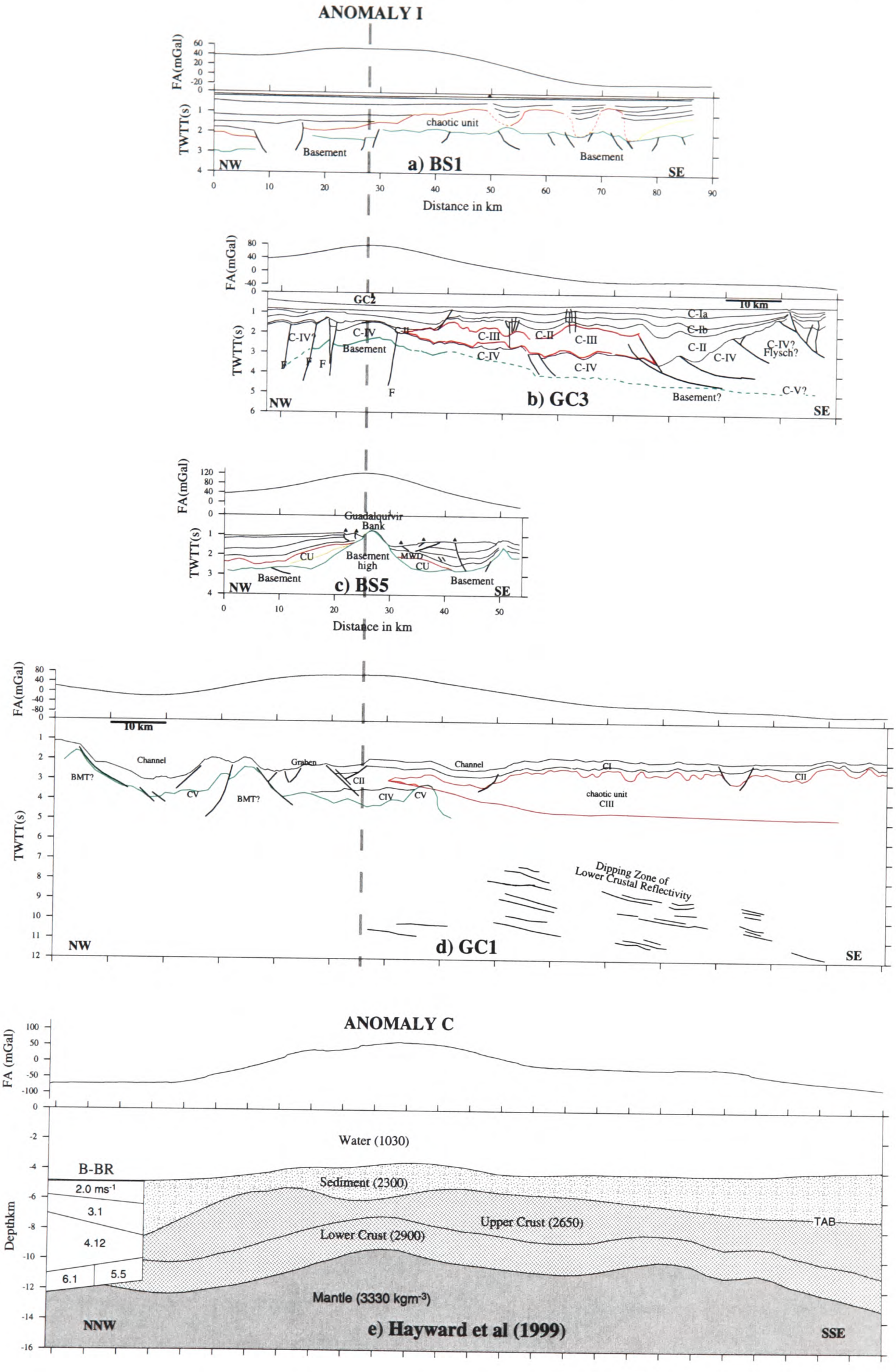


Figure 4.27: Gulf of Cadiz profiles and gravity anomaly I. See Figure 4.25 for locations. a) and c) are interpreted seismic profiles of the BIGSETS project [Bartolomé *et al.*, 1999]. b) and d) are interpreted seismic profiles GC3 and GC1 of this study. e) is profile R4, a seismic- and gravity-constrained model of crustal structure across the Coral Patch Ridge [Hayward *et al.*, 1999], and constrained by refraction data of Purdy [1974] (profile R5, Figure 4.25), and illustrates crustal structure associated with FAA anomaly C.

much shallower depth for the top of reflective lower crust, as shown on Figure 4.29 where a depth of ~10 km beneath gravity anomaly I. Due to this discrepancy, the crust was modelled as a single layer.

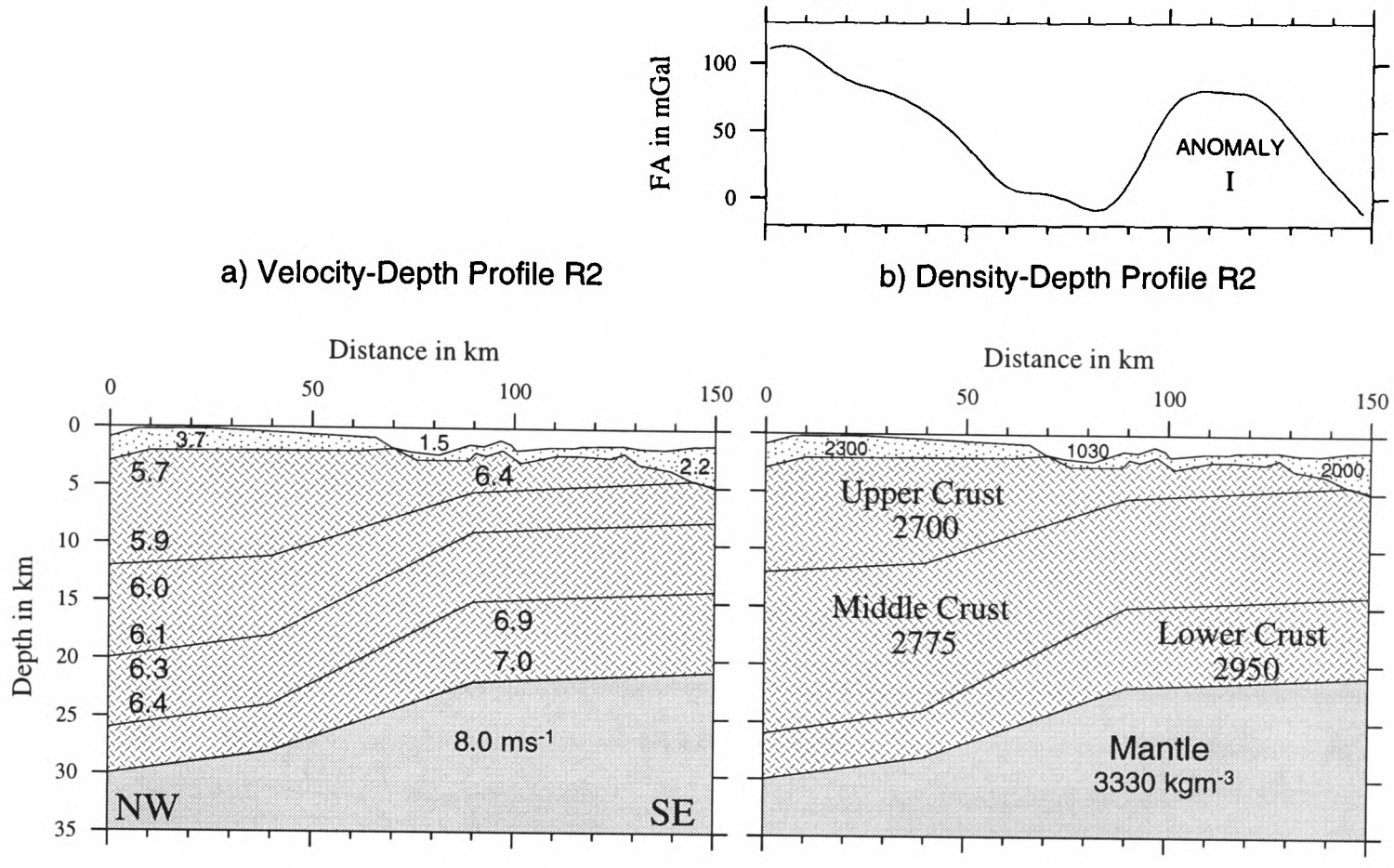


Figure 4.28: a) Wide-angle profile R2 with velocity structure as reported in González [1996]; Dañobeitia *et al.* [1999]. See Figure 4.25 for the location of this profile. b) Densities obtained through conversion of the wide-angle velocities, using the method of Nafe & Drake [1957] for the sediments and that of Christenson & Mooney [1995] for the crust and upper mantle. Seawater density was used for the water layer. The free air gravity anomaly shown above the profile is taken from Sandwell & Smith [1997].

The initial model was constrained offshore Iberia by wide-angle profile R2 (basement and Moho) [Dañobeitia *et al.*, 1999] and seismic reflection profile GC1 (basement), and offshore Morocco by Tadili *et al.* [1986]; Favre [1995](Moho) and Pratsch [1996] (top of magnetic basement), as shown in Figure 4.29c. Averaged densities were derived from the wide-angle data of Figure 4.28 to produce a density model: seawater (1030 kgm^{-3}), sediment (2100 kgm^{-3}), crust (2800 kgm^{-3}) and mantle (3330 kgm^{-3}). The program **GBOTT** was used to compute the gravity anomaly of the density model, based on a 2-D line integral technique (Section C.4.1).

The water and sediment bodies shown on Figure 4.29c are relatively well-constrained, and their combined gravity effect explains the overall concave-up shape of the observed free-air anomaly, but not the short wavelength anomalies I and J shown on Figure 4.29b.

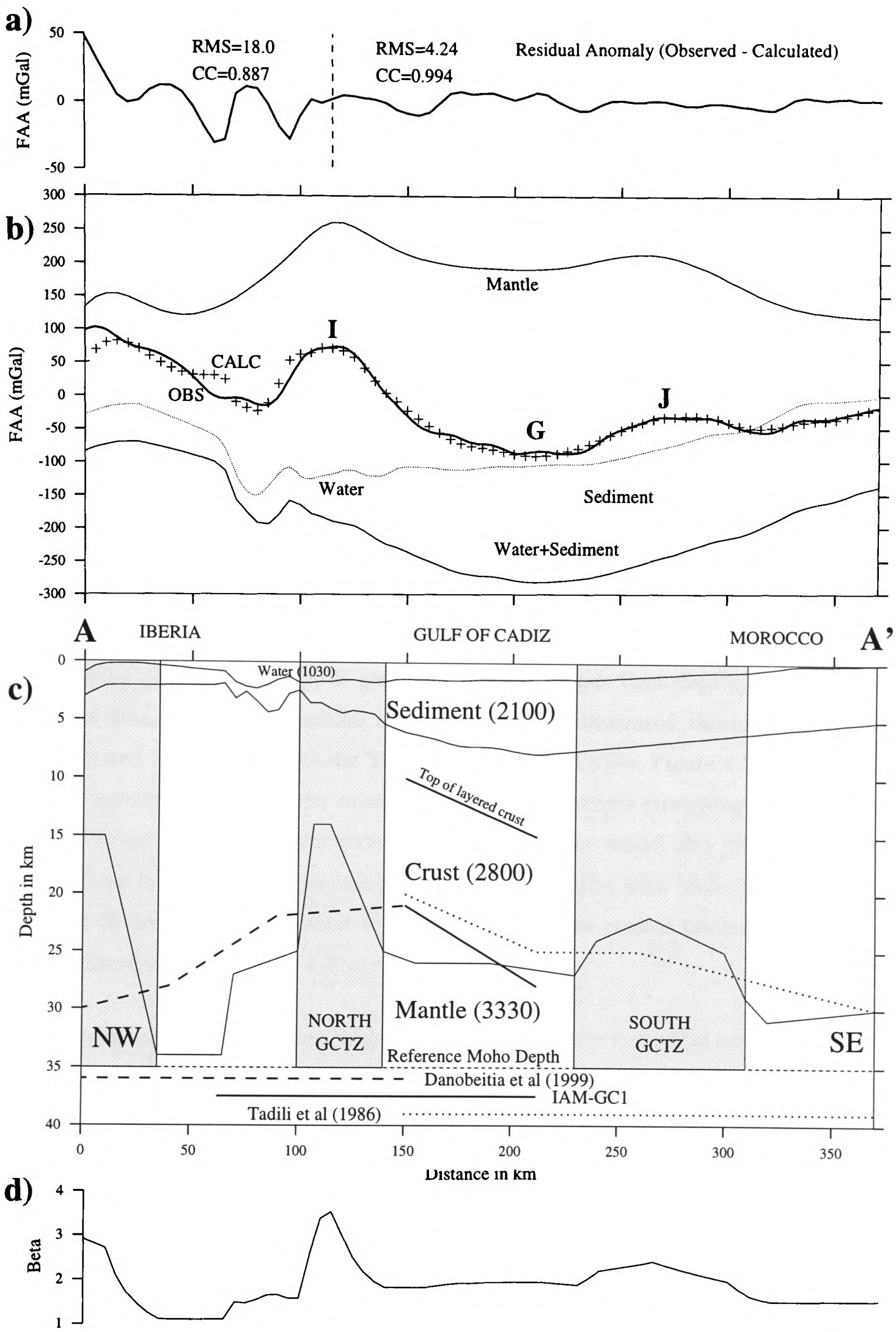


Figure 4.29: Free-air anomaly gravity model **A–A'** (South Portugal to Morocco profile) for a layered density model of seawater (1030 kgm^{-3}), sediment (best-fit 2100 kgm^{-3}), crust (2800 kgm^{-3}) and mantle (3330 kgm^{-3}). Modelled gravity shown above crustal model, with observed free-air gravity (corrected for OSU91 field) shown as a thick line with prominent anomalies from the GOC labelled I, G and J. Moho depths published in [Dañobeitia *et al.*, 1999; Tadili *et al.*, 1986] as well as the base of reflective lower crust from IAM profile GC1 are also shown for comparison. Regions of greatest crustal thinning are shown in grey; GCTZ = Gulf of Cadiz Thinned Zone.

To explain these, crustal thickness and reference Moho depth were the body parameters adjusted until a good fit was obtained between the modelled and observed free-air gravity anomaly (Figure 4.29b). A reference Moho depth of 35 km was found to produce a modelled gravity close in magnitude to the observed when an initial crustal configuration based on published data was used (as shown on Figure 4.29c). Moho depths were then adjusted to obtain the closest fit. Figure 4.29a shows the residual anomaly between observed and modelled gravity, and that a much closer fit was achieved south of anomaly I, as evidenced by a higher correlation coefficient (CC) and much lower RMS value. The differences between observed and calculated north of anomaly I are short wavelength and therefore hard to resolve through changes in Moho depth.

Three zones of crustal thinning have been invoked to fit the calculated anomaly to the observed, shown shaded grey on Figure 4.29b. The modelled zone beneath Iberia at the northern end of Figure 4.29c illustrates a sharp decrease in Moho depth to 15 km, which disagrees with that of the wide-angle data in Dañobeitia *et al.* [1999] which indicates a Moho depth approaching 30 km beneath Iberia. Beneath the rest of the profile, the modelled gravimetric Moho is generally 2–3 km deeper than depths from GC1 and published data, with the exception of two zones of concentrated thinning, labelled as the North and South Gulf of Cadiz Thinned Zones (GCTZ) on Figure 4.29c. The South GCTZ is associated with gravity anomaly high J, and involves stretching factors up to a factor of 2 over a zone $\sim$ 90 km wide (Figure 4.29d). The model also indicates a North GCTZ where intense thinning occurs over a zone 40 km wide, with Moho shallowing from 25 km to 15 km depth (equivalent to β=3.5 if a reference crustal thickness of 35 km is used, as illustrated on Figure 4.29d).

The degree of crustal thinning proposed beneath anomaly I was also investigated using the power spectrum of the gravity anomaly. This method of estimating the mean depth of compensating interfaces for potential field data was developed for aeromagnetic data by Spector & Grant [1970], and subsequently applied to gravity data, in order to estimate density interfaces, by Karner & Watts [1983]; Coudert *et al.* [1995]; Vidotti *et al.* [1998]. The mathematics of the procedure used is outlined in Coudert *et al.* [1995] and involves plotting the logarithm of the average gravity power spectrum of the anomaly against wavenumber, which should produce a series of linear segments, the slopes of which will be equivalent to the mean two-way depths related to each interface [e.g., Karner & Watts, 1983]. This procedure was carried out over the extent of seismic profile IAM-GC1 associated with free-air anomaly I (Figure 4.29). The results of each step are illustrated in Figure 4.30, where the 22.7 km interface is within 3 km of the average modelled

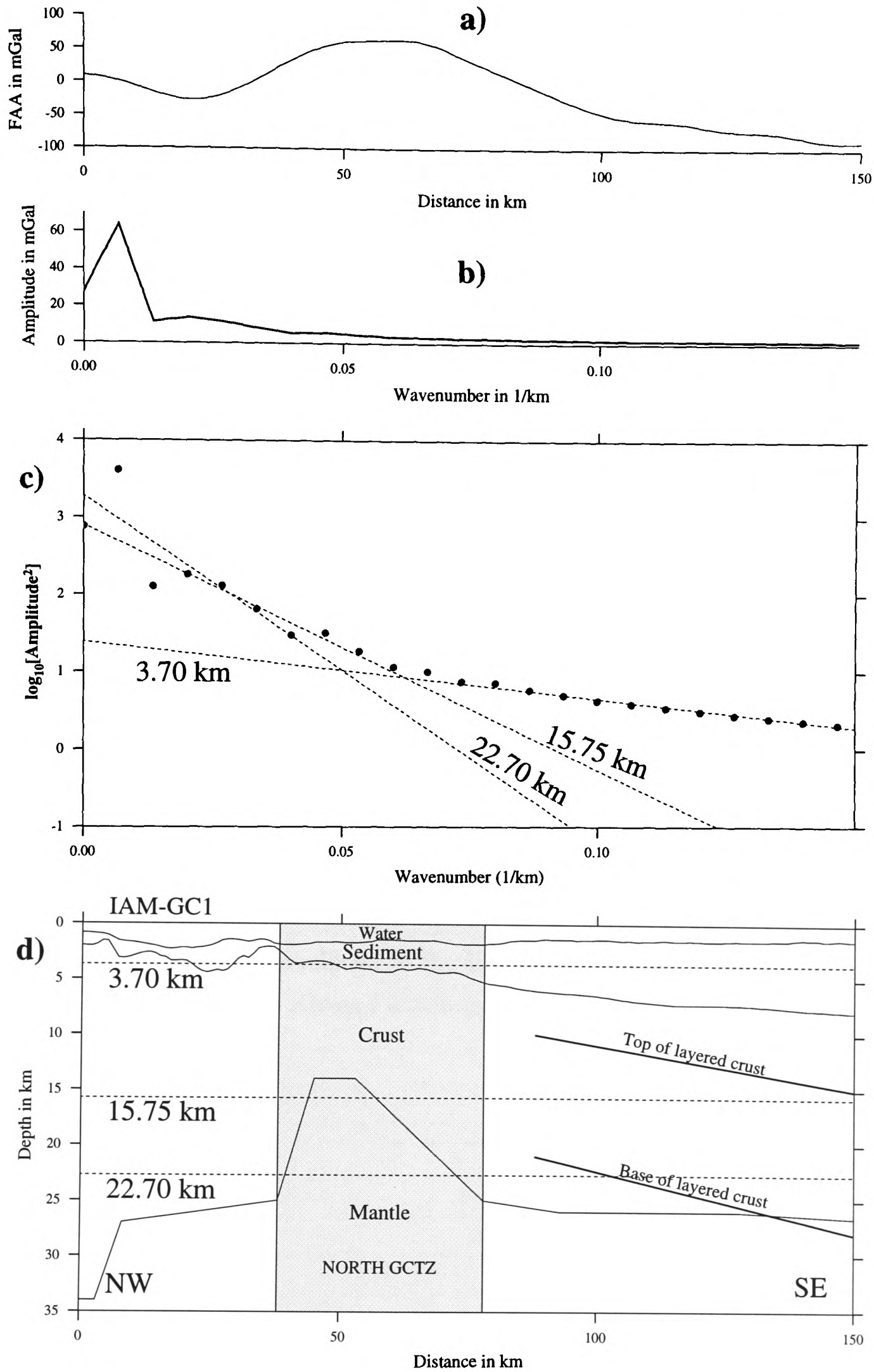


Figure 4.30: Estimate of depths to discrete density boundaries using the power spectrum of the free-air gravity anomaly over profile GC1 [e.g., Karner & Watts, 1983; Coudert *et al.*, 1995]. a) Free-air anomaly (FAA) over seismic profile GC1; b) Amplitude spectrum obtained through Fourier Transform of the FAA; c) Logarithm of the power spectrum of FAA against wavenumber. Three linear segments are picked, corresponding to depths to major density constrasts. The density interfaces are interpreted to correspond to Moho at 22.7 km, upper/lower crust boundary at 15.75 km, and sediment/basement interface at 3.7 km.

Moho depth, and also coincides with the base of layered crust picked from the seismic reflection data (Figure 4.15). The 3.7 km interface matches basement depths within the North GCTZ well and the 15.75 km layer matches the top of the stretched crust. Over the entire profile, however, the 15.75 km layer may indicate the presence of a density contrast connected with the presence of an intra-crustal discontinuity. The results of this method broadly validate those obtained from the forward gravity model.

The North and South GCTZ are associated with large positive gravity anomalies (I and J, Figure 4.25). The modelled thinning of crust producing these anomalies is supported by the seismic- and gravity-constrained model of Hayward *et al.* [1999] over the Coral Patch seamount chain to the west (profile R4, Figure 4.25) as shown in Figure 4.27e. The Hayward *et al.* [1999] profile is constrained by the refraction data of Purdy [1974] (profile R5, Figure 4.25), and clearly illustrates crustal thinning beneath the positive anomaly C seen in the free-air gravity. Large fluctuations in the depth of Moho (and thus crustal thickness) are needed to fit the calculated to the observed free-air gravity anomaly in Figure 4.29. Such variations are discussed in Lambeck *et al.* [1988], who argues (based on P-wave travel time anomalies beneath Australian cratonic basins) that such large variations over short horizontal distances can exist. However, the thinned zone beneath Iberia is not realistic, as a normal thickness (30 km) crust is indicated by wide-angle profile R3 [González *et al.*, 1996]. The thinning offshore, in the North and South GCTZ, is thought to be real and a possible explanation for such variations could be the Mesozoic rifting of these margins and transform fault tectonics that are known to have affected this region in relation to the activity of the Azores–Gibraltar Fracture Zone since the Mesozoic [e.g., Klitgord & Schouten, 1986; Dewey *et al.*, 1989; Srivastava *et al.*, 1990].

4.8.4 Mapping of stretching factors

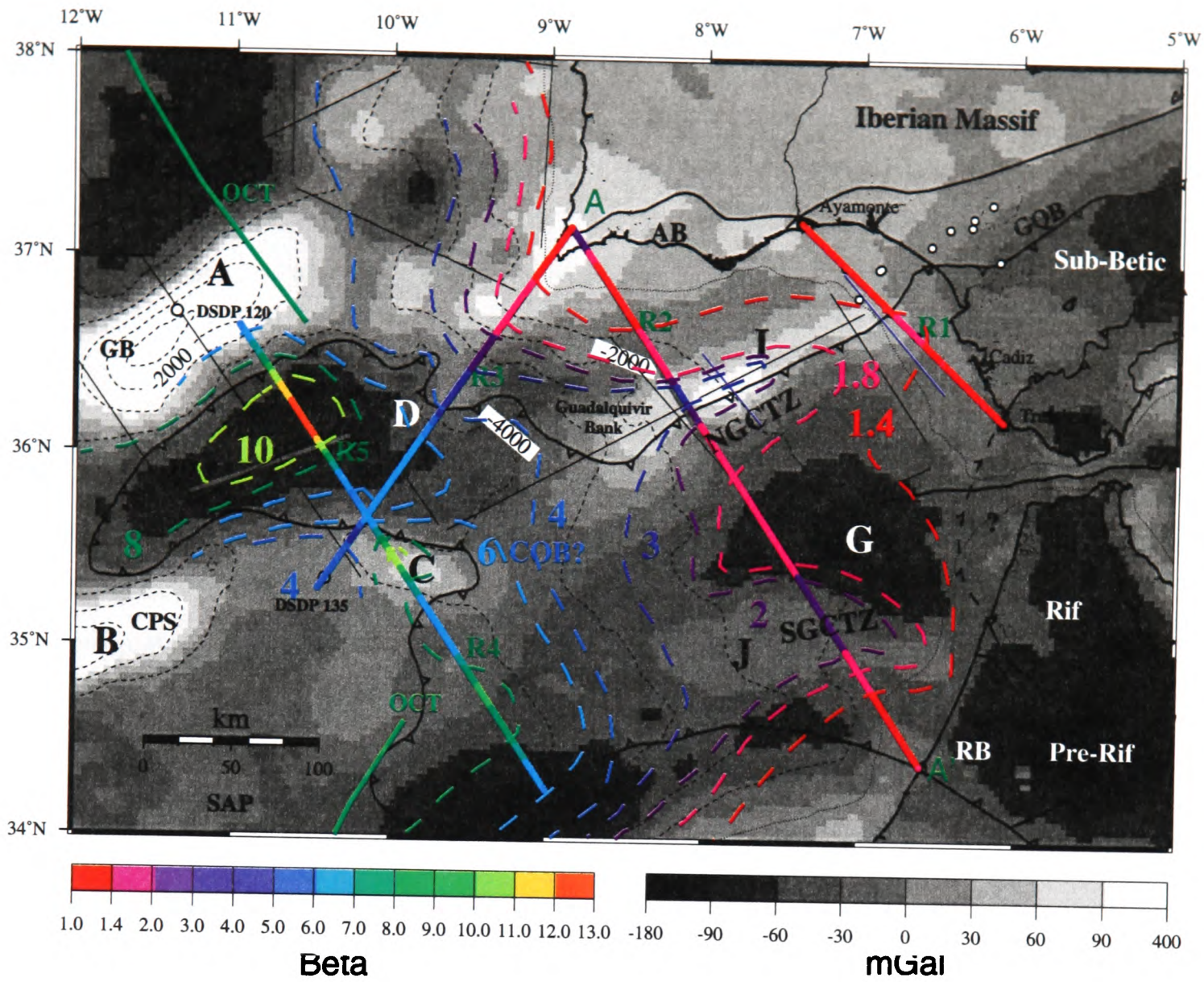


Figure 4.31: Map of contoured stretching factors (β) superimposed on regional topographic contours (dashed black lines) themselves superimposed on shaded gravity anomalies of the Gulf of Cadiz region. Letters A–J label prominent gravity anomalies, and COB refers to the possible continent-ocean boundary zone. The thick green lines offshore labelled OCT indicate the position of the ocean-continent transition reported by Mauffret *et al.* [1989]; Verhoef *et al.* [1991], as shown in Figure 4.1. NGCTZ and SGCTZ are the North and South Gulf of Cadiz Thinned Zones respectively. β values calculated with respect to a reference crustal thickness of 35 km.

Stretching factors from well backstripping results, refraction/wide-angle profiles (R1, R3, R5) and crustal models from gravity modelling (Profile A–A', Figure 4.29, and profile R4 from Hayward *et al.* [1999]) were used to construct a contoured map of β in the GOC–HAP region of the NE Atlantic, as shown in Figure 4.31. Sediment layers were not included in calculations of β from crustal thicknesses, which were made with respect to a reference crustal thickness of 35 km [González *et al.*, 1998]. Hence, β=2 implies a crustal thickness of 17.5 km, and β=10 implies a crustal thickness of 3.5 km, for example. The lines constraining the contours of constant β are shown as coloured bars. Between

the Gibraltar Straits (6 °W, 36 °N) and the 9°W meridian, β values increase from ~1 (unstretched) to ~4, but in a pattern which is associated with the gravity anomalies observed. The saddle-shape observed in GOC anomalies I, G and J (Figure 4.31) is reflected in the β contours. The gravity low G is associated with a sedimentary depocentre (Figure 4.29), whereas anomalies I and J are associated with zones of localised crustal extension, labelled NGCTZ and SGCTZ on Figure 4.31, which trend parallel to Betic and Rif structures, and perpendicularly to the coasts of southern Spain and northern Morocco.

Oceanwards of 9°W, towards the HAP and SAP, β values rise from 4 to 8 over a narrow NW–SE oriented zone only 50 km wide. Profile R3 indicates greatest thinning beneath the HAP , with a maximum of β ~7, and β ~4 or so beneath the southern boundary of the HAP. Profile R4 of Hayward *et al.* [1999] agrees with R3 where they intersect, but indicates greater thinning over the regions of the HAP and SAP (south of gravity anomaly C, Figure 4.31) which it samples. Thinnest crust is indicated in the central eastern HAP and beneath gravity anomaly C, where β values are greater than 10.

Overall, on Figure 4.31, β values are seen to increase from east to west towards the Atlantic Ocean, due to the transition from continental to oceanic crust. Seafloor spreading is thought to commence at β >4 [e.g., McKenzie, 1978], and the β=4 contour on Figure 4.31 can be taken as an estimate of the continent-ocean boundary (COB) in the absence of magnetic spreading anomalies in this region. The COB coincides with the base of the continental slope and rise of the GOC margin. This is in agreement with the position of the COB in the Tagus Abyssal Plain, off western Iberia, postukated by Mauffret *et al.* [1989], who place the COB at the base of the continental rise.

Two elongate zones of elevated β are seen trending perpendicularly to the margins of SW Spain and NW Morocco (North and South GCTZ), which are interpreted to be caused by the the general orientation of rifting, compression and strike–slip events along this segment of the Azores–Gibraltar plate boundary from the Mesozoic [Dewey *et al.*, 1989]. Their position and orientation in relation to the Gibraltar Arc also suggests an intimate connection to the structure of the Betic–Rif orogen.

4.9 Conclusions

The analysis of well, gravity anomaly, and seismic reflection and refraction data from the Gulf of Cadiz margin have allowed the several conclusions to be drawn with regard to its shallow and deep structure and sediment distribution. The main results of this study are summarised below.

- Well and seismic data were used to construct a regional seismic stratigraphy for the GOC. Seismic profiles were interpreted on the basis of a scheme of five major seismic stratigraphic units (units CI to CV), picked on the basis of seismic character and borehole–calibrated age and lithology, were identified. The sediments are of Triassic to Recent in age, and rest on a Hercynian basement which is an extension of the Iberian Massif. The maximum thickness of sediment in the Gulf of Cadiz is $\sim$ 4 s TWTT or 4–5 km (assuming V_p= 2–2.5 kms^{-1}).

- Seismic interval velocities from profile GC3 broadly agreed with sonic velocity pseudo-funtions for nearby wells, and so seismic velocities were used for depth conversion and tying of well to seismic data.

- Prominent SE–dipping reflections beneath the southern 100 km of profile GC1 are interpreted to be due to a reflective lower crust 3 s thick, typical of Hercynian crust in SW Europe [e.g., Watts *et al.*, 1990]. These reflections stop below a zone of tilted basement/Mesozoic fault blocks and an overlying graben structure, which may indicate these originated with rifting with an asymmetric simple shear component. Alternatively, strike slip motion may have juxtaposed two different crusts.

- A complex tectonic history is indicated by the presence of extensional, compressional and diapiric structures, and the widespread occurrence of allochthonous sediments.

- Two major events were recorded in the well backstrip curves of Figure 4.23. A period of rapid subsidence in the Late Jurassic (154.1 Ma) which correlated with the M25 (157 Ma) spreading anomaly in the NE Atlantic, which is the oldest magnetic spreading anomaly west of the Gulf of Cadiz (Figure 2.4). The second major observation was of accelerating subsidence in the Miocene as a foreland basin developed ahead of the advancing Betic–Rif thrust wedge.

- β values averaging 1.2–1.5 were obtained from wells in the northeast GOC, using a finite duration rifting model, with a Upper Jurassic time of rifting and a rift duration of $\sim$10 Ma. Assuming an unstretched crustal thickness of 35 km, these results produced backstrip Moho estimates that were in agreement with seismic

refraction/wide-angle reflection data of González *et al.* [1998]. This suggests that the thinned crust observed in the NE GOC at the present day is a relict of the original rifting event.

- The saddle-shape observed in GOC gravity anomalies I, G and J (Figure 4.31) is due to variations in crustal thinning, as confirmed through gravity modelling and power spectrum analysis of the free-air gravity anomaly over profile GC1 [e.g., Karner & Watts, 1983; Coudert *et al.*, 1995]. The gravity low G is associated with a sedimentary depocentre (Figure 4.29), whereas anomalies I and J are associated with zones of localised crustal extension, labelled NGCTZ and SGCTZ on Figure 4.31, which trend parallel to Betic and Rif structures.

- Mapping and contouring of stretching factors reveals lateral zones of thinning in the GOC, which trend away from the margin. These are thought to be a result of Mesozoic rifting, subsequent lateral movements and the structure of the Betic–Rif belt. A possible continent–ocean boundary zone runs approximately at the base of the continental slope, on the basis $\beta > 4$ produces oceanic crust.

Chapter 5

A Seismic Study of Hydrates and Mass Wasting in the Gulf of Cadiz

5.1 Introduction

Gas hydrates have generated much scientific interest because of their potential as a major new energy source for methane [e.g., Okuda, 1998; Subrahmanyam *et al.*, 1998], their role in global climate change as a source and sink of methane which is a "greenhouse" gas, and the relationship between hydrate destabilization and submarine slope failure [e.g., Haq, 1998; Mienert & Posewang, 1999]. Gas hydrates occur naturally in a variety of locations worldwide: associated with permafrost in polar regions, and in sediments of outer continental margins and insular margins such as the Mediterranean [Kvenvolden, 1999].

Geophysical methods of tracing gas-hydrate zones, like identifying markers such as bottom simulating reflectors (BSRs) and blanking zones on seismic reflection sections, are well-established [Subrahmanyam *et al.*, 1998]. BSRs are thought to coincide with the base of the gas hydrate stability zone (GHSZ) through analogy with bottom simulating seismic reflections observed on seismic profiles from outer continental margins worldwide [e.g., Shipley *et al.*, 1979; Kvenvolden, 1998] which correlate with drilled hydrate/free gas interfaces in places such as the Cascadia accretionary prism [e.g., Westbrook *et al.*, 1993] and the Blake Spur off southeast USA [ODP Leg 164, Pecher *et al.*, 1997]. Gas hydrates have been associated with submarine mass wasting, for example the giant Storegga Slides off the Norwegian margin [Mienert & Bryn, 1997] and at the Beaufort Sea margin of Alaska [Kayen & Lee, 1993].

This study presents a previously unreported gas hydrate deposit located beneath the lower continental slope of the Gulf of Cadiz, as inferred from the presence of a bottom–simulating reflection (BSR) seen on multichannel seismic data of the IAM project [Banda *et al.*, 1995], the acquisition and processing of which has been described in Section 3.1. A

description of the seismic character of this BSR and associated features is presented here, along with an analysis of the observations. Seismic data also reveal mass flow features in the Pliocene–Recent fill of the Gulf of Cadiz continental slope. Possible connections between mass–wasting and the presence of gas hydrates are explored.

5.2 Background to gas hydrates

5.2.1 Occurrence

Gas hydrates (also known as clathrates) are solid, non-stochiometric mixtures of water and gas molecules, which chemists have studied since the early 19th Century [Sloan, 1990]. Water molecules form a rigid lattice of cages, which hold molecules of natural gas [Kvenvolden, 1998]. Booth *et al.* [1998] estimate that 99% of marine hydrates are methane-bearing, but molecules of other hydrocarbons up to the size of butane can be held in certain lattice structures. Each volume of a fully saturated methane hydrate can yield up to 164 volumes of gas, which has led to interest in natural hydrates as an important future natural energy resource. Other important aspects of gas hydrate occurrence are hazards such as slope instability, and the effects on climate of the hydrate source/sink system for methane. Current estimates generally agree that gas hydrates are by far the largest reservoir of organic carbon on Earth [e.g., Kvenvolden, 1998]. The resource, hazard and climate issues involved with gas hydrates are discussed at length in a number of recent review papers [Booth *et al.*, 1998; Lerche & Bagirov, 1998; Subrahmanyam *et al.*, 1998; Haq, 1998; Kvenvolden, 1998, 1999].

The known and inferred locations of gas hydrate worldwide are shown on Figure 5.1, from Kvenvolden [1998]. Globally, marine hydrates (filled circles) occur beneath continental margins, whereas the onshore hydrates (filled diamonds) occur in regions of permafrost at high latitudes. The spatial distribution is such because these regions represent the combination of the availability of large amounts of methane with fluid transport pathways, and appropriate thermobaric conditions of relatively low temperature and high pressure i.e., a gas hydrate stability zone (GHSZ) [Ginsburg, 1998].

The calculation of the GHSZ for continental slope environments is illustrated on Figure 5.2 [Kayen & Lee, 1993]. Figure 5.2a is the phase diagram for methane hydrate, and Figure 5.2b is a schematic section through a continental slope. Figure 5.2 indicates that in depths exceeding 300 m, the pressure is high enough and the temperature low enough for hydrate to occur at the seafloor. The fraction of hydrate in the sediment usually increases with depth. The base of the hydrate zone is a phase boundary between

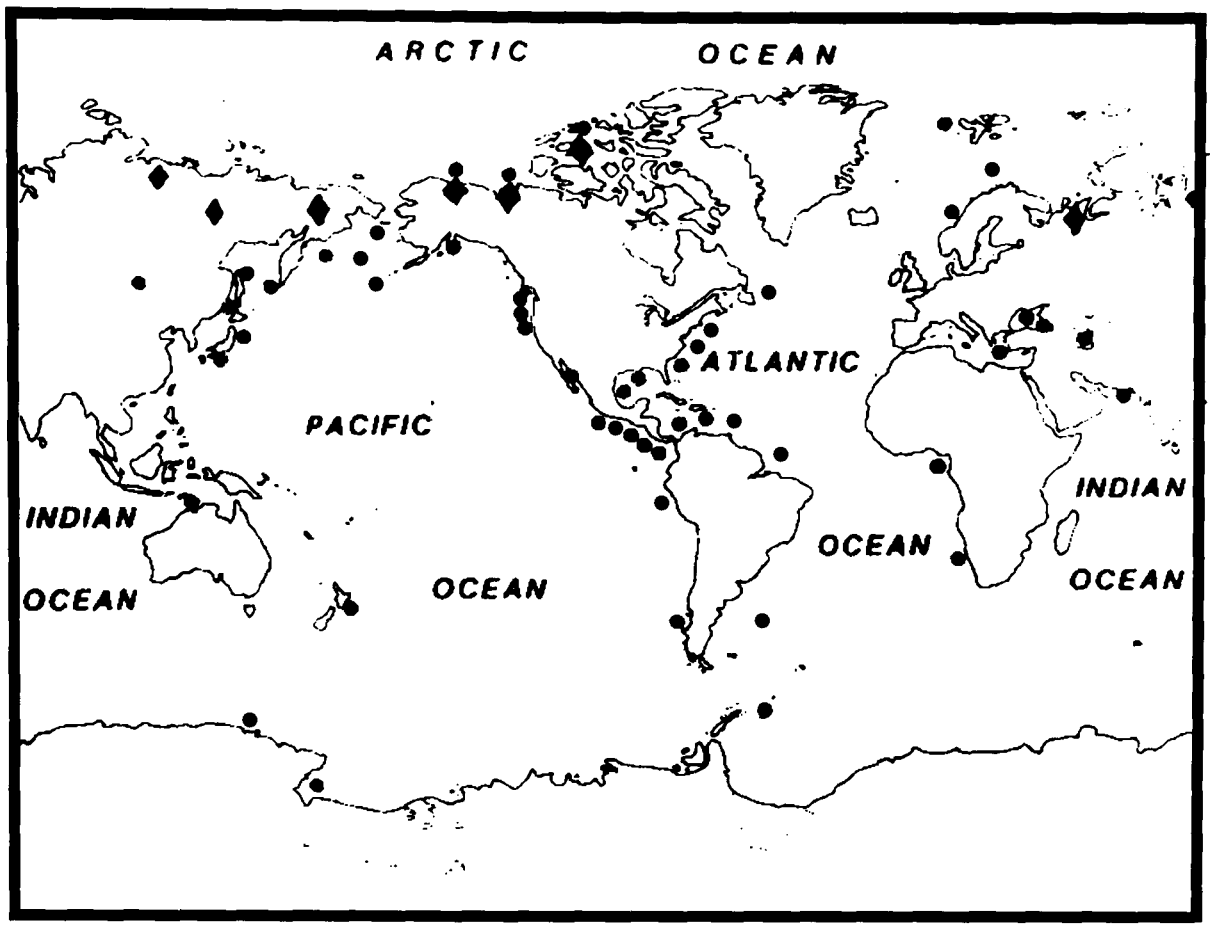


Figure 5.1: Global gas hydrate occurrence (after Kvenvolden [1998]). Known and inferred locations of gas hydrate in offshore sediments (filled circles) and beneath continental permafrost (filled diamonds).

solid hydrate and free gas and water, whose depth is determined principally by the value of the geothermal gradient. An additional factor that affects the GHSZ is the composition of the hydrate; the presence of molecules of salt, carbon dioxide, and hydrogen sulphide all affect the position of the hydrate solidus [Kvenvolden, 1998]. There is also a documented affinity between gas hydrate occurence and the presence of faults or other tectonic features (e.g., diapirism) which would promote the upward migration of gas or gas–rich fluids [Ginsburg & Soloviev, 1997; Booth *et al.*, 1998; Ginsburg *et al.*, 1999]. *In situ* gas hydrates have usually been sampled well above the base of the GHSZ, and in relatively thin horizons up to 30 m thick and with a vertical range of 200 m) [Booth *et al.*, 1998]. ODP Leg 164 has drilled through the GHSZ at the Blake Ridge, offshore SE USA, which has allowed detailed measurements to be made [e.g., Holbrook *et al.*, 1996; Pecher *et al.*, 1997].

5.2.2 Bottom Simulating Reflectors

A majority of gas hydrate deposits beneath continental margins have been inferred from the observation of an anomalous bottom-simulating reflector on reflection seismic profiles

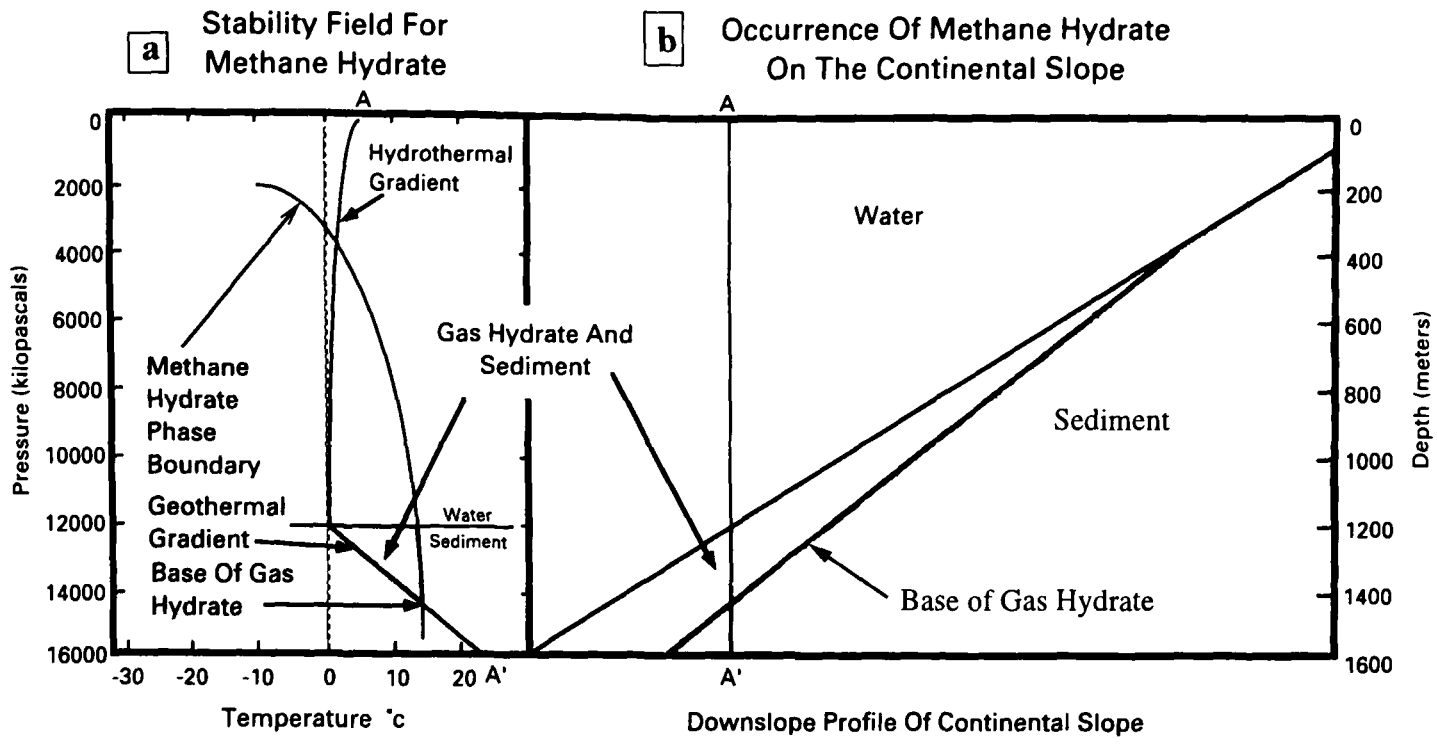


Figure 5.2: a) is a phase diagram showing the gas hydrate P-T stability field for a pure methane–pure water system. Gas hydrate is formed at conditions beneath the marked phase boundary. b) is a schematic of the continental slope, and the P-T conditions of profile A-A' are drawn on phase diagram a) to show how conditions at the sea floor are well within the hydrate stability field but the depth of the base of the hydrates is controlled by the geothermal gradient.

[Shipley *et al.*, 1979; Kvenvolden, 1998], commonly associated with a zone of reduced-amplitude reflections above the BSR (blanking) [e.g., Veerayya *et al.*, 1998]. The BSR is thought to mark the base of the GHSZ, where a phase transition occurs (within the pore space of the sediments) with small amounts of solid gas hydrate above the reflector to free gas below [see general study of Kremlev *et al.*, 1997]. The phase transition is largely temperature–controlled in deep water (Figure 5.2), and so locally follows the sub-seabed isotherms that approximately parallel the seabed [e.g., Hobro *et al.*, 1998], hence the "bottom-simulating" appellation.

BSRs generally exhibit negative polarity relative to the seafloor due to the transition from higher P-wave velocity hydrate–cemented sediment above the base of the GHSZ, and the uncemented sediment below, containing free gas and water, which has a low compressional velocity. For example, the BSRs of the Blake Outer Ridge exhibit negative reflection co-efficients of -0.12±0.04 [Shipley *et al.*, 1979]. ODP drilling and recent waveform inversion studies such as Katzman *et al.* [1994]; Holbrook *et al.* [1996] and Korenaga *et al.* [1997] indicate that strong BSRs are usually caused by free gas–bearing sediments below the GHSZ. From their general study, Kremlev *et al.* [1997] concluded that the thickness of the hydrate-bearing sediment above the BSR has little effect on the BSR reflection characteristics as the diffuse upper boundary (where the proportion of hy-

drate in the sediment pores is variable) does not produce a significant acoustic impedance contrast. As a result of this, the total mass of hydrate cannot be reliably determined by seismic measurements alone.

5.2.3 Hydrates and Slope Stability

Gas hydrates are thought to play a part in several types of geohazard, such as blowouts which could affect conventional hydrocarbon operations in the Arctic and offshore Gulf of Mexico for example, and failures of the seafloor [e.g., Haq, 1998; Kvenvolden, 1999]. Figure 5.3 illustrates the broad categories of gravity–driven mass transport seen on continental slopes [Shanmugam *et al.*, 1995]. Slides occur on planar glide surfaces, slumps occur as rotational mass movements on concave-up glide planes, and debris flows occur as a fluidized chaotic mass which produces a chaotic deposit. These successive groupings represent increasing mass disaggregation and fluidisation.



Figure 5.3: Schematic figure of mass flow processes operating on the continental slope (after Shanmugam *et al.* [1995]; Haq [1998]).

During gas hydrate formation, as solid methane and water progressively fill up sedimentary pore space, a situation will eventually arise where the hydrates fill much of the GHSZ, and the base of the deposits are driven below the GHSZ through deeper burial by ongoing sedimentation. These basal deposits will become unstable and revert to a fluid gas–water mixture from a solid hydrate, thus forming a zone of lowered shear strength at the base of the GHSZ. This forms a potential slide surface which dips more steeply than the seafloor surface (Figure 5.2b), along which failure could be triggered by a seismic

shock or gravitational loading [McIver, 1982; Ashi, 1999]. Apart from continued sedimentation, a lowering of sealevel or an increase in water–bottom temperature can also change the ambient thermobaric condition of the gas–hydrates such that they dissociate to gas and water [Kvenvolden, 1998]. Such decomposition of hydrate and weakening of sediment strength would tend toward failure along low–angle slopes, generally producing slides and slumps rather than debris flows [Haq, 1998].

McIver [1977] first identified the possible link between hydrates and submarine slide and slump features. Subsequently, several examples where gas hydrates may have played a role have been described, such as the giant Storegga Slides off the Norwegian margin [Bugge *et al.*, 1988; Mienert & Bryn, 1997], in the western Mediterranean [Rothwell *et al.*, 1998] and off the Beaufort Sea margin of Alaska [Kayen & Lee, 1993].

5.3 Tectonic and geological setting

The Gulf of Cadiz (GOC) lies in the eastern Atlantic between southern Iberia and north Africa, landward of the Horseshoe and Seine abyssal plains and seaward of the Straits of Gibraltar (Figure 5.4). The continental margin occupying most of the Gulf has the morphology of a large mass–wasting depositional feature, such as a submarine fan, and is flanked on either side by the steep, more typically Atlantic-type passive margins of Iberia and Africa (Figure 5.4). The GOC margin is situated at the intersection between the active African-Eurasian plate boundary, marked by the Azores-Gibraltar Fracture Zone and the Betic-Rif orogenic belt, and the more typical passive margins of the eastern Atlantic. The present-day regional stress regime is one of NW-SE compression with dextral strike-slip (transpression), with large strike-slip displacements known to have occurred since the Mesozoic [Dewey *et al.*, 1989].

Previous observations of gas and its related seismic and sedimentary manifestations have been limited to the upper slope and shelf regions of the GOC. Dry, biogenic gas has been drilled since the 1970s from the "Atlantida" formation of Middle–Late Miocene sands in the northeast GOC upper continental slope and shelf region [Delaplanche *et al.*, 1982; Melendez-Hevia & Alvarez de Buergo, 1996]. The occurrence of gas–charged sediment on the central to eastern upper slope in the GOC was deduced from acoustic turbidity and gas–escape pockmarks on seismic reflection data [Baraza & Ercilla, 1996]. The gassy sediment was noted over $\sim$200 km^2 at about 20 m depth below the seabed, and a link between the gassy sediment and sediment failure (shown by broken shallow reflections just downslope of the gassy sediment) was proposed by Baraza & Ercilla [1996].

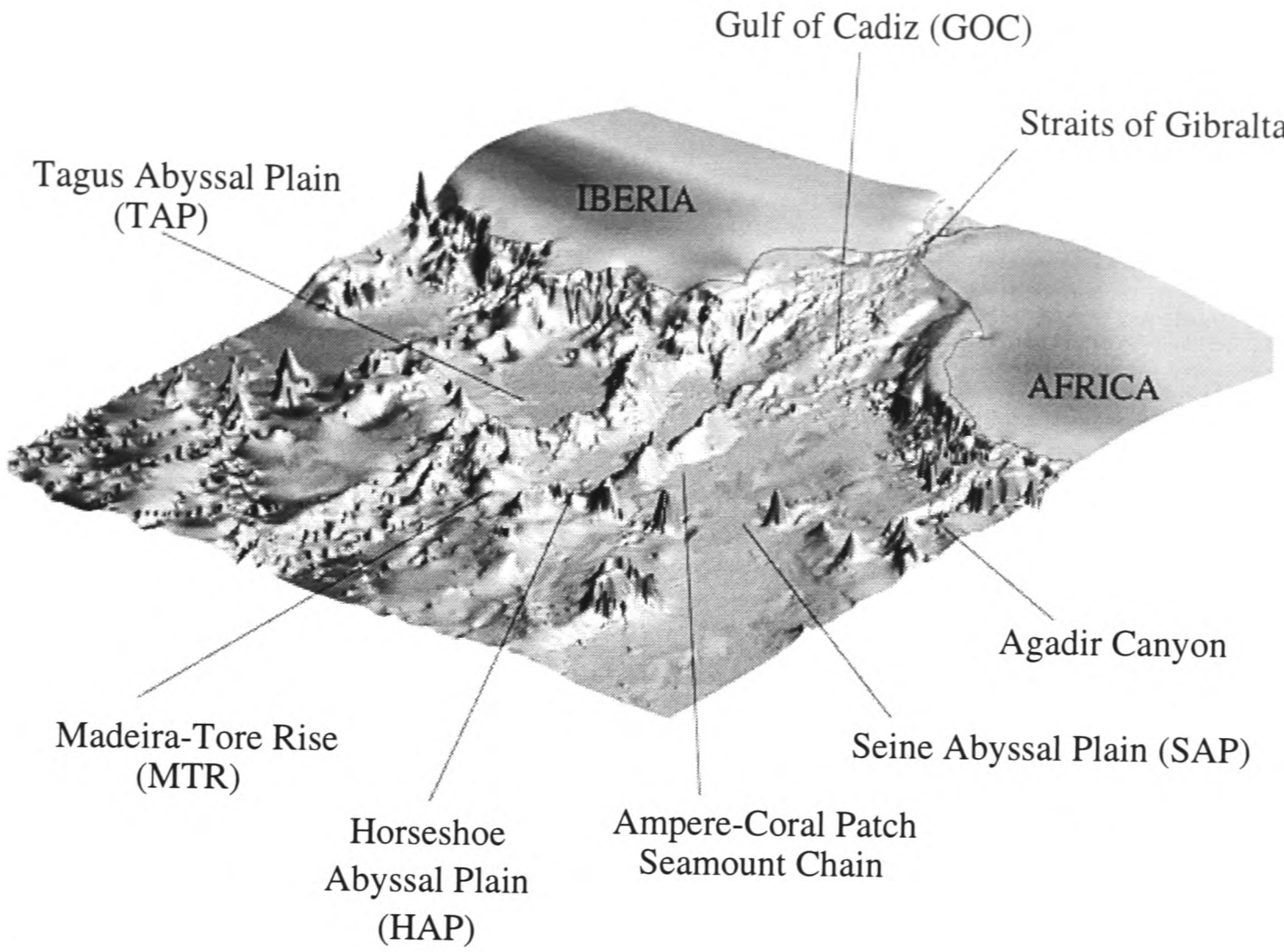


Figure 5.4: Perspective image of the bathymetry of the central North Atlantic viewed from the SW, with illumination from the SE.

The presence of the gas has been described as a slope-stability hazard, that could affect pipelines, cables and structures over the region of the seabed affected [Baraza *et al.*, 1999].

In this study, seismic indications of deep–water gas and gas hydrates are investigated on MCS profiles over the continental slope of the GOC margin. In addition, the nature of gas migration upslope from deep sources, and the possible effects of free gas in the sediment on mass wasting through time, are explored.

5.4 Multichannel Seismic Reflection Data

5.4.1 Seismic Profiles

In late 1993, the Iberian Atlantic Margins (IAM) group carried out a seismic reflection survey with the aim of acquiring a series of deep crustal images [Banda *et al.*, 1995]. In order to maximise acoustic penetration a powerful 116 litre volume airgun array was deployed, with shot returns recorded by a 5 km long streamer of 192 channels. Standard processing techniques [Yilmaz, 1987] were applied to produce filtered stacks of 32–fold data, as described in Banda *et al.* [1995]. Post-stack processing carried out at Oxford University included phase-shift migration, trace mixing, dip filtering and dynamic signal-to-noise filtering. The final migrated profiles were displayed with a 500 ms AGC scalar, using Seismic Unix [Cohen & Stockwell, 1996] and GMT [Wessel & Smith, 1991] software packages. In this chapter, IAM profiles GC1 and T3 are studied (Figure 5.5). For the studies of reflection amplitude, only migration was performed post-stack, with no filtering applied in order to preserve relative amplitudes.

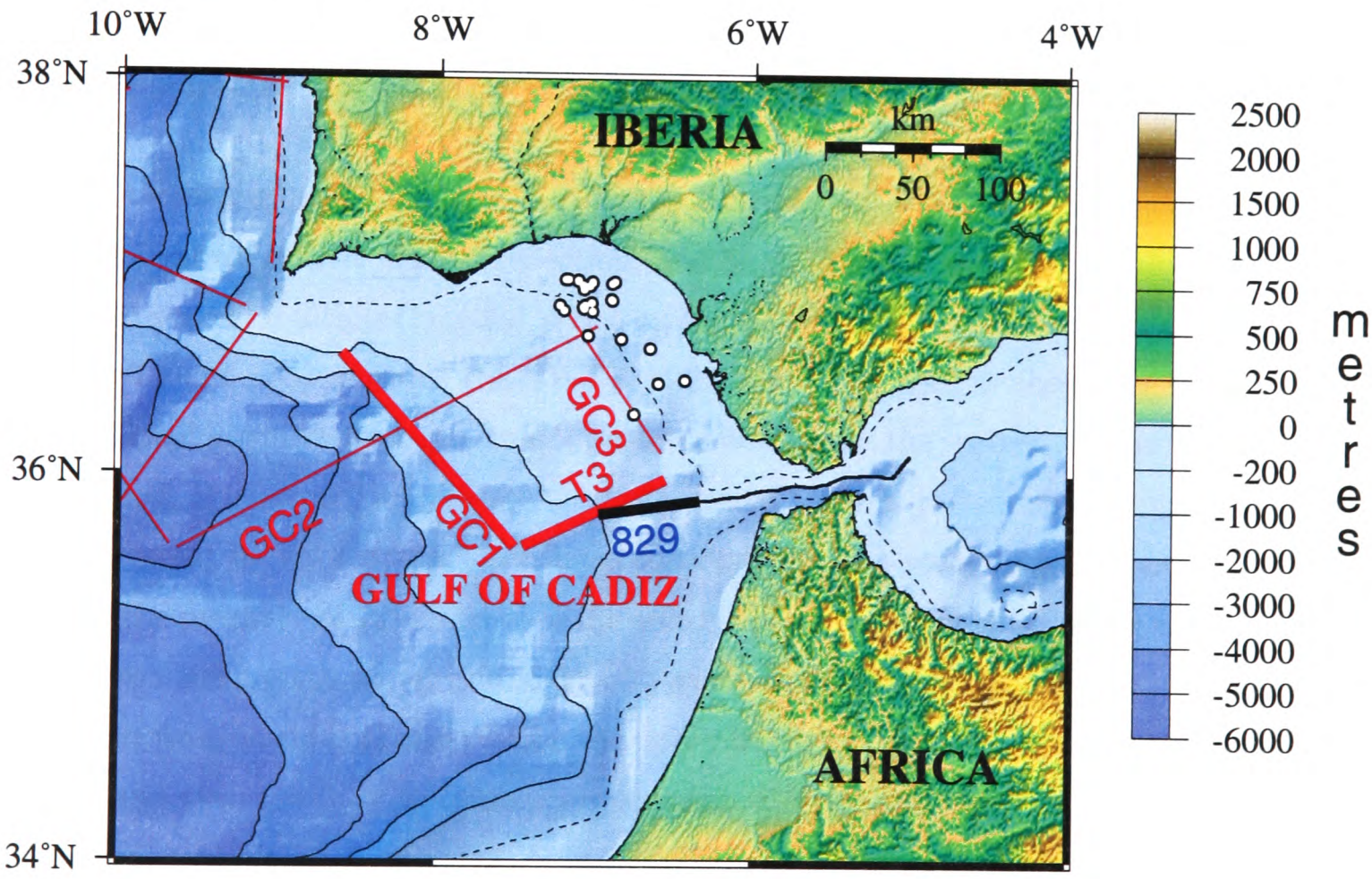


Figure 5.5: Location map of MCS profiles from the Gulf of Cadiz studied in this chapter (heavy lines). Well data from IGME [1987] shown as white circles.

In addition to the IAM profiles, MCS profile 829 (Figure 5.5) of the Lamont–Doherty RC-2911 cruise in the Gibraltar Straits–Western Mediterranean area was also utilised for

extra information on upper slope sedimentation. This data was acquired by Lamont–Doherty Geophysical Observatory (LDGO) vessel *R/V Robert D. Conrad*, using a tuned 5346 cubic inch airgun array and 2.4 km streamer with 48-channel recording. The initial processing and post-stack processing carried out for this study are described in Section 3.5.

5.4.2 Observations of Anomalous Reflectivity

A bright reflection running approximately parallel to the seabed is observed beneath the lower continental slope of the central GOC margin, on the profiles IAM–T3 (CDPs 1-1500, 2-2.5s TWTT, Figure 5.6) and IAM-GC1 (CDPs 4000-6000, 2-3s TWTT, Figure 5.7) . The reflection is not due to normal marine sedimentary layering as it appears to cut across bedding plane reflections of seismic units C–II, and diapirs of C–III (Figure 5.6 and Figure 5.7, and in more detail on Figure 5.8), which means it is younger than, and superimposed upon, the acoustic structure of C-II and C-III sediments. This peculiar reflection is observed over a limited extent of profiles GC1 and T3 (Figure 5.8) in water depths of 1275–1575 m (1.7–2.1 s TWTT), at an average subbottom TWTT of $\sim$ 0.4 s on T3 (Figure 5.6) and a slightly greater 0.5s on GC1 (Figure 5.7).

The anomalous reflection is not a simple multiple, as it only approximately reflects the relief shown by the seabed reflection, and is at far shallower TWTT than the first expected seabed multiple (labelled WBM on Figure 5.6, Figure 5.7), which is observed on profiles T3 and GC1 at twice the TWTT of the seabed arrival, at about 4 s TWTT. No other plausible source for a multiple is observed other than the seabed, and as that can be discounted, the anomalous reflection is interpreted to be a *bottom-simulating reflection* (BSR) caused by an acoustic impedance contrast due to a secondary diagenetic feature such as the presence of gas hydrate in the sediment [e.g., Shipley *et al.*, 1979]. No distinct reflection marking the upper boundary of a gas hydrate zone is observed on either T3 or GC1, but from worldwide observation the upper boundary has been generally found to be diffuse and thus produce no impedance contrast which would result in a clear reflection [Kremlev *et al.*, 1997].

The BSR exhibits reverse polarity with respect to the seabed reflection, as displayed in Figure 5.9, which indicates that the BSR represents an interface across which there is a significant decrease in acoustic impedance. Negative polarity is characteristic of BSRs worldwide [e.g., Haq, 1998; Kvenvolden, 1998]. If the BSR marks the base of the GHSZ, a drop in velocity and thus, acoustic impedance, would be expected between hydrate and gas-filled sediments, observed as a negative excursion on a seismogram equivalent to the

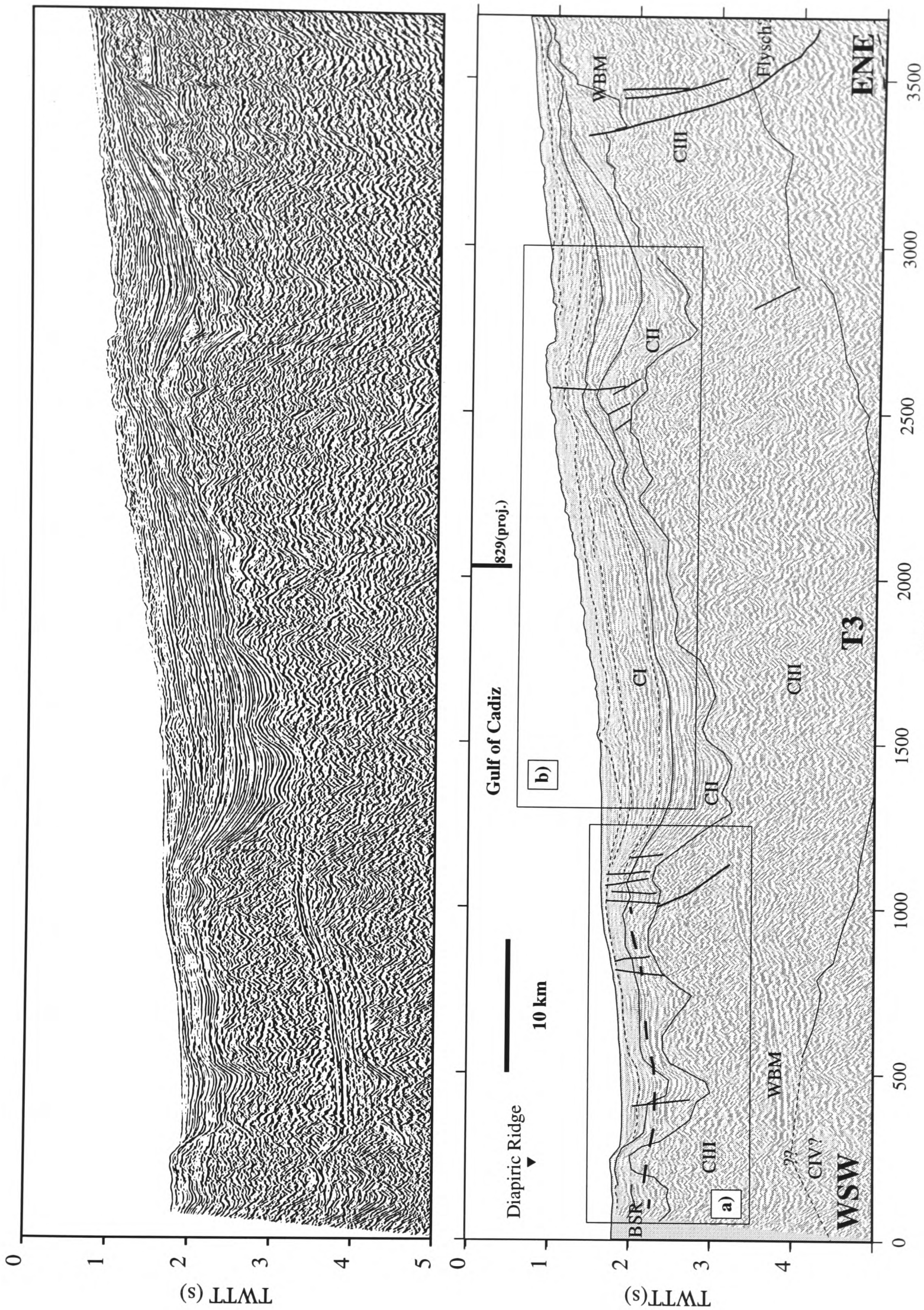


Figure 5.6: Interpreted Migrated Profile T3. Seismic stratigraphic units labelled according to the scheme outlined in Table 4.1. WBM=Primary Water Bottom Multiple; BSR=Bottom Simulating Reflector. Box a) indicates the enlarged portion of the profile shown in Figure 5.8, and box b) is shown enlarged in Figure 5.12.

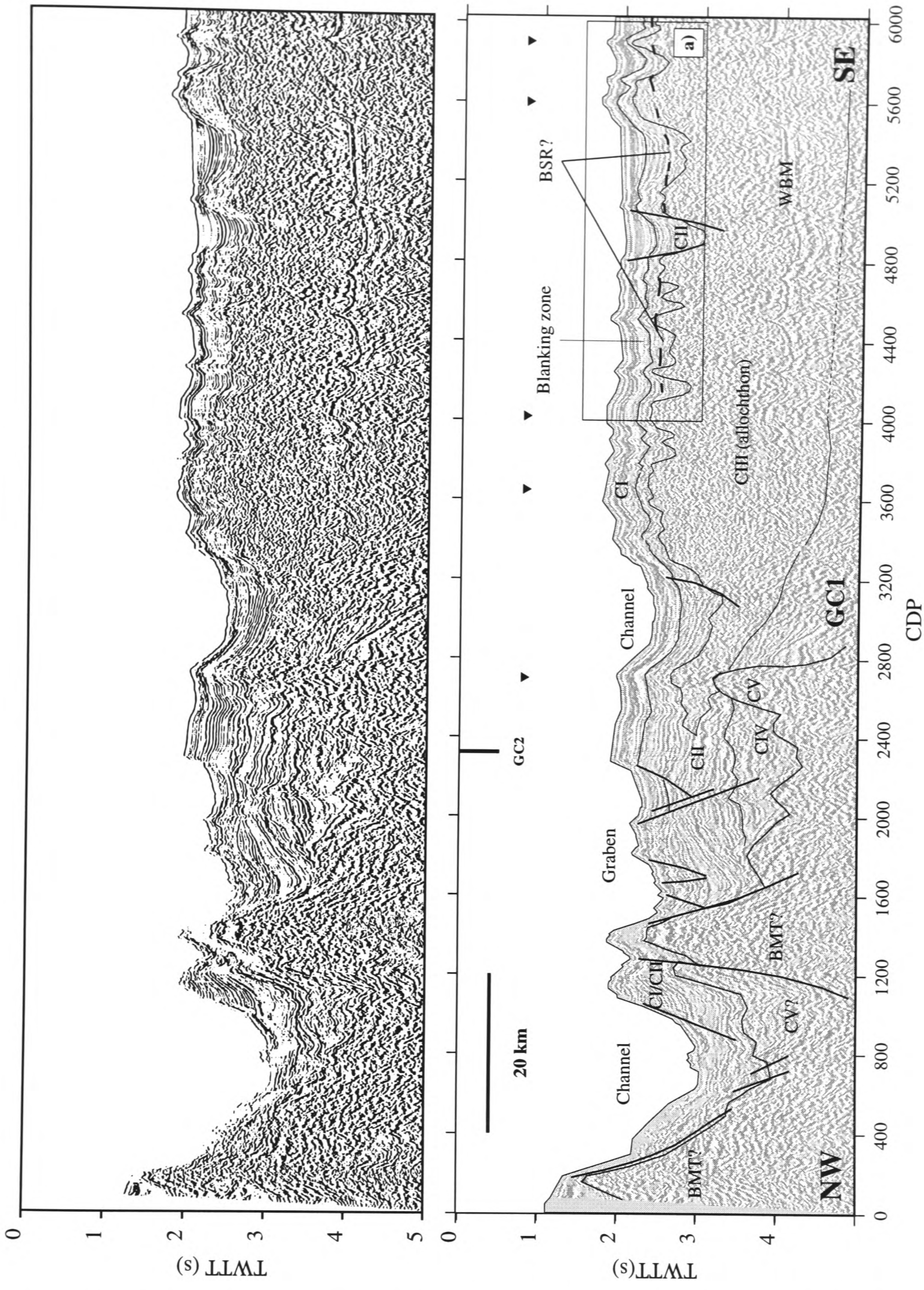


Figure 5.7: Interpretion of migrated seismic reflection profile IAM–GC1. WBM=Primary Water Bottom Multiple; BSR=Bottom Simulating Reflector. Box a) indicates the enlarged portion of the profile shown in Figure 5.8. Inverted and filled triangles indicate the positions of the larger ridges, formed through folding and diapirism of sediments in C-III, that are plotted on Figure 5.16.

convolution of the impulsive source signal with the negative reflectivity coefficient associated with the hydrate-gas boundary. The BSR reflection, as observed in Figure 5.9C, is a single, symmetrical pulse which is indicative of a simple, sharp interface. The negative BSR is associated with a strong positive reflection immediately below it.

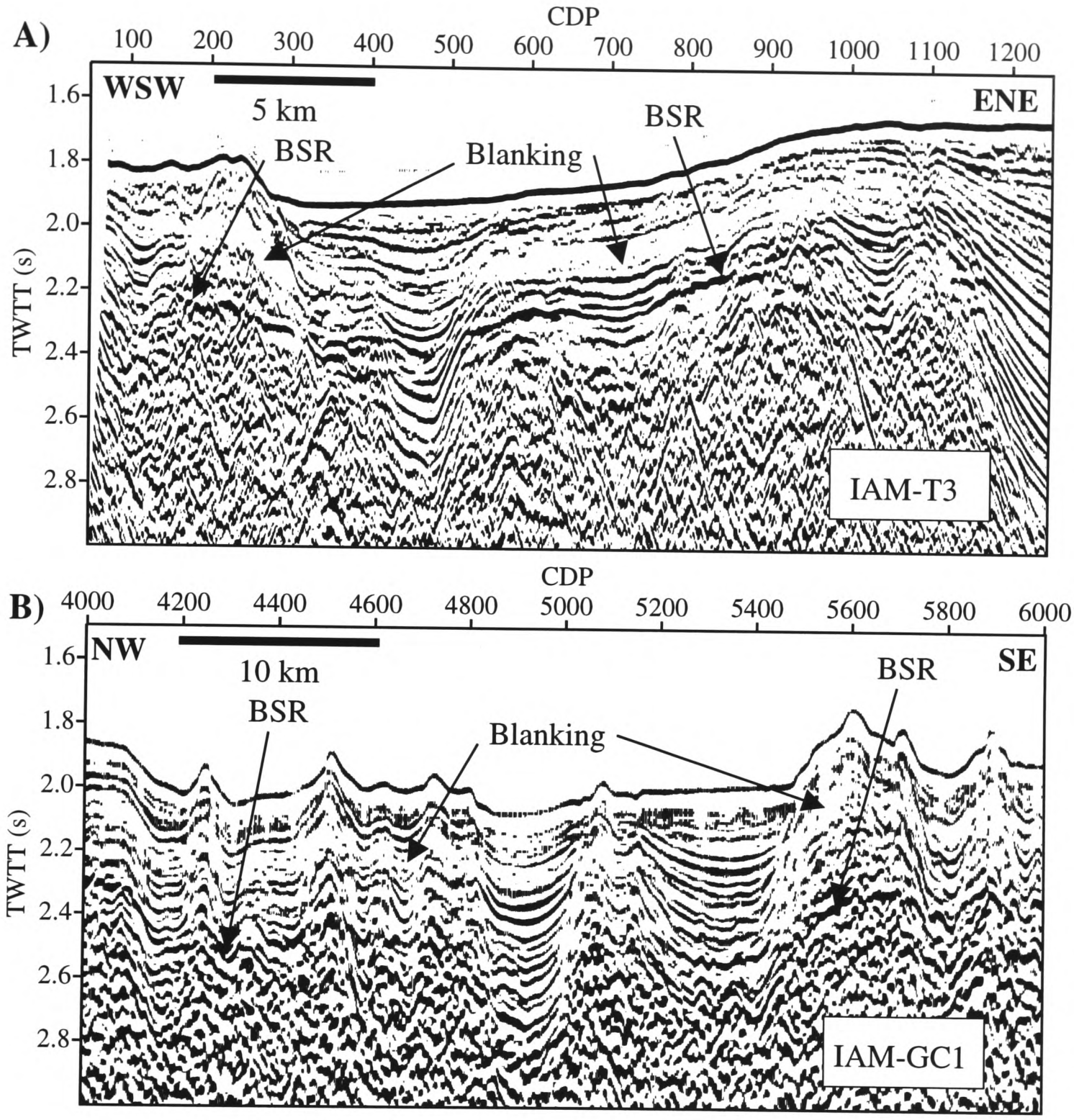


Figure 5.8: a) is the enlarged box from the WSW end of Profile T3 (Figure 5.6) illustrating a subbottom reflector labelled BSR (Bottom-Simulating Reflector) which appears to cut across different sedimentary units. b) is the enlarged box from the SE end of Profile GC1 (Figure 5.7, also illustrating the BSR and associated blanking effect.)

The region of the anomalous reflection is observed to coincide with a region where the top of allochthonous unit C-III displays relief of up to 1 s TWTT (1 km if a velocity of 2 kms^{-1} for the overlying sediment is assumed), associated with diapirism within the unit.

The BSR appears to be brightest where it co-incides with the adjacent diapiric highs of seismic unit C-III seen at the SE end of GC1 (Figure 5.7) and the WSW end of T3 (Figure 5.6).

The BSR is observed to be associated with an overlying "blanking zone" of much reduced reflection amplitudes result in a more transparent appearance when compared to sediments of equivalent age elswhere on the same section (Figure 5.7, Figure 5.6). Figure 5.8 shows that the blanking occurs locally over the same portions of the profile as the BSR, so an intimate relation between the two is inferred.

5.4.3 Analysis of the interpreted BSR

Depth of BSR occurrence

The BSR observed on profiles GC1 and T3 (Figure 5.8), occurs in water depths of 1275–1575 m (1.7–2.1 s TWTT). It occurs at ~0.4 s below the seabed reflection on T3 (Figure 5.6) and ~0.5s on GC1 (Figure 5.7). Assuming a shallow sediment velocity of 1800 ms^{-1}, from interval velocities obtained during commercial processing of the IAM data [Banda *et al.*, 1995], 0.4s on T3 is ~360 m and 0.5 s on GC1 is ~450 m depth, and these values can be taken as approximate depths for the reflector generating the BSR.

Indications of Possible Hydrate and Gas Distributions

Interval velocities between the seafloor and the BSR vary from 1730–1950 ms^{-1}, which is not measurably higher than at similar subbottom depths where there is no observable BSR. This may be interpreted as indicating that hydrate concentrations are low above the BSR, or that hydrate is concentrated in a thin layer above the BSR. Blanking zones are thought to be caused by hydrate cementation of sediment producing a more uniform velocity structure [e.g., Haq, 1998], or more rarely by very uniform lithology [e.g., Holbrook *et al.*, 1996]. The uniform lithology argument is unlikely to be the case here as the zones of amplitude reduction are localised over the same regions as the BSR (Figure 5.8). A more likely explanation is that the blanking zones associated with the GOC BSR, and the lack of any obvious increase in compressional velocity, indicate that hydrates are dispersed in the shallow sediment in low concentration.

Interval velocities also indicate local velocity inversions associated with the BSR and blanking zones. Beneath CDP 5600 of IAM–GC1 (Figure 5.8), the interval velocity drops from 1785 ms^{-1} between seabed and BSR, to 1595 ms^{-1} at the BSR. At the shallowest seafloor depths at which blanking is observed on IAM–T3, at CDP 1050 (Figure 5.8),

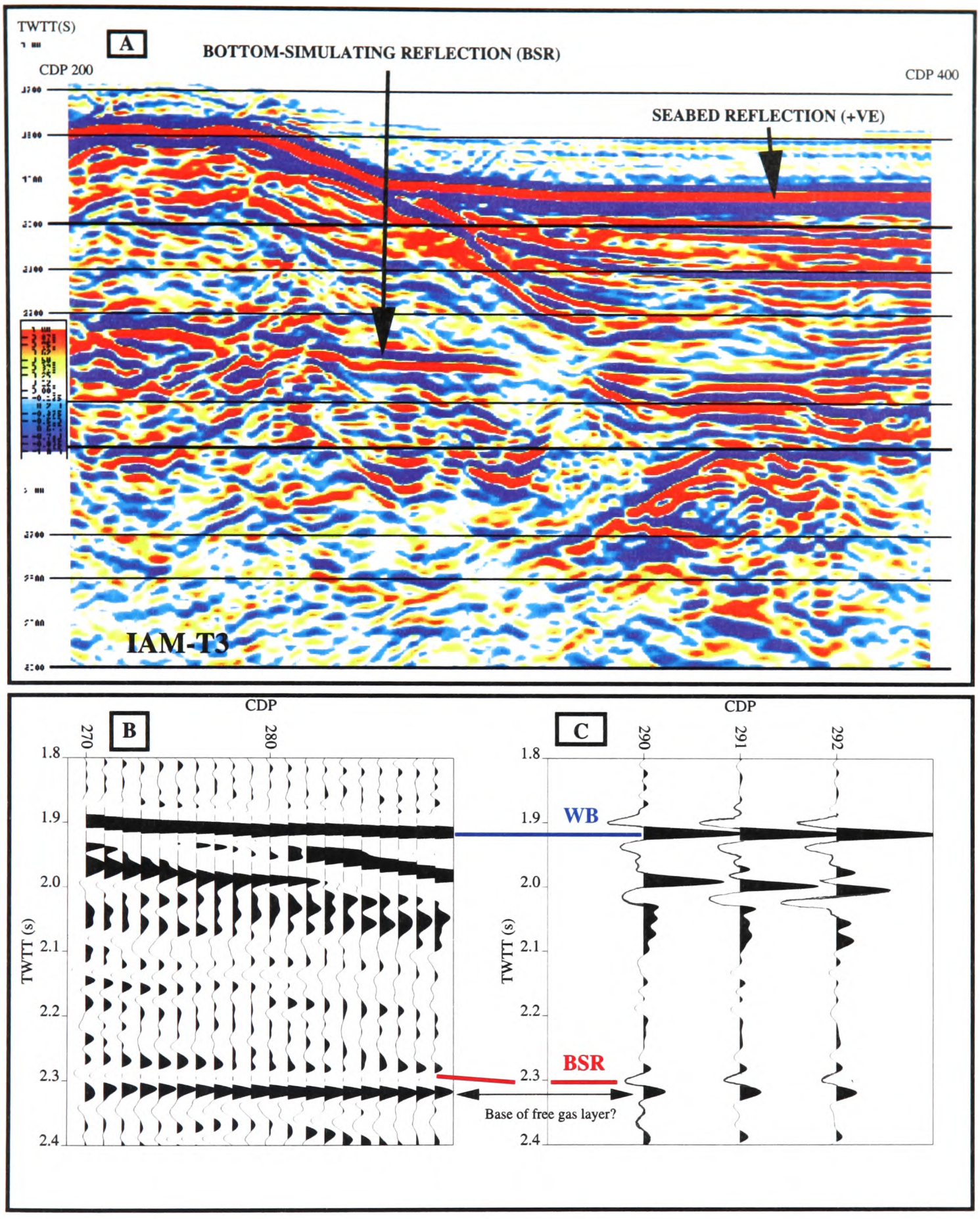


Figure 5.9: a) Seismic display scaled by normalised amplitude of Profile T3 CDPs 200-400. Normal polarity is used, with red colours showing amplitudes of reflections from positive impedance contrasts and blues showing reflections from negative impedance contrasts. b) Wiggle trace-variable area plot showing opposite polarity of main seabed reflection (WB=water-bottom) and Bottom Simulating Reflector (BSR). c) Traces showing relative amplitude of seabed and BSR reflections. No trace equalisation or AGC applied.

a velocity decrease from 1847 ms^{-1} to 1814 ms^{-1} is recorded between 1.9 and 2.05 s TWTT, increasing to 1916 ms^{-1}. This implies a zone of over a hundred metres thickness (0.15/2 s x 1814 ms^{-1} = 136 m) of reduced velocity, but the velocity drop is small. There is no clear BSR in this area, but amplitude blanking is observed from 1.8–1.9 s TWTT, and the velocity drop may be associated with small concentrations of free gas below the blanking zone.

Reduction in velocity, such as noted on CDP 1050, T3, and CDP 5600, GC1, is explicable by the presence of free gas with sedimentary pore space. Free gas is known to cause a large reduction in the compressional velocity, V_p, of clastic sediments [e.g., Domenico, 1976; Gregory, 1977]. Figure 5.10 illustrates the empirical relation between compressional velocity and percentage of porosity occupied by free gas bubbles that was derived by Gregory [1977]. This relation has been used to calculate that the velocity inversion to a V_p of 1814 ms^{-1}, at CDP 1050 on T3, is possibly due to a low free gas concentration of 0.25%. Likewise, the greater fall in velocity to a V_p of 1595 ms^{-1}, observed at the BSR (CDP 5600) on GC1, is explicable through a free gas concentration of ~0.8%.



Figure 5.10: Relation of observed seismic velocity inversions from IAM-T1 and GC1 to free gas concentration as a percentage of pore space. A velocity of 1814 ms^{-1}, at CDP 1050 on T3, can be explained with free gas concentration of 0.25%; the velocity of 1595 ms^{-1}, at CDP 5600 on GC1, is explicable through a free gas concentration of ~0.8%. The relation shown is based on the experimental work of Gregory [1977] (figure modified after Andreassen *et al.* [1995]).

The above observations of interval velocity would indicate a probability that the BSR is caused by free gas in pore space below rather than hydrate above, although the velocity data are not detailed enough to show this conclusively. As noted in Section 5.4.2, the

BSR is a single, symmetrical pulse (Figure 5.9C) which is indicative of a simple interface [Hyndman & Spence, 1992]. If the BSR reflection is generated by a layer, the layer must be at least 1/8 dominant wavelength thick i.e., the approximate limit of vertical resolution of the seismic reflection method [Widess, 1973]. The threshold resolution is largely controlled by the dominant frequency of the seismic waves [Yilmaz, 1987], but there are other factors such as signal-to-noise ratio and the shape of incident wavelet [e.g., Widess, 1973]. The dominant wavelength $\lambda = c/f$ where c is the velocity in the medium and f is the dominant seismic frequency. For the IAM data, the dominant frequency is $\sim$ 25 Hz (see Figure 3.3), and taking the average interval velocity above the BSR, 1800 ms^{-1}, the value of λ = 72 m and the maximum resolution $\lambda/8$ = 9 m. The negative excursion of the BSR spans $\sim$20 ms, which is equivalent to 16 m thickness (at a velocity of 1600 ms^{-1} e.g., CDP 5600, IAM-GC1) up to 18 m (at a velocity of 1800 ms^{-1}).

A gassy layer in normal sediment will have a negative contrast at the top and a positive one at its base. If it were thick enough to produce two distinguishable reflections one would expect to see a strong positive reflection marking the base of the layer, as well as a strong negative at the top. Hyndman & Spence [1992] have commented that the base of gas zones in commercial gas-producing regions are often marked by a strong reflection, known as a "flat spot". A gas layer model would be expected to produce such a reflection, unless it was consistently less than $\lambda/8$ thick. The strong positive excursion immediately beneath the BSR (Figure 5.9) is of similar amplitude to the BSR negative excursion, as expected for a gas-bearing layer sandwiched between water–bearing sediment of normal velocity. This is a possible base gas layer reflection, and the negative BSR excursion plus the positive excursion below span $\sim$40 ms, which is equivalent to a possible gas layer thickness of 32 m (1600 ms^{-1}) to 36 m (1800 ms^{-1}). It is inferred from the above observations that the BSR in this region of the GOC is most likely generated by a low-velocity layer of gas–bearing sediment, the thickness of which lies between the limit of vertical seismic resolution, $\sim$9 m, to $\sim$36 m.

BSR Reflection Coefficients

BSR reflection coefficients (R_{bsr}) can be estimated by comparison of the amplitude of the BSR (A_{bsr}) with the amplitude of the seafloor reflection (A_{sf}). To do this, it was first necessary to estimate the reflection co-efficient of the seafloor, R_{sf}. This was done from estimates of velocity and density at the seafloor, as used in Hyndman & Spence [1992]; Andreassen *et al.* [1995]. The equation for the calculation of the reflection co-efficient across a boundary between two media, 1 and 2 (in this case water and sediment

respectively) is given below:

$$R_{sf} = \frac{\rho_2 V_2 - \rho_1 V_1}{\rho_2 V_2 + \rho_1 V_1} = 0.25 \tag{5.1}$$

where water P-wave velocity, $V_1 = 1500$ ms^{-1} and density, $\rho_1 = 1030$ kgm^{-3}; seafloor sediment velocity, $V_2 = 1550$ ms^{-1} and density, $\rho_2 = 1650$ kgm^{-3}, which are reasonable estimates for seafloor acoustic properties [Hamilton & Bachman, 1982; Andreassen *et al.*, 1995].

A region of IAM-T3 (CDPs 100–400, Figure 5.6, Figure 5.9) with a clear BSR, beneath both a seafloor high and a relatively flat seabed, was chosen for analysis. With a known seafloor reflection coefficient, R_{sf}, the BSR reflection coefficient is calculated by

$$R_{bsr} = \frac{AR_{sf}}{1 - R_{sf}^2} \tag{5.2}$$

where A is the BSR/seafloor amplitude ratio (A_{bsr}/A_{sf}) [Warner, 1990] and (1 - R_{sf}^2) is the term accounting for transmission loss at the seafloor [Yuan *et al.*, 1999]. Other studies [e.g., Hyndman & Spence, 1992; Andreassen *et al.*, 1995] have estimated R_{bsr} assuming that the ratio of maximum amplitudes of BSR to seabed primary is the same as the ratio between the respective reflection coefficients [Warner, 1990], but this approximation does not include transmission loss at the seabed. The coefficients are also affected by attenuation and scattering to a limited extent, but a consideration of these factors is beyond the scope of this study. The amplitudes of seafloor and BSR reflections were measured in PROMAX; the amplitude values were then normalised and the ratio, A, calculated, as shown in Figure 5.11 (a). From the amplitude ratio of A (A_{bsr}/A_{sf}), it can be observed that the BSR reflection strength varies from a weak 10% to a strong 30% of the seafloor reflection. At one point, where a small peak in A_{bsr} coincides with a low in A_{sf} at CDP 280, the BSR reflection is about 50% of the seafllor value, and this region also coincides with the clearest BSR on IAM-T3 (Figure 5.9).

BSR co-efficients were calculated using the values of amplitude ratio A and Equation (5.2). The seafloor coefficient, R_{sf} used was 0.25, as calculated above; in addition R_{bsr} values for R_{sf}=0.2 and R_{sf}=0.3 were calculated, in order to cover a reasonable variation in seafloor reflectance [e.g., Yuan *et al.*, 1999]. The results of this analysis are shown in Figure 5.11 (b), with the bars indicating the range of values for R_{sf}=0.2–0.3, with values from the preferred R_{sf} of 0.25 shown as filled squares. The general range of the BSR reflection coefficient is -0.02 to -0.07, with a large coefficient of -0.12 at CDP 280. This strong reflection in the vicinity of CDP 280, may be caused by a locally high concentration of hydrate above, or free gas below, the BSR.

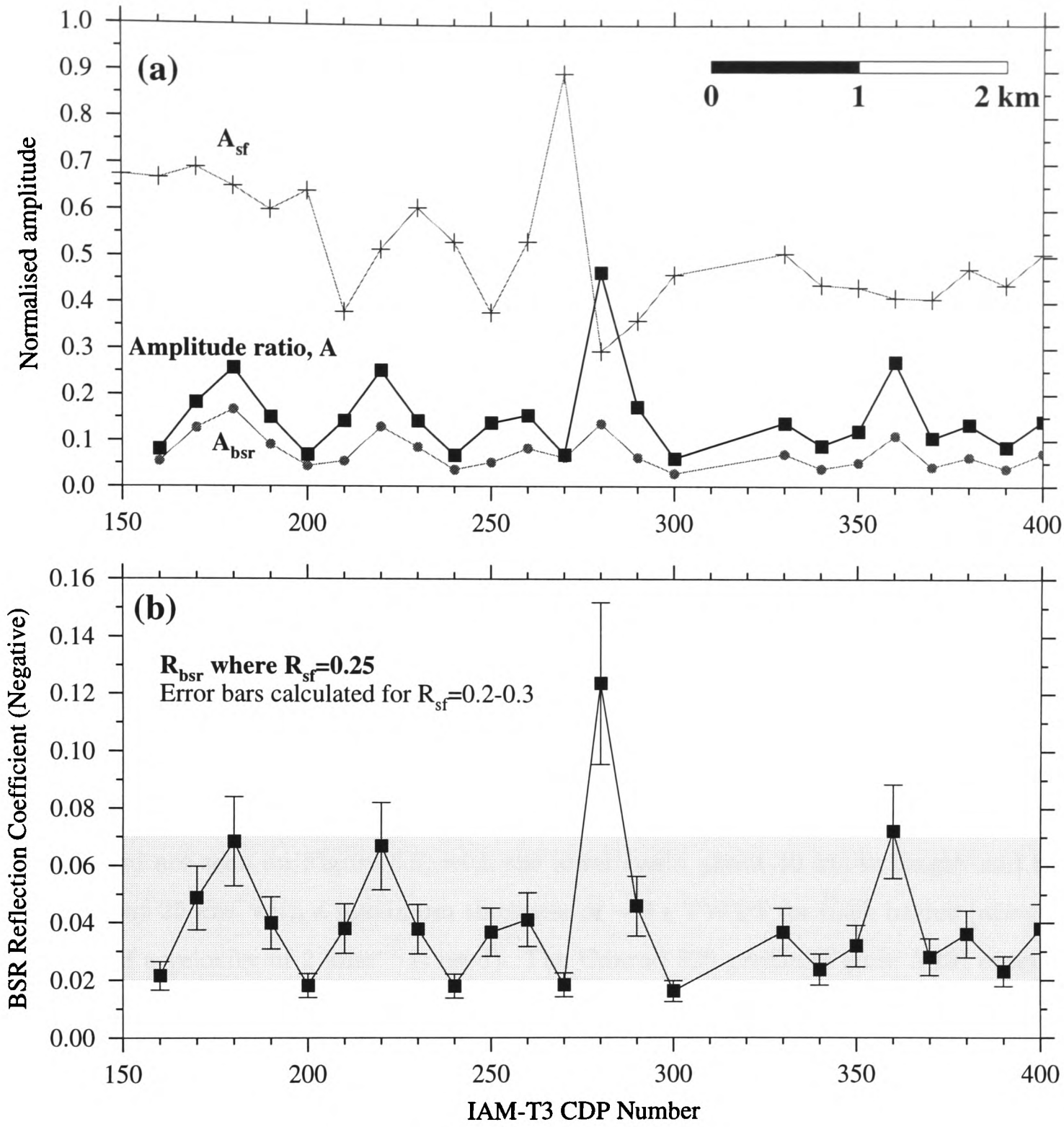


Figure 5.11: Analysis of the reflection character of a 6 km segment of BSR from IAM-T3 (see Figure 5.6 and Figure 5.9). (a) show the normalised amplitudes of seafloor and BSR reflections and the ratio, A, between them. (b) is an illustration of the BSR reflection coefficients,R_{bsr}, calculated using a seafloor coefficient, R_{sf}= 0.25±0.05. The grey shading shows the general range in R_{bsr} values, from -0.02 to -0.07.

The positive polarity reflection below the BSR, clearly observed on Figure 5.9, is also of interest. It was found to have approximately the same maximum amplitudes as the BSR reflection above it, and so has a similar magnitude, but positive, range of reflection coefficients. This strongly suggests that it is a base reflection of a low velocity layer causing the BSR reflection from its upper surface.

5.4.4 Intraslope Basins and Observations of Mass Wasting Upslope of the Observed BSR

The types of mass wasting feature expected at a continental margin are shown in Figure 5.3 and the mechanism by which hydrates can contribute to slope failure is described in Section 5.2.3. Mass flow features are observed in the sediments of the GOC continental slope above the BSR, and these are described using portions of MCS profiles IAM-T3 (Figure 5.12) and Conrad RC2911 829 (Figure 5.13) from the central sector of the GOC slope. These profiles run approximately at right angles to the bathymetric contours on the continental slope west of the Gibraltar Straits (Figure 5.5).

Figure 5.6 images the acoustic structure of the continental slope from about 500–1500 m water depths from its ENE to WSW end, and reveals that the slope sediments of the central GOC have been deposited into two asymmetrical sub-basins whose location is controlled by the underlying morphology of allochthonous unit C-III (Table 4.1). The observed BSR on profile T3 (Figure 5.6) extends downslope from CDP 1000 (~1300 m waterdepth) for at least 25 km to the end of the profile, and presumably further. Upslope of the BSR two sub-basins comprising C-I and C-II seismic units (sediments of Miocene–Recent age) are seen on Figure 5.6, with the lower basin about 40 km in length and the upper about 25 km, with a maximum thickness of $\sim$ 2 s TWTT for both basins (about 2 km thick if a velocity of 2 kms^{-1} is used). The Conrad 829 profile (Figure 5.13) extends from the upper GOC slope west of the Gibraltar Straits to within 3 km of IAM–T3 (Figure 5.5, Figure 5.6), and records the same basins (with a much reduced upper basin) at its western end. The slope basins have the appearance of growth fault bounded basins, which Somoza *et al.* [1999] have recently suggested were controlled by salt withdrawal in deeper sediments. However, the basal C-II reflections at CDP 1300, Figure 5.6, do not terminate at the contact between the units but show divergence, which indicate that the C-III relief was already present but still undergoing movements.

Seismic unit C-II (Miocene) displays variable character on Figure 5.6 and in more detail in Figure 5.12. The deepest sediments of the upper slope basin (CDP 2700, 2.5 s TWTT), have been interpreted as C-II because they lie above a high amplitude surface and display a clear difference in character from C-III below, with high amplitude reflections at intervals, with intervening low-amplitude to transparent sediments in between. This part of the Miocene sediment is thrusted in similar fashion to the sediments of C-III below it (see Figure 4.14) and has the shape of a thrust "horse". This is interpreted as being due to deposition coeval with the emplacement of C-III in the mid–Miocene. This layer is overlain by an unconformity, then well-bedded divergent fill thinning onto highs

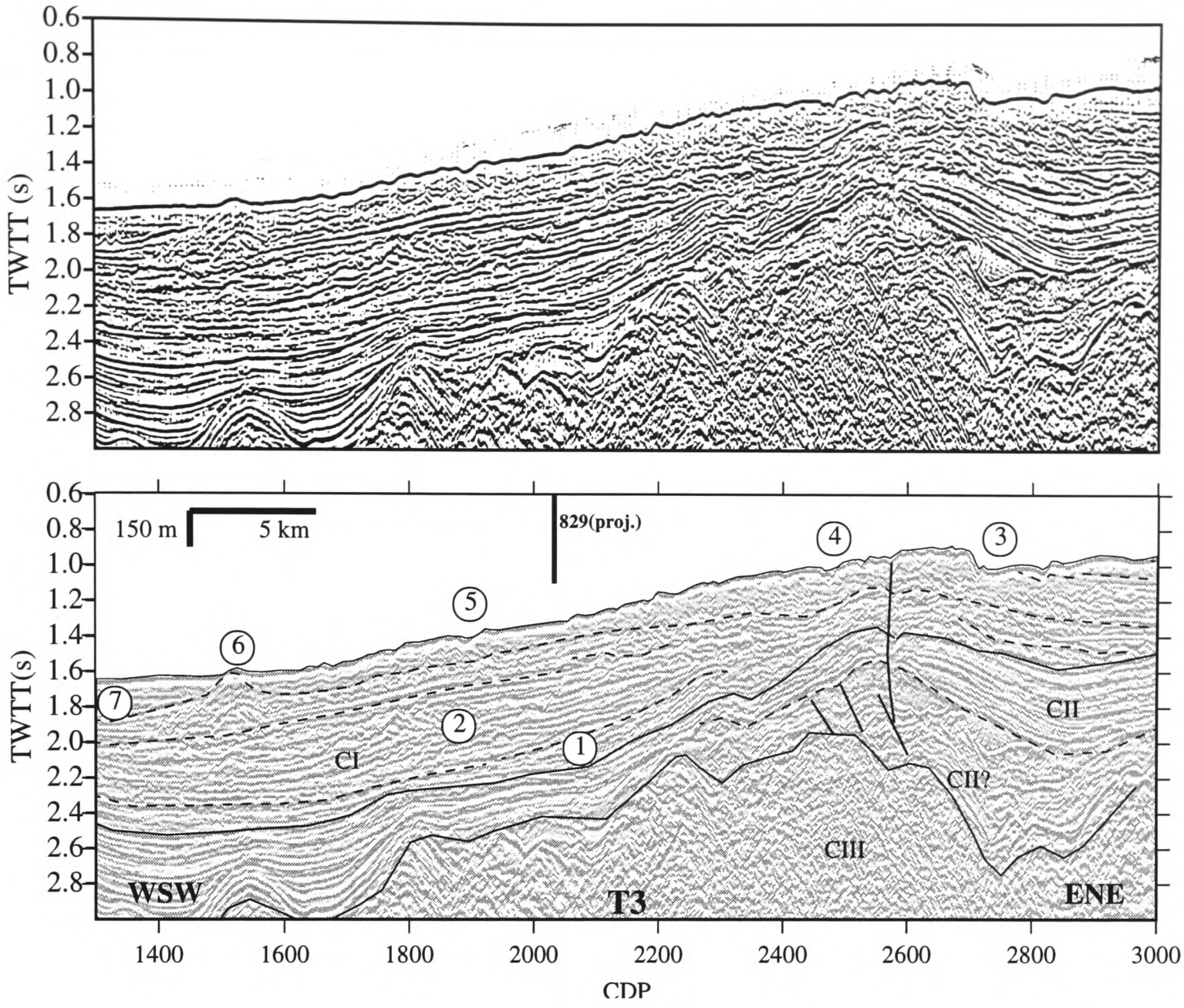


Figure 5.12: Mid- to upper slope features of the central GOC as seen on migrated Profile IAM-T3 (enlargement of box b) on Figure 5.6. Seismic units follow the scheme of Table 4.1. C-I comprise Pliocene–Recent sediment; C-II is Miocene; allochthonous sediments making up C-III are thought to be of various ages, but emplaced in the mid–Miocene (Tortonian). Numbers 2–4 and 8–9 on the profile refer to points discussed in the text (Section 5.4.4). Points 2–4 also relate to Figure 5.13.

either side, of later Miocene sediments deposited after C-III tectonic activity had ceased. This well-bedded Miocene fill is also seen above C-III in the lower subbasin between CDPs 1000–2000 of Figure 5.6.

Separating Miocene C-II sediments from overlying unit C-I is a high amplitude reflection above which C-I sediments lie unconformably as in the upper slope basin, where C-I appear to downlap at the bottom, or disconformably, as at the south end of T3 from CDPS 0–1000 (Figure 5.6). The Pliocene to Recent sediments of seismic unit C-I (Table 4.1) beneath the GOC upper slope on Figure 5.6 is observed to be well–layered downslope of CDP 1000, but in the basins upslope displays a number of features related to mass-flow. The main observations regarding these features are made with respect to

the regions of the seismic profiles numbered on Figure 5.12 and Figure 5.13.

The basal C-I sediments of the lower slope basin appear to be made up of two wedges of material showing progradational fill from ENE to WSW (Number 1, Figure 5.12) and laminar fill from WSW to ENE (e.g., CDP 1400, 2.4 s TWTT, Figure 5.12). These two wedges may be interpreted as fans sourced from two highs present in the early Pliocene, above CDP 1000 and CDP 2500 on Figure 5.6. Sediments of this basal sequence also appear to downlap the Messinian surface separating Miocene C-II from overlying C-I in the upper slope basin at CDP 2900, 1.5 s TWTT on Figure 5.6, again indicating deposition from the high at CDP 2500.

A lens–shaped body is observed above the basal sediment wedges in the lower slope basin (Number 2, Figure 5.12). Its internal reflection configuration is complex, and appears to be a combination of hummocky, laminar and chaotic reflections, which have locally erosive contacts (Number 2, Figure 5.13). Its top is defined by layers of even, parallel and high amplitude events. This body is interpreted to be made up of a series of mass flow deposits which have been sourced upslope. The chaotic deposits may be interpreted to be due to debris flows and slumping, whereas the more laminar reflections may be due to slides or turbiditic deposition. Sediments in the upslope basin (Number 3, Figure 5.12) also have a complex fill with chaotic and hummocky reflections truncated by parallel reflection horizons, implying a series of slope failure events with intervals of erosion and sedimentation.

Above the lens-like body of failure events are two more identifiable sedimentary bodies, which both pinch out downslope (Figure 5.12). The shallower of these bodies is about 0.2 s TWTT thick, and forms the present-day seafloor from CDP 1500–2700 on IAM-T3, with a slope of 1:50 or 1.2°, which is the steepest portion of T3. This upper body is approximately 20 km long and is bounded by a scarp at CDP 2700 (Number 3, Figure 5.12) which is about 0.2 s TWTT high, or 150 m (water velocity 1500 ms^{-1}). The body shows a distinct change in reflection character from the chaotic reflectivity and possible extensional faulting reaching the seabed at the upslope end of the block (Number 4, Figure 5.12 and Figure 5.13) to layered reflectivity and compressional folds at its downslope end (Number 5, Figure 5.12), separated by a 2km zone of no deformation seen between CDPs 1950–2050 Figure 5.12. This body is interpreted to be made up of a higher, *in situ* part continuous with the sediment infill of the upper slope basin (Number 4 to Number 3, Figure 5.12 and Figure 5.13), and a lower part of layered turbidites and debris flows formed by failure of the sediments upslope. These latter mass flows

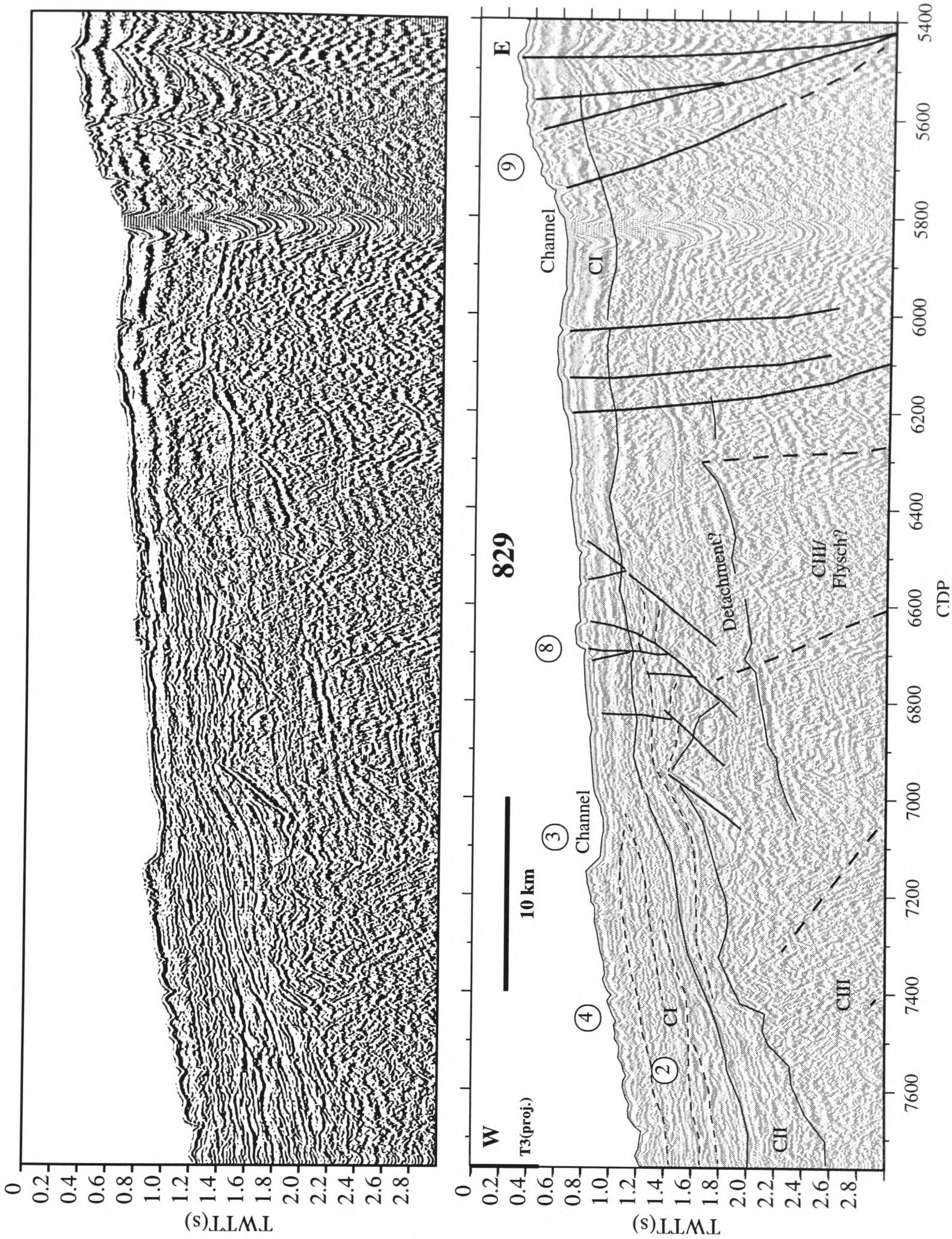


Figure 5.13: Upper slope features of the central GOC illustrated with migrated MCS profile Conrad 829. Seismic units as for Figure 5.12. Numbers 2–4 and 8–9 on the profile refer to points discussed in the text (Section 5.4.4). Points 2–4 also relate to Figure 5.12.

are stopped by the topographic obstacle of a mound (Number 6, Figure 5.12), which itself pinches out beneath parallel, even reflections of onlap fill (Number 7, Figure 5.12) belonging to a small basin (CDP 1300, 2 s TWTT, Figure 5.6). The mound at (Number 6, Figure 5.12) is unusual and must be competent in order to form a barrier to sediment either side of it. It sits above a local high in unit C-III, and the sediments beneath it are disturbed, which may indicate small-scale faulting, such as is clearly seen above the high in C-III at IAM-T3 CDP 2600 on Figure 5.12 and at CDP 1000 on Figure 5.6. It is speculated that the mound is a bioherm formed by marine organisms drawn to an area of fluid expulsion from unit C-III, which may include methane.

It has been observed that the shape and internal reflectivity of sediments infilling the two intraslope basins indicate much of the deposition took place by mass flow processes from local seafloor highs at the time of deposition, and also from further upslope (Number 2, Figure 5.13). A potential upslope source region for the infill of the slope basins is imaged on Figure 5.13, where units C-I and C-II thicken downslope into the lower slope basin seen on Figure 5.6, NE of the observed BSR. Seaward–dipping normal faults are seen in the sediments between 1.2–2.0 s TWTT, with "flower–structure" type faults above them, which may indicate some component of strike slip deformation (Number 8, Figure 5.13). The normal faults may be associated with very bright, high amplitude, low frequency reflection seen on Figure 5.13 from CDP 6300–7000 and 1.8–2.4 s TWTT, which may act as a possible detachment layer for these sediments. Such faulting in slope sediments can facilitate slope failure.

Present–day erosion can be inferred from the two erosional channels that can be seen adjacent to the scarp at Number 3, Figure 5.13 and at the base of the thrust faulted seabed high seen at the upper slope end of the Conrad 829 profile (Number 9, Figure 5.13). The erosional effects of the Mediterranean Outflow current are of importance in this region of the GOC upper slope [e.g., Nelson *et al.*, 1993, 1999].

5.5 Discussion

Characteristics of the Gulf of Cadiz BSR

The BSR observed in the GOC is a single, symmetrical pulse (Figure 5.9) which is indicative of a simple interface of negative impedance contrast as the BSR has negative polarity relative to the seabed (Section 5.4.2). This distinctive reflection appears to cut across bedding plane reflections of seismic units, indicating it is a younger interface. It is also associated with a zone of amplitude blanking in sediments that overly it. Such characteristics are typical of BSRs worldwide [e.g., Kvenvolden & Barnard, 1983; Hyndman & Spence, 1992; Kvenvolden, 1998; Veerayya *et al.*, 1998]. The Blake Ridge, off the SE coast of the USA, is well studied, and seismic reflection and vertical seismic profiling [e.g., Shipley *et al.*, 1979; Pecher *et al.*, 1997] together with direct sampling [ODP Leg 164, Holbrook *et al.* [1996]] confirms the presence of hydrates and free gas. The Blake Ridge data indicates that the BSR is caused largely by a velocity drop in sediments containing free gas, rather than a velocity rise in sediments cemented by solid hydrates. Figure 5.14 is an example of seismic data displaying a sharp BSR and blanking from the Outer Blake Ridge (off SE USA) [Shipley *et al.*, 1979], to which the features seen in Figure 5.8 are comparable, albeit weaker.



Figure 5.14: A seismic line from the Blake Ridge, offshore SE USA, showing a classic example of a BSR and acoustic blanking, which drilling has confirmed is associated with subbottom gas-hydrates. This figure has been modified after Shipley *et al.* [1979].

The BSR is observed to be found in slope sediments at water depths of 1275–1575 m (1.7–2.1 s TWTT) and from 0.4–0.5 s TWTT beneath the seabed on IAM-T3 and GC1. This range of values for the GOC BSR was plotted on Figure 5.15 with data on BSR

TWTT against seafloor depth for BSRs observed worldwide on seismic data, including the Blake Outer Ridge and the western Indian margin [Veerayya *et al.*, 1998]. The range of the observed GOC BSR is in the central region of BSR results, and satisfies the overall trend of BSR TWTT increasing with water depth. This trend is to be expected if TWTT is proportional to depth, as the phase diagram showing the gas hydrate P-T stability field predicts that the GHSZ becomes thicker with increasing water depth (Figure 5.2b).

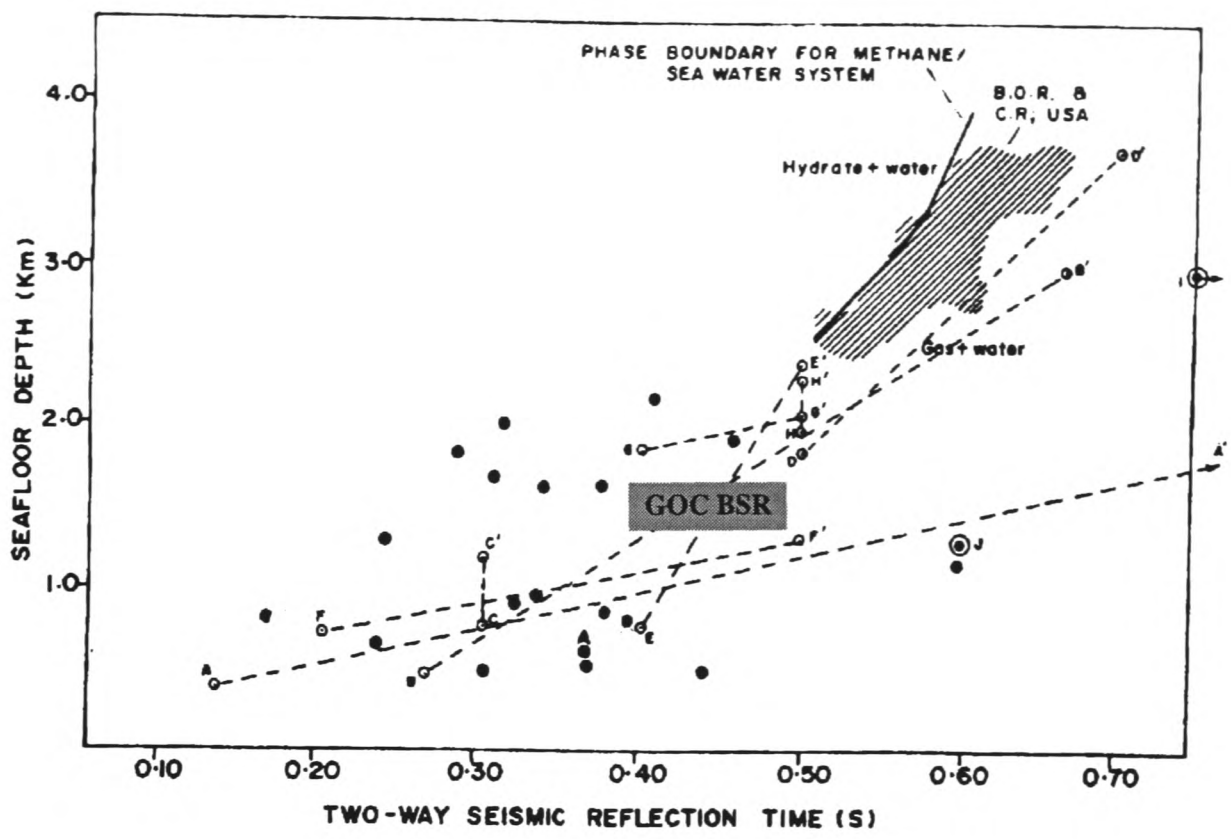


Figure 5.15: Observed BSR burial TWTT versus water depth for worldwide BSRs. Gulf of Cadiz BSR shown as a grey box. Filled dots represent values from seismic profiles off western India [Veerayya *et al.*, 1998]. Values from the Blake Outer Ridge (B.O.R.) and continental rise (C.R.) off SE USA are shown as a striped region. BSRs designated A–A' etc from Kvenvolden & Barnard [1983]; Kvenvolden [1993]. Figure modified after Veerayya *et al.* [1998].

The BSR is observed from the seismic data to be limited in extent over the lower continental slope, being identifiable over 20 km of IAM-T3 and 40km of IAM-GC1 (Figure 5.8, Figure 4.15). Such limited occurence on the continental slope, rather than in all sediment which falls into the predicted GHSZ (Figure 5.2), is a common feature of gas hydrate distribution [Ginsburg, 1998]. Previous seismic data from the lower continental slope of the GOC (Torelli *et al.* [1997]), displayed no discernable BSR which suggests that the deposits of hydrate are localised in the central GOC.

The study of BSR amplitude and reflection over a region of IAM-T3 (CDPs 100–400, Figure 5.6) revealed that the amplitude of the BSR reflection varied from 10–30% of that of the seafloor (Figure 5.11a). Using an estimated seafloor reflection coefficient of 0.25±0.05, the range of BSR coefficients were in the range of -0.02 to -0.07, with a maximum of -0.12±0.02 (Figure 5.11b), with values beneath the seafloor high from CDP 150–300 generally higher than those from CDP 300–400 (Figure 5.9). These values are consistent with those calculated from a BSR off Vancouver Island [Hyndman & Spence, 1992; Fink & Spence, 1999], with values from -0.05 to -0.15 reported, the higher values being observed under topographic highs. However, these values are low compared to offshore Peru, where Miller *et al.* [1991] estimate an average R_{bsr} of -0.135 with a maximum of -0.25, and a BSR offshore Colombia has been reported to have R_{bsr} between -0.2 to -0.3, exceeding the seafloor coefficient [Minshull *et al.*, 1994].

A strong positive excursion immediately beneath the BSR (Figure 5.9) is of similar amplitude to the BSR negative excursion, and is a possible base–gas layer reflection, as a free gas–bearing layer would be expected to produce a strong negative impedance contrast with the sediments above and a strong positive contrast with sediments below it, assuming the layer is thicker than the limit of vertical resolution. Interval velocities discussed in Section 5.4.3 indicate that velocities between the seafloor and the BSR are not measurably higher than at similar subbottom depths away from the BSR (1730–1950 ms^{-1}). There is no clear seismic reflection on the profiles examined that could be the top of any hydrate–bearing sediments; the amplitude blanking observed may indicate the presence of some hydrate but in low concentrations. ODP drilling and recent waveform inversion studies [e.g., Katzman *et al.*, 1994; Holbrook *et al.*, 1996; Korenaga *et al.*, 1997], and general surveys of BSRs [Kremlev *et al.*, 1997; Andreassen *et al.*, 1997] indicate that BSRs are generally attributable to free gas–bearing sediments below the GHSZ. Interval velocities also indicate local velocity inversions associated with the BSR, with velocities as low as 1600 ms^{-1}, which corresponds to free gas in 0.8% or less of pore space (Figure 5.10). The negative excursion of the BSR and the positive excursion below it span ~40 ms (Figure 5.9), which is equivalent to a possible gas layer thickness of 32 m (velocity = 1600 ms^{-1}) to 36 m (velocity = 1800 ms^{-1}), so a gas layer which produces such a signature is predicted to be between 9–36 m thick, where 9 m is the limit of vertical resolution. To increase the accuracy of this estimate, other procedures such as AVO (amplitude variation with offset) modelling, detailed velocity analysis and waveform inversion on reprocessed pre–stack data is required.

Source of Hydrate Methane and Possible Transport Routes

The occurrence of gas hydrate is governed by the combination of a prolific source of gas [Kvenvolden, 1998], and migration pathways to regions where such gases can accumulate in appropriate thermobaric conditions (GHSZ) for hydrate formation [Ginsburg, 1998]. The worldwide distribution of observed and inferred hydrate deposits (Figure 5.1) reflects that hydrates are common at continental margins, where the development of thick sedimentary sections rich in organic matter favour the formation of hydrocarbon gases [Booth *et al.*, 1998].

The marginal sediments of the Gulf of Cadiz can reach thicknesses of several kilometres (Section 4.6), and organic matter is delivered into the Gulf by several rivers (e.g., Guadiana, Tinto-Odiel and Guadalquivir rivers in Iberia), as well as being derived from water column productivity. Buried organic matter undergoes diagenesis, breaking down to methane and other hydrocarbons through microbial and thermogenic action [Kvenvolden, 1998]. Thermogenic gas generation is linked to burial as pressure and temperature both rise, whereas micobial action may occur at all levels of the stratigraphic column. The Gulf of Cadiz margin has all the ingredients for large–scale thermogenic gas generation (thick sediments, organic input), and an assessment of the importance of microbial action is outside the purview of this study.

The map of Figure 5.16 summarizes the results of the seismic interpretation of IAM and Conrad data in this study, which have been combined with previous structural data to provide a novel map of potential gas migration in the GOC margin. NE–SW trending fault and diapir systems have a strong bathymetric expression in the northern GOC where they formed a series of curvilinear ridges and valleys which have been recognised for decades [e.g., Roberts, 1970]. With improved seismic images the relationship between the slope ridges and underlying folding and diapirism of units C-V (Triassic) and C-III (allochthon) has become clearer, and recent publications combined with this study have allowed the construction of a map of diapiric ridges down to the lower continental slope. The published locations of diapiric ridges and associated faults are shown in Figure 5.16. Their NE–SW trend, has been correctly interpreted as due to flow of mobile shales and evaporites to a tectonic NW–SE compression that has taken place across this region since the late Miocene [Dewey *et al.*, 1989], and which is continuing today at a rate of 4–5 mmyr^{-1} according to the recent NUVEL-1A model of DeMets *et al.* [1990, 1994]. A distinct change in structural style is seen east of 6.45°W where radial thrust faulting structure related to the Betic–Rifian Arc is prevalent over the NW–SE African–Eurasian convergence.

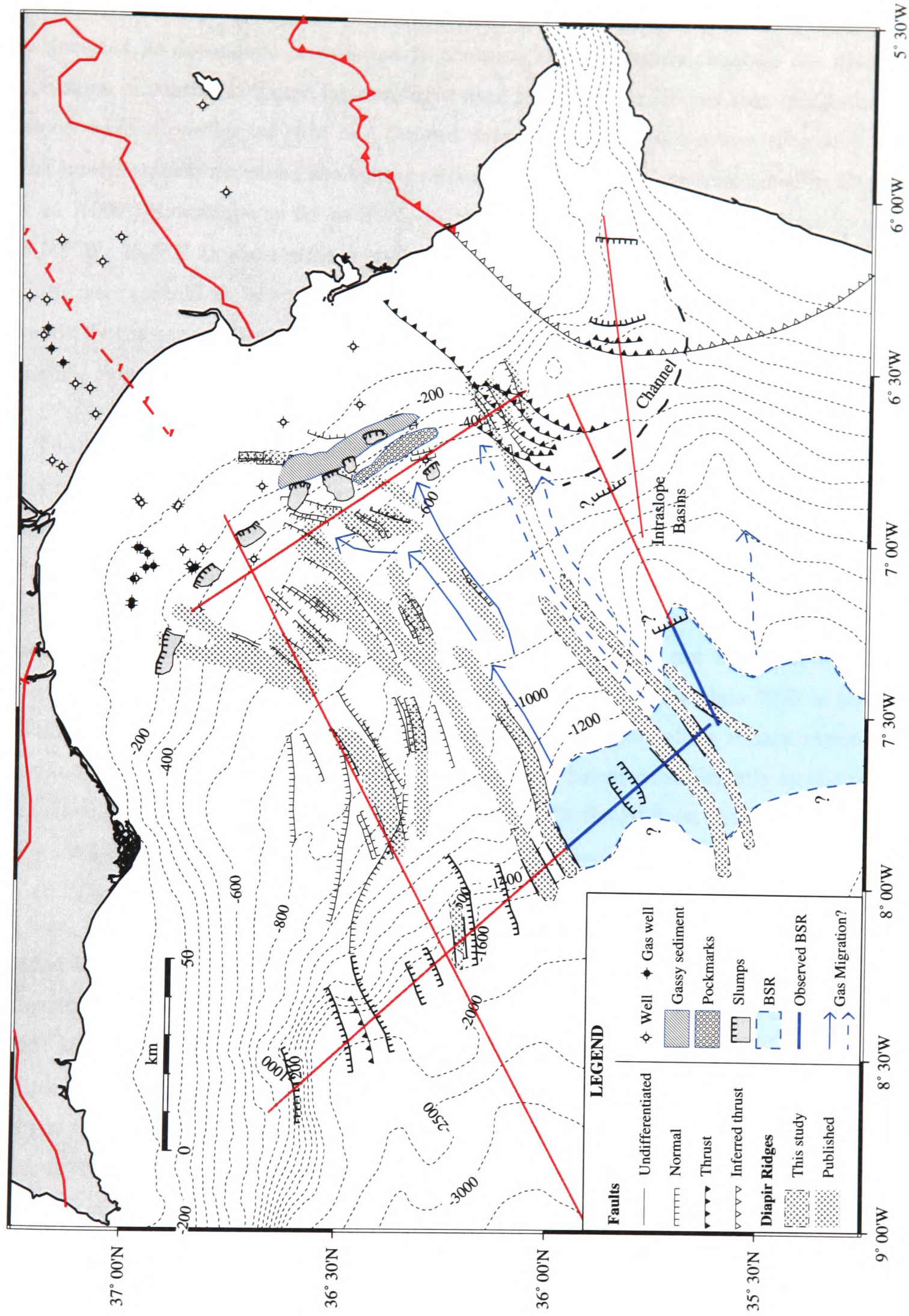


Figure 5.16: Summary map of gas–related observations in the Gulf of Cadiz, taken from this study and prior publications. Offshore seismic profiles used to constrain interpretation are shown in red. Published fault data from Baraza *et al.* [1999]; Dañobeitia *et al.* [1999]; Maldonado *et al.* [1999] and prior data on diapirism–related ridges from Roberts [1970]; Nelson *et al.* [1999]; Baraza *et al.* [1999].

The NE-SW trends in structure are also reflected in the bathymetry, where ridges can be detected as downslope protrusions in contours and conversely channels are upslope intrusions in contours. These features were used to extend structures seen on the interpreted seismic profiles, of IAM and Conrad datasets, up- and downslope (Figure 5.16). The interpretation extended the extent of two long diapiric ridges (published in Baraza *et al.* [1999]) downslope as far as 8°W, 36°N. Other diapirs seen on seismic are located at 7.5°W, 35.5°N at the southern ends of profiles GC1 and T3 (Figure 5.7,Figure 5.6). These were tentatively interpreted to extend up- and down slope on the basis of NE-SW trends, bathmetry indications of a ridge, and possible connection with a series of small diapiric ridges reported on the upper slope at 6.5°W–7°W, 36°N [Baraza *et al.*, 1999].

The extent of the BSR observed on Figure 5.7 and Figure 5.6 is mapped on Figure 5.16, and from the depth range observed (~1275 m to ~1575 m) a contiguous area satisfying depth constraints and the extent of seismically observed BSR was mapped out (in light blue on Figure 5.16, Figure 5.17), covering an area of ~3500 km^2. The upper depth limit is constrained by profile IAM-T3 but the lower limit shown is unconstrained, and may extend further downslope than shown. The BSR should not be taken to mark the extent of free gas and hydrate, as both can exist even where a clear BSR is absent [Holbrook *et al.*, 1996]. Rather, the BSR represents the region where concentrations of gas and hydrate are sufficient to produce an impedance constrast sufficiently strong to be seismically detectable. As blanking was coincident with the BSR on the seismic profiles (Figure 5.8), this phenomenom is assumed to be of the same areal extent.

Gas, being a less dense fluid than water, will tend to migrate upwards where not impeded by a sealing medium. The GOC BSR appears to be stronger under topographic highs caused by folding and diapirism in unit C-III (Figure 5.9, Figure 5.11). Greater BSR amplitudes beneath topographic highs have also been observed off Vancouver Island [Fink & Spence, 1999]. This strongly indicates that the BSR may be linked to a supply of gas from unit C-III and below, with free gas naturally collecting beneath the highs. Acoustically turbid zones interpreted as containing biogenic gas have been observed over an area of 173 km^2 between 130 m and 220 m contours in upper slope GOC sediments [Baraza & Ercilla, 1996]. This zone of gassy sediment, thought to be due to low permeability muds trapping gas, is plotted on Figure 5.16 with a diagonal fill. A region of pockmarks, v-shaped depressions similar to gas–escape structures seen in the North Sea and Scotian margins [e.g., Hovland *et al.*, 1984; Hovland & Judd, 1988], were also reported on the Gulf of Cadiz slope [Baraza & Ercilla, 1996; Baraza *et al.*, 1999]. These pockmark features are up to 600m in diameter and between 13–19 m deep, cover some

72 km^2 of the slope between 250 and 380 m water depth, and occur on the slope below the gassy sediments, as shown in Figure 5.16 [Baraza *et al.*, 1999].

This study suggests that the areas of pockmarks and gassy sediment are supplied by gas which is generated downslope, through thermogenic processes of burial and heating in the thick sediments beneath the continental slope, as well as by microbial generation of biogenic gas. The continental slope below about 1300 m water depth falls within the GHSZ and gas is converted to hydrate, which then impedes further local upward migration of gas, creating local concentrations of gas which cause a velocity drop and a negative impedance contrast which may be imaged seismically as a BSR. Figure 5.16 suggests that free gas from below the GHSZ (and BSR) may migrate tens of kilometres upslope through fault and diapir systems (Figure 5.16) associated with seismic units C-V (Triassic evaporites) and C-III (allochthonous evaporites and mobile shales). The GOC diapric ridge system therefore acts as a series of gas conduits to both the hydrate zone and regions upslope of it. This study also suggests that the "Atlantida" offshore gas reservoirs drilled in the northeast Gulf [Delaplanche *et al.*, 1982; Melendez-Hevia & Alvarez de Buergo, 1996] may also be charged from this source (Figure 5.16). Ginsburg [1998] stressed the importance of the study of methane migration to global estimates of the gas hydrate reservoir. The recognition of a possible gas generation and transport system in the Gulf of Cadiz is an important first step in such a study in this region. Veerayya *et al.* [1998] have speculated on a relationship between deep hydrates and shallower pockmarks and gas seepages observed on the western Indian margin, and a fault and diapir migration system. This study provides an example of such a system in the Gulf of Cadiz.

Relation of BSR, hydrates and free gas to mass flow observed in the GOC slope sediments

A connection between gas hydrates and submarine mass flow has been postulated since the 1970s [McIver, 1977, 1982]. Examples of margins where hydrates are considered to have played a major role in downslope gravity–driven transport are the Norwegian margin (Storegga slides) [Bugge *et al.*, 1988; Mienert & Bryn, 1997], the western Mediterranean [Rothwell *et al.*, 1998] and off the Beaufort Sea margin of Alaska [Kayen & Lee, 1993].

In the previous section, the possible upward migration routes for free gas from the downslope region to shallow upper slope and shelf regions have been discussed. The presence of gas in the upper slope between 100–400 m is associated with a series of rotational slumps originating at this level (Figure 5.16). Wells that have drilled biogenic

gas on the NE GOC shelf since the 1970s [Delaplanche *et al.*, 1982; Melendez-Hevia & Alvarez de Buergo, 1996] are also upslope of observed slumps (Figure 5.16). This slumping is likely caused by a drop in sediment strength due to interstitial gas.

Haq [1998] considers that hydrates may play an important role in reshaping the structure of continental margins through the effects of destabilization and dissociation of gas hydrates, which might be connected to slope failure as well as normal and growth faulting. Changes in temperature and pressure conditions can cause hydrate dissociation if hydrates previously in the GHSZ are moved out of it Figure 5.2. Burial below the GHSZ through continued sedimentation, a lowering of sealevel or an increase in water–bottom temperature will all change the ambient thermobaric condition of the gas–hydrates such that they dissociate to gas and water [Kvenvolden, 1998], leading to sediment failure along slide planes or catastrophic failure if gas pressure builds up in the sediments before release, as described in Kayen & Lee [1993]. Hydrates and slumps can sometimes be observed together, on the US continental slope, for example [Carpenter, 1981].

Immediately downslope of the Gibraltar Straits, two intraslope basins have been observed (Figure 5.6), as described in Section 5.4.4. The lower of these basins, in particular, shows evidence of downslope mass wasting units infilling it above the unconformity between the Miocene and Pliocene seen between seismic units C-I and C-II on Figure 5.6. The change from parallel and even reflectivity of Upper Miocene C-II sediments to the presence of irregular and complex reflectivity in Pliocene to Recent sediments of unit C-I (Figure 5.6), Figure 5.13) indicates a change in depositional style across the Messinian unconformity between the two units. This evidence of mass flow in sediments of unit C-I (Pliocene to Recent), may be explained by gravitational failure on a steep slope triggered by seismic activity as the region of the GOC central slope marked by diapiric ridges (Figure 5.16) is seismogenic [e.g., Udias *et al.*, 1976]. However, the region was seismically active prior to the Pliocene, so an additional factor must also be invoked to explain the changes. The intraslope basins are observed 50 km downslope of the Gibraltar Straits and immediately upslope of the observed BSR (Figure 5.16).

Considering the location and timing of the change of depositional style in the intraslope basins just south of the diapiric ridge systems (Figure 5.16), it is possible that the opening of the Gibraltar Straits in the late Messinian which established the Mediterranean Outflow Water in early Pliocene times [Campillo *et al.*, 1992], was responsible for an increase in mass wasting processes on the slope. After the Straits opened and the Mediterranean Outflow was established, the GHSZ on the slope would have been de-

pressed by the higher bottom–water temperatures of the outflow compared to the prior Atlantic waters. This would have dissociated hydrates to free gas and water, particularly at the shallower levels of the hydrates, and contributed to slope weakening and failure.

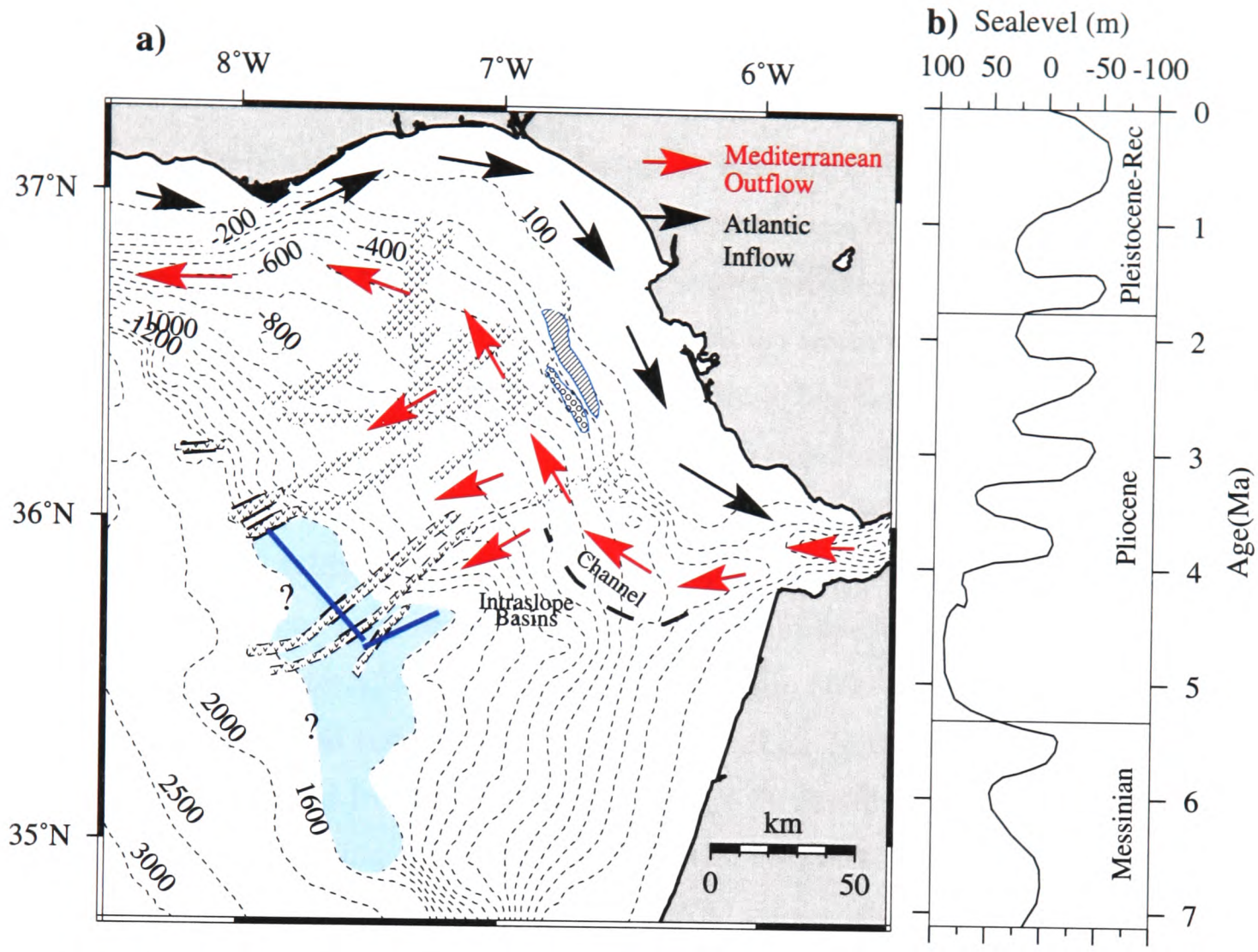


Figure 5.17: **a)** The current system of the Gibraltar Straits and Gulf of Cadiz in relation to the region of downslope transverse ridges, and gas–related features (BSR, pockmarks and gassy sediment). The Mediterranean impinges the bottom on regions of the shelf below the 300 m contour [Nelson *et al.*, 1999]. Legend as for Figure 5.16 above. **b)** Short–term sealevel curve of Haq *et al.* [1987] over the Messinian to Recent period.

Figure 5.17 illustrates the present–day current system of the Gibraltar Straits and Gulf of Cadiz, the dynamics and sedimentary effects of which have been well–studied [e.g., Kenyon & Belderson, 1973; Price *et al.*, 1993; Shapiro & Meschanov, 1996; Baringer & Price, 1999; Nelson *et al.*, 1999]. Above 300 m water depth, a strong flow of North Atlantic Surficial Water (NASW) heads southwestward along the shelf to eventually inflow into the Mediterranean basin [Nelson *et al.*, 1999]. The Mediterranean Outflow Water (MOW) flows westward over the Gibraltar sill, and on exiting the Gibraltar Straits, it sinks and shears sharply northwestward (Figure 5.17), flowing as a deep current over the Gulf of Cadiz at depths between 300–1800 m [Baraza *et al.*, 1999]. The MOW interacts with the

zone of linear ridges and valleys and leaves scour-and- fill features, as well as contourites which end in the large Faro Drift sediment body south of Portugal [Kenyon & Belderson, 1973; Stow *et al.*, 1996]. The erosive effects of the MOW can be seen in the 150 m deep channel seen on seismic data in the upper slope (Number 3, Figure 5.12, Figure 5.13).

The MOW forms a deep water outflow because it is denser than the Atlantic inflow of NASW. The MOW is known to be very saline, and a tongue of saline MOW is detectable as far into the North Atlantic as the Bermuda Rise [e.g., Rahmstorf, 1998; Baringer & Price, 1999]. The MOW is also warm, with temperatures greater than 12°C , as shown on Figure 5.18, where the uppermost temperature profile (see small map below). The uniform reds at the east end of this profile indicate the warm waters of the Mediterranean, and the warm MOW is seen as a region of elevated temperature above 1500 m depth, extending away to the west above the cooler intermediate Atlantic waters (<6–7°C). The temperature-salinity-depth plot at the bottom left of Figure 5.18 illustrates the various trends in salinity and temperature sampled from the water column. The MOW is shown by the trend from high salinity of 36–38 psu and temperatures >12.5°C, whereas Atlantic intermediate(AIW) to deep waters (1500m to 5000 m deep) fall on a trend from salinity 35–36 psu and temperatures <8°C. A trend for North Atlantic Shallow Water is discernable on a trend from 10-15°C and salinity ~36 psu, but of water depths <300–400 m. The region of mixing falls where these trends intersect (bottom right, Figure 5.18). At similar depths, say 1000 m, the MOW is 3–5°C warmer than the intermediate Atlantic waters. In the absence of the MOW therefore, the waters of the Gulf Cadiz at depths of 300 m would be up to 5°C cooler, and controlled by the Atlantic intermediate–deep water temperatures.

A eustatic sealevel rise [Haq *et al.*, 1987] of 75–100 m in the early Pliocene (Figure 5.17b) led to the establishment of a Mediterranean overflow and the development of a strong Mediterranean Outflow Water (MOW) undercurrent, which has been of great oceanographic significance since those times [e.g., Rahmstorf, 1998; Dañobeitia *et al.*, 1999]. It is hypothesized that gas hydrates were present at much shallower depths due to the colder bottom–water temperatures than at present. In this model, the initial Mediterranean outflow waters increased the seabed temperature west of the Gibraltar Straits, and depressed the top of the GHSZ in the early Pliocene, causing dissociation of the shallower gas hydrates beneath the continental slope. For the hydrate stability field given in Figure 5.2a, a movement of the hydrothermal gradient curve 5°C to the right, would lead to a reduction in the top of the GHSZ of ~200 m, and would decrease the thickness of sediment to the base of the GHSZ [Bratton, 1999]. MacDonald [1990]

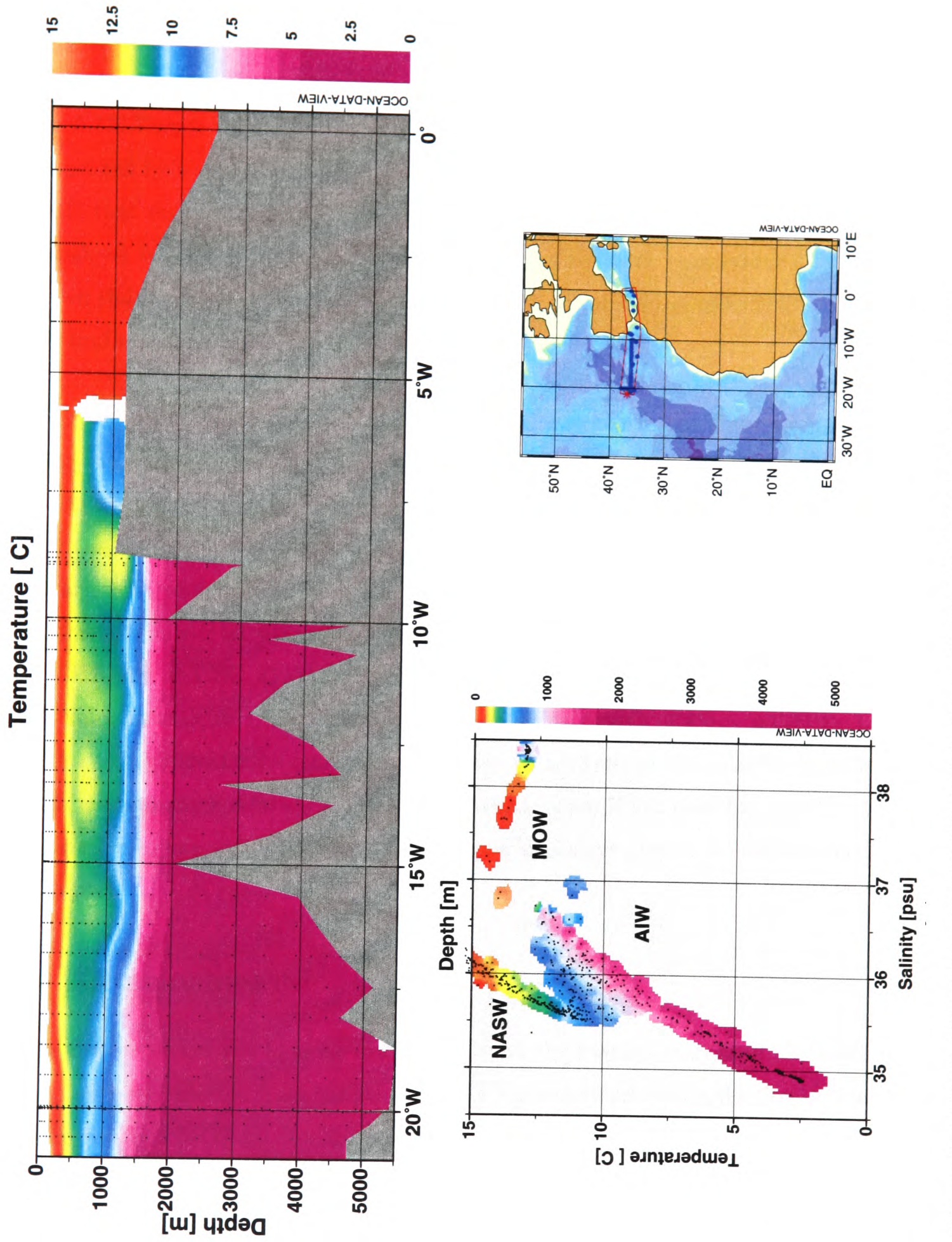


Figure 5.18: Salinity and temperature of water bodies either side of the Gibraltar Straits. The figure was produced using the World Ocean Circulation Experiment (WOCE) datasets accessed using the Ocean Data Viewer freeware of Schlitzer [1999]. NASW = North Atlantic Surficial Water; MOW = Mediterranean Outflow Water; AIW = Atlantic Intermediate Water.

has demonstrated that thermal conductance caused by warming of bottom waters could dissociate 10–100 m of hydrate in the GHSZ in a period of a few thousand years. The data suggests that such dissociation in the GOC hydrates may have caused the earlier mass wasting events observed in the Pliocene-Recent sedimentary unit C-I (Figure 5.6, Figure 5.12, Figure 5.12). Maslin *et al.* [1998] have suggested that destabilized continental slope gas hydrates are one factor in the deposition of huge regional mass-transport deposits that make up a significant component of the Amazon Fan. However, they suggest sealevel fall is the cause rather than changes in seawater temperature. However, it is known that bottom–water temperature is an important control of hydrate distribution [e.g., MacDonald, 1990; Bratton, 1999].

Alternative causes for the mass wasting events observed in the Pliocene-Recent sedimentary unit C-I (Figure 5.12) include earthquake disturbance or the presence of a slope that has been steepened through ongoing depositional and tectonic processes. There is no data regarding palaeoseismicity at the end of the Miocene, but as the area was tectonically active throughout the Miocene it is likely to have been affected by earthquakes at that time. Deformation and sediment mobility affecting unit C-III led to the formation of a C-III high at CDP 2500 on Figure 5.12, with sediments thickening away from it on either side. Seismicity and tectonic oversteepening on the GOC slope are likely to have played a role in downslope mass movement but an analysis of the relative contributions of each mechanism in relation to gas hydrate dissociation is not possible with the current data available, but it is probable that all three causative factors considered had some role to play.

5.6 Conclusions

The first reported gas hydrate occurrence from the eastern margin of the central Atlantic, has been inferred from the presence of a bottom-simulating reflection and acoustic blanking on two MCS profiles from the Gulf of Cadiz. A BSR and amplitude blanking are diagnostic of the presence of gas hydrates [Hyndman & Spence, 1992; Subrahmanyam *et al.*, 1998; Haq, 1998]

The bottom-simulating reflection observed was a single, symmetrical pulse with negative polarity relative to the seabed. Interval velocity data indicate that the negative impedance contrast is largely due to a free gas layer in the sedimentary section. Velocities implied hydrate concentrations were low above the BSR, and that gas volumes below the BSR may be <1% of pore volume. A positive reflection beneath the BSR may

mark a base of the gas layer, which may be up to 36 m thick. BSR reflection coefficients varied from -0.02 to -0.07, which were comparable to values observed from a BSR off the Cascadia Margin [Fink & Spence, 1999].

The BSR is observed in slope sediments at water depths of 1275–1575 m (1.7–2.1 s TWTT) and from 0.4–0.5 s TWTT beneath the seabed on IAM-T3 and GC1, and on the basis of these depths may cover 3500 km^2, but this may be an underestimate if hydrate exists at depths below 1575 m. The extent of the BSR implies that hydrates are limited to a local concentration in the Gulf of Cadiz. Possible migration pathways between the BSR region, a system of of longitudinal diapiric ridges and valleys (and associated faults), and gas–affected sediments in the upper slope and shelf area have been mapped.

Mass wasting associated with free gas has been noted in certain areas of the Gulf of Cadiz. Large mass wasting events appear to have been recorded in the Pliocene to Recent sediments of intraslope basins downslope of the Gibraltar Straits. It has been shown that bottom waters were up to 5°C colder before the onset of the Mediterranean outflow, and so hydrates would have been stable at much shallower depths. Dissociation of these hydrates caused by the warm Mediterranean Outflow Water at the early Pliocene highstand may have been responsible for the observed mass wasting in Pliocene sediments. Tectonic oversteepening of the GOC slope and accompanying seismicity may also have played a role in triggering large mass movements in the late Miocene to early Pliocene.

Further work on seismic data involving detailed velocity analysis, amplitude-variation-with-offset (AVO) analysis, and waveform inversion should be carried out to ascertain what earth models produce the best fit to the observed BSR. Drilling would provide useful tests of such models, and information on the chemistry and habitat of the hydrates. The preliminary indications of low hydrate and gas concentrations on the basis of this study, suggest that the GOC hydrate deposits may have low economic potential for future exploitation.

Chapter 6

A Seismic Study of The Giant Chaotic Body Beneath the Horseshoe Abyssal Plain

6.1 Introduction

The existence of large allochthonous masses west of Gibraltar has been reported since the early 1970s [Beck, 1972; Mulder, 1973]. Situated on the eastern Atlantic margin between 34°–37°N and 6°–12°W is an acoustically chaotic body thought to comprise of these allochthonous masses, and it has most recently been imaged on deep seismic reflection data of the Iberian Atlantic Margins Project [Banda *et al.*, 1995]. The body is located in a complex tectonic zone where the continental margins of southern Iberia and north Africa are intersected by the late Tertiary Gibraltar Arc and Betic-Rif orogenic belt, and the seismically active Azores-Gibraltar plate boundary marking the zone of convergence of Africa and Eurasia (Figure 6.1).

The giant chaotic body (GCB)forms the most external element of the Gibraltar Arc and its areal extent is outlined in white on Figure 6.1. It is observed to occur as far as 600 km west of the Straits of Gibraltar, in water depths up to 5 km. The study of this body is important because of its size and the complexity of its tectonic setting. This study presents the results of the interpretion of recent, high quality deep seismic reflection images over the body, collected by the IAM Group in 1993. This survey provides the most extensive regional coverage over the chaotic body to date, increasing greatly the amount of deep reflection data available for study of this feature of interest. In particular, this study focuses on the lobe of the body beneath the eastern Horseshoe Abyssal Plain (EHAP), refining its timing of emplacement, describing its geometry and seismic character, and proposing a mechanism for its origin.

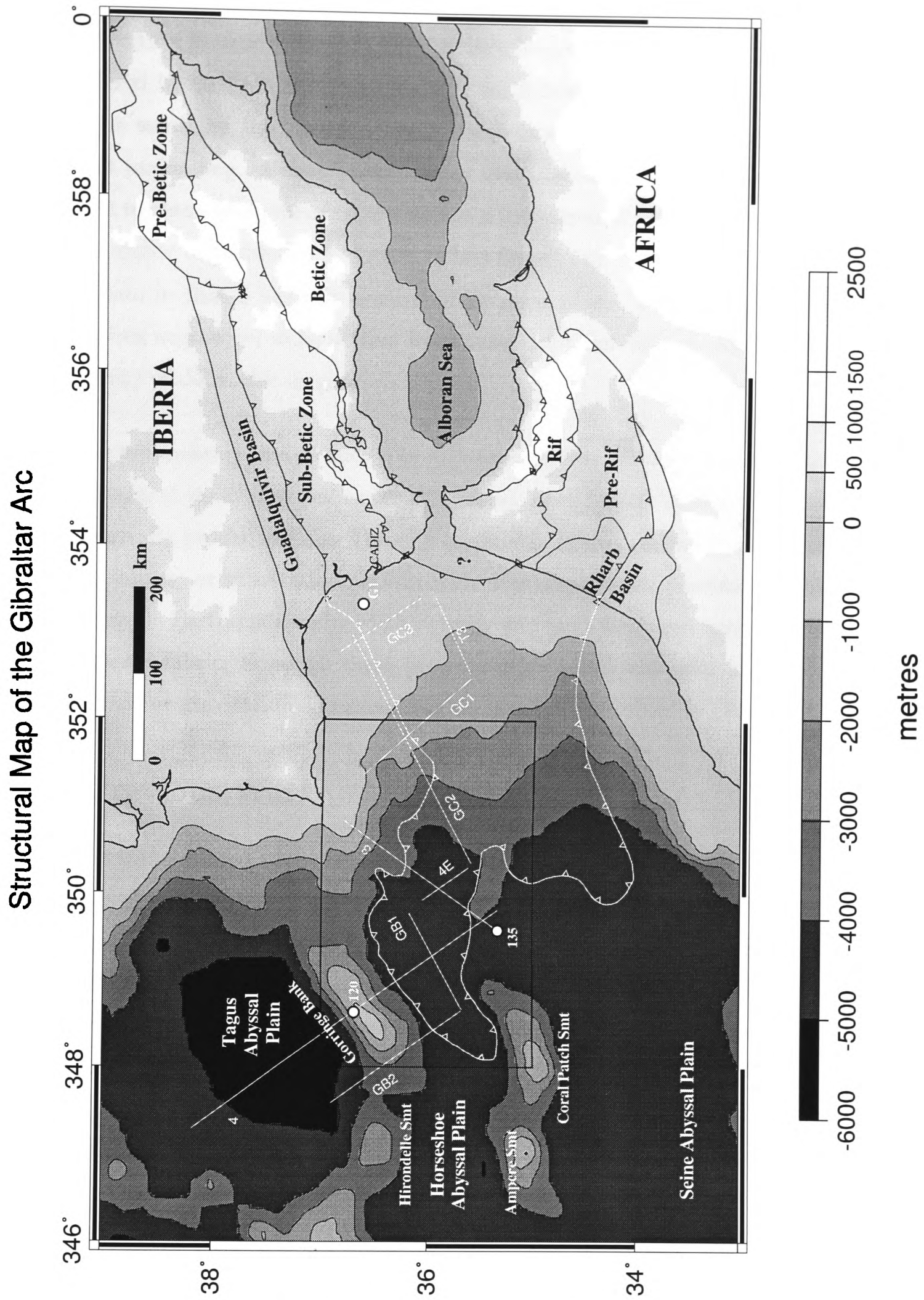


Figure 6.1: Structural map of the Gibraltar Arc-eastern Atlantic region. The location of IAM seismic profiles used in this study are shown in white. The locations of DSDP wells 120 and 135, and exploration well G1 (245, IGME [1987], Appendix B) are shown in white. The study area of interest is shown within the black box.

The Horseshoe Abyssal Plain is a narrow and elongated basin some 356 km long by 64 km wide, with a surface area of 21,157 square kilometres (beneath the 4800 m isobath). It is enclosed by bathymetric highs, being bounded to the north by the Gorringe Bank and to the south by the Ampere–Coral Patch Seamount chain (Figure 6.1). Studies of abyssal plains (e.g. Pilkey [1987]) show that the characteristic types of sediments attributed to these bathymetric domains are a succession of pelagites/hemipelagites (10-20%), a number of turbidites and rarer debris flows. The EHAP subbasin is an unusual abyssal plain in that a large proportion of its fill appears (from its seismic appearance and sampling nearshore) to be neither from pelagic nor turbiditic deposits, but of a large, chaotic body of debatable origin.

Chaotic sedimentary bodies known as melanges are formed through a variety of geological processes, at many different scales [Raymond, 1984]. Large chaotic sedimentary bodies are generally produced either through tectonic deformation, resulting in accretionary wedge melanges, or gravitationally, through downslope mass movement (debris flows, olistostromes). Earthquake-induced thixotropy and mud diapirism may also cause a pervasive chaotic fabric, although these produce more small-scale and localized melanges than tectonic or gravitational mechanisms are generally observed to [Torelli *et al.*, 1997].

6.2 Previous Work

Roberts [1970] hinted at the offshore extension into the Gulf of Cadiz of the seismically chaotic body observed in the flexural foredeep of the Betic orogen during petroleum exploration of the Guadalquivir Basin. This onshore body was found after drilling to be composed of allochthonous Triassic clays, gypsum and salt [Perconig, 1962]. Early work within the exploration department of Shell International Petroleum Company led to two publications reporting the existence of large, allochthonous masses extending into the Atlantic, west of Gibraltar. These workers interpreted these masses as gravity-induced thrusts/olistostromes from the convex, uplifted outer part of the orogenic arc during late Cenozoic Alpine phases of uplift and folding [Beck, 1972; Mulder, 1973].

Lajat *et al.* [1975] and Bonnin *et al.* [1975] published maps based on seismic reflection data which delineated the interpreted offshore extensions of the gravity-driven nappes of the Guadalquivir and Rharb basins, which represented the most external part of the Betic-Rif Arc. Both groups of workers had the chaotic body extending well into the Horseshoe Abyssal Plain, but Bonnin *et al.* [1975] mapped it 100 km further west in both the Seine and Horseshoe Abyssal Plains with the benefit of more regional seismic data.

Purdy [1975] interpreted a zone of seismic opacity in the eastern Horseshoe Abyssal Plain as due to slumped sediments from the northwest which had rested on slices of African oceanic crust before being overthrust onto the Eurasian plate to form Gorringe Bank. Royden [1993a] also interpreted the body as indicating active subduction, with it marking the westernmost limit of the arcuate Betic-Rif thrust belt system.

Bonnin *et al.* [1975] subdivided the body into three zones from the Gulf of Cadiz coast in the east to the Seine Abyssal Plain in the west, based on sedimentary cover: Zone 1 (0–1500 m depth) with normal sedimentary cover of variable thickness; Zone 2 (1500m to continental rise) where the body has little sedimentary cover; Zone 3 in the abyssal plains occurs within normal sedimentary layers. Auzende *et al.* [1981] followed this same scheme, but whereas Bonnin *et al.* [1975] attributed the different units to westward gravity-emplaced sediments derived from the Betic-Rif orogen, the later authors attributed Zone 2 to an emergent pre-Messinian collisional feature due to folding of sediments between the African and Eurasian plates, and Zone 3 to olistostromes from this emergent "South Iberian Spur", which they invoked in order to explain Messinian sediments in a core taken to the west of the Straits of Gibraltar. Malod & Mougenot [1979] and Malod [1982] also interpreted the chaotic body as an olistostrome of eastern provenance. All the above authors published short lines of seismic data that passed over the chaotic body. Other short sections have been published by Watkins & Hoppe [1979], Hinz *et al.* [1982] and Veeken & Schwander [1988]. Generally these lines failed to penetrate the chaotic body in all but the areas of pinchout.

Hayward [1996] mapped the chaotic body to the south of Gorringe Bank in the Eastern Horseshoe basin as olistostrome unit EH-II, and debris flows to the north of Gorringe as unit T-II. This was the first survey of large mass movements in the sedimentary record in the Gorringe region. Hayward *et al.* [1999] present seismic reflection and GLORIA side-scan sonar data and structural models of the Gorringe Bank, Tagus and Horseshoe Abyssal Plain regions. They include seismic profiles showing the nature of the edges of the chaotic body in the HAP, and concluded that regional compression is mostly taken up on the northern flanks of Ampere, Coral Patch seamounts and the Coral Patch ridge. Sartori *et al.* [1994] and Torelli *et al.* [1997] published deep multichannel seismic reflection data across the giant chaotic body. The latter was a study of the giant chaotic body based on a series of regional lines, and they hypothesized that the northern sector (above ~35°) was made up of gravitational mass flow deposits (olistostromes/debris flows) of intrabasinal provenance from structural highs generated during a Miocene paroxysmal phase of Africa-Iberia convergence. They interpret the southern sector as having a tectonically-produced

chaotic fabric and being emplaced as an accretionary wedge, during the Pliocene. Tortella *et al.* [1997] published a first-order attempt to map the thickness of the chaotic unit in the HAP, but their figure was based only on interpretations from six IAM profiles. The above authors all agreed on a mid-late Miocene (Tortonian) age for emplacement of the chaotic body, on the basis of correlations between the offshore deposit and similar deposits drilled in the Guadalquivir and Rharb basins (e.g.Perconig [1962] and Feinberg [1976]).

6.3 Mass Flow Processes in the Deep Sea

Mass flow (gravity-driven) mechanisms are extremely important in the transfer of sediment from source to depocentre on continental margins and their adjacent abyssal plains. They are discussed briefly here to introduce the different types of gravity-driven process and typical deposits that result from them.

Early in the twentieth century, it was generally thought that the deep ocean was undisturbed, with deposition of only hemipelagic and pelagic material. However, as terrigenous sands were being discovered in deep oceans, it was clear that a range of processes could transport sediment hundreds of kilometres from the continental slope to the rise and abyssal plain. Such mass flow processes range from catastrophic failures such as avalanches, slumps and slides, to slower creep mechanisms. The transport of sediment for very long distances into deep water is largely due to turbidity currents, debris flows and slides [e.g., Masson *et al.*, 1996].

Figure 6.2 lists the range of processes acting in marine environments and their subsequent deposits. These have been divided up into resedimentation (mass flow) processes, bottom currents, surface currents and pelagic settling, and authigenic (*in situ*) processes. At continental margins and seamount flanks, there is a sufficient slope to cause sediment movement by a variety of resedimentation processes, some of which operate at a large-scale. It has been estimated from studies of the infilling of abyssal plains, that as much as 90% of the sedimentary flux is due to mass flows such as turbidite currents or debris flows and avalanches [e.g., Weaver & Rothwell, 1987; Pilkey, 1987], with the remainder being made up of pelagites/hemipelagites.

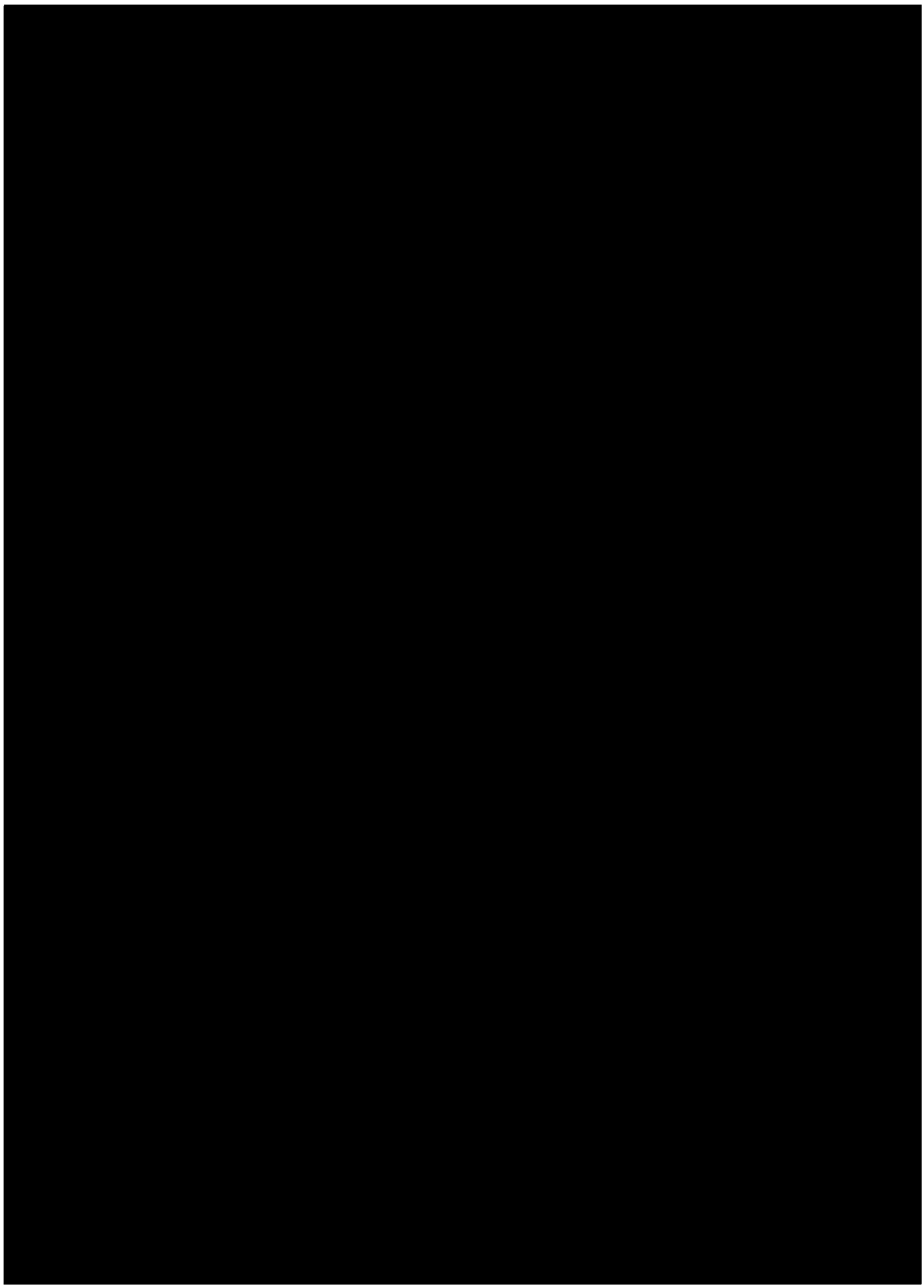


Figure 6.2: Seafloor processes and their resultant deposits. After Stow *et al.* [1996].

6.4 Data Acquisition and Processing

Seismic Experiment

In the latter part of 1993, 3800 km of near-vertical seismic reflection data were collected offshore Spain and Portugal by the IAM group, aboard the vessel Geco-Sigma [Banda *et al.*, 1995]. The profiles used for this study are shown in Figure 6.1. The seismic survey utilized a very large,116 litre volume airgun array, and a 5 km long streamer of 192 channels, resulting in high quality images which penetrated the chaotic body in all but its thickest parts in the Gulf of Cadiz.

Seismic Data Processing

Processing to brute stack was carried out by GECO-PRAKLA Ltd after the cruise, using standard processing techniques. The processing steps followed were: reformat to SEGY, bandpass filter, resample to 8 ms, trace edit, trace equalisation, sum adjacent traces, CDP gather with 25m bin and 32 fold, spherical divergence correction, deconvolution, fk demultiple, NMO correction, front end and inner trace mute, spherical divergence correction using stacking velocity field to replace initial correction, CDP stack, noise attenuation, time and space variant bandpass filter.

For this study, further post-stack processing was carried out using the Promax Version 6.0 processing package on a Sun Sparcstation 20 platform. The profiles were migrated using a phase-shift algorithm, which produced clear images down to acoustic basement. Trace mixing after migration removed some of the migration-introduced noise, and some degree of dip filtering removed the very steep coherent noise present through processing due to the large number of discontinuities and irregularities in the sediments that were imaged. The final migrated profiles were displayed with a 500 ms AGC scalar, using Seismic Unix [Cohen & Stockwell, 1996] and GMT [Wessel & Smith, 1991] software packages. Processing is described in detail in Section 3.1.

Other data

This study uses previous multichannel seismic data shot on the 1992 CD64 cruise of the *Charles Darwin* by the Oxford group over the eastern Horseshoe Abyssal Plain and reported in Hayward [1996] and Hayward *et al.* [1999], in addition to the IAM deep seismic profiles. Figure 6.3 compares acquisition parameters for the Oxford data, and that of the 1992 *Explora* cruise which collected deep seismic data over the chaotic body reported in Sartori *et al.* [1994] and Torelli *et al.* [1997]. The IAM data, with the largest source, longest streamer and greatest fold and regional coverage, is the most comprehensive

deep reflection survey data reported to date over the chaotic body. Using the extensive coverage afforded by access to CD64 and IAM datasets allow us to accurately delineate the shape and thickness of the chaotic body in its northern sector.

TABLE 1 COMPARISON OF ACQUISITION PARAMETERS FOR DATA ACROSS THE EASTERN HORSESHOE ABYSSAL PLAIN

PARAMETER	CRUISE	
	EXPLORA	IAM
YEAR	1992	1993
SOURCE	32 airgun array 80 litres capacity	36 airgun array 116.2 litres
STREAMER	3000m length 120 channels	4800 m length 192 channels
GROUP INTERVAL	25 m	25 m
SHOT INTERVAL	50 m	75m
CMP SPACING	12.5 m	25m
CMP FOLD	30	32
SAMPLE RATE	2 ms	4 ms
RECORDING LENGTH	13	25 s
PROCESSING	"DISCO" from Cogniseis	GECO-PRAKLA Promax.
MIGRATION	Finite-difference wave-eqaution using 90% Vrms	Phase shift

Figure 6.3: Comparison of acquisition parameters for IAM and AR92 profiles data shot across the eastern Horseshoe Abyssal Plain.

6.5 Observations

6.5.1 Seismic Character and Correlation

Well correlations

There is a general lack of detailed sampling in the Gorringe Bank and Horseshoe Abyssal Plain regions, and no complete stratigraphic record for the EHAP. Figure 6.1 shows positions of DSDP sites 120 [Ryan *et al.*, 1973] and 135 [Hayes *et al.*, 1972]. Drilling at Site 120 penetrated 246 m of sediments of 2 distinct facies: a lower Miocene-Pleistocene highly calcareous biogenic ooze rich in coccolithophora and foraminifera, separated by a major hiatus from a series of Lower Cretaceous marls of Albian-Barremian age. Another unconformity was present between the Miocene and Pliocene sediments, which the scientific staff hypothesized could be due to the missing unit slumping downslope into the Tagus Abyssal Plain. Indeed, a pair of inferred olistostromes can be seen as sub-bottom chaotic bodies at the base of the north slope of Gorringe Bank (Figure 6.5), the upper one having a probable Pliocene date of emplacement [Mauffret *et al.*, 1989]. The oldest cored sediments, of Barremian (120 Ma) age, rest on metamorphosed basalts and gabbros forming the basement at a depth of 246 m below the seabed. Profile IAM-4 (Figure 6.5) could not be tied stratigraphically to Site 120, as the resolution of this shallow well was at a far smaller scale than the vertical resolution of the IAM dataset, which was designed to image crustal profiles. However, inferences of age and seismic character have been made, as discussed below.

Site 135 penetrates 689 m of sediment on a smaller bathymetric high to the east of Coral Patch seamount [Hayes *et al.*, 1972]. Profile IAM-3 passed directly over the DSDP site and this allowed correlation of the seismic data with the well data (Figure 6.4). Reflection **a** corresponds to the major unconformity between the Pleistocene–Late Oligocene nanno-chalk oozes of DSDP Unit 1 and the Early Eocene–Maastrichtian silty muds, sands and clays of Unit 2 [DSDP volume 14, Hayes *et al.*, 1972]. Reflection **b** is a bright reflection, which is tentatively correlated with the major contrast in lithology between nanno-marl ooze and a limestone bed in the early Aptian Unit 4, following Hayes *et al.* [1972]. Intermediate boundaries between Units 2, 3, and 4 are not easily correlated with any regional reflections. However, their correlation is not within the scope of this study. The portions of profiles IAM-3 and IAM-4 shown in Figure 6.4 illustrate the major seismic facies considered in this study of the EHAP.

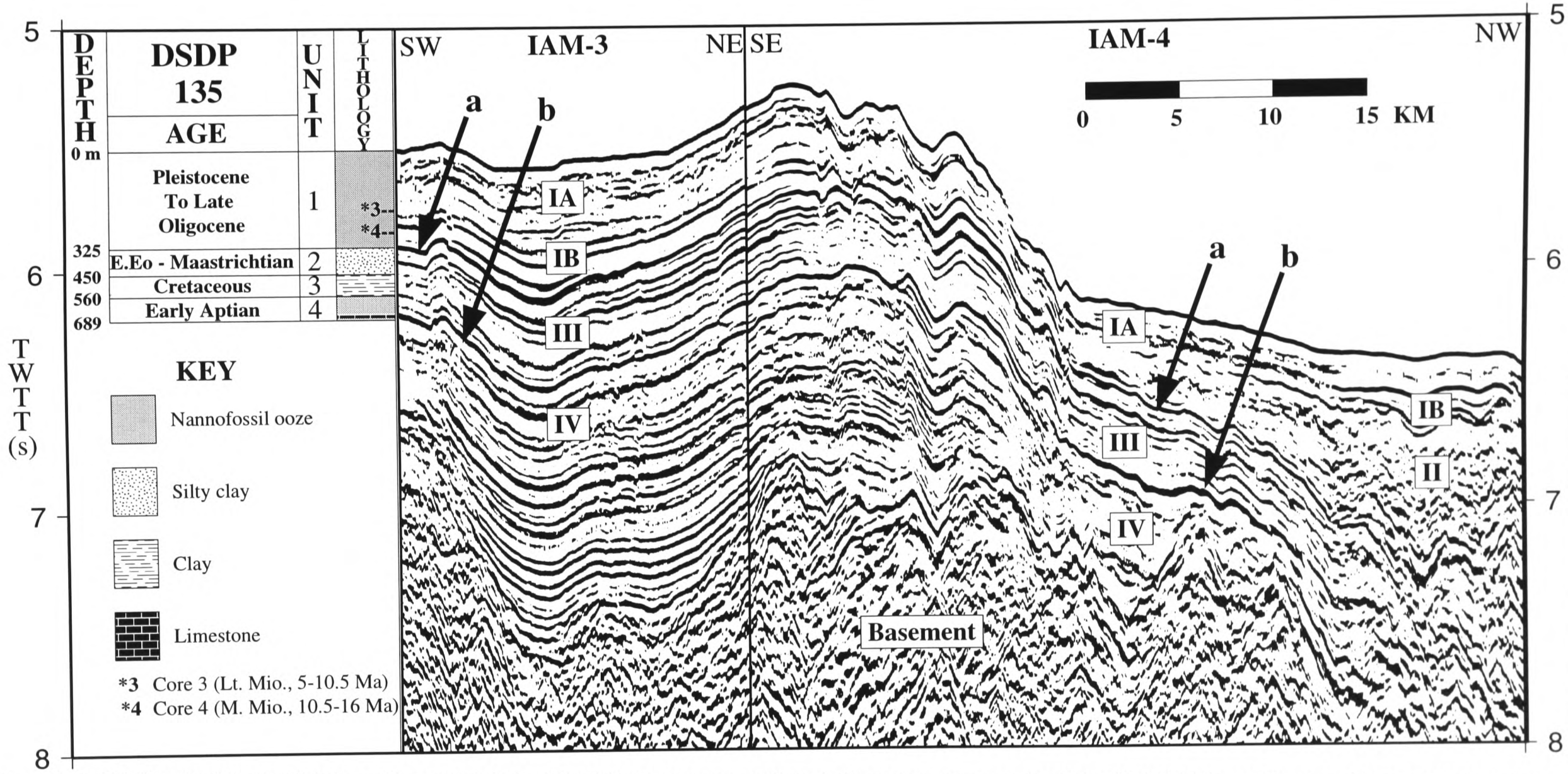


Figure 6.4: DSDP site 135 correlation with seismic data. The lithology nomenclature follows the scheme set out in DSDP Volume 14. **a** and **b** represent major reflections correlated with the well. See text for explanation of the seismic facies.

Seismic Facies

In this study, four seismic stratigraphic units are defined on the basis of seismic character and age correlation with well 135, as depicted on Figure 6.4. The top basement is generally easily picked on the abyssal plain seismic profiles (e.g., Figure 6.5, Figure 6.8). The four seismic facies are described below, in order of deposition.

Facies IV is very variable in amplitude and thickness, with an overall wavy parallel reflection character. The lower reflective layers are seen to onlap onto acoustic basement. It has not been sampled anywhere, but by extrapolation of sedimentation rates from DSDP site 135 an early to late Jurassic (155-180 ma) age for the oldest sediments of this facies was deduced by Hayes *et al.* [1972].

Facies III consists of low-medium, parallel wavy continuous reflections, where the unit has not been affected by faulting. By correlation with DSDP site 135 the top and base of the unit are marked by reflections **a** and **b** respectively, and thus this facies corresponds to an early Aptian-early Eocene interval.

Facies II has a generally horizontal to sub-horizontal, small scale, chaotic fabric on the reflection profiles. It also exhibits regions that are seismically transparent. The large number of discontinuities within it produce an image dominated by steep noise on unfiltered sections. There are some reflections within the unit which appear to be semi-continuous over several kilometres. This unit is the chaotic body with which this study is primarily concerned. It rests above reflector **a**, so it is younger than late Oligocene. The lowermost cycle of **Facies I** also underlies **Facies II** as seen on Figure 6.4, and this falls between the positions of Cores 3 and 4 when correlated with DSDP site 135. This is gives an age bracket of mid-late Miocene (5-16 Ma) for this body, with a probable age in the Tortonian at ~10 Ma. This unit is equivalent to unit C-III defined earlier in the Gulf of Cadiz seismic stratigraphic scheme (Section 4.5).

Facies I is subdivided into two sub-units on the basis of reflection character. **IA** consists of low amplitude, continuous and parallel reflections. This can pass laterally into, or sit conformably above **IB**, which is characterised by medium amplitude, continuous reflections. However, on the portion of IAM-3 adjacent to DSDP site 135 on Figure 6.4, the basal layers of **IA** appear to onlap **IB**, in a local depocentre. The base of **Facies I** correlates with the early Eocene to late Oligocene unconformity at DSDP site 135.

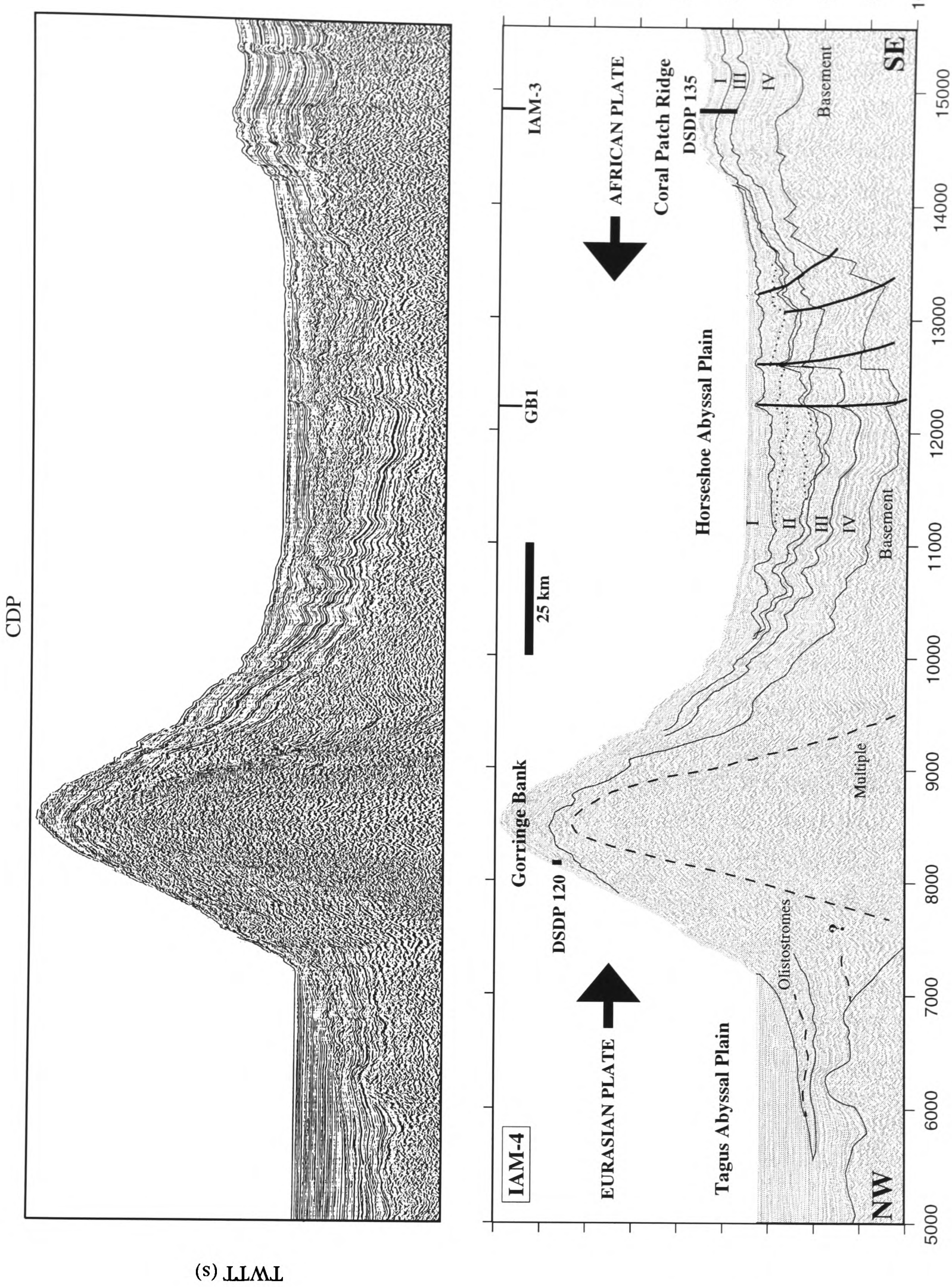


Figure 6.5: Interpreted seismic profile IAM-4 across the Gorringe Bank and Horseshoe and Tagus abyssal plains.

6.5.2 Observations from Seismic Profiles

Figure 6.5 is a 250 km long NW-SE oriented profile from the Tagus Abyssal Plain over the major bathymetric high that is Gorringe Bank, to the Horseshoe Abyssal Plain, and terminating over the Coral Patch Ridge, which has been drilled at DSDP site 135. This transect illustrates several salient features regarding the chaotic body (Facies II) which infills the basinal trough between the Gorringe Bank and Coral Patch Ridge. Water depths in the TAP average 4.5 km whereas those in the shallower HAP average some 4 km. The Gorringe Bank feature is thought to be due to partial overthrusting of the African plate over the Eurasian plate. Compressive deformation across the Horseshoe Abyssal Plain is illustrated by the folding of all the sediments up until a post-Tortonian time, after which deformation is seen to be affecting sediments only at Gorringe Bank and Coral Patch Ridge (Figure 6.5). Internal semi–continuous reflections can be seen within facies C-II, which terminate at the edges of the body. The major basement–involved faulting, and folding in the southern half of this profile are indicative of a relatively large amount of shortening being taken up in this region, and this region is a locus of seismicity [e.g., Udias *et al.*, 1976].

Age relations with Gorringe Bank uplift imply that the chaotic unit was deposited post-uplift, as its basin–shaped fill implies. The assertion of Torelli *et al.* [1997] that a substantial amount of material came from the Bank during uplift is not borne out by a comparison of chaotic deposits to the north and to the south of the Gorringe Bank. The steeper north flank has a set of three large debris flow events at its base, which pass into the mid-Miocene (end Serravalian, 12 Ma) unconformity of the Tagus Abyssal Plain [Mauffret *et al.*, 1989], and which are buried below undeformed sediments. These chaotic events are tiny when compared to the huge chaotic body in the HAP to the south, at the base of a less steep slope. The emplacement of chaotic Facies II predates the onset of the deformation which folds the sediments at the south base of Gorringe, so a further date bracket is available. The present day deformation and uplift at the Coral Patch Ridge [e.g., Hayward *et al.*, 1999] is also reflected in the observation that the corpus of chaotic sediments here is tilted away from the Ridge, and has a thicker overburden of sediment at its NW end, beneath a flat seabed.

Figure 6.6 is a depth–converted profile over the EHAP. This profile illustrates the great thickness the chaotic body can attain, being up to 4 km in the centre of the profile. The Horseshoe basin appears to be bounded by a major normal fault at the base of the continental slope, at the NE end of the profile, where a faulted Mesozoic carbonate platform of the former South Iberian Margin is also seen. The chaotic unit

is observed to be a composite unit here: seismically transparent bodies A and B may represent slumps due to their lack of internal structure; internal reflections within the giant chaotic body appear to differentiate smaller bodies which pick out a southerly direction of flow. However, the chaotic body, at its northern end, has the appearance of an advancing wedge, as unit C-III does on profiles upslope in the Gulf of Cadiz (e.g., IAM-GC3, Figure 4.11).

Figure 6.7 from the eastern end of the lobe of the chaotic unit (Figure 6.1), illustrates the effects of convergence of the Eurasian and African plates in the folding and faulting across this section. The most interesting feature of the profile, however, is the clear presence within the large chaotic body of reflections marking internal boundaries. The thickness of these sub-units is seen to decrease to the west, towards the pinchout of the chaotic body to the west (Figure 6.8). This strongly suggests that the body is a result of cumulative mass flow into the Horseshoe basin, from an easterly direction. Three individual layers separated by clear reflections within the body have been picked out (II-a, II-b, and II-c on Figure 6.7).

Figure 6.8 images the pinchout of Facies II in the EHAP. The unit is thin here (<0.5 s TWTT) and thins out against the base of Gorringe Bank to the NW (Figure 6.1). A possible fault affecting Units IV, III and II can be seen at CDP 600. At the SE end of the profile Unit II is unclear due to migration-induced noise from processing. At its leading edge, however, an internal reflection can be seen which appears to be deformed or cut into small thrust slices.

6.5.3 Age of Emplacement of the Chaotic Body

Previous age estimates have been based on correlations with onshore deposits in the Guadalquivir and Rharb foreland basins. In general, workers agree on a mid-late Miocene age for the body [e.g., Perconig, 1962; Feinberg, 1976; Malod, 1982]. This study presents a seismic correlation with DSDP Site 135 (Figure 6.4) giving the most direct dating constraint on the chaotic body in the Horseshoe Abyssal Plain. The top and base of the chaotic body in the abyssal plain are bracketed by reflections interpreted as far as DSDP site 135. The unit equivalent in age to the olistostrome is between Cores 3 and 4. Core 3 is late Miocene (Globorotalia acostaensis zone) [Hayes *et al.*, 1972]. Core 4 biostratigraphy indicates an early Middle Miocene age. The age brackets on the deposition of the chaotic body are thus between 5-16 Ma, with a probable Tortonian age of ~10 Ma, from this seismic correlation with DSDP 135.

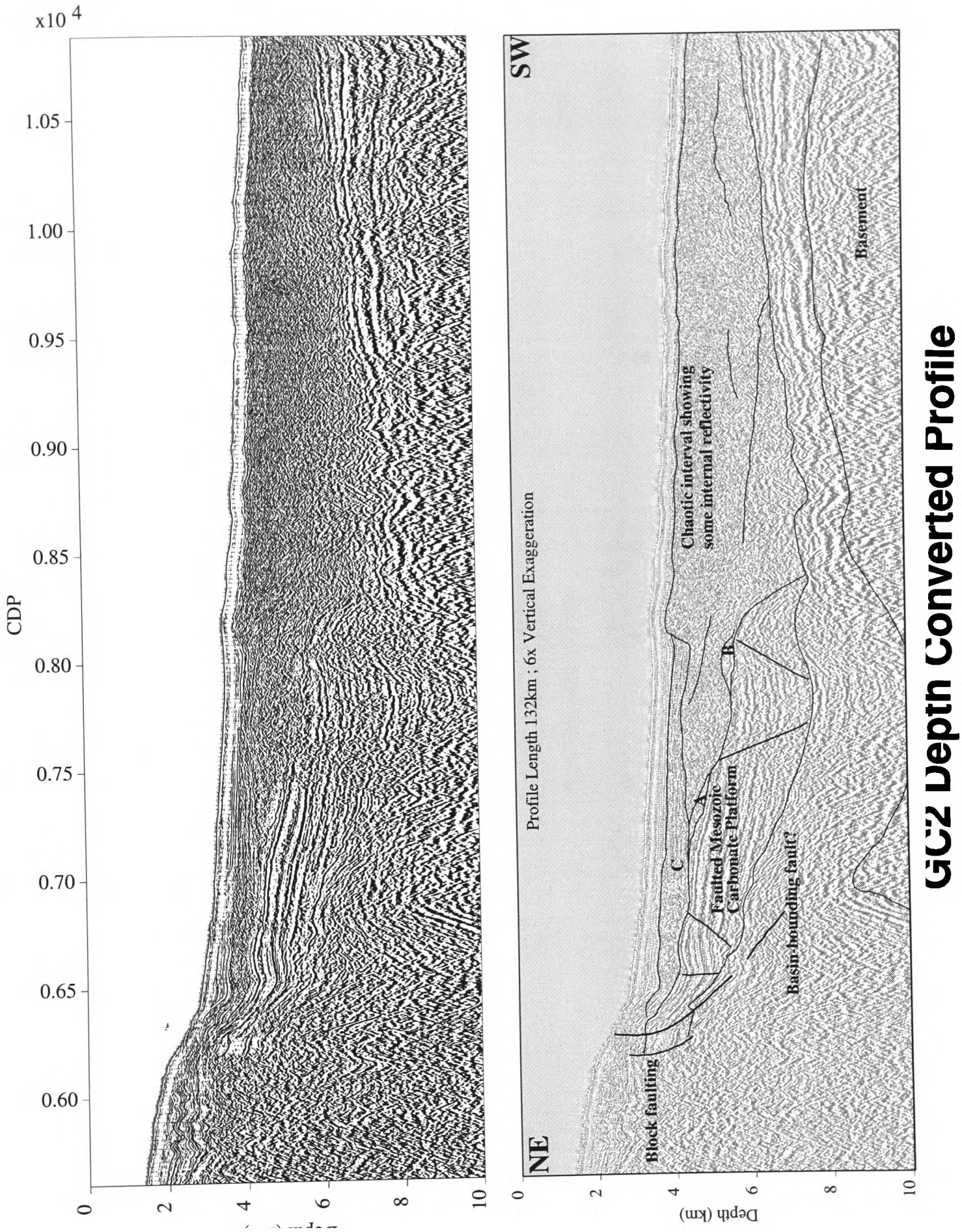


Figure 6.6: Interpreted depth-converted seismic profile GC2 from the lower continental slope of the Gulf of Cadiz margin (NE end) to the Horseshoe Abyssal Plain.

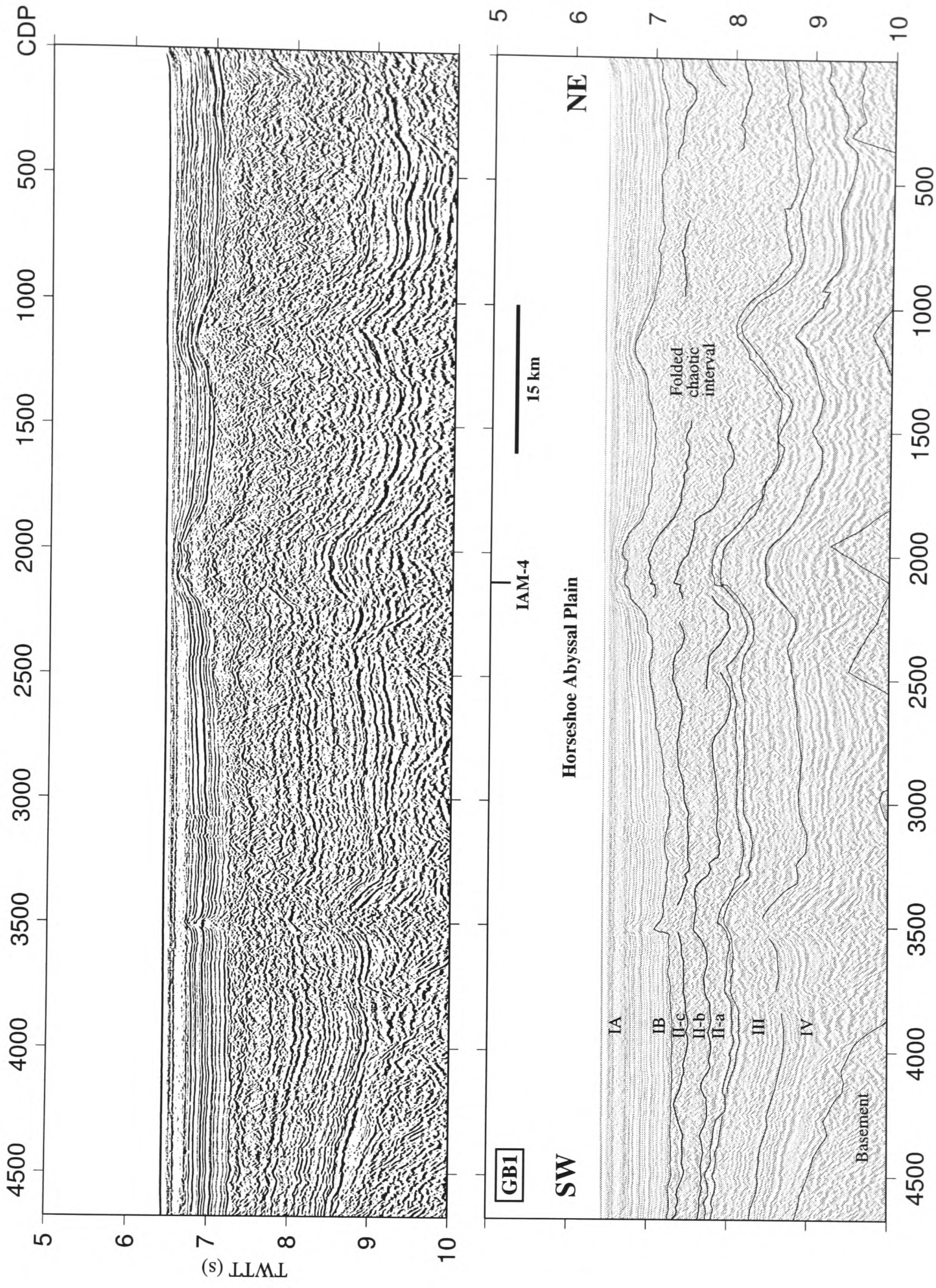


Figure 6.7: Interpreted seismic profile GB1.

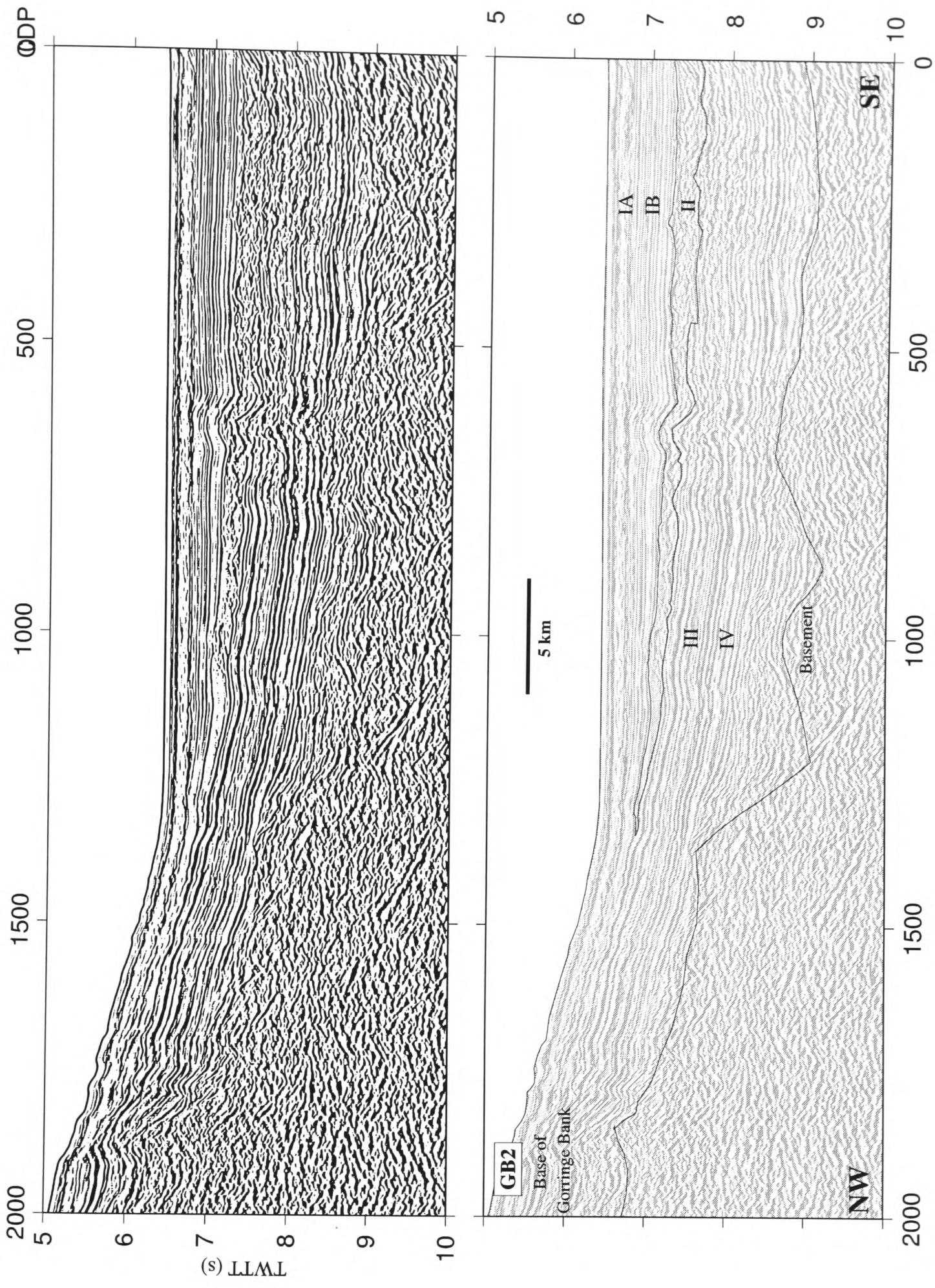


Figure 6.8: Interpreted seismic profile GB2.

6.5.4 Dimensions

Depth Conversion

TWTT picks for the top and base of Facies II sediments were digitised from IAM and CD64 seismic profile data, incorporating the published lines of Sartori *et al.* [1994] and Torelli *et al.* [1997]. These picks were then compiled into a regional database of TWTT thickness values for Facies II, which was then gridded to provide an isochronopach of the body. Using results from refraction surveys in the EHAP reported by Purdy [1975] and Bonnin [1978], a velocity of 3.1 km/s was used to depth–convert the isochronpach into an isopach of the body, which is illustrated in Figure 6.9.

Area and Volume

Figure 6.9 illustrates the extent and thickness of the chaotic body. The seismic profiles on which this work is based are shown in grey. Question marks illustrate areas where lack of coverage or seismic penetration lead to uncertain thicknesses. The body is seen to extend 600 km west of the Straits of Gibraltar. A thick region, of >5 km thickness, is in the Gulf of Cadiz, where the computer-contoured thickness is possibly an underestimate due to an unclear base of the body on some of the seismic profiles. There is also a major depocentre at the base of the continental slope at 9°W, where a thickness of over 5 km is seen (see also Figure 6.6). The Horseshoe lobe then thins progressively towards the west and follows the shape of current bathymetry, implying it was originally emplaced into a similar trough as today's EHAP, which in turn implies that the crustal warping that produced the GB and Coral Patch highs was already in evidence at the time of emplacement of Unit II.

Integrating the Unit II isopach over the whole area of Figure 6.9 gives a volume for the whole body of ~230 000 km^3, and a volume in the EHAP (in the box shown) of ~72 000 km^3. The former figure is inclusive of all the material taken up in thrust wedges in the Gulf of Cadiz (e.g., GC1,GC3,T3), whereas the latter figure for the EHAP basin is interpreted to reflect the volume of gravity-emplaced mass–wasting deposits. Figure 6.9 clearly illustrates that the volume of sediment in the northern lobe of the chaotic body is far greater than the southern lobe, and the contention that the southern lobe is emplaced through tectonic rather than gravitational processes is borne out by its far shorter extent. The northern lobe extends 300 km from the thick depocentre at its landward end, which suggests the more distal parts have been emplaced by long–runout mechanisms such as turbidites and debris flows, whereas the thicker proximal parts may be more like olistostromes [e.g., Stow *et al.*, 1996].

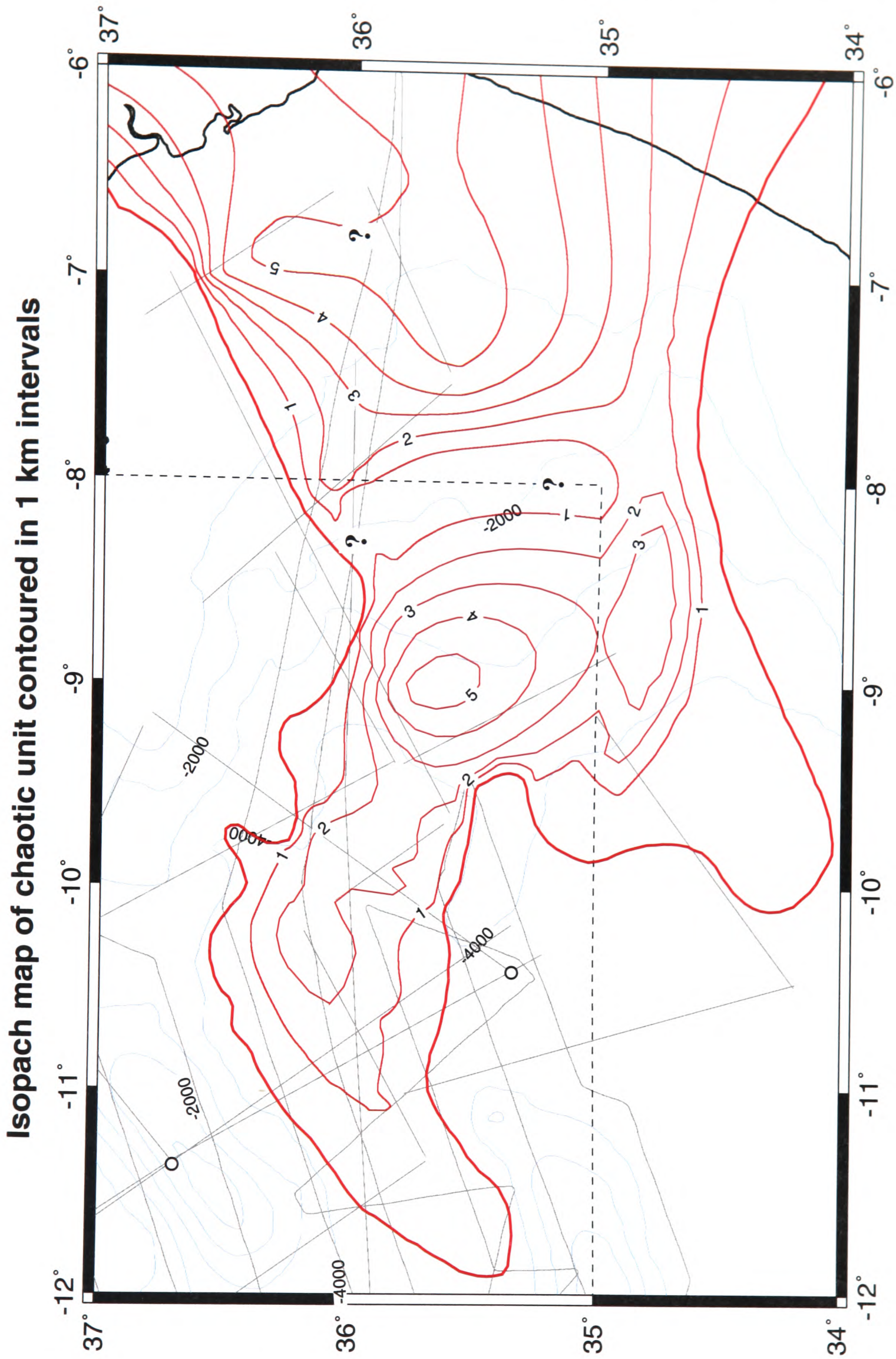


Figure 6.9: Depth-converted thickness of unit C-III/HAP-II in the Gulf of Cadiz to Horseshoe Abyssal Plain region. Single digits refer to isopachs in km; bathymetry contours in blue, every 1000m.

6.6 Discussion

What causes a chaotic seismic fabric?

A chaotic fabric can be produced in sediments through fluidisation, anomalous density stratification leading to mixing of sedimentary layers, gravity–driven depositional processes (e.g., debris flow), and tectonic deformation producing a melange. The sediments of seismic unit C-III (the equivalent allochthonous unit in the GOC to seismic facies II) display evidence of internal angular unconformities as the unit is deformed into a series of thrust packages (e.g., Figure 4.14). The overall morphology of the frontal units of C-III is that of an accretionary wedge (Chapter 4). However, the chaotic facies, C-II, beneath the HAP appears to be made up of many discrete events. These are internally chaotic but their boundaries may be imaged as seismic reflections (e.g., three individual layers separated by clear reflections within the chaotic body have been picked out: II-a, II-b, and II-c on Figure 6.7). The most plausible mechanism for the deposition of such sediments hundreds of kms from the base of the continental slope are gravity-driven mass movements such as long runout debris flows, and slides [e.g., Embley, 1976, 1980; Masson *et al.*, 1996]. Long distance turbidite flows have been correlated over the HAP by Hoyt & Fox [1977], whose study showed that sediments can be deposited over very wide areas of the basin from single events.

What is the age of emplacement of the chaotic body?

This study brackets the age of emplacement of the chaotic body in the HAP between 5 and 16 Ma (mid–late Miocene), and likely to be ~10 Ma, on the basis of seismic correlation with biostratigraphically dated cores at DSDP site 135. The emplacement age is probably Tortonian (Figure 6.4) and occurred after the initial uplift of Gorringe Bank (Figure 6.5), which formed by overthrusting of the African plate upon the Eurasian plate in the Middle Miocene at ~ 10 Ma [e.g., LePichon *et al.*, 1970; Hayward *et al.*, 1999]. This suggests that the chaotic unit was emplaced in the Tortonian soon after 10 Ma.

The age of emplacement from this study, agrees with previous estimates of a mid–late Miocene age, although they were indirect as they were based on correlations with onshore deposits in the Guadalquivir and Rharb foreland basins. Both contain large allochthonous bodies which have been classified as olistostromes [e.g., Perconig, 1962], although this is now a matter of debate in respect of the Guadalquivir Basin [Berastegui *et al.*, 1998]. For example, a chaotic unit ("olistostrome") is also found within the Miocene sediments of the Prerif foreland basin of Morocco [e.g., Pratsch, 1996]. Early Tortonian marine

fauna have been found within the rocks below the chaotic unit, and late Tortonian marine fauna above [Michard, 1976] and thus this unit is contemporaneous with, and analogous to, that within the Guadalquivir foreland basin. However, well data from the GOC (see Figure 4.4) suggest that the age of sediments above and below the allochthonous chaotic sediments is not always the same e.g., in well 245, the sediment overlying C-III is mid-Miocene in age; above 225 it is basal Tortonian (late Miocene); above 604 in the Guadalquivir Basin it is mid-upper Miocene. This suggests that perhaps the thick southern part of the chaotic body in the GOC/GQB foreland basin was emplaced earlier, and that the timing of emplacement is diachronous.

How does the GCB compare to other large mass movements?

Location	Type	Volume (10^3 km^3)	REFERENCE
Horseshoe A.P., Atlantic	giant chaotic body	72	**This study**
N.E. Atlantic inc. H.A.P.	giant chaotic body	85	Torelli *et al.* [1997]
Madeira A.P., Atlantic	debris flow	0.6	Embley [1976]
Storegga, Norway	3+ slides	6	Bugge *et al.* [1988]
Hawaii	slides & slumps	up to 5 (per slide)	Moore *et al.* [1989]
Agulhas, SE Africa	slides and slump	20	Dingle [1977]

Table 6.1: Volumes of rock involved in mass wasting.

The estimated volumes of a number of different mass wasting events are tabulated in Table 6.1, in comparison to the estimate of 72 000 km^3 for just the northern lobe of the chaotic body seen beneath the sediments west of Gibraltar. Torelli *et al.* [1997] estimated a value of up to 85 000 km^3 for the volume of GCB sediments beneath the continental rise and Seine and Horseshoe Abyssal Plains. They remarked that the hypothesis of a purely gravity–driven body is problematic due to the size of the GCB. However, this study suggests that in the GOC–EHAP area at the time of emplacement, the presence of thick sediments, a sloping seafloor, and tectonic steepening at the Gibraltar Arc, were favourable conditions for gravitational failure (see Hampton *et al.* [1996] for an analysis on the causes of slope failure). The largest recorded failure events are the Agulhas slides off SE Africa [Dingle, 1977], which are of the same magnitude as the HAP estimate presented here.

The seismic data indicate that the GCB beneath the HAP was created by multiple events, with at least three discrete deposits at the distal pinchouts at the base of Gorringe

Bank (Figure 6.7. Taking the maximum values recorded for an individual submarine slide, of 5000 km^3 [Moore *et al.*, 1989], the HAP lobe would require 14–15 events of this size; for the largest debris flow volume reported, of 0.6 km^3 [Embley, 1976], 120 equivalent events would be required. A number in between these two may represent the true number of mass wasting events that make up the present–day GCB beneath the EHAP.

A conceptual model for the emplacement of the chaotic body.

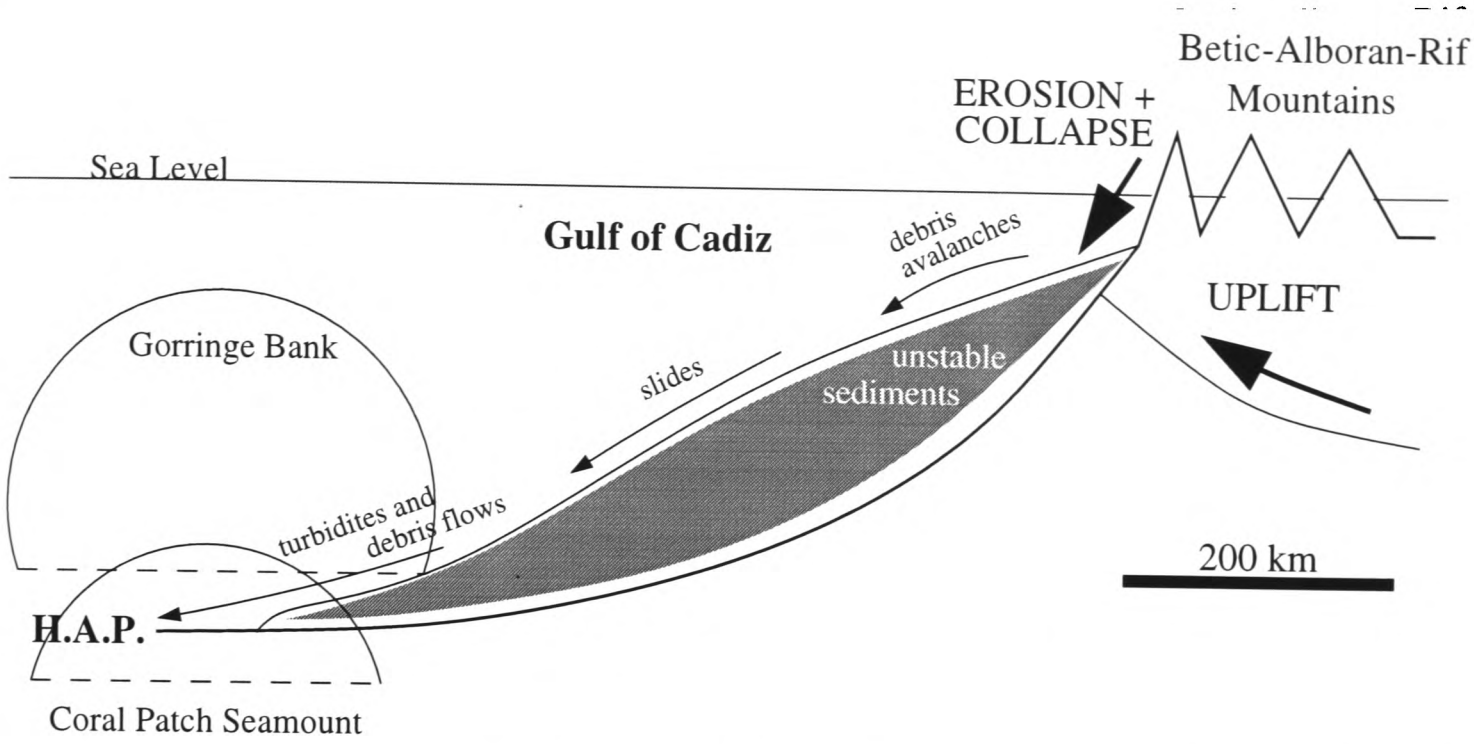


Figure 6.10: Model for the formation of the giant chaotic body in the Gulf of Cadiz and Horseshoe Abyssal Plain (H.A.P.), in the Upper Miocene.

Figure 6.10 illustrates the model suggested for the emplacement of the GCB west of the Gibraltar, in the Upper Miocene. At this time, NW–SW directed convergence between the African and Eurasian plates had produced deformation over a wide region, leading to the formation of a series of NE-SE oriented structures in response to the regional stress. These structures, included the Gorringe Bank (~10 Ma) and the Coral Patch Seamount chain [e.g., Purdy, 1975; Hayward *et al.*, 1999]. At the end of the Tortonian, the area now occupied by the Betic–Rif orogen and the Alboran Sea Basin was composed of elongate mountainous islands surrounded by marine basins [e.g., Watts *et al.*, 1993; Vissers *et al.*, 1995]. Uplift at the Coral Patch is thought to have commenced at ~20 Ma and at the Gorringe Bank at ~10 Ma, which both predate the emplacement of units of the GCB.

Figure 6.10 shows the situation in the Upper Miocene after the uplift of Gorringe Bank at 10 Ma. High rates of uplift in the Betics have been reported between 15–22

Ma [Zeck *et al.*, 1992], which would have resulted in high rates of erosion. It is inferred that the bulk of sediments produced by the uplift and westward tectonic transport of the Gibraltar Arc were deposited in flysch basins, and the subsident Gulf of Cadiz. The GOC basin filled with rapidly deposited sediments which included highly mobile shales and Triassic evaporites. The westward transport of the Betic–Rif orogenic uplift led to the formation of a wedge of sediment ahead of it, and this led to the accumulation of sediments on the GOC slope. Tectonic steepening of the slope led to gravitational instability and the production massive gravity–driven flows, which may also have been triggered by seismicity.

Sediments in Betic Rif foreland basins were constrained by the forebulge ahead of the advancing thrust load. The allochthonous chaotic units onshore were incorporated into accretionary wedges [e.g., Flinch *et al.*, 1996] as were the sediments of the central GOC slope (e.g., profiles GC1, GC3 in Figure 4.15, Figure 4.11) In the Seine Abyssal Plain the GCB also has the form of an accretionary wedge [Torelli *et al.*, 1997]. The HAP lobe of the GCB, however, is interpreted as being almost entirely due to gravity-driven mass flow, evidenced by its seismic character and long runout. This was due to the fact that sediments deposited in the GOC ahead of the advancing fold-and-thrust belt were not constrained by a forebulge, but were able to flow down a steep slope bounded by the South Iberian Margin to the north, and along a pre-existing deep trough between Gorringe Bank and Coral Patch chains (see Figure 6.1), which acted as a funnel for the sediment (see Figure 6.10). It is inferred that at the time of GCB emplacement, the dominant mass wasting process in the upper GOC slope would have produced debris avalanches (Figure 6.2), and in the mid–lower slope, slumping and slides would have been common. The long runouts seen in the HAP would have been the result of debris flows and turbidites, which may have been triggered by slide events upslope (Figure 6.10).

In summary, products of mass flow processes such as slides and olistostromes are thought to comprise much of the sediment seen infilling the basins of the study area, as observed on seismic data in this study. Seismically chaotic units are widespread in the area and it is thought that mass wasting, from avalanches to turbidites, has occurred along the Atlantic-facing Iberian and Moroccan continental margins over a down-dip distance up to 600 km west of the Gibraltar Straits, possibly lubricated by salts and clays. Tectonic oversteepening of the Atlantic facing Iberian-Moroccan continental margins through westward Gibraltar arc migration, salt and shale diapirism, seismicity and the presence of gas hydrates may all have contributed to mass wasting processes from the mid–late Miocene at this segment of the north Atlantic margin.

6.7 Conclusions

Recently acquired seismic reflection profiles from the 1993 Iberian Atlantic Margins (IAM) project have been used to study a giant, acoustically chaotic body which underlies the Iberian continental slope and parts of the Horseshoe and Seine Abyssal Plains west of Gibraltar. The data, acquired with a powerful 116 litre airgun array and a 192-channel 5 km long streamer, have been used to constrain the age, thickness and origin of the chaotic body.

Profile IAM-3, which crosses the Horseshoe Abyssal Plain and DSDP Site 135, suggests a mid-late Miocene age for the chaotic body. This age is comparable to the ages of similar chaotic deposits seen onshore in the Guadalquivir and Rharb foreland basins, which have been interpreted as subaqueous gravitational slumps deposited in the flexural depressions that flank migrating thrust and fold loads in the Betic and Rif orogens.

IAM profiles provide excellent coverage of the northern lobe of the chaotic body, beneath the Horseshoe Abyssal Plain. A simple seismic stratigraphic scheme was adopted for interpretation of the profiles and isochronopach maps derived. The isochronopach to isopach depth conversion was carried out using velocities from earlier refraction studies. The depth converted data indicates that the chaotic units form a lobate body beneath the Horseshoe Abyssal Plain, of a maximum thickness of 5 km beneath the base of the continental rise and thinning westwards over some 250 km.

Calculations of thickness and area allow a volume estimate of some 72,000 km^3 to be made for the HAP lobe of the chaotic body, which extends west of 8°W. In this region the HAP lobe has several features that suggest an origin through cumulative gravity-driven mass flow processes, as evidenced by the imaging of three individual flows on Profiles 4E and GB1.

Based on its large volume, seismic fabric and the regional physiographic and tectonic settings, the Horseshoe lobe is interpreted to be a giant cumulative mass wasting deposit from several pulses of slope failure caused by seismicity or tectonic oversteepening upslope near the Gulf of Cadiz "hinge" of the Gibraltar Arc (Betic and Rif orogens), associated with its westward movement and rapid uplift. The geometries observed on seismic profiles indicate that the chaotic units have an eastern origin, rather than being sourced from bathymetric highs flanking the Horseshoe Abyssal Plain. The pre-existing trough between Gorringe Bank and Coral Patch seamounts provided the accomodation space, and possibly the constraint which allowed long runouts, for the GCB.

Chapter 7

A Seismic Study of the Alboran Sea Basin in the Western Mediterranean

7.1 Introduction

The Alboran Sea is a semi–enclosed basin at the westernmost end of the Mediterranean. It is flanked by the Betic–Rif orogenic belt (Figure 7.1) and opens out to the east into the Algerian Basin (Figure 7.2), which is known to be floored by oceanic crust [Mauffret *et al.*, 1992]. This Neogene extensional basin is situated between the African and Eurasian plates, and formed in a region of overall convergence during the Miocene [e.g., Watts *et al.*, 1993]. The tectonic units of the Betic–Rif orogenic belt have been described in Section 2.2, which also describes the regional setting of the Alboran Sea Basin in relation to the Neogene basins of the western Mediterranean. The Internal Betic-Rif Zones are considered part of the Alboran Domain, most of which underlies the Alboran Sea. The ABS is known to be underlain by thin continental crust of a suite of metamorphic rocks similar to those found in the Internal Zones onshore [Comas *et al.*, 1992; Platt *et al.*, 1996]. The current Alboran Sea area was a Mesozoic marine basin that closed progressively in the Tertiary such that in the Oligocene an emergent collisional orogen stood in its place [Platt & Vissers, 1989]. Early to mid-Miocene extension and subsidence created the present-day Alboran Sea Basin, and smaller onshore basins [Watts *et al.*, 1993], accompanied by volcanism [Hernandez *et al.*, 1987]. From the Messinian a regional transpressional regime prevailed [e.g., Watts *et al.*, 1993], and the Betic-Rif was uplifted while the Alboran Sea subsided [Vissers *et al.*, 1995]. This apparent paradox of extension within a collisional setting has led to much interest in this basin, and the proposal of a number of models to explain its formation, which have been outlined earlier (Section 2.2.4).

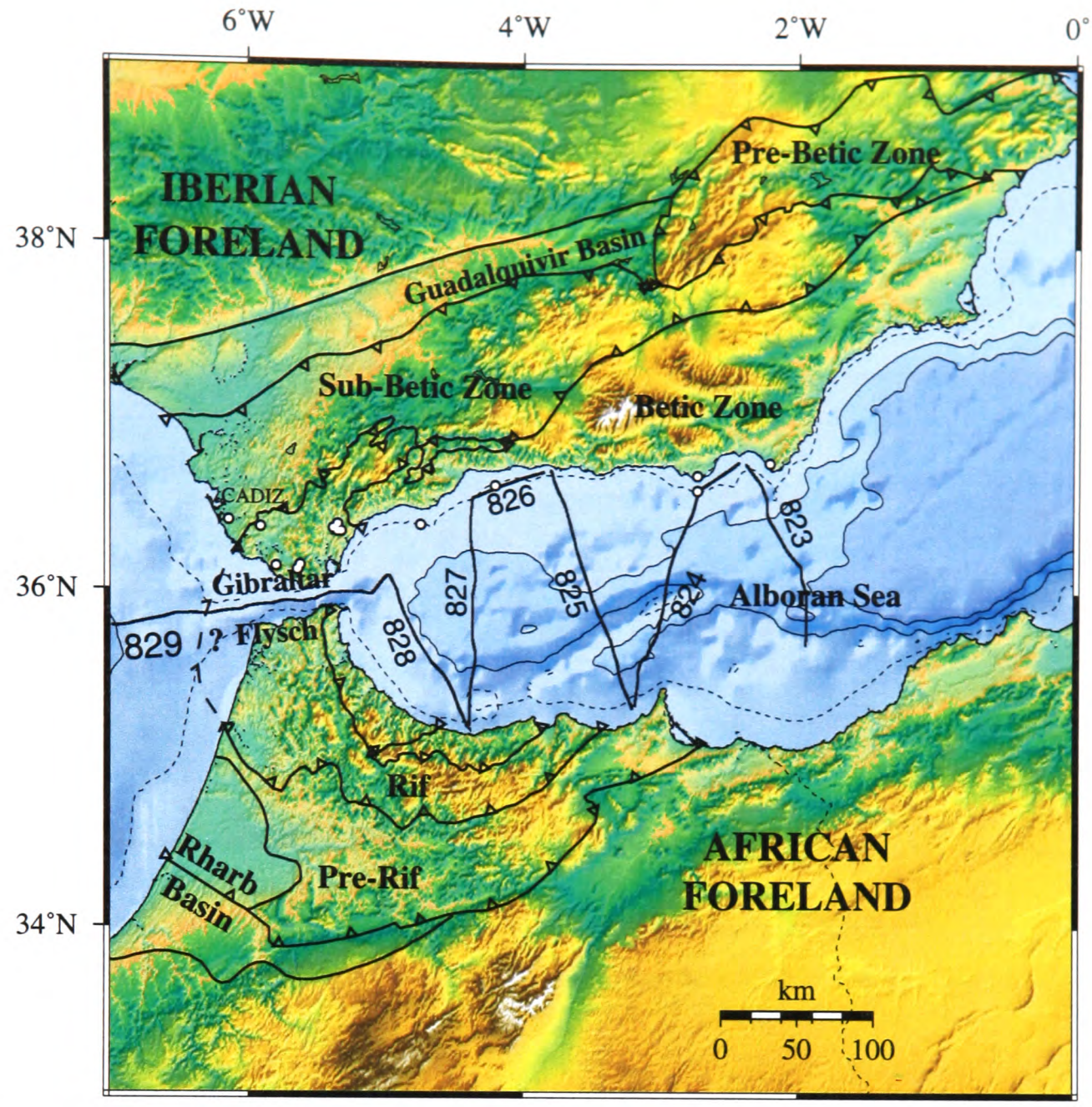


Figure 7.1: Location of the Alboran Sea Basin in relation to elements of the Betic–Rif orogenic belt, superimposed on relief. Bathymetry contoured at 1000m intervals. Lines of LDGO RC2911 cruise shown and labelled. See Section 2.2 for detailed description.

The Alboran Sea has a number of bathymetric features, which are shown on Figure 7.2. The largest of these is the volcanic Alboran Ridge (Figure 2.2), which rises to the surface at Alboran Island. The seafloor morphology separates the Alboran Sea Basin into three sub–basins of the West Alboran, South Alboran and East Alboran Basins (Figure 7.2). The SW–NE trending Alboran Ridge separates the shallower West Alboran Basin from the deeper sub-basins between it and the oceanic Algerian Basin to the east [e.g., Willet, 1996].

The work described in this study was undertaken as a contribution to a synthesis paper on the origin and tectonic history of the Alboran Basin, for the ODP, Scientific Results, Leg 161 volume [Comas *et al.*, 1999]. Multichannel seismic profiles of the 1989 cruise of the R/V Conrad (RC2911 cruise) in the western Mediterranean were re-processed,

migrated and interpreted on the basis of the improved images. The processing is described in detail in Section 3.5. The aim of the study in the Alboran Sea was to produce an improved interpretation of regional profiles of the RC2911 cruise, to better constrain the present day distribution of sediments and deep structures, with which the development of the main features of the Alboran Sea Basin could be analysed.

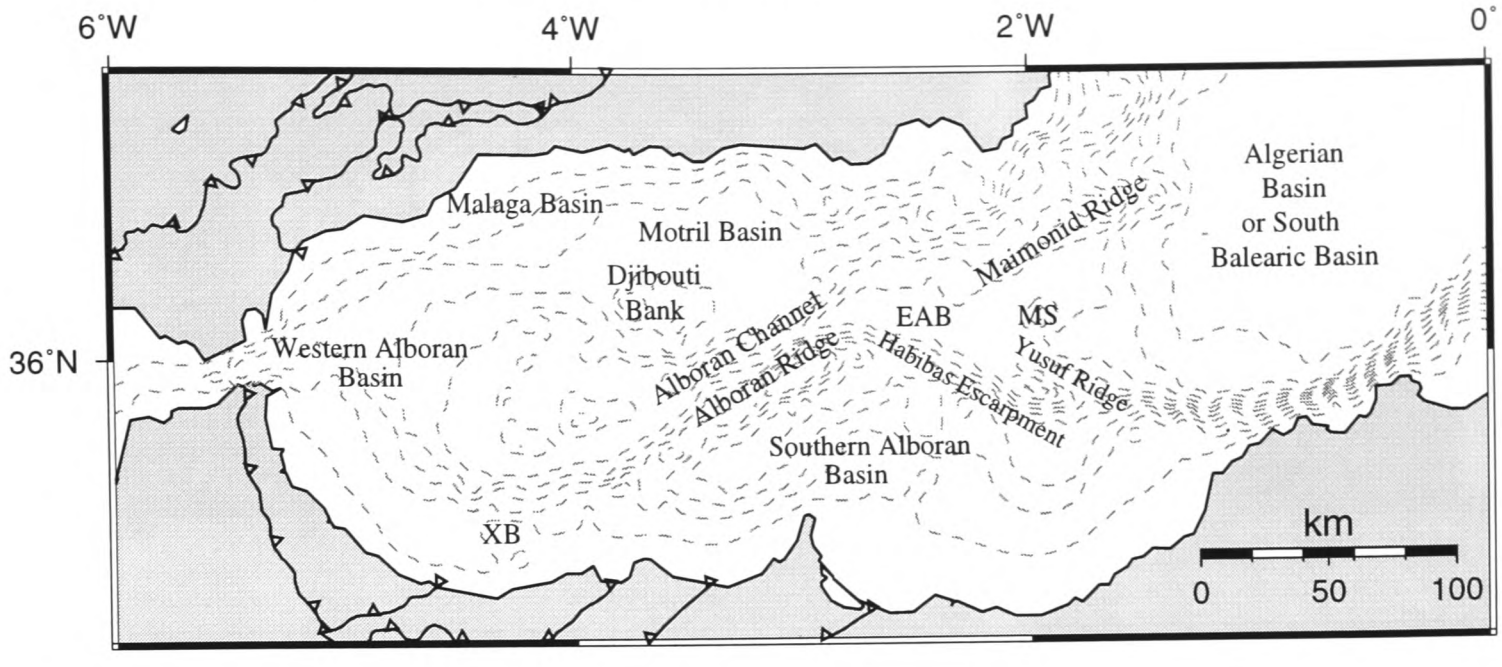


Figure 7.2: Major bathymetric features of the Alboran Sea Basin. EAB = East Alboran Basin; MS = Mansour Seamount; XB = Xauen Bank. Bathymetric contours every 250m.

7.2 Methodology

Multichannel seismic data of cruise RC2911 were acquired in the western Mediterranean in 1989 by the Lamont–Doherty Geophysical Observatory (LDGO) vessel *R/V Robert D. Conrad.* The locations of the profiles from this cruise are shown in Figure 7.1. Processing and interpretation of these data was carried out at Oxford University. The original data was in stacked form, but only 827 had previously been migrated [Watts *et al.*, 1993]. On the original profiles the basement was not always well defined, and many structures were obscured by diffraction hyperbolae [e.g., Watts *et al.*, 1993]. These images were improved by migration, and post-stack filtering (e.g., Figure 3.13). Time migration using a variation of Gazdag's phase-shift method was applied to the stacks of Lines 823 and 827; Lines 824 and 825 were migrated using Stolt's F-K method.

Figure 7.3 shows the locations of the four regional seismic lines included in this study, numbered 1 to 4 and shown as thick lines. These were tied with commercial and ODP Leg 161 well data (locations shown in Figure 7.3, well data in Figure 7.4).

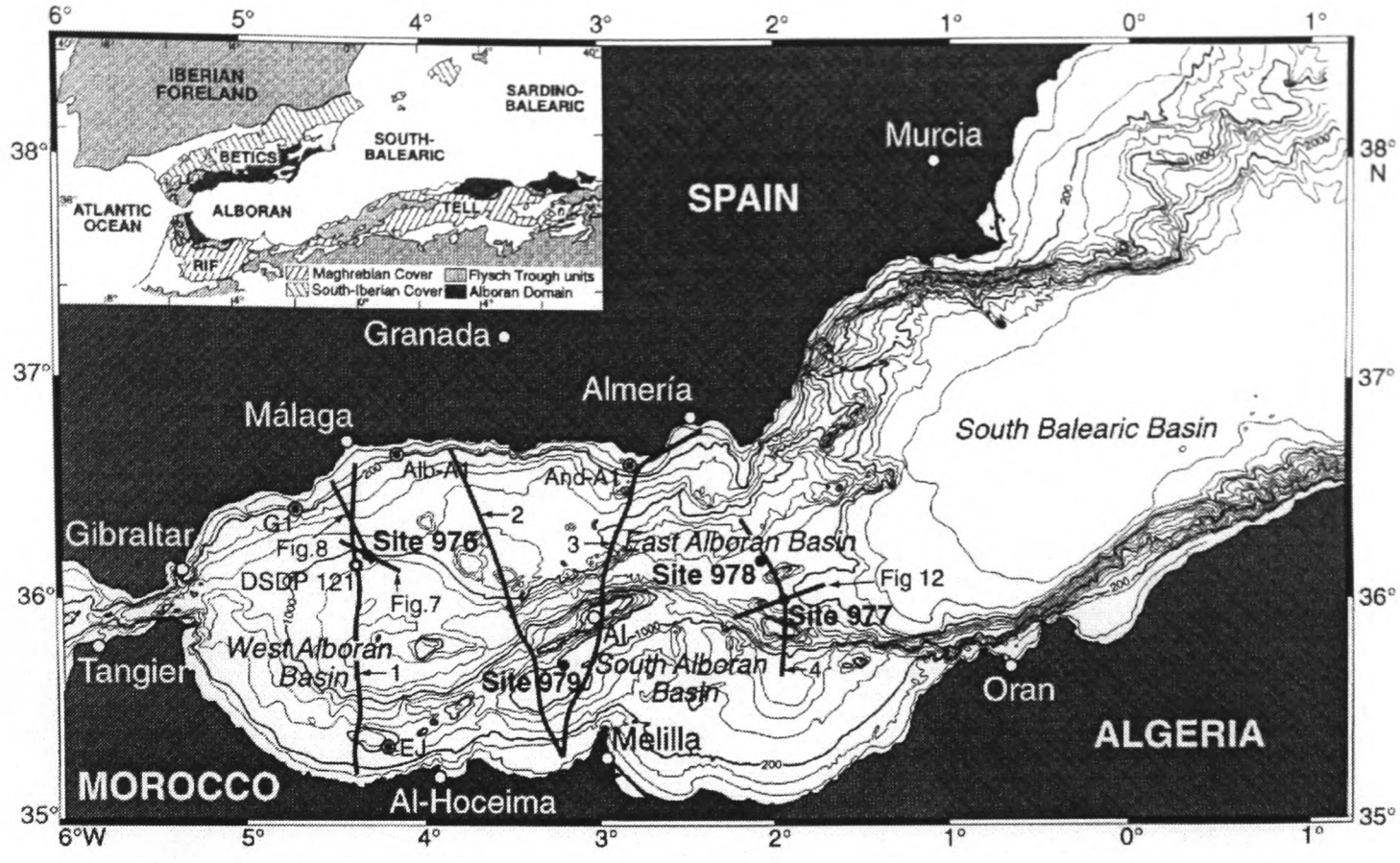


Figure 7.3: Seismic profile and well locations in the Alboran Sea Basin. Location of *Conrad* RC2911 data: 1 = Line 827; 2 = 825; 3 = Line 824; 4 = Line 823. Commercial wells: G1 = Andalucia G1, Alb-A1 = Alboran A1, And-A1 = Andalucia A1, EJ = El Jebha. ODP Leg 161 well sites 976, 977, 978, 979 are labelled, as is the older DSDP Site 121.

Figure 7.4 illustrates the ages of sediments drilled in the ABS, the oldest of which are biostratigraphically dated to the Early Miocene (well Alboran-A1). The seismic stratigraphic scheme of Comas *et al.* [1992] is shown, which divides the basin fill into six units: Unit I correlates with Pliocene to Recent sediments, and Units II–VI are subdivisions of rocks of Miocene age. For the basinwide interpretation carried out in this study, a simpler scheme was adopted. An acoustically bright, basin-wide erosional unconformity is known to correlate with the top of the Messinian evaporite sequence recognized throughout the Mediterranean (the "M"-reflector of Ryan *et al.* [1973]). This Messinian unconformity was a useful marker horizon [e.g., Watts *et al.*, 1993] and was picked on all the profiles, thus dividing the basin fill into Pliocene–Recent sediments of Unit I above from Miocene sediments below, on a seismostratigraphic basis. Hummocky, chaotic reflections associated with volcanic features, such as the Alboran Ridge, were interpreted to be Miocene volcanics [J.Platt, pers. comm.]; the base of these deposits was interpreted. The top of metamorphic basement was interpreted on the basis of a change to a uniform seismic character, and on the basis of the well Andalucia-A1 which drilled basement (see Figure 7.4, and profile 824 in Figure 7.5). Finally, structures were also interpreted, including faults and intra–basement reflectivity. The new migrated

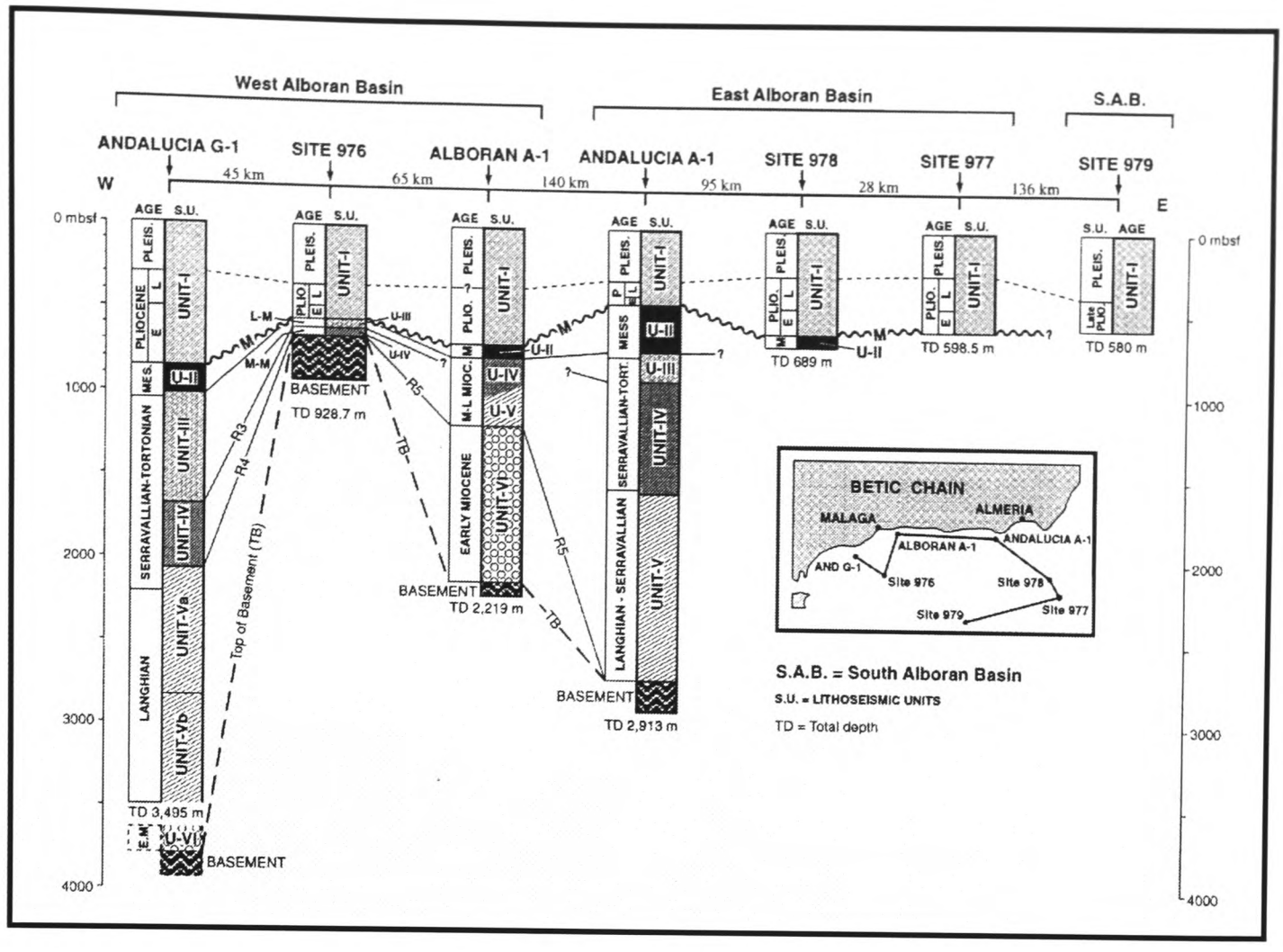


Figure 7.4: Correlation of ODP and commercial wells in the Alboran Sea Basin. M = Messinian unconformity, TB = Top of Basement. Seismic units (S.U.) are those of Comas *et al.* [1992]. Figure taken from Comas *et al.* [1999].

images and interpretations produced in this study, for the regional profiles 823, 824, 825, and 827, have since been published in the regional synthesis paper of Comas *et al.* [1999].

7.3 Observations from Seismic Profiles

The profiles are displayed as uninterpreted profiles at upper plots, and the lower plots are interpretations. The following abbreviations are used: M = Messinian unconformity; B = top of acoustic basement; BV = interpreted base of Miocene volcanics above metamorphic basement; ICR = intracrustal reflectors, possibly representing mylonite zones along extensional detachments [Watts *et al.*, 1993]; TRLC = interpreted top of reflective lower crust. Faults are shown as heavy lines. Numbers on the lines are points referred to in the text. The profiles are discussed in east to west order.

Conrad Line 823

Figure 7.5 of Line 823 images across the East Alboran Basin (Line 4, Figure 7.3). Chaotic reflectivity, with some internal layering, is observed in the lowest sections (2 s

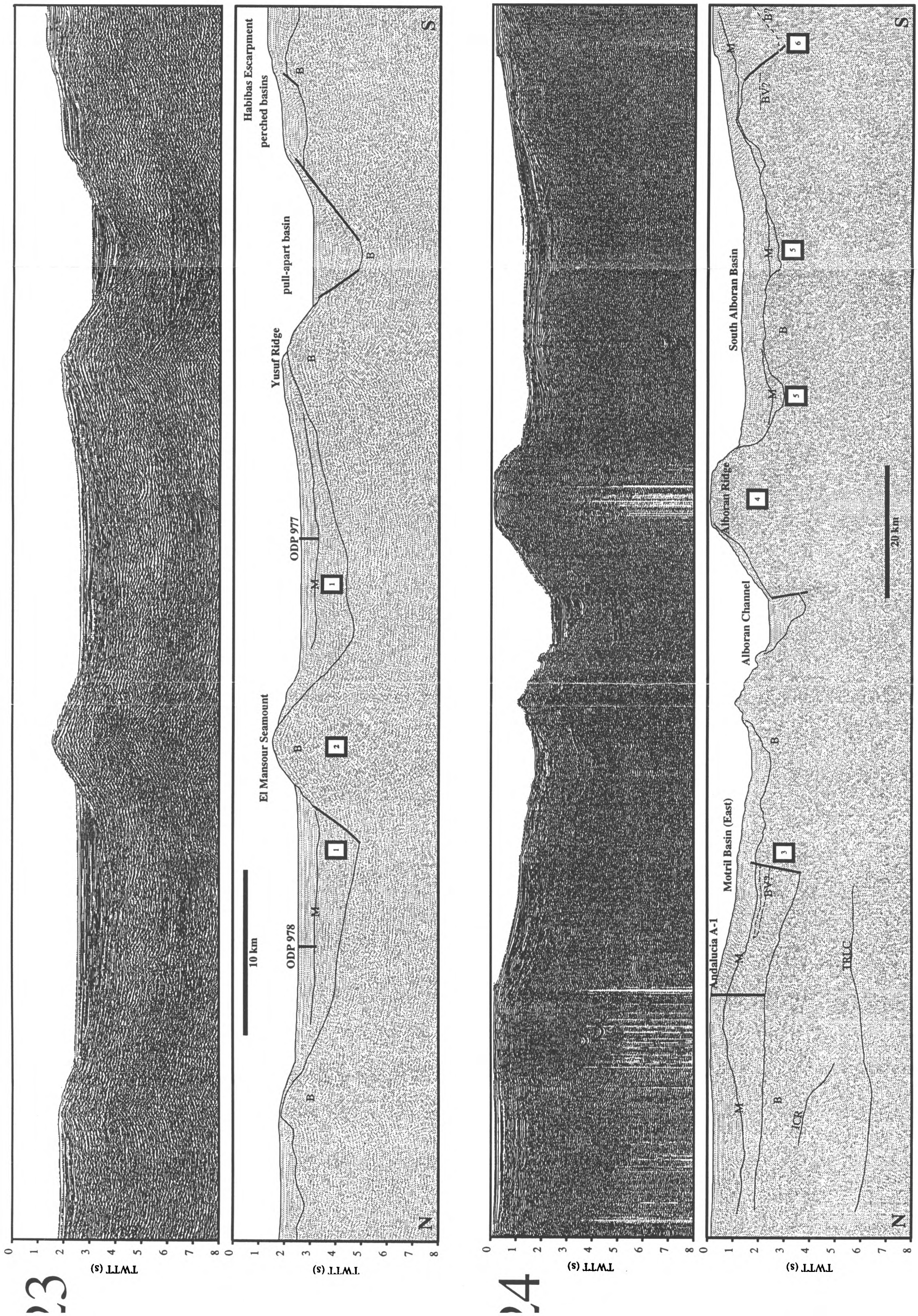


Figure 7.5: RC2911 Profiles 823 and 824. See text for explanation

TWTT thick) of the sub-basins basins imaged either side of Mansour seamount, which is of volcanic origin [Willet, 1996]. This is interpreted to be caused by interlayered sedimentary and volcanic material (Point 1, 823, Figure 7.5). El Mansour seamount is a volcanic feature which may be fault-bounded, but faulting would predate the M-reflector, which onlaps onto it (Point 2, 823, Figure 7.5). However, the symmetry and thickening towards the seamount of the basins flanking it, are reminiscent of a flexural moat, as seen around many ocean islands and seamounts [e.g., Watts & ten Brink, 1989; Watts, 1994]. However, there is insufficient seismic data around the seamount to confirm this hypothesis. ODP wells 977 and 978 have penetrated the Recent–Pliocene section in these basins, but not into the deposits beneath the M-reflector.

The rhomboid–shaped basin at the south end of the profile is bounded by faults marking the edges of the Yusuf Ridge and Habibas Escarpment. The Yusuf Fault bounding the Yusuf Ridge is thought to be part of a major strike–slip fault system [Comas *et al.*, 1999] and the rhomboid-shaped basin has been interpreted as a pull–apart basin [e.g., Zahn *et al.*, 1999]. From the profile, this appears to be inactive at the present day, whereas the fault bounding the Habibas Escarpment to the south appears to be a former normal fault re-activated by compression, as evidenced by the uplift of the "perched basins" to the south. On GLORIA data discussed by Willet [1996], surface features from the southern margin of the Alboran suggested strike-slip motion through their continuation into onshore structures.

Conrad **Line 824**

This profile in Figure 7.5 images the central part of the Alboran Sea, from the East Alboran Basin in the north to the South Alboran Basin to the south, across the Alboran Ridge (Line 3, Figure 7.3). Acoustic basement is not always easily picked, for example south of the N-dipping normal fault beneath the Motril Basin (Point 3, 824, Figure 7.5) where the basement is probably middle to late Miocene volcanics, coeval with sediment in the basin to the north of the fault. Volcanics may be interlayered with sediments across the fault and wedge out to the north.

Sediments are less thick than seen on Line 823, varying from 1–2 s TWTT total thickness, with a thin Miocene succesion beneath the South Alboran Basin which appears to infill basement topography (Point 5, 824, Figure 7.5). These localized packages of sediment, possibly intercalated with volcanics, occur below the M-reflector. The nature of the acoustic basement in this region is uncertain, but it is probably volcanic.

An unknown thickness of volcanic rocks forms the acoustic basement beneath the Alboran Ridge and the adjacent basins (Point 4, 824, Figure 7.5). The attitude of the young S-dipping reverse (or transpressive) fault on the north side of the Alboran Ridge and its continuation to depth are poorly constrained, but indicates compression. The Alboran Ridge has been interpreted by Comas *et al.* [1999] to be a pop-up structure relating to a sinistral strike–slip system.

Conrad Line 825

This NW–SE profile shown in Figure 7.6 images across the Djibouti Bank, which forms the southern limit of the Motril Basin, and the Alboran Ridge to the south (Line 2, Figure 7.3). The top of basement can generally be picked, and is interpreted to be overlain by Miocene volcanics in some regions, such as below the Djibouti Bank, where the base of volcanics and their thickness is obscured by strong multiples (Point 8, 825, Figure 7.6). The acoustic basement beneath the Alboran Ridge and the adjacent basins is probably volcanic, with discontinuous reflections at depth (BV?) which may mark the base of the volcanic sequence (e.g., Point 9, 825, Figure 7.6). A lenticular body of volcanic rocks may form the upper part of the acoustic basement beneath the South Alboran Basin (Point 10, 825, Figure 7.6). The attitude of the young S-dipping reverse (or transpressive) fault on the north side of the Alboran Ridge is better constrained here than on Line 824 in Figure 7.5.

Conrad Line 827

Line 827 in Figure 7.6 is the only profile in this study which images across the West Alboran Basin (Line 1, Figure 7.3). The thickest depocentres (up to 5 s TWTT thick) in the Alboran Sea are found in the West Alboran Basin [Comas *et al.*, 1992; Willet, 1996], and two thick basins can be seen on Line 827, separated by a basement high which has been drilled at ODP site 976. A ~1 s TWTT thick succesion of Unit I sediments drapes the "976 High" and covers the Malaga and West Alboran Miocene basins, before thinning and pinching out against the faulted nothern parts of the Xauen Bank (Figure 7.6).

The "976 High" is a basement high bounded by normal faults active in the Miocene, but which are inactive today, as can be seen in the lack of deformation in the sediments above the high (e.g., Point 12, 827, Figure 7.6). The thick sediments in the West Alboran Basin depocentres are associated with extensive mud diapirism, but mud diapirs are not observed on Line 827. However, sediments imaged on Line 828 of the RC2911 cruise are affected by extensive mud diapirism (Figure 7.1, Fig. 9 in Watts *et al.* [1993], Willet

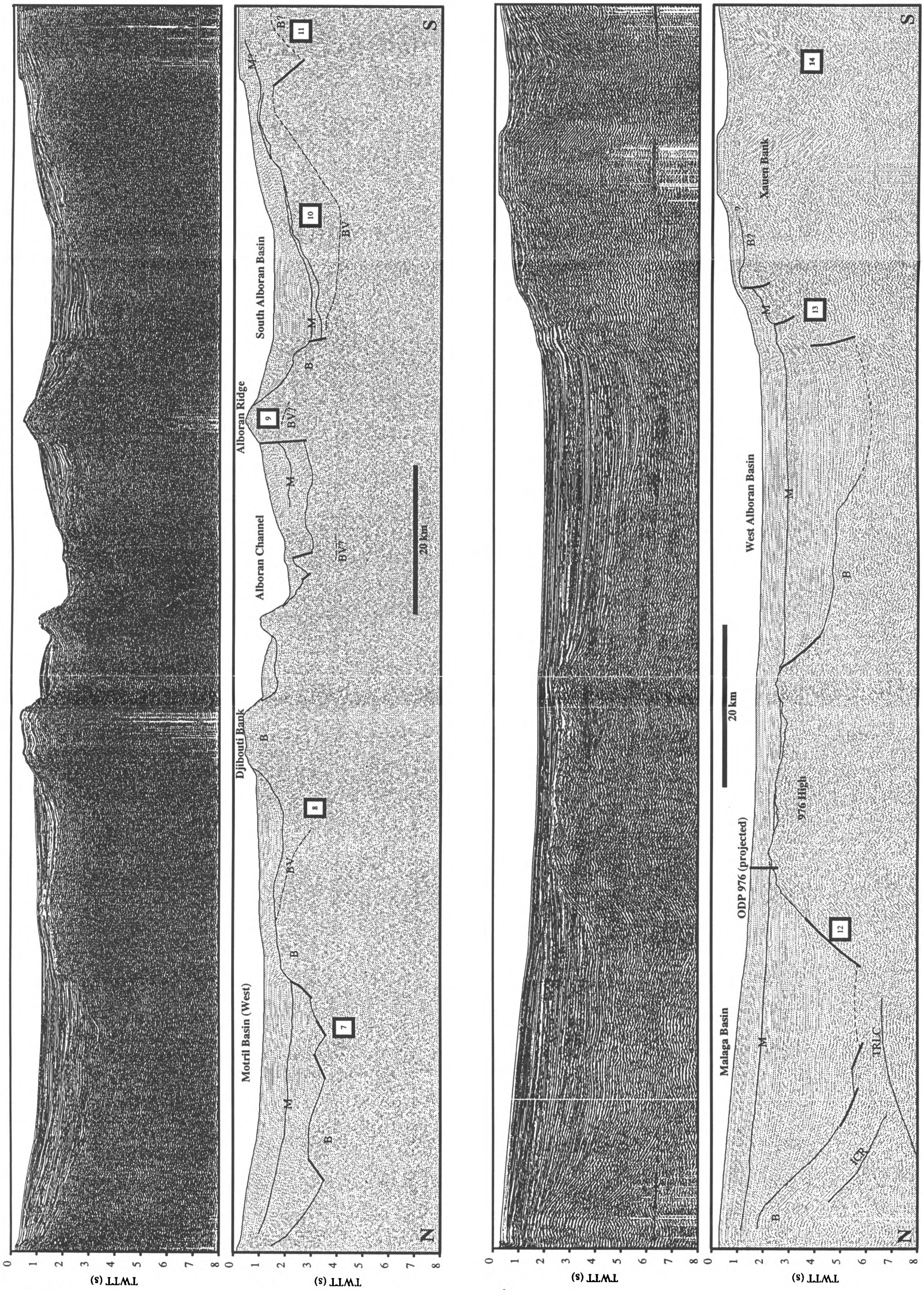


Figure 7.6: RC2911 Profiles 825 and 827. See text for explanation

[1996]). Post–Miocene compression has been taken up largely on reverse faults seen bounding the Xauen Bank at the south end of Line 827, a feature which Comas *et al.* [1999] have interpreted as being a strike-slip feature asscociated with the Alboran Ridge (see Figure 7.2).

A south–dipping intra-crustal reflection (ICR) is seen between 4–7 s TWTT beneath the northern end of Line 827, Figure 7.6, and is similar to an ICR seen between 3–5 s TWTT on Line 824 (Figure 7.5). Layered lower crust is also seen as high amplitude laminar reflections beneath these ICRs on both profiles 824 and 827, between 4–8 s. The top of this deep layering is shown by the TRLC reflection marked on Figure 7.5 and Figure 7.6. The dipping ICRs have previously been reflected as extensional shear zones associated with the early Miocene rifting of the Alboran Sea. The top of the reflective lower crust probably marks the compositional Conrad discontinuity in the crust [e.g., Meissner *et al.*, 1986].

7.4 Conclusions

- Migration and dip filtering have improved the interpretability of regional seismic profiles of Conrad cruise RC2911 across the Alboran Sea.
- The thickest sediments were observed in the West Alboran Basin where thick Miocene successions were up to 5 s TWTT thick, indicating a thickness of several kms.
- A large volume of volcanic material is present in this basin, both overlying basement, and as ridges and seamounts. This is related to thinning and heating of the crust during Miocene rifting [e.g., Watts *et al.*, 1993; Willet, 1996].
- A possible flexural moat has been observed around El Mansour seamount.
- Normal faulting has been observed affecting Miocene sediments in the West Alboran Basin, indicating an extensional regime in the Miocene. Reverse faults are seen bounding the Alboran Ridge and Xauen Bank basement highs, indicating a compressive regime after the Miocene. Strike-slip systems also affect the present day ABS, and have produced a pull–apart basin south of the Yusuf fault.
- South-dipping intracrustal reflections and layered lower crust have been imaged on Lines 824 and 827. These may be associated with the early Miocene rifting of the Alboran Sea, although the lower crustal layering may have been a feature of the crust prior to stretching.

Chapter 8

Conclusions

The goal of this research was to use marine geophysical techniques to understand a tectonically complex area at the convergent eastern segment of the Azores–Gibraltar plate boundary zone between Africa and Eurasia, offshore southern Iberia. New multichannel seismic reflection images have been produced and interpreted, in conjunction with previous geophysical and geological data, to study structure, sedimentary fill, and evolution of the Gulf of Cadiz continental margin, the Gorringe Bank Region (GBR) and the Alboran Sea (ABS) in the western Mediterranean. The main findings of this research are summarised below.

8.1 Gulf of Cadiz

Five major seismic stratigraphic units. The sediments are of Triassic to Recent in age, and rest on a Hercynian basement which is a seaward extension of the Iberian Massif. A complex tectonic history is indicated by the presence of extensional, compressional and diapiric structures, and the widespread occurrence of allochthonous sediments.

Backstripping of well data in the Gulf of Cadiz have indicated a period of rapid subsidence in the Late Jurassic (154.1 Ma) which correlated with magnetic anomaly M25 (157 Ma) in the NE Atlantic - the oldest magnetic spreading anomaly west of the Gulf of Cadiz. This rifting phase was followed by a long period of gentle tectonic subsidence, reflecting post-rift cooling when the region as a whole was a passive margin. The tectonic subsidence curves revealed an accelerating subsidence in the Miocene as a foreland basin developed ahead of the advancing Betic–Rif thrust wedge.

Prominent SE–dipping reflections in the western Gulf of Cadiz are interpreted to be due to a reflective lower crust about three seconds thick, typical of Hercynian crust in southwest Europe [e.g., Watts *et al.*, 1990]. These reflections stop below a zone of tilted basement/Mesozoic fault blocks and an overlying graben structure, which may indicate these originated with rifting with an asymmetric simple shear component. Alternatively, strike slip motion may have juxtaposed two different crusts.

β values averaging 1.2–1.5 were obtained from wells in the northeast Gulf of Cadiz, using a finite duration rifting model, with a Upper Jurassic time of rifting and a rift duration of ~10 Ma. Assuming an unstretched crustal thickness of 35 km, these results produced backstrip Moho estimates that were in agreement with seismic refraction/wide-angle reflection data of González *et al.* [1998]. This suggests that the thinned crust observed in the NE Gulf of Cadiz at the present day is a relict of the original rifting event.

The high-low-high saddle-shaped gravity anomaly pattern observed in Gulf of Cadiz is interpreted as being due to variations in crustal thinning, as confirmed through gravity modelling and power spectrum analysis of the free-air gravity anomaly over profile GC1 [e.g., Karner & Watts, 1983; Coudert *et al.*, 1995]. The gravity low is associated with a sedimentary depocentre whereas the adjacent gravity highs are associated with zones of localised crustal extension, the North and South Gulf of Cadiz Thinned Zones, which trend parallel to Betic and Rif structures.

Mapping and contouring of stretching factors reveals lateral zones of thinning in the Gulf of Cadiz, which trend away from the margin. These are thought to be a result of Mesozoic rifting, subsequent lateral movements and the structure of the Betic–Rif belt. A possible continent–ocean boundary zone runs approximately at the base of the continental slope, on the basis β >4 produces oceanic crust.

The first reported gas hydrate occurrence from the eastern margin of the central Atlantic, has been inferred from the presence of a bottom-simulating reflection (BSR) and acoustic blanking on two MCS profiles from the Gulf of Cadiz. The BSR is observed in slope sediments at water depths of 1275–1575 m (1.7–2.1 s TWTT) and from 0.4–0.5 s TWTT beneath the seabed. Velocities implied hydrate concentrations were low above the BSR, and that gas volumes below the BSR may be <1% of pore volume. A positive reflection beneath the BSR may mark a base of the gas layer, which may be up to 36 m thick. BSR reflection coefficients varied from -0.02 to -0.07, which were comparable to values observed from a BSR off the Cascadia Margin [Fink & Spence, 1999]. The BSR may cover 3500 km^2, but this may be an underestimate if hydrate exists at depths below 1575 m. The extent of the BSR implies that hydrates are limited to a local concentration in the Gulf of Cadiz. Possible migration pathways between the BSR region, a system of longitudinal diapiric ridges and valleys (and associated faults), and gas–affected sediments in the upper slope and shelf area have been mapped.

Mass wasting associated with free gas has been noted in certain areas of the Gulf of Cadiz. Large mass wasting events appear to have been recorded in the Pliocene to Recent sediments of intraslope basins downslope of the Gibraltar Straits. It has been shown that bottom waters were up to 5°C colder before the onset of the Mediterranean outflow, and so hydrates would have been stable at much shallower depths. Dissociation of these hydrates caused by the warm Mediterranean Outflow Water at the early Pliocene highstand may have been responsible for the observed mass wasting in Pliocene sediments.

8.2 Gorringe Bank and Horseshoe Abyssal Plain

Recently acquired seismic reflection profiles were used to study a giant, acoustically chaotic body which underlies the Iberian continental slope from the Gulf of Cadiz to the Horseshoe and Seine Abyssal Plains west of Gibraltar. The data, acquired with a powerful 116 litre airgun array and a 192-channel 5 km long streamer, have been used to constrain the age, thickness and origin of the chaotic body.

Seismic data correlated with core data from DSDP Site 135, suggests a mid-late Miocene age for the chaotic body. This age is comparable to the ages of similar chaotic deposits seen onshore in the Guadalquivir and Rharb foreland basins, which have been interpreted as subaqueous gravitational slumps deposited in the flexural depressions that flank migrating thrust and fold loads in the Betic and Rif orogens.

A simple seismic stratigraphic scheme was adopted for interpretation of the profiles and an time thickness map of the chaotic body was produced, which was subsequently depth converted to produce an isopach. Depth conversion was carried out using velocities from earlier refraction studies. The depth converted data indicates that the chaotic units form a lobate body beneath the Horseshoe Abyssal Plain, of a maximum thickness of 5 km beneath the base of the continental rise and thinning westwards over some 250 km.

Calculations of thickness and area allow a volume estimate of some 72,000 km^3 to be made for the HAP lobe of the chaotic body, which extends west of 8W. In this region the HAP lobe has several features that suggest an origin through cumulative gravity-driven mass flow processes, as evidenced by the imaging of three individual flows on Profiles 4E and GB1.

Based on its large volume, seismic fabric and the regional physiographic and tectonic settings, the Horseshoe lobe is interpreted to be a giant cumulative mass wasting deposit from several pulses of slope failure caused by seismicity or tectonic oversteepening

upslope near the Gulf of Cadiz "hinge" of the Gibraltar Arc (Betic and Rif orogens), associated with its westward movement and rapid uplift. The geometries observed on seismic profiles indicate that the chaotic units have an eastern origin, rather than being sourced from bathymetric highs flanking the Horseshoe Abyssal Plain. The pre-existing trough between Gorringe Bank and Coral Patch seamounts provided the accomodation space, and possibly the constraint which allowed long runouts, for the GCB.

8.3 The Alboran Sea

A variety of structural features observed on reprocessed and re-interpreted seismic data provide evidence for the extensional nature of the Alboran Sea, and a transpressive regime after the Messinian. Normal faulting has been observed affecting Miocene sediments in the West Alboran Basin, indicating an extension in the Miocene. Reverse faults are seen bounding the Alboran Ridge and Xauen Bank basement highs, indicating a compressive regime after the Miocene. Strike-slip systems also affect the present day ABS, and have produced a pull–apart basin south of the Yusuf fault. South-dipping intracrustal reflections and layered lower crust have been imaged on Lines 824 and 827. These may be associated with the early Miocene rifting of the Alboran Sea, although the lower crustal layering may have been a feature of the crust prior to stretching.

The thickest sediments were observed in the West Alboran Basin where thick Miocene successions were up to 5 s TWTT thick, indicating a thickness of several kms. A large volume of volcanic material is also present in this basin, both overlying basement, and as ridges and seamounts. This is related to thinning and heating of the crust during Miocene rifting [e.g., Watts *et al.*, 1993; Willet, 1996]. A possible flexural moat has been observed around El Mansour seamount.

8.4 Further Work

Stratigraphy and Basin Structure There is reasonable deep reflection seismic coverage of the Gulf of Cadiz margin, but there is a lack of published data from the Atlantic margin of Morocco. Greater well coverage, particularly in the lower continental slope and abyssal plain areas, would have been helpful in accurately identifying the ages of sediments and the therefore the evolution of the basin on a seismostratigraphic basis. Data on the offshore crustal structure is also sparse, and a reversed refraction profile, using the latest digital ocean bottom seismometers, across the Gulf of Cadiz slope to Horseshoe Abyssal Plain, would clarify the debates about the position of the OCT, the nature of

the crust beneath the Horseshoe Abyssal Plain, and the position of the African-Eurasian plate boundary. An east-west refraction experiment across the Straits of Gibraltar would be pivotal in resolving the arguments about the causative mechanism of the Miocene extension in the Alboran Sea Basin.

Hydrates Further work on gas hydrates is suggested, as these may be a possible future energy resource, as well as an important factor in stability studies of the Gulf of Cadiz slope, which has been associated with tsunamis in the recent past. Further work on seismic data involving detailed velocity analysis, amplitude-variation-with-offset (AVO) analysis, and waveform inversion should be carried out to ascertain what earth models produce the best fit to the observed BSR. Drilling would provide useful tests of such models, and information on the chemistry and habitat of the hydrates. The preliminary indications of low hydrate and gas concentrations on the basis of this study, suggest that the Gulf of Cadiz hydrate deposits may have low economic potential for future exploitation.

Hydrocarbon potential Pratsch [1996], in a study of the oil and gas potential of the Prerif foreland basin of Morocco, has looked at the implications for petroleum geology of the intra-Tortonian chaotic unit ("olistostrome") within the Miocene sediments, which is very similar to that found in the Guadalquivir foreland basin and GOC. The unit can act as a regional seal, due to its impermeable clay matrix. The basal detachment and salt tectonics also cause two tectonic levels separated by the chaotic layer. A thick chaotic unit overburden has a thermal effect on underlying potential source beds. The same arguments can be applied to similar plays such as the GOC. Successful hydrocarbon plays beneath olistostromes have been reported in southern France, eastern Italy and Sicily and eastern Turkey [Pratsch, 1996]. An idea of a play involving allochthonous blocks in the GOC chaotic unit as hydrocarbon traps, with salt or clay seals, has recently been suggested [Somoza *et al.*, 1999]. This seems plausible in the light of this study and may merit further work.

Appendices

Appendix A

Regional datasets

This section describes study-wide datasets that have been compiled from commercial and published sources, for use throughout this thesis. The compilation and processing of relief, gravity, borehole, seismicity, and heat flow data are described.

A.1 Topography/Bathymetry

Figure A.1 is a map of relief constructed from the synthesis of three datasets. Onshore relief is based from the public domain USGS GTOPO30 dataset, which is a global digital elevation model (DEM) resulting from a collaborative effort led by the staff at the U.S. Geological Survey's EROS Data Center in Sioux Falls, South Dakota. Elevations in GTOPO30 are regularly spaced at 30 arc seconds (approximately 1 kilometer). Over the study area of this thesis, the data has been resampled from a 3 arc seconds resolution (approximately 90 m) Digital Terrain Elevation Database (DTED) produced by the National Imagery and Mapping Agency (NIMA) of the USA. Alboran Sea bathymetric relief was constructed from available ship data from a cruise database pioneered at the Lamont-Doherty Earth Observatory (GMT database, see Wessel & Watts [1988], which include 3.5 kHz and 12 kHz echosounder records reported in Willet [1996]. West of Gibraltar ($\sim 5^{\circ}$W) the cruise database had relatively sparse and non-uniform coverage, and so relief data from the Western Europe Gravity Project (WEEGP) data base, compiled by GETECH at Leeds, were used. WEEGP relief data were supplied as a 4 km grid, which was converted to latitude-longitude points before smoothing over $2.5'$ x $2.5'$ squares and gridding on a $5'$ grid using a curvature spline in tension technique [Smith & Wessel, 1990].

A.2 Gravity

Figure A.2 is a composite gravity anomaly map, compiled from onshore West European Gravity Project (GETECH Leeds) Bouguer data, and offshore satellite-derived free-air gravity measurements [Sandwell & Smith, 1997]. The onshore Bouguer gravity data of

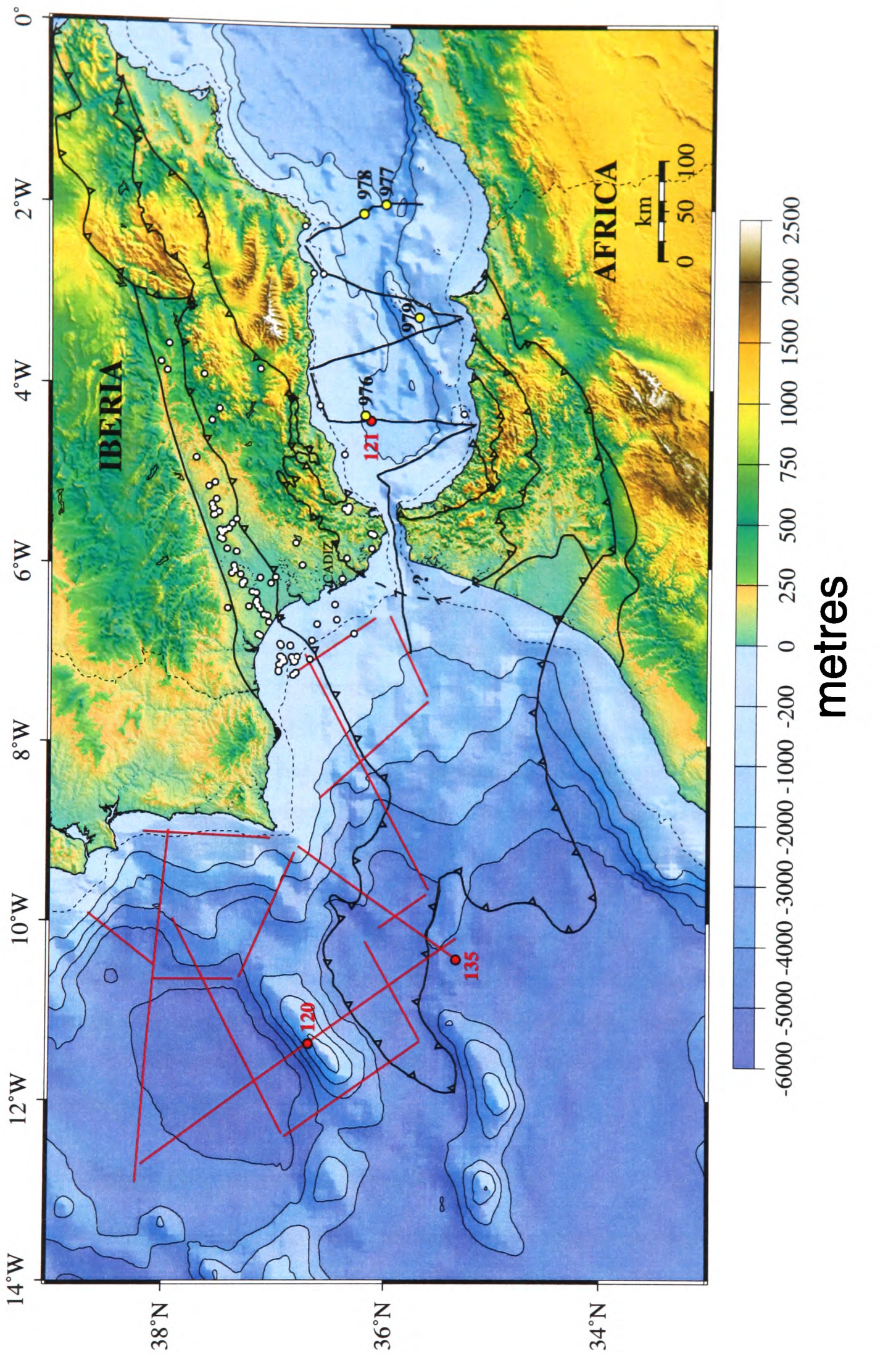


Figure A.1: Illuminated relief map and well locations in the study region. DSDP wells shown as circles filled in red, ODP wells as circles filled in yellow, and other well locations from IGME [1987] shown as circles filled in white. Multichannel seismic data is also shown: IAM in red, RC2911 in black. Bathymetric contours at 1000m intervals, plus dashed line for the 200m shelf break.

the Western Europe Gravity Project (WEEGP) data base were smoothed and gridded on a $5'$ grid using a curvature spline in tension technique [Smith & Wessel, 1990]. This data was then resampled at 2 arc min intervals and spliced with the offshore 2 arc min x 2 arc min free-air anomaly dataset of Sandwell & Smith [1997]. The resulting anomaly map provides important information for interpretation of crustal structure.

Several prominent anomalies are labelled A-J on Figure A.2, illustrating major tectonic trends. The composite map here details the regional gravity field more comprehensively than previous work such as Roberts [1970]; Bonini *et al.* [1973]. Anomalies **A, B, C** trend approximately perpendicularly to the direction of Africa–Eurasia convergence [Dewey *et al.*, 1989] and are associated with the seafloor highs of Gorringe Bank, Coral Patch Seamount and Ridge respectively.

On the margins west of the Gibraltar Straits, the free-air anomaly or "edge effect" commonly seen at rifted continental margins is absent. This is almost certainly due to tectonic modification/overprinting by the Africa-Eurasian plate boundary and Gibraltar Arc systems. Anomalies **G, I, J** in the Gulf appear unrelated to present-day bathymetry (contrast Figure A.2 with Figure A.1), trending almost perpendicular to the slope. Anomaly **I** is narrow and linear, and has a similar orientation to anomalies B and C which are associated with submarine ridges to the west. The approximate symmetry of anomalies north and south of an E-W axis through the Straits of Gibraltar has been associated with the structure of Betic–Rifian Arc [e.g., Roberts, 1970; Bonini *et al.*, 1973]. Anomalies I, G, J appear to converge at $\sim 11^\circ$ W, and anomalies **E, F, G and H** make up an arcuate gravity negative zone coincident with the Betic and Rif orogens. The symmetry appears indicative of a relationship to deeper structures of the Betic–Rif/Gibraltar Arc system. In the Alboran Sea, coastal gravity highs coincide with outcrops of ultramafic rocks [Bonini *et al.*, 1973].

A.2.1 Global Geopotential Model OSU91a

When modelling gravity anomalies related to lithospheric processes, in addition to the standard gravity corrections (free-air, Bouguer, terrain, Eotvos etc), gravity effects due to sub-lithospheric processes need to be compensated [Blakely, 1995]. To this end, the OSU91a global geopotential model is used [Rapp *et al.*, 1991], which expresses the Earth's geopotential in a spherical harmonic form. The highest order of expansion is 360 - equivalent to a 55 km wavelength. An order of 16 corresponds to a 2500 km wavelength, which is dominated by sub-lithospheric contributions (Figure A.3 below).

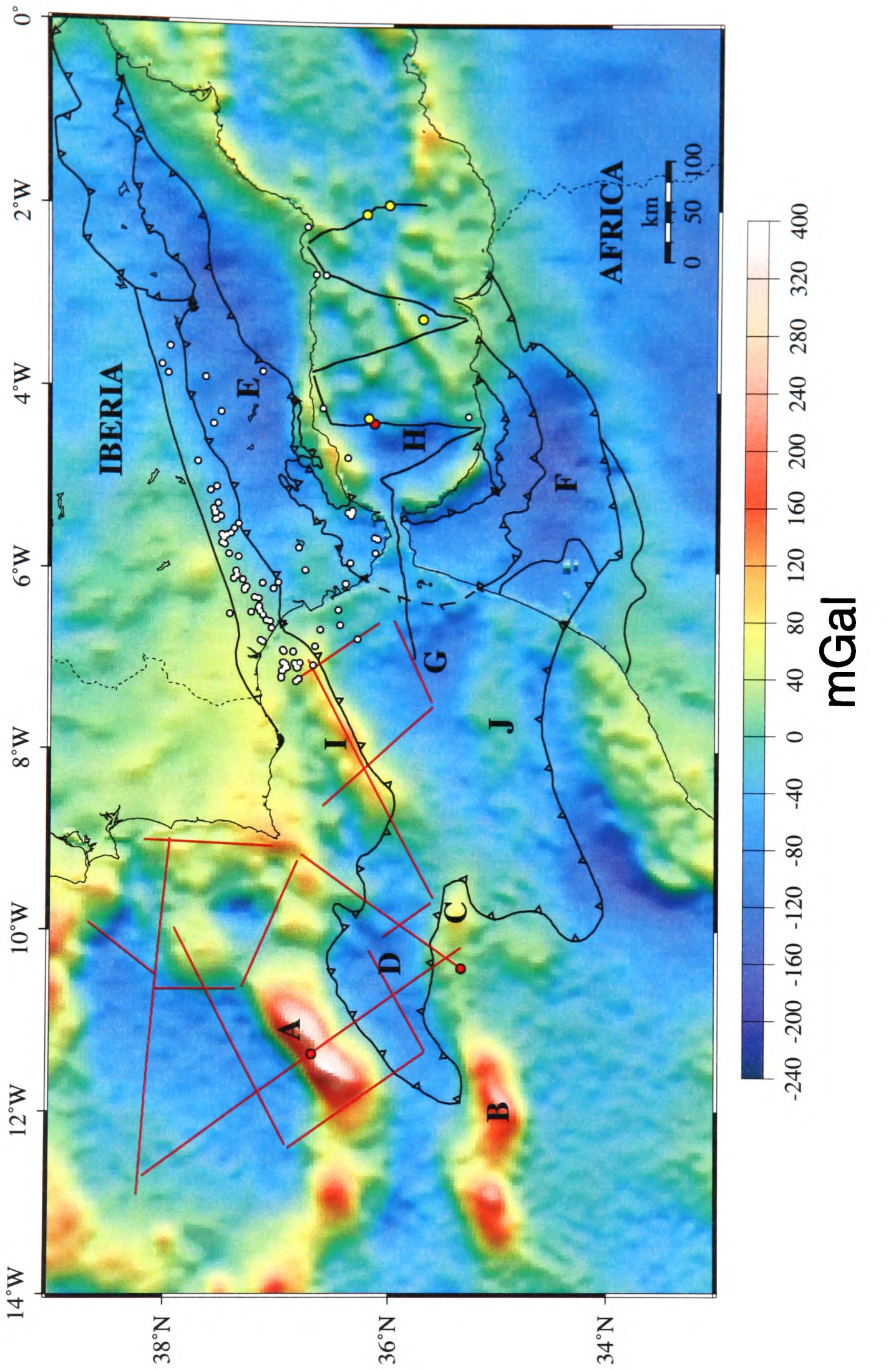


Figure A.2: Composite gravity anomaly map of the Gibraltar Arc-eastern Atlantic area: free air anomalies offshore, Bouguer anomalies onshore. Locations of seismic profiles and well data as in Figure A.1. Significant anomalies A-J labelled, see text for further explanation.

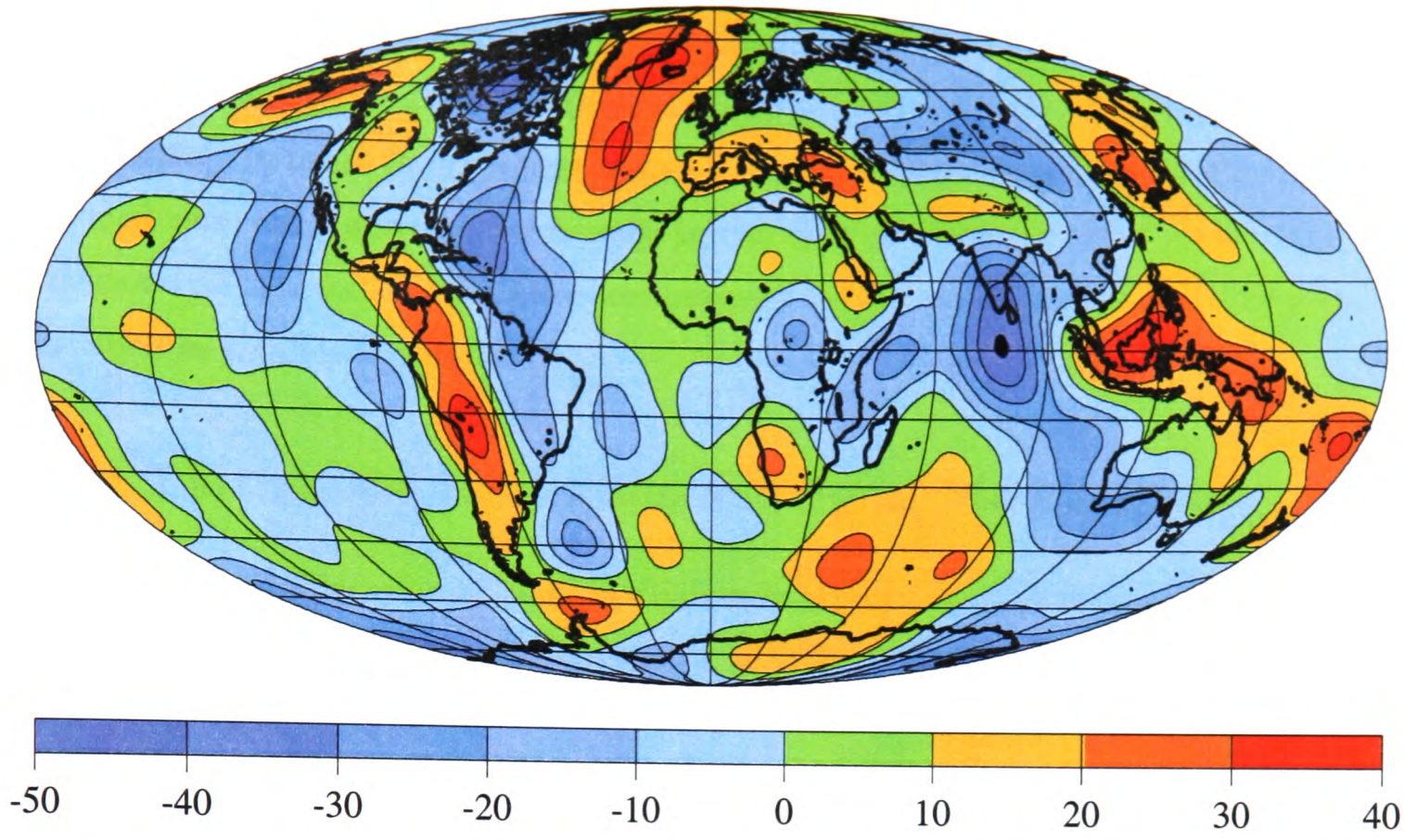


Figure A.3: Degree and order 16 gravity field determined from OSU91a [Rapp *et al.*, 1991]. Values in mGal, contours every ten mGal; positive values hot, negative cold. Mollweide projection centred on the Greenwich meridian.

Of importance to this study is the large North Atlantic positive anomaly centred on Iceland (Figure A.3), caused by the Iceland Plume. A lower amplitude positive anomaly is coincident with the location of the Alpine-Himalayan orogenic belt caused west of India by Africa-Eurasia collision. The degree and order 16 long-wavelength gravity field calculated from the OSU91a geopotential model was subtracted from the observed free air and Bouguer gravity anomalies prior to gravity modelling, in order to compensate for sub-lithospheric contributions which would be expected from the polyphase tectonic evolution of the North Atlantic. As Figure A.3 shows this field is positive in the study region, with values $\sim$ 10–20 mGals, so the long wavelength adjustment is negative and around 5–10% of the total anomaly (e.g., Figure A.2).

A.3 Well Data

The locations of well data available for this study are shown as small circles on Figure A.1. **DSDP** sites 120, 121 [Ryan *et al.*, 1973] and 135 [Hayes *et al.*, 1972] are shown as red circles. **ODP** (Ocean Drilling Program) sites 976, 977, 978, 979 (yellow circles) were drilled in the Alboran Sea during the 1995 Western Mediterranean Leg 161 [Comas *et al.*, 1995]. Other public domain well data locations are shown as white circles on Figure A.1. This data is mainly from a government compilation of oil industry wells drilled

in Spain [IGME, 1987], which includes well positions, lithologies and ages in most cases. Published sonic logs for 4 wells in the Gudalquivir Basin were digitised from Fernandez *et al.* [1998a]. In terms of proprietary commercial data, Shell International Oil Company provided composite well logs for 5 wells in the Gulf of Cadiz, while Chevron (COPI) provided well logs for 3 wells in the westernmost Guadalquivir Basin. The well data is described in detail in Appendix B.

A.4 Earthquake Relocation and Focal Mechanisms

The hypocentral location is the most fundamental quantification of an earthquake, and is described by the four basic parameters of latitude, longitude, origin time and depth. The aim of hypocentre location is to find the location which minimises the residuals between the observed and theoretical traveltimes based on a generalised earth model. At present the most complete global catalogue of earthquake hypocentres is the Bulletin of the International Seismological Centre (ISC), which contains arrival times of seismic phases from a global network of stations along with calculated hypocentral locations and origin times for earthquakes from 1962 through 1997. The ISC locates each earthquake individually, which means that events may be relatively mislocated by tens of kilometres [e.g., Pegler, 1995]. In areas of complex tectonics, such as the Azores–Gibraltar Fracture Zone, it is desirable to improve on the accuracy of locations available from the standard ISC hypocentral bulletin, and so a joint hypocentre determination (JHD) technique was applied, in which a number of events are analysed simultaneously such that relative mislocations are minimised. All earthquakes relocated in this study use ISC arrival times and hypocentral parameters as an initial estimate.

A.4.1 Methodology

ISC–recorded earthquakes in the study area with magnitude greater than 4 have been relocated. In order to produce well-constrained relocated hypocentres, the region of interest was sub-divided into seven surface boxes, the largest being 4 arc min x 4 arc min. This was done as the method assumes that the distance between stations is small relative to the distance to the recording station. The area covered by these relocations is shown in the upper map of Figure A.5. For each block, representative earthquakes recorded by a large number of stations (generally the largest events) were relocated using the standard joint hypocentre determination (JHD) procedure of [Dewey, 1971], summarised in Figure A.4. Stations were rejected if they displayed high variance in readings, and earthquakes with a small number of readings were dropped in cases where solutions failed to converge. Once a convergent solution for each box was obtained,

smaller events were relocated using the SE89 (single event) algorithm [Dewey, 1971] with station corrections determined during the JHD procedure. Finally, all the relocated hypocentres were combined into a single catalogue. The method has been successfully applied to several seismotectonic studies e.g., Pegler *et al.* [1995]; Pegler & Das [1996, 1998]; Schöffel & Das [1999].

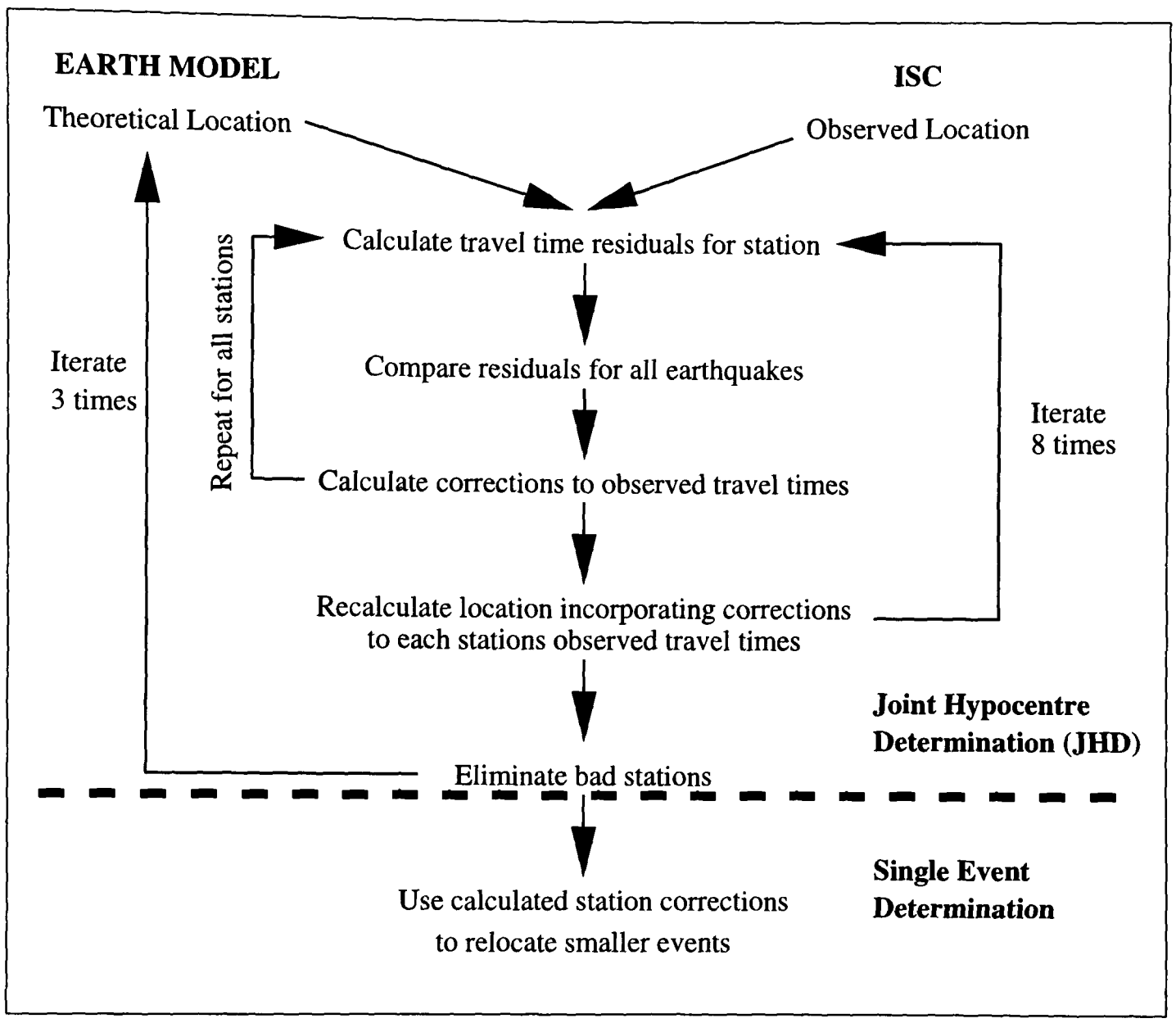


Figure A.4: Flow chart of earthquake hypocentre relocation method utilising the joint hypocentre determination technique of [Dewey, 1971]. The initial Earth model used was that of Jeffreys & Bullen [1940].

A.4.2 Relocation Results

Figure A.5a shows the location of recording stations used by the ISC. The study area shown is located near many stations, which provided good coverage for the relocation procedure. Figure A.5b illustrates the relocation vectors by which ISC events were relocated horizontally, with the relocated event shown as a small black circle. Figure A.5b illustrates that the largest displacements are over 50 km. Figure A.5c shows both the original ISC and relocated locations. Some ISC events that were judged poorly constrained

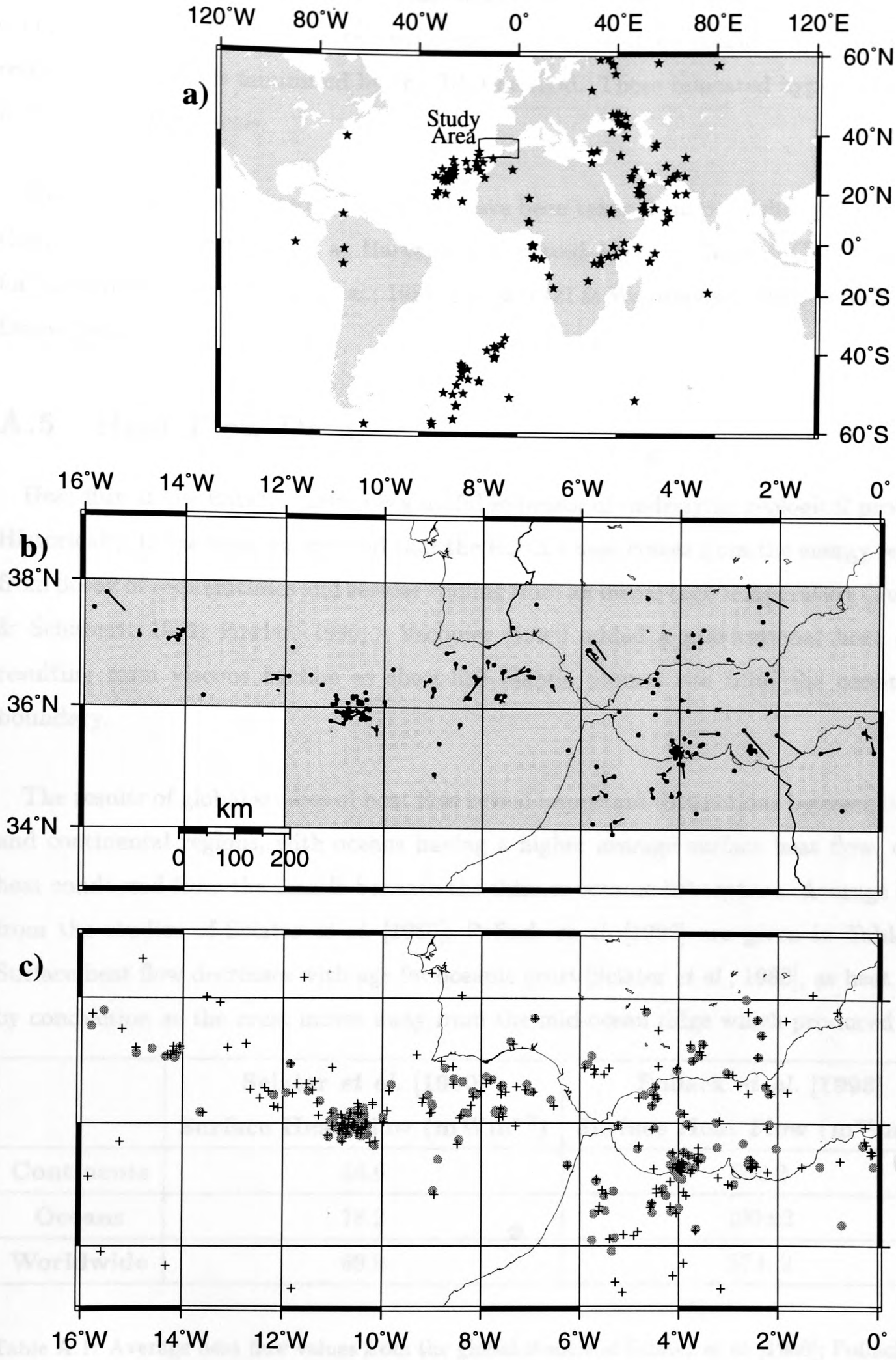


Figure A.5: Results of JHD hypocentre relocation. a) Location of recording stations used by the ISC; b)Relocation vectors over the study area. The area covered by JHD boxes is in grey, with relocated events (black circles) and relocation vectors for ISC events shown; c) relative positions of ISC events (crosses) and relocated events (grey-filled circles).

have not been relocated, but no obvious changes in the overall pattern of seismicity have occurred. However, the relocated hypocentres are now more confidently located, with relative mislocations minimised by the JHD method. These relocated hypocentres have been used in this thesis.

Focal mechanisms utilised in this study have been taken from published data and from the public-domain catalogue at Harvard of Centroid Moment Tensor (CMT) solutions for earthquakes [Dziewonski *et al.*, 1981; Dziewonski & Woodhouse, 1983; Woodhouse & Dziewonski, 1984].

A.5 Heat Flow Data

Heat flux at the Earth's surface is a useful indicator of underlying geological processes. Historically, it has been understood that the Earth's heat comes from the energy released from decay of radionuclides and secular cooling from an initial high temperature [Turcotte & Schubert, 1982; Fowler, 1990]. Vacquier [1998] added a gravitational heat source resulting from viscous friction as sheet-like mantle plumes rise from the core-mantle boundary.

The results of global studies of heat flow reveal important distinctions between oceanic and continental regions, with oceans having a higher average surface heat flow, due to heat conducted from the mantle beneath the thinner oceanic lithosphere. Average values from the studies of Sclater *et al.* [1980]; Pollack *et al.* [1993] are given in Table A.1. Surface heat flow decreases with age for oceanic crust [Sclater *et al.*, 1980], as heat is lost by conduction as the crust moves away from the mid-ocean ridge which produced it.

	Sclater *et al.* [1980] Surface Heat Flow (mWm^{-2})	**Pollack *et al.* [1993] Surface Heat Flow (mWm^{-2})**
Continents	56.6	66±2
Oceans	78.2	100±2
Worldwide	69.9	87± 2

Table A.1: Average heat flow values from the global studies of Sclater *et al.* [1980]; Pollack *et al.* [1993]

A dataset of 370 data points has been compiled from the literature to produce a new map of surface heat flow in the study region (Figure A.6). The data is taken from oil, water and mining wells, as well as seafloor probes [e.g., Verzhbitsky & Zolotarev,

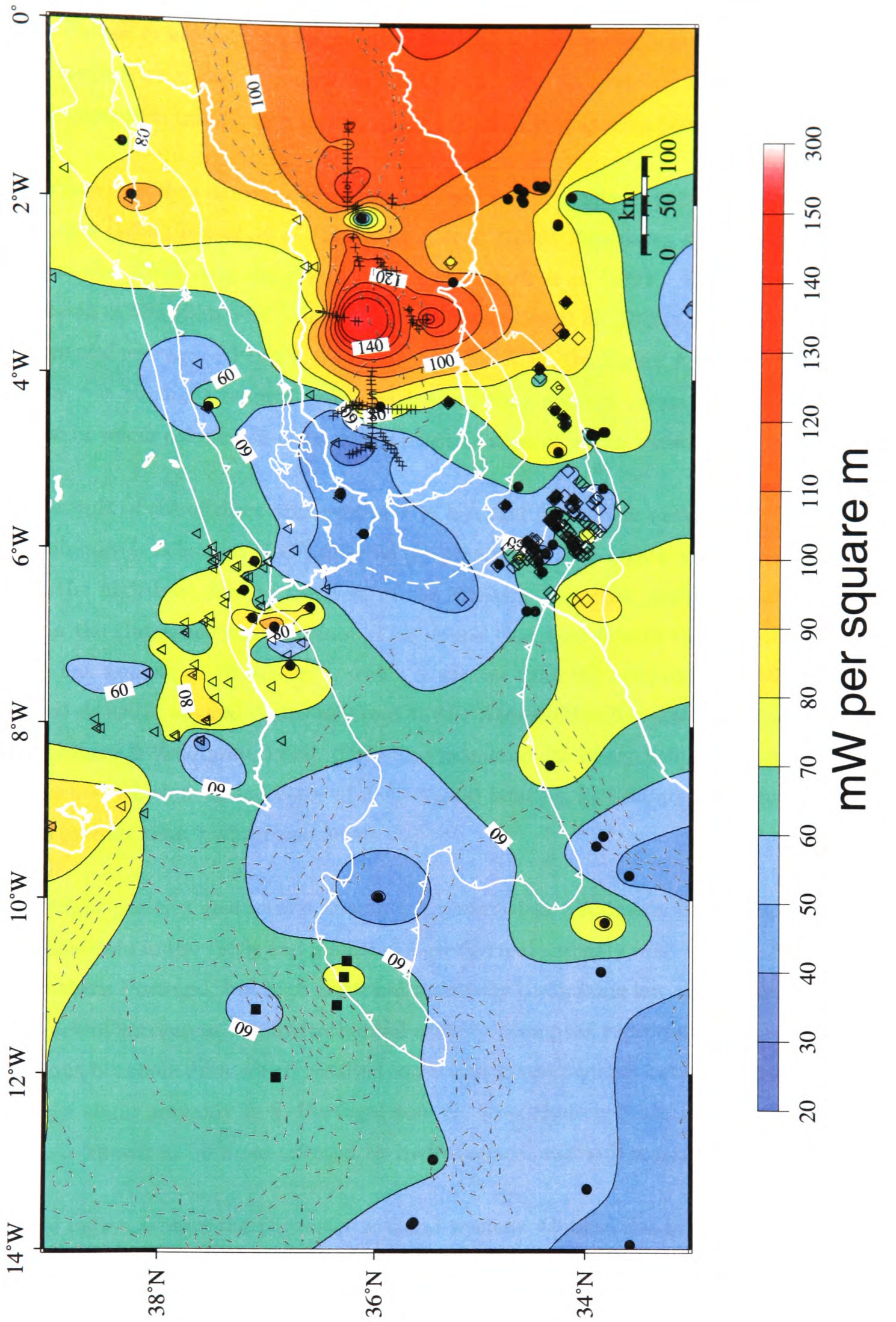


Figure A.6: Surface heat flow density map of study region, based on a compilation of oil. mining, water wells and seafloor measurements. Data points are shown according to source publication: Verzhbitsky & Zolotarev [1989] (filled squares); Pollack *et al.* [1993] (filled circles); Polyak *et al.* [1996] (crosses); Rimi *et al.* [1998] (open diamonds); and Fernandez *et al.* [1998b]; Correia & Ramalho [1998](open triangles).

1989; Polyak *et al.*, 1996]. The irregular distribution of readings has been dealt with by blockmedian weighting of points into 10' boxes, prior to gridding with a GMT tension spline algorithm using a tension of 0.25 at 1 arc min grid spacing [Wessel & Smith, 1995].

Surface heat-flow density data was compiled from the regional papers of Verzhbitsky & Zolotarev [1989]; Polyak *et al.* [1996]; Rimi *et al.* [1998]; Fernandez *et al.* [1998b]; Correia & Ramalho [1998] and the global dataset of Pollack *et al.* [1993]. The average heatflow for Iberia of 65±10 mWm^{-2} determined by Fernandez *et al.* [1998b] is close to the global continental average of Pollack *et al.* [1993] (Table A.1). On Figure A.6, the interval 60-70 mWm^{-2} is shaded a neutral green, with lower than average values in blues and higher values in warm colours, in order to aid identification of major variations.

The bulk of the offshore area west of 9°W has heat flow values between 50–70 mWm^{-2}. Verzhbitsky & Zolotarev [1989] inferred the presence of deep crustal faulting in this region from the high heat flow to the west of the Madeira-Tore Rise, north of Gorringe Bank and in the Horseshoe abyssal plain. They found that heat flow in the Horseshoe abyssal plain has a mean of 70 mWm^{-2}, which is greater than the recorded 45 mWm^{-2} in the central Atlantic abyssal plains adjacent to the Azores-Gibraltar fracture zone [Figure 1, Verzhbitsky & Zolotarev, 1989]. They also measured the heavy helium isotope (He–4) in sediments, which is an indicator of deep crustal faulting, and found values to be 2.5 to 5 times greater than background levels.

A slight positive geothermal anomaly is observed in SW Iberia (Figure A.6). Mining borehole data in the 1980s had indicated a geothermal anomaly with values >200 mWm^{-2} in southern Portugal, but high electrical resistivity (indicating low crustal temperatures) and lack of accompanying hydrothermal activity prompted reprocessing and retesting of previous borehole data which resulted in revised measurements between 50–90 mWm^{-2}. Thus, a slight anomaly in S. Portugal and W. Guadalquivir Basin is registered, but the latter is known to be more affected by hydrothermal effects [Fernandez *et al.*, 1998a].

The region around the Gibraltar Arc and western Alboran Sea is seen to have a lower heat flow than average, whereas a high is noted in the eastern Alboran Sea with local heat flow densities reaching values >200 mWm^{-2} [Polyak *et al.*, 1996]. Heat flow values are observed to be significantly greater along the Mediterranean coasts of Iberia and North Africa (80–120 mWm^{-2}) than along their Atlantic coasts (50–90 mWm^{-2}).

A.6 Summary

The following regional datasets were used or compiled from published data:

- A relief map of the study area was produced by merging the onshore USGS GTOPO30 digital elevation model with an offshore compilation by WEEGP west of Gibraltar, and shiptrack data in the Alboran Sea.

- A 2' gravity anomaly map, Bouguer onshore and Free-Air offshore, was produced by merging WEEGP (GTECH Leeds) Bouguer data, and offshore satellite-derived free-air gravity measurements from recently declassified datasets Sandwell & Smith [1997]. The order 16 (2500 km) wavelength OSU91a gravity field [Rapp *et al.*, 1991] was subtracted to account for sub-lithospheric contributions to the gravity field.

- Well data was available from several sources: DSDP, ODP, the Spanish compilation published in IGME [1987], published data, and well logs from Shell International and Chevron oil companies.

- Earthquake hypocentre locations, from the global catalogue of hypocentres from the Bulletin of the International Seismological Centre (ISC), were more accurately constrained through relocation using the joint hypocentre determination (JHD) procedure of [Dewey, 1971]. Focal mechanisms were compiled from published data, and to a lesser degree from the Harvard CMT catalogue.

- A new heat flow density map of the study region was produced by compiling a total of 370 points from published sources.

Appendix B

Well Data

[redacted]

Table B.1: Well data from the Gulf of Cadiz, Campo de Gibraltar and Alboran Sea, as outlined in IGME[1987].

Table B.2: Wells from the western Betic Cordillera and Guadalquivir Basin, as outlined in IGME[1987].

B.1 Description of wells

This section is concerned with a detailed description of wells studied in Chapter 4, in particular Figure B.1, Figure B.2 and Figure 4.5 of Section 4.4. The location of the studied wells and the well profile A-A' are shown on Figure 4.4. The lithological and stratigraphic data derived from commercial well logs are shown on Figure B.1 and Figure B.2A, while Figure B.2B illustrates three wells in the GQB, with sonic data digitised from Fernandez *et al.* [1998a], and lithological and stratigraphical information taken from IGME [1987]. In both Figure B.1 and Figure B.2, the sonic velocities are obtained by simply taking the reciprocal of sonic interval velocities measured from the given logs. The densities shown are derived directly from the sonic velocities using the empirical "Gardner's Rule" [Gardner *et al.*, 1974] for sediments:

$$\rho = aV^{1/4} \tag{B.1}$$

where formation density, ρ, is in gcm^{-3} and sonic velocity, V, is in ms^{-1} and the constant of proportionality, a, is 0.31.

B.1.1 Wells with available logs

The locations of wells with available downhole log data are shown in red on Figure 4.4. Figure B.1 illustrates wells from the GOC arranged from NW to SE. On examining the 3 northern offshore wells, **241, 296, 314**, it is evident that the Recent–Miocene deposits are dominated by shales, with a roughly linear increase in velocity with depth. This trend is disturbed by the presence of limestone and dolomite layers in the pre-Miocene section, with sonic velocities up to 6000 m/s. The late Neogene sediment sonic velocities are generally less than 3000 m/s. Well **296** penetrates through to Triassic Keuper facies-type red beds, containing volcanics, above which lie Jurassic marls, limestones and dolomites, marked by high sonic velocities. The dolomite is overlain by Cretaceous shales, then Palaeogene interbedded limestones and shales. Miocene deposits are absent in this well (Shell composite well log), implying erosion or lack of deposition on a possible Miocene high. This unconformity is clearly resolved by the sonic log, exhibiting a large decrease in sonic velocity as the section passes into Pliocene-Recent shales and silts. This well has no gas shows despite being surrounded by gas-bearing wells (Figure 4.4).

Wells **314** and **241** are adjacent wells, and are the closest offshore wells to the GQB. Both wells penetrate thick sections (≈2000 m) of Neogene, mainly deep-water, clastic sediments. Both wells TD in Upper Jurassic carbonates of Kimmeridgian-Tithonian age (154-144 Ma). Stratigraphic breaks occur in the early Cretaceous, early Eocene and late

Oligocene–early Miocene in well **314**, whereas an Eocene-early Oligocene break is seen in well **241**.

Well **288** samples upper Miocene to Recent sediments, and then passes into a Triassic evaporitic sequence comprising halite with some anhydrite, K-Mg salts and claystone intercalations. Over 1000 m of the Triassic salt layer was penetrated (1720–2763 m), and this was interpreted as saltdome material. The well shows anomalous velocities in the Messinian-Pliocene section, possibly due to the presence of consolidated calacareous intercalations, although there maybe some effect due to the saline diapir beneath. Figure 4.2A illustrates a previous interpretation of the NW GOC using wells **288** and **241**, plus onshore well **47** (see Table B.2). Well **245** drilled through a series of mid-Miocene to Recent shales into an allochthonous deposit at 975m depth below seafloor. The sonic log registered a large fall in velocity across this boundary. The upper part of this unit consists of redeposited Paleocene to mid-Eocene deep-water sediments, while the lower part is a chaotic mixture of Triassic clay with some halite and anhydrite, thought to have be supratidal flat deposits redeposited in a deepwater environment. Sonic velocities in the allochthon (1600–1800 ms^{-1}) are anomalously low relative to the normal velocity increase with depth seen in the sediments higher in the well. This indicates that normal compaction processes have not been able to operate, and hence that this unit is overpressured and undercompacted.

Onshore well logs from the western GQB are shown in Figure B.2. All of these have penetrated pre-Miocene basement. Well **482** penetrates 575 m of Pliocene shales, then 782 m of Miocene mudstones and shales, before reaching Upper Jurassic limestone. Only location data is published by IGME [1987] on well **482**. This description is based on the composite well log: 1107 m of Upper Miocene sediments with sandstone intervals (with gas shows), overlying weakly metamorphosed limestone of apparent Mesozoic age. Well **482** provides the northernmost well logs examined here. No ages are given in IGME [1987] or in the well logs for the uppermost section, but Upper Miocene sediments are found below. Again, these are mudstones and shales, with sandstone intervals, which are not gas-bearing in this instance. At the base of the well a 20 m thick, glauconitic, fossiliferous sandstone of Tortonian age unconformably overlies slates of Palaeozoic age.

Figure B.2B is of special interest as the three wells represent a section perpendicular to the regional structures, and cross the front of the widespread allochthonous deposits of the GQB shown on Figure 4.4 [e.g., Perconig, 1962; Flinch *et al.*, 1996; Berastegui *et al.*, 1998]. The three wells shown, **223** (Villamanrique I), **225** (Casa Nieves 1) and **604**

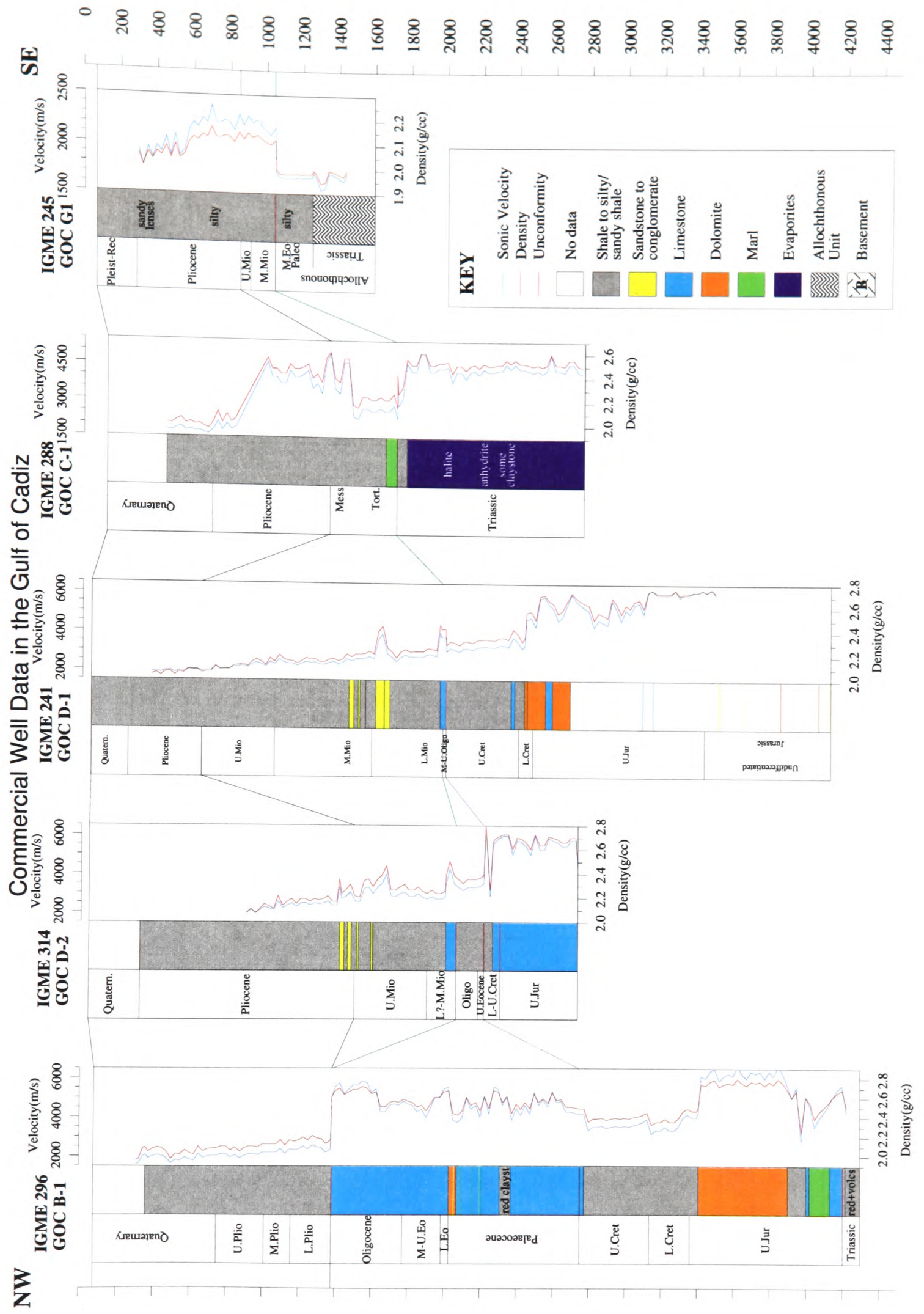


Figure B.1: Wells for which composite logs were available in the Gulf of Cadiz. Lithology is plotted against sonic velocity and density derived from the sonic log using the empirical relationship of Gardner *et al.* [1974] ("Gardner's Rule"). Correlations of the base Pliocene (black), base Miocene (green), and base Tertiary (purple) are also shown.

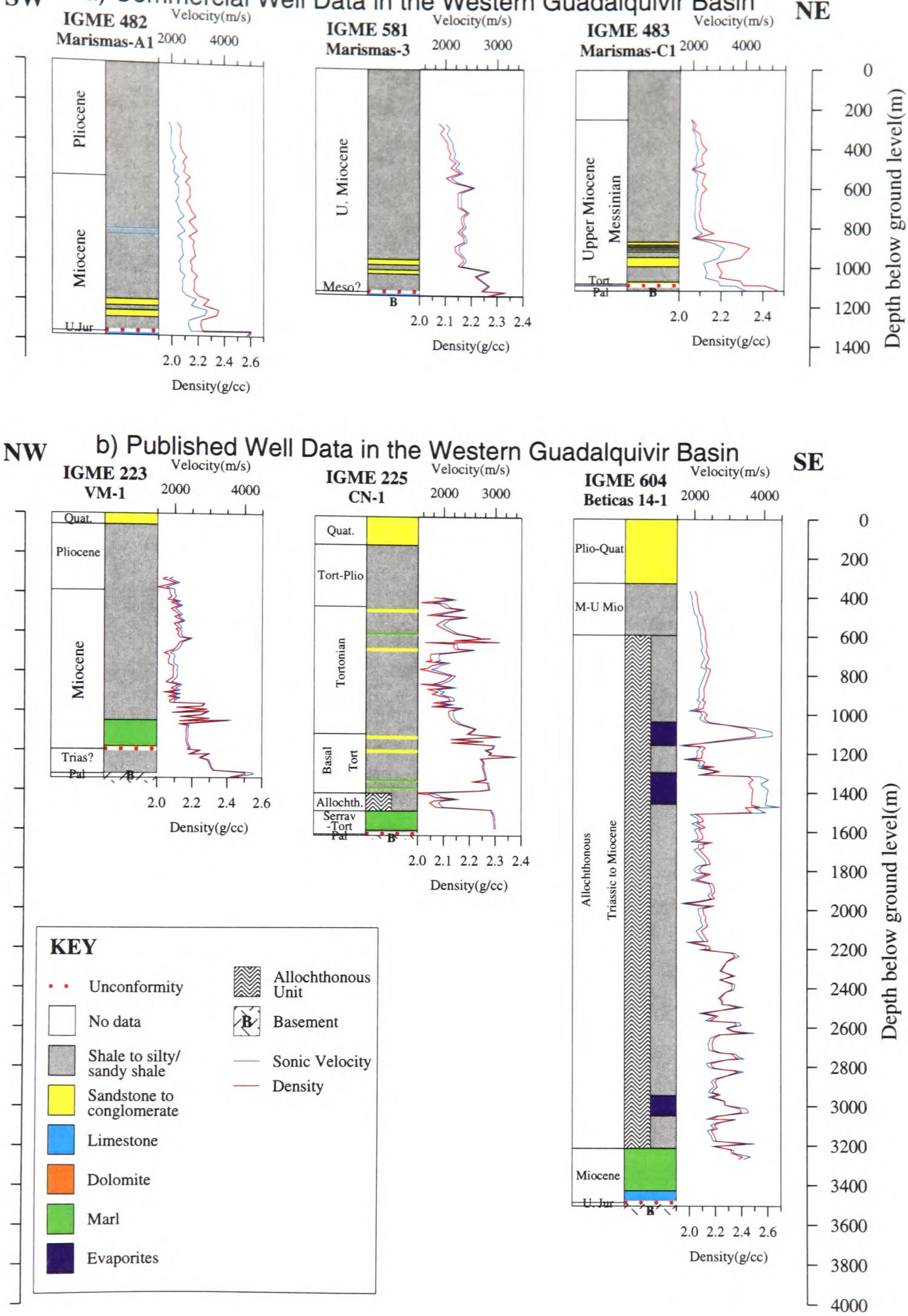


Figure B.2: Well lithology versus sonic velocity and density for boreholes in the western GQB. a)Logs obtained from Chevron; b)Logs digitised from published data.

(Beticas-14), were used to constrain the northern end of the Guadalquivir allochthonous unit (see Figure 4.2C crossection, for example). In well **223** Quaternary sands lie above Pliocene shales. The Miocene interval is marly at the base, where it overlies sediments of probable Triassic age, under which Palaeozoic basement has been drilled. Well **225** has Quaternary sands, sandstones, and conglomerates, below which are Pliocene and Miocene intervals of shale and mudstone with sandy intervals. 87 m of allochthonous clays are present between basal Tortonian sediments above, and Serravalian–basal Tortonian marls below, giving an earliest Tortonian time for emplacement of the allochthon. The allochthonous sediments are marked by sonic velocities which are much lower than those of the autochthonous rocks that envelope it (see dip in velocities on Figure B.2B). Well **604** has also been drilled right through the allochthonous unit. The Plio-Quaternary consists of sands due to proximity to the course of the River Guadalquivir (Figure 4.4). Mid-Upper Miocene sediments are drilled above, and Miocene sediments below, 2621 m of allochthonous Triassic to Miocene sediments, punctuated by thick layers (up to 150 m) of halite. Halite beds are resolved by large jumps in sonic velocity. It can also be seen that non-evaporitic sonic values stay relatively low (2000–2500 ms^{-1}) until about 2200 m down-section, when velocities average around 3000 ms^{-1}, with no obvious gradational increase in velocity with depth. The unusual velocity distributions may be due to the effects of more salt in the lower allochthon (higher velocities) and compartmentalisation and undercompaction of mudrocks in the upper section, with salt layers sealing compartments. Beneath the allochthon are Miocene marls and a basal limestone, overlying Upper Jurassic carbonates.

B.1.2 Well Correlation Profile A-A'

Stratigraphic and lithologic Profile A-A' (Figure 4.5), was constructed using available well information along an approximately NW-SE transect in the eastern Gulf of Cadiz (Figure 4.4). The profile ran from the northeastern GOC to the western part of the Ultra-Betics, close to the Gibraltar Straits. This exercise was carried out to allow correlation of lithologies and stratigraphic ages across a section cross-cutting the trend of onshore Betic–related structural units. This transect runs parallel to seismic profile GC3 (Figure 4.1 and Figure 4.4), aiding seismic interpretation. The sedimentary record sampled by the wells of Profile A-A' is described below, in chronological order of deposition, making reference as necessary to the logs described in the previous section.

Palaeozoic basement, drilled in the onshore wells of Figure B.2, is not observed in any well on Figure 4.5. Only well **533** (Figure 4.6) is known to have penetrated Palaeozoic rocks in the GOC (Table B.3), consisting of metasediments, carbon and volcanics. The

oldest rocks seen on the well transect are Triassic, and are of two types: siliciclastic and evaporitic. The siliciclastic Triassic is represented by continental red beds with volcanics seen in well **296**, whereas the evaporitic Triassic is represented by salt deposits such as that drilled at well **288**, which is made up of halite, anhydrite and red claystone layers (see also Figure B.1).

Lower-mid Jurassic rocks have only been drilled in well **533** and comprise thick deposits of dolomite, limestone and marls, as shown on Figure 4.6, but the Upper Jurassic is not present. Rocks of this age are not seen on Figure 4.5. Maldonado *et al.* [1999] report Lower-mid Jurassic sediments in wells **241** and **296**, which conflicts with the proprietary well logs, which report the same sections in the the same wells as undifferentiated Jurassic and Upper Jurassic sediments respectively. Upper Jurassic platform carbonates have been drilled in only three of the most northern wells - **241, 296,314**. However, this is probably because most wells in the GOC were not drilled below the Tertiary e.g., Figure 4.5.

Upper Jurassic sediments generally pass conformably up into Lower Cretaceous ones, with the exception of well **314** which contains a minor stratigraphic break at the top of the Jurassic. Like the Jurassic, the Cretaceous has mainly been drilled in the northern GOC. The lower Cretaceous consists of a lower level of limestones and dolomites, which pass upwards into silts and shales of the mid- and Upper Cretaceous (wells **296, 427, 433** of Figure 4.5 and **241, 296, 414** of Figure B.1).

Above the correlated base Tertiary unconformity between Palaeogene and Cretaceous rocks seen in the northern end of profile A-A', are rocks ranging from Palaeocene-Oligocene in age. Lithologies are varied, with sands, shales, limstones and dolomites all represented. Limestones of shallow carbonate shelf origin of up to 1200 m thickness (well **296**) are seen in the northern GOC, within the Palaeogene interval (wells **296, 398, 421, 433**). Away from this carbonate platform, drilled Palaeogene thicknesses are variable, ranging from ≈200 m of shales, to complete absence - as above the saline diapir of well **288** and the mid-lower Jurassic carbonates of well **533** (Figure 4.6). The top of this unit is marked by a basin-wide erosional unconformity, which represents an Oligocene–lower Miocene stratigraphic break, and is marked as the basal Miocene unconformity on Figure 4.5. The ages of rocks directly below it are Palaeocene–Oligocene; lower-mid Miocene sediments are deposited above it.

The Miocene interval is variable in lithology, ranging from marly shales to shaly marls, sandstones and limestone intercalations. This interval also varies greatly in thickness.

It is thinnest above the diapir in well **288** and above the chaotic allochthonous unit in well **245**. It is completely absent above the Palaeogene limestones in the NW (wells **433, 296,421,398**) which could have formed a palaeohigh. The allochthonous unit comprising Palaeogene deep water sediments, and a chaotic mixture of Triassic evaporites and clays, is present below the mid-Miocene at well **245**, and has also been drilled below the Tortonian at well **495** [IGME, 1987]. No wells have penetrated through the allochthonous unit in the GOC. There is no obvious stratigraphic break between upper Miocene and Pliocene sediments documented from the well data, but the contact can be correlated over the basin (Figure 4.5), with the Plio-Quaternary lying above.

The Plio-Quaternary sediments along the transect consist largely of calcareous muds, shales and some sandy intercalations. This unit thins overall towards the SE, ranging in thickness from a minimum of 515 m at well **342** in the southern part of the profile, to a maximum of 1462 m in well **413** to the north-west. The Quaternary is identified separately in only a minority of wells, mainly because this interval is unconsolidated and often not logged (note "No Data" intervals at the top of wells shown on Figure 4.5 and Figure B.1).

The two onshore wells form the southernmost end of the transect (**21, 35**). Well **21** is from the southern Sub-Betics (Figure 4.4) and illustrates the presence of complex thrust tectonics, with the Triassic appearing at least twice in the sequence. Well **35** is from the Ultra-Betics (Flysch of Campo de Gibraltar units) and is composed of thick Cretaceous and Palaeogene sediment, with thrusting indicated by the repetition of stratigraphic intervals.

B.2 Backstripping Input and Output Tabulated For Selected Wells

Well 296 – Cadiz B1

Horizon Top	Depth (m)	Age* (Ma)	Palaeowaterdepth		Watts & Steckler†	Pitman‡
			Min	Max		
Quaternary (Seabed)	0	0	0	0	0	0
Upper Pliocene	671.4	1.64	100	1000	-2	6.2
Mid–Pliocene	931.4	2.8	200	2000	-3.4	10.9
Lower Pliocene	1079.4	4.0	200	2000	-4.8	15.4
Unconformity	1301.6	5.2	0	0	0	0
Oligocene	1301.6	23.3	0	100	27.8	90.8
Mid–Upper Eocene	1693.4	35.4	0	100	52.8	165.4
Lower Eocene	1905.4	50	0	100	72	232.3
Palaeocene	1948.4	56.5	0	20	79.2	273.8
Unconformity	2672.4	65	0	0	0	0
U. Camp.–L. Maast.	2672.4	68	200	2000	103.6	329.1
Barremian–Albian	3056.4	98.9	100	2000	14.0	286.0
Valangian–Hauterivian	3106.4	127.0	100	2000	9	280.0
Berriasian	3248.4	137.0	100	2000	24.7	295.7
U. Jur (Kimm–Tith)	3281.4	144.2	0	200	-44.4	226.6
Unconformity	4123.4	154.1	0	0	0	0
Triassic	4123.4	205.7	0	0	0	200
T.D.	4219.1	-	-	-	-	-
Top basement	-	-	-	-	-	-

Table B.3: IGME 296 (Cadiz B1) stratigraphy.

Age* (Ma)	Observed Sediment Thickness	Decompacted Sediment Thickness	Tectonic Subsidence (W and S†)			Tectonic Subsidence (Pitman‡)		
			Min	Max	Mean	Min	Max	Mean
0.0	4.123	4.123	1.600	1.600	1.600	1.600	1.600	1.600
1.6	3.452	3.645	1.560	2.460	2.010	1.548	2.448	1.998
2.8	3.192	3.439	1.597	3.397	2.497	1.577	3.377	2.477
4.0	3.044	3.318	1.561	3.361	2.461	1.532	3.332	2.432
5.2	2.822	3.130	1.294	1.294	1.294	1.294	1.294	1.294
23.3	2.822	3.130	1.254	1.354	1.304	1.162	1.262	1.212
35.4	2.430	2.781	1.101	1.201	1.151	0.938	1.038	0.988
50.0	2.218	2.582	1.004	1.104	1.054	0.772	0.872	0.822
56.5	2.175	2.541	0.979	0.999	0.989	0.698	0.718	0.708
65.0	1.451	1.809	0.823	0.823	0.823	0.823	0.823	0.823
68.0	1.451	1.809	0.873	2.673	1.773	0.547	2.347	1.447
98.9	1.067	1.385	0.733	2.633	1.683	0.339	2.239	1.289
127.0	1.017	1.328	0.717	2.617	1.667	0.324	2.224	1.274
137.0	0.875	1.164	0.625	2.525	1.575	0.233	2.133	1.183
144.2	0.842	1.124	0.607	0.807	0.707	0.215	0.415	0.315
154.1	0.000	0.000	0.000	0.000	0.000	0.000	0.000	0.000
205.7	0.000	0.000	0.000	0.000	0.000	0.000	0.000	0.000

Table B.4: IGME 296 (Cadiz B1) backstripping results. Thickness and subsidence values in kilometres.

Well 241 – Cadiz D1

Horizon Top	Depth	Age*	Palaeowaterdepth		Watts & Steckler†	Pitman‡
			Min	Max		
Quaternary (Seabed)	0	0	0	0	0	0
Pliocene	200	1.64	0	100	-2	6.2
Upper Miocene	600	5.2	100	200	-5.6	20.0
Mid–Miocene	1000	10.4	100	1000	4.95	40.0
Lower Miocene	1740	16.3	100	1000	12.3	63.0
Upper to Mid–Oligocene	1937	23.3	0	100	25.5	90.8
Unconformity	1953	29.3	0	0	0	0
Lower Maastrichtian	1953	68	200	2000	103.6	329.1
Campanian	2120	71.3	200	2000	107.6	332.0
Santonian	2317	83.5	200	2000	76.4	342.8
Coniacian	2337	85.8	200	2000	67.2	340.6
Turonian	2342	89.0	200	2000	59.7	330.7
Cenomanian	2347	93.5	200	2000	58.2	329.2
Albian	2358	98.9	0	1000	14.0	286.0
Barremian–Aptian	2380	112.2	0	200	-1.6	269.5
L.Cret. (Berr.–Haut.)	2390	127.0	0	20	9	280.0
U. Jur. (Kimm.–Tith.)	2437	144.2	0	20	-44.4	226.6
Undifferentiated Jurassic	3390	154.1	0	20	-34.0	236.6

Table B.5: IGME 241 (Cadiz D1) stratigraphy.

Age* (Ma)	Observed Sediment Thickness	Decompacted Sediment Thickness	Tectonic Subsidence (W and S†)			Tectonic Subsidence (Pitman‡)		
			Min	Max	Mean	Min	Max	Mean
0.0	3.390	3.390	1.405	1.405	1.405	1.405	1.405	1.405
1.6	3.190	3.250	1.362	1.462	1.412	1.350	1.450	1.400
5.2	2.790	2.949	1.365	1.465	1.415	1.328	1.428	1.378
10.4	2.390	2.618	1.234	2.134	1.684	1.183	2.083	1.633
16.3	1.650	1.937	0.969	1.869	1.419	0.895	1.795	1.345
23.3	1.453	1.740	0.771	0.871	0.821	0.677	0.777	0.727
29.3	1.437	1.724	0.802	0.802	0.802	0.802	0.802	0.802
68.0	1.437	1.724	0.852	2.652	1.752	0.525	2.325	1.425
71.3	1.270	1.551	0.776	2.576	1.676	0.451	2.251	1.351
83.5	1.073	1.339	0.733	2.533	1.633	0.347	2.147	1.247
85.8	1.053	1.318	0.737	2.537	1.637	0.341	2.141	1.241
89.0	1.048	1.313	0.745	2.545	1.645	0.353	2.153	1.253
93.5	1.043	1.307	0.745	2.545	1.645	0.353	2.153	1.253
98.9	1.032	1.295	0.604	1.604	1.104	0.211	1.211	0.711
112.2	1.010	1.272	0.617	0.817	0.717	0.224	0.424	0.324
127.0	1.000	1.261	0.597	0.617	0.607	0.205	0.225	0.215
144.2	0.953	1.209	0.653	0.673	0.663	0.260	0.280	0.270
154.1	0.000	0.000	0.049	0.069	0.059	-0.343	-0.323	-0.333

Table B.6: IGME 241 (Cadiz D1) backstripping results. Thickness & subsidence in kilometres.

Well 314 – Cadiz D2

Horizon Top	Depth	Age*	Palaeowaterdepth		Watts & Steckler†	Pitman‡
			Min	Max		
Mid–Plio. to Recent (Seabed)	0	0	0	0	0	0
Lower Pliocene	907.3	4.0	200	2000	-4.8	15.4
Upper Miocene	1455.3	5.2	150	2000	-5.6	20.0
Mid–Miocene	1857.3	10.4	150	2000	4.95	40.0
Unconformity	2019.3	16.3	0	0	0	0
Oligocene	2019.3	23.3	150	2000	27.8	90.8
U. Eocene (Priab.)	2140.3	35.4	150	2000	52.8	165.4
Unconformity	2172.3	38.6	0	0	0	0
Lower Maastrichtian	2172.3	68	150	2000	103.6	329.1
U. Cret (Cenom.–Campan.)	2221.8	71.3	0	2000	107.6	332.0
Mid–Cret. (Barrem.–Albian)	2257.3	98.9	0	200	14.0	286.0
Unconformity	2264.3	127.0	0	0	0	0
U. Jur (Kimm.–Tith.)	2264.3	144.2	0	100	-44.4	226.6
Mid–U. Jur?	2694.3	154.1	0	100	-34.0	236.6

Table B.7: IGME 314 (Cadiz D2) stratigraphy.

Age* (Ma)	Observed Sediment Thickness	Decompacted Sediment Thickness	Tectonic Subsidence (W and S†)			Tectonic Subsidence (Pitman‡)		
			Min	Max	Mean	Min	Max	Mean
0.0	2.694	2.694	1.183	1.183	1.183	1.183	1.183	1.183
4.0	1.787	2.002	1.138	2.938	2.038	1.109	2.909	2.009
5.2	1.239	1.492	0.886	2.736	1.811	0.849	2.699	1.774
10.4	0.837	1.070	0.688	2.538	1.613	0.637	2.487	1.562
16.3	0.675	0.888	0.461	0.461	0.461	0.461	0.461	0.461
23.3	0.675	0.888	0.571	2.421	1.496	0.480	2.330	1.405
35.4	0.554	0.746	0.469	2.319	1.394	0.306	2.156	1.231
38.6	0.522	0.707	0.376	0.376	0.376	0.376	0.376	0.376
68.0	0.522	0.707	0.376	2.226	1.301	0.050	1.900	0.975
71.3	0.472	0.646	0.190	2.190	1.190	-0.135	1.865	0.865
98.9	0.437	0.602	0.304	0.504	0.404	-0.090	0.110	0.010
127.0	0.430	0.593	0.320	0.320	0.320	0.320	0.320	0.320
144.2	0.430	0.593	0.384	0.484	0.434	-0.008	0.092	0.042
154.1	0.000	0.000	0.049	0.149	0.099	-0.343	-0.243	-0.293

Table B.8: IGME 314 (Cadiz D2) backstripping results. Thickness & subsidence in kilometres.

Well 288 – Cadiz C1

Horizon Top	Depth	Age*	Palaeowaterdepth		Watts & Steckler†	Pitman‡
			Min	Max		
Quaternary (Seabed)	0	0	0	0	0	0
Pliocene	573	1.64	100	1000	0	0
Messinian	1223	5.2	100	1000	0	0
Tortonian	1332	6.7	100	1000	0	0
Unconformity	1594	10.4	100	1000	0	0
Triassic	1594	206	0	0	0	0
T.D.	2636	-	-	-	-	-

Table B.9: IGME 288 (Cadiz C1) stratigraphy.

Age* (Ma)	Observed Sediment Thickness	Decompacted Sediment Thickness	Tectonic Subsidence	
			Min	Max
0.0	1.594	1.594	0.757	0.757
1.6	1.021	1.126	0.559	0.559
5.2	0.371	0.464	0.250	0.250
6.7	0.262	0.337	0.185	0.185
10.4	0.000	0.000	0.1	1.000

Table B.10: IGME 288 (Cadiz C1) backstripping results. Thickness & subsidence in kilometres. Sealevel corrections not applied as negligible in Neogene and Quaternary.

Well 245 – Cadiz G1

Horizon Top	Depth	Age*	Palaeowaterdepth		Watts & Steckler†	Pitman‡
			Min	Max		
Quaternary (Seabed)	0	0	0	0	0	0
Pliocene	218	1.64	0	100	0	0
U. Miocene (Tor–Mes)	785	5.2	50	200	0	0
Mid-Miocene (Lan–Srv)	840	10.4	100	1000	0	0
Unconformity	975	16.3	100	1000	0	0
Top Allochthon	975	-	-	-	-	-
T.D.	1527	-	-	-	-	-

Table B.11: IGME 245 (Cadiz G1) stratigraphy.

Age* (Ma)	Observed Sediment Thickness	Decompacted Sediment Thickness	Tectonic Subsidence	
			Min	Max
0.0	0.975	0.975	0.503	0.503
1.6	0.757	0.776	0.404	0.504
5.2	0.190	0.209	0.164	0.314
10.4	0.135	0.150	0.182	1.082
16.3	0.000	0.000	0.100	1.000

Table B.12: IGME 245 (Cadiz G1) backstripping results. Thickness & subsidence in kilometres. Sealevel corrections not applied as negligible in Neogene and Quaternary.

Well 533

Horizon Top	Depth	Age*	Palaeowaterdepth		Watts & Steckler†	Pitman‡
			Min	Max		
Plio-Quat.(Seabed)	0	0	0	0	0	0
Miocene	728.3	5.2	0	0	-5.6	20.0
Unconformity	752.3	23.3	0	0	25.5	90.8
Mid-Jurassic (Dogger)	752.3	159.4	0	0	-34	236.9
L. Jur (U. Lias)	1974.3	180.1	0	0	-32	239
L. Jur (M.-L. Lias)	2089.3	189.6	0	0	-32	239
Unconformity	2704.3	208	0	0	-32	239
Palaeozoic	2704.3	248.2	0	0	-32	239
T.D.	3054.3	-	-	-	-	-

Table B.13: IGME 533 stratigraphy. Sealevel corrections prior to the mid-Jurassic are extrapolated constants from the oldest mid-Jurassic sealevel curve values. Palaeobathymetry not available.

Age* (Ma)	Observed Sediment Thickness	Decompacted Sediment Thickness	Tectonic Subsidence	
			Watts & Steckler†	Pitman‡
0.0	2.704	2.704	1.151	1.151
5.2	1.976	2.137	0.956	0.919
23.3	1.952	2.117	0.904	0.809
159.4	1.952	2.117	0.990	0.598
180.1	0.730	0.915	0.497	0.105
189.6	0.615	0.786	0.440	0.047
208.0	0.000	0.000	0.046	-0.346
248.2	0.000	0.000	0.046	-0.346

Table B.14: IGME 533 backstripping results. Thickness & subsidence in kilometres.

GQB Well 223 (VM-1)

Horizon Top	Depth (km)	Age*	Observed Sediment Thickness	Decompacted Sediment Thickness	Tectonic Subsidence
Quaternary	0.000	0.0	1.196	1.196	0.612
Pliocene	0.056	1.64	1.140	1.151	0.591
U. Miocene (Tor-Mes)	0.389	5.2	0.807	0.866	0.455
Serravalian	0.966	10.4	0.230	0.278	0.157
Unconformity	1.196	14.2	0.000	0.000	0.000
Triassic	1.196	205.7	-	-	-
Palaeozoic	1.196	248.2	-	-	-

Table B.15: IGME 223 stratigraphy and backstripping results. Sealevel corrections not applied as negligible in Neogene and Quaternary. Palaeobathymetry not available.

GQB Well 225 (CN-1)

Horizon Top	Depth (km)	Age*	Observed Sediment Thickness	Decompacted Sediment Thickness	Tectonic Subsidence
Quaternary	0.000	0.0	1.623	1.623	0.798
Pliocene	0.145	1.64	1.478	1.506	0.745
U.Tor (assumed)	0.459	5.2	1.164	1.233	0.620
M. Tor (assumed)	0.701	7.9	0.922	1.005	0.514
Ser – L. Tor (assumed)	1.111	9.2	0.512	0.590	0.313
Unconformity	1.623	14.2	0.000	0.000	0.000
Palaeozoic	1.623	248.2	-	-	-
T.D.	1630	-	-	-	-

Table B.16: IGME 225 stratigraphy and backstripping results. Sealevel corrections not applied as negligible in Neogene and Quaternary. Palaeobathymetry not available.

* Ages of Harland *et al.* [1990] in the Cenozoic and Gradstein *et al.* [1995] in the Mesozoic.

† Sea-level corrections of Watts & Steckler [1979]

‡ Sea-level corrections of Pitman [1978]

B.3 Backstripping Results For All Available Gulf of Cadiz Wells

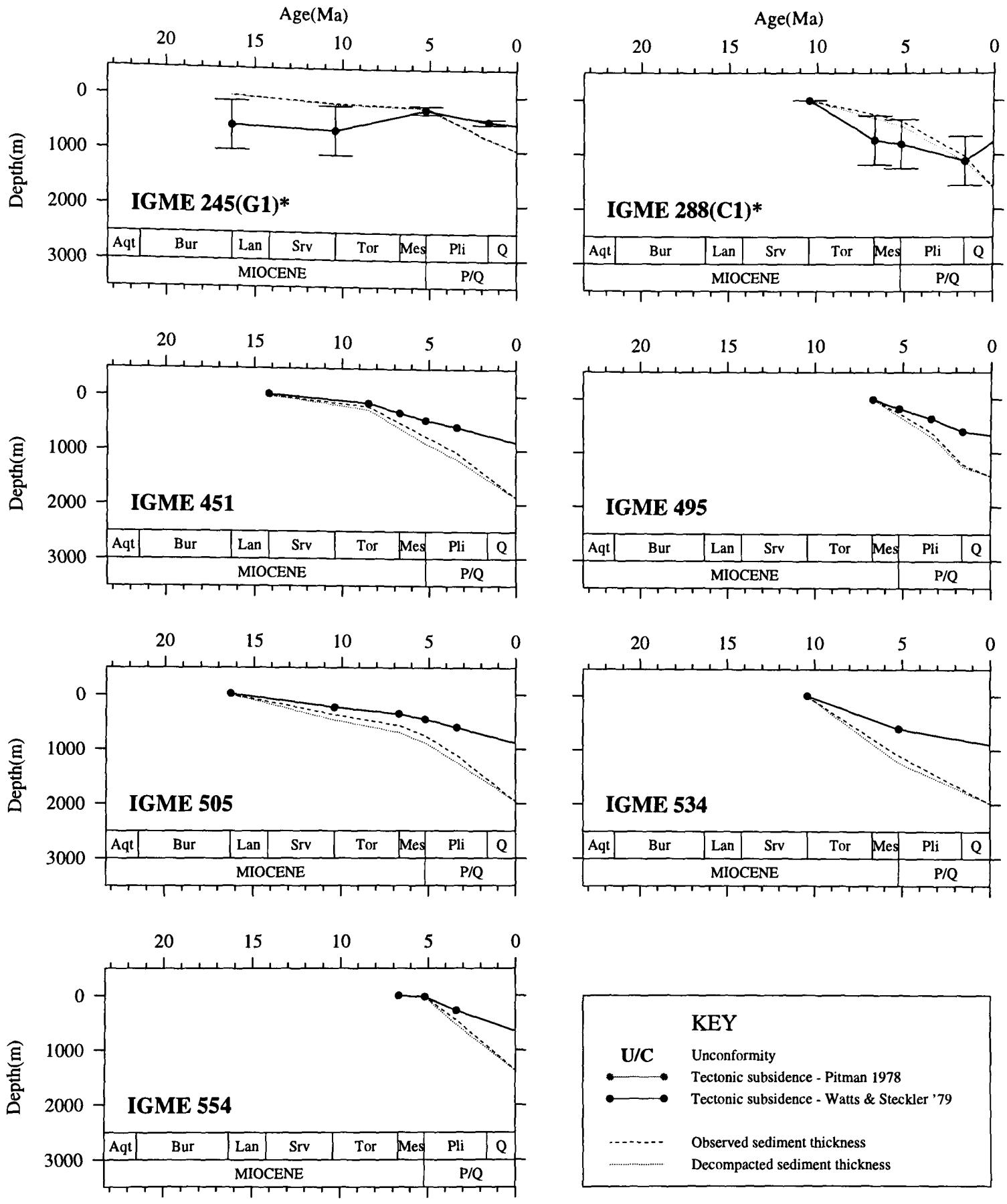


Figure B.3: 1-D backstripping results for wells penetrating only the Miocene to Recent of the GOC. Only the tectonic subsidence curves calculated with the Watts & Steckler [1979] sealevel correction are shown, as there is negligible difference between Watts & Steckler [1979] and Pitman [1978] sealevel curves in the Neogene (Miocene, Pliocene) and Quaternary.

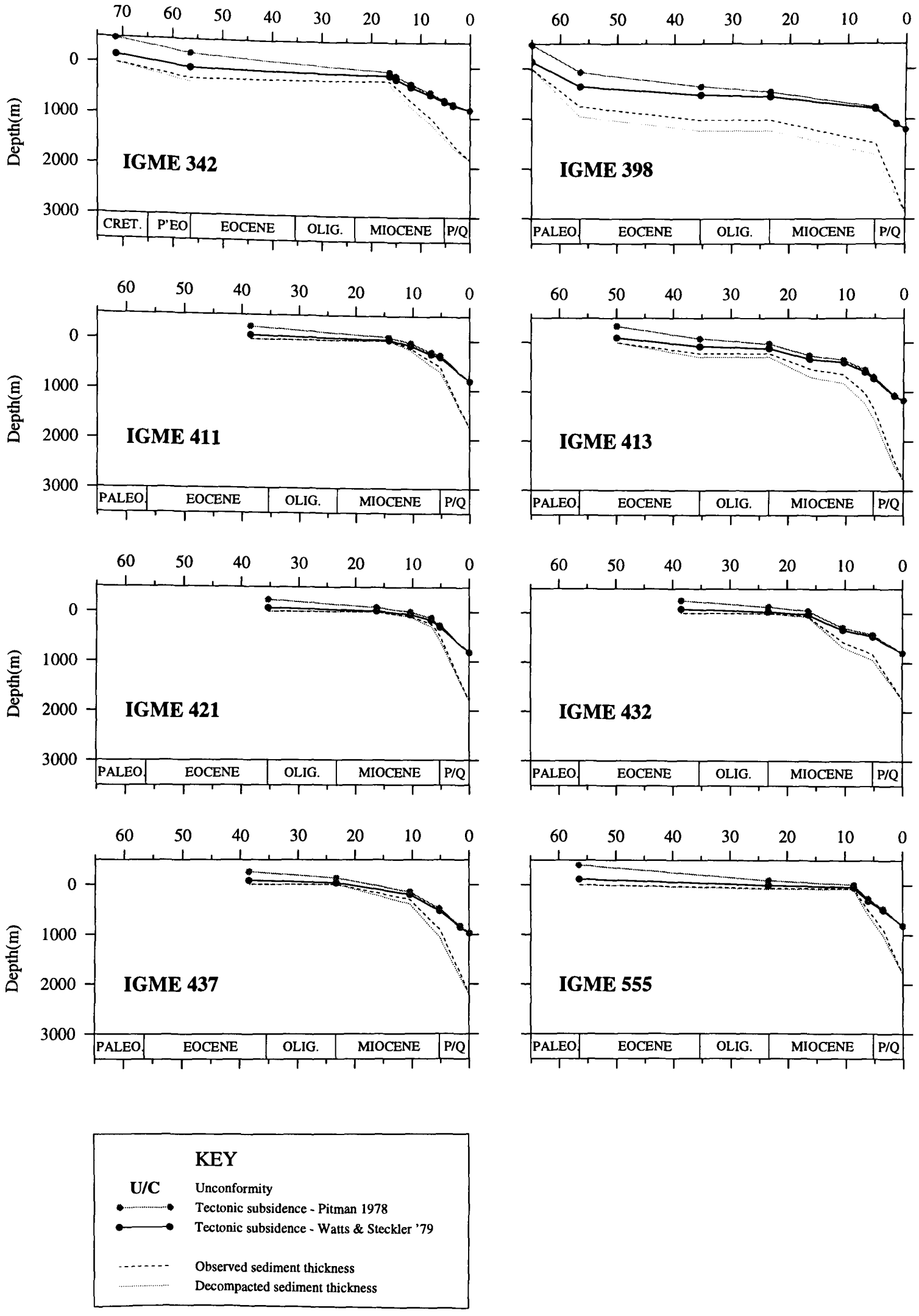


Figure B.4: 1-D backstripping results for wells penetrating only the Tertiary of the GOC.

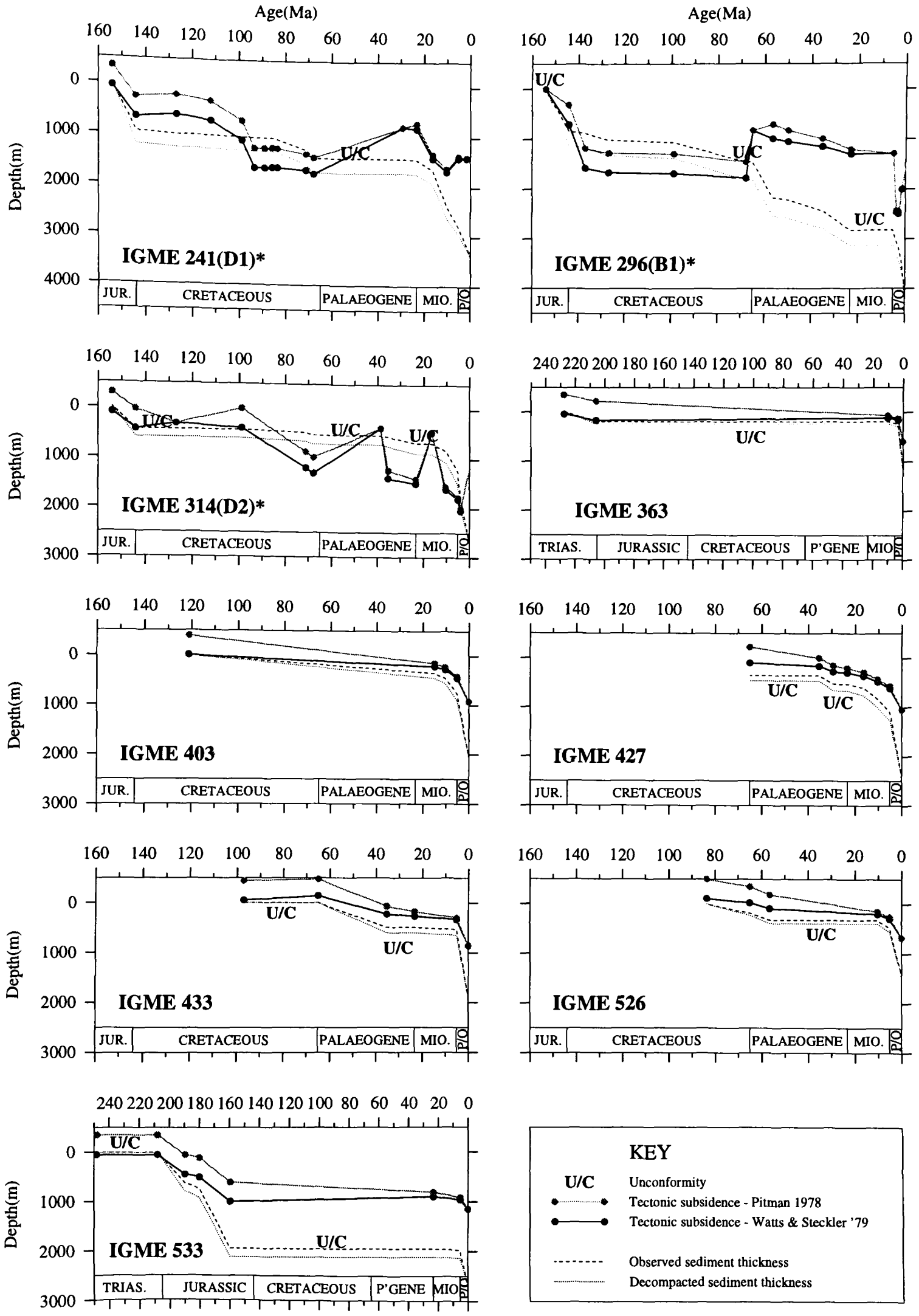


Figure B.5: 1-D backstripping results for wells penetrating the Mesozoic of the GOC. Backstrips for starred wells have incorporated palaeobathymetric data.

Appendix C

Basin Analysis Methods

C.1 Introduction

The basin analysis methods of seismic interpretation, backstripping, subsidence analysis, thermal modelling for β calculations, and gravity modelling, are used in this thesis. Through inverse and forward modelling these methods provide a powerful suite of tools with which to examine basin subsidence history, crustal structure, lithospheric type and its isostatic response to loading. Further constraints on models are provided by well logs, refraction profiles and stratigraphic data. The seismic interpretation and compilation of stratigraphic data is described in the relevant chapters, while this chapter is concerned with the explanation of the quantitative analysis methods of backstripping (with a new approach to the porosity-depth determination), β calculation, and gravity modelling, as used in this study.

C.2 Backstripping Methodology

Backstripping [Watts & Ryan, 1976] is a quantitative technique which allows the contribution to the subsidence and uplift of sediment loading to be evaluated at a well site, along a seismic reflection profile, or over an isopach map. Backstripping yields the depth that basement would be in the absence of sediment and water loads and, hence, the initial shape of the water-filled basin that resulted from rifting. The technique assumes either Airy isostasy or a finite flexural rigidity for the strength of the lithosphere.

The two steps in backstripping are **decompaction** and **unloading**. Sediment fill in a basin is made up of a series of layers resulting from deposition during specific time intervals. The process of backstripping allows the burial history of each sediment layer and the basement to be traced through time. As each layer is stripped off the thicknesses of the remaining, unloaded layers are decompacted by moving them up the porosity-depth function. At every incremental stage the palaeodepths (depths to the tops of each remaining layer) are calculated. The palaeodepth curve for the top of the basement represents the tectonically-driven subsidence, as sediment- and water-loading effects have



Figure C.1: The backstripping method (modified from Steckler & Watts 1978; Gallagher 1989). The aim is to isolate the tectonic subsidence Y from the original sediment thickness S.

been removed. Subsequently, the basement subsidence curve can be compared to theoretical subsidence curves - from the uniform lithospheric stretching model of McKenzie [1978], for example - in order to obtain an estimate for the lithospheric stretching factor, β. The β estimate is a useful parameter in terms of evaluating the thermal history of a basin, and lithospheric configuration.

Figure C.1 schematically illustrates the main steps in the backstripping method as described above.

C.2.1 Sediment Compaction and Decompaction

Rock volumes change with time and depth due to several factors. Before the final backstripping stage it is necessary to correct for these changes so true thicknesses at the time of deposition can be estimated for the backstripping process (Figure C.1a,b). Mechanical compaction is the major process, but the amount of compaction is very dependent on factors such as lithology, overpressuring and diagenetic effects. Clean sandstones compact far less than shales over similar depths and timescales, for example. Due to the reactivity of carbonates with water, limestones are liable to suffer a large amount of chemical alteration which cannot be accounted for by simple mechanical decompaction.

When modelling the mechanical compaction of a sedimentary layer it is commonly asssumed that during burial of a sedimentary layer the mass of sediment is constant and density increases, as the volume and thickness of the layer decrease because the the increase in overburden stress produces a progressive reduction in porosity through fluid expulsion. These assumptions imply conservation of mass and incompressibility of the matrix material. Conservation of mass is valid as long as dissolution and precipitation are local effects; the matrix incompressibility assumption is generaly justified because of the low compressibility of sedimentary grains. Effects of changes in lithology between sandstones, shales, limestones and dolomites are taken into account during decompaction studies, but secondary factors such as diagenesis and overpressure are not considered further.

In order to account for sediment compaction, porosity variation with depth in a compacting sedimentary basin must be known. There are a variety of methods of determining porosity in the subsurface, from direct core measurements to data from sonic, neutron and density well logs. For work on numerical decompaction, simple empirical porosity–depth functions are fitted to observed data.

Well Log to Porosity Conversion

Porosity can be estimated from downhole electrical logs, with sonic, neutron and density logs being the most sensitive to porosity. In this study , sonic logs have been used to derive porosity(Φ) in the Gulf of Cadiz, whereas all three types of well log listed above have been used in the Guadaquivir Basin studies.

A **sonic log** measures the interval transit time (Δt) of a compressional sound wave to travel one foot(traditionally) across a formation. The modern borehole compensated (BHC) sonic log consists of a pair of transmitters and a pair of receivers, whose readings are averaged. Δt is inversely proportional to the P-wave velocity (in feet per second) and so can be tied in with seismic velocities from reflection surveys. Sound velocity within a formation, and thus Δt, is a function of both its lithology and its porosity. It is therefore necessary to know a formation's matrix velocity in order to derive a sonic porosity either by chart or using an equation [Asquith & Gibson, 1982]. Matrix velocities (*ie.* rock porosity is zero) and corresponding interval transit times for the most common sedimentary rock types are given in Table C.1.

Various relationships exist for converting sonic log interval transit times into porosity values, which are all based on fitting theoretical values calibrated to observed data points

[redacted]

Table C.1: Sonic velocities and interval transit times for various rock types. ϕ=0 in all cases. (After Schlumberger Well Interpretation Charts, 1972 and 1991).

from cores and logs from a large number of wells. Figure C.2 illustrates how sonic-to-porosity equations are derived. The **time-average equation** of Wyllie *et al.* [1956, 1958] was the first widely used Δt–ϕ conversion method. These workers found that the readings of the sonic curve (Δt) represented the sum of two individual responses: that of the matrix (Δt_{ma}) and that of the fluid-filled porosity (Δt_f). The total response is controlled by the relative amounts of matrix and fluid as well as their individual responses, so that total response Δt_{log} is given by

$$\Delta t_{log} = (1 - \phi)\Delta t_{ma} + \phi \Delta t_f \tag{C.1}$$

Solving Equation (C.1) for ϕ the time-average equation is derived:

$$\phi_{sonic} = \frac{\Delta t_{log} - \Delta t_{ma}}{\Delta t_f - \Delta t_{ma}} \tag{C.2}$$

The time-average equation has been shown to hold reasonably well in consolidated sands and limestones with little vuggy/fracture porosity. For unconsolidated sands serious errors occur unless an empirical compaction factor modifies Equation (C.2).

The method of Wyllie *et al.* [1956, 1958] has been widely used, but has been gradually superceded by the empirical method of Raymer *et al.* [1980] who proposed a new relationship based on the comparison of transit times with core porosities (eg., Figure C.2) *and* porosities from other logs. For porous media, the relationship is approximated by the equation:

$$\phi_{sonic} = 0.63 \left[1 - \frac{\Delta t_{ma}}{\Delta t_{log}}\right] \tag{C.3}$$

which has the dual advantage of not requiring different matrix times for a given lithology and giving reasonable porosities in uncompacted sands in the Δt=100-150 microsecs/foot range. A good empirical fit for **sandstone** (Δt_{ma}=54 $\mu s/ft$), **limestone** (Δt_{ma}=48 $\mu s/ft$) and **dolomite** (Δt_{ma}=44 $\mu s/ft$) have been demonstrated [Raymer *et al.*, 1980], and because of its reliability this method was used for these three lithologies.



Figure C.2: Schematic diagram of the calibration procedure for porosity—sonic transit time equations used to derive porosities from sonic logs for use in compaction curve construction. Note that although a linear porosity-depth (ϕ–Z) curve is shown, this is not always the case. With respect to lab core measurements, PV=pore volume and BV=bulk volume.(After Issler [1992]).

The empirical regression equation of Raiga-Clemenceau *et al.* [1988] is an alternative equation for sonic transit time-to-porosity conversion, and introduces the concept of the acoustic formation factor x

$$\phi_{sonic} = 1 - \left[\frac{\Delta t_{ma}}{\Delta t_{log}}\right]^{1/x} \tag{C.4}$$

Issler [1992] calibrated this power-law function for thick shale sequences of the Beaufort-Mackenzie Basin, northern Canada, with a best-fit value of x=2.19. Thick shale sequences are also found in the Gulf of Cadiz and Guadalquivir Basin but because no shale or mudstone core data was available it was not possible to derive an acoustic formation factor

for the shales in this area, so the values given by Issler [1992] were used to convert **shale** transit times to porosity: Δt_{ma}=66 $\mu s/ft$, x=2.19.

Porosity–Depth Functions

The decompaction of a sedimentary layer are shown in Figure C.1 a,b. The mean porosity of the decompacted layer, $\bar{\phi}$, is just the mean value of the porosity function with depth, ϕ(z), over the interval $z_1' - z_2'$

$$\bar{\phi} = \frac{1}{(z_2' - z_1')} \int_{z_1'}^{z_2'} \phi(z) dz \tag{C.5}$$

which is a useful expression for inputting into the general flexural backstripping equation Equation (C.21) through the expression Equation (C.22). Our porosity information comes from well data, from which porosity values are extracted by methods explained in the previous section. The next stage is to find compaction trends in the data.

That porosity is a function of depth is an assumption which implies that the basin under consideration is, and has been, under hydrostatic pressure. Overpressures can be incorporated into the expressions if necessary [e.g., Thorne & Watts, 1989]), but overpressures are not considered in this study. Porosity reduction by cementation is important for diagenetic and reservoir studies within the hydrocarbon industry. However, for tectonic studies simple compaction models are sufficiently comprehensive [Gallagher, 1989]. Porosity-depth functions are generally derived by the fitting of empirical curves to observed data. Depending on data distribution workers have generally calculated porosity-depth curves with either a linear regression with the equation

$$\phi(z) = \phi_0 - -cz \tag{C.6}$$

or the commonly used exponential relation [Athy, 1930]

$$\phi(z) = \phi_0 \mathrm{e}^{-cz} \tag{C.7}$$

where ϕ = porosity, a function of depth, z, ϕ_0 = porosity at the surface and c is the compaction constant.

Workers such as Korvin [1984] and Gallagher [1989] have compiled lists of porosity studies showing an exponential decrease of porosity with depth, but other workers [e.g., Magara, 1980; Selley, 1978] agree that while an exponential relationship for shales is appropriate, a linear relationship can result as a result of diagenetic processes such as cementation. Figure C.3 shows some published, empirically derived curves for sandstone

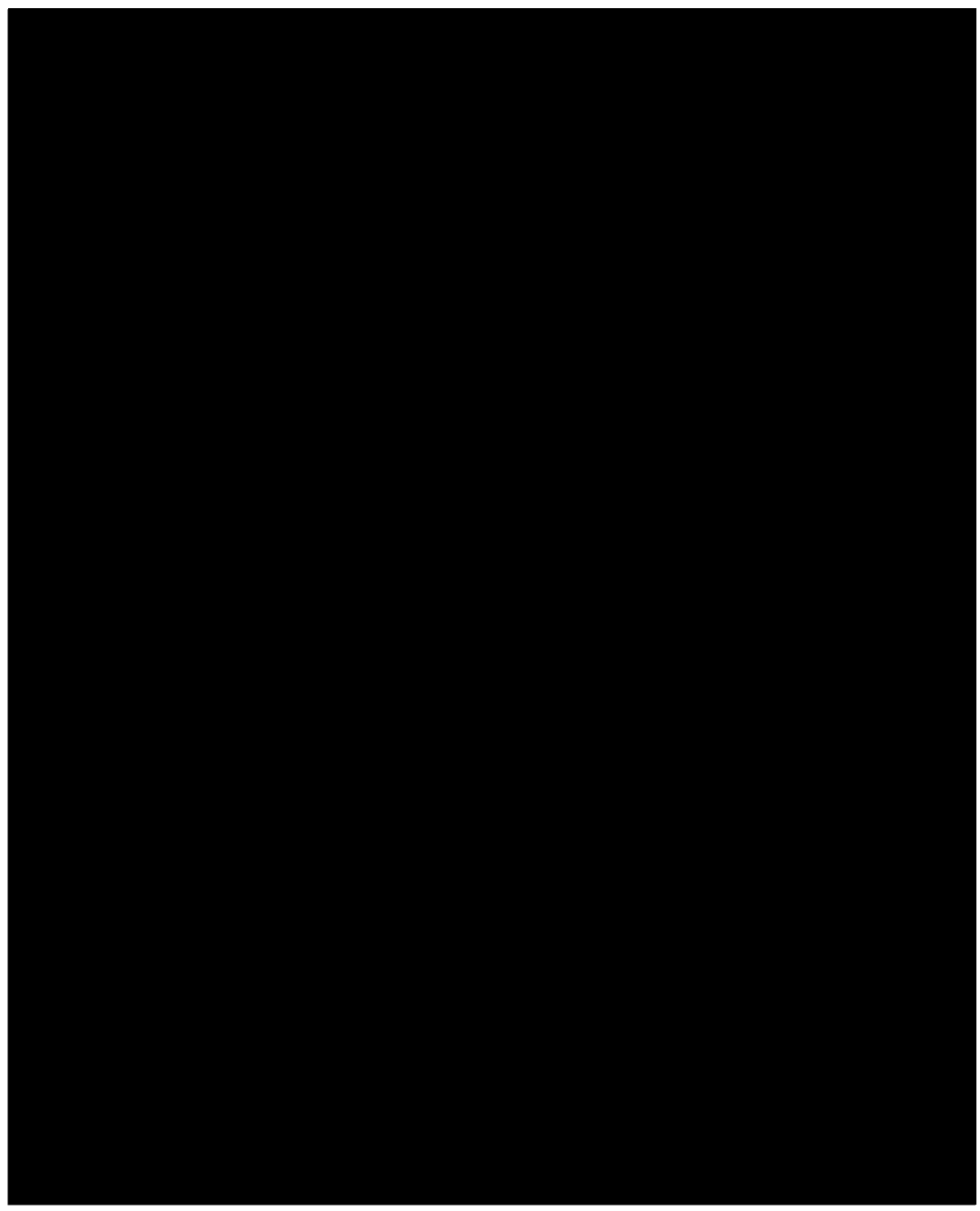


Figure C.3: Published porosity-depth relationships for sandstones and shales. After Gallagher [1989].

and shale, and a large spread of values for both lithologies is immediately noticeable. Bond & Kominz [1984] try to deal with the uncertainties in the data by specifying maximum and minimum porosities for lithologies based on published material. Gallagher [1989] tries to deal with the same problem by looking at errors associated with specified porosity-depth functions and compaction versus cementation as the primary mechanism of porosity reduction. For this study, however, what must be borne in mind is that as any assumptions involving porosity reduction are only first-order approximations, there are a wide range of possible mathematical relationships that could fit a given dataset.

This study follows the recent method of Audet [1995] who proposed an alternative method based on theoretical compaction curves. These derived from a continuum mechanics model for the gravitational compaction of sediments, which are assumed to be normally pressured and in a 1-D state of stress (uniaxial vertical compression ie zero hor-

izontal strain). The ability of sediments to sustain mechanical loading (their *strength*) is dependent on effective stress, which is related to the sediment porosity. It can be shown that two mechanical parameters are sufficient to describe a realistic porosity-depth function: the compression index C_c and the void ratio e_{100} which is the ratio of pores to matrix. Both parameters can be determined in the laboratory using uniaxial compression methods, and many such values for both clays and coarser clastics are found in the geotechnical literature [e.g., Burland, 1990]. C_c values have been found to be 0.1–0.3 for silts and sandy clays, 0.4–0.6 for non-expandable clays, and 0.7 or more for colloidal and organic -rich clays. An expression for theoretical compaction can be derived:

$$\exp_{10}\left(\frac{e_{100}-e}{C_c}\right)\left(1+\frac{C_c}{\ln 10}+e\right)=\frac{d}{L}+K \tag{C.8}$$

which relates porosity (expressed as the void ratio e) and depth. L is a length constant and is given by

$$L=\frac{\sigma_{100}}{(\rho_s-\rho_f)g}$$

K is dimensionless and defined as

$$K=\left(\frac{\sigma_0}{\sigma_{100}}\right)\left(1+\frac{C_c}{\ln 10}+e_0\right)$$

where σ_0 is the effective stress at initial void ratio e_0 and may be evaluated for the given effective stress at the depositional surface of the model ($d = 0$), which in reality corresponds to a a very shallow burial depth (σ_0=10 kPa is equivalent to d≈2m, for example) where sediments become cohesive and soil-like in behaviour. Audet [1995] has shown that the curve-fitting procedure is not very sensitive to the boundary condition σ_0, showing that curves fitted using σ_0=10 kPa and σ_0=100 kPa are almost identical below 50 m depth for shallow calcareous marine oozes. A value σ_0=10 kPa results in a higher initial porosity and is more appropriate for shallow, marine oozes, but in this study σ_0=100 kPa as the wells are either shallow marine or terrestrial and kilometres deep.

The derivation of Equation (C.8) from soil mechanics theory, and its ties with experimental work, are described in Audet [1995, 1996]. The theoretical curves thus derived account for both the sharp decrease in porosity at shallow depths that would be expected, as well as the less steep, almost linear decreases in porosity with greater depths, as seen on Figure C.3. The method of Audet [1995] is preferable for fitting functions

to the log-derived porosity data due to its advantages over the purely empirical linear and exponential fits: namely, its sounder theoretical foundation and better calibration through experimental work for clays,oozes and fine sands and silts. As sediments in the Guadalquivir and Gulf of Cadiz wells are largely shales and mudrocks this method can be used.

C.2.2 Absolute Ages, Palaeobathymetry and Sea Level

The data points on a subsidence curve originate from the stratigraphic boundaries, of presumed known absolute age, defining stratigraphic units of known present-day thickness. The stratigraphic periods for horizons given in IGME [1987] and commercial well data were converted to absolute ages using the following standard time scales:Harland *et al.* [1990] for the Cenozoic and Gradstein *et al.* [1995] for Mesozoic. Thus, each horizon top had a given age. Unconformities were given age brackets *ie.* two ages, to represent the period of non-deposition or erosion. The periods of unconformities were shown simply as periods of non-deposition as estimates of erosion were beyond this study, though they are possible [e.g., Issler, 1992].

Palaeobathymetric corrections can be very significant when constructing burial histories for a given sedimentary sequence. Palaeodepth (the water depth at time of deposition of a given stratigraphic horizon) is difficult to estimate, but the main sources of information on this parameter are benthic microfossils, most importantly, and less importantly, sedimentary facies and geochemical signatures [Allen & Allen, 1990]. A palaeontologist will use various techniques to derive an estimate of the environment of deposition and its depth range. These estimates were not always available, but where they were palaeobathymetry ranges for input into the backstripping process were estimated from descriptions of environment of deposition, to the scheme set out below in Table C.2.

A correction also needs to be made for the ambient sealevel relative to that of today at time of deposition *ie.* absolute change in sea level (eustatic correction). The issue of absolute versus relative sealevel changes, and the production of various global sea level curves [e.g., Vail *et al.*, 1979; Haq *et al.*, 1987]) is a major area of controversy in itself, and will not be discussed further here. Backstripping was carried out using sea level corrections from two first-order eustatic sea level curves: that of Pitman [1978] based on volume changes in the ocean ridge system, and that of Watts & Steckler [1979] based on backstripping studies. As the oldest sediments backstripped in the study are Upper Jurassic in age the Pitman curve had to be extended back beyond 85 Ma, and this was done by taking the difference between the Pitman [1978] and Watts & Steckler [1979]

Environment of Deposition	Assumed Depth Range (m)
Continental/Tidal Flat	0
Neritic–Inner Shelf	0–50
Neritic–Middle Shelf	50–100
Neritic–Outer Shelf	100–200
Carbonate Shelf–Restricted	0–20
Carbonate Shelf–Open	0–100
Continental Shelf	0–150
Deep Clastic Shelf	100–150?
Shallow Marine	0–200
Continental Slope	150–2000
Bathyal	200–2000
Bathyal to Abyssal	1500–2500?
Abyssal	>2000

Table C.2: List of assumed palaeodepth ranges for given environments of deposition, for use in backstripping corrections.

at 85 Ma and maintaining this difference back to 165 Ma which is the oldest given age for the Watts & Steckler [1979] curve. Figure C.4 illustrates the two curves used for sea level corrections.

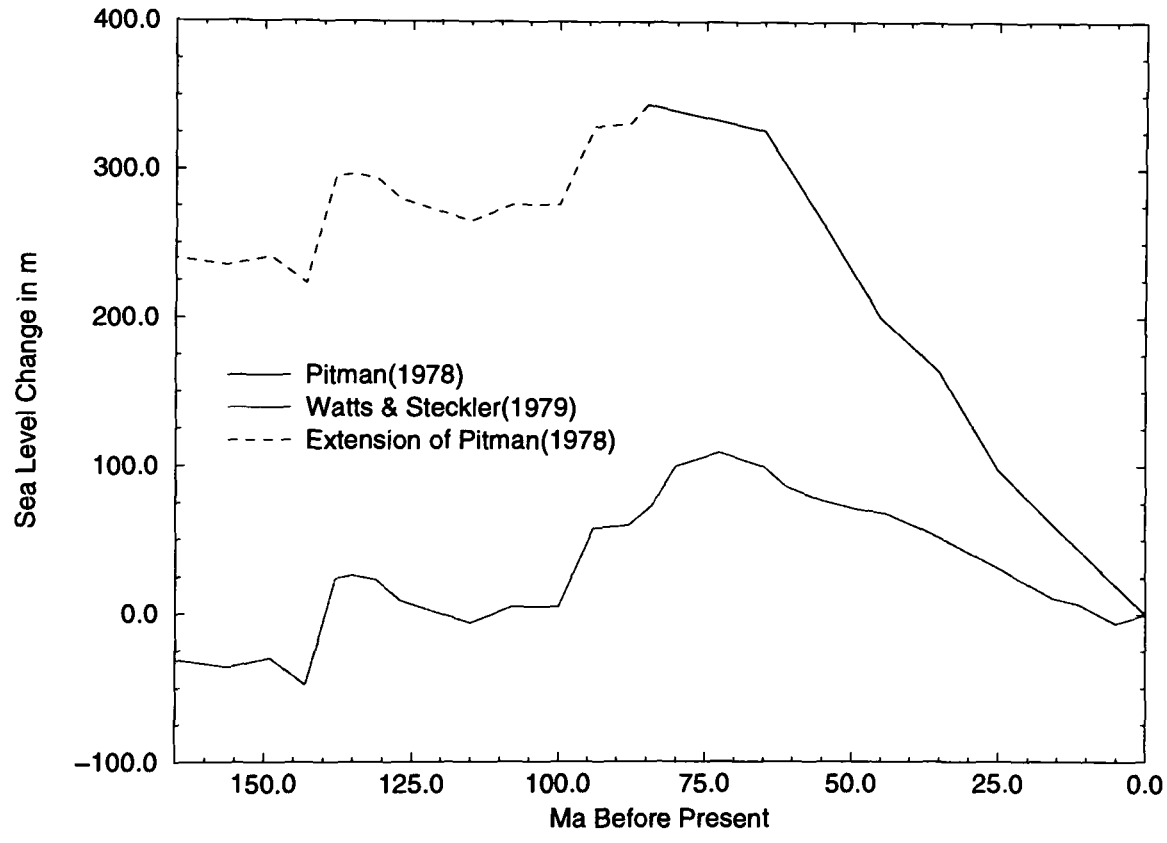


Figure C.4: Sea level curves used for backstripping corrections.

C.2.3 Airy (1D) Backstripping

Where sedimentary history is known only at a point, such as a well, Airy (1-D) backstripping is used [Watts & Ryan, 1976; Steckler & Watts, 1978; Watts, 1988]. The 1-D backstripping equation is based on simple balancing of columns of unit cross-sectional

area (columns b) and c) of Figure C.1), assuming Airy isostatic compensation . In this simple case, the following expression for the water-filled tectonic subsidence for Airy isostasy, Y, can be derived [Steckler & Watts, 1978]:

$$Y = S^* \left[\frac{\rho_m - \rho_s}{\rho_m - \rho_w}\right] - \Delta_{sl} \left[\frac{\rho_w}{\rho_m - \rho_w}\right] + W_d \qquad (C.9)$$

where S^*=decompacted sediment thickness; ρ_m, ρ_s and ρ_w are the densities of mantle, sediment and water respectively; W_d is water depth at time of deposition and Δ_{sl} is the sea level relative to the present day.

Core data and geophysical logs allow high quality information on lithology, porosity, palaeobathymetry and biostratigraphic age to be input into the subsidence analysis process. Figure C.5 illustrates the data inputs into the 1D backstripping program, and how β is derived by comparison with theoretical curves [e.g., McKenzie, 1978; Jarvis & McKenzie, 1980]). One limitation of the Airy approach is that the estimate of tectonic subsidence is confined to the immediate vicinity of the well.

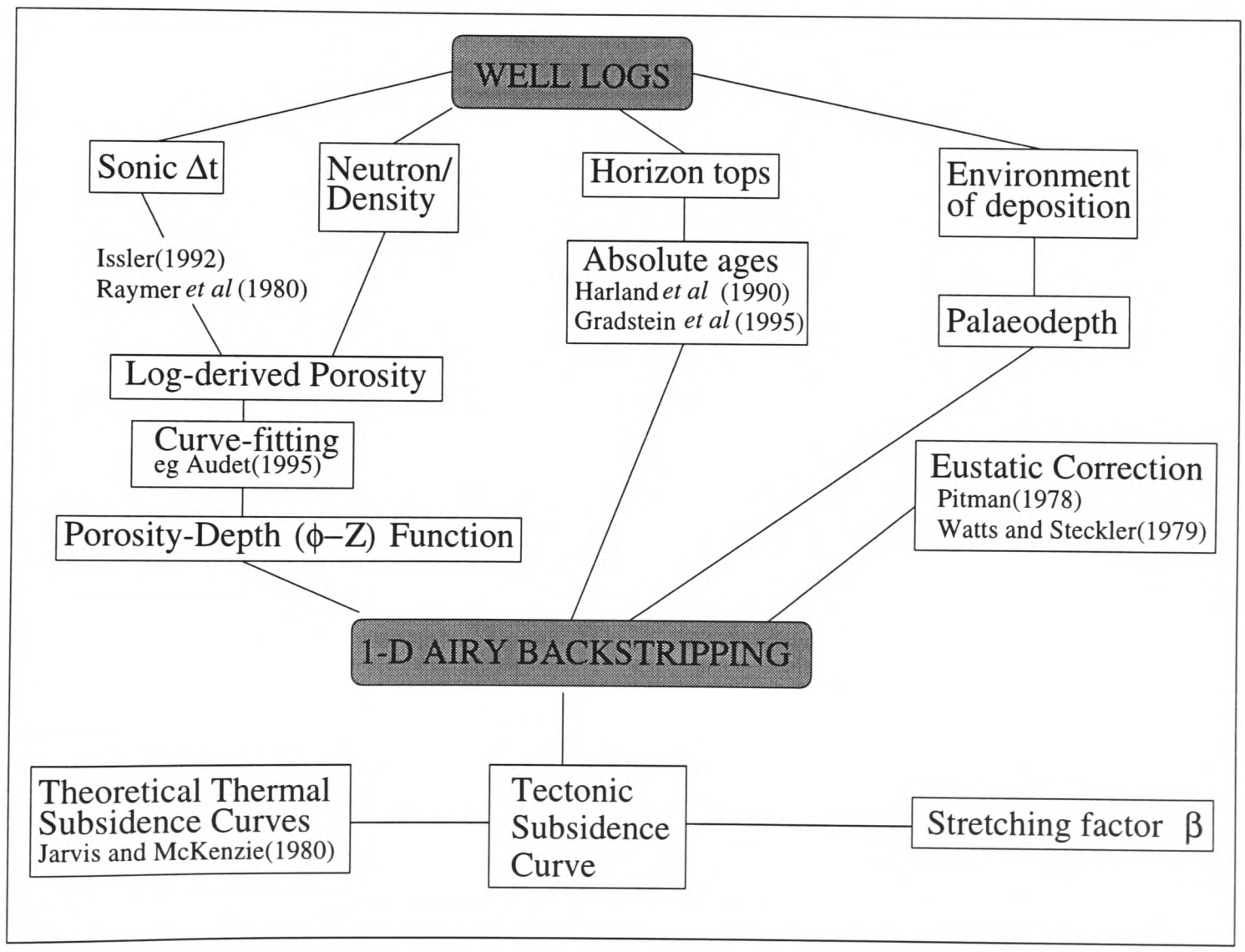


Figure C.5: Flowchart illustrating the methodology of 1D Airy backstripping as carried out with well data in this study.

C.2.4 Flexural Backstripping

Airy, or local, isostasy is often assumed for backstripping as the calculations are simpler and only require well data. However, if the lithosphere possesses any flexural rigidity (an ability to support a load) then an assumption of Airy isostasy will overcorrect for the sediment load and thus underestimate the tectonic subsidence [Gallagher, 1989]. The values of some parameters inferred from subsidence curves, such as β, may be up to 40% in error [Watts *et al.*, 1982]. Flexural corrections can be made when there is a regional constraint on sediment thicknesses.

2D flexural backstripping can be applied when seismic reflection profiles are available, [e.g., Watts & Ryan, 1976; Sawyer, 1985; Bessis, 1986]. Where sufficient density of seismic data exists, isopach maps of sediment thicknesses are constructed and backstripped using the flexural backstripping method extended to 3D. Such studies have been carried out in the Valencia Trough [Watts & Torné, 1992], the North Sea [Thorne & Watts, 1989] and offshore Namibia [Stewart *et al.*, Submitted].

After the decompaction stage of backstripping the loading effects of sediment and water(from sea level changes) can be removed (Figure C.1c). The solution of the **flexure equation** below gives the response (w) of the lithosphere to a sediment load l and a water load Δ_{sl}:

$$D\frac{d^4w}{dx^4} + (\rho_m - \rho_{infill})gw = (\rho_s - \rho_w)gl + \rho_w g\Delta_{sl} \tag{C.10}$$

where g is gravitational acceleration, ρ_m is the density of the mantle, ρ_{infill} is the density of the material infilling the flexural depression, ρ_w is the density of water.
The average density of the sediment load, ρ_s where ρ_{sg} is the density of sediment grains, is given by

$$\rho_s = \bar{\phi}\rho_w + (1 - \bar{\phi})\rho_{sg} \tag{C.11}$$

The flexure equation is a fourth-order differential equation for the deformation of a thin elastic plate overlying a weak, fluid substratum [Gunn, 1947] and has a solution of the form

$$w = Pe^{-\lambda x}(\cos\lambda x + \sin\lambda x) \tag{C.12}$$

with bending wavelength λ given by

$$\lambda = \left[\frac{(\rho_m - \rho_{infill})g}{4D}\right]^{\frac{1}{4}} \tag{C.13}$$

and D is the flexural rigidity of the plate, which determines the wavelength over which the plate bends. The flexural rigidity can be expressed in terms of an equivalent elastic plate thickness, T_e

$$D = \frac{ET_e^3}{12(1-\sigma^2)} \tag{C.14}$$

where E is Young's modulus and σ is Poisson's ratio. For constant flexural rigidity D, Equation (C.10) can be solved by taking the Fourier transform of both sides

$$\begin{aligned} \bar{W}(Dk^4 + (\rho_m - \rho_{infill})g) &= (\rho_s - \rho_w)g\bar{L} + \rho_w g\bar{\Delta}_{SL} \\ \bar{W} &= \Phi\left[\bar{L}\frac{\rho_s - \rho_w}{\rho_m - \rho_{infill}} + \bar{\Delta}_{SL}\frac{\rho_w}{\rho_m - \rho_{infill}}\right] \end{aligned} \tag{C.15}$$

where k is the wavenumber related to the wavelength of the load, λ, by $2\pi/\lambda$; barred uppercase variables denote the Fourier transform of the lower case variable and Φ is the flexural parameter

$$\Phi = \left[1 + \frac{Dk^4}{(\rho_m - \rho_{infill})g}\right]^{-1} \tag{C.16}$$

Φ is also known as the basement response function or wavenumber parameter which represents the modification to an Airy solution to produce flexure [Allen & Allen, 1990; Watts, 1983].

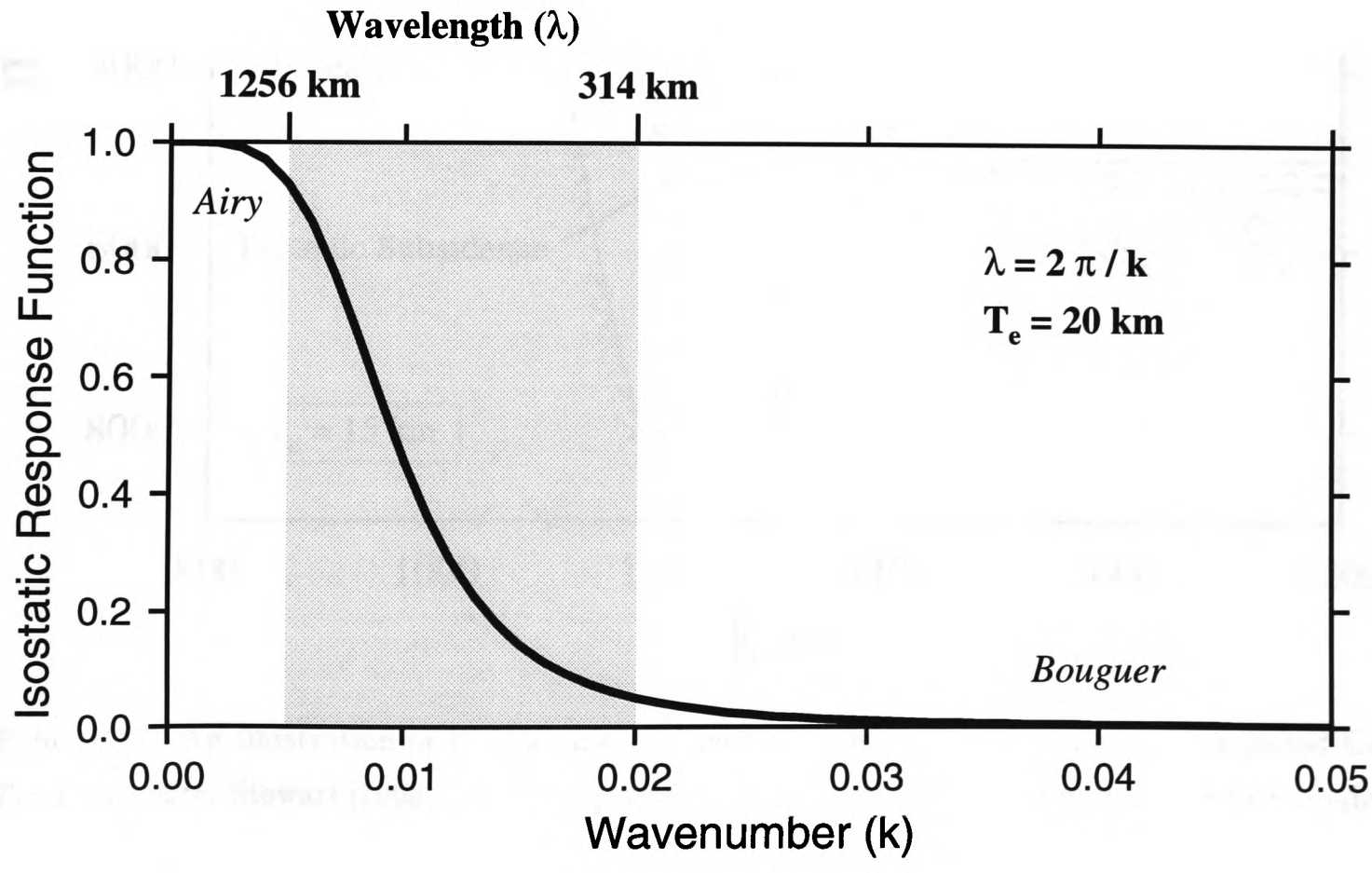


Figure C.6: Variation of response function Φ with wavenumber,and correspondingly, load wavelength, for lithosphere of T_e=20km.

Figure C.6 illustrates the variation of the response function with load wavelengths for a constant T_e (and therefore a constant D). It can be seen that at short wavelengths (k >0.02) Φ tends to zero, *ie.* the elastic plate appears rigid. The grey area shows the region of transition between rigid (Bouguer slab) behaviour and zero rigidity (Airy) behaviour for a lithosphere of T_e=20km. For lower T_e and lower D, the Φ curve will be to the right of that shown *ie.* Airy behaviour will be approached at smaller load wavelengths. In the Airy case, D=T_e=0, thus Φ=1, so that upon substituting for Φ and taking the inverse Fourier transform of Equation (C.15) the following solution for the flexural deflection w is arrived at:

$$w = l\left[\frac{\rho_s - \rho_w}{\rho_m - \rho_{infill}}\right] + \Delta_{sl}\left[\frac{\rho_w}{\rho_m - \rho_{infill}}\right] \tag{C.17}$$

Figure C.7 shows that S^* (the decompacted thickness of a sedimentary layer) can be

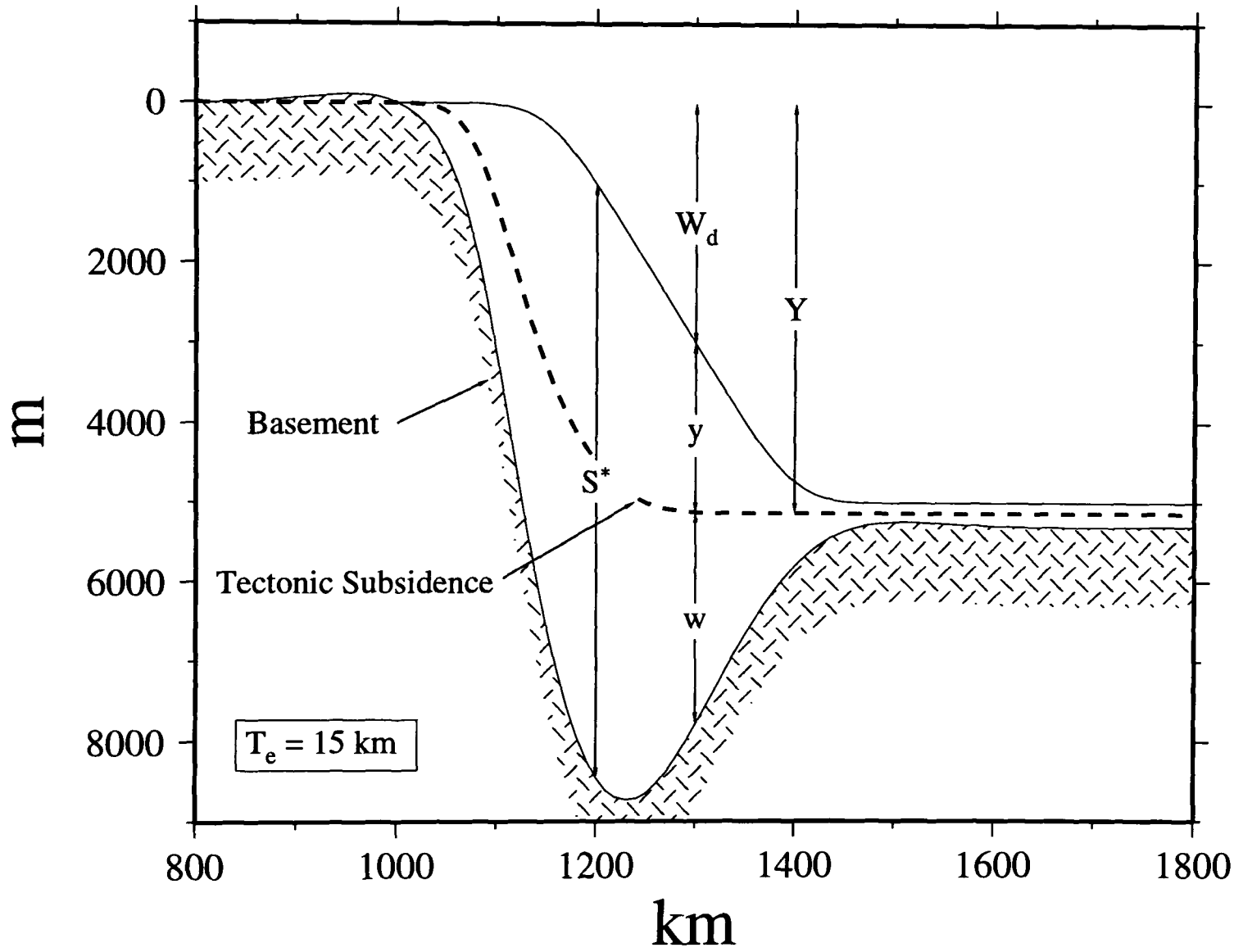


Figure C.7: An illustration of the parameters involved in flexural backstripping, calculated for T_e=15km (after Stewart [1998]). A decompacted sedimentary layer of thickness S^* can be thought of as the sum of a load y and its flexure w. The tectonic subsidence $Y = y + W_d$ is shown in the thick dashed line. The backstripping process takes the decompacted sediment thickness S^* and calculates y to which either an estimate of W_d or any remaining water is added to obtain the tectonic subsidence Y.

considered as the sum of a load y and its flexure w *ie.* $S^* = y + w$, and that the tectonic subsidence $Y = y + W_d$ where W_d is the water depth. Y is shown as a thick dashed line on the figure. The load height y is most easily obtained from the observed sediment thickness, S^* by replacing l by S^* in Equation (C.17) and setting $\rho_{infill} = \rho_w$.

$$w = S^* \left[\frac{\rho_s - \rho_w}{\rho_m - \rho_w}\right] + \Delta_{sl} \left[\frac{\rho_w}{\rho_m - \rho_w}\right] \tag{C.18}$$

A term for the tectonic subsidence can be obtained through a series of substitutions as follows

$$\begin{aligned} Y &= y + W_d \\ &= S^* - w + W_d \\ &= S^* - \left(S^* \left[\frac{\rho_s - \rho_w}{\rho_m - \rho_w}\right] + \Delta_{SL} \left[\frac{\rho_w}{\rho_m - \rho_w}\right] \right) + W_d \\ &= S^* \left[\frac{\rho_m - \rho_s}{\rho_m - \rho_w}\right] - \Delta_{SL} \left[\frac{\rho_w}{\rho_m - \rho_w}\right] + W_d \end{aligned} \tag{C.19}$$

which is the water filled tectonic subsidence for Airy isostasy given in Equation (C.9). For typical densities, the loading correction term (first term on RHS of Equation (C.19)) is about 2/3 of the sediment thickness.

The tectonic subsidence term for the flexural case is obtained by substituting S^* for l, and ρ_w for ρ_{infill} in Equation (C.15) and proceeding as above. The tectonic subsidence is then

$$Y = S^* - \mathcal{F}^{-1} \left\{ \Phi \bar{S}^* \left[\frac{\rho_s - \rho_w}{\rho_m - \rho_w}\right] + \bar{\Delta}_{SL} \left[\frac{\rho_w}{\rho_m - \rho_w}\right] \right\} + W_d \tag{C.20}$$

where $\mathcal{F}^{-1}$ represents the inverse Fourier transform. For a basin comprising n layers Equation (C.20) becomes a sum over the n layers and thus, the tectonic subsidence (Y_i) at the time of deposition of layer i, is

$$Y_i = \sum_{i=1}^{n} \left(S_i^* - \mathcal{F}^{-1} \left\{ \Phi \bar{S}_i^* \left[\frac{\rho_{si} - \rho_w}{\rho_m - \rho_w}\right] + \bar{\Delta}_{SL} \left[\frac{\rho_w}{\rho_m - \rho_w}\right] \right\} \right) + W_{di} \tag{C.21}$$

where S_i^* =total thickness of all decompacted layers at time i, W_{di} =water depth at time i. ρ_{si} =average density of the entire decompacted column at time i such that

$$\rho_{si} = \frac{\sum_{i=1}^{n} \left[\bar{\phi}_i + \rho_{sgi}(1 - \bar{\phi}_i)\right] z_i^*}{S_i^*} \tag{C.22}$$

where z_i^* is the thickness, ρ_{sgi} is the density of the sediment grains and $\bar{\phi}_i$ is the mean porosity of the i^{th} decompacted layer. Backstripping variable lithologies is thus possible with this term.

The methodology for flexural backstripping can be summarised as follows

1. Interpret regional seismic profiles, using well and other stratigraphic data, to construct 2-D basin profiles or 3-D sediment thickness grids. Where picks are carried out in TWTT(s) rather than depth, depth convert the picks using appropriate velocity models.

2. Assuming the lithosphere has strength, its behaviour can be described by a thin elastic sheet model. The most recent startigraphic unit is removed and the new position of the remaining sediments and backstripped basement is calculated and recorded.

3. Remove the next layer and calculate as in the above step. Continue the backstripping for each stratigraphic interval until only the final unloaded basement is left.

4. Calculate the crustal structure from the final position of the backstripped basement, and input to the gravity modelling procedure.

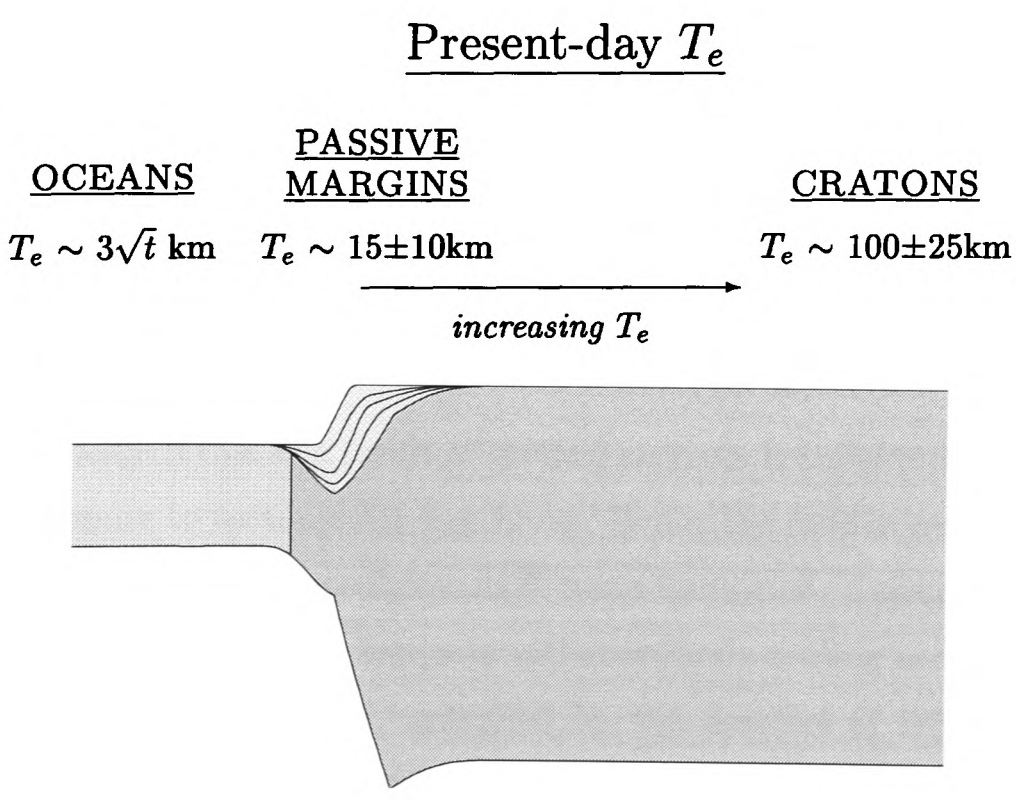


Figure C.8: A schematic illustration of representative present-day T_e values from oceanic to continental lithosphere, based on compilations in Stewart [1998]. The oceanic variation in T_e is based on the cooling plate model (fits shown on Figure C.9).



Figure C.9: Plot of T_e against age for the oceanic lithosphere at the time of loading (Watts, 1994). The solid and dash lines show the 300, 450 and 600°C isotherms based on a cooling plate model.

C.3 Calculation of Stretching Factor, β

C.3.1 Thermo-Mechanical Models of Extensional Basins

A sedimentary basin forms as a result of vertical motions ie subsidence and uplift of the lithosphere in response to tectonic driving forces. Hence the fundameental importance of subsidence studies in explaining mechanisms of basin formation. Subsidence is principally driven by lithospheric extension, subsequent asthenospheric cooling and sediment loading. Initially, the depth of the basin is controlled by the amount of lithospheric thinning (stretching factor β) and the interplay of thermally-induced uplift and sediment-loaded subsidence. As time passes, the asthenosphere cools and thermal contraction contributes to basin subsidence.

The thermo-mechanical consequences of lithospheric extension, and subsequent basin evolution, can be explored using simple physical models. According to Coward [1986] the range of possible mechanisms of basin formation are encompassed between two end member models: the pure shear model of McKenzie [1978] and the simple shear model of Wernicke [1985]. The uniform stretching model of McKenzie [1978] thins the lower lithosphere by ductile extension beneath a brittle crust thinned by faulting, and then imposes a thermal subsidence on the early fault-bounded basin [Kearey & Vine, 1990]. The Wernicke [1985] model, on the other hand, involves whole lithospheric shear along low angle normal faults, offsetting the regions of lower lithospheric stretching and thermal subsidence. Both models have been found to explain observations in different settings, e.g., the McKenzie model in the North Sea Central Graben [Barton & Wood, 1984], and the Wernicke model in the Basin and Range Province of the western USA [Wernicke, 1981; Wernicke & Burchfiel, 1982; Wernicke, 1985]. Other models mix pure- and simple-shear models in differing amounts, a common example being the flexural–cantilever model [Kusznir *et al.*, 1991; Kusznir & Ziegler, 1992] in which the brittle upper crust deforms along planar normal faults by simple shear, and the ductile lower crust and mantle deform through pure shear.

The pure shear model of uniform lithospheric stretching has proved generally successful in explaing the first-order geometry, and observed subsidence, of many extensional basins worldwide. It is therefore examined more closely in the next section.

C.3.2 Pure Shear Model of Lithospheric Extension [McKenzie, 1978]

McKenzie [1978] outlined a simple quantitative model of the response of the lithosphere to instantaneous and uniform stretching, as shown in Figure C.10, assuming **local** (Pratt) isostatic equilibrium, as illustrated further in Figure C.11.

In Figure C.10, a lithospheric segment of length a and thickness L is instantaneously stretched by a factor β, yielding a new length and thickness L/β. The extension also causes upwelling of hot asthenosphere , causing a thermal anomaly and producing an initial subsidence (S_i) as an isostatic response. After a sufficient length of time - at least greater than the lithospheric time constant, τ (see Table C.3)- the thermal anomaly totally decays, and the original lithopsheric thickness and thermal structure are restored, although the crust remains thinned. During the decay of the asthenospheric thermal anomaly, the basin undergoes thermal subsidence which, along with the initial subsidence, makes up the total subsidence. If there no longer exists a thermal perturbation, this total subsidence equals the subsidence in the absence of sediment loading - the total tectonic

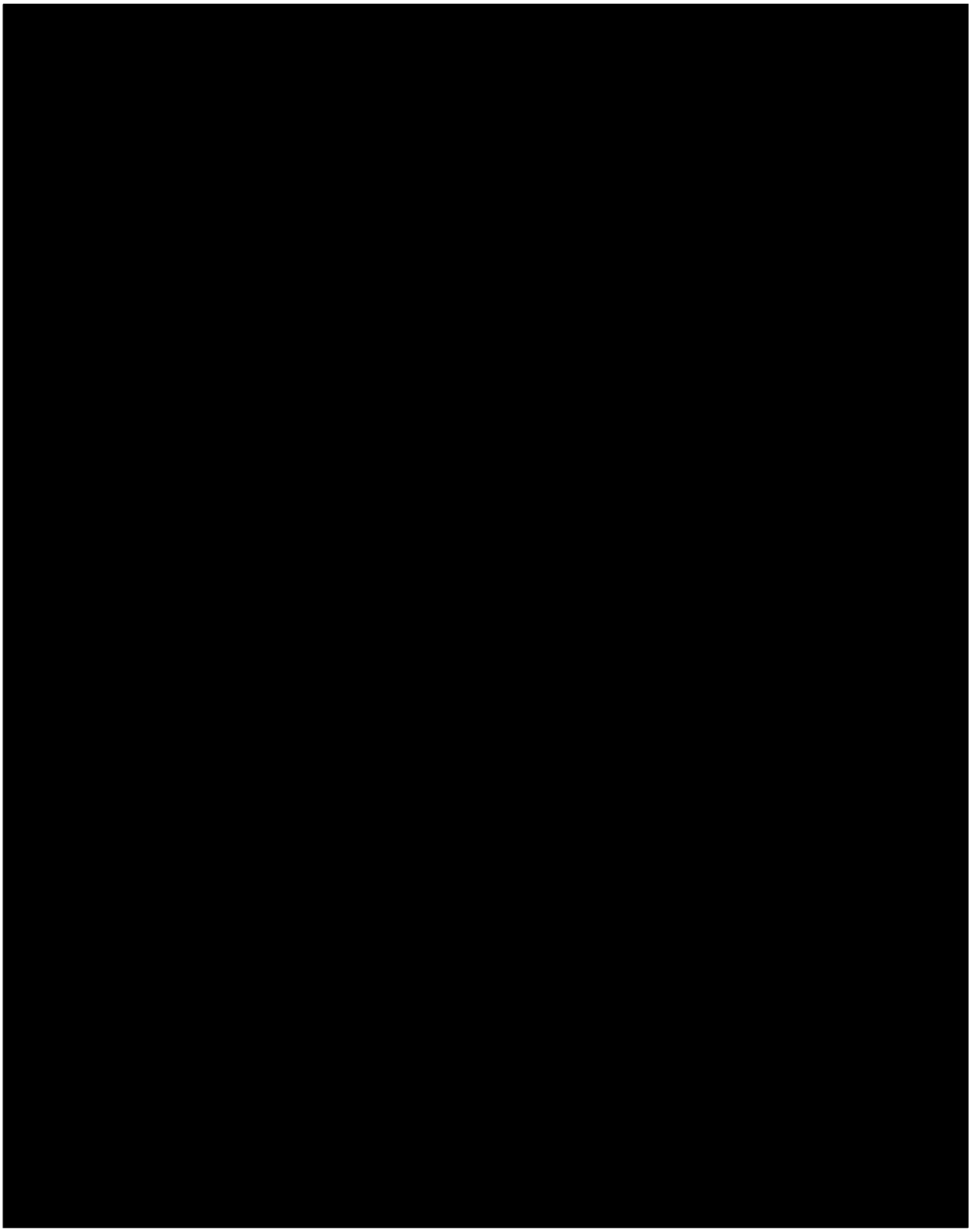


Figure C.10: Uniform stretching model of McKenzie [1978] where a region of length a is extended by a factor β. **a)** shows the pre-rift configuration and thermal structure of the lithosphere. **b)** shows the configuration of stretched lithosphere immediately after rifting, with the higher temperature gradient to the base of the lithosphere. **c)**As time tends to infinity, the lithosphere relaxes to its pre-stretching temperature structure. S_i is the initial subsidence and TTS is the total tectonic subsidence. See text for further explanation. (Modified from Allen & Allen [1990]).

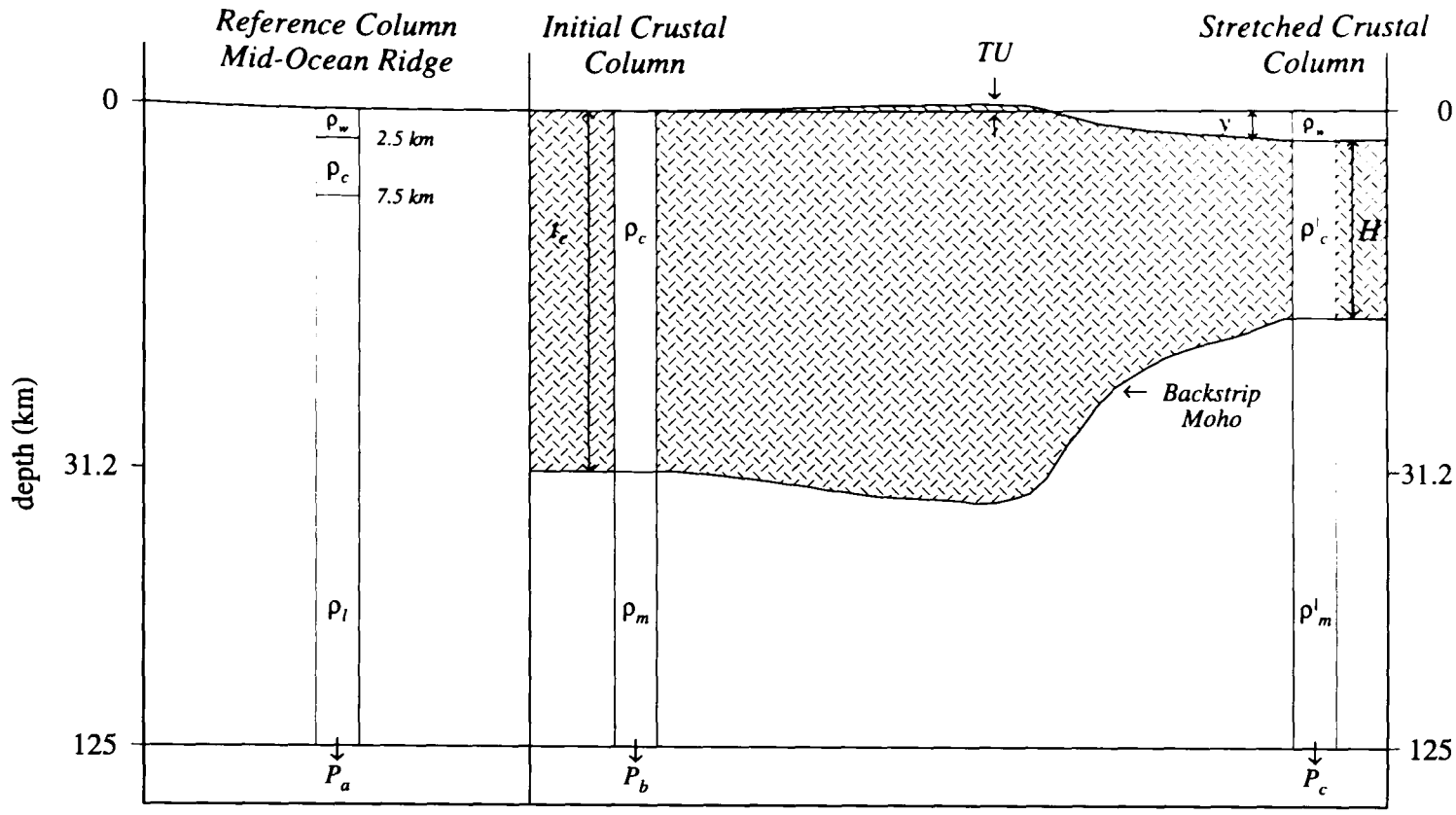


Figure C.11: Illustration of how local (Pratt) isostasy is used in the uniform stretching model to calculate tectonic subsidence. The initial and stretched crustal columns are balanced against a reference mid-ocean ridge column. The columns shown are balanced at lithospheric thickness L= 125 km *ie.* pressures at base of columns are all equal: P_a=P_b=P_c. TU = tectonic uplift.

subsidence TTS.

Figure C.11 shows how a column of standard, unstretched continental crust balances a mid-ocean ridge reference column with 2.5 km water, 5 km of oceanic crust and 117.5 km of mantle lithosphere, assuming local, Pratt isostasy. This also balances the stretched continental crust with thickness $H = t_c/\beta$, and the example illustarted is shown for standard values, which are given in Table C.3.

Many subsequent variations and improvements to the McKenzie [1978] model have been proposed, namely:

a) models with finite durations of rifting, including consideration of lateral heat flow [Jarvis & McKenzie, 1980; Cochran, 1983]. Heat loss through conduction occurs during the prolonged rift event, resulting in reduced thermal subsidence, and thus an increased initial subsidence.

b) models with non-uniform stretching between crust and mantle lithosphere [e.g., Royden & Keen, 1980].

Parameter	Definition	Value
ρ_w	water density	1030 kg m^{-3}
ρ_{sg}	sediment grain density	2650 kg m^{-3}
ρ_c	crustal density	2800 kg m^{-3}
ρ_m	mantle density	3330 kg m^{-3}
t_c	crustal thickness	31.2 km
L	lithospheric thickness	125 km
T_m	temperature of mantle	1330 ° C
α	coefficient of volume expansion	$3.28x10^{-5}$ ° C^{-1}
κ	thermal diffusivity	10^{-6} m^2 s^{-1}
$\tau(L^2/\pi^2\kappa)$	lithospheric time constant	50.2 Ma

Table C.3: List of physical parameters used in backstripping and gravity modelling analysis.

In order to calculate theoretical subsidence curves to compare with the susbidence history obtained by backstripping, the uniform stretching model with possible finite rift duration of Jarvis & McKenzie [1980] was used. These authors showed that the instantaneous stretching model of McKenzie [1978] was adequate where the rift duration was <20 Ma and β <2. However, the finite rifting duration has a major effect on heat flow, and thus the thermal and subsidence history of a basin.

C.4 Gravity Modelling

Forward and inverse methods are commonly applied to the analysis and interpretation of gravity data. The inverse method of gravity modelling calculates the body parameters of a gravity source directly from the observed anomaly. Conversely, forward modelling involves the initial construction of body parameters, using other observations such as seismic constraints, and the subsequent calculation of the resulting gravity anomaly and its comparison to the observed anomaly. Body parameters are iteratively adjusted until calculated and observed anomalies agree to a sufficient fit. The forward modelling strategy was generally employed in this study, as extra input observations such as seismic reflection and refraction data were available in addition to gravity and topography data.

Like many modelling techniques, gravity modelling is subject to problems of non-uniqueness in its solutions, but nevertheless it constitutes a powerful tool in crustal structure studies, especially when the model is well–constrained by good quality seismic reflection profiles, refraction data and well logs. Stratigraphic units picked on seismic profiles provide geometrical constraints on bodies to be modelled, and well as the input to enable the basin under investigation to be modelled through time. Seismic velocity is related to density [e.g., Nafe & Drake, 1957; Christenson & Mooney, 1995] and so initial density models can be obtained from seismic velocity analysis. Crustal thickness esti-

mates can be obtained through gravity modelling because of the significant contribution to the observed field of Moho sources.

C.4.1 Two-Dimensional Gravity modelling - forward method

The program **GBOTT** (written by M.H.P. Bott) was used to compute the gravity anomaly of the density model. **GBOTT** is based on a 2-D line integral technique which calculates gravity anomalies using the formula for a semi-infinite slab with a density contrast across a *sloping edge* shown in Equation (C.23) [e.g. Talwani *et al.*, 1959] and depicted in (Figure C.12).

$$\begin{aligned} \Delta g \;=\; & 2G\Delta\rho(-\{x_1 \sin\theta + z_1 \cos\theta\}\{\sin\theta \log(r_2/r_1) \\ & + \cos\theta(\phi_2 - \phi_1)\} + z_2\phi_2 - z_1\phi_1) \end{aligned} \tag{C.23}$$

where Δg is the calculated gravity anomaly, G is the acceleration due to gravity and $\Delta\rho$ is the density difference across the sloping boundary. The remainder of the semi-infinite body is constructed by extending the top and lower edges of the sloping edge horizontally to infinity in the x and y directions (Figure C.12). Several sloping edges may be used to build up a single large body in which the edges describe a closed polygon. Where a low density body is surrounded by a country rock of high density material, a *mass deficit* is said to occur. The opposite is a *mass excess*, where a high density body occurs within low density country rock. Alternatively, several sloping edges may be used to define a single *interface* across a 2-D profile (such as the boundary between a sedimentary layer and the oceanic crust), which does not constitute a closed body.

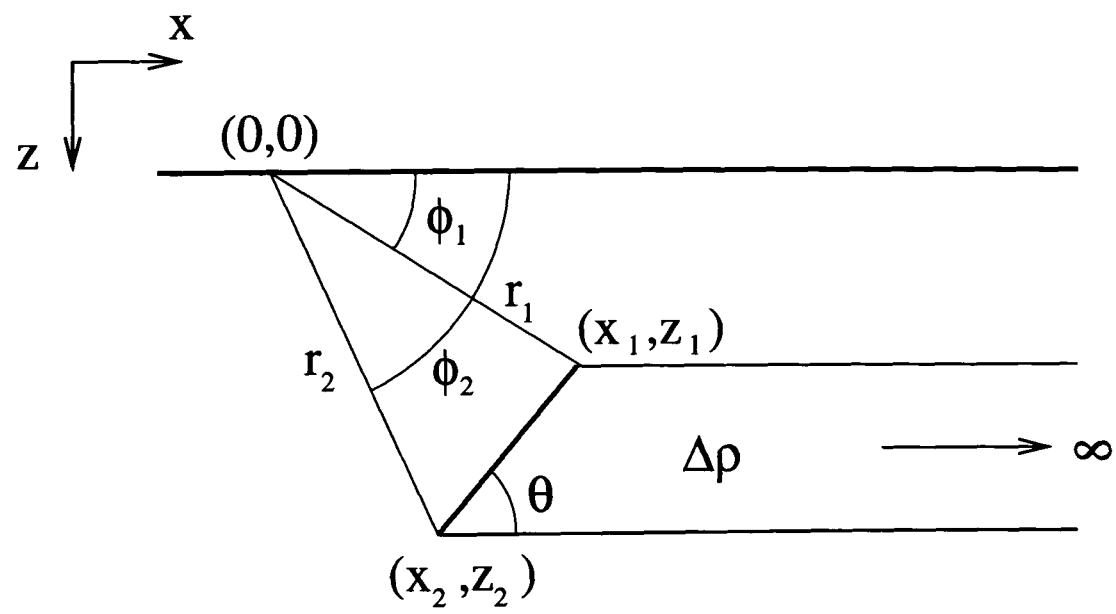


Figure C.12: Parameters used in calculating the gravity field caused by a semi-infinite slab with a sloping edge.

The gravity field of a flat interface will be constant and no anomaly will occur, but if the interface changes in depth, a gravity anomaly will be created (i.e. gravity anomalies

are caused by lateral changes in density). In general, crustal rocks increase in density with depth so that an upper layer of a low density overlies a lower layer of high density. Therefore, if the interface increases in depth a mass deficit occurs and a gravity low will be created. If the interface decreases in depth a mass excess occurs and a gravity anomaly high is created. Separate interfaces may also be defined to build up a complex 2-D profile consisting of water, sediments, crustal and mantle layers.

A caveat of this modelling technique is the assumption that the body is 2-D. In the third dimension the body is assumed to extend to infinity. This is not the case where rock structures do not have a large spatial extent. The model may predict a larger gravity anomaly using the 2-D assumption than is observed in the data.

Bibliography

ABRAMOVITZ, T., BERTHELSEN, A., SCHJOTH, F., THYBO, H., BALLING, N., NIELSEN, L., FLUEH, E.R., HUBINGER, S., RESTON, T., PEDERSEN, L.B., SCHMIDT, J., ENGLAND, R.W., HOBBS, R.W., & MAGUIRE, P.K.H. 1997. MONA LISA - Deep seismic investigations of the lithosphere in the southeastern North Sea. *Tectonophysics*, **269**(1–2), 1–19.

AGER, D.V. 1980. *The Geology of Europe.* McGraw-Hill Book Company UK Ltd. 535pp.

ALA, M. 1993. *Basic to Intermediate Open Hole Logging and Log Interpretation.* Course Notes, Imperial College, London.

ALLEN, P.A., & ALLEN, J.R. 1990. *Basin analysis: Principles and applications.* 1st edn. Osney Mead, Oxford: Blackwell.

ALLERTON, S., LONERGAN, L., PLATT, J.P., PLATZMAN, E.S., & MCCLELLAND, E. 1993. Paleomagnetic rotations in the eastern Betic Cordillera, southern Spain. *Earth and Planetary Science Letters*, **119**, 225–241.

ANDREASSEN, K., HART, P.E., & GRANTZ, A. 1995. Seismic studies of a bottom simulating reflection related to gas hydrate beneath the continental margin of the Beaufort Sea. *Journal of Geophysical Research*, **100**(B7), 12659–12673.

ANDREASSEN, K., HART, P.E., & MACKAY, E. 1997. Amplitude versus offset modeling of the bottom simulating reflection associated with submarine gas hydrates. *Marine Geology*, **137**(1–2), 25–40. Volume on "Gas in marine sediments: geology/ geochemistry/ microbiology".

ANDRIEUX, J., FONTBOTE, J.M., & MATTAUER, M. 1971. Sur un modele explicatif de l'Arc de Gibraltar. *Earth and Planetary Science Letters*, **12**, 191–198.

ARANA, V., & VEGAS, R. 1974. Plate Tectonics and Volcanism in the Gibralter Arc. *Tectonophysics*, **24**, 197–212.

ARGUS, D.F., GORDON, R.G., DEMETS, C., & STEIN, S. 1989. Closure of the Africa-Eurasia-North America Plate Motion Circuit and Tectonics of the Gloria Fault. *Journal of Geophysical Research*, **94**(B5), 5585–5602.

ASHI, J. 1999. Large submarine landslides associated with decomposition of gas hydrate. *Landslide News*, **12**, 17–20.

ASQUITH, G.B., & GIBSON, C.R. 1982. *Basic Well Log Analysis for Geologists.* American Association of Petroleum Geologists. Page 72.

ATHY, L.F. 1930. Density, porosity and compaction of sedimentary rocks. *American Association of Petroleum Geologists Bulletin*, **14**, 1–24.

AUDET, D.M. 1995. Modelling of porosity evolution and mechanical compaction of calcareous sediments. *Sedimentology*, **42**, 355–373.

AUDET, D.M. 1996. Compaction and overpressuring in Pleistocene Sediments on the Louisiana Shelf, Gulf of Mexico. *Marine and Petroleum Geology*, **13**, 467–474.

AUZENDE, J.M., OLIVET, J.L., & PASTOURET, L. 1981. Implications structurales et paléogeographiques de la presence de Messinien a l'ouest de Gibraltar. *Marine Geology*, **43**, 9–18.

BALANYA, J.C., & GARCIADUENAS, V. 1987. Structural trends of the Alboran domain on both sides of the Straits of Gibraltar. *Comptes Rendus De L'Academie Des Sciences Serie Ii-Mecanique Physique Chimie Sciences De L'Univers Sciences De La Terre*, **304**, 929–933.

BALDWIN, B., & BUTLER, C.O. 1985. Compaction Curves. *American Association of Petroleum Geologists Bulletin*, **69**, 622–626.

BANDA, E. 1988. Crustal parameters in the Iberian peninsula. *Physics of the Earth and Planetary Interiors*, **51**, 222–225.

BANDA, E., & GARIN, J. 1975. Primeros perfiles sismicos profundos en España. *Rev. Ibérica*, **162**, 430–433.

BANDA, E., RANERO, C.R., DANOBEITIA, J.J., & RIVERO, A. 1992. Seismic boundaries of the eastern Central Atlantic Mesozoic crust from multichannel seismic data. *Geological Society of America Bulletin*, **104**(October), 1340–1349.

BANDA, E., TORNE, M., & THE IAM GROUP. 1995. Iberian Atlantic Margins Group Investigates Deep Structure of Ocean Margins. *E.O.S. Transactions of the American Geophysical Union*, **76**(3), 25–29.

BANKS, C.J., & WARBURTON, J. 1991. Mid-crustal detachment in the Betic system of southern Spain. *Tectonophysics*, **191**, 275–289.

BARAZA, J., & ERCILLA, G. 1996. Gas-charged sediments and large pockmark-like features on the Gulf of Cadiz slope (SW Spain). *Marine Petroleum Geology*, **13**, 253–261.

BARAZA, J., ERCILLA, G., & NELSON, C.H. 1999. Potential geologic hazards on the eastern Gulf of Cadiz slope (SW Spain). *Marine Geology*, **155**, 191–215.

BARINGER, M.O., & PRICE, J.F. 1999. A review of the physical oceanography of the Mediterranean outflow. *Marine Geology*, **155**, 63–82.

BARRY, K.M., CAVERS, D.A., & KNEALE, C.W. 1975. Recommended standards for digital tape formats. *Geophysics*, **20**(2), 344–352.

BARTOLOMÉ, R., DANOBEITIA, J.J., CORDOBA, D., ZITELLINI, N., TERRINA, P., SANDOVAL, S., GRACIA, E., MENDES-VICTOR, L., & THE BIGSETS TEAM. 1999. New insights into the structure if the Gulf of Cadiz - first results of the BIGSETS 98 cruise (abstract). *Geophysical Research Abstracts*, **1**(1), 183.

BARTON, P.J., & WOOD, R.J. 1984. Tectonic evolution of the North Sea Basin: Crustal stretching and subsidence. *Earth and Planetary Science Letters*, **49**, 987–1022.

BECK, R.H. 1972. The Oceans, the new frontier in exploration. *Australian Petroleum Exploration Association Journal*, **12**, 1–21.

BERASTEGUI, X., BANKS, C., PUIG, C., TABERNER, C., WALTHAM, D., & FERNANDEZ, M. 1998. Lateral diapiric emplacement of Triassic evaporites at the southern margin of the Guadalquivir Basin, Spain. *Pages 49–68 of: Cenozoic Foreland Basins of Western Europe.* Geological Society Special Publications., no. 134. Geological Society of London. London, United Kingdom.

BESSIS, J. 1986. Some remarks on the studies of continental rifting: Application to the Gulf of Lions margin (Western Mediterranean). *Marine and Petroleum Geology*, **3**, 37–63.

BLAKELY, R.J. 1995. *Potential Theory in Gravity and Magnetic Interpretation.* Cambridge University Press.

BLANCO, M.J., & SPAKMAN, W. 1993. The P-wave velocity structure of the mantle below the Iberian Peninsula: evidence for subducted lithosphere below southern Spain. *Tectonophysics*, **221**(1), 13–34.

BOILLOT, G., WINTERER, E.L., & MEYER, A.W. 1987. Site 637, Site 639. *In: Initial Reports of the Ocean Drilling Program, Volume 103.* Washington: U.S. Government Printing Office.

BOILLOT, G., MOUGENOT, D., GIRARDEAU, J., & WINTERER, E.L. 1989. Rifting processes on the West Galicia Margin, Spain. *Pages 355–363 of:* TANKARD, A.J., & BALKWILL, H.R. (eds), *Extensional tectonics and stratigraphy of the North Atlantic Margins.* American Association of Petroleum Geology Memoir 46. Tulsa, OK: American Association of Petroleum Geologists.

BOND, G.C., & KOMINZ, M.A. 1984. Construction of tectonic subsidence curves for the early Paleozoic miogeocline, southern Canadian Rocky Mountains: Implications for subsidence mechanisms, age of breakup, and crustal thinning. *Geological Society of America Bulletin*, **95**(February), 155–173.

BONINI, W.E., LOOMIS, T.P., & ROBERTSON, J.D. 1973. Gravity anomalies, ultramafic intrusions,and the tectonics of the region around the Strait of Gibraltar. *Journal of Geophysical Research*, **78**(8), 1372–1382.

BONNIN, J. 1978. *Evolution géodynamique de la ligne Açores-Gibraltar.* Ph.D. thesis, Universite de Paris.

BONNIN, J., OLIVET, J.L., & AUZENDE, J.M. 1975. Structure en nappe a l'Ouest de Gibraltar. *C.R. Acad. Sci. Paris Series D*, **280**, 559–562.

BOOTH, J.S., WINTERS, W.J., DILLON, W.P., CLENNELL, M.B., & ROWE, M.M. 1998. Major occurences and reservoir concepts of marine clathrate hydrates: implications of field evidence. *Pages 113–127 of: Gas hydrates; relevance to world margin stability and climate change.* Geological Society Special Publications., no. 137. Geological Society of London. London, United Kingdom.

BOUILLIN, J.P., BROQUET, P., & TUBIA, J.M. 1987. The thermo-luminescence of the quartz in nodules in the migmatites associated to the emplacement of the periodotites of Andalusia (Spain) and of lesser Kabylia (Algeria) a marker of the Alboran block motion. *Comptes Rendus De L'Academie Des Sciences Serie Ii-Mecanique Physique Chimie Sciences De L'Univers Sciences De La Terre*, **305**, 287–291.

BRATTON, J.F. 1999. Clathrate eustasy: methane hydrate melting as a mechanism for geologically rapid sea–level fall. *Geology*, **27**(10), 915–918.

BUFORN, E., UDIAS, A., & COLUMBAS, M.A. 1988. Seismicity, source mechanisms and tectonics of the Azores-Gibralter plate boundary. *Tectonophysics*, **152**, 89–118.

BUFORN, E., UDIAS, A., & MADARIAGA, R. 1991. Intermediate and deep earthquakes in Spain. *Pure Applied Geophysics*, **136**, 375–393.

BUGGE, T., BELDERSON, R.H., & KENYON, N.H. 1988. The Storegga slide. *Philosophical Transactions of the Royal Society of London*, 357–388.

BURLAND, J.B. 1990. On the compressibility and shear strength of natural clays. *Géotechnique*, **40**, 329–378.

CAMPILLO, A.C., MALDONADO, A., & MAUFFRET, A. 1992. Stratigraphic and tectonic evolution of the western Alboran sea - late Miocene to recent. *Geo-Marine Letters*, **12**, 165–172.

CAREY, S.W. 1958. The tectonic approach to continental drift. *Pages 177–355 of:* CAREY, S.W. (ed), *Continental drift; a symposium.* Tasmania, University Geology Department.

CARMINATI, E., WORTEL, M.J.R., SPAKMAN, W., & SABADINI, R. 1998a. The role of slab detachment processes in the opening of the western- central Mediterranean basins: some geological and geophysical evidence. *Earth and Planetary Science Letters*, **160**, 651–665.

CARMINATI, E., WORTEL, M.J.R., MEIJER, P.T., & SABADINI, R. 1998b. The two-stage opening of the western-central Mediterranean basins: a forward modeling test to a new evolutionary model. *Earth and Planetary Science Letters*, **160**, 667–679.

CARPENTER, G. 1981. Coincident sediment slump/clathrate complexes on the U.S. Atlantic continental slope. *Geo-Marine Letters*, **1**, 29–32.

CHASE, C.G. 1978. Plate kinematics: The Americas, East Africa and the rest of the world. *Earth and Planetary Science Letters*, **37**, 355–368.

CHOWDHURY, S. 1994. *Processing of multichannel seismic reflection data from the Tagus Abyssal Plain, offshore Portugal.* Royal School of Mines, Imperial College, London University. MSc.Thesis.

CHRISTENSON, N.I., & MOONEY, W.D. 1995. Seismic velocity structure and composition of the continental crust: a global view. *J. Geophys. Res.*, **100**(B7), 9761–9788.

CLAERBOUT, J.F. 1985. *Imaging the Earth's Interior.* Blackwell Scientific Publications.

COCHRAN, J.R. 1983. Effect of finite rifting times on the development of sedimentary basins. *Earth and Planetary Science Letters*, **66**, 289–302.

COHEN, J.K., & STOCKWELL, JR.J.W. 1996. *CWP/SU: Seismic Unix Release 29: a free package for seismic research and processing.* Tech. rept. Center for Wave Phenomena, Colorado School of Mines.

COLLETTE, B.J., & ROEST, W.R. 1992. Further investigations of the North Atlantic between 10- degrees N and 40-degrees N and an analysis of spreading from 118 Ma ago to present. *Proceedings Koninklijke Nederlandse Akademie Van Wetenschappen-Biological Chem. Geological Phys. Medical Sciences*, **95**, 159.

COLLIER, J.S., HENSTOCK, T.J., PEIRCE, C., & WATTS, A.B. 1998. A detailed geophysical study in the Canary Basin (eastern Atlantic) : Implications for the internal structure of 130 Ma oceanic crust. *Geophysical Journal International*, **135**, 943–963.

COMAS, M.C., GARCIADUENAS, V., & JURADO, M.J. 1992. Neogene tectonic evolution of the Alboran Sea from MCS data. *Geo-Marine Letters*, **12**, 157–164.

COMAS, M.C., ZAHN, R., & KLAUS, A. 1995. Mediterranean Sea Leg 161. *Joides Journal*, **21**, 25–27.

COMAS, M.C., PLATT, J.P., SOTO, J.J., & WATTS, A.B. 1999. The origin and tectonic history of the Alboran Basin: Insights from ODP Leg 161 Results. *Pages 555–580 of:* ZAHN, R., COMAS, M.C., & KLAUS, A. (eds), *Proceedings of the ODP, Scientific Results, 161.* College Station, TX (Ocean Drilling Program). Foldout of seismic profiles by S. Chowdhury.

CORREIA, A., & RAMALHO, E.C. 1998. New heat flow density data from southern Portugal: a geothermal anomaly revisited. *Tectonophysics*, **291**(1-4), 55–62.

COUDERT, L., FRAPPA, M., VIGUIER, C., & ARIAS, R. 1995. Tectonic subsidence and crustal flexure in the Neogene Chaco Basin of Bolivia. *Tectonophysics*, **243**, 277–292.

COWARD, M.P. 1986. Heterogeneous stretching, simple shear and basin development. *Earth and Planetary Science Letters*, **80**, 325–336.

DAÑOBEITIA, J.J., BARTOLOME, R., CHECA, A., MALDONADO, A., & SLOOTWEG, A.P. 1999. An interpretation of a prominent magnetic anomaly near the boundary between the Eurasian and African plates (Gulf of Cadiz, SW margin of Iberia). *Marine Geology*, **155**, 45 (16 pages).

DAVIES, G.R., NIXON, P.H., PERSON, D.G., & OBATA, M. 1993. Tectonic implications of graphitized diamonds fom the Ronda peridotite massif, S. Spain. *Geology*, **21**, 471–474.

DEGALDEANO, C.S. 1990. Geologic evolution of the Betic Cordilleras in the western Mediterranean, Miocene to the present. *Tectonophysics*, **172**, 107–119.

DEJONG, K. 1990. Alpine tectonics and rotation pole evolution of Iberia. *Tectonophysics*, **184**, 279–296.

DELAPLANCHE, J., LAFET, Y., SINERIZ, B.G., & GIL, M.A.R. 1982. Seismic-reflection applied to sedimentology and gas discovery in the Gulf of Cadiz. *Geophysical Prospecting*, **30**, 1–24.

DEMETS, C., GORDON, R.G., ARGUS, D.F., & STEIN, S. 1990. Current Plate Motions. *Geophysical Journal International*, **101**, 425–478.

DEMETS, C., GORDON, R.G., ARGUS, D.F., & STEIN, S. 1994. Effect of recent revisions to the geomagnetic reversal time scale on estimates of current plate motions. *Geophysical Research Letters*, **21**(20), 2191–2194.

DEREGOWSKI, S.M. 1986. What is DMO? *First Break*, **4**(7), 7–24.

DEWEY, J.F. 1988. Lithospheric stress, deformation, and tectonic cycles: the disruption of Pangaea and the closure of Tethys. *Pages 23–40 of:* AUDLEY-CHARLES, M.G., & HALLAM, A. (eds), *Gondwana and Tethys.* Geological Society of London Special Publication, no. 37. Geological Society of London. London, United Kingdom.

DEWEY, J.F., PITMAN III, W.C., RYAN, W.B.F., & BONNIN, J. 1973. Plate Tectonics and the Evolution of the Alpine System. *Geological Society of America Bulletin*, **84**, 3137–3180.

DEWEY, J.F., HELMAN, M.L., TURCO, E., HUTTON, D.H.W., & KNOTT, S.D. 1989. Kinematics of the Western Mediterranean. *Pages 265–283 of:* COWARD, M.P., DIETRICH, D., & PARK, R.G. (eds), *Alpine Tectonics.* Geological Society Special Publications, vol. 45. Geological Society of London.

DEWEY, J.W. 1971. *Seismic studies with the method of joint hypocenter determination.* Ph.D. thesis, University of California, Berkeley.

DIDON, J. 1977. Role des phenomenes de glissement et d'ecoulement par gravite dans la mise en place du materiel flysch a la peripherie de l'arc de Gibraltar. Translated Title: Role of sliding phenomena and gravity sliding in the emplacement of flysch material at the periphery of the Gibraltar Arc. *Bulletin de la Societe Geologique de France*, **19**(4), 765–771.

DINGLE, R.V. 1977. The anatomy of a large submarine slump on a sheared continental margin (SE Africa). *Journal of the Geological Society of London*, **134**, 293–310.

DIX, C.H. 1955. Seismic velocities from surface measurements. *Geophysics*, **20**, 68–86.

DOBLAS, M., & OYARZUN, R. 1989. Neogene extensional collapse in the western Mediterranean (Betics-Rif Alpine orogenic belt) - implications for the genesis of the Gibraltar Arc and magmatic activity. *Geology*, **17**, 430–433.

DOCHERTY, C., & BANDA, E. 1995. Evidence for eastward migration of the Alboran Sea based on regional subsidence analysis: A case for basin formation by delamination of the subcrustal lithosphere. *Tectonics*, **14**(4), 804–818.

DOMENICO, S.N. 1976. Effect of brine–gas mixture on velocity in an unconsolidated sand reservoir. *Geophysics*, **41**, 882–894.

DRAKE, C.L., GAIBAR, P.C., LANGSETH, M., & NAFE, J.E. 1959. Prospeccion sismica submarina en el Golfo de Cadiz. *Revista de Ciencia Aplicada. Consejo Superior de Investigaciones Cientificas. Patronato Juan de la Cierva de Investigacion Tecnica. Madrid, Spain.*

DRUMMOND, B.J., GOLEBY, B.R., GONCHAROV, A.G., WYBORN, L.A.I., COLLINS, C.D.N., & MACCREADY, T. 1998. Crustal-scale structures in the Proterozoic Mount Isa Inlier of north Australia: their seismic response and influence on mineralisation. *Tectonophysics*, **288**(1–4), 43–56.

DUBOURDIEU, G. 1964. La formation des chaines mediterraneennes. *Compte Rendus Hebdomadaires des Seances de l'Academie des Sciences*, **258**(11), 3061–3063.

DUNBAR, J.A., & SAWYER, D.S. 1987. Implications of continental crust extension for plate reconstruction: an example from the Gulf of Mexico. *Tectonics*, **6**, 739–755.

DZIEWONSKI, A.M., & WOODHOUSE, J.H. 1983. An experiment in the systematic study of global seismicity: centroid-moment tensor solutions for 201 moderate and large earthquakes of 1981. *Journal of Geophysical Research*, **88**, 3247–3271.

DZIEWONSKI, A.M., CHOU, T.A., & WOODHOUSE, J.H. 1981. Determination of earthquake source parameters from waveform data for studies of global and regional seismicity. *Journal of Geophysical Research*, **86**, 2825–2852.

EMBLEY, R. W. 1976. New evidence for occurrence of debris flow deposits in the deep sea. *Geology*, **4**, 371–374.

EMBLEY, R. W. 1980. The role of mass transport in the distribution and character of deep-ocean sediments in the Atlantic. *Mar. Geol*, **38**, 23–50.

EMERY, K.O., & UCHUPI, E. 1984. *The Geology of the Atlantic Ocean.* Springer.

ENGLAND, P.C., & HOUSEMAN, G. 1986. Finite strain calculations of continental deformation 2. Comparison with the India-Asia collision zone. *Journal of Geophysical Research*, **91**, 3664–3676.

FAVRE, P. 1995. Quantitative-analysis of rifting and thermal relaxation in the western part of the North African transform margin - external Rif (Morocco). *Geodinamica Acta*, **8**, 59–81.

FEINBERG, H. 1976. Mise en place, au Pliocene, d'une nappe de glissement à l'extrémité sud-occidentale de la chaine du Rif (Maroc). *C.R. somm. Soc. geol. France*, **6**, 273–276.

FERAUD, G., YORK, D., MEVEL, C., CORNEN, G., HALL, C.M., & AUZANDE, J.M. 1986. Additional Ar40-Ar39 dating of the basement and the alkaline volcanism of Gorringe Bank (Atlantic Ocean). *Earth and Planetary Science Letters*, **79**, 255–269.

FERNANDEZ, M., BERASTEGUI, X., PUIG, C., GARCIA-CASTELLANOS, D., JURADO, M.J., TORNE, M., & BANKS, C. 1998a. Geophysical and geological constraints on the evolution of the Guadalquivir foreland basin, Spain. *Pages 29–48 of: Cenozoic Foreland Basins of Western Europe.* Geological Society Special Publication, no. 134. Geological Society of London. London, United Kingdom.

FERNANDEZ, M., MARZAN, I., CORREIA, A., & RAMALHO, E.C. 1998b. Heat flow, heat production, and lithospheric thermal regime in the Iberian Peninsula. *Tectonophysics*, **291**(1-4), 29–53.

FINK, C.R., & SPENCE, G.D. 1999. Hydrate distribution off Vancouver island from multifrequency single-channel seismic reflection data. *Journal of Geophysical Research - Solid Earth*, **104**, 2909–2922.

FLINCH, J.F. 1993. *Tectonic evolution of the Gibraltar Arc.* Ph.D. thesis, Rice University, Texas.

FLINCH, J.F., BALLY, A.W., & WU, S. 1996. Emplacement of a passive-margin evaporitic allochthon in the Betic Cordillera of Spain. *Geology*, **24**(1), 67–70.

FLOWER, M.F.J., SCHMINCKE, H.-U., & BOWMAN, H. 1976. Rare earth and other elements in historic Azorean lavas. *Journal of Volcanology and Geothermal Research*, **1**, 127–147.

FOR DEEP SEISMIC SOUNDING IN THE ALBORAN SEA 1974, WORKING GROUP. 1978. Crustal Seismic Profiles in the Alboran Sea - Preliminary Results. *Pure and Applied Geophysics*, **116**, 167–180.

FOWLER, C.M.R. 1990. *The Solid Earth.* Cambridge University Press.

FRIEND, P.F., & DABRIO, C.J. (eds). 1996. *Tertiary Basins of Spain: the stratigraphic record of crustal kinematics.* World and Regional Geology, vol. 6. Cambridge University Press.

FRIZON DE LAMOTTE, D., ANDRIEUX, J., & GUÉZOU, J.C. 1991. Cinématique des chevauchements néogènes dans l'Arc bético-rifain: discussion sur les modèles géodynamiques. *Bulletin de la Societe Geologique de France*, **162**, 611–626.

FUKAO, Y. 1973. Thrust Faulting at a Lithosphere Plate Boundary. The Portugal Earthquake of 1969. *Earth and Planetary Science Letters*, **18**, 205–216.

GALDEANO, A., MOREAU, M.G., POZZI, J.P., BERTHOU, P.Y., & MALOD, J.A. 1989. New paleomagnetic results from Cretaceous sediments near Lisboa (Portugal) and implications for the rotation of Iberia. *Earth and Planetary Science Letters*, **92**, 95–106.

GALINDO-ZALDÍVAR, J., GONZÁLEZ-LODEIRO, F., & JABALOY, A. 1993. Stress and palaeostress in the Betic-Rif Cordilleras (Miocene to present). *Tectonophysics*, **227**, 105–126.

GALLAGHER, K. 1989. An examination of some uncertainties associated with estimates of sedimentation rates and tectonic subsidence. *Basin Research*, **2**, 97–114.

GALLART, J., VIDAL, N., DANOBEITIA, J.J., SABAT, F., POUS, J., SURINACH, E., & SANTISTEBAN, C. 1994. Lateral variations in the deep–crustal structure at the Iberian margin of the Valencia Trough imaged from seismic reflection methods. *Tectonophysics*, **232**, 59–75.

GARCIA-HERNANDEZ, M., LOPEZ-GARRIDO, A.C., RIVAS, P., SANZ DE GALDEANO, C., & VERA, J.A. 1980. Mesozoic paleogeographic evolution of the Betic Cordillera. *Geologie en Mijnbouw*, **59**(2), 155–168.

GARCIA-HERNANDEZ, M., LOPEZ-GARRIDO, A.C., MARTIN-ALGARRA, A., MOLINA, J.M., RUIZ-ORTIZ, P.A., & VERA, J.A. 1989. Las discontinuidades mayores del Jurasico de las Zonas Externas de las Cordilleras Beticas: analisis r interpretacion de los ciclos sedimentarios. *Cuad. Geol. Iberica*, **13**, 35–52.

GARCIADUENAS, V., BALANYA, J.C., & MARTINEZ, J.M. 1992. Miocene extensional detachments in the outcropping basement of the northern Alboran basin (Betics) and their tectonic implications. *Geo-Marine Letters*, **12**, 88–95.

GARDNER, G.H.F., GARDNER, L.W., & GREGORY, A.R. 1974. Formation velocity and density – the diagnostic basics for stratigraphic traps. *Geophysics*, **39**, 770–780.

GAZDAG, J. 1978. Wave-equation Migration with the Phase Shift Method. *Geophysics*, **43**, 1342–1351. also in Gardner 1985.

GINSBURG, G.D. 1998. Gas hydrate accumulation in deep-water marine sediments. *Pages 51–62 of: Gas hydrates; relevance to world margin stability and climate change.* Geological Society Special Publication, no. 137. Geological Society of London. London, United Kingdom.

GINSBURG, G.D., & SOLOVIEV, V.A. 1997. Methane migration within the submarine gas-hydrate stability zone under deep-water conditions. *Marine Geology*, **137**(1–2), 49–57. Volume on "Gas in marine sediments: geology/ geochemistry/ microbiology".

GINSBURG, G.D., MILKOV, A.V., SOLOVIEV, V.A., EGOROV, A.V., CHERKASHEV, G.A., VOGT, P.R., CRANE, K., LORENSON, T.D., & KHUTORSKOY, M.D. 1999. Gas hydrate accumulation at the Hakon mosby mud volcano. *Geo-Marine Letters*, **19**, 57–67.

González, A. 1996. *Analisis de señales sismicas. Estudio de la estructura de la litosfera en el margen suroccidental ibérico.* Ph.D. thesis, Facultad de Ciencias, Universidad Complutense de Madrid. 180 pp.

González, A., Torné, M., Córdoba, D., Vidal, N., Matias, L.M., & Díaz, J. 1996. Crustal thinning in the southwestern Iberia margin. *Geophysical Research Letters.*, **23**(18), 2477–2480.

González, A., Córdoba, D., Vegas, R., & Matias, L.M. 1998. Seismic crustal structure in the southwest of the Iberian peninsula and the Gulf of Cadiz. *Tectonophysics*, **296**, 317–331.

Gradstein, F.M., Agterberg, F.P., Ogg, J.G., Hardenbol, J., van Veen, P., Thierry, J., & Huang, Z. 1995. A Triassic, Jurassic and Cretaceous Timescale. *SEPM Special Publication*, **54**, 95–121.

Gregory, A.R. 1977. Aspects of rock physics from laboratory and log data that are important to interpretation. *Pages 15–46 of:* Payton, C.E. (ed), *Seismic stratigraphy - applications to hydrocarbon exploration.* AAPG Memoir 26. Tulsa, OK: American Association of Petroleum Geologists.

Grimison, N.L., & Chen, W.P. 1986. The Azores-Gibralter plate boundary: Focal mechanisms, depths of earthquakes, and their tectonic implications. *Journal of Geophysical Research*, **91**(B2), 2029–2047.

Grow, J.A., Mattick, R.A., & Schlee, J.S. 1979. Multichannel seismic depth sections and internal velocities over outer continental shelf and upper continental slope between Cape Hatteras and Cape Cod. *Pages 65–83 of: AAPG Memoir 29.* AAPG Memoir 29. Tulsa, OK: American Association of Petroleum Geologists.

Grupo de Trabajo de perfiles sísmicos profundos. 1983. Perfiles sísmicos profundos en España 1981. *Bol. Geol. Miner.*, **XCIV-IV**, 339–347.

Gunn, R. 1947. Quantitative aspects of juxtaposed ocean deeps, mountain chains and volcanic ranges. *Geophysics*, **12**, 238–255.

Gutenberg, B., & Richter, C.F. 1954. *Seismicity of the Earth.* Princeton University Press.

Hamilton, E.L., & Bachman, R.T. 1982. Sound Velocity and Related Properties of Marine Sediments. *Journal Acoustic Society of America*, **72**(6), 1891–1903.

Hampton, M. A., , Lee, H.J., & Locat, J. 1996. Submarine landslides. *Reviews of Geophysics*, February, 33–59.

Haq, B.U. 1998. Natural gas hydrates: searching for the long–term climatic and slope–stabilityrecords. *Pages 303–318 of: Gas hydrates; relevance to world margin stability and climate change.* Geological Society Special Publication, no. 137. Geological Society of London. London, United Kingdom.

HAQ, B.U., HARDENBOL, J., & VAIL, P.R. 1987. Chronology of fluctuating sea levels since the Triassic. *Science*, **235**, 1156–1167.

HARDY, R.J.J., & HOBBS, R.W. 1991. A strategy for multiple suppression. *First Break*, **9**(4), 139–144.

HARLAND, W.B., ARMSTRONG, R.L., COX, A.V., CRAIG, L.E., SMITH, A.G., & SMITH, D.G. 1990. *A Geologic Time Scale 1989.* Cambridge University Press.

HAYES, D.E., PIMM, A.C., BENSON, W.E., BERGER, W.H., VON RAD, U., SUPKO, P.R., BECKMAN, J.P., & ROTH, P.H. 1972. Site 135, Site 136. *Pages 15–48 of: Initial Report of the Deep Sea Drilling Program-Volume 14.* Washington: U.S. Government Printing Office.

HAYWARD, N. 1996 (September). *Marine Geophysical Study of the Eurasian-African Plate Boundary in the Vicinity of the Gorringe Bank.* Ph.D. thesis, University of Oxford.

HAYWARD, N., WATTS, A.B., WESTBROOK, G.K., & COLLIER, J. 1999. A seismic reflection and GLORIA study of compressional deformation in the Gorringe Bank region. *Geophysical Journal International*, **138**, 831–850.

HERNANDEZ, J., DELAROUZIERE, F.D., BOLZE, J., & BORDET, P. 1987. Le magmatisme Neogene betico-rifian et le coulouir de decrochement trans-Alboran. *Bulletin De La Societe Geologique De France*, **8**, 257–267.

HEYMANN, M.A.W. 1989. Tectonic and depositional history of the Moroccan margin. *Pages 323–340 of:* TANKARD, A.J., & BALKWILL, H.R. (eds), *Extensional tectonics and stratigraphy of the North Atlantic Margins.* AAPG Memoir 46. Tulsa, OK: American Association of Petroleum Geologists.

HINZ, K., DOSTMANN, H., & FRITSCH, J. 1982. The Continental Margin of Morocco: Seismic Sequences, Structural Elements and Geological Development. *Chap. 3, pages 34–59 of:* VON RAD, U., HINZ, K., SARNTHEIN, M., & SEIBOLD, E. (eds), *Geology of the northwest African continental margin.* Berlin, Heidelburg, New York: Springer-Verlag.

HOBBS, R., & SNYDER, D. 1992. Marine seismic sources used for deep seismic reflection profiling. *First Break*, **10**(11), 417–426.

HOBRO, J.W., MINSHULL, T.A., & SINGH, S.C. 1998. Tomographic seismic studies of the methane hydrate stability zone in the Cascadia Margin. *Pages 133–140 of: Gas hydrates; relevance to world margin stability and climate change.* Geological Society Special Publication, no. 137. Geological Society of London. London, United Kingdom.

HOLBROOK, W.S., HOSKINS, H., WOOD, W.T., STEPHEN, R.A., & LIZARRALDE, D. 1996. Methane hydrate and free gas on the Blake ridge from vertical seismic profiling. *Science*, **273**, 1840–1843.

HOUSEMAN, G. A., MCKENZIE, D. P., & MOLNAR, P. 1981. Convective instability of a thickened boundary layer and its relevance for the thermal evolution of continental convergent belts. *Journal of Geophysical Research*, **86**, 6115–6132.

HOVLAND, M., & JUDD, A.G. 1988. *Seabed pockmarks and seepages: impact on geology, biology and the marine environment.* Graham and Trotman. 293 pp.

HOVLAND, M., JUDD, A.G., & KING, L.H. 1984. Characteristic features of pockmarks on the North Sea floor and Scotian shelf. *Sedimentology*, **31**, 471–480.

HOYT, W.H., & FOX, P.J. 1977. Long-distance turbidite correlations in Horseshoe abyssal plain. *American Association of Petroleum Bulletin*, **61**(5), 797.

HYNDMAN, R. D., & SPENCE, G. D. 1992. A seismic study of methane hydrate bottom simulating reflectors. *J. Geophysical Research-Solid Earth*, **97**, 6683–6698.

IGME. 1987. *Contribucion de la exploracion petrolifera al conocimiento de la geologia de España.* Instituto Geologico y Minero de España. 465pp.

ILIHA DSS GROUP. 1993. A deep seismic sounding of lithospheric heterogeneity and anisotropy beneath the Iberian Peninsula. *Tectonophysics*, **221**(1), 35–52.

ISSLER, D.R. 1992. A new approach to shale compaction and stratigraphic restoration, Beaufort-Mackenzie Basin and Mackenzie Corridor, northern Canada. *American Association of Petroleum Geologists Bulletin*, **76**(8), 1170–1189.

JARVIS, G.T., & MCKENZIE, D.P. 1980. Sedimentary basin formation with finite extension rates. *Earth and Planetary Science Letters*, **48**, 42–52.

JEFFREYS, H., & BULLEN, K.E. 1940. Seismological Tables.

KAHLE, H.G., & MUELLER, S. 1998. Structure and dynamics of the Eurasian-African/Arabian plate boundary system: Objectives, tasks and resources of the WEGENER group. *Journal of Geodynamics*, **25**(3-4), 303–325.

KAMPSCHUUR, W., & RONDEEL, H.E. 1975. The origin of the Betic Orogen, southern Spain. *Tectonophysics*, **27**(1), 39–56.

KARNER, G.D., & WATTS, A.B. 1983. Gravity Anomalies and Flexure of the Lithosphere at Mountain Ranges. *Journal of Geophysical Research*, **88**(B12), 10449–10477.

KATZMAN, R., HOLBROOK, W.S., & PAULL, C.K. 1994. Combined vertical-incidence and wide-angle seismic study of a gas hydrate zone, Blake Ridge. *Journal of Geophysical Research*, **99**(B9), 17975–17995.

KAYEN, R.E., & LEE, H.J. 1993. Slope stability in regions of sea-floor gas hydrate: Beaufort Sea Continental Slope. *Pages 97–103 of:* SCHWAB, W.C., LEE, H.J., & TWITCHELL, D.C. (eds), *Submarine Landslides: Selected studies in the U.S. Exclusive Economic Zone.* U.S. Geological Survey Bulletin.

KEAREY, P., & VINE, F.J. 1990. *Global Tectonics.* 1st edn. Oxford: Blackwell Scientific Publications.

KEEN, C.E., & DE VOOGD, B. 1988. The continent-ocean boundary at the rifted margin off Eastern Canada: New results from deep seismic reflection studies. *Tectonics*, **7**(1), 107–124.

KEEN, C.E., MACLEAN, B.C., & KAY, W.A. 1991. A deep seismic reflection profile across the Nova Scotia continental margin offshore Eastern Canada. *Canadian Journal of Earth Sciences*, **28**, 1112–1120.

KENYON, N.H., & BELDERSON, R.H. 1973. Bed forms of the Mediterranean Undercurrent observed with side–scan sonar. *Sedimentary Geology*, **9**, 77–99.

KIRATZI, A.A., & PAPAZACHOS, C.B. 1995. Active crustal deformation from the Azores triple junction to the middle-east. *Tectonophysics*, **243**, 1–24.

KLEMPERER, S.L. 1987. *Digital Seismology and fine modelling of the lithosphere.* Ettore Majorana international science series. Physical sciences, vol. 42. New York: Plenum. Chap. 4: Processing BIRPS deep seismic reflection data: A tutorial review, pages 229–257.

KLITGORD, K.D., & SCHOUTEN, H. 1986. *The Geology of North America: the western Atlantic region.* DNAG, vol. M. Geological Society of America. Chap. 22: Plate kinematics of the central Atlantic, pages 351–378.

KORENAGA, J., HOLBROOK, W.S., SINGH, S.C., & MINSHULL, T.A. 1997. Natural gas hydrates on the southeast US margin: constraints from full waveform and travel time inversions of wide-angle seismic data. *Journal of Geophysical Research - Solid Earth*, **102**, 15345–15365.

KORVIN, G. 1984. Shale compaction and statistical physics. *Geophysical Journal of the Royal Astronomical Society*, **28**, 35–50.

KREMLEV, A.N., SOLOVIEV, V.A., & GINSBURG, G.D. 1997. Reflecting seismic horizon at the base of the submarine zone of gas hydrate stability. *Geologiya I Geofizika*, **38**, 1747–1759.

KUSZNIR, N.J., & ZIEGLER, P.A. 1992. The mechanism of continental extension and sedimentary basin formation: a simple-shear/pure-shear flexural cantilever model. *Tectonophysics*, **215**, 117–131.

KUSZNIR, N.J., MARSDEN, G., & EGAN, S.S. 1991. A flexural-cantilever simple-shear/pure-shear model of continental lithosphere extension: Applications to the Jeanne d'Arc Basin, Grand Banks and Viking Graben, North Sea. *Pages 41–60 of:* ROBERTS, A.M., YIELDING, G., & FREEMAN, B. (eds), *The Geometry of Normal Faults.* Geological Society of London Special Publication, no. 56. Geological Society of London.

KVENVOLDEN, K. 1993. Gas hydrates – geological perspective and global change. *Reviews of Geophysics*, **31**, 173–187.

KVENVOLDEN, K., & BARNARD, L. 1983. Hydrates of natural gas in continental margins. *Pages 631–640 of: Studies in Continental Margin Geology.* AAPG Memoir 34. Tulsa, OK: American Association of Petroleum Geologists.

KVENVOLDEN, K.A. 1998. A primer on the geological occurrence of gas hydrate. *Pages 9–30 of: Gas hydrates; relevance to world margin stability and climate change.* Geological Society Special Publication, no. 137. Geological Society of London. London, United Kingdom.

KVENVOLDEN, K.A. 1999. Potential effects of gas hydrate on human welfare. *Proceedings National Academy Sciences United States America*, **96**, 3420–3426.

LAJAT, D., BIJU-DUVAL, B., GONNARD, R., LETOUZEY, J., & WINNOCK, E. 1975. Prolongement dans l'Atlantique de la partie externe de l'Arc Betico-Rifaine. *Bulletin De La Societe Geologique De France*, **17**(4), 481–485.

LAMBECK, K., BURGESS, G., & SHAW, R.D. 1988. Teleseismic travel-time anomalies and deep crustal structure in central Australia. *Geophysical Journal*, **94**, 105–124.

LAUGHTON, A.S., & WHITMARSH, R.B. 1974. *The Azores-Gibraltar Plate Boundary.* Dordrecht, Holland: D. Reidel Publishing Company. Pages 63–81.

LAUGHTON, A.S., WHITMARSH, R.B., RUSBY, J.S.M., SOMERS, M.L., REVIE, J., MCCARTNEY, B.S., & NAFE, J.E. 1972. A Continuous East-West Fault on the Azores-Gibralter Ridge. *Nature*, **237**(May), 217–220.

LEBLANC, D. 1990. Tectonic adaptation of the external zones around the curved core of an orogen - the Gibraltar Arc. *Journal of Structural Geology*, **12**, 1013–1018.

LEBLANC, D., & OLIVIER, P. 1984. Role of strike-slip faults in the Betic-Rifian orogeny. *Tectonophysics*, **101**, 345–355.

LEBREIRO, S.M. 1995. *Sedimentation history off Iberia: Tore Seamount, Tagus and Horseshoe abyssal plains.* Ph.D. thesis, University of Cambridge.

LEPICHON, X., BONNIN, J., & PAUTOT, G. 1970 (July). *The Gibraltar end of the Azores-Gibraltar plate boundary: an example of compressive tectonics (Abstract), Upper Mantle Committee Symposium, Flagstaff, Arizona.*

LERCHE, I., & BAGIROV, E. 1998. Guide to gas hydrate stability in various geological settings. *Marine and Petroleum Geology*, **15**, 427–437.

LIE, J.E., PEDERSEN, T., & HUSEBYE, E.S. 1990. Observations of seismic reflectors in the lower lithosphere beneath the Skagerrak. *Nature*, **346**, 165–168.

LITVIN, V.M., MATVEYENKOV, V.V., ONISHCHENKO, E.L., RUDENKO, M.V, & SAGALEVICH, A.M. 1982. New Data on the Structure of Ampere Seamount. *Oceanology*, **22**(1), 62–64.

LONERGAN, L., & MANGE-RAJETSKY, M. 1994. Evidence for Internal Zone unroofing from foreland basin sediments, Betic Cordillera, SE Spain. *Journal of the Geological Society of London*, **151**, 515–529.

LONERGAN, L., & WHITE, N. 1997. Origin of the Betic-Rif mountain belt. *Tectonics*, **16**, 504–522.

MACDONALD, G. 1990. Role of methane clathrates in past and future climates. *Climate Change*, **16**, 247–281.

MAGARA, K. 1980. Comparison of porosity-depth relationships of shale and sandstone. *Journal of Petroleum Geology*, **3**(2), 175–180.

MALDONADO, A., BARAZA, J., CHECA, J., NELSON, C.H., BARBER, J.H., HAMPTON, M.H., KAYEN, R.E., & LEE, H.J. 1989. Tectonic framework, pattern of sedimentation, and potential environmental problems of the Cadiz Continental Margin, Spain. *Pages 2–356 of: 28th International Geological Congress, Washington.*, vol. 2-3.

MALDONADO, A., SOMOZA, L., & PALLARES, L. 1999. The Betic orogen and the Iberian-African boundary in the Gulf of Cadiz: geological evolution (central North Atlantic). *Marine Geology*, **155**, 9–43.

MALOD, J.A. 1982. *Comparaison de l'evolution des marges continentales au nord et au sud de la Peninsula Iberique.* Ph.D. thesis, Univ. Pierre et Marie Curie, Paris.

MALOD, J.A., & MAUFFRET, A. 1990. Iberian plate motions during the Mesozoic. *Tectonophysics*, **184**, 261–278.

MALOD, J.A., & MOUGENOT, D. 1979. L'histoire géologique néogène du golfe du Cadiz. *Bulletin De La Societe Geologique De France*, **21**(5), 603–611.

MANDEVILLE, C.R.M. 1993. *A structural study of an arcuate thrust belt, Prebetic Zone, Southern Spain.* Ph.D. thesis, University of Oxford.

MARCH, D.W., & BAILEY, A.D. 1983. A review of the two-dimensional transform and its use in seismic processing. *First Break*, **1**(1), 9–21.

MAROVA, N.A., & YEVSYUKOV, Y.U.D. 1988. The Geomorphology of the Ampere Submarine Seamount (in the Atlantic Ocean). *Oceanology*, **27**(4), 452–455.

MASLIN, M., MIKKELSEN, N., VILELA, C., & HAQ, B. 1998. Sea-level- and gas-hydrate-controlled catastrophic sediment failures of the Amazon Fan. *Geology*, **26**(12), 1107–1110.

MASSON, D.G., KENYON, N.H., & WEAVER, P.P.E. 1996. Slides, debris flows and turbidity currents. *Chap. 9, pages 136–151 of:* SUMMERHAYES, C.P., & THORPE, S.A. (eds), *Oceanography, an illustrated guide.* Manson Publishing Ltd, London.

MATVEYENKOV, V.V., POYARKOV, S.G., DMITRIYENKO, O.V., AL'MUKHAMEDOV, A.I., GAMSAKHURDIA, G.R., & KUZNETSOV, O.L. 1994. Geological Particularities of the Seamount Structure in the Azoro-Gibraltar Zone. *Oceanology*, **33**(5), 664–673.

MAUFFRET, A., MOUGENOT, D., MILES, P.R., & MALOD, J.A. 1989. Cenozoic deformation and Mesozoic abandoned spreading center in the Tagus Abyssal plain (West of Portugal): results of a multichannel seismic survey. *Canadian Journal of Earth Science*, **26**, 1101–1123.

MAUFFRET, A., MALDONADO, A., & CAMPILLO, A. C. 1992. Tectonic framework of the eastern Alboran and western Algerian basins, western Mediterranean. *Geo-Marine Letters*, **12**, 104–110.

MCIVER, R.D. 1977. Hydrates of natural gas – important agent in geological processes. *Geological Society of America Bulletin*, **9**, 1089–1090.

MCIVER, R.D. 1982. Role of naturally–occurring gas hydrates in sediment transport. *American Association of Petroleum Geologists Bulletin*, **66**, 789–792.

MCKENZIE, D. 1972. Active Tectonics of the Mediterranean Region. *Geophysical Journal of the Royal Astronomical Society*, **30**, 109–185.

MCKENZIE, D.P. 1978. Some remarks on the development of sedimentary basins. *Earth and Planetary Science Letters*, **40**, 25–32.

MEDIALDEA, T., SURINACH, E., VEGAS, R., BANDA, E., & ANSORGE, J. 1986. Crustal structure under the western end of the Betic- cordillera (Spain). *Annales Geophysicae Series B-Terrestrial Planetary Phys.*, **4**, 457–464.

MEGHRAOUI, M., MOREL, J.C., ANDRIEUX, J., & DAHMANI, M. 1996. Tectonique Plio-Quaternaire de la chaîne tello-rifaine de la mer d'Alboran. Une zone complexe de convergence continent-continent. *Bulletin De La Societe Geologique De France*, **167**, 141–157.

MEISSNER, R., MATTHEWS, D., & WEVER, T. 1986. The Moho in and around Great-Britain. *Annales Geophysicae Series B-Terrestrial Planetary Phys.*, **4**, 659–663.

MELENDEZ-HEVIA, F., & ALVAREZ DE BUERGO, E. 1996. Oil and gas resources of the Tertiary Basins of Spain. *In:* Friend & Dabrio [1996].

MEZCUA, J., & RUEDA, J. 1997. Seismological evidence for a delamination process in the lithosphere under the Alboran Sea. *Geophysical Journal International*, **129**, F1–F8.

MICHARD, A. 1976. *Elements de Géologie Marocaine.* Notes et Mém., vol. 252. Serv. Géol. Maroc. 408 pp.

MIENERT, J., & BRYN, P. 1997. Gas hydrate drilling conducted on the European margin. *E.O.S. Transactions of the American Geophysical Union*, **78**(49), 567,571.

MIENERT, J., & POSEWANG, J. 1999. Evidence of shallow- and deep-water gas hydrate destabilizations in North Atlantic polar continental margin sediments. *Geo-Marine Letters*, **19**, 143–149.

MILLER, J.J., LEE, M.W., & VON HUENE, R. 1991. An analysis of a seismic reflection from the base of a gas hydrate zone, offshore Peru. *American Association of Petroleum Geologists Bulletin*, **75**, 910–924.

MINSHULL, T.A., SINGH, S.C., & WESTBROOK, G.K. 1994. Seismic velocity structure at a gas hydrate reflector, offshore western Columbia, from full waveform inversion. *Journal of Geophysical Research*, **99**(B3), 4715–4734.

MINSTER, J.B., & JORDAN, T.H. 1978. Present-day plate motions. *Journal of Geophysical Research*, **83**, 5331–5354.

MITCHUM, R.M., VAIL, P.R., & SANGREE, J.B. 1977. Stratigraphic interpretation of seismic reflection patterns in depositional sequences. *Pages 117–133 of:* PAYTON, C.E. (ed), *Seismic Stratigraphy - applications to hydrocarbon exploration.* Tulsa, Oklahoma, U.S.A.: The American Association of Petroleum Geologists.

MOORE, J. G., CLAGUE, D. A., HOLCOMB, R. T., LIPMAN, P. W., NORMARK, W. R., & TORRESAN, M. E. 1989. Prodigious submarine landslides on the Hawaiian Ridge. *J. Geophys. Res.*, 17465–17484.

MOORE, R.B. 1990. Volcanic geology and eruption frequency, Sao Miguel, Azores. *Bull. Volcanology*, **52**, 602–614.

MORLEY, C.K. 1992. Notes on Neogene basin history of the western Alboran Sea and its implications for the tectonic evolution of the Rif- Betic orogenic belt. *Journal of African Earth Sciences*, **14**, 57–65.

MORLEY, C.K. 1993. Discussion of origins of hinterland basins to the Rif-Betic Cordillera and Carpathians. *Tectonophysics*, **226**, 359–376.

MUELLER, S., PRODEHL, C., MENDES, A.S., & MOREIRA, V.S. 1973. Crustal structure in the Southwestern Part of the Iberian Peninsula. *Tectonophysics*, **20**, 307–318.

MUELLER, S.T., & KAHLE, H.G. 1993. Crust-mantle evolution, structure and dynamics of the Mediterranean-Alpine region. *Pages 249–298 of:* SMITH, D.E., & TURCOTTE, D.L. (eds), *Contributions of space geodesy to geodynamics: crustal dynamics.* A.G.U.

MULDER, C.I. 1973. Tectonic framework and distribution of Miocene chemical sediments with emphasis on the eastern Mediterranean. *Pages 44–59 of:* DROOGER, C.W. (ed), *Messinian events in the Mediterranean.* Amsterdam: Elsevier.

MUZCUA, J., RUEDA, J., & SOLARES, J.M. MARTINEZ. 1991. Seismicity of the Ibero-Maghrebian Region. *Pages 17–28 of:* MEZCUA, J., & UDIAS., A. (eds), *Seismicity, Seismotectonics and Seismic Risk of the Ibero-Maghrebian Region MONOGRAFIA 8.* 28003 Madrid Spain: Instituto Geografico Nacional.

NAFE, J.E., & DRAKE, C.L. 1957. Variation with depth in shallow and deep water marine sediments of porosity, density and the velocities of compressional and shear waves. *Geophysics*, **22**(3), 523–552.

NAT STUDY GROUP. 1985. North Atlantic Transect: A Wide-Aperture, Two-Ship Multichannel Seismic Investigation of the Oceanic Crust. *Journal of Geophysical Research*, **90**(B12), 10321–10341.

NELSON, C. H., BARAZA, J., & MALDONADO, A. 1993. Mediterranean undercurrent sandy contourites, Gulf of Cadiz, Spain. *Sedimentary Geology*, **82**, 103–131.

NELSON, C.H., BARAZA, J., MALDONADO, A., RODERO, J., ESCUTIA, C., & BARBER, J.H. 1999. Influence of the Atlantic inflow and Mediterranean outflow currents on late Quaternary sedimentary facies of the Gulf of Cadiz continental margin. *Marine Geology*, **155**, 99–129.

OKUDA, Y. 1998. Introduction to exploration research on gas hydrates in Japan. *Bulletin of the Geological Survey of Japan.*

OLIVET, J.L. 1996. Kinematics of the Iberian plate. *Bulletin des centres des recherches exploration-production Elf Aquitaine*, **20**(1), 131–195.

OLIVET, J.L., BONNIN, J., BEUZART, P., & AUZENDE, J.M. 1984. Cinematique de l'Atlantique nord et central. *Rapports scientifiques et techniques de Centre Nationale pour l'Exploitation des Océans, Brest.*, **54**, 1–108.

PARASNIS, D.S. 1986. *Principles of Applied Geophysics.* Fourth edn. Chapman & Hall.

PAUTOT, G., AUZENDE, J., & LEPICHON, X. 1970. Continuous deep sea salt layer along North Atlantic margins related to early phase of rifting. *Nature*, **227**(July), 351.

PAYO, G. 1972. Crust-Mantle Velocities in the Iberian Peninsula and Tectonic Implications of the Seismicity in this Area. *Geophysical Journal of the Royal Astronomical Society*, **30**, 85–99.

PECHER, I.A., HOLBROOK, W.S., STEPHEN, R.A., HOSKINS, H., LIZARRALDE, D., HUTCHINSON, D.R., & WOOD, W.T. 1997. Offset-vertical seismic profiling for marine gas hydrate exploration; is it a suitable technique? First results from ODP Leg 164. *Pages 193–200 of: 29th Offshore Technology Conference, Dallas.*

PEGLER, G. 1995. *Studies in seismotectonics.* Ph.D. thesis, University of Oxford.

PEGLER, G., & DAS, S. 1996. The 1987-1992 Gulf of Alaska earthquakes. *Tectonophysics*, **257**, 111–136.

PEGLER, G., & DAS, S. 1998. An enhanced image of the Pamir Hindu Kush seismic zone from relocated earthquake hypocentres. *Geophysical Journal International*, **134**, 573–595.

PEGLER, G., DAS, S., & WOODHOUSE, J. H. 1995. A seismological study of the eastern New Guinea and the western Solomon Sea regions and its tectonic implications. *Geophysical Journal International*, **122**, 961–981.

PEIRCE, C., & BARTON, P.J. 1991. Structure of the Madeira-Tore Rise, eastern North Atlantic. Results of DOBS wide angle and normal incidence seismic experiment in the Josephine Seamount Region. *Geophysical Journal International*, **106**, 357–378.

PEPER, T., & CLOETINGH, S. 1992. Lithosphere dynamics and tectono-stratigraphic evolution of the Mesozoic Betic rifted margin (southeastern Spain). *Tectonophysics*, **203**, 345–361. Special Issue on Geology and Geophysics of the Valencia Trough, Western Mediterranean.

PERCONIG, E. 1962. Sur la constitution geologique de l'Andalousie Occidentale en particulier du bassin du Guadalquivir (Espagne meridionale). *Pages 231–256 of: Livre a la memoire de Prof. Paul Fallot.* Soc. Geol. Fr.

PICKUP, S.L.B., WHITMARSH, R.B., FOWLER, C.M.R., & RESTON, T. J. 1996. Insight into the nature of the ocean-continent transition off west Iberia from a deep multichannel seismic reflection profile. *Geology*, **24**, 1079 (6 pages).

PILKEY, O.H. 1987. Sedimentology of basin plains. *Pages 1–12 of:* WEAVER, P.P.E., & THOMPSON, J. (eds), *Geology and Geochemistry of Abyssal plains.* Geological Society Special Publication, vol. 31. Geological Society of London. London, United Kingdom.

PINHEIRO, L.M. 1994. *The crustal structure under the Tagus Abyssal Plain and the Ocean-Continent Transition off western Iberia.* Ph.D. thesis, Imperial College, University of London.

PINHEIRO, L.M., WHITMARSH, R.B., & MILES, P.R. 1992. The ocean-continent boundary off the western continental margin of Iberia; II, Crustal structure in the Tagus abyssal plain. *Geophysical Journal International*, **109**(1), 106–124.

PITMAN, W.C. 1978. The relationship between eustasy and stratigraphic sequences at passive margins. *Geological Society of America Bulletin*, **89**, 1389–1403.

PLATT, J., ALLERTON, S., KIRKER, A., & PLATZMAN, E. 1995. Origin of the western subBetic arc (south Spain) - paleomagnetic and structural evidence. *Journal of Structural Geology*, **17**, 765–775.

PLATT, J.P., & VISSERS, R.L.M. 1989. Extensional collapse of thickened continental lithosphere - a working hypothesis for the Alboran Sea and Gibraltar arc. *Geology*, **17**, 540–543.

PLATT, J.P., SOTO, J.I., & COMAS, M.C. 1996. Decompression and high-temperature-low-pressure metamorphism in the exhumed floor of an extensional basin, Alboran-sea, western Mediterranean. *Geology*, **24**, 447–450.

PLATZMAN, E.S. 1992. Paleomagnetic rotations and the kinetmatics of the Gibraltar arc. *Geology*, **20**, 311–314.

PLATZMAN, E.S., PLATT, J.P., & OLIVIER, P. 1993. Paleomagnetic rotations and fault kinematics in the Rif arc of Morocco. *Journal of the Geological Society of London*, **150**, 707–718.

POLLACK, H.N., HURTER, S.J., & JOHNSON, J.R. 1993. Heat flow from the earth's interior: Analysis of the global data set. *Reviews of Geophysics*, **31**, 267–280.

POLYAK, B.G., FERNANDEZ, M., KHUTORSKOY, M.D., SOTO, J.I., BASOV, I.A., COMAS, M.C., KHAIN, V.Y., ALONSO, B., AGAPOVA, G.V., MAZUROVA, I.S., NEGREDO, A., TOCHITSKY, V.O., DELALINDE, J., BOGDANOV, N.A., & BANDA, E. 1996. Heat flow in the Alboran sea, western Mediterranean. *Tectonophysics*, **263**, 191–218.

PRATSCH, J.C. 1996. Oil and gas potential of the pre-Rif foreland basin, onshore northern Morocco. *Journal of Petroleum Geology*, **19**, 199–214.

PRICE, J.F., BARINGER, M.O., LUECK, R.G., JOHNSON, G.C., AMBAR, I., PARRILLA, G., CANTOS, A., KENNELLY, M.A., & SANFORD, T.B. 1993. Mediterranean outflow mixing and dynamics. *Science*, **259**, 1277–1282.

PURDY, G.M. 1974. *A geophysical study of the eastern end of the Azores-Gibralter fracture zone.* Ph.D. thesis, University of Cambridge, Darwin College, Cambridge, England.

PURDY, G.M. 1975. The eastern end of the Azores-Gibraltar plate boundary. *Geophysical Journal of the Royal Astronomical Society*, **43**, 973–1000.

RAHMSTORF, S. 1998. Influence of Mediterranean Outflow on climate. *E.O.S. Transactions of the American Geophysical Union*, **79**(24), 281–282.

RAIGA-CLEMENCEAU, J., MARTIN, J.P., & NICOLETIS, S. 1988. The concept of acoustic formation factor for more accurate porosity determination from sonic transit time data. *The Log Analyst*, **29**(1), 54–60.

RAPP, R.H., WANG, Y.M., & PAVLIS, N.K. 1991. *The Ohio State 1991 geopotential and sea surface topography harmonic coefficient models.* Tech. rept. 410. Department of Geodesy Science and Surveying, Ohio State University, Columbus.

RAYMER, L.L, HUNT, E.R., & GARDNER, J.S. 1980. An improved sonic transit time-to-porosity transform. *Pages 1–13 of: Transactions of the SPWLA Twenty-First Annual Logging Symposium.* Society of Professional Well Log Analysts.

RAYMOND, L.A. 1984. Classification of mélanges. *Geological Society of America Special Paper*, **198**, 7–20.

REILLY, W.I., FREDRICH, G., HEIN, G.W., LANDAU, H., ALMAZÁN, J.L., & CATURLA, J.L. 1992. Geodetic determination of crustal deformation across the Strait of Gibraltar. *Geophysical Journal International*, **111**, 391–398.

REY, J. 1998. Extensional Jurassic tectonism of an eastern Subbetic section (southern Spain). *Geological Magazine*, **135**(5), 685–697.

REY, P.A. 1954. Estudio morfo-tectonico de la falla del Guadalquivir. *Mem. Inst. Geog., Spain*, **24**(1), 1–48. Monograph.

RIAZA, C., & MARTINEZ DEL OLMO, W. 1996. Depositional model of the Guadalquivir–Gulf of Cadiz Tertiary basin. *In:* Friend & Dabrio [1996].

RIMI, A., CHALOUAN, A., & BAHI, L. 1998. Heat flow in the westernmost part of the Alpine Mediterranean system (the Rif, Morroco). *Tectonophysics*, **285**, 135–146.

ROBERTS, D.G. 1970. The Rif-Betic orogen in the Gulf of Cadiz. *Marine Geology*, **9**, 31–37.

ROESER, H.A. 1982. Magnetic Anomalies in the Magnetic Quiet Zone off Morocco. *Chap. 4, pages 60–68 of:* VON RAD, U., HINZ, K., SARNTHEIN, M., & SEIBOLD, E. (eds), *Geology of the northwest African continental margin.* Berlin, Heidelburg, New York: Springer-Verlag.

ROEST, W.R., & SRIVASTAVA, S.P. 1991. Kinematics of the plate boundaries between Eurasia, Iberia, and Africa in the North Atlantic from the Late Cretaceous to the present. *Geology*, **19**(June), 613–616.

ROEST, W.R., DANOBEITIA, J.J., VERHOEF, J., & COLLETTE, B.J. 1992. Magnetic Anomalies in the Canary Basin and the Mesozoic Evolution of the Central North Atlantic. *Marine Geophysical Researches*, **14**, 1–24.

ROSENDAHL, B.R., MEYERS, J., GROSCHEL, H., & SCOTT, D. 1992. Nature of the transition from continental to oceanic crust and the meaning of reflection Moho. *Geology*, **20**, 721–724.

ROTHÉ, J.P. 1954. La zone sismique mediane Indo-Atlantique. *Proceedings of the Royal Society of London, Series A: Mathematical and Physical Sciences.*, **222**.

ROTHWELL, R. G., THOMSON, J., & KÄHLER, G. 1998. Low sea–level emplacement of a very large Late Pleistocene "megaturbidite" in the western Mediterranean Sea. *Nature*, **392**, 377–380.

ROYDEN, L., & KEEN, C.E. 1980. Rifting processes and thermal evolution of the continental margin of eastern Canada determined from subsidence curves. *Earth and Planetary Science Letters*, **51**, 343–361.

ROYDEN, L.H. 1993a. Evolution of retreating subduction boundaries formed during continental collision. *Tectonics*, **12**(3), 629–638.

ROYDEN, L.H. 1993b. The tectonic expression of slab pull at continental convergent boundaries. *Tectonics*, **12**, 303–325.

RYAN, W.B.F., HSU, K.J., CITA, M.B., LORT, J., MAYNC, W., PAUTOT, G., STRADNER, H., & WEZEL, F.C. 1973. Gorringe Bank - Site 120. *Pages 19–41 of: Initial Reports of the Deep Sea Drilling Project, Volume 13.* Washington: U.S. Government Printing Office.

RYU, J.V. 1982. Decomposition (DECOM) approach applied to wave field analysis with seismic reflection records. *Geophysics*, **47**, 869–883.

SANDWELL, D.T., & SMITH, W.H.F. 1997. Marine gravity anomaly from Geosat and ERS 1 satellite altimetry. *Journal of Geophysical Research*, **102**, 10039–10054.

SARTORI, R., SCHETORELLI, L., ZITELLINI, N., PEIS, D., & LODOLO, E. 1994. Eastern segment of the Azores-Gibraltar line (central-eastern Atlantic): An oceanic plate boundary with diffuse compressional deformation. *Geology*, **22**(June), 555–558.

SAWYER, D. S. 1985. Total tectonic subsidence: A parameter for distingushing crust type at the U.S. Atlantic continental margin. *J. Geophys. Res.*, **90**, 7751–7769.

SCHEIRER, D.S., & HOBBS, R.W. 1990. Seismic attenuation in the continental crust SW of England. *Geophysical Journal International*, **103**, 533–540.

SCHLITZER, R. 1999. *Ocean Data Viewer*. http://www.awi-bremerhaven.de/GEO/ODV.

SCHÖFFEL, H-J., & DAS, S. 1999. Fine details of the Wadati-Benioff zone under Indonesia and its geodynamic implications. *Journal of Geophysical Research*, **104**, 13101–13114.

SCLATER, J.G., JAUPART, C., & GALSON, D. 1980. The heat flow through oceanic and continental crust and the heat loss of the Earth. *Reviews of Geophysics and Space Physics*, **18**, 269–311.

SEARLE, R. 1980. Tectonic pattern of the Azores spreading centre and triple junction. *Earth and Planetary Science Letters*, **51**, 415–434.

SEARLE, R.C. 1979. Side-scan sonar studies of North Atlantic fracture zones. *Journal of the Geological Society of London*, **136**, 283–292.

SEBER, D., BARAZANGI, M., IBENBRAHIM, A., & DEMNATI, A. 1996. Geophysical evidence for lithospheric delamination beneath the Alboran-sea and Rif-Betic mountains. *Nature*, **379**, 785–790.

SELLEY, R.C. 1978. Porosity gradients in the North Sea oil-bearing sandstones. *Journal of the Geological Society of London*, **135**, 119–132.

SETTO, I., & MEISSNER, R. 1987. Support from gravity modeling for seismic interpretation. *Annales Geophysicae Series B-Terrestrial Planetary Phys.*, **5**, 389–393.

SHANMUGAM, G., BLOCH, R.B., MITCHELL, S.M., BEAMISH, G.W.J., HODGKINSON, R.J., DAMUTH, J.E., STRAUME, T., SYVERTSEN, S.E., & SHIELDS, K.E. 1995. Basin-floor fans in the North Sea – sequence stratigraphic models vs sedimentary facies. *American Association of Petroleum Geologists Bulletin*, **79**(4), 477–512.

SHAPIRO, G. ., & MESCHANOV, S.L. 1996. Spreading pattern and mesoscale structure of Mediterranean outflow in the Iberian basin estimated from historical data. *Journal of Marine Systems*, **7**, 337–348.

SHERIFF, R.E., & GELDART, L.P. 1983. *Data-processing and interpretation.* Exploration Seismology, vol. 2. Cambridge University Press.

SHIPLEY, T.H., HOUSTON, M.K., BUFFLER, R.T., SHAUB, F.J., MCMILLEN, K.J., LADD, J.W., & WORZEL, J.L. 1979. Seismic evidences for widespread possible gas hydrate horizons on continental slopes and rises. *American Association of Petroleum Geologists Bulletin*, **63**, 2204–2213.

SIMKIN, T., & SIEBERT, L. 1994. *Volcanoes of the World.* Geoscience Press,Tucson, Arizona. 349pp.

SLOAN, E.D. 1990. *Clathrate hydrates of natural gas.* Marcel Dekker, New York.

SMITH, W.H.F., & WESSEL, P. 1990. Gridding with continuous curvature splines in tension. *Geophysics*, **55**, 293–305.

SOMOZA, L., MAESTRO, A., & LOWRIE, A. 1999. Proposed vast hydrocarbon play along the Gulf of Cadiz continental margin (abstract). *In: Proceedings of AAPG and SEPM Annual Meeting April 11-14, 1999.* American Association of Petroleum Geologist (AAPG) and SEPM (Society for Sedimentary Geology).

SPECTOR, A., & GRANT, F.S. 1970. Statistical models for interpreting aeromagnetic data. *Geophysics*, **35**, 293–302.

SRIVASTAVA, S.P., ROEST, W.R., KOVACS, L.C., OAKEY, G., LEVESQUE, S., VERHOEF, J., & MACNAB, R. 1990. Motion of Iberia since the Late Jurassic: Results from detailed aeromagnetic measurements in the Newfoundland Basin. *Tectonophysics*, **184**, 229–260.

STANLEY, D.J., & WEZEL, F.C. (eds). 1985. *Geological Evolution of the Mediterranean Basin.* Springer-Verlag. Raimondo Selli Commemorative Volume.

STECKLER, M.S., & WATTS, A.B. 1978. Subsidence of the Atlantic-type continental margin off New York. *Earth and Planetary Science Letters*, **41**, 1–13.

STEWART, J. 1998. *Gravity Anomalies and Lithospheric Flexure: Implications for the Thermal and Mechanical Evolution of the Continental Lithosphere.* Ph.D. thesis, Univ. of Oxford, Oxford, England.

STEWART, J., & WATTS, A.B. 1997. Spatial variations of flexural rigidity at mountain ranges. *J. Geophys. Res.*, **102**, 5327–5352.

STEWART, J., WATTS, A.B., & BAGGULEY, J.G. Submitted. 3-D subsidence analsyis and gravity modelling of the continental margin offshore Namibia. *Submitted to Geophysical Journal International.*

STOCKMAL, G. S., BEAUMONT, C., & BOUTILIER, R. 1986. Geodynamic models of convergent margin tectonics: Transition from rifted margin to overthrust belt and consequences for foreland basin development. *AAPG Bull.*, **70**, 181–190.

STOLT, R.H. 1978. Migration by Fourier Transform. *Geophysics*, **43**, 23–48.

STOW, D.A.V., READING, H.G., & COLLINSON, J.D. 1996. Deep seas. *Chap. 10, pages 395–453 of:* READING, H. G. (ed), *Sedimentary Environments and Facies*, 3 edn. Oxford, UK: Blackwell Science.

STROMBERG, S.G., & BLUCK, B. 1998. Turbidite facies, fluid-escape structures and mechanisms of emplacement of the Oligo-Miocene Aljibe flysch, Gibraltar arc, Betics, southern Spain. *Sedimentary Geology*, **115**, 267–288.

SUBRAHMANYAM, C., REDDI, S.I., THAKUR, N.K., GANGADHARA-RAO, T., & SAIN, K. 1998. Gas-hydrates: a synoptic view. *Journal of the Geological Society of India*, **52**(5), 497–512.

TADILI, B., RAMDANI, M., BENSARI, D., CHAPOCHNIKOV, K., & BELLOT, A. 1986. The crustal structure in the northern part of morocco. *Annales Geophysicae Series B-Terrestrial Planetary Phys.*, **4**, 99–104.

TALWANI, M., WORZEL, J.L., & LANDISMAN, M. 1959. Rapid gravity computations for two-dimensional bodies with application to the Mendocino submarine fracture zone. *Journal of Geophysical Research*, **64**, 49–59.

THORNE, J., & WATTS, A.B. 1989. A quantitative analysis of North Sea subsidence. *American Association of Petroleum Geologists Bulletin*, **73**, 88–116.

TORELLI, L., SARTORI, R., & ZITELLINI, N. 1997. The giant chaotic body in the Atlantic Ocean off Gibraltar: new results from a deep seismic reflection survey. *Marine and Petroleum Geology*, **14**(2), 125–138.

TORNE, M., & BANDA, E. 1992. Crustal thinning from the Betic cordillera to the Alboran sea. *Geo-Marine Letters*, **12**, 76–81.

TORNE, M., COLLIER, J., PERRY, M., & GAMEIRA, J. 1993. *Iberian Atlantic Margins Project: Marine Data Acquisition Report.* Tech. rept. Iberian Atlantic Margins Group. Acquisition and Onboard Processing Report.

TORRESROLDAN, R. L., POLI, G., & PECCERILLO, A. 1986. An early Miocene arc-tholeiitic magmatic dike event from the Alboran Sea - evidence for precollisional subduction and back-arc crustal extension in the westernmost Mediterranean. *Geologische Rundschau*, **75**, 219–234.

TORTELLA, D., TORNE, M., & PÉREZ-ESTAÚN, A. 1997. Geodynamic evolution of the eastern segment of the Azores-Gibraltar Zone: The Gorringe Bank and the Gulf of Cadiz Region. *Marine Geophysical Researches*, **19**, 211–230.

TUBIA, J.M., & CUEVAS, J. 1987. Structures and kinematics related to the Ronda peridotites emplacement. *Geodinamica Acta*, **1**(1), 59–69.

TURCOTTE, D. L., & SCHUBERT, G. 1982. *Geodynamics: Applications of Continuum Physics to Geological Problems.* John Wiley and Sons.

UDIAS, A. 1985. Seismicity of the Mediterranean. *In:* Stanley & Wezel [1985]. Raimondo Selli Commemorative Volume.

UDIAS, A., & BUFORN, E. 1991. Regional Stresses Along the Eurasian-Africa Plate Boundary Derived from Focal Mechanisms of Large Earthquakes. *Pure and Applied Geophysics*, **136**(4), 433–448.

UDIAS, A., ARROYO, A.L., & MEZCUA, J. 1976. Seismotectonic of the Azores-Alboran Region. *Tectonophysics*, **31**, 259–289.

VACQUIER, V. 1998. A theory of the origin of the Earth's internal heat. *Tectonophysics*, **291**, 1–7.

VAIL, P.R., MITCHUM, R.M., & THOMPSON, S. 1979. Seismic stratigraphy and global changes in sea level, Part 4: Global cycles of relative change in sea level. *Pages 145–163 of:* PAYTON, C. E. (ed), *Seismic Stratigraphy - Applications to Hydrocarbon Exploration, AAPG Memoir 26.* Tulsa, Oaklahoma: American Association of Petroleum Geologists.

VEEKEN, P.C.H., & SCHWANDER, M.M. 1988. A regional line across the Gulf of Cadiz,offshore southwestern Spain. *Pages 185–187 of:* BALLY, A.W. (ed), *Atlas of Seismic Stratigraphy.* AAPG Studies in Geology, vol. 3. Tulsa: American Association of Petroleum Geologists.

VEERAYYA, M., KARISIDDAIAH, S.M., VORA, K.H., WAGLE, B.G., & ALMEIDA, F. 1998. Detection of gas-charged sediments and gas hydrate horizons along the western continental margin of India. *Pages 239–253 of: Gas hydrates; relevance to world margin stability and climate change.* Geological Society Special Publications., no. 137. Geological Society of London. London, United Kingdom.

VEGAS, R. 1991. Present-Day Geodynamics of the Ibero-Maghrebian Region. *Pages 193–203 of:* MEZCUA, J., & UDIAS, A. (eds), *Seismicity, Seismotectonics and Seismic Risk of the Ibero-Maghrebian Region.* 28003 Madrid Spain: Instituto Geografico Nacional.

VERA, J.A., MOLINA, J.M., MONTERO, P., & BEA, F. 1997. Jurassic guyots on the Southern Iberian Continental Margin: a model of isolated carbonate platforms on volcanic submarine edifices. *Terra Nova*, **9**, 163–166.

VERHOEF, J., COLLETTE, B.J., NOBEITIA, J. DA ROESER, H.A., & ROEST, W.R. 1991. Magnetic anomalies off West Africa (20–38° N). *Marine Geophysical Research*, **13**, 81–103.

VERZHBITSKY, E.V., & ZOLOTAREV, V.G. 1989. Heat Flow and the Eurasian-Africa Plate Boundary in the Eastern Part of the Azores-Gibraltar Fracture Zone. *Journal of Geodynamics*, **11**, 267–273.

VIDOTTI, R.M., EBINGER, C.J., & FAIRHEAD, J.D. 1998. Gravity Signature of the western Paraná Basin. *Earth and Planetary Science Letters*, **159**, 117–132.

VISSERS, R.L.M., PLATT, J.P., & VAN DER WAL, D. 1995. Late orogenic extension of the Betic Cordillera and the Alboran Domain: a lithospheric view. *Tectonics*, **14**, 786–803.

WARNER, M.R. 1987. Migration: why it doesn't work for deep continental data? *Geophysical Journal of the Royal Astronomical Society*, **89**, 21–25.

WARNER, M.R. 1990. Absolute reflection coefficients from deep seismic reflections. *Tectonophysics*, **173**, 15–23.

WATKINS, J.S., & HOPPE, K.W. 1979. Seismic reflection reconnaissance of the Atlantic margin of Morocco. *Pages 205–217 of:* TALWANI, M., HAY, W., & RYAN, W.B.F. (eds), *Deep drilling results in the Atlantic Ocean: Continental margins and palaeoenvironment.* Maurice Ewing Series, vol. 3. American Geophysical Union.

WATTS, A.B. 1983. The strength of the Earth's crust. *Marine Technology Society Journal*, **17**(1).

WATTS, A.B. 1988. Gravity anomalies, crustal structure and flexure of the lithosphere at the Baltimore Canyon Trough. *Earth and Planetary Science Letters*, **89**, 221–238.

WATTS, A.B. 1992. The effective elastic thickness of the lithosphere and the evolution of foreland basins. *Basin Research*, **4**, 169–178.

WATTS, A.B. 1994. Crustal structure, gravity anomalies and flexure of the lithosphere in the Canary Islands. *Geophys. J. Int.*, **119**(2), 648–666.

WATTS, A.B., & MARR, C. 1995. Gravity anomalies and the thermal and mechanical structure of rifted continental margins. *Pages 65–94 of:* E.BANDA, M.TORNÉ, & TALWANI, M. (eds), *Rifted Ocean-Continent Boundaries.* NATO ASI Series. Netherlands: Kluwer Academic Publishers.

WATTS, A.B., & RYAN, W.B.F. 1976. Flexure of the lithosphere and continental margin basins. *Tectonophysics*, **36**, 25–44.

WATTS, A.B., & STECKLER, M.S. 1979. Subsidence and eustasy at the continental margin of eastern North America. *Pages 218–234 of: Deep Drilling Results in the Atlantic Ocean: Continental Margins and Palaeoenvironments.* Maurice Ewing Series, vol. 3. American Geophysical Union.

WATTS, A.B., & TEN BRINK, U.S. 1989. Crustal structure, flexure, and subsidence history of the Hawaiian Islands. *Journal of Geophysical Research*, **94**(B8), 10473–10500.

WATTS, A.B., & TORNÉ, M. 1992. Subsidence history, crustal structure and thermal evolution of the Valencia Trough: A young extensional basin in the western Mediterranean. *Journal of Geophysical Research*, **97**, 20021–20041.

WATTS, A.B., KARNER, G.D., & STECKLER, M.S. 1982. Lithospheric flexure and the evolution of sedimentary basins. *Philosophical Transactions of the Royal Society of London*, **305**, 249–281.

WATTS, A.B., TORNÉ, M., BUHL, P., MAUFFRET, A., PASCAL, G., & PINET., B. 1990. Evidence for reflectors in the lower continental crust beforerifting in the valencia trough. *Nature*, **348**(6302), 631–635.

WATTS, A.B., PLATT, J.P., & BUHL, P. 1993. Tectonic evolution of the Alboran Sea basin. *Basin Research*, **5**, 153–177.

WEAVER, P.P.E., & ROTHWELL, R.G. 1987. Sedimentation on the Madeira Abyssal Plain over the last 300,000 years. *Pages 71–86 of:* WEAVER, P. P. E., & THOMPSON, J. (eds), *Geology and Geochemistry of Abyssal plains*, geological society special publication edn., vol. 31. Geological Society of London. London, United Kingdom.

WEIJERMARS, R. 1985a. In search for a relationship between harmonic resolutions of the geoid, convective stress patterns and tectonics in the lithosphere: a possible explanation for the Betic-Rif orocline. *Physics of the Earth and Planetary Interiors*, **37**, 135–148.

WEIJERMARS, R. 1985b. Uplift and subsidence history of the Alboran basin and a profile of the Alboran diapir (W-Mediterranean). *Geologie En Mijnbouw*, **64**, 349–356.

WERNICKE, B. 1981. Low angle normal faults in the Basin and Range Province – nappe tectonics in an extending orogen. *Nature*, **291**, 645–648.

WERNICKE, B. 1985. Uniform-sense normal simple shear of the continental lithosphere. *Canadian Journal of Earth Science*, **22**, 108–125.

WERNICKE, B., & BURCHFIEL, B.C. 1982. Modes of extensional tectonism. *Journal of Structural Geology*, **4**, 105–115.

WESSEL, P., & SMITH, W. H. F. 1995. New version of the Generic Mapping Tools released. *E.O.S. Transactions of the American Geophysical Union*, **76**, 329.

WESSEL, P., & SMITH, W.H.F. 1991. Free software helps map and display data. *E.O.S. Transactions of the American Geophysical Union*, **72**(41), 441–446.

WESSEL, P., & WATTS, A.B. 1988. On the Accuracy of Marine Gravity Measurements. *Journal Geophysical Research*, **93**(B1), 393–413.

WESTAWAY, R. 1990. Present Day Kinematics of the Plate Boundary between Africa and Europe, from the Azores to the Aegean. *Earth and Planetary Science Letters*, **96**, 393–406.

WESTBROOK, G., CARSON, B., MUSGRAVE, R., & SHIPBOARD SCIENTIFIC PARTY. 1993. *Initial Reports of the ODP, Volume 146 Part 1.* Ocean Drilling Program.

WEVER, T., & MEISSNER, R. 1987. About the nature of reflections from the lower continental-crust. *Annales Geophysicae Series B-Terrestrial Planetary Phys.*, **5**, 349–351.

WHITMARSH, R.B., & MILES, P.R. 1995. Models of the development of the West Iberia rifted continental margin at 40'30' deduced from surface and deep tow magnetic anomalies. *J. Geophys. Res.*, **100**(B3), 3789–3806.

WHITMARSH, R.B., AVEDICK, F., & SAUNDERS, M.R. 1986. The seismic structure of thinned continental crust in the northern Bay of Biscay. *Geophysical Journal of the Royal Astronomical Society*, **86**, 589–602.

WHITMARSH, R.B., MILES, P.R., & MAUFFRET, A. 1990. The ocean-continent boundary off the western continental margin of Iberia-I. Crustal structure at 40° 30min N. *Geophysical Journal International*, **103**, 509–531.

WHITMARSH, R.B., PIHEIRO, L.M., MILES, P.R., RECQ, M., & SIBUET, J.C. 1993. Thin Crust at the Western Iberia Ocean-Continent Transition and ophiolites. *Tectonics*, **12**(5), 1230–1239.

WIDESS, M.B. 1973. How thin is a thin bed? *Geophysics*, **38**(6), 1176–1180.

WILLET, A. 1996. *Geophysical Investigations of the Alboran Sea Basin, Western Mediterranean.* Ph.D. thesis, University of Oxford.

WOODHOUSE, J.H., & DZIEWONSKI, A.M. 1984. Mapping the upper mantle: three dimensional modelling of Earth structure by inversion of seismic waveforms. *Journal of Geophysical Research*, **89**, 5953–5986.

WORKING GROUP FOR DEEP SEISMIC SOUNDING IN SPAIN 1974-1975. 1977. Deep Seismic Soundings in southern Spain. *Pure and Applied Geophysics*, **115**, 721–735.

WYLLIE, M.R.J., GREGORY, A.R., & GARDNER, L.W. 1956. Elastic Wave Velocities in heterogeneous and porous media. *Geophysics*, **21**, 41–70.

WYLLIE, M.R.J., GREGORY, A.R., & GARDNER, L.W. 1958. An experimental investigation of the factors affecting elastic wave velocities in porous media. *Geophysics*, **23**, 459–493.

YILMAZ, O. 1987. *Seismic Data Processing.* Investigations in Geophysics, vol. 2. PO Box 702740/ Tulsa, OK 74170-2740: Society of Exploration Geophysicists.

YUAN, T., SPENCE, G.D., HYNDMAN, R.D., MINSHULL, T.A., & SINGH, S.C. 1999. Seismic velocity studies of a gas hydrate bottom-simulating reflector on the northern Cascadia continental margin: amplitude modeling and full waveform inversion. *Journal of Geophysical Research - Solid Earth*, **104**, 1179–1191.

ZAHN, R., COMAS, M.C., & KLAUS, A. 1999. *Proceedings of the ODP, Scientific Results, 161.* College Station, TX (Ocean Drilling Program).

ZECK, H.P. 1996. Betic-Rif orogeny - subduction of Mesozoic Tethys lithosphere under eastward drifting Iberia, slab detachment shortly before 22ma, and subsequent uplift and extensional tectonics. *Tectonophysics*, **254**, 1–16.

ZECK, H.P. 1997. Mantle peridotites outlining the Gibraltar arc - centrifugal extensional allochthons derived from the earlier Alpine, westward subducted nappe pile. *Tectonophysics*, **281**, 195–207.

ZECK, H.P., MONIE, P., VILLA, I.M., & HANSEN, B.T. 1992. Very high rates of cooling and uplift in the Alpine belt of the Betic Cordilleras, southern Spain. *Geology*, **20**(January), 79–82.

ZIEGLER, P.A. 1989. Evolution of the North Atlantic: an overview. *Pages 111–130 of:* TANKARD, A.J., & BALKWILL, H.R. (eds), *Extensional tectonics and stratigraphy of the North Atlantic Margins.* AAPG Memoir 46. Tulsa, OK: American Association of Petroleum Geologists.